Suivi et modélisation du bilan de masse de la calotte Cook aux îles Kerguelen - lien avec le changement climatique

Deborah Verfaillie

UNIVERSITÉ DE GRENOBLE

THÈSE

Pour obtenir le grade de

DOCTEUR DE L'UNIVERSITÉ DE GRENOBLE

Spécialité : **Océan Atmosphère et Hydrologie**

Arrêté ministériel : 7 août 2006

Présentée par

Deborah Verfaillie

Thèse dirigée par **Hubert Gallée** et **Vincent Favier**

préparée au sein du **Laboratoire de Glaciologie et Géophysique de l'Environnement (LGGE, UMR 5183, CNRS - UJF)**
dans l'École Doctorale **Terre Univers Environnement**

Suivi et modélisation du bilan de masse de la calotte Cook aux îles Kerguelen
lien avec le changement climatique

Thèse soutenue publiquement le **24 novembre 2014**,
devant le jury composé de :

Mme Sandrine ANQUETIN
Directrice de Recherche CNRS, LTHE (Présidente)
M. Michiel R. van den BROEKE
Professeur, IMAU Utrecht (Rapporteur)
M. Pierre RIBSTEIN
Professeur, UPMC Paris (Rapporteur)
Mme Masa KAGEYAMA
Directrice de Recherche CNRS, LSCE (Examinatrice)
Mme Françoise VIMEUX
Directrice de Recherche CNRS, LSCE (Examinatrice)
M. Hubert GALLÉE
Directeur de Recherche CNRS, LGGE (Directeur de thèse)
M. Vincent FAVIER
Physicien Adjoint OSUG, LGGE (Co-Directeur de thèse)

Résumé

Les glaciers des régions sub-polaires entre 45 et 60° S ont reculé dramatiquement au cours du dernier siècle. L'archipel des Kerguelen (49° S, 69° E) constitue un site unique dans ces régions où peu d'observations sont disponibles pour comprendre le recul glaciaire. Situés à faible altitude et proches de l'océan, ses glaciers ont montré une sensibilité particulière aux variations atmosphériques et océaniques. Ainsi, depuis les années 60, la calotte Cook (∼400 km^2) a reculé de manière spectaculaire, perdant 20% de sa surface en 40 ans. L'objectif de mon travail de thèse était d'évaluer l'état actuel et futur de la calotte, et de comprendre les causes de ce recul tout en les replaçant dans un contexte global.

Pour ce faire, un réseau météorologique et glaciologique a été mis en place en 2010 sur l'archipel et des campagnes de mesures ont depuis été réalisées annuellement. L'analyse de ces mesures nous permet de confirmer le bilan de masse négatif de la calotte. Parallèlement, l'étude de l'albédo de l'ensemble de la calotte Cook à partir d'images satellites MODIS (MODerate resolution Imaging Spectroradiometer) permet d'évaluer l'évolution de la ligne de neige de la calotte depuis 2000, mettant en évidence une réduction importante de sa zone d'accumulation au cours des dix dernières années. La modélisation du bilan de masse de la calotte Cook à l'aide d'un modèle degré-jour couplé à une routine dynamique révèle par ailleurs que son retrait est principalement dû à une forte diminution des précipitations sur l'archipel depuis les années 60.

Afin de replacer le recul des glaciers aux îles Kerguelen dans un contexte global, les tendances climatiques sur l'ensemble des zones subpolaires sont étudiées, faisant apparaître que la zone sub-Antarctique est actuellement celle où les retraits sont les plus forts à l'échelle du globe. Pour comprendre ces variations, nous analysons un ensemble complet de jeux d'observations de terrain, de satellites et de résultats de modélisation : réanalyses, modèles de l'exercice CMIP5 (Coupled Model Intercomparison Project phase 5), observations de température atmosphérique et océanique, précipitations, etc. Ceux-ci révèlent un réchauffement et un assèchement quasi généralisé de l'ensemble de la zone 40° S - 60° S, lié à un déplacement vers le sud des zones dépressionnaires en réponse aux phases de plus en plus fréquemment positives du mode annulaire austral (Southern Annular Mode, SAM). Le recul récent des glaciers des îles Kerguelen, mais également d'autres zones glaciaires des régions subpolaires de l'hémisphère sud, est donc principalement lié à un déficit d'accumulation causé par le SAM, et amplifié par le réchauffement atmosphérique.

L'évolution future du bilan de masse de la calotte Cook aux îles Kerguelen est évaluée grâce au Modèle Atmosphérique Régional (MAR), forcé à ses frontières par les modèles de l'exercice CMIP5. Des simulations du bilan de masse récent sont d'abord effectuées sur base des réanalyses ERA-Interim et NCEP1, et comparées aux observations in situ. Parallèlement, des simulations d'un an sont réalisées avec le désagrégateur de précipitations SMHiL (Surface Mass balance High resolution downscaLing) en sortie du MAR, à différentes échelles, afin d'évaluer l'impact du changement d'échelle sur la représentation des précipitations. Une évaluation des modèles CMIP5 par rapport à ERA-Interim sur la période récente est ensuite réalisée sur base de certaines variables climatiques-clé. Le modèle le plus proche d'ERA-Interim sur la période récente, et les deux modèles les plus extrêmes sont ensuite utilisés pour forcer le MAR sur le prochain siècle, et les sorties de bilan de masse de surface sont analysées de manière critique.

L'analyse du retrait de la calotte des îles Kerguelen à l'aide de différents outils a permis de mieux comprendre le lien entre glaciers et climat, mettant en évidence le rôle majeur du SAM, mais a également soulevé de nouvelles questions.

Abstract

Glaciers of the southern hemisphere sub-polar regions between 45 and 60° S have declined dramatically over the last century. The islands of Kerguelen archipelago (49° S, 69° E) represent a unique location in regions where few data are available to understand glacier retreat. Situated at low altitudes and close to the ocean, their glaciers have shown particular sensitivity to atmospheric and oceanic variations. Thus, since the 1960s, the Cook Ice Cap ($\sim$400km^2) has retreated spectacularly, losing 20% of its area in 40 years. The aim of my thesis was to assess the present and future state of the ice cap, and to understand the causes of this decline while putting them in a global context.

To do so, a meteorological and glaciological network was set up in 2010 on Kerguelen archipelago and field campaigns have been carried out annually since then. Analysis of these measurements confirms the negative mass balance of Cook Ice Cap. In parallel, the study of the albedo over the whole ice cap from MODIS satellite images (MODerate resolution Imaging Spectroradiometer) gives us access to the evolution of the snow line since 2000, highlighting an important reduction of Cook Ice Cap accumulation area over the last decade. Mass balance modelling of the Cook Ice Cap using a degree-day model coupled to a simple ice motion routine further reveals that its retreat is mainly due to a strong decrease in precipitation over the Kerguelen Islands since the 1960s.

In order to put the decline of the cryosphere on Kerguelen in a global context, climatic trends over the whole sub-polar regions are studied, revealing that the sub-Antarctic area is currently the one where glacier retreat is the strongest. To understand these variations, we analyse a complete set of field and satellite observations and modelling results : reanalyses, models from the CMIP5 (Coupled Model Intercomparison Project phase 5) experiment, atmospheric and oceanic temperature and precipitation observations, etc. The latter show warming and quasi-generalised drying of the whole 40 ° S - 60° S area, linked to the southward shift of storm tracks in response to the more frequent positive phases of the Southern Annual Mode (SAM). Recent glacier retreat on Kerguelen archipelago, and for other glaciers and ice caps located at similar latitudes, is thus mainly due to a deficit of accumulation caused by the SAM, and amplified by atmospheric warming.

The future evolution of Cook Ice Cap mass balance is evaluated using the MAR (Modèle Atmosphérique Régional) model, forced at its boundaries by CMIP5 models. Recent mass balance simulations are first carried out using ERA-Interim and NCEP1 reanalyses, and compared to in situ observations. In parallel, one-year simulations are produced with the precipitation desagregation scheme SMHiL (Surface Mass balance High resolution downscaLing) on MAR outputs, at various scales, in order to evaluate the impact of downscaling on precipitation. An evaluation of CMIP5 models over the recent period against ERA-Interim is then carried out, considering certain key climatic variables. The model closest to ERA-Interim as well as the two most extreme models are then used to force the MAR model over the next century, and surface mass balance outputs are critically analysed.

The analysis of the decline of the Kerguelen ice cap using different tools and techniques brought new insights on the link between glaciers and climate, highlighting the major role of the SAM, but also raised new questions.

Table des matières

Introduction

Les glaciers des régions subpolaires : un recul marqué...

La compréhension des mécanismes du réchauffement climatique actuel constitue l'une des questions scientifiques majeures pour le 21^{e} siècle. L'évolution des surfaces englacées à l'échelle du globe est l'un des indicateurs naturels sélectionnés par le GIEC (Groupe d'experts intergouvernemental sur l'évolution du climat) pour évaluer la variabilité et les tendances climatiques au cours du 20^{e} et 21^{e} siècles (Vaughan et al., 2013). Au sein des surfaces englacées, les glaciers des régions sub-polaires de l'hémisphère sud, situées entre 45 et 60° S, sont particulièrement indiqués pour cette évaluation. En effet, ces régions jouent un rôle-clé dans la circulation atmosphérique globale (e.g. Garreaud et al., 2009; Thompson et al., 2011; Purich et al., 2013) car elles constituent le lieu où se mélangent les masses d'air tropicales et polaires, à l'origine d'une forte activité cyclonique.

En raison d'un transport important d'humidité par les vents d'ouest, la formation de grandes calottes est possible en Patagonie, Nouvelle-Zélande et dans les îles subantarctiques malgré la faible altitude des chaînes de montagnes (e.g. Fitzharris et al., 1997; Takeuchi et al., 1999; Fitzharris et al., 2007; Garreaud et al., 2009). Comme la plupart des glaciers mondiaux, ces glaciers subissent actuellement un retrait important. Tandis que les glaciers de Nouvelle-Zélande ont montré un retrait limité voire même une légère avancée entre 1976 et le début des années 2000, suivi par des reculs marqués depuis lors (Fitzharris et al., 2007), les glaciers de Patagonie et des îles Kerguelen (49° S, 69° E) ont reculé de manière importante tout au long de cette période. Par exemple, les surfaces englacées patagoniennes ont diminué de 0,4% à 36% depuis 1945 (Lopez et al., 2010; Melkonian et al., 2013), avec une accélération de leur retrait après les années 90 (Rignot et al., 2003; Lemke et al., 2007; Willis et al., 2012a,b).

... Mais pourtant peu documenté

En dépit du recul dramatique de la cryosphère observé au sein de l'ensemble de cette gamme latitudinale au cours du 20^{e} siècle, très peu de données permettant de comprendre ce recul sont aujourd'hui disponibles. La réponse des glaciers au réchauffement climatique a été étudiée via la télédétection, principalement sur les champs de glace patagoniens, où la perte de masse a été mesurée précisément à partir d'images satellites (e.g., Rignot et al. (2003); Willis et al. (2012a,b)). Les études se sont également tournées vers la modélisation glaciologique en Patagonie (Schaefer et al., 2013; Lenaerts et al., 2014), mais les modèles utilisés étaient forcés par des données de réanalyses présentant des biais (principalement en ce qui concerne l'humidité) et les processus de vêlage, pourtant importants au niveau de ces champs de glace, étaient négligés. Peu de données de bilan de masse dans les régions sub-polaires sont par ailleurs disponibles. En effet, à l'exception du glacier de Brewster en Nouvelle-Zélande, dont le bilan de masse de

surface est mesuré annuellement depuis 2005 (Anderson et al., 2010), les bilans de masse de ces régions ont rarement été étudiés sur de longues périodes de temps, limitant notre connaissance des processus glaciologiques en jeu. De plus, les programmes de mesure du bilan d'énergie de surface dans ces régions ont été réalisés durant des périodes de temps trop courtes (e.g. Takeuchi et al., 1999; Schneider et al., 2007) et sont trop peu abondants pour représenter clairement les changements climatiques des deux derniers siècles.

L'archipel des Kerguelen : un site d'étude unique du recul glaciaire...

Au sein des zones sub-polaires, l'archipel des Kerguelen (49° S, 69° E), représente un site d'observation unique. En effet, il se situe au sud de l'océan Indien (Figure 1) dans une zone où les observations (glaciologiques, mais aussi atmosphériques et océaniques) sont extrêmement rares de par son éloignement des zones habitées. Les glaciers des îles Kerguelen, situés à faible altitude et sur des îles, sont particulièrement sensibles aux variations atmosphériques et océaniques. La cryosphère aux îles Kerguelen a montré d'importantes fluctuations au cours des deux derniers siècles (Frenot et al., 1993). Après une période stable jusqu'en 1961, la calotte a subi un retrait très important et extrêment rapide, perdant 20% de sa surface au cours des 40 dernières années (Berthier et al., 2009). Cette accélération avait généralement été attribuée au réchauffement de l'atmosphère, alors que l'importance des changements de précipitations était minimisée (e.g., Frenot et al. (1993, 1997); Berthier et al. (2009)). Pourtant, en raison de notre manque de connaissances sur la relation entre climat et glaciers et sur la dynamique glaciaire dans cette région, il était jusqu'à présent difficile de déterminer avec précision quelles ont été les principales causes du recul.

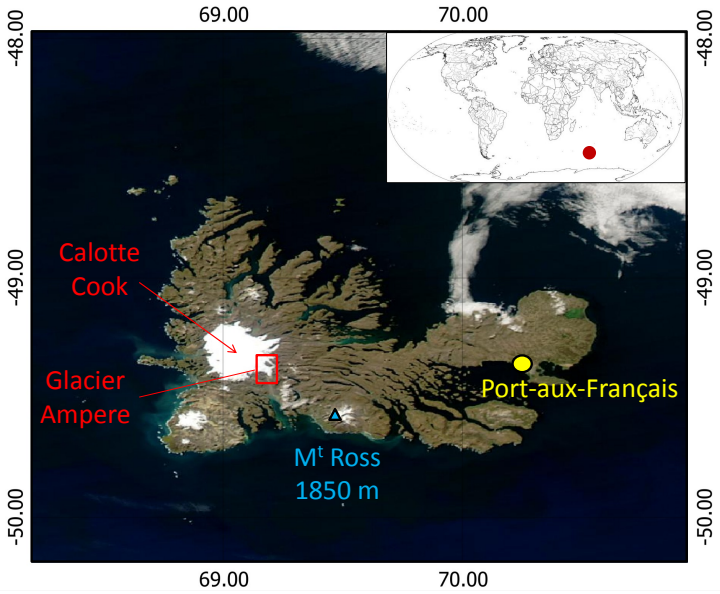

FIGURE 1 – Image MODIS© des îles Kerguelen montrant les principaux sites d'étude en rouge, et la localisation de Port-aux-Français, la base scientifique. La situation géographique des îles Kerguelen sur une carte mondiale est montrée en haut à droite.

Le premier chapitre de cette thèse présentera le contexte de l'étude : la localisation et l'intérêt des îles Kerguelen, une description du climat et de la cryosphère de cet archipel ainsi que la méthodologie adoptée au cours de cette thèse.

... Grâce à une approche globale utilisant un jeu de données complet

L'objectif de ce travail de thèse est donc d'évaluer l'état actuel et futur des zones englacées des îles Kerguelen, et de comprendre les causes locales et globales de leur recul, en combinant observations de terrain, images satellites et modélisation.

Mesures de terrain, observations satellites et modélisations

Pour déterminer l'origine des variations récentes de la cryosphère aux îles Kerguelen, un réseau de mesures météorologique et glaciologique a été mis en place à proximité de la calotte Cook (Figure 1) en 2010, et des campagnes de mesure ont depuis été réalisées chaque année. L'analyse des données glaciologiques de terrain, couplée à l'étude de l'albédo de la calotte à partir d'images satellites MODIS, nous permet de suivre l'évolution du bilan de masse de la calotte, tandis que les données issues de stations météorologiques pré-existantes ou installées par nos soins nous renseignent sur l'évolution climatique associée. Par ailleurs, l'utilisation d'un modèle degré-jour couplé à une routine d'écoulement simple nous fournit des indications précieuses concernant les causes du recul glaciaire actuel. Afin de comprendre les causes de grande échelle de ce recul, nous avons également étudié les tendances climatiques de l'ensemble de la zone sub-polaire à partir d'un ensemble de jeux d'observations et de modélisations.

Modélisation régionale du climat

Parallèlement, pour prévoir l'évolution future de la cryosphère aux îles Kerguelen, un important chantier de modélisation a dû être mis en oeuvre. Une modélisation climatique régionale des îles Kerguelen a été effectuée au cours de cette thèse, utilisant le Modèle Atmosphérique Régional (MAR) forcé à ses frontières par des champs issus de réanalyses (sur la période récente) ou de modèles de l'exercice CMIP5 (pour les simulations futures). En effet, l'accumulation et la fonte sont contrôlées par des effets de seuil qui demandent une analyse au niveau événementiel, voire horaire. De plus, étant donné la topographie complexe de l'archipel et la taille de ses glaciers (quelques dizaines de km^2), la résolution typique des modèles utilisés doit être de l'ordre de quelques kilomètres. La résolution des sorties de Modèles de Circulation Globale (de l'ordre de plusieurs dizaines de km) est donc inadaptée au problème posé. Un effort supplémentaire de régionalisation est par conséquent indispensable. En raison de la faible densité du réseau de mesures de surface dans les régions englacées, une désagrégation statistique est impossible et le développement d'une approche par désagrégation physique est primordial. Si l'utilisation de modèles complets d'atmosphère pour passer aux échelles qui nous intéressent est trop lourde, il est néanmoins possible de se pencher sur des modèles simplifiés. C'est le cas de l'outil de désagrégation physique du bilan de masse et d'énergie développé par le LGGE. Ce modèle a été testé en Antarctique dans le cadre de la thèse de Luc Gential (Gential, 2007), et perfectionné dans le cadre de la thèse de Cécile Agosta (Agosta, 2012). Dans le cadre de ce travail de thèse, on se propose de tester ses performances dans une zone de topographie plus complexe telle que l'archipel des Kerguelen.

Le deuxième chapitre de cette thèse décrira les deux paramètres clés étudiés, le bilan de masse de surface et le bilan d'énergie de surface, ainsi que les données disponibles pour mon travail de thèse, les données d'observations d'une part (mesures de terrain et satellites), et la modélisation d'autre part.

Les résultats de cette étude seront présentés dans le troisième chapitre. Le quatrième et dernier chapitre sera finalement consacré à mes conclusions générales ainsi qu'aux perspectives de cette étude.

Chapitre 1

Contexte d'étude

1.1 Situation géographique et intérêt des îles Kerguelen

Les îles Kerguelen constituent un archipel français de plus de 300 îles situé dans le sud de l'océan Indien à 49° S, 70° E (Figure 1). Ce territoire d'environ 7200 km^2 fait partie des Terres Australes et Antarctiques Françaises (TAAF) depuis 1955. Les TAAF comportent cinq disctricts : Crozet, Kerguelen, Saint-Paul et Amsterdam, les Iles Eparses ainsi que la Terre Adélie (Antarctique). Située sur la Grande Terre (l'île principale) et sur la partie orientale appelée Péninsule Courbet, la base scientifique de Port-aux-Français ne compte pas d'habitants permanents. Durant la saison hivernale elle rassemble une soixantaine d'hivernants, nombre qui peut monter jusqu'à 120 entre novembre et avril lors des campagnes d'été. En effet, ces îles, localisées en plein océan Austral, à près de 3500 km de toute terre habitée constituent un observatoire unique de la biosphère, la géologie, la climatologie,..., a priori peu impacté par l'homme. Malgré certains changements tout de même apportés par les intrusions d'homme sur l'archipel au cours des dernières décennies (introductions volontaires ou non d'espèces invasives, modification des zones de pêche de la faune locale, ...), il s'agit d'un cas idéal pour l'étude de milieux ayant subi un impact humain minimal. L'archipel des Kerguelen constitue donc un lieu idéal notamment pour l'analyse de l'impact de la variabilité climatique sur l'environnement, réalisée dans le cas de cette étude au travers des glaciers.

La présence aux îles Kerguelen de forts vents d'ouest (Westerlies) et d'un climat subpolaire a permis la mise en place et le maintien de glaciers à de faibles altitudes. La calotte Cook, située à l'ouest des îles Kerguelen et culminant à 1049 m d'altitude, représente la plus grande masse englacée de l'archipel (environ 400 km^2). Parmi les glaciers émissaires de la calotte, le glacier Ampère, situé au sud-est, est le plus long glacier français (12 km de long et environ 60 km^2 en superficie). Cependant, depuis quelques décennies, la cryosphère montre un recul marqué, la calotte Cook ayant perdu environ 20% de sa surface entre 1963 et 2001 (Berthier et al., 2009). Cependant les causes premières de ce recul n'ont encore jamais été clairement définies. L'archipel des Kerguelen constitue donc un observatoire privilégié du recul glaciaire et du lien glacier-climat associé.

1.2 Climat et cryosphère

Le climat aux îles Kerguelen, de type subpolaire, est caractérisé par de forts vents d'ouest, nommés Westerlies en anglais, caractéristiques de la bande latitudinale 45° S - 55° S. Le vent

moyen quotidien mesuré à la station de Port-aux-Français (PAF) est de l'ordre de 10-20 m s^{-1} (ou 36-72 km h^{-1}) et les rafales peuvent atteindre près de 200 km h^{-1}. Une autre caractéristique de ce climat subpolaire réside dans le taux humidité et les précipitations importants, liés au passage régulier de dépressions se formant au-dessus de l'océan en amont de l'archipel. Malgré une forte humidité (humidité relative moyenne annuelle à PAF de l'ordre de 75%), les précipitations n'atteignent que 700 mm an^{-1} à PAF alors qu'elles sont supérieures à 3000 mm an^{-1} sur la partie orientale de l'île. Un très fort effet de foehn a en effet lieu entre la partie ouest de l'archipel, où se situe la plupart des reliefs (et la calotte Cook), et la partie est, plus plate, où un assèchement de l'air est observé (près de 80% de précipitations en moins par rapport à l'ouest). Le climat est également caractérisé par des températures fraîches (environ 5°C en moyenne annuelle à PAF, pour des températures oscillant entre -1°C et +10°C en moyenne mensuelle selon la saison), ainsi que par une faible saisonnalité des températures et des précipitations.

Ces conditions climatiques caractéristiques d'un climat subpolaire ont permis la mise en place de calottes et leur maintien à des altitudes relativement peu élevées, tout comme en Patagonie ou en Nouvelle-Zélande (e.g. Fitzharris et al., 1997; Takeuchi et al., 1999; Fitzharris et al., 2007; Garreaud et al., 2009). En particulier, aux îles Kerguelen, plusieurs ensembles glaciaires sont observés. La figure 1.1, issue de Berthier et al. (2009), représente l'ensemble des zones englacées des îles Kerguelen ainsi que la topographie de l'archipel. L'ensemble des calottes et glaciers actuels aux îles Kerguelen est situé sur la partie occidentale de l'archipel, reflétant l'influence de l'orographie sur les précipitations et la présence d'un effet de foehn. Les superficies de ces zones englacées (en 2001) sont renseignées dans le Tableau 1.1. Il est important de noter que ces ensembles glaciaires, avec ceux de Heard Island, sont les seuls de l'océan Indien austral, constituant le chaînon manquant entre les glaciers de Patagonie, de Géorgie du Sud et de Nouvelle-Zélande.

TABLE 1.1 – Superficie des zones englacées des îles Kerguelen en 2001 (d'après Berthier et al. (2009)).

Zones englacées	Superficie en 2001 (km^2)
Calotte Cook	410,0
Péninsule Rallier du Baty	79,2
Mont Ross	35,1
Presqu'île de la Société de Géographie	4,7

Dans le cadre de cette thèse, je me suis intéressée à la calotte Cook, qui représente la principale zone englacée des îles Kerguelen (environ 400 km^2, voir Table 1.1). La calotte présente une étendue très plate à son sommet, culminant à 1049 m d'altitude, et dix-sept glaciers émissaires s'écoulant dans toutes les directions depuis celui-ci (Figure 1.2). La plupart de ces glaciers émissaires ont un terminus terrestre, à l'exception des glaciers Ampère, Vallot & Naumann, Agassiz, Dumont-d'Urville et Descartes qui vêlent dans un lac proglaciaire et du glacier Pasteur qui vêle directement dans l'océan.

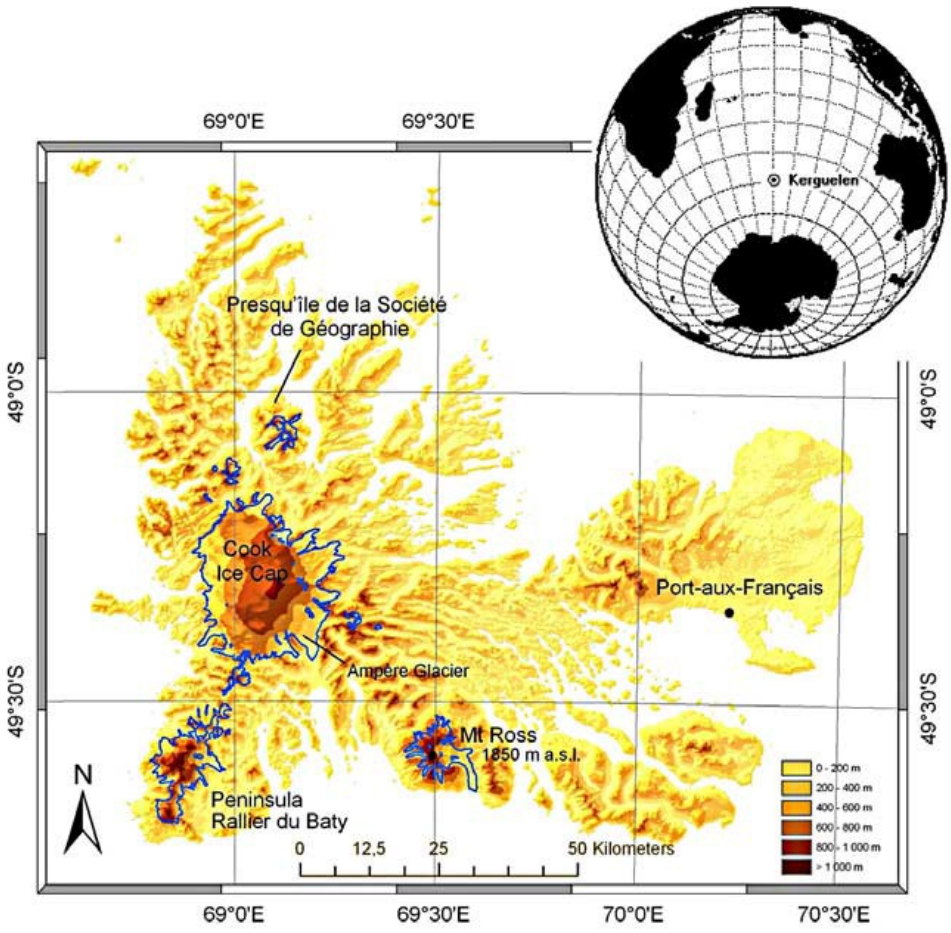

FIGURE 1.1 – Topographie des îles Kerguelen (en couleur) et principales zones englacées (délimitées par les lignes bleues) de l'archipel (Figure issue de Berthier et al. (2009)).

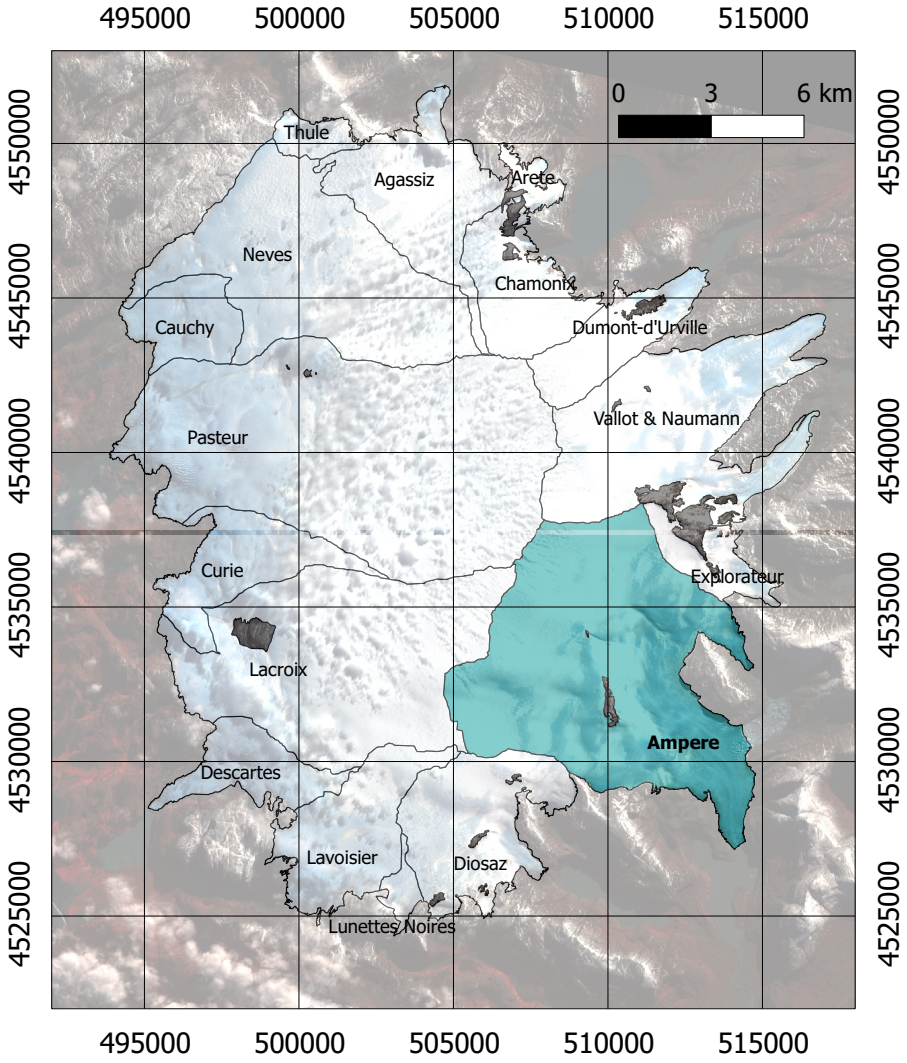

FIGURE 1.2 – Délimitations des dix-sept glaciers émissaires de la calotte Cook. Le glacier Ampère est indiqué en bleu. L'image en arrière-plan est une image ASTER prise le 23 avril 2009. Les coordonnées sont en UTM (zone 42S).

1.3 Objectifs et méthodologie adoptée

L'objectif de mon travail de thèse est de comprendre les causes du recul glaciaire récent aux îles Kerguelen, pour (1) évaluer l'état passé, présent et futur de la calotte Cook et (2) comprendre le changement climatique (et/ou dynamique) à l'origine de ce recul. Pour ce faire, une méthodologie basée sur une approche régionale est nécessaire. Cette approche régionale nécessite la mise en oeuvre d'une modélisation (régionale), ainsi que de données de validation. Ces dernières sont issues d'observations (locales) sur le terrain, permettant de mettre en évidence les différents processus glaciologiques, mais également de données distribuées (sur l'ensemble de la calotte).

La méthodologie adoptée au cours de cette thèse se déroule en quatre points :

1. Afin de comprendre les processus glaciologiques entrant en jeu, il est nécessaire d'analyser des données ponctuelles (météorologiques, de bilan de masse et d'énergie, ...) obtenues sur le terrain. Ces données seront présentées dans la section 2.3.1.
2. Ces diverses données doivent ensuite être spatialisées afin d'obtenir le bilan de masse de surface (BMS) de la calotte Cook. La spatialisation des précipitations (et températures) est mise en oeuvre *via* un réseau de mesure (LEFE Kcrumble) et une modélisation régionale. De même, la télédétection permet d'obtenir la variable clé que constitue l'albédo de surface. La section 2.3.2 traitera des ces données spatialisées.
3. Par ailleurs, il est nécessaire de déterminer si le BMS obtenu est en accord avec les pertes glaciaires de surface et de volume. Cela nécessite d'avoir une idée quantitative de ces pertes (Section 2.3.3) et de pouvoir les modéliser (Section 2.4.6).
4. Finalement, la dernière étape consiste à mettre en relation les pertes de masse observées ci-dessus avec des variations climatiques régionales et globales. Ceci passe par une modélisation globale et régionale de ces variations (Section 2.4).

Chapitre 2

Paramètres étudiés - Mesures et modélisation

2.1 Bilan de masse de surface

Le bilan de masse (BM) d'un glacier ou d'une calotte peut être défini comme la somme algébrique de deux termes : l'accumulation sur la calotte et son ablation. L'accumulation en surface a lieu principalement sous forme de précipitations neigeuses, mais également par la formation de givre ou par dépôt éolien. Elle peut être complétée par du regel basal. L'ablation peut se manifester par la sublimation, la fonte basale ou de surface, l'érosion par le vent et, le cas échéant, le vêlage d'icebergs. L'ensemble de ces processus est repris dans la Figure 2.1. Le bilan de masse de surface (BMS) ou bilan de masse climatique (d'après le Glossary of Mass Balance (Cogley et al., 2011)) ne prend en compte que les processus affectant la surface, c'est-à-dire les précipitations, le givrage et le dépôt par le vent pour le terme d'accumulation, et la sublimation, la fonte de surface et l'érosion par le vent pour le terme d'ablation.

Sur la calotte Cook (cf Section 1.2), le terme d'accumulation du BMS est dominé par les précipitations. Le dépôt éolien joue également un rôle important dans certaines zones localisées à l'aval du relief (voir Section 3.2). Par ailleurs, en raison du fort taux d'humidité dans l'air, la sublimation reste faible sur la calotte Cook (Poggi, 1977b). Le terme d'ablation en surface est donc principalement représenté par la fonte de surface et, dans une moindre mesure et plus localement, par l'érosion éolienne. Le réseau de mesure du BMS sur le glacier Ampère sera présenté dans la section 2.3.1.

Pour déterminer le BM (total) des glaciers et calottes, de nombreuses techniques existent. Lorsque le vêlage et la fonte basale sont négligeables, les méthodes de mesure du BMS sont utilisées pour évaluer le BM (et les différentes méthodes sont alors intercomparables). Les différentes techniques utilisées sont :

1. la méthode glaciologique (BMS) : l'implantation de balises d'accumulation ou d'ablation, relevées d'une année sur l'autre et couplées à la mesure de la densité du matériau, permet d'obtenir des valeurs ponctuelles de bilan qui sont ensuite interpolées pour obtenir le bilan de masse spécifique (ou climatique selon le Glossary of Mass Balance (Cogley et al., 2011))). Cette technique est utilisée dans le cadre de notre étude sur le glacier Ampère (Section 2.3.1). En zone d'accumulation, la mesure de l'accumulation (en mètres équivalent eau, m eq. e.) en un point consiste à réaliser un carottage jusqu'à la couche correspondant à la fin de la saison d'ablation précédente et à multiplier la hauteur de cette carotte par

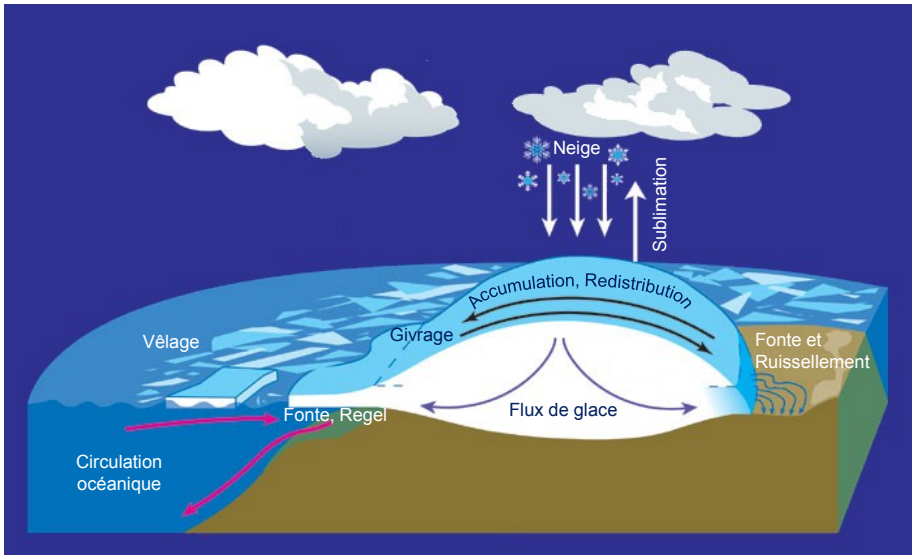

FIGURE 2.1 – Les différents termes du bilan de masse d'une calotte. D'après une image de la NASA (2005) : `http://en.wikipedia.org/wiki/Image:Mass_balance_atmospheric_circulation.png`

sa densité (Figure 2.2 a). En zone d'ablation, la mesure, au bout d'un an, de la hauteur de neige perdue le long d'une balise permet, après multiplication par la densité de celle-ci, d'obtenir l'ablation (en m eq. e.) en ce point (Figure 2.2 b). Le bilan ponctuel $b_{i,t}$ ainsi obtenu au niveau de chaque balise peut ensuite être multiplié par une certaine proportion de la surface du glacier (déterminée en fonction de rangs altitudinaux et d'orientation), afin d'obtenir le bilan volumique (en m^3 d'eau) B_t (Figure 2.2 c). Le bilan spécifique du glacier (en m eq. e) b_t est calculé en divisant le bilan volumique par la surface totale du glacier.

2. l'approche hydrologique (BMS) : le bilan spécifique b_t d'un glacier peut être estimé à partir des apports en eau provenant des précipitations (mesurés par un pluviomètre), auquel on soustrait les pertes par fonte (mesurées par une station hydrologique installée sur le torrent émissaire, avec prise en compte des apports provenant de surfaces non englacées) et par sublimation (mesurées par une station météorologique). Cette technique ne sera pas utilisée au cours de cette étude.
3. la gravimétrie : la répartition des masses glaciaires et son évolution temporelle sont déterminées par la mesure des variations de la gravité terrestre. A l'aplomb des masses englacées, les variations de gravité terrestre dépendent au premier ordre des pertes de glace et de l'ajustement isostatique post-glaciaire causé par la fonte des glaces. Les mesures par gravimétrie dépendent donc fortement du modèle d'ajustement isostatique utilisé. Les données de gravimétrie actuellement utilisées proviennent de la mission GRACE (Gravity Recovery And Climate Experiment) lancée en 2002 (voir p.ex. les travaux de Velicogna and Wahr (2005); Chen et al. (2011); Ivins et al. (2011); Jacob et al. (2012)).
4. la comparaison de modèles numériques de terrain (MNTs) : des MNTs obtenus à différentes époques sont comparés afin de déduire la variation d'altitude des surfaces englacées, et en la multipliant par les surface concernées, la variation de volume. Les MNTs peuvent être

obtenus à partir de l'altimétrie, de photographies aériennes, d'images satellites ou d'un maillage GPS dense. Une estimation de la densité du matériau est nécessaire pour obtenir le BM à partir de la variation du volume glaciaire. Les principales sources d'erreur, à part l'erreur possible sur la densité, proviennent des différences de résolution et d'aspect entre les deux MNTs. Les MNTs doivent donc subir un ensemble de corrections (ajustement planimétrique, corrections verticales, ...) avant de pouvoir être comparés l'un à l'autre. La mesure du BM à partir de photographies aériennes et d'images satellites a notamment été utilisée en Amérique du Sud pour l'étude des champs de glace patagoniens (Rignot et al., 2003; Willis et al., 2012a,b) et de la cordillère Darwin (Melkonian et al., 2013), ou en Himalaya (Berthier et al., 2007; Gardelle et al., 2012). L'altimétrie (radar et laser) consiste en la mesure des variations de l'altitude des calottes et glaciers par des altimètres laser ou radar embarqués à bord de satellites, permettant une estimation des variations de volume, et après prise en compte de la densité, du BM. Les mesures récentes de BM basées sur l'altimétrie sont issues des missions radar ERS-1 et -2 (p.ex. Johannessen et al. (2005); Zwally et al. (2005)), Envisat (Wingham et al., 2009) et CryoSat-2 (Wingham et al., 2006) et de l'altimètre laser ICESat (Zwally et al., 2002; Moholdt et al., 2010b; Kääb et al., 2012)).

Des méthodes complémentaires existent par ailleurs pour calculer certains termes du bilan de masse total (tels que les pertes par vêlage, l'accumulation sur des inlandsis, etc.) :

1. l'implantation de capteurs à ultrasons : elle sert à mesurer les variations de la surface (par rapport au capteur) liées à l'ablation de surface et aux précipitations neigeuses (puis au métamorphisme de la neige).
2. le Ground Penetrating Radar (GPR) : cette technique, qui a l'avantage d'être réalisée en continu, utilise la différence entre le moment d'émission et d'arrivée d'ondes radar réfléchies sur des surfaces isochrones en profondeur dans le manteau neigeux afin de calculer l'épaisseur d'une couche (située entre la surface et une isochrone en profondeur, ou entre deux isochrones en profondeur). Grâce à l'estimation de l'âge des réflecteurs (via des forages ponctuels) et de la densité des couches traversées, l'accumulation moyenne au cours d'une période donnée peut donc être évaluée. Le traitement et l'analyse de mesures GPR réalisées en Terre Adélie en 2008-2009 ont fait l'objet de mon stage de M2R et sont repris dans l'Annexe A.
3. l'interférométrie radar : l'évaluation des flux de glace (via leur vitesse) permet d'estimer les pertes par vêlage. Ces flux de glace sont ensuite additionnés au BMS et à l'estimation de la fonte basale (plus difficile à évaluer) afin d'obtenir le BM total. C'est le cas notamment des études réalisées sur Pine Island Glacier en Antarctique (voir p.ex. Thomas et al. (2004)).

A l'heure actuelle, de nombreuses études tentent, afin de réduire les incertitudes sur les valeurs de BM, de combiner plusieurs de ces techniques (Shepherd et al., 2012; Gardner et al., 2013). Cependant, de part l'étendue des surfaces englacées et la complexité des mesures à mettre en oeuvre, une évaluation complémentaire du BMS par modélisation est primordiale. Les différentes données de modèles et les modèles utilisés dans le cadre de cette thèse seront repris dans la section 2.4.

Pour évaluer l'état de santé d'un glacier, d'autres mesures que celle du BM peuvent être effectuées, notamment concernant son étendue. L'analyse de l'étendue des surfaces glaciaires fait appel à certaines notions, présentées succintement ci-après. La ligne de neige (transitoire) d'un glacier correspond à la limite, à l'échelle journalière, entre la zone du glacier recouverte de neige (à l'amont de la ligne de neige) et la zone recouverte de névé (c'est-à-dire dans ce sens-ci, la neige

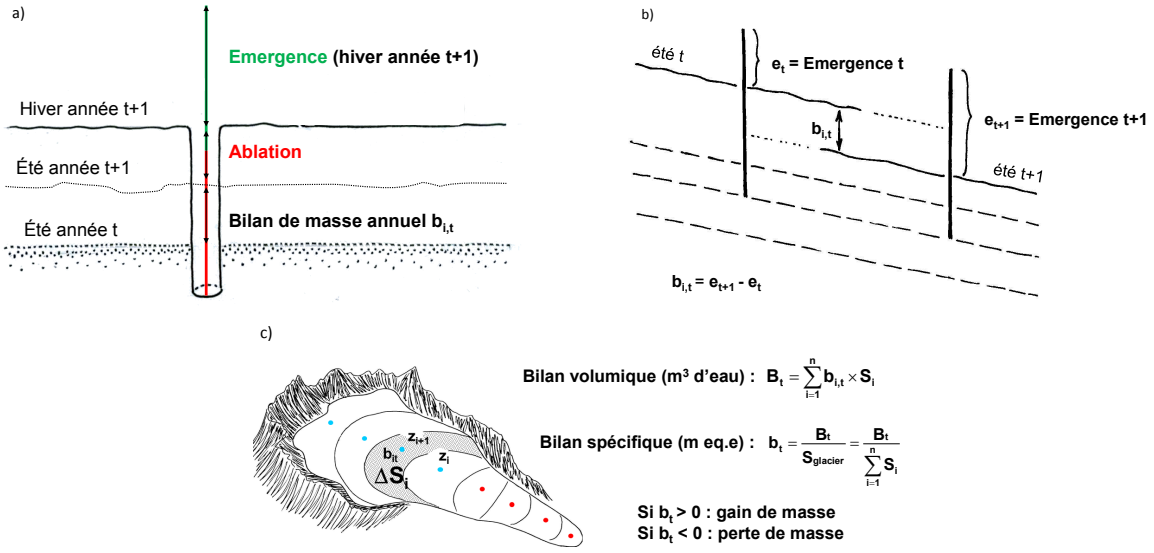

FIGURE 2.2 – Mesure du bilan de masse de surface (a) ponctuel en zone d'accumulation (b) ponctuel en zone d'ablation (c) volumique et spécifique sur l'ensemble du glacier. D'après une présentation de Favier (2011).

de la saison précédente n'ayant pas encore été transformée en glace, voir Cogley et al. (2011)) ou de glace (à l'aval de la ligne de neige). La ligne de névé (transitoire), quant à elle, sépare la zone du glacier recouverte de névé de celle recouverte de glace. A la fin de la saison d'ablation (décembre à mai environ aux îles Kerguelen), l'altitude de la ligne de neige offre une bonne approximation de l'altitude de la ligne d'équilibre du glacier (seulement si la majeure partie des échanges de masse se fait en surface du glacier et s'il n'y a pas de glace surimposée, ce qui est une bonne approximation aux îles Kerguelen). La ligne d'équilibre (Figure 2.3) représente l'endroit où le BM climatique (Cogley et al., 2011) est nul (au niveau annuel). Elle sépare donc la zone dite d'accumulation (zone du glacier où le BM cumulé depuis le début de l'année glaciologique est positif) de la zone d'ablation (zone où le BM cumulé depuis le début de l'année glaciologique est négatif). Une mesure de l'étendue de la zone d'accumulation d'un glacier consiste à calculer son AAR (Accumulation Area Ratio), c'est-à-dire le rapport (en %) de l'étendue de la zone d'accumulation sur l'étendue totale du glacier (au niveau annuel). Une analyse de l'étendue et de la ligne de neige de la calotte cook au cours des dernières décennies sera présentée dans la section 3.2.

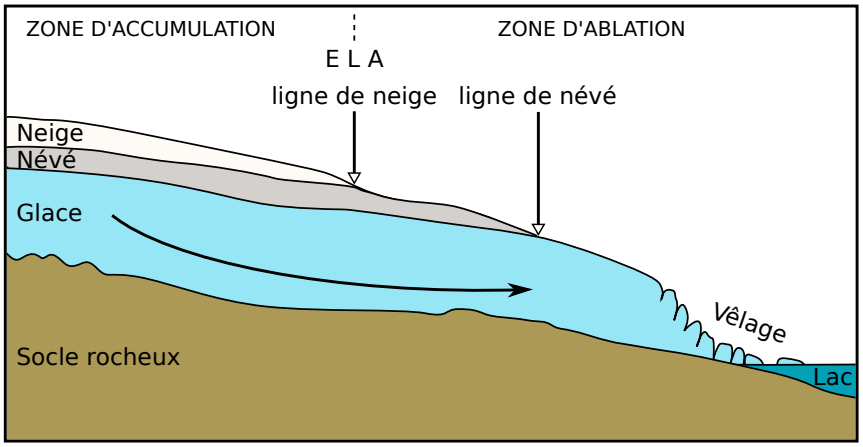

FIGURE 2.3 – Profil schématique du Glacier Ampère, montrant ses zones d'accumulation et d'ablation ainsi que la position de son ELA, de sa ligne de neige et de sa ligne de névé en fin de saison d'ablation.

2.2 Bilan d'énergie de surface

Après sa chute la neige subit des transformations. Elle est érodée ou redéposée, et subit des métamorphoses conséquentes des processus de fusion/regel et de la sublimation/condensation solide. Avec les processus de frittage et de tassement elle évolue vers la glace, qui est vouée à disparaitre par fonte ou sublimation. Ces processus de changement d'état sont directement reliés à des échanges d'énergie. En surface, les échanges sont effectués avec l'atmosphère, et avec les couches sous-jacentes (par conduction, et advection d'air et d'humidité dans le névé).

Le bilan d'énergie de surface (BES) représente la somme des flux d'énergie qui arrivent à la surface du glacier et en partent (Figure 2.4). Nous utiliserons l'approche de Favier et al. (2011), dont je ne développerai ici que les éléments essentiels. Le BES est généralement traduit par l'équation suivante (en négligeant les transferts horizontaux) :

$$R + H + LE + P = F_{surface}, \tag{2.1}$$

exprimée en W m^{-2} et où les flux sont comptés positivement lorsqu'ils arrivent à la surface et négativement quand ils en repartent.

R est le rayonnement net toutes longueurs d'onde, c'est à dire la somme du bilan radiatif net de courtes longueurs d'onde S et de grandes longueurs d'onde L :

$$R = S + L = S\downarrow + S\uparrow + L\downarrow + L\uparrow = S\downarrow(1-\alpha) + L\downarrow + L\uparrow, \tag{2.2}$$

où $S\downarrow$ est le rayonnement incident de courtes longueurs d'onde, $S\uparrow$ est le rayonnement réfléchi de courtes longueurs d'onde, $L\downarrow$ est le rayonnement incident de grandes longueurs d'onde, $L\uparrow$ est le rayonnement de grandes longueurs d'onde émis et réfléchi par la surface et α est l'albédo de surface de la neige ou de la glace.

H est le flux turbulent de chaleur sensible et LE le flux turbulent de chaleur latente. P représente la quantité de chaleur apportée par les précipitations (généralement négligée par rapport aux autres termes).

$F_{surface}$ représente donc la quantité d'énergie emmagasinée par la surface. En réalité, $F_{surface}$ peut être séparée en deux termes :

$$F_{surface} = G_0 + (1 - a)S, \tag{2.3}$$

où G_0 correspond à l'énergie effectivement emmagasinée par la surface, tandis que $(1 - a)S$ représente une partie (fraction a) du rayonnement net de courtes longueurs d'onde qui va pénétrer dans la neige et la glace. Lorsque la température de la surface est inférieure à 0°C, cette quantité d'énergie G_0 est stockée en surface et contribue à augmenter la température de la surface et des couches sous-jacentes. Si au contraire la température de surface est égale à 0°C, G_0 sera utilisée pour la fonte.

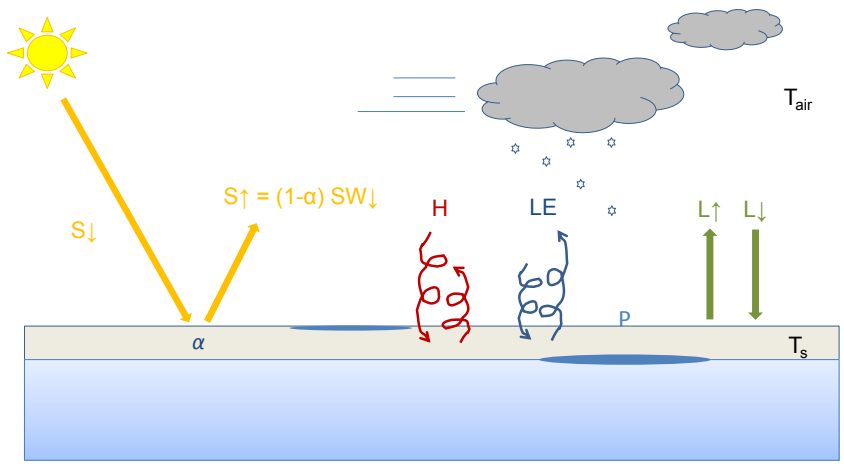

FIGURE 2.4 – Les différents termes du bilan d'énergie de surface d'une calotte.

Le réseau de mesure du BES sur le glacier Ampère est présenté ci-dessous.

2.3 Données d'observation

2.3.1 Mesures de terrain

2.3.1.1 Réseau de mesures glaciologiques, hydrologiques et météorologiques 2010-2014

Un réseau de mesures glaciologiques, hydrologiques et météorologiques a été mis en place sur et à proximité du glacier Ampère en décembre 2010 lors de la première mission de terrain réalisée dans le cadre du programme IPEV GLACIOCLIM-KESAACO. Ce réseau a par la suite été entretenu et renouvelé au cours des trois campagnes suivantes (2011-2012, 2012-2013 et 2013-2014). J'ai pour ma part participé aux campagnes 2011-2012 et 2012-2013. La Figure 2.5 présente l'ensemble des mesures réalisées sur ou à proximité du glacier Ampère au cours de ces 4 campagnes.

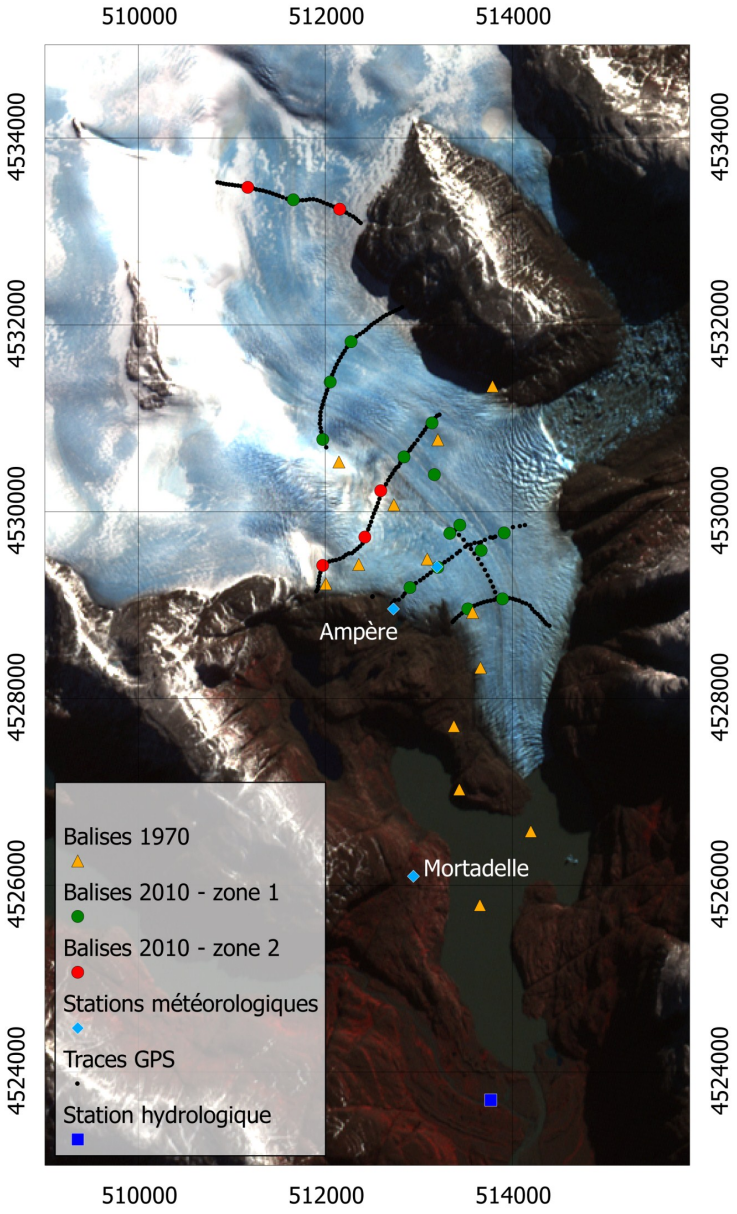

FIGURE 2.5 – Réseau de mesures installé en 2010 sur et aux abords du glacier Ampère. Les balises d'ablation de l'étude de Vallon dans les années 70 sont également positionnées. L'image de fond est une image ASTER prise le 23 avril 2009. Les coordonnées sont en UTM (Zone 42S).

a) Mesures glaciologiques

Premièrement, un réseau de vingt balises a été installé en décembre 2010 sur la zone d'ablation du glacier Ampère (Figure 2.5). L'ablation au niveau de ces balises a ensuite été mesurée annuellement afin d'évaluer le bilan de masse de surface ponctuel (voir Section 2.1), et les balises remplacées d'une année sur l'autre. La gamme d'incertitude sur la mesure des balises est évaluée à ±10cm. Les balises sont séparées en deux catégories dans la Figure 2.5 : les balises présentes dans la zone d'ablation classique (zone 1) et celles placées dans des zones spécifiques

de surraccumulation neigeuse en hiver liée à un dépot par le vent (zone 2). Nous verrons par la suite que malgré cette surraccumulation, la zone 2 reste marquée par une forte ablation. Ces balises font donc elles aussi partie de la zone d'ablation, et lors de leur installation elles ont été implantées sur de la glace. Des balises équipées d'une pastille Recco® ont également été placées dans la zone d'accumulation du glacier Ampère en 2010. Cependant, alors que nous pensions les avoir initialement installées en zone d'accumulation (aux alentours de 800-900 m) celles-ci ont été retrouvées au sol l'année suivante, démontrant l'occurrence d'une importante ablation sur les points analysés. Nous ne disposons donc pas de mesures directes du BMS ponctuel en zone d'accumulation.

Des mesures glaciologiques avaient déjà été réalisées sur le glacier Ampère au cours de campagnes de terrain entre 1970 et 1974 (Vallon, 1977a,b). L'existence de ces données antérieures représente un grand avantage dans le cadre de mon étude car elles me permettent de réaliser une comparaison avec mes données récentes (donc avec un intervalle d'environ 40 ans). Un réseau de balises similaire au nôtre et utilisant les mêmes protocoles d'installation et de mesure fut installé en 1970 et relevé les années suivantes afin d'évaluer le BMS ponctuel du glacier (Vallon, 1977a). La position de ces balises est reportée dans la Figure 2.5. La comparaison des valeurs de BMS et de vitesses de surface des années 1970 avec mes données récentes sera détaillée dans la section 3.2.

Par ailleurs, la mesure au GPS différentiel du déplacement annuel de chaque balise a permis une évaluation des vitesses de surface du glacier. L'utilisation d'un système différentiel permet de minimiser les erreurs de positionnement à la surface du glacier (erreurs horizontales et verticales de quelques centimètres seulement). La mesure de la perte d'altitude de la surface du glacier le long de traces réalisées au GPS différentiel (Figure 2.5) a également permis une estimation de la perte d'épaisseur glaciaire, qui peut être comparée au BMS ponctuel mesuré au niveau des balises.

b) Météorologie et bilan d'énergie de surface

Deuxièmement, deux stations météorologiques automatiques de type CR1000 (Campbell Scientific) ont été mises en place en 2010 (Figure 2.5 et 2.6), afin d'évaluer les conditions météorologiques sur et aux alentours du glacier. Ces mesures permettent aussi d'évaluer le BES en zone d'ablation. L'une a été installée à proximité de la cabane de la Mortadelle (env. 200m asl), située à 1-2 km du glacier (Figure 2.5). La deuxième station était positionnée sur la zone d'ablation du glacier lors des campagnes d'été, et déplacée sur un affleurement rocheux attenant au glacier pendant la saison d'hiver (station "Ampère", Figure 2.5). Malheureusement, la station du glacier présente de nombreuses ruptures dans les données au cours de la saison 2010-2011 liées à un problème de batterie. J'ai donc principalement utilisé les données de la station de la Mortadelle, qui sont constituées de moyennes demi-horaires de température et humidité de l'air, vitesse et direction du vent, précipitations, et rayonnement de courtes et grandes longueurs d'onde incident et émis/réfléchi. Néanmoins, les calculs d'ablation en été ont été calculés avec les données de la station du glacier. Cette station permet le suivi, lors de son installation sur le glacier, de la température et de l'humidité de l'air, de la vitesse et direction du vent, du rayonnement de courtes et grandes longueurs d'onde incident et émis/réfléchi par le glacier, mais également de la hauteur de la surface du glacier grâce à l'utilisation d'une sonde à ultrasons SR50. Le Tableau 2.1 présente les caractéristiques des différents capteurs de la station de la Mortadelle et d'Ampère.

TABLE 2.1 – Caractéristiques des capteurs installés sur les stations météorologiques de la Mortadelle et d'Ampère : Nom, Données mesurées, Précision (selon la notice du fabricant) et Hauteur de mesure (la Mortadelle / Ampère).

Nom	Données	Précision	Hauteur
Anémomètre Young 05103	Vitesse du vent	± 0.3 m s^{-1}	5 m / 2,1 m
	Direction du vent	$\pm 3^{\circ}$	
Vaisala HMP45C	Température de l'air	± 0.4 °C	5 m / 2,1 m
	Humidité relative	$\pm 3\%$	
Radiomètre Kipp and Zonen CG3	Rayonnement incident L	$\pm 10\%$ [1]	2 m / -
Radiomètre Kipp and Zonen CMP3	Rayonnement incident & réfléchi S	$\pm 10\%$ [1]	- / 2 m
Pluviomètre PRECIS MECANIQUE 3029	Hauteur de précipitations	$\pm$0,5 mm	0,85 m / -
Capteur de pression Campbell Sc. SC100	Pression	± 1.5 mbar	2 m / -
Capteur de distance Campbell Sc. SR50A	Hauteur de surface	± 1 cm	- / 1,6 m

[1]précision pour totaux journaliers

FIGURE 2.6 – Stations météorologiques installées sur le glacier (image de gauche) et à proximité (la Mortadelle, image de droite).

Par ailleurs, Poggi (1977a,b) réalisa une étude du BES du glacier Ampère entre janvier et mars 1972 grâce à un mât de vent et une station météorologique classique équipés de capteurs de leur propre fabrication (température, humidité, vent et rayonnement mesurés à différents niveaux entre 0 et 4m).

c) Mesures hydrologiques

Finalement, une station hydrologique constituée d'une échelle limnigraphique et d'un capteur de pression OTT-CTD a été installée en 2011 dans la Diosaz, le torrent émissaire du glacier Ampère (Figure 2.5), afin d'obtenir une estimation indépendante des pertes glaciaires par la méthode hydrologique (voir section 2.1). Ces mesures n'ont cependant pas été exploitées dans le cadre de ma thèse. L'échelle limnigraphique permet de vérifier l'exactitude des valeurs de hauteur d'eau mesurées par l'OTT-CTD (de précision ±0.05%). Ce capteur mesure également la température et la salinité de l'eau.

2.3.1.2 Suivi météorologique à Port-aux-Français 1951-2014

Météo France réalise le suivi de nombreux paramètres météorologiques depuis 1951 à proximité de Port-aux-Français. Dans le cadre de mon étude, j'ai utilisé les données journalières de température (à 2 m), précipitations, vitesses et direction du vent (à 10 m), humidité relative et rayonnement incident de courtes longueurs d'onde. Des radiosondages sont également réalisés, au départ hebdomadairement et à présent quotidiennement, depuis les années 1960. Ces données de radiosondages sont également précieuses car elles permettent une vision des variations de température, humidité et vitesse du vent avec l'altitude. L'analyse de ces données sera effectuée dans la section 3.3, afin de retrouver les causes climatiques du recul des glaciers aux îles Kerguelen. En effet, il s'agit d'un série de données unique par sa longueur, sa faible quantité de lacunes, et le suivi de protocoles stricts (protocoles de l'Organisation Météorologique Mondiale).

2.3.1.3 Suivi météorologique complémentaire depuis 2012 : le réseau Kcrumble

Afin de permettre une estimation distribuée du BMS et du BES sur l'ensemble de la calotte Cook, des données spatialisées (sur l'ensemble de l'archipel) des variables-clés que constituent les températures et les précipitations sont nécessaires. Au début de ma thèse, seules les stations

de la Mortadelle (et celle d'Ampère présentant des lacunes en 2010) et de Météo France à Port-aux-Français étaient disponibles pour la fourniture de ces données. Un réseau de quatre nouvelles stations météorologiques (réseau LEFE-KCRUMBLE) a donc été mis en place par mes soins lors de la seconde campagne de terrain en 2012. Ces stations Campbell Scientific CR200 (Figure 2.7) enregistrent les moyennes demi-horaires de température et humidité de l'air à 2 m, de direction et vitesse du vent à 2 m, et de précipitations. Le Tableau 2.2 présente les caractéristiques des différents capteurs et des données enregistrées. La position des différentes stations météorologiques dont je dispose est illustrée dans la figure 2.8, ainsi que les valeurs de température moyenne et précipitations cumulées enregistrées sur une période commune de mesure du 15 février au 9 juillet 2012.

FIGURE 2.7 – Station météorologique CR200 et pluviomètre du réseau LEFE-KCRUMBLE installés sur le site de Sourcils Noirs (Photo : Nina Marchand).

TABLE 2.2 – Caractéristiques des capteurs installés sur les stations météorologiques du réseau LEFE-KCRUMBLE : Nom, Données mesurées, Précision (selon la notice du fabricant) et Hauteur de mesure

Nom	Données	Précision	Hauteur
Anémomètre Young 05103	Vitesse du vent	± 0.3 m s^{-1}	2 m
	Direction du vent	$\pm 3^{\circ}$	
CS215	Température de l'air	± 0.9 °C	2 m
	Humidité relative	$\pm 4\%$	
Pluviomètre CS ARG100	Hauteur de précipitations	$\pm 8\%$	1 m

Afin d'implanter ces stations sur des sites intéressants, la modélisation régionale au moyen du modèle MAR (voir Section 2.4.3) m'a permis de réaliser des cartes distribuées de température et de précipitations. La Figure 2.9 montre les sorties de température moyenne de surface et de précipitations cumulées du modèle au cours de l'année 2012. Les sites Kcrumble ont ainsi été choisis de façon à représenter la variabilité spatiale des températures et précipitations. En effet les sites situés à l'ouest sont légèrement plus froids qu'à l'est, mais surtout beaucoup plus humides (Figures 2.8 et 2.9). En effet, un fort effet de foehn prévaut, avec des précipitations près

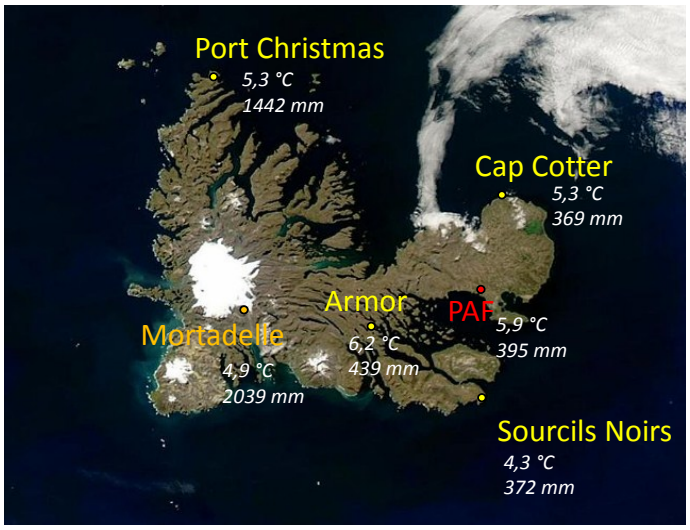

FIGURE 2.8 – Localisation des stations de la Mortadelle et de Météo France à Port-aux-Français (PAF) et des quatre stations du réseau LEFE-KCRUMBLE installées en 2012. Les valeurs de température moyenne et de précipitations cumulées mesurées aux différentes stations au cours d'une période commune de mesure (15/02/2012 au 09/07/2012) sont également présentées. L'image de fond est une image provenant de MODIS©.

de quatre fois plus importantes sur la partie occidentale de l'archipel (environ 4000 mm an^{-1} mesurés en 2012 à la station de la Mortadelle) que sur sa partie orientale (environ 900 mm an^{-1} mesurés à Port-aux-Français en 2012).

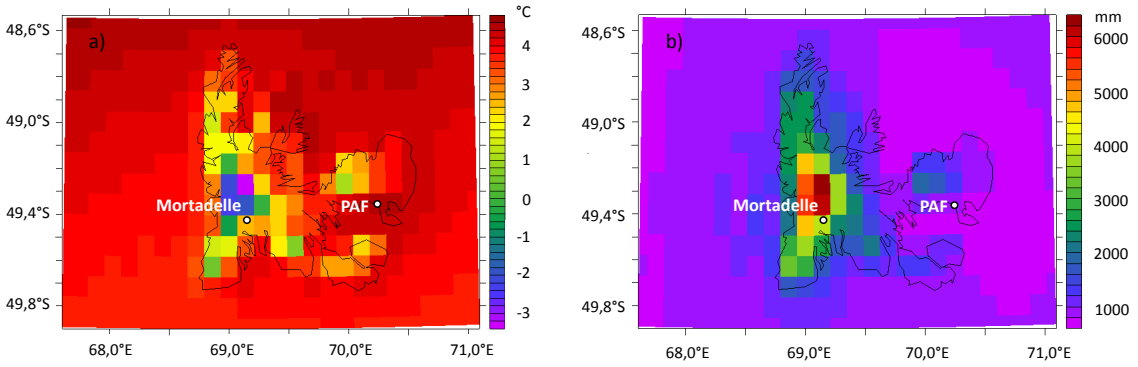

FIGURE 2.9 – Cartes distribuées de température moyenne (a) et précipitations cumulées (b) en 2012 modélisées avec le modèle MAR forcé par ERA-Interim (avec correction de +10% de l'humidité spécifique, voir Sect. 2.4.5).

2.3.2 Données spatialisées

2.3.2.1 Estimation de l'albédo de surface par télédétection

Un autre paramètre-clé pour l'étude du bilan d'énergie du surface est l'albédo de surface, c'est-à-dire la part du rayonnement incident de courtes longueurs d'onde qui est réfléchi par la surface. Celui-ci est aussi appelé albédo bolométrique ou bi-hémisphérique à bande large, c'est-à-dire intégré sur tout le spectre solaire (Dumont, 2010). Des cartes distribuées de l'albédo sur la calotte Cook ont été obtenues grâce au traitement d'images MODIS (Dumont et al., 2012), résumé ci-après. Pour cette étude, j'ai utilisé les produits MODIS Level-1B Swath (Tableau 2.3) produits par le capteur MODIS à bord de la plateforme EOS/AM-1 Terra depuis 2000. Cette plateforme circule à une altitude 105 km sur une orbite héliosynchrone quasi-polaire circulaire lui permettant de passer au-dessus de l'équateur vers 10h30 tous les matins. Les images MODIS permettent donc un échantillonnage à haute résolution temporelle (plus d'une image par jour aux îles Kerguelen) tout en offrant une résolution spatiale suffisante (250 m) pour l'étude du couvert neigeux et de la ligne d'équilibre de la calotte. D'autres produits MODIS (MOD10 et MCD43) auraient pu être utilisés dans ce but. Les produits MOD10 créés par le National Snow and Ice Data Center (NSIDC) offrent une estimation journalière de l'albédo à une résolution de 500 m spécifiquement pour les surfaces enneigées. Les produits MCD43 sont un autre produit MODIS d'albédo à 500 m, offrant des valeurs de réflectance directionnelle-hémisphérique et bihémisphérique de l'ensemble des surfaces terrestres. Cependant, les images MODIS décrites dans le Tableau 2.3 ont été préférées aux produits MOD10 et MCD43 en raison de (1) leur meilleure résolution spatiale, (2) la possibilité d'extraire différents types d'albédo (blue sky et white sky, voir Dumont et al. (2012)), (3) leur faible incertitude (Dumont et al. (2012) ont montré une différence de 0,05 entre l'albédo issu d'images MODIS et l'albédo mesuré sur le glacier de Saint-Sorlin (massif des Grandes Rousses, Alpes)) et (4) une confusion entre surfaces enneigées et nuages dans les produits MOD10 observée en Nouvelle-Zélande (Hall et al., 2002; Sirguey et al., 2009) et en Patagonie (Lopez et al., 2008).

Table 2.3 – Description des produits MODIS utilisés dans cette étude (IR : Infrarouge, SWIR : IR de courtes lognueurs d'onde, SA : sommet de l'atmosphère).

Nom	Donnée	Bande(s)	Résolution (m)	Gamme (nm)	
MOD03	Géolocation		1000		
MOD02QKM	Radiance au SA	1	250	620–670	Rouge
		2		841–876	Proche IR
MOD02HKM	Radiance au SA	3	500	459–479	Bleu
		4		545–565	Vert
		5		1230–1250	SWIR
		6		1628–1652	SWIR
		7		2105–2155	SWIR
MOD021KM	Radiance au SA	8–36	1000	variable	Thermique

Les capteurs MODIS ne fournissent pas directement des valeurs d'albédo, mais des valeurs de radiance mesurées au sommet de l'atmosphère. Un traitement des valeurs mesurées par le

capteur est donc nécessaire pour obtenir des valeurs d'albédo de surface utiles à l'estimation du bilan d'énergie de surface. La réflectance hémisphérique-conique (appelée ainsi car l'éclairement solaire de la surface provient d'une hémisphère entière tandis que le capteur MODIS ne mesure le rayonnement réfléchi que sur un cône, voir Dumont (2010)) en surface est tout d'abord estimée pour chaque bande spectrale (7 bandes dans le cas de MODIS). Cette estimation est faite grâce à un premier algorithme corrigeant les effets atmosphériques et les réflections multiples qui ont lieu sur les reliefs environnants. Un second algorithme permet ensuite de transformer la réflectance hémisphérique-conique de surface en réflectance directionnelle-hémisphérique, ou albédo spectral (correspondant à un éclairement selon une direction et une observation sur l'ensemble d'une hémisphère, voir Dumont (2010)). Un dernier algorithme permet de tranformer la réflectance directionnelle-hémisphérique en réflectance bi-hémisphérique (éclairement et observation hémisphériques, voir Dumont (2010)), puis en albédo bolométrique (c'est-à-dire une réflectance bi-hémisphérique intégrée sur l'ensemble du spectre solaire). Par la suite, pour simplifier le discours, l'albédo bolométrique sera simplement noté albédo. La détermination de l'albédo à partir d'images MODIS et son rôle dans le bilan de masse de la calotte Cook a fait l'objet d'un article qui sera présenté dans la Section 3.2.

2.3.2.2 Evaluation de la ligne de neige et de l'étendue des surfaces englacées

Les images satellites ASTER et Landsat ont une bien meilleure résolution spatiale (15 et 30 m respectivement) que les images MODIS, mais sont disponibles beaucoup moins fréquemment. J'en ai utilisées certaines pour tracer un masque de la calotte pour chaque carte d'albédo issue de MODIS et évaluer le seuil d'albédo pour la ligne de neige. Ces images sont décrites dans le Tableau 2.4. L'analyse de l'évolution de l'étendue de la calotte Cook et des variations de la ligne de neige sera présentée dans la Section 3.2.

Table 2.4 – Description des images ASTER et Landsat utilisées dans cette étude.

Satellite	Date	Référence	Résolution
ASTER	23 April 2009	SC :AST_L1A.003 :2072780070	15 m
Landsat	11 January 2001	LE71390942001011SGS00	30 m
Landsat	27 November 2001	LE71390942001331SGS00	30 m
Landsat	11 March 2005	LE71390942005070ASN00	30 m
Landsat	10 August 2008	LE71390942008223SGS00	30 m
Landsat	24 February 2011	LE71390942011055ASN00	30 m

2.3.3 Evaluation des bilans de masse

A l'échelle de l'ensemble de la calotte Cook, la soustraction de deux modèles numériques de terrain (MNTs) d'âges différents permet l'estimation des pertes de volume (méthode décrite dans la Section 2.1). En faisant des hypothèses sur l'estimation de la densité de la neige et de la glace, il est alors possible de retrouver le bilan de masse total de la calotte. Les MNTs utilisés sur l'archipel des Kerguelen sont issus (1) d'une image de la mission SRTM (Shuttle Radar Topographic Mission) en février 2000 et (2) d'un couple d'images optiques stéréo SPOT5 (Satellite Pour l'Observation de la Terre) prises en décembre 2009. Les biais systématiques horizontaux et verticaux pouvant affecter les MNTs (voir Section 2.1) ont été modelisés et

corrigés avant le calcul du BM. Les différents traitements effectués sont détaillés dans Gardelle et al. (2013). L'évaluation des pertes glaciaires et du bilan de masse de l'ensemble de la calotte Cook a fait l'objet d'un article dont je suis co-auteur et qui sera présenté dans la Section 3.3.

2.4 Modélisation

2.4.1 Réanalyses

Les réanalyses correspondent à des sorties de modèles réalisant l'assimilation de données (de température, humidité, vitesse du vent, ...). Cette dernière consiste à combiner, durant un certain cycle (généralement toutes les six heures), des observations (issues de radiosondages, bouées, satellites, etc.) avec l'information antérieure provenant de modèles de prévision, afin d'obtenir une estimation physiquement cohérente et proche de la réalité de l'état de l'atmosphère à un instant donné. La principale différence avec les analyses opérationnelles, utilisées pour la prévision météorologique à court terme, réside dans le fait que chaque réanalyse est produite avec une seule version d'un système d'assimilation de données (y compris le modèle de prévision), afin d'éviter les incohérences liées à des modifications du système d'assimilation au cours du temps. Dans le cadre de ma thèse, j'ai utilisé les données des réanalyses ERA-Interim et ERA-40 (Uppala et al., 2005; Dee et al., 2011) du Centre Européen de Prévision Météorologique à Moyen Terme, et des Réanalyses 1 et 2 (Kalnay et al., 1996; Kanamitsu et al., 2002) du NCEP-NCAR et NCEP-DOE (National Centers for Environmental Prediction, National Center for Atmospheric Research and Department of Energy). Les observations de surface et de radiosondages effectuées à Port-aux-Français sont assimilées dans ERA depuis 1967 et 1968 respectivement et dans NCEP depuis 1967 et 1970 respectivement.

Dans le cadre de cette étude, j'ai comparé les données de température, précipitations, rayonnement et couvert nuageux issues d'ERA-40, ERA-Interim, NCEP1 et NCEP2 aux observations réalisées à la station Météo France de Port-aux-Français (Sections 3.2 et 3.4). Certaines données supplémentaires telles que la hauteur du géopotentiel ont été comparées à celles issues des modèles CMIP5 (Section 2.4.2). Par ailleurs, certaines variables-clés (telles que la température ou l'humidité spécifique) d'ERA-Interim et de NCEP1 ont été utilisées pour forcer le modèle régional MAR à ses frontières (Section 2.4.3). Le Tableau 2.5 reprend l'ensemble des données issues de réanalyses utilisées au cours de cette thèse.

TABLE 2.5 – Description des données issues de réanalyses utilisées dans cette étude.

Donnée	Réanalyse(s)	Niveau	Fréquence	Utilisation
Température	Toutes	2 m	Mensuel	Comparaison PAF, CMIP5
	ERA-40	Surface (skin T)	Mensuel	Tendance T2m - Tskin
	ERA-Int, NCEP1	Tous	6 h	Forçage du MAR
	ERA-Int, NCEP1	Surface océan (SST[1])	6 h	Forçage du MAR
Précipitations	Toutes	-	Mensuel	Comparaison PAF, CMIP5
Rayonnement SW	Toutes	Surface	Journalier	Comparaison PAF
Rayonnement LW	Toutes	Surface	Journalier	Intercomparaison
Couvert nuageux	Toutes	Tous (total)	Mensuel	Comparaison CMIP5
Humidité	ERA-Int, NCEP1	Tous	6 h	Forçage du MAR
Vent (U, V)	ERA-Int, NCEP1	Tous	6 h	Forçage du MAR
Pression atm.	ERA-Int, NCEP1	Tous	6 h	Forçage du MAR
Géopotentiel	ERA-40, NCEP1	500, 700hPa	Mensuel	Comparaison CMIP5
Glace de mer[2]	ERA-Int, NCEP1	Surface	6 h	Forçage du MAR

[1]Sea Surface Temperature.
[2]Concentration en %. La glace de mer n'est jamais présente à la latitude des îles Kerguelen.

2.4.1.1 NCEP

Les données des Réanalyses 1 du NCEP-NCAR (NCEP1) sont disponibles depuis 1948 jusqu'à aujourd'hui (Kalnay et al., 1996). Le modèle utilisé produit des données toutes les six heures à une résolution spectrale T62 ($\sim$ 210 km) et selon 28 niveaux verticaux (situés entre 5 hPa au-dessus de la surface et 3 hPa). Un schéma d'assimilation (variationnel-3D) séquentiel avec un cycle de six heures est employé. Les Réanalyses 2 du NCEP-DOE (NCEP2) constituent un nouveau jeu de données depuis 1979 jusqu'à aujourd'hui, dans lequel certaines erreurs de NCEP1 ont été corrigées (erreur de localisation des observations, problème de couvert neigeux, d'albédo océanique, ...) et la physique du modèle a été améliorée (changements concernant l'humidité du sol, la couche limite, les courtes longueurs d'onde, les nuages, ...) (Kanamitsu et al., 2002).

2.4.1.2 ERA

Les réanalyses ERA-40 utilisent un modèle différent de NCEP1 & 2, et couvrent la période de 1957 à 2002 (Uppala et al., 2005). Elles emploient également un schéma d'assimilation variationnel-3D avec un cycle de six heures pour produire des données à une résolution spectrale T159 ($\sim$ 125 km) et selon 60 niveaux verticaux (de la surface jusqu'à 0,1 hPa). ERA-Interim fournit des données de réanalyses depuis 1979, utilisant un schéma d'assimilation plus avancé (variationnel-4D, cycle de 12h) et une nouvelle version du modèle de prévision (Dee et al., 2011). Sa résolution est meilleure que celle d'ERA-40 (résolution T255 correspondant à $\sim$ 80 km) et la physique du modèle a également été améliorée.

2.4.2 Modèles CMIP5

Au cours de cette thèse, j'ai analysé les sorties de température atmosphérique, précipitations, couvert nuageux et hauteur de géopotentiel des modèles CMIP5 (Coupled Model Intercomparison Project 5). CMIP5 (Taylor et al., 2012) rassemble vingt groupes d'étude du climat, qui ont réalisé deux grands types d'expériences :

1. Des simulations à court-terme (10 à 30 ans), forcées par des observations océaniques et de glace de mer.
2. Des simulations à long terme (à l'échelle du siècle) utilisant des modèles globaux de climat couplés océan-atmosphère (AOGCMs, parfois couplés à un modèle de cycle de carbone) initialisés à partir de résultats de simulations sur la période pré-industrielle.

Pour l'analyse des tendances climatiques récentes (deuxième moitié du 20^{e} siècle), j'ai utilisé les sorties de simulations historiques (issues de l'expérience long terme). Pour l'estimation des tendances futures, j'ai utilisé les sorties des projections à long terme CMIP5 (2006 à 2100). Celles-ci sont produites en forçant les différents AOGCMs avec des concentrations spécifiques de gaz à effet de serre correspondant à différents scénarii appelés RCPs (Representative Concentration Pathways). Quatre RCPs ont été définis (RCP 2.6, 4.5, 6 et 8.5), faisant référence à différentes valeurs de forçage radiatif attendu à la fin du 21^{e} siècle (Moss et al., 2010).

L'ensemble des modèles CMIP5 analysés dans cette étude est repris dans l'Annexe B. Dans les sections 3.3 et 3.5, j'analyse les sorties récentes et futures de chaque modèle CMIP5 ainsi que de la moyenne multi-modèles (MMM).

2.4.3 Modèle Atmosphérique Régional (MAR)

Le Modèle Atmosphérique Régional (MAR) est un modèle climatique développé à l'Université Catholique de Louvain (Belgique), couplé à un schéma de surface (1D) nommé SISVAT (Soil Ice Snow Vegetation Atmosphere Transfer) au travers de l'échange des flux d'énergie (Figure 2.10). Ce modèle atmosphérique à aire limitée (LAM) simule l'atmosphère en résolvant complètement l'équation de continuité (Gallée and Schayes, 1994). Il s'agit d'un modèle hydrostatique aux équations primitives utilisant les coordonnées sigma de pression :

$$\sigma = \frac{p - p_t}{p_s - p_t}, \tag{2.4}$$

où p est la pression atmosphérique, p_t est la pression constante au sommet du modèle et p_s est la pression de surface. L'équation de conservation de la masse est écrite dans sa forme compressible, donc sans approximation. Dans le cas de mes simulations, le MAR présente 23 niveaux sigma allant de 0,11 (environ 15km d'altitude) à ∼1 (3 m au-dessus de la surface). Les flux sous-maille sont résolus grâce à l'utilisation du modèle de fermeture de Duynkerke (1988) (modèle K-ϵ), qui permet à la longueur de mélange turbulent d'être définie comme fonction des caractéristiques locales du flux. Un modèle de microphysique nuageuse est également inclus, utilisant les équations de conservation des concentrations en gouttelettes de nuages, gouttes d'eau, cristaux de glace nuageux et cristaux de neige basées sur Kessler (1969) et Lin et al. (1983). Le schéma convectif de Bechtold et al. (2001) est également employé. Les schémas radiatifs utilisés sont basés sur Fouquart and Bonnel (1980) pour le solaire et Morcrette (2002) pour l'infra-rouge (schémas utilisés initialement dans le modèle du Centre Européen de Prévision Météorologique à Moyen Terme). Les équations constitutives du modèle MAR sont présentées en détail dans Gallée and Schayes (1994).

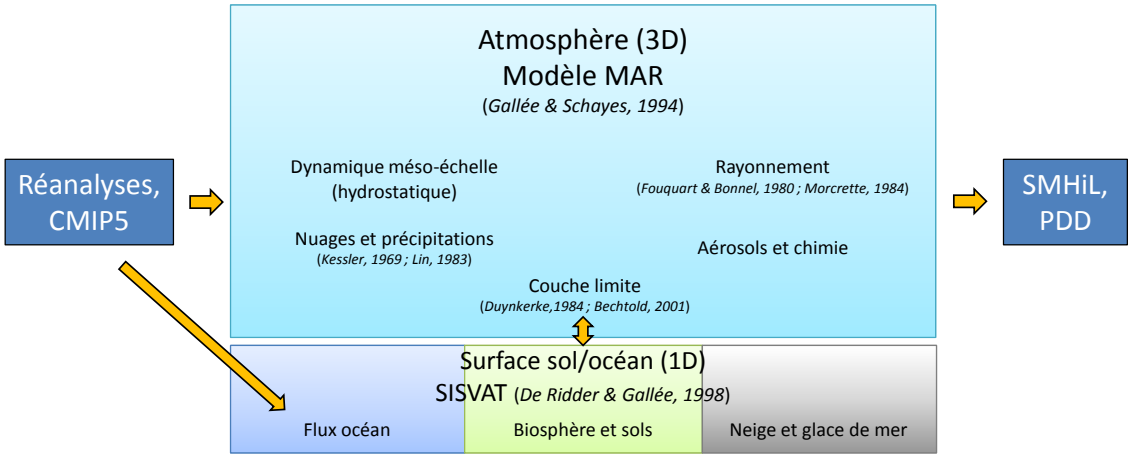

FIGURE 2.10 – Schéma décrivant les différents composants du modèle MAR (adapté d'une présentation de X. Fettweis, 2012).

Le schéma de surface SISVAT (De Ridder and Gallée, 1998; Gallée et al., 2001) détermine les échanges entre les différents composants de la surface. Un module de végétation et sol ainsi qu'un module de neige et glace sont présents dans SISVAT. Dans le cadre des îles Kerguelen,

dépourvues d'arbres, la seule végétation considérée est la toundra. Les pixels peuvent donc être recouverts de manière fractionnaire de neige ou glace, de sol nu, de toundra ou d'eau (océan ou lacs). Le module décrivant la neige et la glace dans SISVAT a été développé par Gallée and Duynkerke (1997), Gallée et al. (2001) et Lefebre et al. (2002). Il s'agit d'un modèle multicouches qui détermine les échanges entre la surface de la calotte, la glace de mer (non présente aux îles Kerguelen), la toundra couverte de neige et l'atmosphère. La partie sol - végétation utilisée pour la toundra a été développée par De Ridder and Gallée (1998). SISVAT prend en compte l'écoulement de l'eau et son regel dans le manteau neigeux, la fermeture des pores dans le névé et l'écoulement de l'eau de fonte sur la glace et son influence sur l'albédo. La conduction de chaleur au sein de la neige est basée sur la formulation de Yen (1981), qui dépend de la masse volumique de la neige. La paramétrisation du métamorphisme de la neige est quant à elle basée sur le modèle CROCUS développé au Centre d'Étude de la Neige (Brun et al., 1992), ce qui permet une représentation fine de l'albédo de surface qui dépend de la forme et de la taille des grains de neige. Les flux turbulents sont calculés selon la théorie des similitudes de Monin and Obukhov (1954) en utilisant les relations entre flux et gradients de Duynkerke and van den Broeke (1994).

Le modèle MAR est forcé à ses frontières par des champs météorologiques (température, humidité, vents, pression) issus de réanalyses ou de modèles grande échelle tels que les modèles CMIP5 (voir Section 2.4). L'archipel des Kerguelen constitue un objet d'étude idéal pour la modélisation régionale, parce qu'il est entouré d'océan. En effet, le fait de placer les frontières latérales du domaine au-dessus de l'océan permet d'éviter les problèmes d'extrapolation et de génération de bruit liés à une topographie complexe aux frontières ainsi que les calculs non réalistes du BES aux frontières (Giorgi and Mearns, 1999). La topographie est issue du modèle topographique global ETOPO1 (résolution 1 arc-minute, Amante and Eakins (2009)), qui fournit une meilleure représentation de la topographie des îles Kerguelen que d'autres modèles de topographie tels qu'ETOPO5 ou GTOPO30. La création de la grille du MAR, la préparation des champs de forçage de grande échelle (champs météorologiques et topographie) pour le modèle MAR et leur initialisation au début de la simulation sont réalisés par une première composante du modèle appelée NESTOR (NESTing Organization for the preparation of meteorological and surface fields in Regional models). Le MAR à proprement parler est ensuite lancé à une résolution de 10 km (limite inférieure de validité de l'approximation hydrostatique, voir Giorgi and Mearns (1999)), sur un domaine de 80 x 80 mailles (soit 800 x 800 km) centré sur les îles Kerguelen.

2.4.4 Désagrégateur SMHiL

Le désagrégateur SMHiL (Surface Mass balance High resolution downscaLing) a été présenté en détail dans les thèses de Gential (2007) et Agosta (2012) ; la présentation réalisée ici sera donc assez succincte. SMHiL est un modèle de désagrégation des précipitations et des bilans d'énergie utilisant des champs atmosphériques de grande échelle issus de réanalyses, de GCM ou de modèles régionaux (tels que le MAR) pour estimer les différentes composantes du BMS à plus haute résolution. La prise en compte par SMHiL de la topographie à haute résolution permet d'évaluer son influence sur les précipitations solides et liquides, la sublimation, la fonte de surface et le regel (le dépôt et l'érosion par le vent ne sont par contre pas pris en compte). Le fonctionnement de SMHiL est repris dans la Figure 2.11. Deux types d'interpolation sont utilisées pour passer de la grande échelle (le MAR dans notre cas) à la plus fine échelle du modèle SMHiL, et sont présentées dans Agosta (2012). Le désagrégateur est composé de deux

parties qui sont utilisées à la suite l'une de l'autre :

1. Un désagrégateur de précipitations (s'appuyant sur les travaux de Sinclair (1994) et Funk and Michaelsen (2004)) qui calcule l'effet de la topographie fine sur les précipitations solides et liquides
2. Un schéma de surface (SISVAT, utilisé dans le MAR) forcé par les champs météorologiques de grande échelle (MAR) interpolés sur la grille de SMHiL et par les précipitations désagrégées précédemment calculées. Cette deuxième partie du modèle permet de calculer la sublimation, la fonte et le regel à haute résolution.

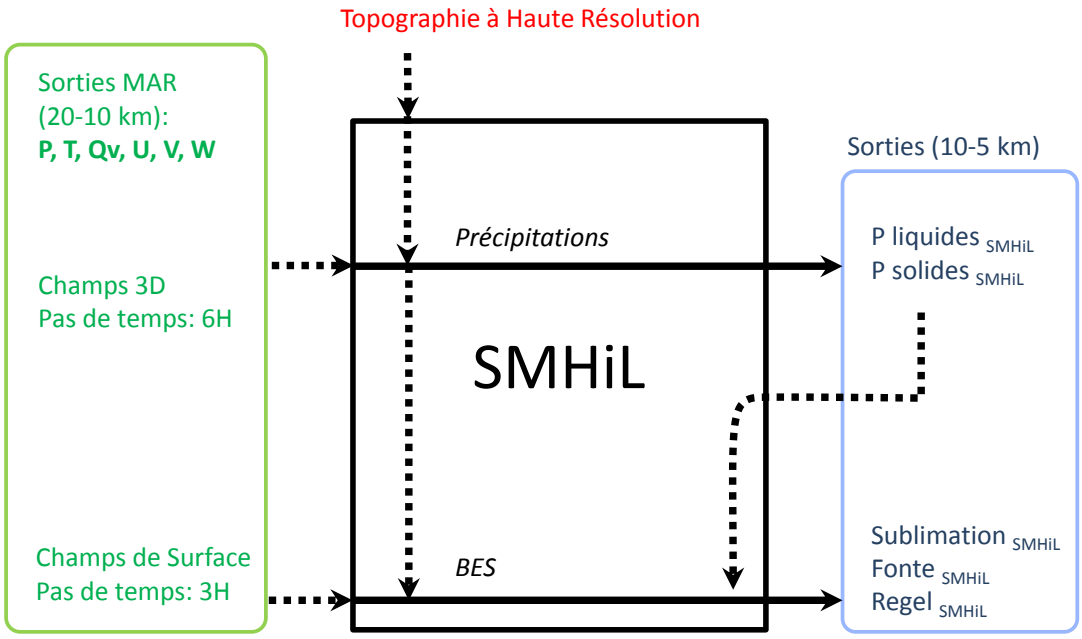

FIGURE 2.11 – Schéma décrivant le fonctionnement du modèle SMHiL. D'après une présentation de Cécile Agosta (2012).

Dans le cadre de cette thèse, j'ai très peu modifié le modèle SMHiL. Celui-ci étant initialement utilisé sur l'Antarctique, je me suis contentée de l'adapter au nouveau domaine des îles Kerguelen. Parmi les différences notables apportées par rapport au cas de l'Antarctique, la réalisation des calculs aux îles Kerguelen a demandé :

1. Le changement de la projection utilisée (passage de la projection stéréographique à la projection UTM 42S)
2. L'utilisation de la topographie issue de SRTM (Shuttle Radar Topography Mission) à 125 m de résolution
3. La suppression de la rotation des vecteurs de vent (qui était effectuée pour désagréger les champs du MAR sur l'Antarctique).

Seul le désagrégateur de précipitations a été utilisé dans ce travail afin d'évaluer l'impact du changement d'échelle sur les précipitations aux îles Kerguelen. Trois simulations SMHiL ont été réalisées sur l'année 2011, passant d'une résolution de 20 à 10 km, 10 à 5 km et 20 à 5 km.

La comparaison entre les sorties de précipitations de SMHiL et du MAR sera présentée à la Section 3.6.3.

2.4.5 Simulations réalisées avec les modèles MAR et SMHiL

Le but des simulations MAR et SMHiL réalisées durant ma thèse était d'évaluer la distribution spatiale des différentes variables climatiques (précipitations, température, vent et humidité) et d'évaluer le BMS de la calotte Cook et son évolution au cours des dernières décennies, mais aussi durant les cent prochaines années. Pour ce faire, dans un premier temps, des simulations MAR multidécennales à 10 km de résolution forcées par les réanalyses ERA-Interim (1980-2014) et NCEP1(1950-2014) ont été réalisées. En raison des différences importantes entre les réanalyses ERA-40 (1957-2002) et ERA-Interim (en terme d'assimilation de données et de résolution, voir Section 2.4.1.2), il n'est pas possible de réaliser des sorties cohérentes en forçant le MAR par ERA-40 suivi d'ERA-Interim. Nous avons donc choisi de n'utiliser qu'ERA-Interim afin de couvrir la période actuelle. NCEP1 a quant à lui été choisi afin d'obtenir des sorties plus anciennes (depuis les années 50), mais tout de même cohérentes jusqu'à la période actuelle. Ces sorties du modèle MAR ont ensuite été évaluées par rapport aux données météorologiques disponibles aux îles Kerguelen (ci-dessous, dans la Sect. 3.6.2). Afin de tester les performances de SMHiL en termes de représentation spatiale et temporelle des précipitations aux îles Kerguelen, une comparaison avec les sorties MAR à différentes échelles est présentée ci-dessous (Sect. 3.6.3) pour l'année 2011. Finalement, pour ce qui est des prévisions futures, les champs de température, précipitation et vitesse du vent de l'ensemble des modèles CMIP5 ont été évalués par rapport à ceux d'ERA-Interim (Sect. 3.5.3) sur la période récente. Pour des raisons de temps de calcul, il n'est pas possible de forcer le MAR avec chaque modèle CMIP5. Le modèle le plus proche d'ERA-Interim (ACCESS1-3, 1975-2005 et 2006-2100), ainsi que les deux modèles présentant les comportements les plus extrêmes (GFDL-CM3 et MRI-CGCM3, 1955-2005 et 2006-2100) ont donc été utilisés pour le forçage du MAR sur la période récente (évaluation de leur climatologie par rapport à ERA-Interim) et sur le siècle prochain (projections futures avec scénario RCP8.5).

2.4.6 Modélisation des pertes glaciaires

Un modèle simple distribué des pertes glaciaires a été développé de façon à reproduire les étendues englacées de la calotte Cook. Celui-ci est constitué d'un modèle degré-jour basé sur Hock (2003) servant à déterminer le BMS distribué sur la calotte, couplé à un automate cellulaire (Harper and Humphrey, 2003) qui permet de simuler l'écoulement glaciaire.

2.4.6.1 Modèle degré-jour

Le modèle degré-jour employé permet de calculer l'ablation journalière de neige ou de glace $A_{\mathrm{j}}(z)$ à une altitude z donnée, et au pas de temps j (Hock, 2003) :

$$A_{\mathrm{j}}(z) = F(T_{\mathrm{j}}(z_{\mathrm{ref}}) + a(z - z_{\mathrm{ref}})) \quad \text{si} \quad T_{\mathrm{j}}(z_{\mathrm{ref}}) + a(z - z_{\mathrm{ref}}) > 0 \tag{2.5}$$

$$A_{\mathrm{j}}(z) = 0 \quad \text{si} \quad T_{\mathrm{j}}(z_{\mathrm{ref}}) + a(z - z_{\mathrm{ref}}) \leq 0, \tag{2.6}$$

où F est le facteur de degré-jour et $T_{\mathrm{j}}(z)$ est la température moyenne journalière. L'épaisseur de neige au pas de temps précédent est $S_{\mathrm{j\text{-}1}}(z)$. Le modèle prend en compte différents facteurs de degré-jour selon la présence ou non de neige à la surface. De la neige est présente si $S_{\mathrm{j}}(z) > 0$.

Le couvert neigeux résulte de la différence entre ablation et accumulation de neige à une altitude z. Des précipitations solides sont considérées si la température de l'air passe en-dessous d'un certain seuil ($T_{\text{snow/rain}} = 1{,}0^{\circ}\text{C}$), sinon la quantité de précipitations solides est nulle. La température aux différentes altitudes est calculée par rapport à la température à Port-aux-Français (altitude de référence z_{ref}) en considérant un gradient de température a constant avec l'altitude, mais qui varie selon l'orientation (azimuth) des glaciers. Les différentes valeurs de a (entre -0,0071 $^{\circ}$C m^{-1} et -0,0087 $^{\circ}$C m^{-1}) ont été déterminées à partir de sorties de température du modèle MAR (Section 2.3.1.3, Figure 2.9 a). Les sorties de précipitations du MAR (Figure 2.9 b) ont également été utilisées afin de déterminer la répartition spatiale des pécipitations. Il existe une forte corrélation entre les précipitations et l'altitude, même si le modèle MAR sous-estime les précipitations à la Mortadelle en raison de l'emplacement du site dans un corridor étroit qui présente des quantités de pécipitations spécifiques. Cette relation entre altitude et précipitations a été utilisée pour représenter les quantités de précipitations aux différentes altitudes du modèle degré-jour.

Dans le modèle degré-jour, la disparition du névé est prise en compte (ce phénomène est discuté dans la Section 3.2). Pour représenter l'épaisseur du névé, l'épaisseur de neige est limitée à une valeur maximale de 15 m équivalent eau (eq. e.) ; si $S_{\text{j}}(z)$ dépasse cette limite, on considère que l'excès est transformé en glace. Des tests de sensibilité ont été effectués concernant l'impact de l'épaisseur de la couche de névé sur le profil à l'équilibre du glacier Ampère (voir Section 3.2).

Les facteurs de degré-jour ont été calibrés avec les mesures réalisées aux balises et une sonde à ultrasons installée sur la zone d'ablation du glacier (à côté de la station météorologique d'Ampère lorsqu'elle est positionnée sur le glacier, voir Figure 2.5). L'ablation modélisée a également été comparée à des estimations de BES réalisées à partir de données des stations météorologiques d'Ampère et de la Mortadelle, entre le 21 décembre 2010 et le 4 janvier 2011 (période durant laquelle la station météorologique d'Ampère est positionnée sur le glacier). Le détail du calcul de BES, qui résoud l'équation 2.1 est repris dans l'Annexe F. Cette modélisation du BES permet de reproduire l'ablation mesurée aux balises et à la sonde à ultrasons (voir Figure S2 des supp. mat. de Favier et al. (in review), Annexe F). La comparaison entre les valeurs d'ablation déterminées par le modèle degré-jour et le modèle de BES permet de calibrer les facteurs de degré-jour F pour la neige et la glace. Cette calibration suggère que

$$F = F_{\text{glace}} = 7,4 \text{ mm } ^{\circ}\text{C}^{-1} \text{ jour}^{-1} \quad \text{si} \quad S_{\text{j-1}}(z) = 0. \tag{2.7}$$

La facteur de la glace F_{glace} est très proche de la valeur moyenne de Radić and Hock (2011), i.e. $F_{\text{glace}} = 7{,}2$ mm $^{\circ}$C^{-1} jour^{-1}. Pour la neige, la calibration ne s'appuie que sur 5 jours de couvert neigeux, entraînant une grande incertitude concernant ce paramètre. Comme la valeur de F_{glace} calibré est très proche de la valeur moyenne de Radić and Hock (2011), nous avons choisi d'utiliser la valeur moyenne de F_{neige} issue de Radić and Hock (2011) dans notre degré-jour :

$$F = F_{\text{neige}} = 4,9 \text{ mm } ^{\circ}\text{C}^{-1} \text{ jour}^{-1} \quad \text{si} \quad S_{\text{j-1}}(z) > 0. \tag{2.8}$$

2.4.6.2 Automate cellulaire

Un automate cellulaire (Harper and Humphrey, 2003) a été couplé au modèle degré-jour afin de simuler l'écoulement de la glace depuis les altitudes élevées jusqu'au front glaciaire. Cette méthode a été largement utilisée auparavant dans différentes études paléoclimatiques (Blard et al., 2007; Jomelli et al., 2011). Le modèle considère la glace comme un matériau plastique se déplaçant par avalanches et par déformation/glissement. Le mouvement de la glace est pris en

compte en considérant une contrainte de cisaillement basal constante de 1 bar (Nye, 1951). Le mouvement est opéré de manière discrète sur une grille hexagonale, permettant six directions cardinales de mouvement différentes. L'écoulement est ensuite largement contrôlé par la pente locale. Le flux de glace est déterminé par la conservation de la masse et les vitesses sont dérivées de ce flux, étant de ce fait fortement reliées à l'idée de vitesse d'équilibre. Il est cependant important de noter que le modèle représente mal les vitesses d'écoulement, et n'est donc pas approprié pour l'analyse des temps de réponse glaciaires ou des régimes glaciaires transitoires. Les simulations ont été effectuées sur une période de 200 ans afin de s'assurer que la calotte Cook soit en équilibre avec les conditions climatiques. Le résultat de la modélisation des pertes sera présenté dans la Section 3.3.

Chapitre 3

Résultats

3.1 Etendue passée des glaciers sur l'archipel

3.1.1 Motivations et principaux résultats

La chronologie de la déglaciation des îles subantarctiques au cours du Quaternaire a fait l'objet d'un article (Hodgson et al., 2014, voir Annexe C) auquel j'ai été associée et dont un extrait concernant les îles Kerguelen est présenté ci-dessous. Cet article constitue l'un des chapitres détaillés d'un compte-rendu plus large concernant la déglaciation de l'ensemble de la zone antarctique depuis le Dernier Maximum Glaciaire (Bentley et al., 2014, voir Annexe D).

L'histoire glaciaire des îles Kerguelen est relativement peu connue. Au dernier maximum glaciaire (il y a -20 000 ans environ, LGM : Last Glacial Maximum dans l'article ci-dessous), on ne sait pas exactement si l'archipel était ou non entièrement recouvert de glace. Au cours de l'Holocène, grâce à la datation de moraines et de tourbes, on sait que les glaciers ont subi de multiples retraits et avancées en réponse aux changements du climat. Plus récemment, après une période relativement stable de 1799 à 1965 (Frenot et al., 1993), les glaciers de l'archipel ont reculé de manière spectaculaire, perdant environ 20% de leur surface en 40 ans (Berthier et al., 2009). Ce recul au cours des dernières décennies ainsi que l'évolution future des étendues glaciaires aux îles Kerguelen fait l'objet de la suite de cette thèse.

3.1.2 Extrait de l'article Hodgson et al. (2014)

Terrestrial and submarine evidence for the extent and timing of the Last Glacial Maximum and the onset of deglaciation on the maritime-Antarctic and sub-Antarctic islands

D.A. Hodgson et al., 2014, Quaternary Science Reviews, 100, 137-158.

3.2.3. The Kerguelen Islands

The Kerguelen Islands (48°30'S, 68°27'E and 50°S, 70°35'E) consist of a main island (7200 km^2) surrounded by numerous smaller islands of mostly ancient (39-17 Ma) volcanic origin. The main island is characterised by mountains up to 1850 m (Mt Ross), the large 403 km^2 (in 2001) Cook Ice Cap on Le Dome (1049 m), and several glaciers on the western part of the island (Fig. 7). The eastern part of the island is generally of lower relief, but includes widespread evidence of glacial striations, glacial outwash and glacial moraines (Quilty, 2007).

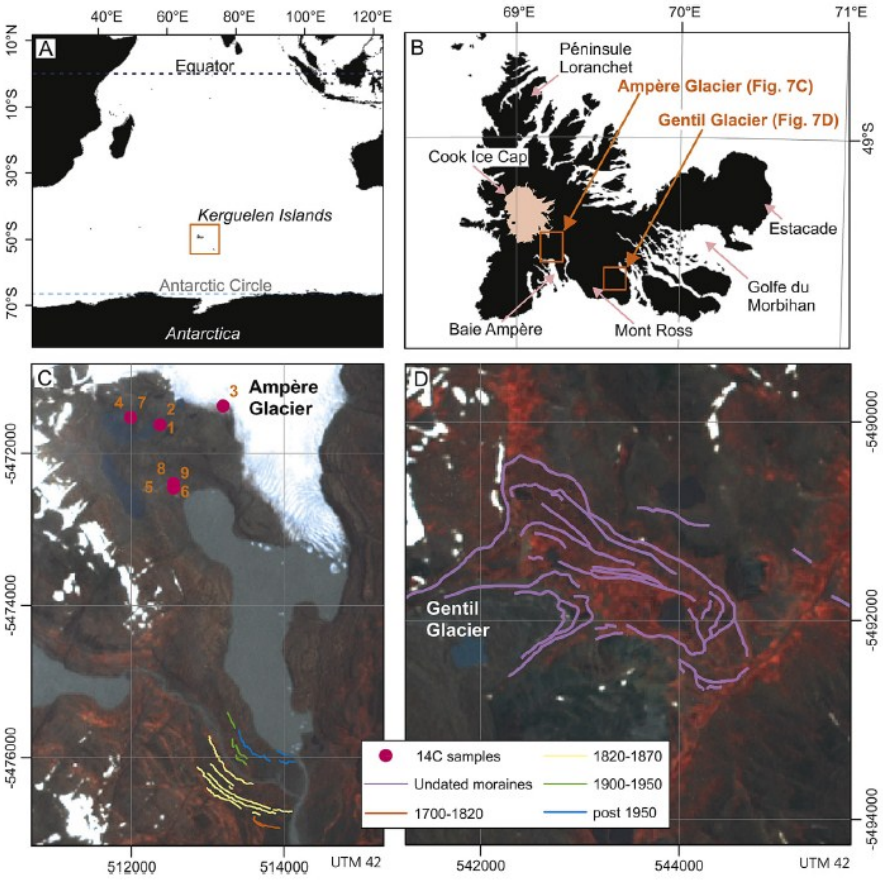

Fig. 7. (A) Location of the Kerguelen Islands. (B) Location of glaciological investigations at the Ampère Glacier and the Gentil Glacier. (C) The Baie d'Ampère showing the location of the 9 radiocarbon dated peat deposits listed in Table 1[1], and more recent moraines post AD 1700. (D) The Gentil Glacier frontal and lateral moraines at the base of Mont Ross that predate AD 934 ± 46 (1016 cal yr BP) based on the absence of a diagnostic ash layer from the Allouarn Volcano (Arnaud et al., 2009).

[1]présentée en Annexe C

Despite being one of the sub-Antarctic islands that remain partially glaciated, there is remarkably little information on the Quaternary glacial history of the Kerguelen Islands. Some studies have suggested that the main island may have been completely covered at the LGM (Hall, 1984) ; an interpretation at least partly supported by the presence of numerous ice-scoured lake basins (Heirman, 2011), U-shaped valleys radiating from the Cook Ice Cap, deeply-incised fjords and the lack of terminal moraines, which implies that ice may have extended offshore (Bellair, 1965). However, other studies have suggested that the LGM glaciation was limited (Nougier, 1972), and this is supported by the absence of present day isostatic rebound (Testut et al., 2006). This latter theory suggests that glaciers were restricted to the central plateau and to the east and south west where there are glacial erratics, aeolian sands, depressions filled with peat, gelifraction soils and moraine complexes, as well

as residual valley glaciers and cirques. Conversely, in the north the highly degraded morphology of the moraines in the Loranchet Peninsula and the near absence of glacial erratics has been interpreted as evidence of more ancient glaciation (Nougier, 1972).

There are no chronological constraints on maximum glacier extent at the LGM. However, there are reliable minimum bulk radiocarbon ages for deglaciation from peat deposits at Estacade, the Golf du Morbihan (Young and Schofield, 1973a), and the Baie d'Ampère (Fig. 7B), and geomorphological observations on the Gentil glacial moraines at the base of Mont Ross (Fig. 7D). The oldest peat deposit at Estacade dates from 15,396-6,624 cal yr BP (Van der Putten et al., 2010) and at the Golfe du Morbihan from 12,765-13,241 and 9141-9912 cal yr BP (Young and Schofield, 1973a,b). In the Baie d'Ampère the recent (post 1990 AD) retreat of the front of Ampère glacier has re-exposed a series of early Holocene peat deposits (Frenot et al., 1997). One group provides minimum ages for deglaciation between 13,241 and 11,212 cal yr BP (Table 1, sample numbers 1-3, Fig. 7C). These can be clearly separated from later periods of Holocene glacial retreat from 5054-5188 cal yr BP (Table 1, sample number 4, Fig. 7C), and 2208 to 716 cal yr BP (Table 1, sample numbers 5-9, Fig. 7C) that may correspond to warm periods inferred from peat deposits (e.g., Young and Schofield (1973a)). Other older frontal and lateral moraines associated with the Gentil Glacier have been identified at the base of Mont Ross (Fig. 7D). It is not known if these date from the LGM, but they must predate AD 934 $\pm$ 46 (1016 cal yr BP) based on the absence of a diagnostic ash layer from the Allouarn Volcano (Arnaud et al., 2009). In terms of maximum ice thickness, erosional evidence produced by the ice flow on rock cliffs on both sides of the valley above Lac d'Ampère reveal that the surface of the glacier was about 150 m higher than today during the maximum Holocene extent. Whether this is equivalent to the LGM ice thickness is not known. The lack of remains of lateral or frontal moraines on the slopes of both sides of the valley may indicate that previous Holocene glacial extents were smaller than those of the last millennium or that at its maximum the glacier reached positions in the fjord that are submerged offshore today. The possibility that cold-based, generally non-erosive glaciers, were present at the LGM has not yet been considered in the literature. Collectively, the evidence from the moraines suggests that the Kerguelen glaciers are highly sensitive to climate changes and that various Holocene ice advances may have approached LGM ice maxima. For example, various studies have shown that the Ampère Glacier has advanced and retreated up to 3.8 km from its 2010 front position on multiple occasions in the late Holocene (Frenot et al., 1993; Frénot et al., 1997; Arnaud et al., 2009).

Recent glacier retreat has been documented from the first half of the 20th century (Aubert De La Rue, 1967; Vallon, 1977a) and the total ice extent on Kerguelen Islands declined from 703 to 552 km^2 between 1963 and 2001, with the Cook Ice Cap retreating from 501 to 403 km^2 in the same period (Berthier et al., 2009). Current rapid deglaciation at the Kerguelen Islands is exceptional (Cogley et al., 2010) and possibly linked to increased temperature (Frenot et al., 1993; Frénot et al., 1997; Jacka et al., 2004), and decreased precipitation since AD 1960 (e.g., Frenot et al. (1993); Frénot et al. (1997); Berthier et al. (2009). An alternative hypothesis is that the retreat is related to migration of the sub-Antarctic convergence from the north to the south of the Kerguelen Islands around AD 1950 (Vallon, 1977a).

3.2 Analyse de l'albédo de surface et de la ligne de neige

3.2.1 Motivations et principaux résultats

Dans la section précédente, nous avons rapidement abordé les variations passées des étendues glaciaires aux îles Kerguelen, montrant que celles-ci ont fluctué depuis le dernier maximum

glaciaire. Le retrait récent (depuis les années 60) des glaciers de l'archipel a cependant été particulièrement rapide, et semble lié à des variations de température et/ou de précipitations (Frenot et al., 1993; Berthier et al., 2009). Dans cette section, nous analysons le retrait récent de la calotte Cook au travers de l'étude de son étendue et de sa ligne de neige. Cette dernière peut en effet servir d'indicateur de l'état de santé des glaciers en fin de saison d'ablation (Rabatel et al., 2012), où elle se confond avec leur ligne d'équilibre (ELA, voir Section 2.1).

La position de la ligne de neige transitoire (et de la ligne de névé transitoire, Section 2.1) est déterminée grâce à l'étude de cartes d'albédo de surface issues du traitement d'images MODIS. Celle-ci révèle que la ligne d'équilibre actuelle de la calotte Cook est située à plus de 800 m d'altitude. Ces cartes d'albédo permettent également de calculer l'AAR pour les dates d'acquisition des images MODIS, ce qui nous fournit une indication supplémentaire de l'état de santé de la calotte, révèlant que l'AAR a diminué d'environ 20% depuis 2000. Les altitudes de ligne de neige et de névé observées sont ensuite comparées aux valeurs estimées grâce à un modèle degré-jour (PDD, voir Section 2.4.6.1), confirmant leur remontée (environ 30 m depuis 2000 et 100 m depuis les années 70).

Ce dernier permet également de modéliser le BMS du glacier Ampère à partir de mesures de température et précipitations réalisées à Port-aux-Français depuis 1950, BMS qui peut ensuite être comparé au BMS mesuré dans les années 70 et en 2010-2011 grâce à la méthode glaciologique (Section 2.1). Le PDD représente bien les variations spatiales du BMS et son évolution avec l'altitude. Cependant, on se rend compte que les valeurs de BMS divergent de plus en plus d'une représentation classique linéaire selon l'altitude, et que les balises à haute altitude présentent des valeurs de BMS beaucoup plus négatives que ce à quoi l'on pourrait s'attendre, causées par la disparition du couvert neigeux et sa rétroaction sur la fonte de surface.

Pour estimer la part relative des différents termes du bilan d'énergie dans l'ablation de surface, le BMS ponctuel au niveau des balises est également estimé à partir des valeurs d'albédo fournies par MODIS et d'une évaluation des précipitations solides sur la calotte. Il révèle l'importance du rayonnement de courtes longueurs d'onde dans le bilan d'énergie de la calotte au travers de l'albédo de surface, qui est confirmée par les résultats d'un modèle de bilan d'énergie de surface. Cependant, certaines zones de la calotte Cook ne sont pas correctement représentées dans notre modèle de bilan d'énergie car elles subissent une suraccumulation de neige liée au dépôt éolien (visible sur le terrain et sur les images satellites).

Finalement, l'analyse des données climatiques de la station de Port-aux-Français ainsi que le modèle PDD révèle que la diminution marquée des précipitations sur l'archipel depuis les années 70 semble être la cause principale de la disparition du couvert neigeux, qui est ensuite amplifiée par le réchauffement atmosphérique.

Ce travail a fait l'objet d'un article soumis à *Journal of Geophysical Research*, présenté ci-dessous. Les données et méthodes ayant déjà été présentées dans la Section 2, afin d'éviter les répétitions, seuls le résumé (abstract), les résultats et la discussion (ainsi que les remerciements) sont présentés ci-dessous. La numérotation de l'article d'origine a été conservée. L'article complet est repris en Annexe E (avec la mise en forme qu'il aurait une fois publié).

3.2.2 Extrait de l'article Verfaillie et al. (soumis)

Recent glacier decline in the Kerguelen Islands (49° S, 69° E) derived from modeling, field observations and satellite data

Verfaillie, D., Favier, V., Dumont, M., Jomelli, V., Gilbert, A., Brunstein, D., Gallée,H., Rinterknecht, V., Memegoz, M. & Frenot, Y., 2014, Journal of Geophysical Research, submitted

Abstract

The retreat of glaciers in the Kerguelen Islands (49° S, 69° E) was analyzed using field data and MODIS images to validate a positive degree-day (PDD) model forced by data from local meteorological stations. Mass balance measurements made during recent field campaigns on the largest glacier of the Cook Ice Cap were compared to data from the early 1970s, providing a 40-year view of the differences in the spatial distribution of surface mass balance (SMB). As these data depend to a great extent on specific years, our interpretation of climate-induced changes was limited. To obtain additional regional data for the validation of our models, we analyzed MODIS images (2000-2012) to determine if our model was capable of reproducing variations in the transient snow line. The PDD model correctly simulated the variations in the snow line, the spatial variations in the SMB and its trend with elevation. Yet, current SMB values diverge from their classic linear representation with elevation, and stake data at high altitudes now display much more negative SMB values than would be expected. By analyzing MODIS albedo values, we observed that these values are caused by the disappearance of snow and associated feedback on melt rates. In addition, we noticed that certain parts of Ampere Glacier could not be reproduced by the surface energy balance model, because overaccumulation appears to occur due to wind deposition. Finally, MODIS and field data and the models demonstrate the acceleration of glacier wastage in Kerguelen up to high altitudes due to reduced net accumulation.

4. Results

4.1. PDD validation using field data

SMB at the ice cap scale was modeled with a simple PDD model based on meteorological measurements and reanalysis data (Section 3.5[1]). Results are shown in Fig. 4 for comparison with stake measurements (presented in Section 4.3). Our PDD model results are in agreement with SMB measurements (Fig. 4) for the recent period (medium correlation (R) of 0.58 discussed below, p-value <0.001 according to a Student's t test) and the 1970s (excellent correlation of 0.99, p-value <0.001). This shows that the PDD model initiated with a 20 year spin-up and a firn cover is capable of reproducing the SMB distribution with elevation and the SMB changes between the 1970s and 2011. However, Fig. 4 shows that the initial amount of firn does not have much impact on modeled SMB. Indeed, a slight difference in SMB (only concerning elevations close to the firn and snow lines) can be observed between 5 m and 15 m firn experiments[1], but higher amounts of initial firn yielded the same final SMB as the 15 m firn experiment.

1. Annexe E

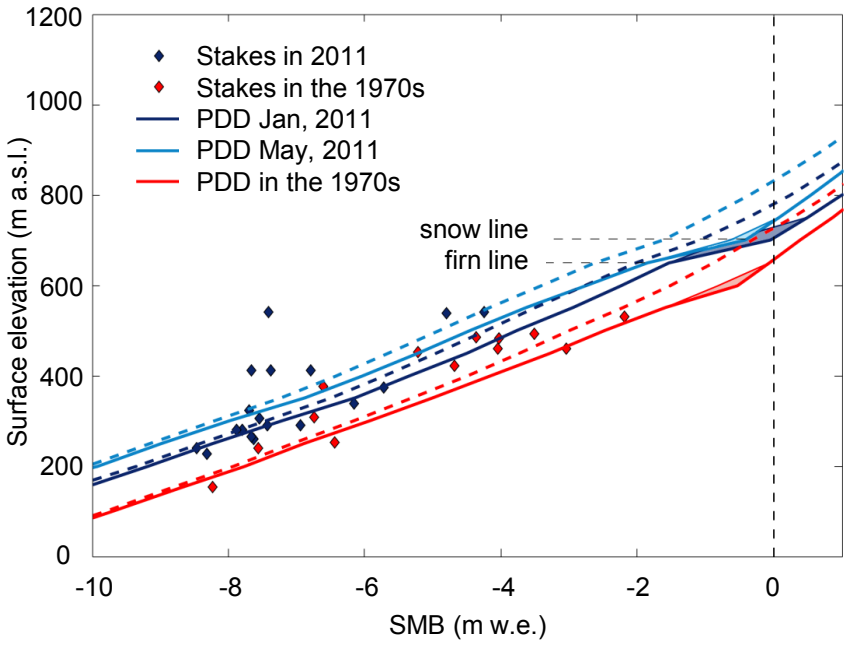

Figure 4. 2011 Ampere Glacier SMB values (m water equivalent, diamonds) at stake locations (see Fig. 1 b[1]) plotted against surface elevation (m above sea level). Values obtained between 1970 and 1974 by Vallon (1977a,b, 1987) are also given for the purpose of comparison. Lines represent ice cap SMB derived from our PDD model, for the early 1970s (red line, average of 1970-1974) and 2011 (blue lines). The PDD SMB for 2011 is calculated from January to January (light blue line) and from May to May (dark blue line). The dotted lines represent the version of the model with no initial firn cover, while the solid lines represent the version with an initial firn cover. Uncertainty intervals ($\pm$ 10 m w.e.) in the initial firn accumulation are also given.

4.2. Recent variations in the snow line and accumulation area derived from MODIS albedo maps

Figure 5 b, c shows changes in the ratio between areas covered by firn and snow (albedo > 0.55) on the ice cap and the entire ice cap surface between 2001 and 2012 calculated from albedo maps (Section 3.2[1]). This ratio may be considered equivalent to the accumulation area ratio (AAR) at the end of the ablation season, if we assume that the snow line elevation is similar to the ELA at the end of summer. In Fig. 5, we use the term "AAR", even though we acknowledge that winter values of this ratio are different from the strict sense AAR which should be based on annual values. Despite the marked scattering of the results and the limited number of good quality images, the ratio decreased between 2001 and 2012. A low firn line appeared on April 5, 2012 followed by a rapid increase that was revealed on April 25, 2012, suggesting that estimates may not reflect the highest annual firn line position, and the trends obtained may not be very accurate due to the small number of images available. However, the same trend was observed in each season, showing that the ratio had decreased by ~ 20 % at the end of the ablation season from 2001 to 2012 (which corresponds to a decrease of ~ 90 km^2 in the firn and snow covered areas). Values for March-April 2008 and 2009 are, however, the highest of the March-April period. The ratio between the area covered by fresh snow (albedo > 0.65) and the entire ice cap (not shown) was about 1.5 times lower than the same ratio for firn- and snow-covered surfaces, showing the potential extent of firn disappearance, while the rate of retreat for the snow line was about the same as that of the firn line in the last decade.

Figure 6 shows two albedo maps obtained for the period March-April (end of the ablation season), in 2001 and in 2012. The difference in the firn line (black line) and snow line (orange line) between the two images is striking. In 2001, the firn (snow) line was about 600 m a.s.l. (700-800 m a.s.l.). In 2012, the firn (snow) line increased to about 700-750 m a.s.l. (800-900 m a.s.l.). Although the images were not acquired at the exact same date, but about six weeks apart, due to the scarcity of clear-sky images, and the disappearance of the snow cover could thus be partly linked to the time lag between the images, PDD modeling showed that this reduction is consistent (Section 4.4), and that the estimated snow line in 2001 was close to its maximum. Moreover, the MODIS images also showed a retreat of the ice cap between 2001 and 2012. Indeed, the disappearance of ice, unlike that of snow, does not depend on the time of year, and Fig. 6 shows that some glacier snouts and termini have disappeared in 2012, especially on the eastern flank of the ice cap (sites are indicated by pink arrows). The glacier retreat was confirmed by comparing Landsat images acquired in 2001 and 2011 (not shown here).

4.3. Current SMB and snow line estimates from stake measurements and comparison with the 1970s

Figure 4 also shows Ampere Glacier SMB values at stake locations in 1970-1974 and 2011 plotted against surface elevation. Despite the marked scattering in the distribution of SMB with elevation, a simple linear extrapolation of stake measurements suggests that, in 2011, the snow line was located at about 800-1000 m a.s.l., in agreement with the transient snow line value obtained for Ampere Glacier from MODIS images in 2012 (Fig. 6). However, the data display marked scattering caused by five values from stakes located at the border of the glacier where snow can accumulate (Fig. 1 b[1], zone 2).

Despite the two short observation periods, we were able to compare SMB and snow line elevation values on Ampere Glacier between 1970 and 1974 (Vallon, 1977a,b, 1987) with our values for 2011 (Fig. 4). The comparison revealed that the spatial distribution of SMB has changed significantly in

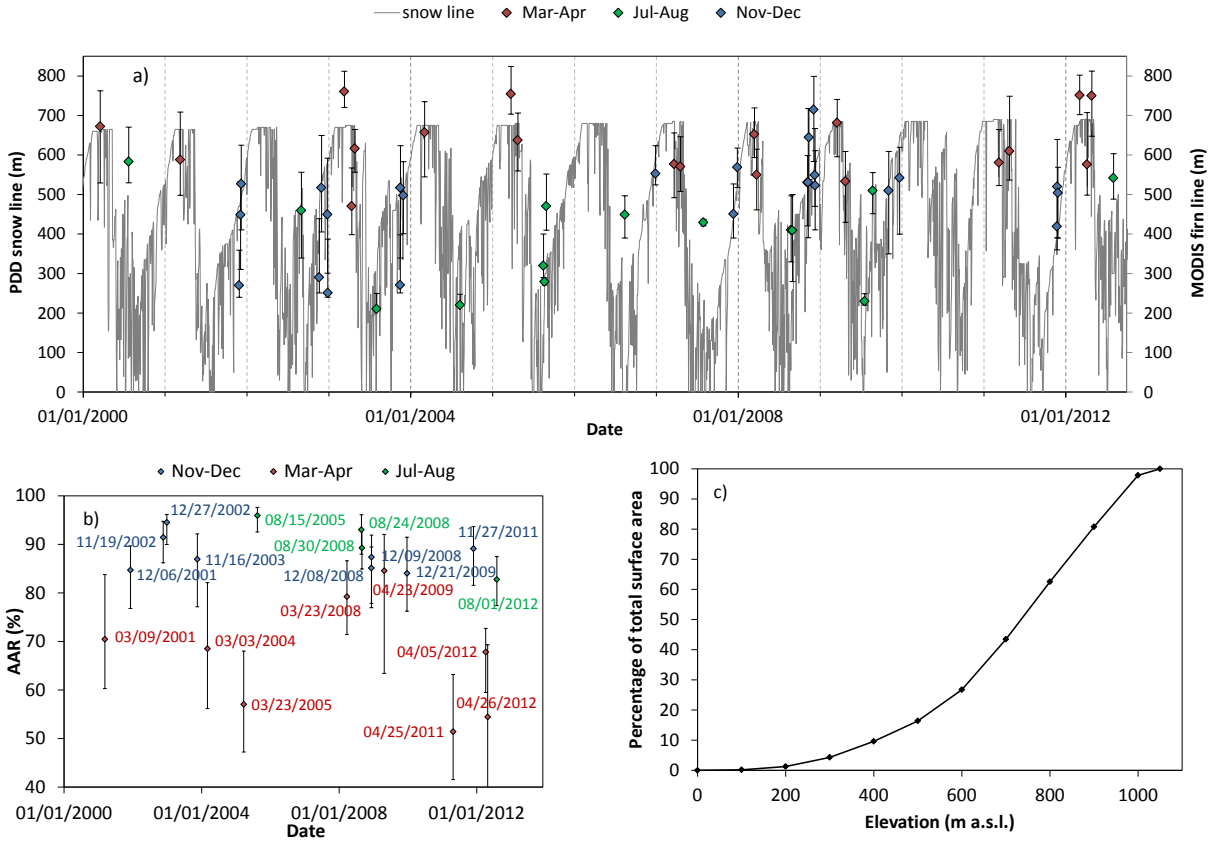

Figure 5. (a) Comparison between Ampere Glacier snow line computed with the PDD model and discrete firn line elevations for the Ampere Glacier obtained from albedo maps derived from MODIS images. Error bars are given for a firn albedo limit between 0.5 and 0.6 on the MODIS images. (b) Changes in the ratio of the accumulation area (firn- and snow-covered area) to the surface area of the entire ice cap between January 2000 and August 2012, for three periods : November-December (blue), March-April (red) and July-August (green) derived from clear-sky MODIS images. Error bars are also indicated for a firn albedo limit between 0.5 and 0.6 on the MODIS images. (c) Hypsometry of the Cook Ice Cap in 2009, i.e. the percentage of the surface area of ice cap below a given elevation.

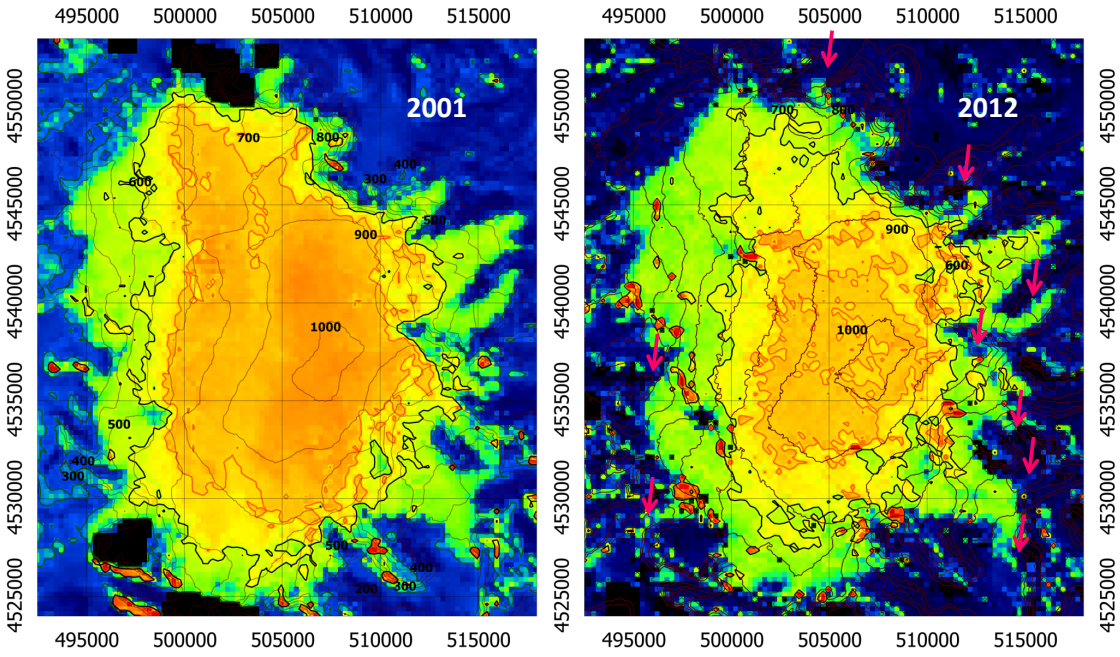

Figure 6. Comparison between albedo maps for March 9, 2001 (left) and April 26, 2012 (right). For key to pixel colours, see Fig. 2[1], panel a. The firn line is represented by a black line, the snow line is in orange, and contour lines in 2000 (SRTM DEM) and 2009 (SPOT DEM) respectively are in burgundy (numbers indicate contour line elevations in m a.s.l.). The pink arrows in the 2012 image point to sites where ice tongues or termini disappeared between 2001 and 2012. Coordinates are in UTM (Zone 42S).

40 years :

1. SMB is more negative at the same elevation
2. SMB extrapolation suggests that the snow line was above 800 m a.s.l. in 2011 (this was confirmed by field observations in 2012 and 2013), whereas it was located around 650 m a.s.l. in the early 1970s. Even if the snow line elevation was computed only using data from one year, the PDD model shows that it was similar between 2008 and 2012, suggesting that this difference makes sense.
3. SMB gradient above 400 m a.s.l. is lower than in the early 1970s.

4.4.Comparison between the PDD snow line and the MODIS transient firn line

PDD model results showed a difference of about 50-100 m between the snow line and the firn line elevations for 2011, in good agreement with MODIS estimates in 2012 (around 100 m, see Section 4.2). Figure 5 a compares the modeled snow line and the transient firn line elevation obtained from MODIS images on Ampere Glacier. Despite its high variability, the modeled snow line agrees well with transient firn line variations in MODIS images (correlation of 0.67 for a transient firn line at an albedo of 0.55, p-value $<$0.001). The mean difference between the PDD-modeled snow line and MODIS-derived transient firn line ($\overline{x}_{PDD} - \overline{x}_{MODIS}$) was 46 m for a transient firn line threshold of 0.5 and -31 m for a threshold of 0.55. This means that the actual threshold should be close to 0.53, and gives us further confidence in our PDD estimates. The annual maximum PDD-modeled snow line elevation (corresponding to the ELA) of the Ampere Glacier increased by $\sim$ 30 m between 2000 and 2012.

4.5. Information provided by SEB modeling and albedo estimates from MODIS

We calculated punctual SMB values at stake locations (see Fig. 1 b[1] for locations) for 2011 and compared them to values measured at the stakes in 2011, as illustrated in Fig. 7.

The poor quality of the information concerning turbulent heat fluxes and precipitation constitutes the main uncertainty in SEB and SMB computation. High $LE + H$ values tend to decrease the local mass balance. Conversely, high precipitation tends to limit negative SMB values. We observed that field SMB data cannot be reproduced if we assume a value of 50 W m^{-2} for turbulent heat fluxes (as measured by Poggi (1977a)) even if we assume a P twice as large as the one calculated from the relationship described in Section 3.4[1] (Fig. 7 a). On the other hand, we observed that SMB is correctly computed assuming calculated precipitation and turbulent heat fluxes $\sim$ 30 W m^{-2} (Fig. 7 b). Preliminary results from our SEB model during 2011 yielded a similar mean value of punctual $LE + H$ of 34 W m^{-2}.

However, even for the case with turbulent heat fluxes of 30 W m^{-2}, points located in overaccumulation areas (zone 2) yield SMB estimates too negative compared to measurements (they fall under the x = y curve), while the ones located in zone 1 agree well with measurements. About three times the amount of P (which is mostly liquid) have to be considered for the computed SMB in zone 2 to agree with measurements, suggesting that they are located in large corniches.

Finally we observed that the point chosen at 990 m a.s.l., where accumulation is expected to occur, displays a negative estimated SMB value (approximately -3200 mm w.e. for the case with turbulent heat fluxes of 30 W m^{-2} at an elevation of 990 m a.s.l.). In the case of $LE+H = 30$ W m^{-2}, accumulation calculated from the relationship described in Section 3.4[1] (approximately +3350 mm w.e.) compensates the SW contribution to SMB (approximately -3140 mm w.e.). This demonstrates that $LE + H$ and LW must decrease with elevation in order to have a slight accumulation at the

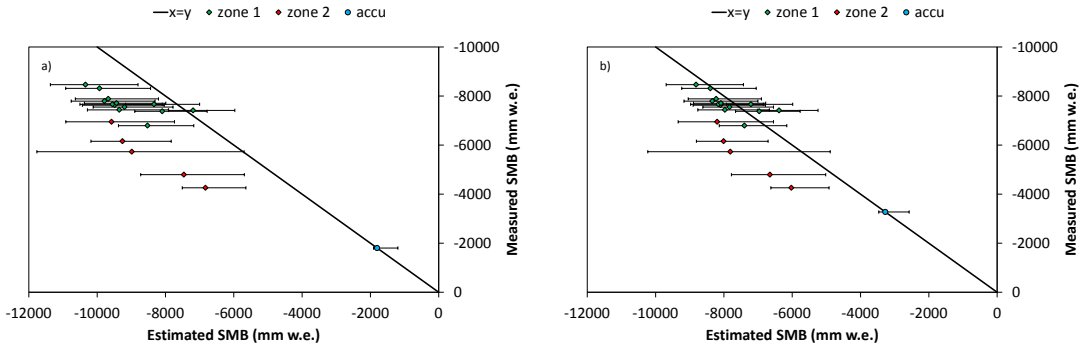

Figure 7. Comparison between field annual SMB measured at stake locations (see Fig. 1 b[1] for locations) and annual SMB estimates. Two cases were used for the computation of SMB : (a) turbulent heat fluxes of 50 W m^{-2} and doubled precipitation compared to estimates, and (b) turbulent heat fluxes of 30 W m^{-2} and estimated precipitation. Values are separated into zone 1 and zone 2 (see Section 2.1[1] for explanations). The point named "accu" corresponds to the x = y SMB value calculated with the albedo of a pixel situated in the accumulation zone of the glacier (990 m a.s.l.). Error bars were estimated by calculating the error introduced when selecting different pixels adjacent to the one in which the stake is located, plus the systematic bias introduced by using clear-sky images.

top of the ice cap, and that constant values used in the ablation zone are not appropriate at such high elevations.

4.6. Long term variations in the snow line and link with climate variability

Measured and reanalyzed temperature and precipitation data over Kerguelen since 1948 are presented in Fig. 8.

Météo France measurements revealed a marked decrease in temperature of about -0.06 °C a^{-1} from 1952 to 1964, followed by a sharp increase of about +0.06 °C a^{-1} from 1964 to 1982. Reanalyses and measurements after 1982 revealed a slight increase (not significant at the 95% confidence level) in temperature of about +0.002 °C a^{-1} to +0.01 °C a^{-1}.

Precipitation measured at Port-aux-Français before 1973 presented a very different variability than precipitation measured after 1973. Measurements after 1973 displayed a significant (at the 95% confidence level) decrease in precipitation of about 25% in the last 40 years, slightly higher than in reanalysis data, which suggest a decrease of 5% to 20%. Analysis of daily precipitation revealed that this decrease is not linked to a decrease in the intensity of precipitation, but rather to a decrease in the frequency of precipitation events (Table 3). However, it should be kept in mind that precipitation measurements using rain gauges are negatively biased in strong wind conditions (Larson and Peck, 1974), which is often the case on the Kerguelen Islands, implying that actual precipitation amounts are probably larger than measured but such a bias was also likely present in past measurements.

Table 4 compares mean ELA values from the PDD model and from MODIS images during the 1950s and the 2000s. The mean modeled ELA for the period 2000-2009 was 127 m higher than the mean ELA for the period 1958-1963 (last period of glacier equilibrium, Frenot et al. (1993)). Considering unchanged precipitation amounts since the 1950s (precipitation from the 1950s repeated during the next decades, labeled P50s) yielded a mean ELA for 2000-2009 ∼100 m lower than the actual modeled ELA, while the same ELA for unchanged temperature (labeled T50s) was only ∼40

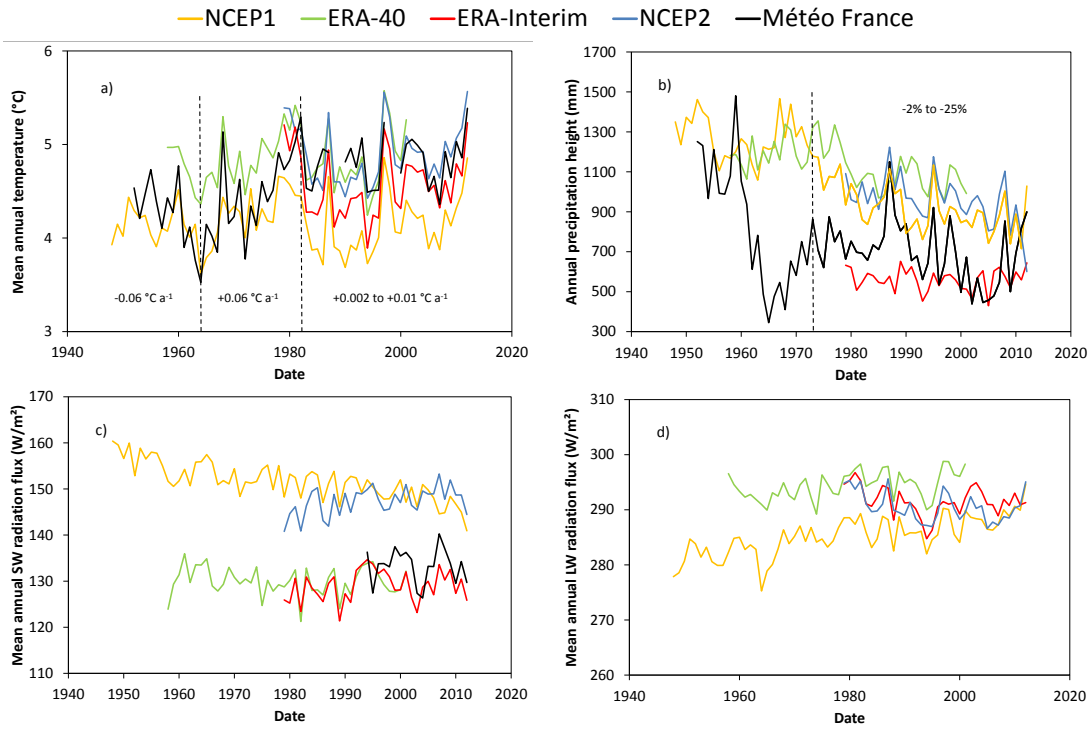

Figure 8. Meteorological (Météo France measurements at Port-aux-Français) and climatic (NCEP Reanalysis 1 and 2, ERA-40 and ERA-Interim reanalysis) data for the Kerguelen Islands since 1948 : (a) temperature 2 m above the surface, (b) precipitation, (c) shortwave (SW) radiation flux and (d) longwave (LW) radiation flux. Temperature and precipitation trends for different periods (delimited by vertical dashed lines) are also shown.

Table 3. Characteristics of precipitation events from Météo France measurements at Port-aux-Français. Total annual amount of precipitation, total number of precipitation events and number of events with less than 20 mm d^{-1} are shown for 10 year-periods since 1953.

	Mean annual precipitation (mm a^{-1})	Total number of precipitation events	Precipitation events < 20 mm d^{-1}	Ratio of events < 20 mm d^{-1} on total number of events (%)
1953 - 1962	1055	2402	2298	95.7
1963 - 1972	567	2113	2083	98.6
1973 - 1982	743	2102	2051	97.6
1983 - 1992	789	2013	1947	96.7
1993 - 2002	649	1928	1888	97.9
2003 - 2012	626	1814	1764	97.2

Table 4. Comparison of mean ELA values calculated by the PDD model and estimated from MODIS images over the periods 1958-1963 and 2000-2009. PDD values are calculated with measured precipitation and temperature from Port-aux-Français (Measured), with normal precipitation but temperature from the 1950s repeated until the 2000s (T50s) and with normal temperature but precipitation from the 1950s repeated every decade until the 2000s (P50s). Uncertainty estimates for 2000-2009 mean ELA correspond to the standard deviations of centered snow line values.

Climate forcing	Measured		T50s	P50s
Time period	1958–63	2000–09	2000–09	2000–09
PDD ELA (m)	549	677±182	638±196	578±175
MODIS ELA (m)		668±142		

m lower. This indicates that precipitation decrease has contributed for about 70% to the rise in ELA from the 1950s to date, while temperature has had a much smaller contribution. The agreement between modeled and measured mean ELA for the period 2000-2009 (compared to the P50s and T50s hypothetical cases) should be noted anew, although standard deviation of the measured ELA is smaller than the ones for modeled values, indicating that the model could be slightly too sensitive compared to measurements. A similar analysis was carried out on mass balance measurements (obtained from the difference between two digital elevation models) and estimates using the same PDD. The PDD forced with measured values from Port-aux-Français indicates an equilibrium in 1960 (Frenot et al., 1993) and a similar modeled mass balance between 1963 and 2000 (-1.13 $\pm$ 0.13 m w.e. a^{-1}) as the one measured by Berthier et al. (2009) (-1.33 $\pm$ 0.90 m w.e. a^{-1}). When comparing these values with the ones modeled for 2000-2009 using measured values and hypothetical cases P50s and T50s, we find that, similarly to ELA, 77% of the differences in surface mass balance can be explained by the decrease in precipitation.

Changes in precipitation occurrence were likely associated to variations in other climatic settings which may have had significant impact on glaciers, as for instance cloudiness. We analyzed the variations of this variable, which may have changed significantly during the last 50 years. Figure 8, panels c and d show incident shortwave and incoming longwave radiation trends that differ depending on the reanalysis. Recent reanalyses show a slight increase in incident SW radiation and a slight decrease in incoming LW radiation in recent decades. This indicates a decrease in cloud cover which certainly played a role in the ice cap wastage, although this result should be interpreted with caution because (1) previous generation reanalyses displayed opposite trends and (2) there are no available long term field measurements in this area to enable us to confirm this result.

5. Discussion and Conclusions

The PDD model reproduced current and past SMB (in the early 1970s) reasonably well, showing that temperature and precipitation were the first order variables that explained the SMB variations. PDD results indicated that the mean firn limit was about 100 m lower in the early 1970s than today. Nevertheless, an acceleration in punctual ablation up to high elevations and a resulting decrease in SMB gradient with elevation have been observed, which are not fully reproduced by the PDD model. Our rough estimates of SEB based on MODIS albedo showed that they result from feedback including albedo and spatial reduction in snow corniches due to lower amounts of solid precipitation. Including wind drift and snow accumulation processes is necessary for the study of fine scale (about 10-100 m) corniche formation. However, at larger scales (1-10 km), a distributed surface heat budget

would be enough to model most processes and feedback that occur at the ice cap scale.

Modeling the punctual SMB for 2011 using albedo estimates from MODIS imagery showed that the LW radiation budget represents 4% to 13% of the available energy for melting, while the SW radiation budget represents 58% to 64%. Consequently, turbulent heat fluxes contribute 29% to 32% to ablation, which is lower than on Patagonian glaciers (i.e. Schneider et al. (2007)), and less than estimates based on the measurements (42%) made in summer by Poggi (1977a). These estimates were confirmed by a one-year (2011) SEB model, yielding mean contributions of 68% for SW, 1% for LW and 31% for turbulent heat fluxes. Albedo thus plays an important role in ablation through the SW radiation budget, which motivated us to undertake a thorough study of changes in the snow line using MODIS data and modeling.

MODIS imagery also revealed a change in the location of the snow line between 2000 and 2012. The current snow line is above 800 m a.s.l. (Fig. 4), but slightly lower on the ice cap's western flank than on its eastern flank (Fig. 6), due to dominant eastward moisture transport (Garreaud et al., 2009). MODIS also showed a decrease in the accumulation area ratio since 2000 (Figs. 5 and 6), despite the larger accumulation area and lower firn line altitude values in March-April 2008 and 2009 compared to other years, that were probably due to the occurrence of large precipitation amounts and relatively low temperatures in 2008 and 2009 (Fig. 8). As the ice cap is very flat between $\sim$ 600 m a.s.l. and its summit (1,030 m a.s.l.), even a small rise in the snow line has dramatic consequences for the reduction of the accumulation area (Fig. 5). The extent of the current accumulation area *sensu stricto* is small and negative SMB can probably be found at high altitudes.

In fact, comparison with field data from the 1970s indicates that the snow line has risen more than 150 m in 40 years. Moreover, the SMB gradient with elevation is lower today than it was in the early 1970s. Indeed, since snow cover is almost continuously absent up to high elevations, the albedo at stakes with distinct elevations is more uniform (as it remains in the albedo range of ice almost all through the entire ablation season), leading to a lower SMB gradient with elevation.

To sum up, the snow line has risen with time, the accumulation area is now reduced and the mean albedo of the ice cap is lower. These processes led to a retreat of the ice cap. Climatic forcings that explain this retreat were investigated using meteorological measurements and reanalysis data (Fig. 8), and showed that changes in precipitation represent the initial first order process that explains the marked increase in ablation and decrease in accumulation since the 1970s. An analysis of the ELA (Table 4) revealed that about 70% of the rise in ELA since the 1950s was due to the decrease in precipitation. We are aware that the analysis of such hypothetical series is rather simplistic and that further analysis should be needed. For instance, a study of the long term trends in incoming SW and LW radiation using reanalysis data (Fig. 8 c, d) revealed that a decreasing trend of the cloud cover was likely, and may have played a significant role in glacier retreat, even though long term field measurements are lacking to definitely conclude on such a trend. In addition, a similar analysis, but concerning mass balance values, was carried out, also indicating a significant contribution from precipitation (77%) compared to temperature. The decrease in precipitation was due to a reduction in the frequency of precipitation events (Table 3). This was probably linked to a southward shift of the storm tracks due to more frequent positive phases of the Southern Annual Mode (SAM) in recent decades, which has had important impacts on the environment (Villalba et al., 2012; Manatsa et al., 2013; Delworth and Zeng, 2014). Combined with a more moderate increase in temperature, this resulted in a rise in the 0 °C level, leading to a decrease in the occurrence of solid precipitation at low to intermediate elevations. The latter caused an albedo feedback, which, combined with the slight increase in SW radiation ($+2\%$ to $+4\%$ according to data from ERA-Interim and NCEP 2 reanalysis), led to more ablation and a rapid rise in the snow line. The subsequent decrease in elevation caused additional positive feedback on ablation due to the local increase in temperature.

However, different behaviors were observed between two zones of the glacier (zone 1 and zone 2, see Fig. 1 b[1]), which are visible as large snow corniches or dunes in the lee of crests. As can be seen in Fig. 1 b[1], the spatial distribution of these zones is not related to elevation but to the distance to the crests. Because rough estimates of SMB using MODIS albedo suggest that large negative SMB should be observed, it is very likely that these zones only exist because of overaccumulation. The limited extent of these local accumulation zones is visible on the MODIS images as well as in the field. These different zones were not fully reproduced by a simple approach based on changes in fluxes with elevation and overaccumulation processes must thereby be accounted for.

As a consequence, a full modeling approach would be useful. To this end, recently initiated regional scale simulations of mass balance processes over the Kerguelen Islands with a downscaling scheme (SMHiL, Agosta (2012)) and the regional climate model MAR (Modèle Atmosphérique Régional, Gallée and Schayes (1994)) should provide new insights into changes in its ice bodies.

Acknowledgements

We would like to thank Julie Gardelle, Etienne Berthier and Yves Arnaud for their help with satellite imagery, and the Météo France team at Port-aux-Français for providing meteorological data and information about the meteorological station. Special thanks to the IPEV logistics team and all the people who helped us during the field campaigns, without whose help this study would not have been possible. We also thank the French Austral and Antarctic Territories (TAAF). NCEP 1 and 2 reanalysis data were provided by the NOAA/OAR/ESRL PSD, Boulder, Colorado, USA, from their Web site at `http://www.esrl.noaa.gov/psd/`. ERA-40 and ERA-Interim reanalysis data were downloaded from the ECMWF data portal at `http://data-portal.ecmwf.int/`. MODIS Level-1B Swath images were retrieved from the LAADS at `http://ladsweb.nascom.nasa.gov/`, and the Landsat images from the USGS at `http://glovis.usgs.gov/`. The ASTER image is courtesy of the GLIMS project. Field measurements and research were funded by IPEV program n° 1048 (GLACIOCLIM-KESAACO) and by INSU program LEFE-KCRuMBLE.

3.3 Etude des variations récentes de bilan de masse et de leur causes de grande échelle

3.3.1 Motivations et principaux résultats

Dans la Section 3.2, nous avons analysé le retrait de la calotte Cook au cours des dernières décennies, et montré que celui-ci semble principalement lié une forte diminution des précipitations sur l'archipel depuis les années 70 environ. Mais cet assèchement est-il purement local ou au contraire concerne-t-il une zone plus étendue que la région des îles Kerguelen ? Quelles en sont les causes ? Ces questions, qui ont fait l'objet d'un article présenté ci-dessous, sont abordées dans cette section. Dans cet étude, j'ai principalement participé à l'analyse des tendances climatiques dans les réanalyses et modèles, ainsi qu'à l'élaboration des cartes de corrélations entre les différentes variables climatiques mettant en évidence des changements en terme de téléconnexions climatiques présentés ci-dessous.

Le bilan de masse récent de la calotte Cook est tout d'abord estimé grâce à la comparaison de deux modèles numériques de terrain, l'un datant de 2000, l'autre de 2009. La valeur de bilan de masse estimée se situe parmi les plus négatives à l'échelle globale, des valeurs similaires sur cette période n'ayant été observées que pour certains champs de glace maritimes en Alaska, pour la cordillère Darwin et le champ de glace sud de Patagonie. La chronologie du retrait de la calotte

Cook depuis les années 50 révèle que celui-ci a commencé dans les années 60, s'intensifiant depuis les années 70 pour atteindre le retrait observé actuellement. Cette chronologie est en accord avec les fluctuations de température, mais surtout de précipitations observées à la station de Port-aux-Français depuis 1951. Une chute brutale des précipitations depuis les années 70 (ainsi qu'une légère augmentation de température) est effectivement observée, et est confirmée par l'analyse des données de radiosondages de Port-aux-Français.

Afin d'estimer les contributions relatives des températures et des précipitations au retrait de la calotte Cook, le modèle degré-jour présenté et utilisé précédemment (Sections 2.4.6.1 et 3.2) est couplé à une routine d'écoulement (Section 2.4.6.2) afin de modéliser l'étendue de la calotte à différentes périodes. Ces modélisations révèlent qu'environ 77% du retrait depuis les années 60 peuvent être expliqués par la diminution des précipitations, tandis que l'augmentation des températures n'a joué qu'un rôle secondaire dans le retrait.

L'assèchement observé depuis les années 60 semble lié à des processus de grande échelle mettant en jeu des intéractions entre océan et atmosphère, que j'ai analysées en détail. Les corrélations entre la température de l'air et les précipitations mesurées à Port-aux-Français et la température de l'océan en surface (SST) issue de différents jeux de données révèle une modification des téléconnexions climatiques dans les années 70. En effet, avant 1975 environ, les SST du courant des Agulhas et du courant circumpolaire antarctique en amont de l'archipel des Kerguelen étaient corrélées positivement aux précipitations observées à PAF, car ces courants contrôlaient l'apport de chaleur facilitant les conditions d'évaporation au sein des zones dépressionnaires qui arrosaient l'archipel. Ces téléconnexions correspondent à la variabilité naturelle attendue pour l'archipel des Kerguelen. La température et les précipitations aux îles Kerguelen étaient alors positivement corrélées (lorsque la température augmentait, les précipitations augmentaient également). Cependant, après 1975, le lien entre température et précipitations aux îles Kerguelen a changé. L'analyse des tendances dans les réanalyses et les modèles CMIP5 (Section 3.5.2 et Informations supplémentaires de l'article en Annexe F) montre que l'assèchement et le réchauffement sur l'archipel depuis les années 70 sont associés à un décalage vers le sud des zones dépressionnaires, ainsi qu'à une assèchement de l'atmosphère et un réchauffement océanique de surface sur de larges zones autour des îles Kerguelen. Ces observations concordent avec les effets connus de l'intensification du Mode Annulaire Austral (Soutern Annular Mode (SAM) en anglais). Nous montrons également que l'intensification du SAM semble avoir modifié les téléconnexions climatiques aux îles Kerguelen depuis 1975 environ. Les corrélations entre les SST en amont des îles Kerguelen et les précipitations mesurées à PAF sont en effet négatives, montrant que les zones océaniques avec lesquelles les précipitations aux îles Kerguelen étaient connectées ont changé après 1975 car l'archipel n'est plus sous l'influence des zones dépressionnaires. Les précipitations et la température de l'air aux îles Kerguelen après 1975 présentent alors des tendances opposées (augmentation de température et diminution des précipitations), qui ont eu un impact sur les glaciers surpassant celui de la variabilité naturelle du climat observée avant les années 70.

L'intensification du SAM est attribuée principalement à la diminution de l'ozone stratosphérique et l'augmentation des gaz à effet de serre. Au cours du prochain siècle, on estime que l'augmentation des gaz à effet de serre devrait compenser l'effet bénéfique du rétablissement de la couche d'ozone sur le SAM. Mon analyse des tendances climatiques dans les modèles CMIP5 pour le 21^{e} siècle (qui, par souci de clarté et de logique de ce document, sera présentée à la Section 3.5.2) révèle que les températures devraient continuer à augmenter sensiblement aux îles Kerguelen, tandis que les précipitations pourraient réaugmenter, mais sans atteindre le niveau qu'elles avaient avant les années 60. Dans ces conditions, la calotte Cook devrait continuer de

reculer à grande vitesse.

Les causes du retrait glaciaire aux îles Kerguelen sont donc un assèchement marqué depuis les années 70 couplé à une augmentation des températures, causés par les phases de plus en plus positives du SAM. De par sa nature hémisphérique, le SAM impacte l'ensemble de la bande latitudinale 30° S - 60° S. Il est donc probable que l'assèchement observé sur l'archipel des Kerguelen affecte également d'autres régions englacées de l'hémisphère sud, telles que la Patagonie. Cet impact probable sur les glaciers de l'ensemble de la zone subpolaire de l'hémisphère sud et les processus de grande échelle associés seront abordés dans la Section 3.4.

3.3.2 Extrait de l'article Favier et al. (en révision)

The ozone hole as the main driver of dramatic glacier wastage in the sub-Antarctic region

Favier, V., Verfaillie, D., Berthier, E., Memegoz, M., Jomelli, V., Kay, J.E., Ducret, L, Malbéteau, Y., Brunstein, D., Gallée, H., Park, Y.-H., 2014, Nature Geoscience, in review.

The ongoing retreat of glaciers at southern sub-polar latitudes is particularly rapid and extensive[1−5]. Akin to northern sub-polar latitudes[6−9] this retreat is generally assumed to be linked to warming[1−5]. However, no long-term and well-constrained glacier modeling has ever been performed to demonstrate this hypothesis. Here we model the Cook Ice Cap mass balance on the Kerguelen Islands (Southern Indian Ocean) to reveal the mechanisms of the ice wastage in the sub-Antarctic region. In contrast to relative stability from 1800 to the 1960s[3,10−11], the ice cap mass balance has become increasingly negative since 1975 and reached -1.51 ± 0.19 m water equivalent (w.e.) a^{-1} between 2000 and 2009, amongst the most negative on Earth[1−9,12−14]. We attribute this wastage to the dryness induced by the positive Southern Annular Mode[15−23] caused by anthropogenically-induced ozone depletion. Since 1975, the storm-tracks have moved poleward leaving Kerguelen Islands behind. Due to the hemispheric signature of the drying resulting from the ozone hole, our findings suggest that the causes of the rapid ice wastage in the sub-polar regions[1−5] of the southern hemisphere should be revisited.

Understanding the climatic origin of glacier retreat is important to reconstruct past climate variations and to assess the future changes of the sub-Antarctic environment and glaciers[5]. Glaciological changes at the southern sub-polar latitudes have been documented with remote sensing data[1−5] to demonstrate the occurrence of a particularly rapid and extensive retreat. A full glaciological modeling of the ice caps over more than half a century has never been performed in these regions, and attribution of the possible origins of the ice wastages is only qualitative and done through simple comparisons with the regional climatic trends. Two exceptions are recent modelling studies of the Patagonian Icefields[24,25], but these studies addressed surface mass balance changes only since 1975 and the climatic interpretation is complicated by the presence of numerous calving glaciers. Because long-term continuous reliable field measurements close to the studied glaciers and ice caps are particularly rare, conclusions on trends and impacts may be uncertain. Nevertheless, akin to northern sub-polar latitudes[6−9], the recent rapid and extensive ice wastage is generally attributed mainly to the global warming[1−5].

Here, we challenge this assumption by using a unique and consistent long term meteorological and glaciological dataset available since 1951 at the Kerguelen Islands in the southern Indian Ocean (49° S, 69° E, Fig. 1a), to model and understand the mechanisms involved in the recent wastage of one sub-polar ice-cap, the Cook Ice Cap (CIC, covering 410 km^2 in 2001). Geomorphologic evidences reveal that the front of the main CIC outlet glacier (Ampere Glacier, maximum elevation 1040 m above sea level (asl), 67 km^2 in 2001) in the mid-1960s was still close to its position during the Little Ice Age (LIA)[3,10,11]. By contrast, between 1963 and 2003 (ref. 3), the glacier retreated 2.8 km (i.e. 18% in length), indicating significant changes in climate settings. We analyze these changes and their impact on CIC mass balance, and examine whether the observed processes offer new understanding to interpret glacier wastage in other sub-polar regions of the southern hemisphere.

Recent CIC mass balance has been assessed by subtracting two digital elevation models (DEM) computed from the Shuttle Radar Topography Mission (SRTM) in 2000 and from a stereoscopic pair of SPOT5 images in 2009 (Fig. 1b). With a total volume loss of 7.0 $\pm$ 0.4 km^3 between 2000 and 2009, we compute a mass balance of -1.51 $\pm$ 0.19 m w.e. a^{-1}. Comparison with information for previous decades[3] confirms a strong acceleration of wastage during the last decade (Table 1). The greatest ice loss occurred at Ampere Glacier, with a mass balance of -2.47 $\pm$ 0.30 m w.e. a^{-1}. Thinning was significant (0.4 $\pm$ 0.1 m a^{-1}) up to the ice cap summit (Fig. 1b, c). Recent mass balance was amongst the most negative on Earth (Fig. 1d). Except for low elevations maritime icefields in Alaska[9], similar values were only observed at comparable south hemisphere latitudes, for the Darwin Cordillera[2] and South Patagonian Icefields[1], (Fig. 1d), demonstrating that Southern Hemisphere mid-latitudes are where glaciers are currently losing mass the most rapidly on Earth.

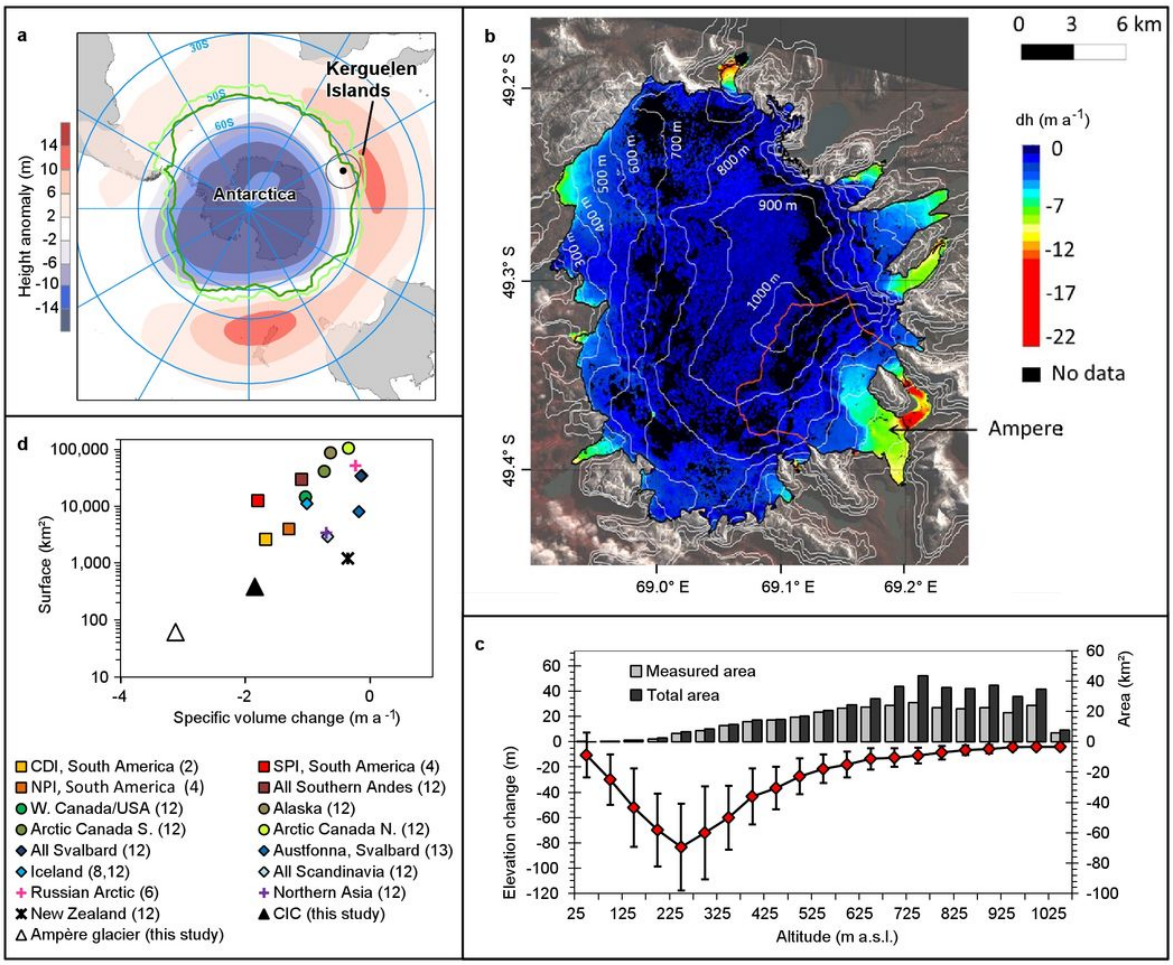

Figure 1. Climate settings of Kerguelen Islands and mass balance of the Cook Ice Cap between 2000 and 2009. a) Map of the sub-Antarctic area, with the mean positions of the sub-Antarctic (light green) and polar (dark green) oceanic fronts between 1993 and 2005 (ref 22). The SAM 850 hPa geopotential heigth anomaly pattern is also shown as blue to red shading[33]. The location of Kerguelen Islands is indicated by the black circle. b) Rate of surface elevation change (in meters per year) on the Cook Ice Cap. The extents of Cook Ice Cap and Ampère Glacier in 2009 are represented by the black and red lines respectively. Elevation changes are measured with an accuracy of $\pm$ 1 m (at the 1-sigma level, see Supplementary Methods). c) Ice cap hypsometry in 2000 and its elevation change between 2000 and 2009 (with standard deviation in each 50-m elevation interval) as a function of elevation. d) Area vs specific volume change (in meters per year) for the different ice caps in the sub-Antarctic and sub-Arctic regions. Numbers associated to each ice cap correspond to the references for the presented values. Our results for CIC and Ampere Glacier are also plotted for comparison.

Table 1. Measured and modeled mass balances for CIC for different periods since the 1960s and at the end of the 21st century.

Climate forcing	With Measured temperature (T) and precipitation (P) at PAF			Without warming[i]	Without drying[ii]	With 1950s climate	Future climate (CMIP5)
Time period	1958–63	1963–2000	2000–09	2000–09	2000–09	2000–09	2090–99
Modeled MB[iii]	-0.01	-1.13±0.13[iv]	-1.64±0.08[v]	-1.15±0.08[v]	0.07±0.08[v]	0.58±0.08[v]	-0.87[vi]/-10.6[vii]
Measured MB[iii]		-1.33±0.90	-1.51±0.19				

[i]T from the 1950s are reported to every following decade, whereas observed P are used
[ii]P from the 1950s are reported to every following decade, whereas observed T are used
[iii]Mass balance in m we a^{-1}
[iv]Mean glacier-wide specific mass balance is the average of values obtained with extents and elevations from years 1963 and 2000 respectively. The uncertainty is the half-difference between minimum and maximum values.
[v]Same as [iv] but with extents and elevations from years 2000 and 2009 respectively. Note that the retreat from 1963 caused the loss of low elevation areas where ablation was the highest.
[vi]In this experiment, precipitation from the 2000s progressively increases and reaches values from the 1950s in 2100, i.e. a twice larger precipitation amount than today. This assumes largely more precipitation increase than suggested by CMIP5 models. Warming is given by the mean trend from CMIP5 models for RCP2.6 scenario. This represents the expected most positive mass balance situation. Mean glacier-wide specific mass balance assumes surface area and elevation from year 2009.
[vii]Same as [vi] but warming is from RCP8.5 scenario.

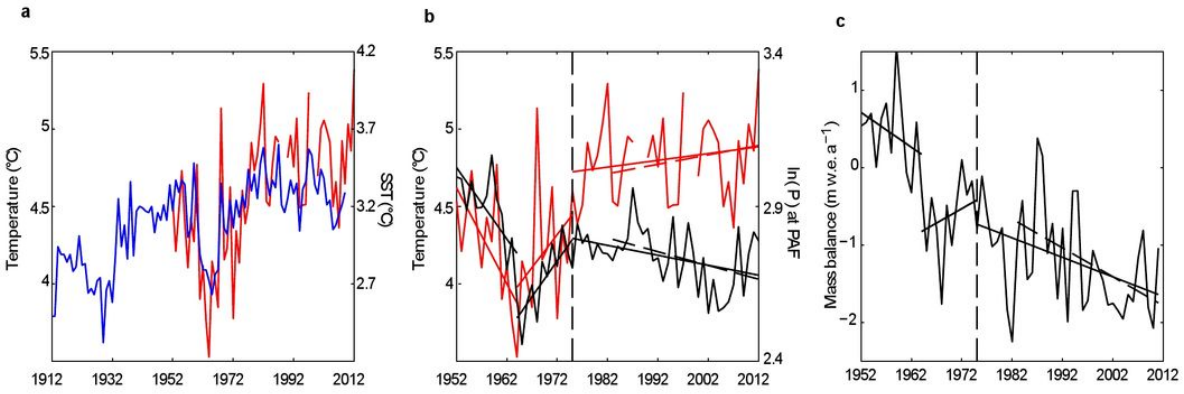

Figure 2. Climate break in 1975 at Kerguelen Islands and impact on CIC mass balance. a&b) Time-series of historical surface ocean temperature from ERSST.v2 dataset (blue line, Fig. 2a), air temperature at PAF (red line, Fig. 2a&b) and of the values of logarithm of precipitation at PAF (black line, Fig 2b). Data are presented a) since 1912, b) and since 1952. c) Time-series of the modeled specific mass balance of CIC assuming that elevation and extent are those observed in 2009. Vertical discontinuous lines represent the year 1975. Thin continuous and discontinuous lines are trends computed over the timespan corresponding to the length of each line.

Our analysis, combined with previous studies[3,10], leads to the following chronology : mass balances were close to 0 at the end of the 1950s, very negative between 1965 and 1970, slightly less negative at the beginning of the 1970s and increasingly negative to present. This chronology is consistent with observations from Port-aux-Français (PAF, a weather station on the east coast of the Kerguelen Islands (Supplementary Fig. 3a)) since 1951. Following a moist and relatively warm period in the 1950s, a striking dry and cool period began in 1963 (Fig. 2a). From 1967 to 1975, both precipitation and temperature re-increased significantly (Fig. 2b), but precipitation did not recover its pre-1963 value. From 1975 to present, annual precipitation decreased again by 15%-20% and temperature increased (0.07 °C/decade). The precipitation events frequency and intensity decreased, while the duration of dry spells increased. The current 10-year mean precipitation is half of what it was in the 1950s[3] and warming was 0.13 °C/decade since the 1950s. Radiosonde observations at PAF (Supplementary Discussion, Supplementary Fig. 6, 7) confirm a large reduction in moisture throughout the troposphere indicating a decreasing large-scale moisture flux since the 1970s. Radiosondes also confirm a warming limited to low elevation levels (below 850 hPa) suggesting that atmospheric warming resulted from surface one. Ocean-forced lower atmospheric warming trends are consistent with sea surface temperature (SST) increases measured by satellites in the Kerguelen region and by a buoy at PAF since 1982 (see Supplementary Discussion, Supplementary Fig. 8).

To assess the relative importance of reduced precipitation and warming to the CIC wastage, we forced a glaciological model with local meteorological station data, available since 1951. The mass balance model computes distributed daily accumulation and ablation based on a positive degree day (PDD) approach[26]. The daily surface mass balance model is coupled with a simple ice motion routine[27] to retrieve glacier snout positions (see Supplementary Methods). Degree day factors were calibrated by comparison with surface energy balance calculations and continuous ablation measu-

rements in the field (see Supplementary Methods, Supplementary Fig. 1). The computed vertical balance profile shows a good agreement with field measurements taken during 1970-74 and 2011 (see Supplementary Methods, Supplementary Fig. 2a). Modeled CIC specific mass balance values between 1963 and 2000 (-1.13 $\pm$ 0.13 m w.e. a^{-1}) and between 2000 and 2009 (-1.64 $\pm$ 0.08 m w.e. a^{-1}) are in particularly good agreement with remotely-sensed estimates (Table 1). The model also reproduces the observed wastage chronology[3,10] (see Table 1 and Fig. 2c). Finally, the ice flow model reproduces the maximum CIC extent in the early 1960s followed by a rapid retreat (see Supplementary Methods, Supplementary Fig. 2b), demonstrating that it captures the main glaciological processes influencing CIC.

After verifying that the model could reproduce observed changes, the glacier model was next driven by hypothetical meteorological datasets in which the observed warming (respectively the observed dryness) was removed since the 1950s (Table 1). Assuming current ice cap hypsometry and extent the model suggests that CIC would logically present a positive balance (0.58 mm w.e. a^{-1}) if precipitation and temperature were at their 1950s level. Indeed, the retreat caused the loss of low elevation areas where ablation is the highest. Despite the warming trend observed at Kerguelen since 1960, modeling suggests that 77% of the current negative mass balance is explained by the dryness (Table 1). Thus, precipitation decrease was the first order driver for glacier mass loss, while atmospheric warming, including the effects of greenhouse gases, played a smaller amplifying role.

An abrupt dry spell observed in 1963 initiated the glacier wastage. This dryness was related to large scale processes involving ocean-atmosphere interactions as suggested by the consistency between variations of surface air temperature and precipitation measurements at PAF before 1975 (Fig. 2b), and between air temperature and ocean surface temperature (ERSST.v2[28] and HadSST2[29]) in the box containing Kerguelen Islands (Fig. 2a). Actually, the historical ERSST.v2 data indicate that SST exhibited large changes on decadal time scales prior to 1960 (Fig. 2a), likely a result of large internal natural climate variability[30]. A correlation map between temperature measured at Kerguelen and SST data (HadSST2) before 1975 shows a typical Subtropical Indian Ocean Dipole[31] pattern (Fig. 3a), whose positive phases are associated to high precipitation in South Africa due to abnormally warm conditions of the Agulhas current. The SST of the Agulhas and Antarctic Circumpolar Currents along the southwestern limb of the south Indian subtropical gyre control the evaporation rates within the storm track that eventually reach Kerguelen Islands (Fig. 3c), yielding positive correlations between precipitation variations at Kerguelen and SST in the latter regions (Fig. 3b).

However, starting in the 1970s, climate drivers and the link between temperature and precipitation at Kerguelen have changed. Our analysis of reanalysis (ERA-40, NCEP-NCAR reanalysis1) and climate models (CMIP5) outputs shows that drying and warming since the 1970s are associated with a storm track shift, atmospheric drying and oceanic warming over large areas around Kerguelen Islands (see Supplementary Discussion, Supplementary Fig. 4,6-9). This observation is in perfect agreement with the expected consequences of the recent increasing shift of the Southern Annular Mode (SAM)[15,18–23,32] to its most positive phase (+SAM) over the last millennium[23]. Here we additionally show that +SAM disrupted climate teleconnections at Kerguelen after 1975. The correlation map between HadSST2 data and temperature at Kerguelen displays a strong dipole-like pattern but with a south-north orientation (Fig. 3d) that differs from the typical Subtropical Indian Ocean Dipole pattern (as observed in Fig. 3a). The correlation map for precipitation changes even more, showing a negative correlation between Kerguelen Islands and regions to the south of South Africa (Fig. 3e). Our analysis suggests that precipitation intensity at Kerguelen is no longer controlled by the Agulhas and Antarctic Circumpolar Currents systems (Fig. 3e), because the islands are not under the direct influence of the storm tracks anymore (Fig. 3f and Supplementary Fig. 9). Climatic change disrupted synchronicity between changes in precipitation and temperature since 1975, and trends are opposite

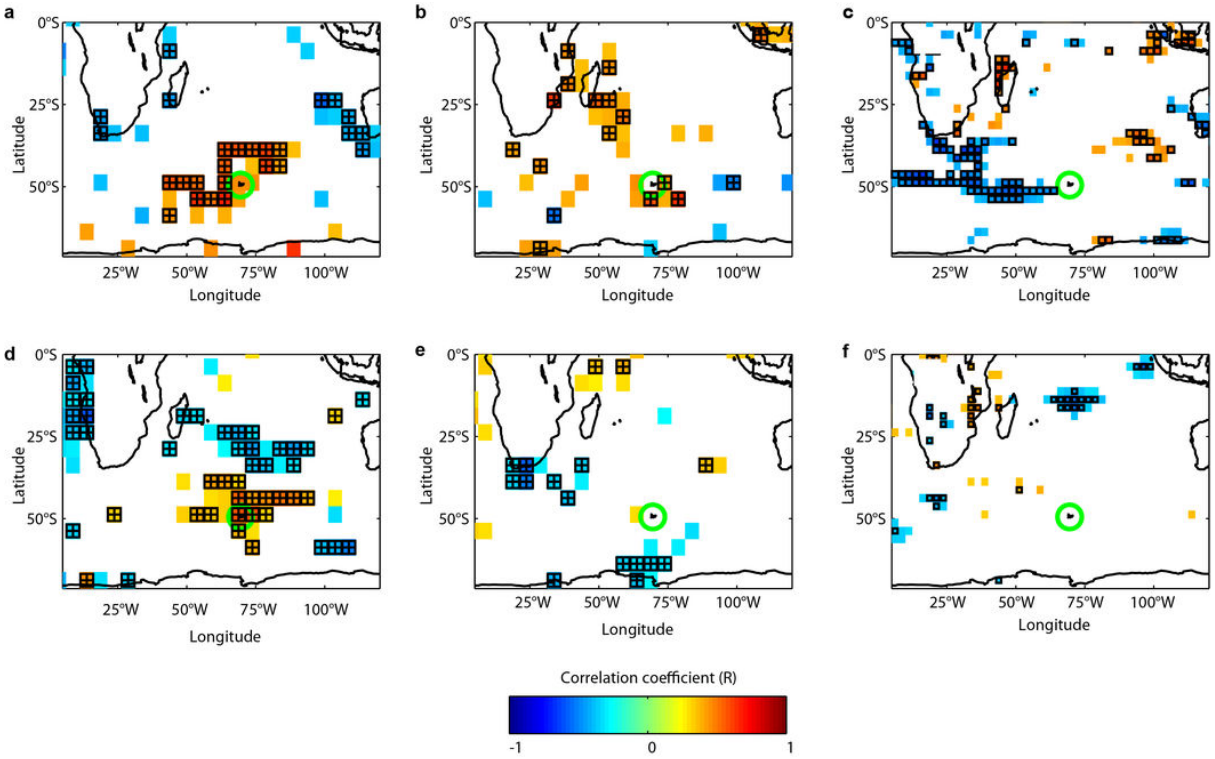

Figure 3. Teleconnections between climate at PAF and conditions in the surrounding oceans. Correlation coefficient (R) is computed between December to March (DJFM) HadSST2 mean Sea Surface Temperature and mean DJFM local atmospheric temperature (a&d) and precipitation (b&e) observed at Kerguelen. c&f) same as previous panels but for correlation between ERA40 precipitation from the pixel including Kerguelen Islands and ERA40 surface latent heat flux during DJFM. Surface latent heat flux is negative when evaporation occurs. Correlation maps are made before 1975 (a, b&c) and after 1975 (d, e&f). All time-series are detrended. Pixels where correlation is significant at 95% are in squared areas, at 90% are in colored areas. Pixels where correlation significance is lower than 90% are not shown. Kerguelen Islands are located inside the green circle.

afterward (Fig. 2b). This situation accelerated the glacier mass loss since 1975 (Table 1, Fig. 2c) and the area reduction since the 1990s (see Figure 2 in (3)), with an impact on glaciers that overpasses the one from internal variability of the climate system as observed before 1975.

The recent +SAM is mainly attributed to hemispheric-scale[17] stratospheric ozone depletion ("the ozone hole") that cooled the stratosphere since the mid-1970s[16]. Greenhouse gases increases also produce a +SAM, though the historical greenhouse gas influence is smaller than that of the ozone hole[15]. Over the next century, projected greenhouse gas increases are expected to lead to additional +SAM intensification in spite of ozone hole recovery[15,32]. At Kerguelen, climate models predict substantial warming by 2100 and that precipitation will not recover their pre-1960 values (see Supplementary Discussion, Supplementary Fig. 5). Because the 0 °C isotherm is now very close to the CIC summit, further warming could eliminate snowfall and accumulation (except in the core of winter) with important albedo feedback on melting. If future warming and sustained dryness are realized, Kerguelen glaciers and ice caps will continue to lose mass at rates that are amongst the fastest on Earth (Table 1).

The CIC wastage demonstrates the unexpectedly large consequences of the ozone hole on climate and environment in the southern sub-polar latitudes. During the last four decades, the extreme ice wastage on Kerguelen Islands was due primarily to drying caused by the unprecedented and anthropogenically-induced +SAM trends[18−23], whereas warming only accounted for one quarter of the mass loss. We suspect similar drying trends are leading to ice wastage at other southern mid- and sub-polar latitudes[1−5] in particular in Patagonia (supplementary Fig. 4,10). Due to the hemispheric nature of the SAM, our findings suggest that the causes of late 20^{th} century glacier wastage at southern mid- and sub-polar latitudes must be re-considered in order to take into account the impact of the ozone hole on climate.

References

(1) Rignot, E., Rivera, A., & Casassa, G., Contribution of the Patagonia Icefields of South America to Sea Level Rise. *Science* **302**, 434-436 (2003).
(2) Melkonian, A.K. et al. Satellite-derived volume loss rates and glacier speeds for the Cordillera Darwin Icefield, Chile. *The Cryosphere* **7**, 823-839 (2013).
(3) Berthier, E., Le Bris, R., Mabileau, L., Testut, L. & Rémy, F. Ice wastage on the Kerguelen Islands (49°S, 69°E) between 1963 and 2006. *J. Geophys. Res.* **114**, F03005 (2009).
(4) Willis, M.J., Melkonian, A.K., Pritchard M.E. & Rivera, A. Ice loss from the Southern Patagonian Ice Field, South America, between 2000 and 2012. *Geoph. Res. Lett.* **39**, L17501 (2012).
(5) Vaughan, D.G.et al. Observations : Cryosphere. In : Climate Change 2013 : The Physical Science Basis. Contribution of Working Group I to the Fifth Assessment Report of the Intergovernmental Panel on Climate Change [Stocker, T.F., D. Qin, G.-K. Plattner, M. Tignor, S.K. Allen, J. Boschung, A. Nauels, Y. Xia, V. Bex and P.M. Midgley (eds.)]. Cambridge University Press, Cambridge, United Kingdom and New York, NY, USA (2013)
(6) Moholdt, G., Wouters, B. & Gardner, A.S. Recent mass changes of glaciers in the Russian High Arctic. *Geoph. Res. Lett.* **39**, L10502 (2012).
(7) Berthier, E., Schiefer, E., Clarke, G.K.C., Menounos, B. & Rémy, F. Contribution of Alaskan glaciers to sea-level rise derived from satellite imagery. *Nature Geosci* **3**, 92-95 (2010).
(8) Bjornsson, H. et al. Contribution of Icelandic ice caps to sea level rise : Trends and variability since the Little Ice Age. *Geoph. Res. Lett.* **40** (8), 1546-1550 (2013).
(9) Trüssel, B.L., Motyka, R.J., Truffer, M. & Larsen, C.F. Rapid thinning of lake-calving Yakutat Glacier and the collapse of the Yakutat Icefield, southeast Alaska, USA. *J. Glaciol.* **59** (213), 149-161

(2013).
(10) Vallon, M. Bilan de masse et fluctuations récentes du Glacier Ampère (Iles Kerguelen, TAAF), *Zeitschrift für Gletscherkunde und Glazialgeologie***13**, 55-85 (1977).
(11) Frenot, Y., Gloaguen, J.C., Picot, G., Bougère, J. & Benjamin, D. Azorella selago Hook. used to estimate glacier fluctuations and climatic history in the Kerguelen Islands over the last two centuries. *Oecologia* **95**, 140-144 (1993).
(12) Gardner, A.S. et al. A Reconciled Estimate of Glacier Contributions to Sea Level Rise : 2003 to 2009. Science 340, 852-857 (2013).
(13) Moholdt, G., Hagen, J.O., Eiken, T. & Schuler, T.V. Geometric changes and mass balance of the Austfonna ice cap, Svalbard. *The Cryosphere* **4**, 21-34 (2010).
(14) Nuth, C., Moholdt, G., Kohler, J., Hagen, J.O. & Kääb, A. Svalbard glacier elevation changes and contribution to sea level rise. *Geoph. Res. Lett.* **115**, F01008 (2010).
(15) Thompson D.W.J. et al. Signatures of the Antarctic ozone hole in Southern Hemisphere surface climate change. *Nature Geosci.* **4**, 741-749 (2011).
(16) Farman, J.C., Gardiner, B.G. & Shanklin, J.D. Large losses of total ozone in Antarctica reveal seasonal ClOx/NOx interaction. *Nature* **315**, 207-210 (1985).
(17) Stolarski, R.S. et al. Nimbus 7 satellite measurements of the springtime Antarctic ozone decrease. *Nature* **322**, 808-811 (1986).
(18) Villalba, R. et al. Unusual Southern Hemisphere tree growth patterns induced by changes in the Southern Annular Mode. *Nature Geosci.* **5**, 793-798 (2012).
(19) Manatsa, D., Morioka, Y., Behera, S.K., Yamagata, T. & Matarira, C.H. Link between Antarctic ozone depletion and summer warming over southern Africa. *Nature Geosci.* **6**, 934-939 (2013).
(20) Yin, J.H. A consistent poleward shift of the storm tracks in simulations of 21st century climate. *Geoph. Res. Lett.* **32**, L18701 (2005).
(21) Gillett, N.P., Kell, T.D. & Jones, P.D. Regional climate impacts of the Southern Annular Mode. *Geoph. Res. Lett.* **33**, L23704 (2006).
(22) Sallée, J.B., Speer, K. & Morrow, R. Response of the Antarctic Circumpolar Current to Atmospheric Variability. *J. Climate* **21**, 3020-3039 (2008).
(23) Abram, N.J., Mulvaney, R., Vimeux, F., Phipps, S.J., Turner, J. & England, M.H. Evolution of the Southern Annular Mode during the past millennium, *Nature Clim. Change*, advance online publication (2014)
(24) Schaefer, M., Machguth, H., Falvey, M., & Casassa G. Modeling past and future surface mass balance of the Northern Patagonia Icefield, *J. Geophys. Res. Earth Surf.* **118**, 571-588 (2013)
(25) Lenaerts, J., van den Broeke, M., van Wessem, J., van de Berg, W., van Meijgaard, E., van Ulft, L., & Schaefer M. Extreme precipitation and climate gradients in Patagonia revealed by high-resolution regional atmospheric climate modelling. *J. Clim.* **27**, 4607-4621 (2014)
(26) Radić, V. & Hock, R. Regionally differentiated contribution of mountain glaciers and ice caps to future sea-level rise. *Nature Geosci.* **4**, 91-94 (2011).
(27) Jomelli, V. et al. Irregular tropical glacier retreat over the Holocene epoch driven by progressive warming. *Nature* **474**, 196-199 (2011).
(28) Smith, T.M. & Reynolds, R.W. Improved Extended Reconstruction of SST (1854-1997). *J. Climate* **17**, 2466-2477 (2004).
(29) Rayner, N.A., et al. Improved analyses of changes and uncertainties in sea surface temperature measured in situ since the mid-nineteenth century : the HadSST2 data set. *J. Climate* **19**, 446-469 (2006).
(30) Deser, C., Phillips, A., Bourdette, V. & Teng, H. Uncertainty in climate change projections : the role of internal variability. *Clim. Dynam.* **38**, 527-546 (2012).

(31) Behera, S. & Yamagata, T. Subtropical SST dipole events in the southern Indian Ocean. *Geoph. Res. Lett.* **28** (2), 327-330 (2001).
(32) Purich, A., Cowan, T., Min, S.-K. & Cai, W. Autumn Precipitation Trends over Southern Hemisphere Midlatitudes as Simulated by CMIP5 Models. *J. Climate* **26**, 8341-8356 (2013).
(33) Trenberth et al. Observations : Surface and Atmospheric Climate Change. In : Climate Change 2007 : The Physical Science Basis. Contribution of Working Group I to the Fourth Assessment Report of the Intergovernmental Panel on Climate Change [Solomon, S., D. Qin, M. Manning, Z. Chen, M. Marquis, K.B. Averyt, M. Tignor and H.L. Miller (eds.)]. Cambridge University Press, Cambridge, United Kingdom and New York, NY, USA (2007).

Acknowledgements. This study was funded by IPEV-1048 GLACIOCLIM-KESAACO and LEFE-INSU KCRuMBLE programs. Logistical supply to Kerguelen Islands was provided by the French Polar institute (IPEV) and we particularly thank Y. Frenot who initially proposed this study. We particularly thank Meteo France for the meteorological and radiosondes data from PAF. E.B. acknowledges support from the French Space Agency (CNES) through the TOSCA and ISIS programs. NCEP 1 and 2 reanalysis data were provided by the NOAA/OAR/ESRL PSD, Boulder, Colorado, USA, from their Web site at `http://www.esrl.noaa.gov/psd/`. ERA-40 and ERA-Interim reanalysis data were downloaded from the ECMWF data portal at `http://data-portal.ecmwf.int/`. We acknowledge the World Climate Research Programme's Working Group on Coupled Modelling, which is responsible for CMIP, and we thank the climate modelling groups (listed in Supplementary Supplementary Table 2) for producing and making available their model output. Sea surface temperature measurements at PAF were provided by ROSAME (Réseau d'Observation Subantarctique et Antarctique du niveau de la MEr) at `http://www.legos.obs-mip.fr/observations/rosame`. ERSST-v2 data were obtained at `http://iridl.ldeo.columbia.edu/SOURCES/.NOAA/.NCDC/.ERSST/.version2/.SST/`. HadSST2 data were obtained at `http://www.metoffice.gov.uk/hadobs/hadsst2/` and AVHRR data were obtained at `http://podaac.jpl.nasa.gov/dataset/NCDC-L4LRblend-GLOB-AVHRR_OI`. CRU TS 3.21 data were provided by the British Atmospheric Data Centre, at `http://badc.nerc.ac.uk/data/cru/`.

Author contributions

VF, DV, VJ, and DB conducted the field work on Kerguelen glaciers ; EB, LD and YM estimated the Cook Ice Cap mass balance using remote sensing data. VF developed the PDD and dynamics numerical modeling. JK interpreted the radio-sounding data. MM, DV, JK and VF interpreted the GCM modeling and Y-HP interpreted oceanographic data. DV and HG performed the regional atmospheric circulation modeling (with MAR model). All authors wrote the paper.

3.4 Analyse des processus à plus grande échelle

3.4.1 Motivations et principaux résultats

Dans la Section 3.2, nous avons analysé le retrait marqué de la calotte Cook aux îles Kerguelen au cours des dernières décennies et montré que celui-ci est lié à un déficit d'accumulation causé par une diminution marquée des précipitations depuis les années 60, ainsi qu'à un léger réchauffement de l'atmosphère. Dans la Section 3.3, nous avons étudié les causes de cet assèchement et réchauffement, montrant que ceux-ci sont liés à l'intensification de plus en plus forte du SAM au cours des dernières décennies. De par la nature hémisphérique du SAM, nous supposons que la majeure partie de la bande latitudinale 30° S - 60° S a dû être affectée par son

intensification. Les zones englacées situées dans ces régions subpolaires, en Patagonie, Géorgie du Sud et en Nouvelle-Zélande, sont donc susceptibles d'avoir été touchées par l'assèchement et le réchauffement observés aux îles Kerguelen. Des analyses indépendantes du changement climatique et du retrait glaciaire dans ces régions ont déjà été menées par le passé, mais aucune analyse combinant ces deux approches n'a jamais été réalisée sur l'ensemble de cette bande latitudinale. C'est ce que nous proposons de faire dans un article en cours de rédaction à soumettre prochainement à *Geophysical Research Letters*, présenté ci-dessous.

Nous analysons donc un jeu de données complet de précipitations et de température de l'air et de l'océan, constitué d'observations de terrain et de satellites, de données de réanalyses, de données composites et de sorties d'un modèle degré-jour. Une analyse critique de ces données est tout d'abord réalisée dans une région centrée autour de l'archipel des Kerguelen. Celle-ci révèle que les SST constituent des données intéressantes pour effectuer une analyse distribuée des changements de température de l'air en surface, grâce à leur excellente corrélation sur les océans. En raison du nombre limité et changeant au cours du temps d'observations disponibles dans la région des Kerguelen, les jeux de données de SST les plus fiables en région côtière se révèlent être ceux issus de mesures satellites (tels que AVHRR) ou ceux produits sans interpolation spatiale (tels qu'HadSST2). Une analyse des températures issues des radiosondages de Port-aux-Français révèle cependant que le réchauffement observé dans les couches les plus basses de l'atmosphère (> 1000 hPa) aux îles Kerguelen est déconnecté de ce qui se passe dans les couches supérieures, où aucun réchauffement n'est observé. Cela signifie que les SST peuvent nous renseigner sur les changements de température en surface et les processus d'ablation des glaciers situés à la côte, mais pas à l'intérieur des terres.

Les jeux de données de SST validés aux îles Kerguelen sont ensuite utilisés pour estimer les tendances climatiques dans l'ensemble des zones subpolaires de l'hémisphère sud, et plus spécifiquement à proximité des zones englacées de Patagonie, Géorgie du Sud et Nouvelle-Zélande. Le réchauffement au cours des trois dernières décennies observé aux îles Kerguelen est quasiment généralisé sur l'ensemble des zones situées au nord de 50° S, affectant l'île Sud de Nouvelle-Zélande où se situe les glaciers de cette région. Une tendance au refroidissement au cours de la même période est cependant observée le long de la côte ouest d'Amérique du Sud, qui draine une grande partie des champs de glace patagoniens et de la cordillère Darwin. En Géorgie du Sud, les différents jeux de données diffèrent et aucune tendance claire n'est donc détectable. En ce qui concerne les changements de précipitations, seules les données observées du CRU et de GPCP ont été utilisées car les précipitations issues de réanalyses sont généralement peu représentatives, en raison de leur dépendance à l'assimilation de données de radiosondages proche de la zone d'étude et de leur faibles performances en région de topographie complexe. Les données du CRU et de GPCP indiquent une tendance marquée à l'assèchement sur une majeure partie de la bande latitudinale étudiée, qui concerne les régions glaciaires de l'archipel des Kerguelen, de la Patagonie, de la Géorgie du Sud et de la Nouvelle-Zélande. Cet assèchement semble avoir commencé dès les années 50 dans la plupart des régions, à l'exception de la Nouvelle-Zélande et de la cordillère Darwin où il n'a commencé qu'à la fin des années 90.

Finalement, les tendances de température et précipitations observées précédemment sont comparées au retrait glaciaire des différentes régions étudiées. Des estimations du bilan de masse glaciaire dans chacune de ces régions grâce au modèle degré-jour utilisé dans les Sections 3.2 et 3.3 seront prochainement effectuées afin d'être intégrées à cette étude. La comparaison des observations dans la littérature du retrait glaciaire dans les différentes régions avec les tendances de température révèle que le retrait glaciaire aux îles Kerguelen et en Nouvelle-Zélande semble cohérent avec le réchauffement observé. En Géorgie du Sud, la tendance est plus difficile à

observer. Par contre, en Patagonie, il est difficile de relier le retrait des glaciers situés sur la façade ouest du continent, dont la plupart se jette dans l'océan, avec la température, car une tendance significative au refroidissement a été observée le long de la côte dans cette région. Un léger réchauffement à l'intérieur des terres pourrait néanmoins être responsable du retrait des glaciers orientaux. Le réchauffement atmosphérique ne peut cependant à lui seul expliquer les retraits de l'ensemble des glaciers de la zone 30° S - 60° S.

L'analyse spécifique du lien entre retrait des glaciers marins et tendances de température en Patagonie révèle une possible atténuation du retrait des glaciers marins du champ de glace patagonien sud liée au refroidissement de l'océan. Dans la cordillère Darwin, l'interprétation est plus complexe. En effet, à taille équivalente, le retrait des glaciers marins ne semble pas différer de celui des glaciers posés. Le retrait des glaciers dans cette région est simplement fonction de leur taille, et plus fort au nord de la cordillère qu'au sud, ce qui reflète sans doute un réchauffement plus marqué au nord qu'au sud (qu'il est cependant difficile de vérifier en raison du faible nombre de données dans cette région).

En ce qui concerne les précipitations, les tendances observées dans les régions subpolaires sont en accord avec le retrait glaciaire. Un assèchement sur les dernières décennies est observé au-dessus de chacune des zones glaciaires étudiées, bien que les tendances varient sensiblement d'une région à l'autre. Aux îles Kerguelen, nous avons montré dans la Section 3.3 que le retrait de la calotte était principalement causé par la sécheresse liée à l'intensification du SAM depuis les années 70. C'est sans doute également le cas dans d'autres régions subpolaires telles qu'en Nouvelle-Zélande et en Géorgie du Sud, bien que le réchauffement observé ait également pu contribuer au retrait glaciaire. En Patagonie, le retrait des glaciers occidentaux du champ de glace patagonien sud n'est pas cohérent avec le refroidissement côtier observé, ce qui suggère que le retrait n'est pas lié au premier ordre à une augmentation de l'ablation ou du vêlage. L'assèchement majeur observé dans cette région a par contre très certainement contribué majoritairement au retrait glaciaire. Finalement, en cordillère Darwin, en raison du manque de données de radiosondages ou de stations météorologiques à long terme, les tendances observées dans le CRU ou dans les réanalyses doivent être considérées avec précaution, et il est difficile de savoir quelles sont les contributions relatives des températures et des précipitations.

L'influence du SAM sur le déplacement vers le sud des zones dépressionaires a été présenté dans la Section 3.3, où l'impact sur les glaciers au travers des précipitations a été démontré. D'autres études ont montré l'impact du SAM sur les précipitations en Nouvelle-Zélande (Villalba et al., 2012) et en Afrique du Sud (Manatsa et al., 2013). L'analyse présentée dans l'article ci-dessous révèle que les zones dépressionnaires semblent avoir également été déplacées vers le sud en Amérique du Sud, où elles n'affectent à présent plus que l'extrême sud du continent.

3.4.2 Extrait de l'article Verfaillie et al. (en préparation)

Reconciling southern hemisphere mid-latitude glacier wastage and climate change

Verfaillie, D., Favier, V., Memegoz, M., Kay, J., Jomelli, V., Berthier, E. & Gallée, H., 2014, Geophysical Research Letters, in prep.

Abstract[1]

1. Introduction

The southern mid- and high latitudes are where glaciers were changing the most during the last decade (Gardner et al., 2013; Favier et al., in review). Very negative mass balances were observed everywhere in this latitudinal range. The combined loss of the Northern and Southern Patagonian Icefields (NPI and SPI) was -0.87 $\pm$ 0.05 m water equivalent per year (w.e. a^{-1}) over 1975-2000 (Rignot et al., 2003), while values of -1.17 $\pm$ 0.09 m w.e. a^{-1} and -1.62 $\pm$ 0.09 m w.e. a^{-1} were measured between 2000 and 2012 for NPI and SPI respectively (Willis et al., 2012a,b). Similarly, the Darwin Cordillera Icefield (DCI) thinned by -1.5 $\pm$ 0.6 m w.e. a^{-1} between 2001 and 2011 (Melkonian et al., 2013). At Kerguelen, glaciated surfaces were reduced by more than 20% between 1963 and 2001 (Berthier et al., 2009), and the Cook Ice Cap experienced a mass balance value of -1.51 $\pm$ 0.19 m w.e. a^{-1} between 2000 and 2009 (Favier et al., in review). Glacier wastage was more reduced in the New Zealand Southern Alps, but still reached values of -0.23 m w.e a^{-1} between 1976 and 2008 (Chinn et al., 2012), and -0.32 $\pm$ 0.78 m w.e. a^{-1} between 2003 and 2009 (Gardner et al., 2013). Finally, Gordon et al. (2008) showed that most South Georgian glacier fronts have retreated since the 1980s.

These variations are generally assumed to mainly reflect global warming (Rignot et al., 2003; Berthier et al., 2009; Lopez et al., 2010; Melkonian et al., 2013; Vaughan et al., 2013), as suggested by the temperature increase proposed by several studies in the southern subpolar regions (Jacka et al., 2004; Trenberth et al., 2007). However, long-term continuous reliable field measurements (i.e., at least before 1970) close to the studied ice bodies are very rare which limits the accuracy of the computed trends. Moreover, the causes of the retreat are still not fully explained because well-constrained glaciological modeling (Schaefer et al., 2013; Lenaerts et al., 2014) has always been forced by reanalysed data, which are believed to present important biases, mainly in the case of precipitation. Moreover, modeling did not consider calving processes which are expected to play an important role in Patagonia for instance.

This leads to several contradictions in the litterature. For instance, warming during the last 40 years (Gordon et al., 2008; Melkonian et al., 2013) is in contraction with observed sea surface temperature (SST) decrease in several regions as for example along the pacific coast of southern Chile (Falvey and Garreaud, 2009; Wang and Kay, 2013). On the other hand, likely as a consequence of inconsistent reanalysed precipitation variations since 1980, the surface mass balance of SPI modeled by (Lenaerts et al., 2014) was increasing over the last decade, in contradiction with the increasing wastage there. As a consequence, conclusions on warming trends and on their impacts on glaciers may be uncertain. Conversely, the impact of precipitation has generally been considered as a second order problem, while precipitation is expected to have decreased almost everywhere in the southern mid- and high-latitudes (Thompson et al., 2011; Hartmann et al., 2013), in particular close to NPI (Garreaud et al., 2013), on Marion Island (le Roux and McGeoch, 2008) or at Kerguelen Islands (Berthier et al., 2009). Revisiting the causes of glacier wastage is thus important in this region. Yet, the drying trend observed at Kerguelen Islands was recently demonstrated as the first order cause of glacier wastage in this region (Favier et al., in review; Verfaillie et al., submitted).

1. section en cours de rédaction.

During the last four decades, this important drying trend resulted from atmospheric circulation changes that occurred in the mid- and high-latitudes of the southern hemisphere. These changes were very likely caused by more frequent positive phases of the Southern Annular Mode (SAM), which reached its most positive phase over the last 1000 years (Abram et al., 2014). The anthropogenically-induced ozone hole is supected to have cooled the stratosphere, and increased the poleward temperature gradient in the troposphere leading to important changes in the SAM phases. This dramatically transformed the post 1970s southern hemisphere climate. A poleward shift of the descending branch of the Hadley cell and the temperate storm tracks (Cai et al., 2012) has been found to affect the Southern hemisphere climate (Thompson et al., 2011). The induced variations in moisture fluxes is expected to have influenced precipitation in Southern Africa (Manatsa et al., 2013), and tree growth in the Southern Hemisphere extra-tropics (Villalba et al., 2012). Yet, a causal relationship between glacier retreat in the sub-polar and mid-latitudes and the SAM-induced dryness has only been clearly demonstrated for Kerguelen Islands (Favier et al., in review). However, due to the hemispheric nature of the SAM (Yin, 2005; Thompson et al., 2011; Abram et al., 2014; Favier et al., in review), its consequences may have impacted other ice bodies in this latitudinal range. Could a drying trend explain the recent glacier wastage in Patagonia or South Georgia ?

Due to the lack of continents over very large areas, trends are based on sporadic field data interpolated by complex statistical approaches including models or remote sensing data. The field data source, coverage and accuracy constantly vary, which tends to limit the significance of the computed trends. Analyzing separately climate change and glacier wastage has been largely performed but both approaches have not been simultaneously analyzed over a large zonal range. In the present study, we compared both approaches and intended to validate or invalidate data sources. A criticial analysis of data sources was performed in a region centered on Kerguelen archipelago (49 °S, 69 °E, Fig. 1) where long term data are available, and glacier behavior is clearly known and constrained. After describing the available data (Section 2), we validate data sources at Kerguelen and select the most adequate source for a spatially distributed analysis (Section 3). These data sources are then used to display climate trends in the SH mid-latitudes and particularly around the main ice bodies (Section 4). Finally, we critically compare these trends with the observed glacier wastage (Section 5).

2. Available Data

2.1. Field observations

2.1.1 Météo France Station at Port-aux-Français, Kerguelen

Météo France installed a meteorological station close to the station of Port-aux-Français (PAF, see Fig. 1) in 1950. Since then, direct meteorological measurements have been performed routinely, including surface air temperature and daily precipitation measurements. These air temperature observations will be considered as the reference dataset against which we will compare other observations or (re)analyses in the following.

2.1.2. Radiosoundings at Kerguelen

Radiosoundings have also been carried out by Météo France at PAF since November 1960. Air temperature, pressure, geopotential height, relative humidity and wind speed and direction are measured daily from the surface up to the maximum elevation reached by the radiosonde (generally between 10,000 and 30,000 m). In this study we will use radiosonde air temperature measurements at 500, 700, 850 and 1000 hPa. Only data since the 1970s, which offer sufficient temporal coverage,

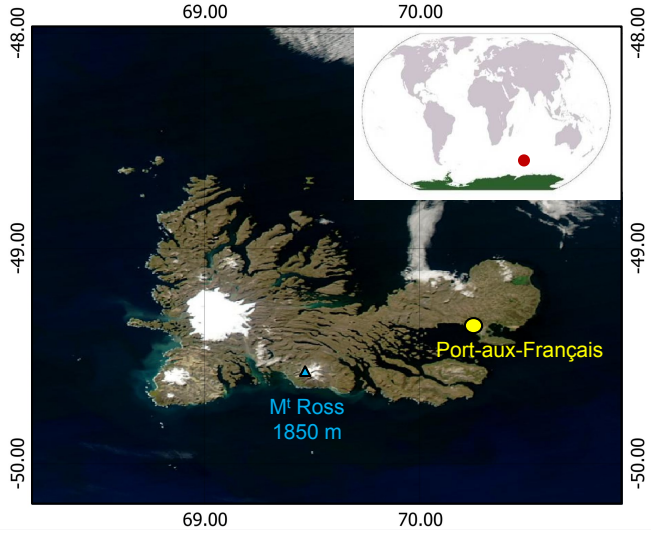

Figure1. MODIS© image of Kerguelen archipelago showing the location of Port-aux-Français station. Location of Kerguelen is shown as a red dot on the global map in the top right corner.

are considered.

2.1.3. ROSAME Tide Gauges at Kerguelen

The ROSAME (Réseau d'Observation Sub-antarctique et Antarctique du niveau de la MEr) network is a set of tide gauges installed at Kerguelen, Crozet and Amsterdam archipelagos and at Dumont-d'Urville station in the 1990s, as part of the international programs WOCE and GLOSS. At Kerguelen, the tide gauge was installed in the Golfe du Morbihan, just off the coast of PAF. In this study we use monthly means of 2 m depth sea surface temperature (SST) since 1994 provided by LEGOS (Laboratoire d'Etudes en Géophysique et Océanographie Spatiales, Toulouse, France).

2.1.4. GPCP Dataset

The Global Precipitation Climatology Project version 2 dataset combines data from worldwide rain gauge stations, satellites and soundings to create a merged estimate of monthly rainfall on a 2.5˚grid from 1979 to the present (Adler et al., 2003). Precipitation over the oceans is based on satellite infrared and passive microwave measurements.

2.1.5. CRU Time-series Dataset

Climatic Research Unit (CRU) time-series (TS) datasets consist in gridded observational data from meteorological stations distributed worldwide (Harris et al., 2014). In this study, we used monthly CRU TS 3.21 precipitation and temperature data calculated on a 0.5˚grid since 1901. The dataset is constructed using the Climate Anomaly Method (Peterson et al., 1998) and a complex gridding

method described in Harris et al. (2014).

2.2. Satellite information

2.2.1 AVHRR Satellite SST Measurements

To get distributed SST values, we first used the AVHRR (Advanced Very High Resolution Radiometer) Optimal Interpolation SST analysis from the Group for High Resolution Sea Surface Temperature (GHRSST) (Reynolds et al., 2007). This analysis, available daily on a 0.25°grid since 1981, uses optimally interpolated (and bias adjusted) SST data from the AVHRR Pathfinder version 5 and observations from ships and buoys.

2.3. Reanalysis data

2.3.1. The ECMWF reanalysis

Reanalyses correspond to outputs from models using data assimilation, ie combination -during a given cycle- of observations (from radiosondes, buoys, satellites, etc.) and prior forecast model information, in order to obtain a physically coherent estimate of the state of the atmosphere as close to reality as possible. Each reanalysis is produced with a single version of a data assimilation system. Reanalysed data are expected to be reliable at Kerguelen, as surface and radiosonde observations performed at Port-aux-Français are assimilated in the reanalyses since 1967 and 1968 respectively for ERA .

We used the ERA-Interim and ERA-40 data (Uppala et al., 2005; Dee et al., 2011) from the European Centre for Medium-Range Weather Forecasts (ECMWF), ERA-40 reanalysis covers the period from 1957 to 2002. ERA40 uses a 6h-cycle 3D-variational assimilation scheme to produce data at a T159 ($\sim$ 125 km) spectral resolution, for 60 vertical levels (from the surface to 0.1 hPa). ERA-Interim offers reanalysis data since 1989, using a more advanced 4D-variational scheme (assimilating data every 12h) and a new version of the forecasting system. The resolution is enhanced compared to ERA-40 (T255 resolution, corresponding to $\sim$ 80 km) and the model physics was also improved. .

2.3.2. The NCEP-NCAR and NCEP-DOE Reanalysis

We also used the Reanalysis 1 and 2 data (Kalnay et al., 1996; Kanamitsu et al., 2002) from the National Centers for Environmental Prediction, National Center for Atmospheric Research and Department of Energy (NCEP-NCAR, NCEP-DOE). NCEP-NCAR Reanalysis 1 (NCEP 1) data are available from 1948 to the present. The model produces 6-hourly data at a T62 spectral resolution ($\sim$ 210 km) and for 28 vertical levels extending from 5hPa from the surface to a top level at 3hPa. It uses a sequential 6h-cycle data assimilation (3D-variational) scheme. NCEP-DOE Reanalysis 2 (NCEP 2) is a new reanalysis dataset extending from 1979 to the present, in which several errors from NCEP 1 were fixed and the model physics was improved. Surface and radiosonde observations performed at Port-aux-Français are assimilated in the reanalyses since and 1967 and 1970 respectively.

As grids and resolution differ between models, reanalysis data for Kerguelen were retrieved for different specific grid cell locations depending on the reanalysis considered. Location of grid cells used in this study for each reanalysis is indicated in Table 1. Air temperature at 2 m, skin temperature and precipitation data were used in this study.

Table 1. Location of the center of specific reanalysis grid cells used in this study.

	ERA-40	ERA-Interim	NCEP-NCAR 1	NCEP-DOE 2
Latitude	50S	48S	48.6S	48.6S
Longitude	70E	69E	69.4E	69.4E

2.4. Composite data

2.4.1. ERSST Dataset

We used SST data from Extended Reconstructed Sea Surface Temperature (ERSST) analyses version 2 and version 3b since 1854 (Smith and Reynolds, 2004; Smith et al., 2008). Sparse SST measurements from ships, moored environmental buoys, drifting buoys and near-surface measurements from oceanographic profiles (ICOADS datasets) are reconstructed using improved statistical methods in 2°latitude $\times$ 2°longitude grid boxes. Near land/surface temperature is accounted for in ERSST version 3b but not in version 2. Satellite data are not used in either datasets.

2.4.2. HadSST2 Dataset

HadSST2 is a monthly global SST dataset produced by the Met Office Hadley Centre covering the period 1850 to date (Rayner et al., 2006). It uses quality-checked in-situ measurements from ships and buoys, without any interpolation of measurements over sparsely documented regions. No satellite data are used. Measurements are then converted into anomalies with respect to 1961-1990 climatology and averaged on a 5°monthly grid. Grid cells without any available measurements present missing values.

2.5. Outputs from a Positive Degree-Day Model

A simple PDD model was used to study the influence of climate change on glacier mass balance in the Southern Hemisphere mid-latitudes. The model has been described in detail in Favier et al. (in review). Briefly, it uses monthly SST data from AVHRR and temperature and precipitation data from CRU to calculate snow accumulation and snow or ice ablation on the various glaciers using degree-day factors for ice and snow.

3. Validating and Selecting Accurate Temperature Data Sources

In order to assess observation data uncertainties in the southern hemisphere mid- and high latitudes, we first focused on Kerguelen region, where a long term, consistent dataset is available (WMO standards). We compared the observed temperature at 2 meters above the surface from the meteorological station at PAF with data from different datasets : radiosonde data, air temperature and skin temperature data from reanalysis, in situ SST in the Golfe du Morbihan from ROSAME and SST from different composite datasets (Fig. 2 and 3). In spite of the resolution difference, all temperature datasets -reanalyses, radiosondes, station measurements and SST measurements and analyses- agree on the same temperature scenario at Kerguelen archipelago : a strong cooling (around -0.5 to -0.7 °C per decade) from the 1950s to the mid-1960s, followed by a strong warming (+0.6 to +0.7 °C per decade) until the 1980s, finally followed by a slight +0.1 °C per decade warming (or a slight cooling in ERSST data) from 1982 onwards.

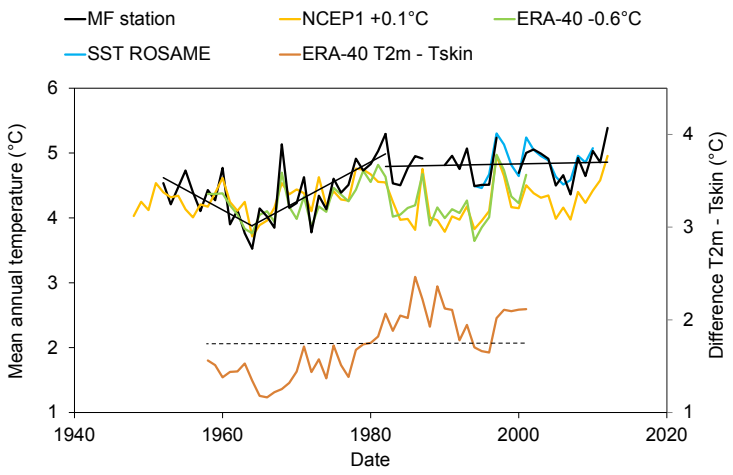

Figure 2. Comparison between air/ocean temperature observations from different datasets over Kerguelen : Météo France temperature measurements at Port-aux-Français, NCEP Reanalysis 1 and ERA-40 reanalysis temperature data, radiosonde observations at 1000 hPa (number of observation exceeding 140 per year) and ROSAME in situ SST. Reanalysis data have been shifted (+0.1 °C and -0.6 °C for NCEP1 and ERA-40 respectively) to show their difference in behaviour after 1980 compared to station measurements. Further evidence of the change in reanalyses after 1980 is shown by the difference between air temperature at 2m and skin temperature in ERA-40 (vertical axis on the right).

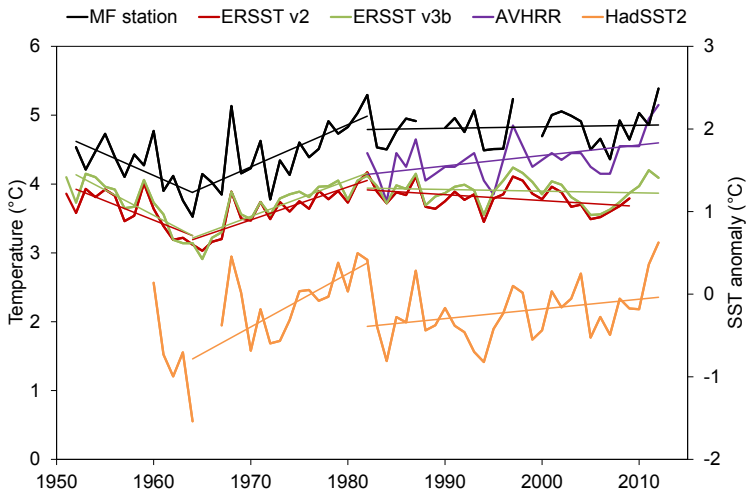

Figure 3. Comparison between air temperature measured at Port-aux-Français and values at Kerguelen from different SST datasets : ERSST analyses v2 and v3b, HadSST2 dataset and AVHRR satellite SST measurements. The vertical axis on the right refers to HadSST2 data, expressed as SST anomalies with respect to 1961-1990 climatology. Each SST dataset has been re-gridded on a 2° x 2° regular grid. Trend lines for the period 1952-1964, 1964-1982 and 1982-present are also represented.

The good quality of reanalysed temperature was expected because radiosonde data and measured SST at Kerguelen are assimilated in the reanalysis procedure. Nevertheless, the trends computed with reanalysis data should be cautiously interpreted. Indeed, temperature measurements are in good agreement with reanalyses before and after 1980 (correlation of 0.91 ($p\sim0$) between ERA-40 and PAF measurements and 0.78 ($p\sim0$) between NCEP 1 and measurements, not shown), but a sharp change in the difference between 2 m air temperature measurements and temperature in ERA 40 appears in 1980 (a shift of about -0.6 °C, see Fig. 2). After 1980, ERA40 and NCEP1 temperature are still in agreement but lower than measurements, and their correlation with measurements are lower than before 1980 (0.82 ($p = 0.0001$) and 0.62 ($p = 0.08$) for ERA-40 and NCEP 1 respectively compared to measurements, not shown). A change in the difference between 2 m temperature and skin temperature in ERA-40 around 1979 is also observed. This discrepancy between reanalysis temperature and observations since 1980 results from reanalysis biases according to the good consistency between surface temperature measurements and radiosonde data at 1000 hPa. This artificial change in reanalysis temperature is likely due to the assimilation of remotely sensed sea surface temperature data since 1979 (beginning of the satellite era, and installation of a buoy in 1982 in the Golfe du Morbihan), which must have changed the models' estimates of surface temperature at Kerguelen. This artefact has been well documented (Kistler et al., 2001; Uppala et al., 2005) in other regions. This leads to important differences if trends are computed on a period including the 1980 shift, even if radiosonde data were assimilated at Kerguelen largely since 1970. This suggests considering cautiously the temperature trends computed with reanalysis data, and to prefer the use of direct consistent observations. However, air temperature measurements over large distances are rare in this region of the world, particularly because inhabited regions are very scarce due to the absence of continents.

Sea surface temperature is thus a potential interesting source of information to estimate surface changes, because these two variables are closely related on the oceans. Indeed, despite its short time span, the ROSAME SST data at Kerguelen are remarkably close to air temperature measured at PAF (Fig. 2). Monthly ROSAME data and air temperature display a correlation of 0.97 ($p\sim0$) on their common period (05-01-1993 to 05-01-2013). The global SST analysis AVHRR satellite measurements at the grid point corresponding to PAF are also significantly correlated ($R=0.83$, $p\sim0$, over the same period). High interannual temperature variability can be noted, both in PAF measurements and SST datasets, but all datasets follow the same general evolution (described above), except for the recent period (1982-present), where ERSST datasets diverge (Fig. 3). Indeed, HadSST2 and AVHRR show an increasing trend of $+0.12$ °C decade^{-1} and $+0.15$ °C decade^{-1} respectively, in agreement with direct measurements (ROSAME data), while ERSSTv2 and ERSSTv3b display decreasing trends of -0.09 °C decade^{-1} (1982-2009) and -0.02 °C decade^{-1} respectively. Although ERSSTv3b might be influenced by PAF temperature as it accounts for near land/surface measurements, its evolution is very close to ERSSTv2 demonstrating that this composite data is mainly constrained by SST observations (ships and buoys) and by data interpolation processes. This suggests that HadSST2 and AVHRR should be preferred to assess SST variations. The spatial distribution of SST variations around the Kerguelen Islands confirms this observation (Fig. 4), because both HadSST2 and AVHRR data display strongly positive temperature trends in a large region around Kerguelen archipelago (significant at 95% for AVHRR according to a Spearman's test), whereas ERSSTv3b shows a decreasing (but not significant) trend west of Kerguelen and on the archipelago (the region of warming seems to be located more eastward).

In order to have a more global view of temperature variations in the southern hemisphere mid- and high latitudes, maps of SST trends over 1982-2012 were extended to the full 30°-70° S zonal belt in Fig. 5. The SST trends over the last 30 years were computed for a) ERSSTv3b, b) HadSST2

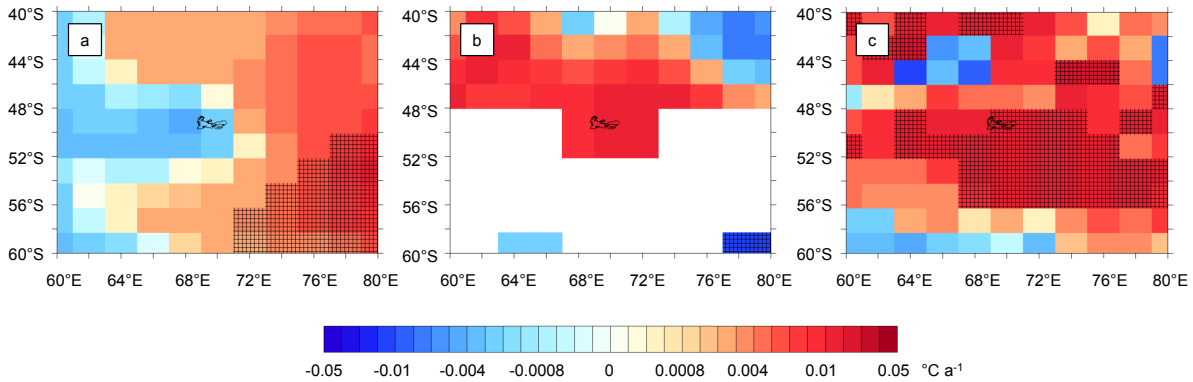

Figure 4. Maps of SST trends in the region of Kerguelen over 1982-2012 from a) ERSSTv3b, b) HadSST2 and c) AVHRR. Each dataset has been re-gridded on a 2° x 2° regular grid. Missing values are indicated in white. Squared areas corespond to regions where trends are significant at the 95% confidence level (Spearman's test).

and c) AVHRR datasets. The general picture of changes is very similar from the three datasets, but the ERSSTv3b dataset does not fully agree with the other two datasets, in particular in the Southern Indian ocean. This raises the questions of (1) the representativity of ERSSTv3b input data in this region, i.e. the fact that the number of buoys and ships and the ship trajectories change through time in this region where a sharp gradient of SST is observed, and (2) the interpolation of SST data in analyses. Indeed, ERSSTv3b use a reconstruction method to fill missing data grid cells, which is not the case of HadSST2 (as can be observed on Fig. 5 b) or AVHRR. Morever, because of the sparsity and changing number of observations around Kerguelen, reconstructed data based on these measurements is likely poorly reliable in this region. This is probably also the case in other remote parts of the Southern ocean, especially at the frontier between SST warming and cooling. SST trends produced with ERSST data should thus be considered with caution in such areas. In better documented areas or where very significant trends appears, ERSST data can be used with more confidence. For example, along the west coast of South America, we find a better consistency in the cooling trend over 1982-2012 displayed by ERSSTv3b, HadSST2 and AVHRR datasets (between -0.01 and -0.03 °C year^{-1}, Fig. 5). This cooling agrees well with the trends found in Falvey and Garreaud (2009) over 1979-2006 for ERSSTv2, HadISST or land coastal stations. Consequently, the most reliable source for the analysis of climatic trends in coastal regions consists in satellite data for the recent period such as AVHRR, and datasets produced without spatial interpolation such as HadSST2.

Nevertheless, surface temperature changes do not inform on variations at high altitudes. For instance, at Kerguelen, a frequency histogram of radiosonde temperature observations since 1973 for four different pressure levels (1000, 850, 700 and 500 hPa) and during two distinct decades (1973-1982 and 2002-2011) (Fig. 6) shows that a slight positive trend in air temperature for the last decade compared to 1973-1982 is only visible at 1000 hPa, whereas it cannot be detected at higher levels. This suggests that only the low atmospheric layers warmed over the last decades in Kerguelen region, and that changes in the low and high atmosphere are disconnected. As a consequence, the analysis performed with SST may inform on ablation processes at the coast, but not further inland.

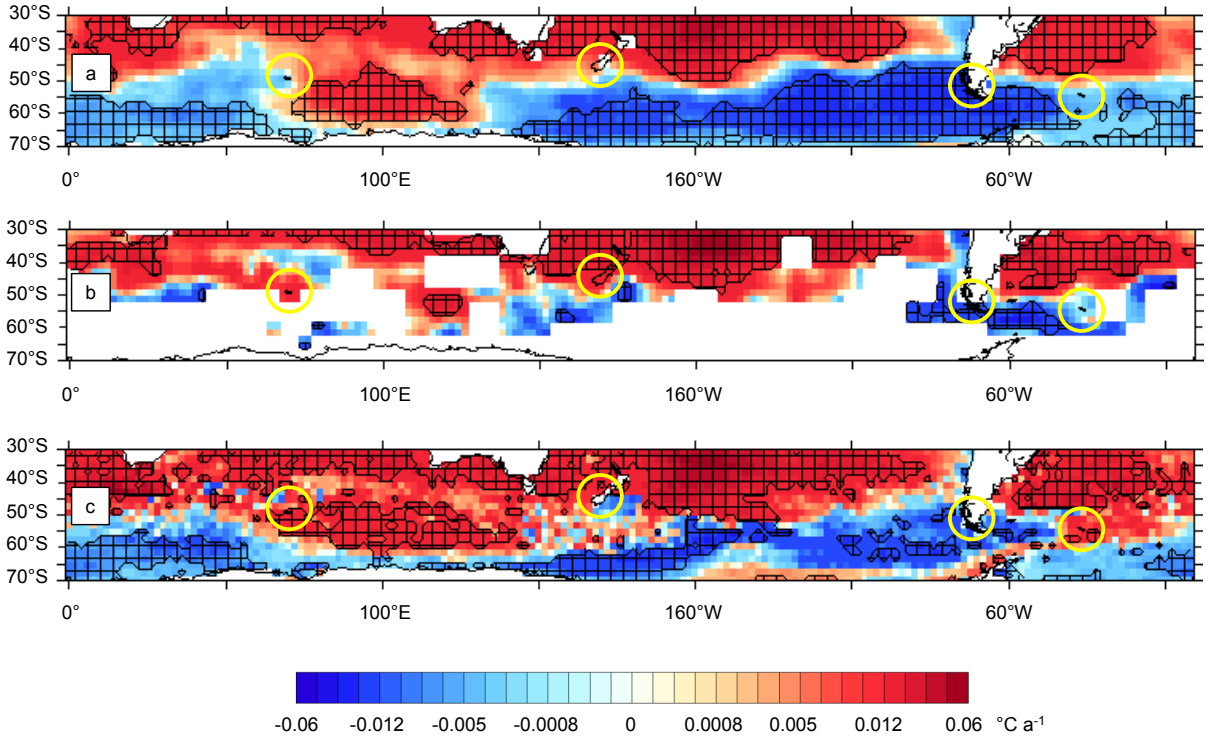

Figure 5. Maps of SST trends on a worldwide 30 °S - 60 °S latitudinal band over 1982-2012 from a) ERSSTv3b, b) HadSST2 and c) AVHRR. Each dataset has been re-gridded on a 2° x 2° regular grid. Missing values are indicated in white. Squared areas corespond to regions where trends are significant at the 95% confidence level (Spearman's test). Yellow circles indicate specific glacier regions discussed in the text.

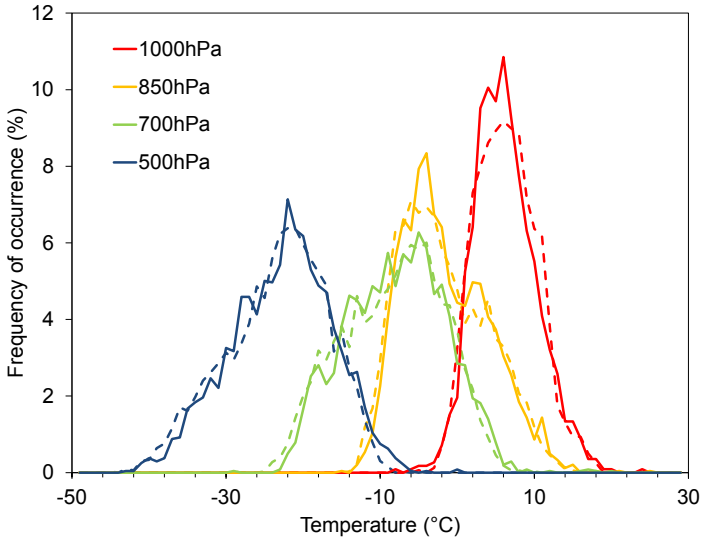

Figure 6. Frequency histograms of Météo France daily radiosonde temperature measurements at Port-aux-Français, for the period 1973-1982 (continuous lines) and 2002-2011 (dashed lines).

4. Defining Climate Trends in the Southern Hemisphere Mid- and High-Latitudes

4.1. Temperature Trends

If we refer to these selected datasets, we observe a particularly good agreement between different sources and the CRU temperature trends. The warming observed over the last 30 years around Kerguelen archipelago is almost general north from 50 °S (Table 2), in particular during the maximum ablation months (DJFM), whereas a significant cooling is observed at the south. A clear frontier between warming and cooling zones is visible, even if it seems to be blurred in AVHRR data probably due to the averaging of several grid cells as a result of regridding of the original 0.25 ° × 0.25 ° dataset. The region affected by a cooling trend is reaching Antarctica, except at the western side of the Antarctic Peninsula and along the coast of the Western Antarctic icecap where very large glacier wastage is caused by changes in oceanic circulation and basal instabilities, which confirms a probable ocean warming (Pritchard et al., 2012; Favier et al., 2014; Rignot et al., 2014; Scambos et al., 2014). In the region of interest for glaciers, warming is observed at Kerguelen and New Zealand, even though the latter is not significant at 95% in every dataset. A consistent cooling trend over 1982-2012 is found along the west coast of South America. Finally, a clear trend in SST is not visible for South Georgia because datasets do not agree in this sector.

Table 2. Temperature (°C per decade, mean over DJFM) and precipitation trends (mm per decade) from CRU and SST trends from HadSST2, AVHRR and ERSSTv3b (mean values in °C per decade, with standard deviation) over the various glaciated regions discussed in this study for the period 1950-2012, 1982-2012 and 2000-2012. Precipitation for the period 2000-2012 is the mean of CRU and GPCP trends, with their standard deviation. Significant values (Student's test) are indicated in bold font. Coordinates of the pixels used in CRU to calculate trends for each glaciated region are also indicated.

		NPI	SPI	DCI	SG	Ker	NZ
Coord.		73.3°W	73.3°W	70.3°W	36.8°W	69.3°E	170.3°E
		46.8°S	49.8°S	54.8°S	54.3°S	49.3°S	43.8°S
1950-2012	T	0.07	0.06	0.07	**0.21**	**0.15**	0.07
	Pr	**-34**	-11	-2	-	**-47**	26
1982-2012	T	-0.07	0.01	0.06	**0.22**	0.13	0.09
	SST	-0.10 ± 0.05	**-0.14 ± 0.07**	**-0.16 ± 0.05**	0.02 ± 0.06	0.06 ± 0.09	0.11 ± 0.05
2000-2012	T	0.38	0.34	0.40	0.08	0.33	0.35
	SST	0.18 ± 0.38	-0.09 ± 0.26	-0.33 ± 0.18	0.17 ± 0.22	0.29 ± 0.17	-0.30 ± 0.24
	Pr	-58 ± 24	-31 ± 6	-47 ± 18	-17[1]	**112 ± 113**	-109 ± 77

[1]Only GPCP values are given for South Georgia.

4.2. Precipitation Trends

Precipitation trends were computed over 2000-2012 in ERA-Interim, NCEP2, GPCP and the CRU TS dataset for the southern mid-latitudes (Fig. 7). Since reanalyzed precipitation is generally considered as poorly representative, we did not use these data here to inform on its large scale changes. Actually, they are more likely to inform on moisture fluxes rather than on actual precipitation amounts. Their quality largely depends on the assimilation of radiosounding data near the study area, and generally decreases in complex topography regions. This is confirmed by the large differences existing between measured and reanalyzed precipitation at Kerguelen, even if radiosondes data, meteorological measurements at PAF and SST from buoys and satellites are assimilated at and around Kerguelen Islands by both ECMWF and NCEP-NCAR or NCEP-DOE reanalysis. This discrepancy is expected to be even larger where radiosoundings are absent, which is the most common in the mid- to high-latitudes regions of the southern hemisphere. For instance, ERA-Interim and NCEP2 reanalyses disagree with precipitation measurements from GPCP and CRU over Patagonia : while reanalyses display an increase of $+15$ to $+70$ mm year^{-1} (95%-significant over most of Patagonia), GPCP and CRU indicate decreases of -5 to -75 mm year^{-1} (95%-significant over Patagonia for GPCP, but not for CRU). This denotes the fact that precipitation from reanalyses cannot be relied upon for this particular region. Several differences also appear elsewhere in the studied latitudinal range (Fig. 7).

Precipitation trends should be analyzed with field data, as for example the available GPCP and CRU precipitation products. These data indicate a strong drying over most of the southern hemisphere mid-latitudes, including glaciated regions in New Zealand and South Georgia (Fig. 7), Kerguelen and over Patagonia. Table 2 indicates that this drying trend had already started in the 1950s over most regions (with the exception of the DCI and New Zealand, where drying initiated in the late 1990s). Note that the Kerguelen Islands display a positive trend over 2000-2012, because of the occurrence of a few wetter years recently, while the drying trend started at the beginning of the 1960s (Verfaillie et al., submitted).

5. Reconciling trends with glacier retreat

5.1. Glacier mass balance variations from the PDD model[1]

5.2. On the role of air temperature

To validate the proposed trends we analyzed whether they were (or not) in agreement with the observed glacier and ice cap wastage in the area.

While recent glacier retreat seems coherent with the SST warming trend observed at Kerguelen and in New Zealand (Fig. 5), the trend in South Georgia is more difficult to assess (positive for AVHRR, negative for HadSST2 and at the limit between warming and cooling for ERSSTv2). The western side of Patagonia, on the other hand, is concerned by a 95%-significant SST cooling along the Chilean coast (Fig. 5), which was also observed in Falvey and Garreaud (2009) over 1979-2006 for ERSSTv2 and HadISST datasets. This latter study showed that this cooling was also measured at coastal meteorological stations. As the western sides of the Patagonian Icefields are located close - and even flowing into - the Southern Pacific Ocean, their fast recent retreat must be explained by something else than temperature. Nevertheless, a slight warming inland (Table 2, Fig. 8) could be partly responsible for glacier wastage on the eastern side of the icefields.

Getting evidences on a link between warming and glacier retreat in the southern hemisphere mid-

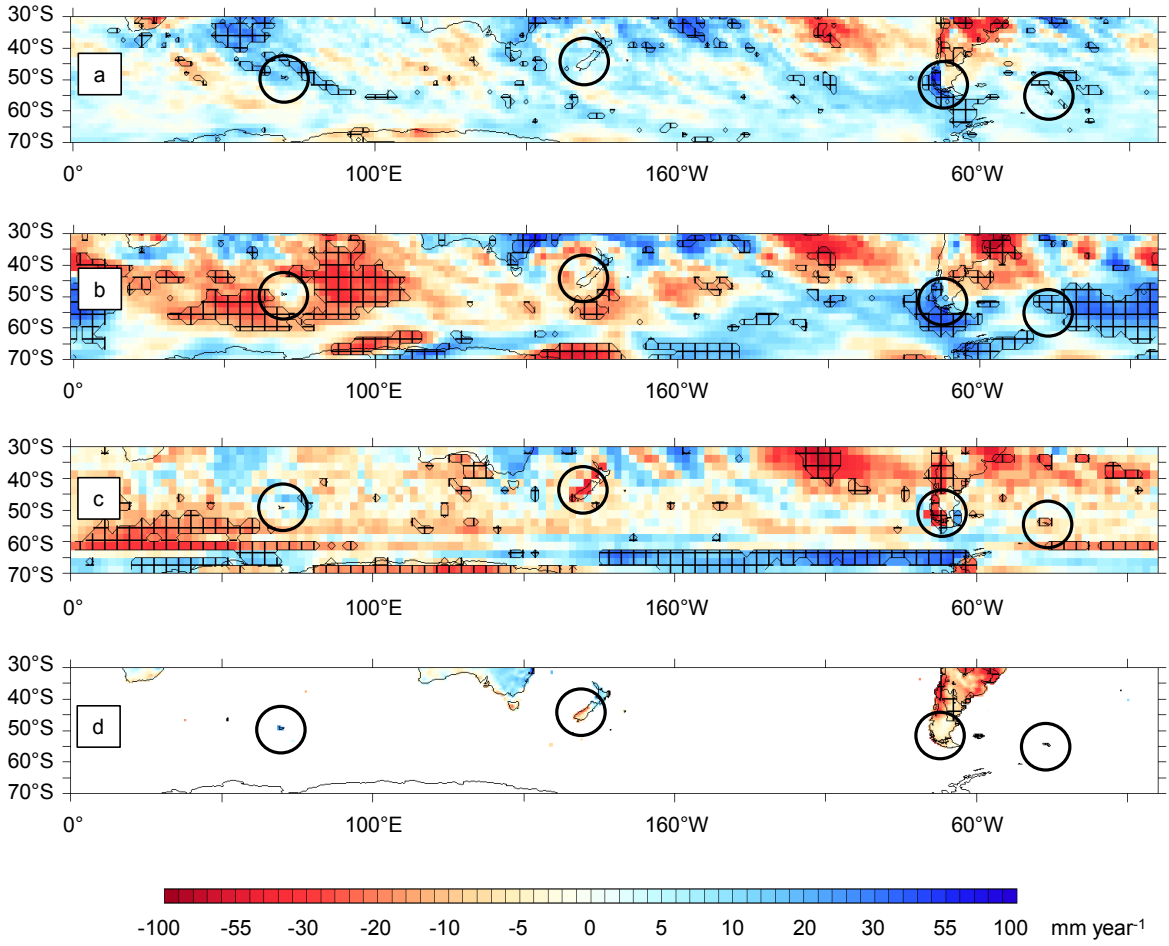

Figure 7. 30 °S - 60 °S maps of precipitation trends over 2000-2012 from a) ERA-Interim reanalysis, b) NCEP2 reanalysis, c) GPCP product and d) CRU dataset. Missing values are indicated in white. Squared areas corespond to regions where trends are significant at the 95% confidence level (Spearman's test). Black circles indicate specific glacier regions discussed in the text.

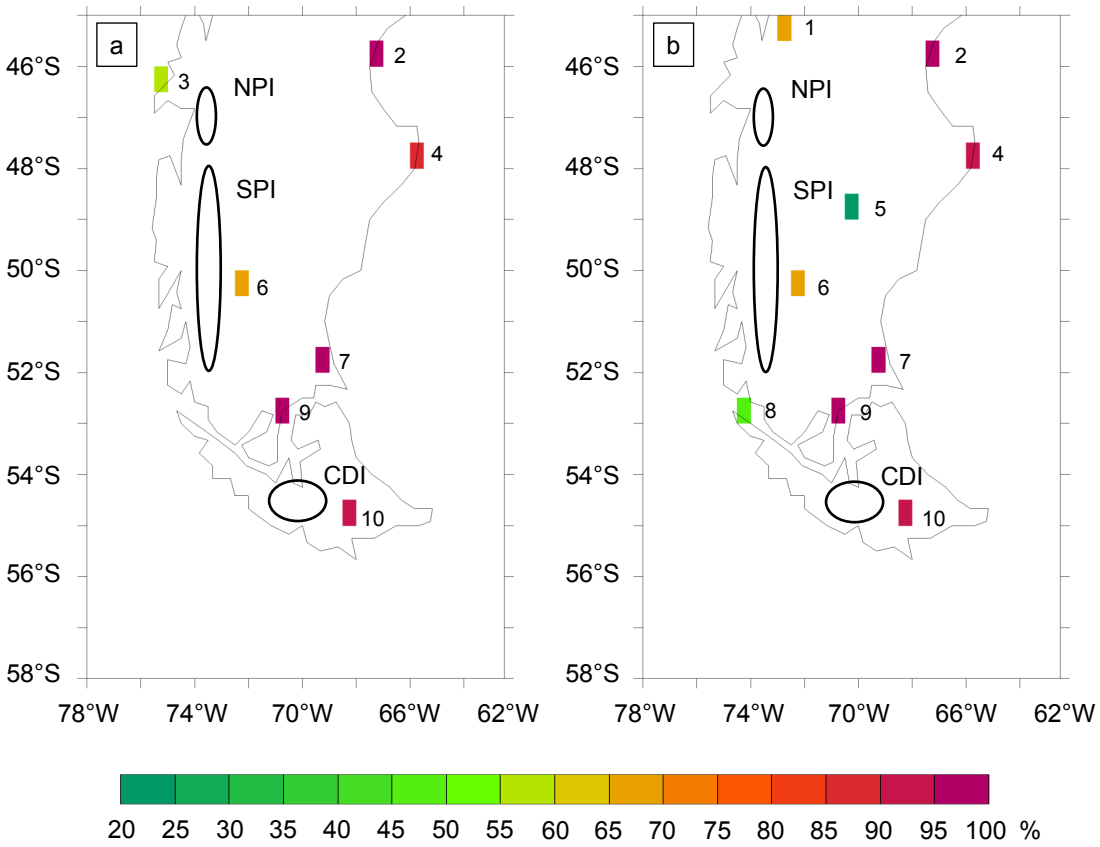

Meteorological stations

1. Puerto Aysén, Chile (8586200)
2. Comodo Rivadavia, Argentina (8786000)
3. Cabo Raper, Chile (8589210)
4. Puerto Deseado, Argentina (8789600)
5. Gobernador Gregores, Argentina (8788000)
6. Lago Argentino, Argentina (8790300)
7. Río Gallegos, Argentina (8792500)
8. Bahia San Félix, Chile (8599700)
9. Punta Arenas, Chile (8593400)
10. Ushuaïa, Argentina (8793800)

Figure 8. Location of Patagonian stations (name, country and WMO number) and percentage of monthly observations used in CRU between 1950 and 2012 for a) temperature and b) precipitation. Location of the Patagonian Icefields is also indicated.

and high-latitude is thus particularly hard. This is even more true if we consider that glacier retreat was mainly controlled by dryness at Kerguelen, since this is the region where the warming is the most significant. Considering Fig 5, it is clear that surface warming alone - linked to SST warming - cannot explain the recent glacier wastage observed in these regions, and particularly in Patagonia.

5.3. Indications given by glaciers on SST changes

SST trends were more particularly analyzed where the icecap or icefield presents numerous tidewater glaciers to assess whether calving processes were a first order cause of the wastage.

If we focus on the South Patagonian Icefield, it appears that tidewater glaciers presented slightly more reduced wastage than the grounded or lake-calving glaciers, which indicates a probable mitigation of the wastage by the nearby cooling ocean (Fig. 9, Table 2). Indeed, on SPI, these glaciers exhibit thinning values closer to zero than surrounding glaciers, while no clear West-East gradient emerges (Fig. 9). This is quite counter intuitive except if we consider that the ocean was cooling during the last decades. Of course, we do not rule out the role of glacier dynamics (i.e. Holmlund and Fuenzalida (1995); Rivera et al. (2012)) in the diversity of retreats observed, but this situation is consistent with SST trends (Table 2) along the Pacific coast of southern Chile (Garreaud et al., 2013). Air temperature at 2 m along the coastal regions of Chile is thus expected to have displayed a similar trend. The observed slight (not significant) warming at the coastal regions is thus likely a consequence of interpolation processes of data from stations located on the Argentinian side because very few stations are used in the CRU dataset in this region, and all of them are either presenting missing data or located inland on the Argentinian side (Fig. 8).

Getting information from SST thanks to tidewater glacier wastage is not possible on the NPI, because the only tidewater glacier is San Rafael glacier. This glacier calves into an extensive laguna, and is thus much farther from the open ocean, which could explain why its retreat is still important compared to nearby non tidewater glaciers. Additionally, SST off the NPI has not experienced the same cooling as further south during the last decade (Table 2).

For the DCI, tidewater glacier response also gives information, even if the interpretation there is much more complex. In Fig. 10, elevation change from 2001 to 2011 for the 16 largest glaciers of the DCI from Melkonian et al. (2013) was plotted against their respective area. A clear distinction arises between glaciers from the north-eastern part of DCI (large elevation changes) and glaciers from the south-western part (smaller elevation changes for similar areas), as already noticed by (Melkonian et al., 2013). The limit between these regions is indicated in Fig. 9 b. Because the number of glaciers considered is rather small, we also included information on additional glaciers given by Holmlund and Fuenzalida (1995) (orange stars in Fig. 9 b) to confirm that southern DCI glaciers were presenting a slower retreat than northern DCI glaciers. Indeed, glaciers at the southern side were close to equilibrium or advancing between 1960 and 1993, in contrast to northern DCI glaciers which were already retreating quickly.

Melkonian et al. (2013) attributed this north-south difference to "warming in the north and changing weather patterns that have increased precipitation on the windward side of the mountains and decreased precipitation on the lee side (e.g., Holmlund and Fuenzalida, 1995), and of course the combination of climate with dynamic instability at (some) glaciers". Indeed, air temperature data from Rio Gallegos, Punta Arenas and Ushuaïa stations (see Fig. 8 for stations location), indicate that warming during the maximum ablation months (DJFM) over the last decade was strongest at the northernmost station (Rio Gallegos, 0.59 °C per decade), still strong at the station located just north of DCI (Punta Arenas, 0.50 °C per decade) but slightly negative at the souternmost one (Ushuaïa, -0.03 °C per decade). But the proposed increasing precipitation appears in contradiction if we refer to the large glacier retreat at the southern side of the Cordillera, while SST and air tempertature

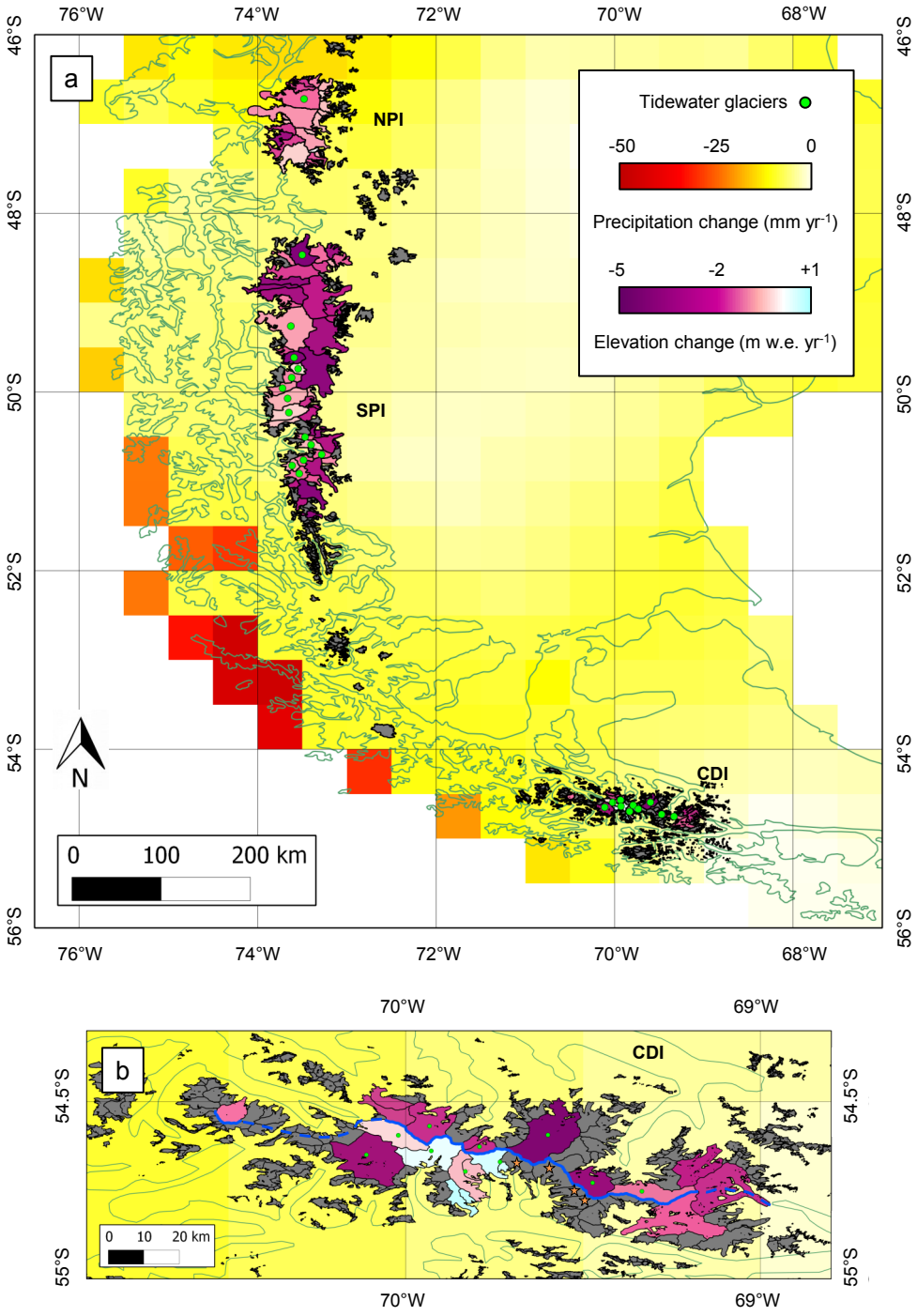

Figure 9. a) Map of Patagonia showing the elevation change over 2000-2012 at NPI and SPI glaciers and over 2001-2011 at DCI glaciers from Willis et al. (2012a,b); Melkonian et al. (2013), as well as the precipitation trend over 2000-2012 from CRU. Grey indicates glaciers not studied in Willis et al. (2012a,b); Melkonian et al. (2013). Tidewater glaciers are marked by a green dot. b) Zoom on the DCI region. The orange stars indicate glaciers for which elevation change over 2000-2012 is not known, but which are discussed in the text. The blue line separates southern side and northern side glaciers discussed in the text.

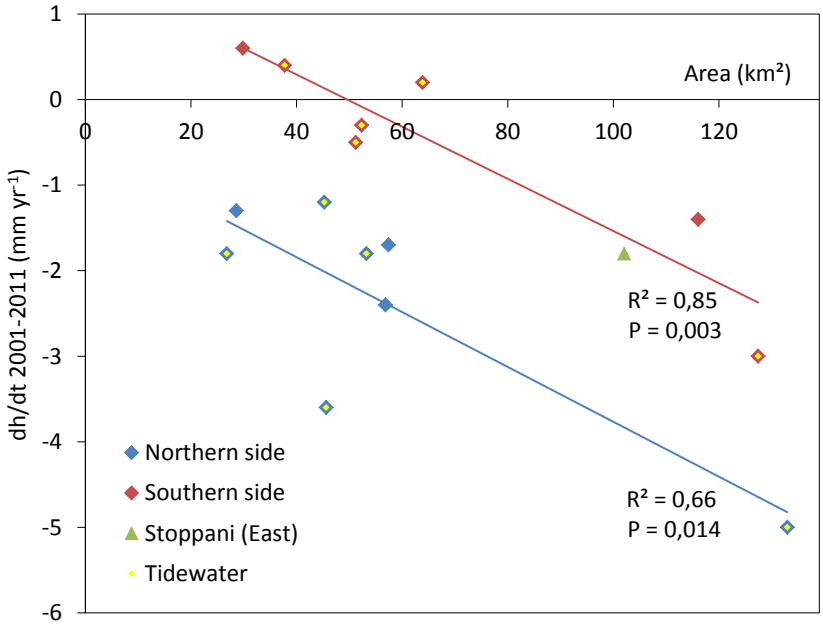

Figure 10. Elevation change between 2001 and 2011 for the 16 largest glaciers of the DCI (from Melkonian et al. (2013)) plotted against their respective area. Glaciers are separated according to their location (northern side, southern side or Stoppani glacier, located on the easternmost part of the DCI). Tidewater glaciers are indicated by overlying yellow markers. Regression lines for the northern and southern glaciers are also indicated, with their determination coefficients (R^2).

were stable during this period.

If we focus on northern and southern parts of DCI, glacier wastage appears as a function of glacier size only. The relationship between ice wastage and glacier size is similar at southern and northern sides, but appears shifted through negative mass balance values in the northern region, reflecting the warming trend at the north while the south was likely influenced by stable or cooler air temperatures. Distinct dynamical responses may hardly explain this difference, because tidewater glaciers do not seem to have behaved differently than non-tidewater glaciers of comparable size (calving processes are the first order difference in the dynamics of these glaciers).

5.4. On the role of precipitation

Except for New Zealand and South Georgia, there is no evidence that atmospheric and oceanic warming was the first order cause of glacier wastage. Conversely, the hemispheric precipitation decrease during the last 30 years at mid- and high latitudes of the southern hemisphere is consistent with glacier retreat.

Precipitation from CRU and GPCP over the last decades (Table 2) presents negative trends everywhere at Kerguelen, South Georgia, the Southern Island of New Zealand, in Patagonia and Darwin Cordillera, even though the observed trends are largely varying in each region.

On the Kerguelen Islands, Favier et al. (in review) showed that dryness since the 1970s induced by the SAM was the main cause of recent glacier retreat, while surface warming amplified it. This is probably also the case in other glaciated regions of the southern hemisphere such as the South Island

of New Zealand and South Georgia, although increasing temperature could also have contributed to glacier wastage in these regions.

The retreat of the western side glaciers of SPI is not coherent with the recent coastal cooling (Fig. 5), suggesting increased ablation and calving were not the first order cause of retreat there. The drying trend observed over the last decades in this region (Table 2) is thus likely a major cause of glacier retreat. The recent acceleration of the wastage (Willis et al., 2012a,b) was possibly linked to the increased drying trend over 2000-2012 (Figs. 7 and 9 and Table 2).

Finally, over the southern tip of South America, based on regional climate modeling using reanalysis data, Garreaud et al. (2013) showed that westerly winds seem to have slightly increased between 1968 and 2001 which caused precipitation to increase on the south-western side of the Andes in this region, and to decrease on the eastern side. However, no radiosonde station exists on the south-west of the DCI, nor long-term meteorological station, and large differences between models and real precipitation are expected. CRU trends there are also the result of interpolation between far-lying stations suggesting that this trend should be considered with caution. Nevertheless, the paradox observed between the SST and air temperature trends at Ushuaia station suggests that a drying trend is likely.

6. Discussion and Conclusion

We observed that after a critical analysis of their consistency in a well documented region (at Kerguelen) several datasets based on field measurements or remote sensing data are sufficiently accurate to assess whether warming or cooling occurred over this latitudinal range. This method is only valid to assess changes in the lowest layers of the atmosphere ($>$ 850 hPa), the higher levels behaving differently as observed in radiosonde measurements at Kerguelen or in Patagonia (Falvey and Garreaud, 2009). After checking the data, we observed that climatic trends were in agreement with glacier retreat over the entire mid- to high latitudes range.

According to precipitation measurements (GPCP and CRU TS), an intense drought has affected almost the entire 40-60°S area. At Kerguelen, glacier modeling based on field measurements since 1951 demonstrated that warming only accounted for one quarter of the ice wastage, whereas the dryness was the first order cause of the glacier retreat (Favier et al., in review; Verfaillie et al., submitted). Here, we suggest that the main cause of glacier wastage in Patagonia was also likely related to the decrease in precipitation since the 1950s, which intensified over the last decade (from -35 to -750 mm decade^{-1} at least for NPI, Garreaud et al. (2013)). A cooling of the nearby ocean seems to have mitigated the retreat of SPI tidewater glaciers and indicates that atmospheric warming was reduced in the low atmosphere. The diversity of glacial responses at the DCI seems to be rather a consequence of temperature gradient across the cordillera, but a reduction in precipitation is necessary to understand the retreat also observed in the southern part of this cordillera. Since CRU data suggest a drying on the northern side, we suppose that the entire cordillera was concerned. Nevertheless, CRU data suggest that the drying trend began more recently in this region. Finally, in the Southern Alps of New Zealand and in South Georgia, a combination of both temperature increase and dryness could explain the recent glacier wastage.

The hemispheric distribution of these glaciers is in agreement with an hemispheric shift in climatic circulation, which is coherent with SAM intensification over the last 50 years. It reflects (1) an hemispherical southwards shift of the storm tracks (Yin, 2005; Favier et al., in review), leading to a decrease in precipitation, (2) a reduction in nebulosity and a resulting increase in temperature on land surfaces (the ocean mixing is expected to limit this warming), (3) an intensification of the westerly winds (Gillett et al., 2006; Thompson et al., 2011; Abram et al., 2014), which induced stronger foehn

winds and thus an increased drying and warming at the lee of the icefields (for instance, in Patagonia (Garreaud et al., 2013)). The positive phases of the SAM are also expeced to have affected the Eckmann transport in the ocean with important changes in the energy distribution. SST changes through the Pacific coast of southern Chile and close to the Antarctic peninsula should thus be revisited according to the increasing magnitude of the SAM.

The recent positive phases of the SAM have been related to the ozone depletion ("the ozone hole") that cooled the stratosphere since the mid-1970s. This suggests that any shorter term (i.e. post 1970s) analysis is doomed to fail in retrieving the glacier wastage origin in the sub-Antarctic region. For instance, because reanalyses are biased by the abrupt introduction of satellite data in the data assimilation system after 1979, any modeling directly forced by ERA40 or NCEP-NCAR Reanalysis1 data is expected to be biased. Moreover, modeling based on ERA-Interim or NCEP-DOE Reanalysis2 ((Schaefer et al., 2013; Lenaerts et al., 2014), i.e. post 1980, will miss the observed changes caused by the SAM. This is all the more true because the coarse resolution of reanalysis data impede getting accurate precipitation estimates, and because no radiosonde data are assimilated close to the glaciers except at Kerguelen Islands.

Impacts of the SAM on storm tracks changes have already been demonstrated at Kerguelen Islands (Favier et al., in review) where the glaciers are not anymore under the direct influence of depression, and where teleconnections with the surrounding oceans largely changed since 1975 (Favier et al., in review). Impacts of the SAM on precipitation changes have also been demonstrated in New Zealand (Villalba et al., 2012) or in Southern Africa (Manatsa et al., 2013). Our results suggest that the storm track was shifted also in South America. The chronology of glacier wastage in Patagonia and Darwin Cordillera suggests that the storm track is progressively moving southwards and now affects the southernmost part of the continent.

Greenhouse gases increases are also expected to produce an increase in the positive phases of the SAM. During the last decades, greenhouse gas influence was smaller than that of the ozone hole (Thompson et al., 2011). Over the next century, in spite of ozone hole recovery, the projected greenhouse gas increase is expected to intensify the SAM. A resulting drying of the southern hemisphere mid- to high latitudes range (Thompson et al., 2011; Purich et al., 2013; Favier et al., in review) and further impact on glaciers is expected. If future warming caused by greenhouse gases increase and sustained dryness are realized, the glaciers and ice caps would likely continue to lose mass at rates that are amongst the fastest on Earth.

Acknowledgements

This study was funded by IPEV-1048 GLACIOCLIM-KESAACO and LEFE-INSU KCRuMBLE programs. Logistical supply to Kerguelen Islands was provided by the French Polar institute (IPEV). We would like to thank Laurent Testut, from LEGOS (Toulouse, France) for providing us with the ROSAME data (see http://www.legos.obs-mip.fr/observations/rosame/ for further infomation). We also thank Météo France for the meteorological and radiosonde data from Port-aux-Français, Kerguelen. NCEP 1 and 2 reanalysis data were provided by the NOAA/OAR/ESRL PSD, Boulder, Colorado, USA, from their Web site at http://www.esrl.noaa.gov/psd/. ERA-40 and ERA-Interim reanalysis data were downloaded from the ECMWF data portal at http://data-portal.ecmwf.int/. ERSST-v2 data were obtained at http://iridl.ldeo.columbia.edu/SOURCES/.NOAA/.NCDC/.ERSST/.version2/.SST/, AVHRR data at http://podaac.jpl.nasa.gov/dataset/NCDC-L4LRblend-GLOB-AVHRR_OI, and HadSST2 data at http://www.metoffice.gov.uk/hadobs/hadsst2/. GPCP precipitation data were provided by the NOAA/OAR/ESRL PSD, Boulder, Colorado, USA, from their Web site at http://www.esrl.noaa.gov/psd/, and CRU TS

precipitation data were provided by the British Atmospheric Data Centre at their website `http://badc.nerc.ac.uk/browse/badc/cru`.

3.5 Compatibilité avec les réanalyses et les modèles CMIP5

3.5.1 Motivations et principaux résultats

Dans la Section 3.2, nous avons montré que le retrait marqué de la calotte Cook aux îles Kerguelen au cours des dernières décennies a été causé par une forte diminution de l'accumulation sur la calotte, accompagnée par une remontée rapide de sa ligne d'équilibre, et que ces phénomènes étaient liés au premier ordre à une diminution marquée des précipitations sur l'archipel (et au second ordre à la température). Nous nous sommes ensuite intéressés, dans la Section 3.3, aux phénomènes de grande échelle pouvant expliquer cette sécheresse. Nous avons montré qu'elle était liée à des changements de téléconnexions dus à un déplacement vers le sud des zones dépressionnaires qui alimentaient jusqu'alors régulièrement l'archipel des Kerguelen. Ces phénomènes, causés par les phases de plus en plus fréquemment positives du SAM, affectent l'ensemble de la bande latitudinale située entre 40° S et 60° S environ. Dans la Section 3.4, nous avons alors analysé plus en détail les différents processus entrant en jeu et l'impact que ces phénomènes de grande échelle ont eu sur l'ensemble des glaciers de la zone subpolaire.

Le but de cette section est de vérifier dans quelle mesure les différents processus observés précédemment sont représentés dans les réanalyses et les modèles de l'exercice CMIP5. En effet, une représentation adéquate de ces différents phénomènes dans les réanalyses et modèles CMIP5 est nécessaire car ce sont ces jeux de données qui seront ensuite utilisés comme forçage du modèle MAR (puis du désagrégateur SMHiL). La qualité de l'information fournie par la régionalisation dépend donc fortement de la qualité des réanalyses ou modèles utilisés en entrée et de leur capacité à représenter les différents processus en jeu.

Dans un premier temps, une analyse des tendances climatiques issues des réanalyses et des modèles CMIP5 reprise dans les informations supplémentaires de l'article de Favier et al. (in review) est présentée (Section 3.5.2). Nous montrons que les réanalyses ERA-40 et NCEP1 indiquent une diminution marquée des précipitations et une augmentation des températures sur une majeure partie de la bande latitudinale 40° S - 60° S entre 1957 et 2002, en réponse au déplacement vers le sud des zones dépressionnaires associé à l'intensification du SAM. La moyenne multi-modèle (MMM) CMIP5 montre également un réchauffement, mais moins marqué, et une zone d'assèchement similaire, bien que celle-ci soit moins marquée et localisée légèrement plus au nord par rapport aux réanalyses. Cette limite entre zone d'assèchement et d'humidification varie selon les modèles CMIP5 (notamment en fonction de leur résolution). En ce qui concerne les tendances futures (2006–2100), la MMM CMIP5 indique un réchauffement important à l'échelle globale (variant selon le scénario considéré) et une augmentation légère des précipitations aux îles Kerguelen, qui sont situées à proximité de la limite entre zone d'assèchement (au nord) et d'humidification (au sud).

Une analyse complémentaire de la relation entre température et précipitations dans ces modèles et réanalyses révèle par ailleurs que malgré leurs tendances très variables d'un modèle à l'autre, à grande échelle (l'ensemble de la bande 40° S - 60° S), l'ensemble des modèles CMIP5 présente une relation de type Clausius-Clapeyron entre précipitations et température. Cela signifie que les précipitations à cette échelle sont presque exclusivement gouvernées par la température (au travers de la capacité de l'air à contenir de l'humidité). A plus petite échelle (pour une région de quelques degrés centrée autour de l'archipel des Kerguelen), cette relation disparait, montrant

que les précipitations à cette échelle dépendent de plusieurs processus propres à chaque modèle, et non pas exclusivement de la température.

Dans un second temps, une évaluation des modèles CMIP5 sur la période récente (Section 3.5.3) est réalisée dans le but de déterminer les modèles les plus aptes à forcer le modèle MAR pour réaliser des prédictions au cours du 21^{e} siècle (présentées dans la Section 3.7). Cette évaluation, s'inspirant des travaux de Fettweis et al. (2013), nous conduit à choisir le modèle ACCESS1-3 comme modèle le plus proche de la réalité, et les modèles GDFL-CM3 et MRI-CGCM3 comme modèles extrêmes. Ces modèles sont ensuite utilisés pour forcer le modèle MAR sur la période récente (évaluation) et future dans la Section 3.7.

3.5.2 Tendances climatiques dans les réanalyses et les modèles CMIP5

Les tendances récentes et futures des températures et précipitations à l'échelle de l'ensemble des zones subpolaires dans les réanalyses et les modèles CMIP5 ont été analysées dans le cadre de notre article Favier et al. (in review) présenté à la Section 3.3. Seule la partie des informations supplémentaires concernant cette analyse est reprise ci-dessous (en conservant la numérotation d'origine). L'ensemble des informations supplémentaires (ainsi que les références) est repris en Annexe F. Une analyse complémentaire du lien entre température et précipitations dans les modèles CMIP5 et les réanalyses est également présentée.

3.5.2.1 Extrait des informations supplémentaires de l'article Favier et al. (en révision)

Supplementary information - The ozone hole as the main driver of dramatic glacier wastage in the sub-Antarctic region

Favier, V., Verfaillie, D., Berthier, E., Memegoz, M., Jomelli, V., Kay, J.E., Ducret, L, Malbéteau, Y., Brunstein, D., Gallée, H., Park, Y.-H., 2014, Nature Geoscience, in review.

S.2. Supplementary Discussion

2.1. Climatic trends from field, CMIP5 and Reanalysis data

We analyzed Reanalyses and CMIP5 models data confirming results from (32).

a. Recent past trends

Additionally to temperature and precipitation data from the meteorological station at Port-aux-Français (Fig. 2), the ERA-40 from the ECMWF and NCEP-NCAR Reanalysis1 (NCEP1) were also analyzed here.

ERA-40 fully covers the 1958-2001 period[56], and is run on a reduced Gaussian grid with T159 spectral truncation that has a nominal resolution of 125 km. NCEP-NCAR Reanalysis1 (NCEP1) are global atmospheric reanalyses available from 1948 to the present[57]. NCEP1 model produces 6-hourly data at a T62 spectral resolution (210 km) and for 28 vertical levels extending from 5hPa from the surface to a top level at 3hPa. It uses a sequential 6h-cycle data assimilation (3D-variational) scheme.

Outputs from models from the Coupled Model Intercomparison Project 5 (CMIP5) were also used to derive current climatic trends. CMIP5[58] involves 20 climatic groups, which performed different

experiments divided into two categories : (1) near-term simulations (10 to 30 years), some forced by observed ocean state and sea-ice and (2) long-term simulations (on a century time-scale) using atmosphere-ocean global climate models (AOGCMs, sometimes coupled to a carbon cycle model) initialized from the end of freely evolving simulations of the historical period[58]. For the second half of the 20^{th} century, we used outputs from historical simulations (from the long-term experiment), and a multi-model mean (MMM) was computed from 49 different versions of different models (interpolated on ERA-40 grid) (Supplementary Table 2[2]).

Precipitation and 850 hPa temperature linear trends from 1957 to 2002 for ERA-40, NCEP1 and the CMIP5 MMM are presented in Supplementary Fig. 4. A Spearman test was applied to detect trends significant at the 95% confidence interval (non-shaded areas in Supplementary Fig. 4). Reanalysis data clearly suggest a temperature increase and a precipitation decrease as a consequence of a poleward shift of storm tracks that was associated with the increase of the SAM[15,18–23].

The CMIP5 MMM also suggests a significant warming, and reproduces the current observed dryness area, even though precipitation decrease area is less significant and the localization of this area is slightly shifted northward in the models. The limit between precipitation decrease and precipitation increase is different according to models, but all the models agree in describing a large area with precipitation decrease around Kerguelen or just a few degrees north from the Kerguelen Islands.

b. Projection for the 21^{st} century

To estimate future climatic trends, we used outputs from the CMIP5 long-term experiment projection simulations[58]. The latter are produced by forcing the different AOGCMs with specified greenhouse gases concentrations corresponding to different scenarios, called representative concentration pathways (RCPs). There are four different RCPs (RCP 2.6, 4.5, 6 and 8.5), which refer to the target radiative forcing at the end of the 21^{st} century. A multi-model mean (MMM) was also computed from the various model outputs (Supplementary Table 2[2]).

Projected precipitation and 850 hPa temperature linear trends from 2006 to 2100 for the CMIP5 MMM under the lowest (RCP 2.6) and the highest (RCP 8.5) scenarios are presented in Supplementary Fig. 5. A Spearman test was applied to detect trends with significance at the 95% confidence interval (non-shaded areas in Supplementary Fig. 5).

CMIP5 MMM clearly suggests an important warming ($+0.0073 \pm 0.0115$ °C a^{-1} for RCP2.6 scenario and $+0.0296 \pm 0.0200$ °C a^{-1} for RCP8.5 scenario) and a slightly increasing precipitation trend ($+0.51 \pm 1.35$ mm a^{-1} for RCP2.6 scenario and $+1.92 \pm 1.86$ mm a^{-1} for RCP8.5 scenario) at Kerguelen as a consequence of global warming. Regarding the CMIP5 MMM, as a consequence of the +SAM increase[15,32], MMM suggest an intensification of the dryness North of the Kerguelen, and a significant moistening over a large band around the Antarctic continent. Due to the coarse resolution of the CMIP5 models, to the possible future shift of the border between these drying and moistening areas, and to the proximity of the Kerguelen Islands with this border, it is difficult to say whether the Kerguelen area will keep drying in the future. In our modeling we assumed however that precipitation will progressively increase and reach the 1950s amount around the end of the 21^{st} century. This assumption supposes severely more humid conditions at the end of the century than projected by CMIP5 models. However, it allows accounting for conditions that should limit glacier wastage at the end of the 21^{st} century so that our projected mass loss for the ice cap is a maximum estimate.

2. correspond au Tableau B.1 présenté en Annexe B.

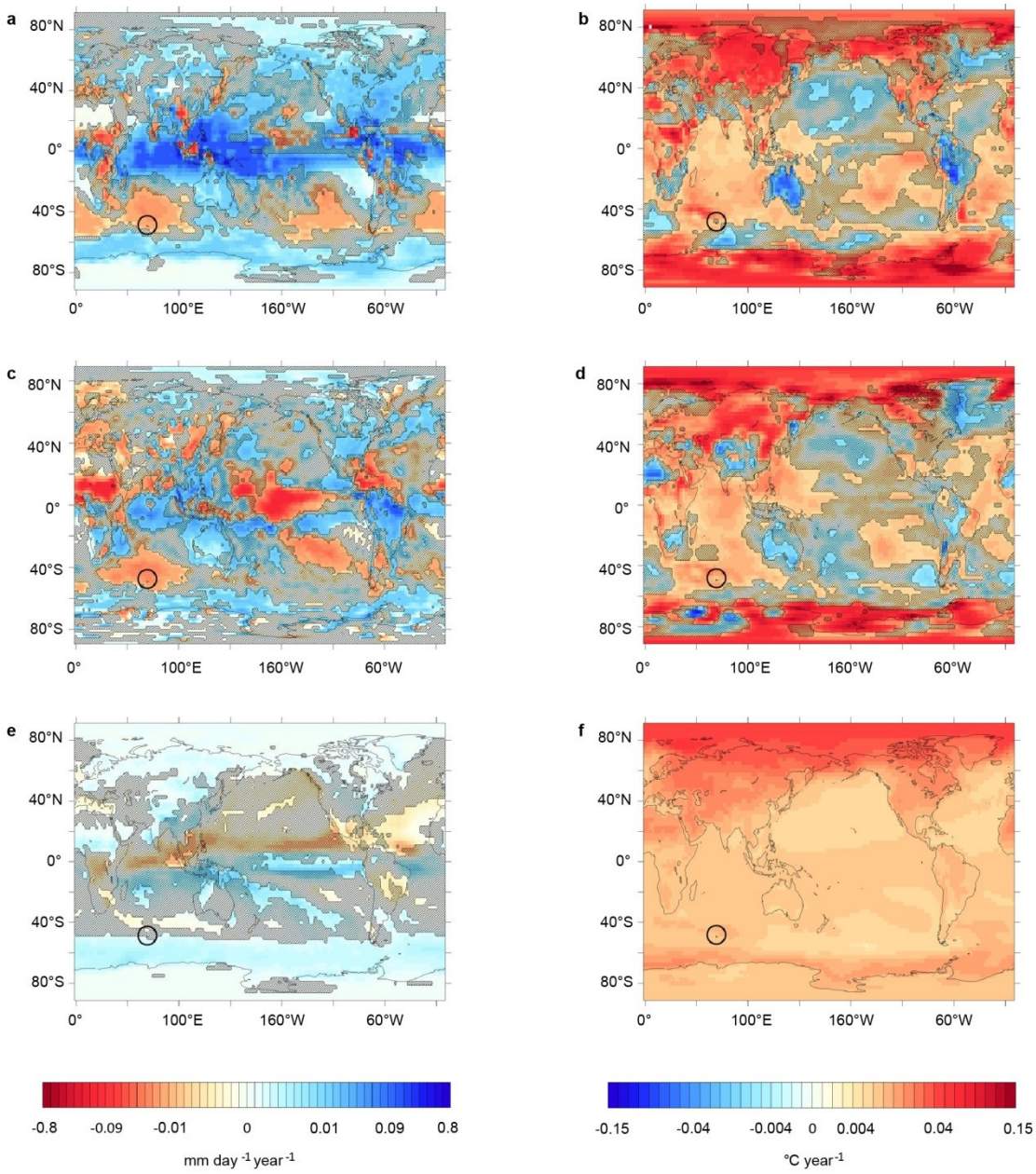

Supplementary Figure 4. Recent large scale precipitation and temperature trends. (left) Precipitation and (right) 850hPa temperature trends for 1957-2002 in ERA-40 (a&b), NCEP1 (c&d) and CMIP5 (e&f) multi-model mean (MMM). Shading indicates areas where the trend is not significant at the 95% confidence interval (Spearman test). Kerguelen's location is indicated by the black circle.

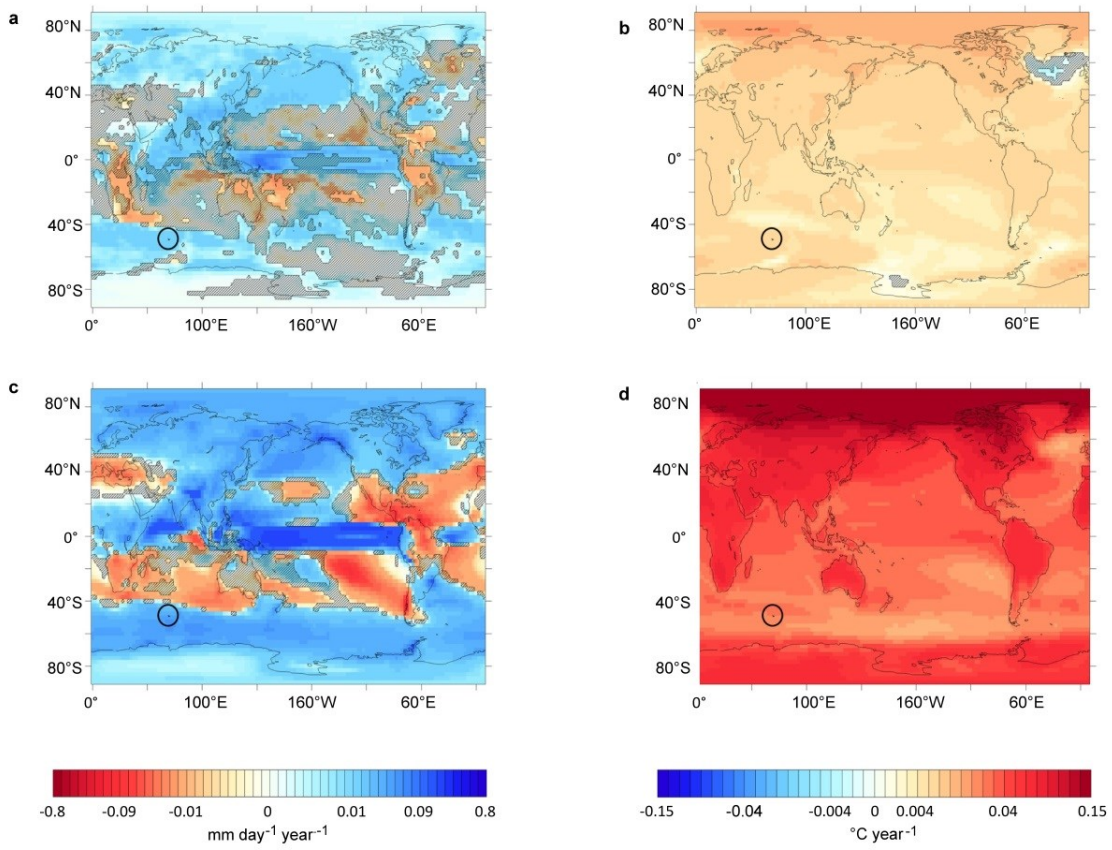

Supplementary Figure 5. Future forecasted large scale precipitation and temperature trends. (left) Precipitation and (right) surface temperature projected trends for 2006-2100 in the CMIP5 multi-model mean (MMM) for RCP 2.6 scenario (a&b) and RCP 8.5 scenario (c&d). Shading indicates areas where the trend is not significant at the 95% confidence interval (Spearman test). Kerguelen's location is indicated by the black circle. Please note the one-order of magnitude difference between current (Supplementary Fig. 4) and projected (this Figure) precipitation trends scale.

3.5.2.2 Analyse complémentaire de la relation entre température et précipitation dans les modèles

Dans l'analyse ci-dessus, on ne s'est intéressé qu'à la MMM CMIP5. Pourtant, lorsque l'on regarde les tendances de température et précipitations de chaque modèle CMIP5 pris séparemment (non montré), on se rend compte de leur diversité, due à des différences de résolution spatiale mais également à des différences de physique des modèles. Cette diversité explique également le fait que la localisation de la limite entre zone d'assèchement et zone d'humidification varie suivant les modèles, parfois quelques dégrés au nord, parfois quelques degrés au sud des îles Kerguelen. Afin de mieux comprendre quelle est la relation entre température et précipitations dans les modèles CMIP5, les anomalies de température par rapport à 1960 sont comparées aux mêmes anomalies de précipitations, pour tous les modèles CMIP5 ainsi que pour ERA-40 et NCEP1 (Figure 3.1).

Lorsque l'on regarde ces anomalies moyennées sur la bande 40° S - 60° S (Figure 3.1 a), les modèles CMIP5 présentent une corrélation positive, proche d'une relation de Clausius-Clapeyron pour certains modèles (pente entre 1% K^{-1} et 6% K^{-1}). Cela signifie qu'à cette échelle-là, les précipitations dans les modèles CMIP5 sont fortement dépendantes de la température : lorsque la température augmente, les précipitations augmentent car la capacité de l'air à contenir de la vapeur d'eau augmente. Ce phénomène classique (effet Clausius-Clapeyron) avait déjà été observé en Antarctique dans les sorties du modèles LMDZ4 et du désagrégateur SMHiL présentées dans Agosta et al. (2013). La relation entre précipitations et température dans les réanalyses est par contre différente d'une simple relation de Clausius-Clapeyron, signifiant que les précipitations dépendent d'autres phénomènes que la température (par exemple la microphysique nuageuse).

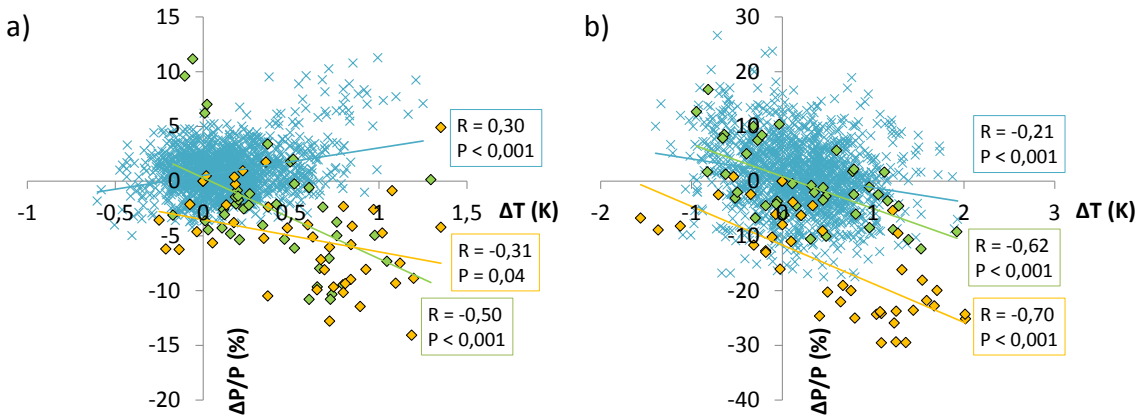

FIGURE 3.1 – Relations entre les anomalies de température et de précipitations par rapport à 1960 dans les modèles CMIP5 (croix bleues) et dans ERA-40 (diamants verts) et NCEP1 (diamants jaunes), (a) moyennées sur l'ensemble de la bande 40° S - 60° S, et (b) moyennées sur une zone réduite autour des îles Kerguelen (45° S - 55° S, 59° E - 79° E). Les courbes de tendances ainsi que les valeurs du coefficient de corrélation (R) et de la p-value (P) pour l'ensemble des modèles CMIP5 et pour ERA-40 et NCEP1 sont indiqués dans les couleurs correspondant aux différents jeux de données.

Cependant, si l'on effectue la même analyse à plus petite échelle, par exemple dans une

région autour des îles Kerguelen (45° S - 55° S, 59° E - 79° E), l'ensemble des corrélations entre précipitations et température (dans les modèles CMIP5 comme dans les réanalyses) est négative (Figure 3.1 b). Les précipitations à plus petite échelle sont alors gouvernées par un ensemble de processus, propres à chaque modèle.

3.5.2.3 Conclusions sur les tendances climatiques dans les réanalyses et les modèles CMIP5

Pour réaliser des prévisions futures, le modèle MAR doit être forcé par les modèles de l'exercice CMIP5 (voir Section 2.4.2). On se rend compte au vu des résultats présentés ci-dessus que considérer la MMM n'est pas forcément judicieux. En effet, la MMM moyenne les réponses de différents modèles construits différemment, avec des physiques différentes (notamment en ce qui concerne le calcul des précipitations), certains divergeant complètement de la réalité, d'autres plus proches de celle-ci. De plus, les champs météorologiques des différents modèles ont un comportement non linéaire, qui implique que les relations dynamiques entre eux sont détruites par l'opération de moyenne. Le résultat (1) n'est donc pas forcément représentatif des processus atmosphériques ayant réellement eu lieu et (2) produit des tendances climatiques très proches de zéro (Figures S4 et S5 présentées ci-dessus) en raison du moyennage de modèles présentant des tendances opposées. La limite entre zone d'assèchement et d'humidification présentée en Section 3.5.2.1 varie également selon les modèles en fonction de leur physique et de leur résolution, ce qui complique l'interprétation des tendances dans les zones proches de cette limite, telles qu'aux îles Kerguelen. Les différents modèles CMIP5 doivent donc être individuellement utilisés pour forcer le MAR. Cette étape sera décrite ci-dessous.

3.5.3 Evaluation des modèles CMIP5 sur la période récente

Parallèlement aux justifications déjà évoquées précédemment, le choix des modèles CMIP5 dépend d'une contrainte liée à l'utilisation du modèle MAR. Le temps de calcul du MAR étant relativement long, il n'est pas possible d'utiliser chaque modèle en entrée du MAR, et un choix doit être effectué. Pour ce faire, nous avons dans un premier temps réalisé une évaluation de chaque modèle CMIP5 sur la période récente par rapport à ERA-Interim, la réanalyse pour laquelle le forçage du MAR se révèle être le plus proche des observations de terrain (voir Section 3.6.2), puis sélectionné le modèle CMIP5 le plus proche d'ERA-Interim ainsi que deux modèles extrêmes afin de forcer le MAR.

3.5.3.1 Evaluation des modèles CMIP5 par rapport à ERA-Interim

Notre évaluation des modèles CMIP5, s'inspirant des travaux de Fettweis et al. (2013), porte sur deux variables-clés du BM aux îles Kerguelen : la température estivale et la vitesse du vent annuelle. La température estivale contrôle l'ablation en surface de la calotte, tandis que la vitesse du vent sert d'indicateur de la circulation de grande échelle (position et intensité des westerlies, influençant les apports d'humidité et donc les précipitations). Pour analyser le recul des glaciers aux îles Kerguelen, en raison de l'impact important de la sécheresse sur le retrait glaciaire dans cette région, et par suite du rôle du SAM, il était intéressant de s'intéresser également à la quantité de précipitations. Cependant, les précipitations du modèle amont n'influencent pas les précipitations modélisées par le MAR car elles ne constituent pas l'un de ses champs de forçage. En effet, le modèle MAR calcule ses propres précipitations sur base des champs de forçage de température, vent, humidité et pression uniquement. Une analyse préalable de l'humidité

spécifique des modèles CMIP5 révèle par ailleurs une bonne représentation de l'humidité dans l'ensemble des modèles comparé à ERA-Interim. La température et la vitesse du vent (ainsi que la hauteur du géopotentiel) sont donc les deux seuls paramètres sur lesquels cette analyse s'est appuyée.

Les Figures G.1 et G.2 en Annexe G représentent les différences de température estivale (DJF) à 850 hPa et de vitesse du vent à 700 hPa entre chaque modèle CMIP5 (ainsi que ERA-40 et NCEP1) et ERA-Interim. La hauteur du géopotentiel 700hPa est également représentée dans la Figure G.2, et est bien reproduite par l'ensemble des modèles CMIP5.

3.5.3.2 Choix des modèles CMIP5

En fonction de l'évaluation réalisée ci-dessus, le modèle le plus proche d'ERA-Interim sur la période récente dans la bande 40° S - 60° S en terme de température et de vitesse du vent est sélectionné pour forcer le modèle MAR. De plus, afin de représenter une enveloppe des bilans de masse possibles autour de ce modèle central, les deux modèles les plus extrêmes en terme de température dans cette région sont également sélectionnés. Cette sélection d'un modèle central et de deux modèles extrêmes repose sur deux hypothèses :

1. le bilan de masse en sortie du MAR est plus influencé par la température du modèle-hôte que par la vitesse du vent (indicatrice de la circulation de grande échelle). Cette hypothèse a déjà été vérifiée au Groenland (Belleflamme et al., 2013; Fettweis et al., 2013) et en Antarctique, où des modèles présentant des différences en terme de circulation atmosphérique générale ont donné des bilans de masse similaires.
2. les anomalies de BM dans le MAR découlant des anomalies de température ont tendance à s'amplifier avec le temps car un modèle trop chaud au départ va se traduire dans le MAR par une fonte beaucoup plus rapide de la calotte et donc un BM directement plus négatif (et inversement pour un modèle trop froid). On a donc une divergence de plus en plus forte des différents BM simulés par le MAR forcé par différents modèles CMIP5 (Fettweis et al., 2013). On peut donc raisonnablement considérer que le modèle qui permet de simuler au mieux les conditions de température (et de circulation) dans le MAR sur la période récente sera celui qui offrira la meilleure prévision future, et que les modèles extrêmes actuels continueront à diverger dans le futur.

Un résumé des Figures G.1 et G.2 en Annexe G pour les modèles CMIP5 utilisés dans cette étude et pour les réanalyses ERA-40 et NCEP1 est présenté ci-dessous en Figures 3.2 et 3.3. ACCESS1-3 constitue le modèle le plus proche d'ERA-Interim sur la période récente dans la bande 40° S - 60° S aussi bien en terme de température que de vitesse du vent. Ses anomalies par rapport à ERA-Interim sont du même ordre de grandeur que celles de ERA-40 ou de NCEP1. Les deux modèles extrêmes sélectionnés sont GFDL-CM3 (le plus froid) et MRI-CGCM3 (le plus chaud, à part GISS-E2-H qui ne présente pas de sorties toutes les 6h nécessaires au forçage du MAR). Ils présentent par ailleurs des biais similaires (légèrement positifs) par rapport à ERA-Interim pour ce qui est de la vitesse du vent (Figure 3.3).

J'ai donc ensuite forcé le modèle MAR sur la période historique (1950-2005) puis sur le 21^{e} siècle (2006-2100) avec les modèles ACCESS1-3, GFDL-CM3 et MRI-CGCM3. Une évaluation des sorties du modèle MAR forcé par ces différents modèles sur la période récente est effectuée dans la Section 3.7.2, tandis que les résultats pour le 21^{e} siècle sont présentés dans la Section 3.7.3.

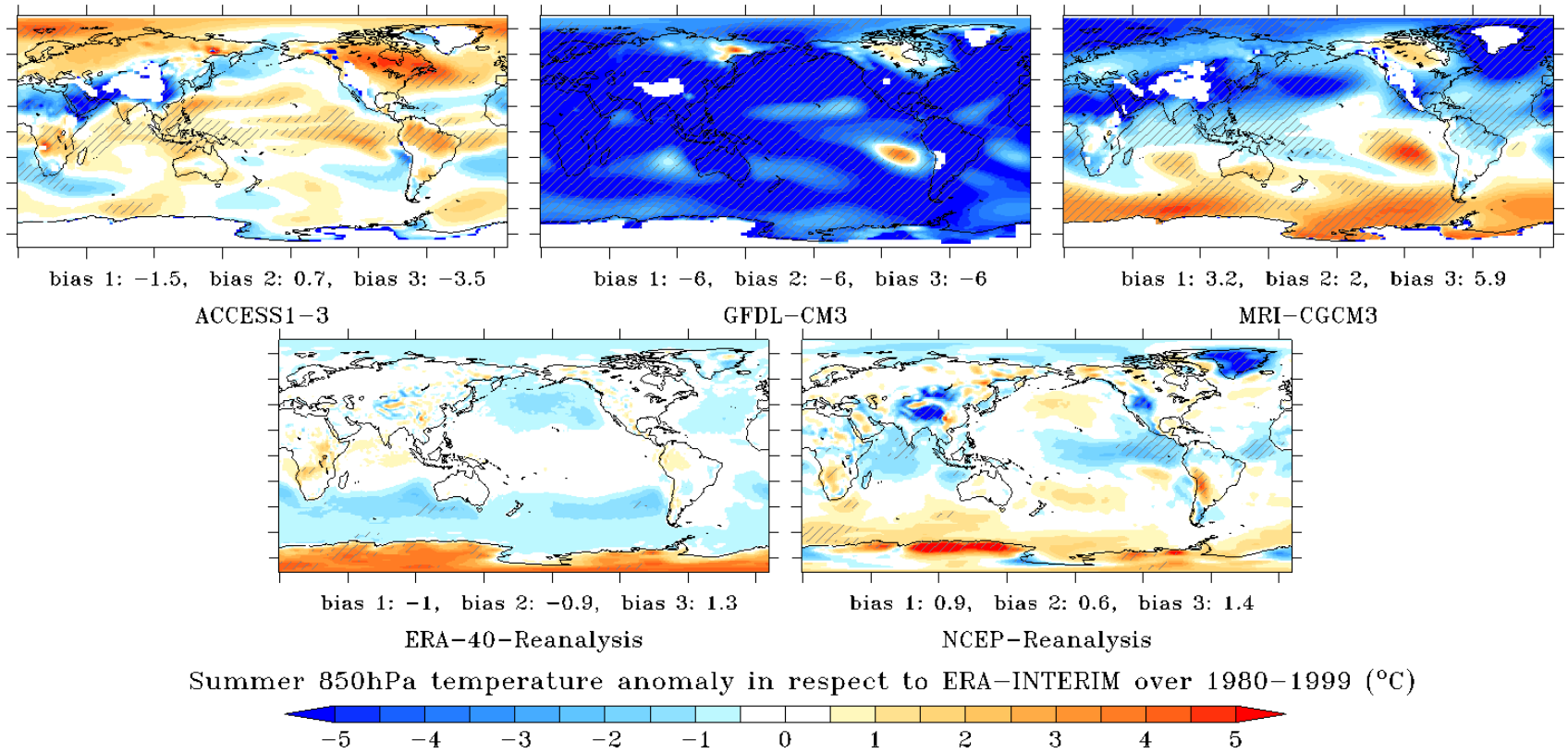

FIGURE 3.2 – Anomalie moyenne ($\overline{T}_{CMIP5} - \overline{T}_{ERA-Int}$) de température estivale (DJF) à 850hPa par rapport à ERA-Interim sur la période 1980-1999, tracée sur la grille d'ERA-Interim, pour ACCESS1-3, GFDL-CM3, MRI-CGCM3, ERA-40 et NCEP1. Les biais indiqués sont calculés de la manière suivante : $(\overline{T}_{CMIP5} - \overline{T}_{ERA-Int})/\sigma(T_{ERA-Int})$, où σ représente l'écart-type. Le biais 1 est calculé sur l'ensemble de la zone 40° S - 90° S, le biais 2 sur la zone 40° S - 60° S et le biais 3 sur la zone 60° S - 90° S. Les zones hâchurées représentent les endroits où l'anomalie de température est plus de deux fois supérieure à l'écart-type de la température dans le modèle CMIP5.

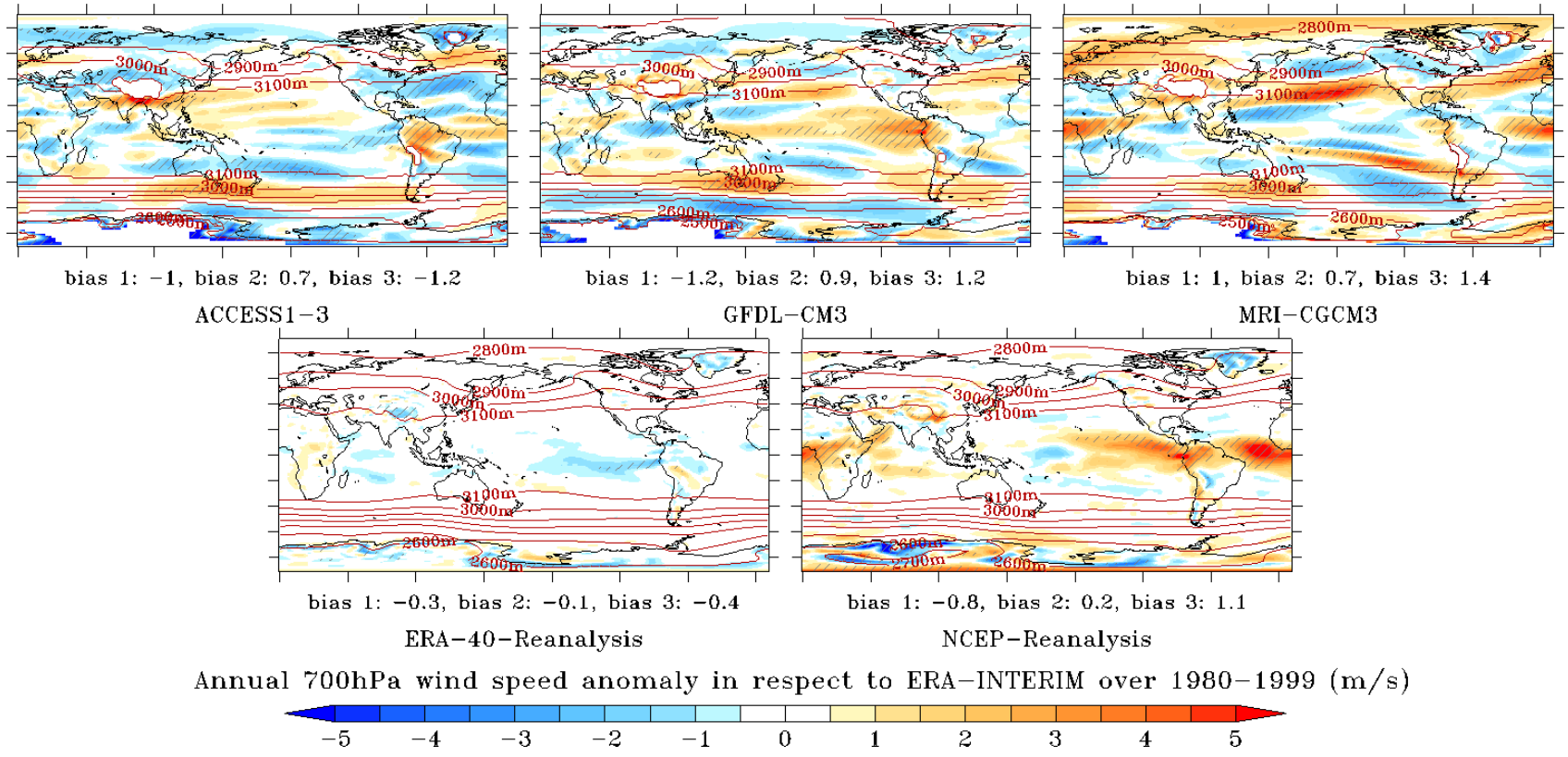

FIGURE 3.3 – Anomalie moyenne ($\overline{WS}_{CMIP5} - \overline{WS}_{ERA-Int}$) de vitesse du vent annuelle à 700hPa par rapport à ERA-Interim sur la période 1980-1999, tracée sur la grille d'ERA-Interim, pour ACCESS1-3, GFDL-CM3, MRI-CGCM3, ERA-40 et NCEP1. Les biais indiqués sont calculés de la manière suivante : $(\overline{WS}_{CMIP5} - \overline{WS}_{ERA-Int})/\sigma(WS_{ERA-Int})$, où σ représente l'écart-type. Le biais 1 est calculé sur l'ensemble de la zone 40° S - 90° S, le biais 2 sur la zone 40° S - 60° S et le biais 3 sur la zone 60° S - 90° S. Les contours correspondent à la hauteur du géopotentiel 700 hPa. Les zones hâchurées représentent les endroits où l'anomalie de vitesse du vent est plus de deux fois supérieure à l'écart-type de la vitesse du vent dans le modèle CMIP5.

3.6 Régionalisation

3.6.1 Motivations et principaux résultats

Nous avons montré dans la section précédente que les réanalyses étaient généralement en accord avec les effets attendus et observés à Port-aux-Français de l'intensification du SAM dans l'hémisphère sud. Les modèles CMIP5 quant à eux présentent une gamme très variée de réponses en raison de leurs différences de résolutions et de physique, qui ne permet pas l'utilisation d'une moyenne multi-modèles. En raison de temps de calcul longs, certains modèles CMIP5 doivent donc être sélectionnés afin de servir de forçage au modèle régional. Le modèle ACCESS-1-3 a été sélectionné comme modèle le plus proche d'ERA-Interim sur la période 1980-1999, et deux modèles extrêmes en terme de température (MRI-CGCM3 et GFDL-CM3) ont également été choisis pour tenter de représenter la gamme de bilans de masse régionalisés à partir des modèles CMIP5 la plus large possible.

Une fois les modèles en entrée du modèle régional sélectionnés, et les simulations sur la période récente effectuées, il faut ensuite analyser les sorties régionalisées pour s'assurer qu'elles soient suffisemment proches des observations. Dans cette section, je compare tout d'abord les résultats des simulations régionalisées à partir des données de réanalyses aux observations de terrain disponibles en différentes stations météorologiques sur l'archipel des Kerguelen. Cette comparaison révèle que les sorties régionalisées à partir d'ERA-Interim sont beaucoup plus proches des observations de terrain que celles obtenues à partir de NCEP1, et que cela est principalement lié au saut de résolution trop important entre NCEP1 ($\sim$210 km) et le modèle régional (10 km) comparé à ERA-Interim ($\sim$80 km). Elle révèle également un déficit de précipitations simulées par le MAR (forcé par ERA-Interim et par NCEP1), qui peut être lié à différents problèmes propres au MAR (représentation des nuages), aux réanalyses (assimilation des radiosondages) ou à la descente d'échelle entre réanalyses et MAR. Une correction de l'humidité spécifique du modèle hôte (ERA-Interim et NCEP1) dans NESTOR est proposée afin de tenter d'améliorer la représentation des précipitations. L'analyse des sorties révèle que la correction d'humidité la plus appropriée est de +10%, et que celle-ci améliore grandement les précipitations simulées sans modifier sensiblement les autres variables.

Par ailleurs, des simulations à 5 km, 10 km et 20 km utilisant le désagrégateur de précipitations SMHiL ont été réalisées afin (1) d'évaluer l'impact du changement d'échelle sur les précipitations aux îles Kerguelen et (2) tester les performances du désagrégateur dans cette région. Dans la seconde partie de cette section, je réalise une intercomparaison en 2011 de ces différentes sorties ainsi qu'une comparaison entre les sorties de SMHiL et celles du MAR. Ces comparaisons nous indiquent que les précipitations sont mieux représentées (en terme de quantités mais également en terme de distribution spatiale) lorsque la résolution augmente, aussi bien dans le MAR que dans SMHiL. SMHiL représente cependant plus de précipitations que le MAR à la même échelle, grâce à la prise en compte des précipitations orographiques de fine échelle. Le MAR offre néanmoins une représentation spatiale plus proche de la réalité que SMHiL (fortes précipitations sur la face ouest de l'archipel, faibles précipitations en aval de la calotte), en raison de la prise en compte de l'advection d'humidité dans MAR qui n'est pas implémentée dans SMHiL. La nécessité d'intégrer un schéma d'advection de l'humidité dans SMHiL, déjà signalée par Agosta (2012) en Antarctique, est confirmée par cette analyse. L'implantation d'un tel schéma, initialement prévue dans le cadre de ma thèse, a cependant été reportée au profit d'autres analyses importantes telles que l'étude des causes de grande échelle du retrait glaciaire sur l'archipel des Kerguelen présentée ci-dessus.

3.6.2 Comparaison entre simulations MAR récentes et observations

3.6.2.1 Analyse des sorties forcées par les réanalyses

Par souci de clarté, la majorité des figures et tableaux présentés dans cette section seront repris en Annexe H. Seuls quelques figures et tableaux résumant les principaux résultats en terme de température et précipitations seront présentés dans cette section.

Dans la Figure 3.4, les températures moyennes de l'air en surface [1] et les cumuls de précipitations aux îles Kerguelen issues du modèle MAR forcé par les réanalyses (ERA-Interim et NCEP1) pour la période allant de février à juillet 2012 sont comparées aux observations réalisées sur l'archipel au cours de cette même période. Les Figures H.1-H.5 en Annexe H montrent une comparaison des séries temporelles de températures, vitesse du vent, humidité relative et précipitations, simulées par le MAR forcé par ERA-Interim et NCEP1 avec les valeurs mesurées aux différentes stations météorologiques. Un résumé pour les températures et les précipitations à la station de la Mortadelle est présenté en Figure 3.5. Les Tableaux H.1-H.4 en Annexe H, quant à eux, révèlent différentes statistiques sur cette comparaison, qui sont résumées pour la station de la Mortadelle dans le Tableau 3.1. Les différences entre observations et valeurs simulées par le MAR sont en partie dues aux différences d'altitude de la topographie du modèle par rapport à la réalité, et à un décalage entre le centre des cellules du modèle et la localisation exacte des stations météorologique sur l'archipel. Cependant, il existe également des différences entre les sorties du MAR forcé par ERA-Interim et par NCEP1.

On remarque une très forte différence de température entre les deux simulations (Figures 3.4-3.5 a, H.1, Tableaux 3.1 et H.1) : celle forcée par ERA-Interim semble un peu trop froide par rapport aux observations (jusqu'à -2,3°C à la station d'Armor), tandis que celle forcée par NCEP1 est clairement trop chaude (jusqu'à +5,4°C à Sourcils Noirs). La saisonnalité des températures est bien reproduite dans les deux simulations (Figures 3.5 a et H.1), bien que le MAR forcé par NCEP1 semble présenter un biais chaud systématique légèrement plus fort en été qu'en hiver (Tableaux 3.1 et H.1). L'écart-type des différences (RMSE : Root Mean Square Error en anglais) reste inférieur à 1,5°C lorsque le MAR est forcé par ERA-Interim, mais peut atteindre 3,3°C lorsqu'il est forcé avec NCEP1. La corrélation entre températures modélisées et mesurées est par ailleurs bien meilleure avec le forçage par ERA-Interim (R=0,90 à 0,95) qu'avec le forçage par NCEP1 (R = 0,39 à 0,66).

La Figure H.2 et le Tableau H.2 comparent la vitesse moyenne journalière du vent en surface en sortie du MAR et dans les observations. Le MAR forcé par ERA-Interim reproduit relativement bien l'intensité du vent aux stations d'Armor et de Sourcils Noirs (Figure H.2 et Tableau H.2, biais annuels proches de zéro : 0.24 et -0.58 respectivement). Par contre il la sous-estime aux stations de Port Christmas, Cap Cotter et Port-aux-Français, avec des biais moyens annuels entre -1,3 et -1,9 m s^{-1}. A Port-aux-Français, le MAR forcé par ERA-Interim et NCEP1 semble indiquer une augmentation de la vitesse moyenne du vent depuis les années 50, qui n'est pas visible dans les mesures. Cependant, la variabilité des mesures en début de séries (dans les années 50 et 60, 4 m s^{-1} environ) est beaucoup plus forte que la variabilité actuelle (2 m s^{-1} environ). De plus, le renforcement du SAM depuis les années 70 est normalement accompagné d'une augmentation de la vitesse des vents d'ouest (voir Section 3.3), ce qui

1. La hauteur des capteurs de température, humidité et vent des stations météorologiques Kcrumble étant de 2 m, et celle de la Mortadelle de 5 m, le niveau de surface considéré dans le MAR correspond au dernier niveau sigma (le $23^{ème}$). A Port-aux-Français, les données de vent (vitesse et direction) disponibles sont mesurées à 10 m, j'ai donc considéré le $21^{ème}$ niveau sigma du MAR dans mes comparaisons concernant le vent (et le $23^{ème}$ pour les autres variables mesurées à 2 m).

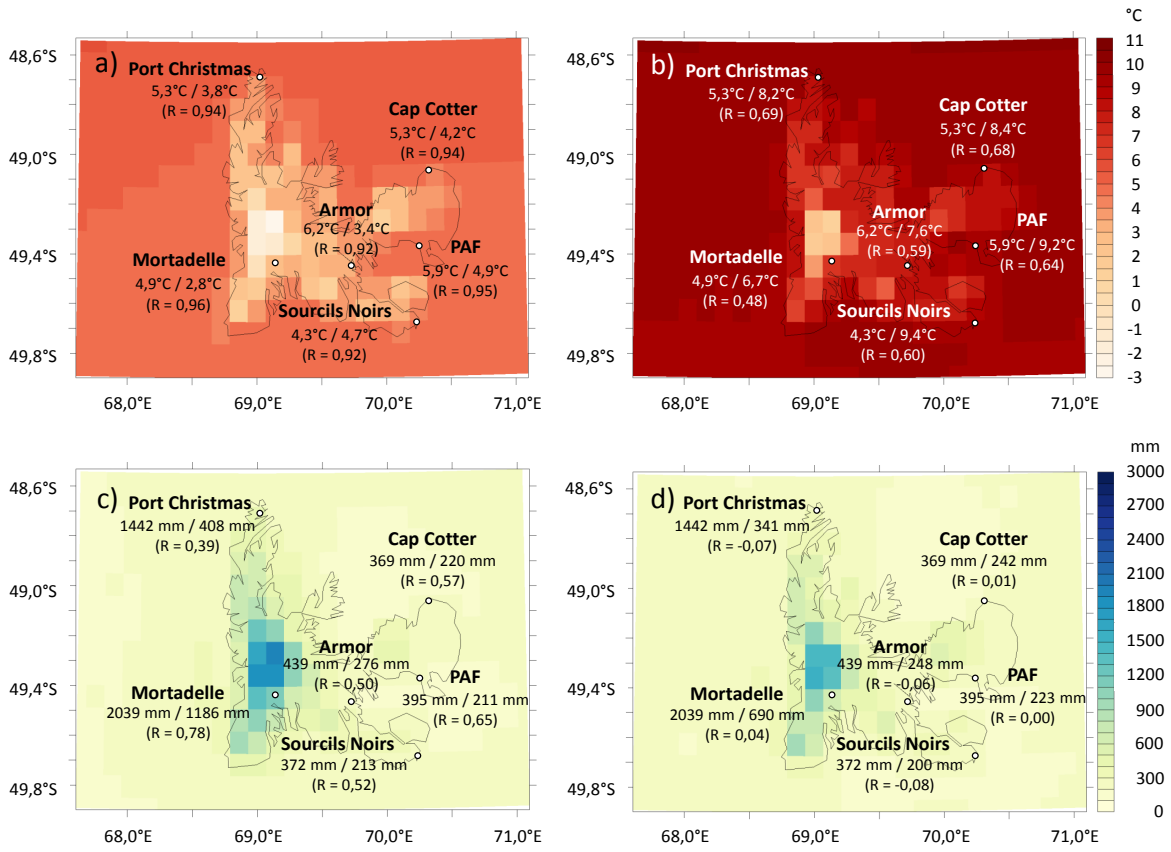

FIGURE 3.4 – Cartes de température moyenne de l'air en surface (a & b) et précipitations cumulées (c & d) aux îles Kerguelen entre le 15/02/2012 et le 09/07/2012 simulées par le MAR lorsqu'il est forcé par ERA-Interim (a & c) et par NCEP1 (b & d). Les valeurs indiquées correspondent à la valeur mesurée suivie de la valeur modélisée, ainsi que le coefficient de corrélation (R) entre parenthèse.

est simulé par le MAR. Cela laisserait penser que les mesures de vitesse du vent à Port-aux-Français présentent des erreurs plus importantes dans les années 50 et 60 qu'actuellement, qui masqueraient la véritable tendance. Le vent à la Mortadelle est fortement surestimé par le MAR forcé par ERA-Interim (Figure H.2 et Tableau H.2). En ce qui concerne le forçage par NCEP (Figure H.2), le vent est sous-estimé (voir Tableau H.2) pour l'ensemble des stations, sauf celle de la Mortadelle où il est légèrement surestimé comme dans le cas du forçage par ERA-Interim. Dans la Figure H.3, le nombre d'événements de vent par classes de vitesse dans les observations est comparé au nombre d'événements simulés par le MAR forcé par ERA-Interim et NCEP1. On remarque que pour la plupart des sites, la distribution des événements de vent dans le MAR est similaire à celle des observations (à Armor, Sourcils Noirs et Port-aux-Français), bien que la distribution d'ERA-Interim soit généralement plus proche de celle des observations que pour NCEP1. A Port-Christmas et à Cap Cotter, le MAR simule légèrement trop de petits événements mais pas assez de forts événements venteux. Par contre, à la Mortadelle, la distribution des événements est très différente dans les observations et dans les sorties du MAR, avec beau-

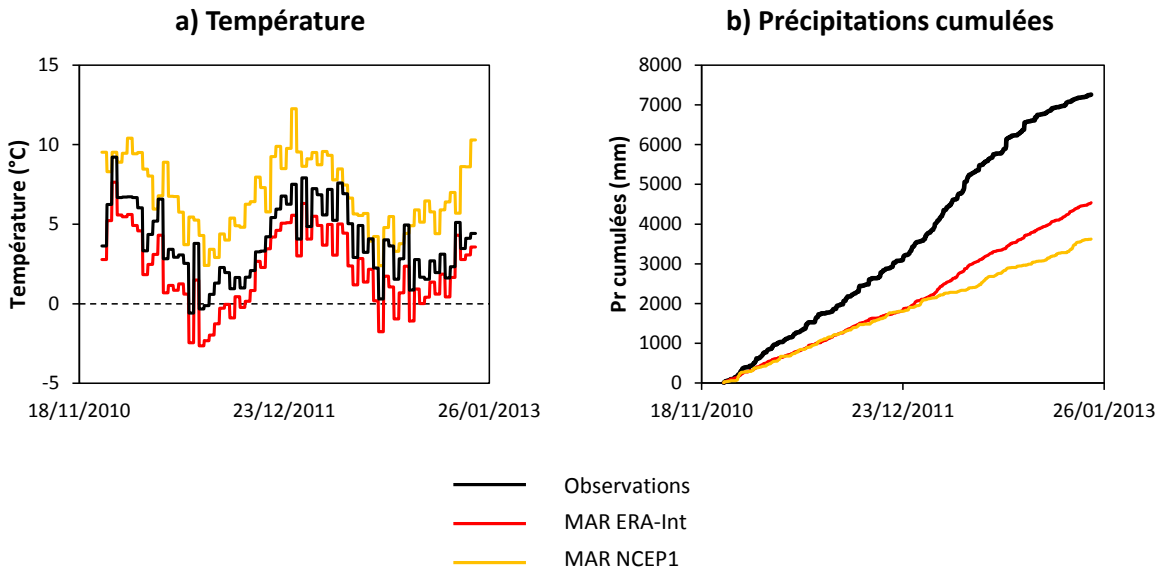

FIGURE 3.5 – Séries temporelles de la température journalière de l'air en surface (a) et des cumuls de précipitations (liquides et solides) journalières (b) simulés par le MAR forcé par ERA-Interim et par NCEP1 au point de grille contenant la station météorologique de la Mortadelle et des valeurs correspondantes mesurées à cette station. Par souci de lisibilité, les mesures et simulations de température sont moyennées sur 10 jours.

coup plus d'événements de forte intensité modélisés que dans les observations. Cela indique probablement que la station de la Mortadelle est légèrement protégée du vent dominant dans ce secteur (par la barre rocheuse de la Mortadelle, voir Figure 2.5), effet local qui n'est visiblement pas capturé par le MAR. Le faible coefficient de corrélation entre vitesse simulée par le MAR forcé par ERA-Interim et mesurée à la Mortadelle (R=0,26 dans le Tableau H.2) par rapport aux coefficients des autres stations (entre 0,70 et 0,78) corrobore cette hypothèse. Les vitesses simulées par le MAR forcé par NCEP1 sont par contre complètement décorrélées des vitesses observées, et les RMSEs systématiquement plus grandes que celles de la simulation forcée par ERA-Interim (Tableau H.2). Les biais moyens, dans les deux simulations, sont par ailleurs plus marqués en hiver qu'en été, à part à la Mortadelle.

En ce qui concerne l'humidité relative, la Figure H.4 nous indique que le MAR forcé par ERA-Interim a tendance à exagérer l'amplitude de la variation saisonnière par rapport aux observations, dans le cas de toutes les stations à part à Sourcils Noirs où le signal saisonnier est relativement bien respecté (à Port-Christmas la durée d'observation est trop courte pour pouvoir en tirer des conclusions). A Armor et à la Mortadelle, le MAR simule trop d'humidité relative en hiver, à Cap Cotter, il en simule trop peu en été, et à Port-aux-Français il en simule trop en hiver et trop peu en été (Figure H.4 et Tableau H.3). La Mortadelle est le site où l'humidité relative simulée est la moins corrélée à l'humidité observée (R=0,39 ; voir Tableau H.3). Le climat simulé par le MAR est globalement plus humide à la Mortadelle que dans les observations, principalement en hiver (Figure H.4 et Tableau H.3). Il pourrait s'agir d'un effet local impactant les mesures lié à la protection de la barre rocheuse de la Mortadelle (comme expliqué plus haut dans le cas du vent), qui dévierait localement une partie des masses d'air humides passant

TABLE 3.1 – Evaluation des températures et précipitations journalières simulées par le MAR forcé par ERA-Interim et NCEP1 par rapport aux observations à la station de la Mortadelle (n=731) : valeur moyenne mesurée à la station sur la période étudiée (Moy), RMSE (Root-Mean-Square Error[1]), coefficient de corrélation (R, les valeurs en gras sont significatives à 95% selon un test de Student ($p < 0,05$)) et biais moyen annuel, en été (DJFMAM) et en hiver (JJASON). Le pourcentage d'événements de précipitation 1) observés et simulés, 2) observés mais non simulés, 3) non observés mais simulés, et 4) ni observés ni simulés pour le MAR forcé par ERA-Interim et NCEP1 est également indiqué. Les sommes 1+4 (accord entre simulations et observations) et 2+3 (désaccord entre simulations et observations) sont aussi renseignées.

Variable		Température (°C)		Précipitations (mm j^{-1})	
Forçage		ERA-Int	NCEP1	ERA-Int	NCEP1
Moy		3,89	3,89	10,0	10,0
RMSE		1,10	3,31	14,9	20,9
R	(s.u.)	**0,94**	**0,39**	**0,72**	0,02
biais	annuel	-1,70	2,91	-3,7	-5,0
	été	-1,65	3,01	-4,5	-6,2
	hiver	-1,74	2,80	-3,0	-3,8
Cas	1			63	47
(%)	2			5	20
	3			22	24
	4			10	9
Cas	1+4			73	56
(%)	2+3			27	44

dans cette région (effet local qui ne peut être capturé par le MAR vu sa résolution). Dans la Figure H.4, on remarque que le MAR forcé par NCEP1 exagère encore plus l'amplitude des variations d'humidité relative. Les RMSEs sont effectivement plus grandes que dans le cas du forçage par ERA-Interim (11 à 25% pour NCEP1 contre 6 à 8% pour ERA-Interim), et aucune corrélation n'apparaît entre humidité simulée et observée, à part à Port-aux-Français (faible corrélation de 0,22 ; voir Tableau H.3, mais si l'on corrèle sur une période similaire aux observations Kcrumble, la corrélation diminue). Les biais moyens sont positifs partout (surtout en hiver), à part à Cap Cotter où l'on observe un biais négatif (surtout en été) par rapport aux observations.

En ce qui concerne les précipitations, les deux simulations diffèrent moins l'une de l'autre. La simulation forcée par NCEP1 produit légèrement moins de précipitations sur la calotte Cook que celle forcée par ERA-Interim (Figures 3.4, 3.5 b et H.5). La simulation forcée par ERA-Interim semble offrir une meilleure représentation du timing des événements de précipitations et de leur intensité relative que celle forcée par NCEP1. En effet, la corrélation entre précipitations modélisées et observées est à nouveau bien plus élevée, et les RMSEs plus faibles, pour le MAR forcé par ERA-Interim (R = 0,41 à 0,72) que par NCEP1 (pas de corrélation) (Tableaux 3.1 et H.4). De plus, les Tableaux 3.1 et H.5 indiquent que le MAR est plus souvent en accord avec les observations lorsqu'il est forcé par ERA-Interim que par NCEP1. Les événements simulés et

observés coïncident mieux (i.e. la somme 1+4 est plus élevée et inversément la somme 2+3 est plus faible) pour ERA-Interim que pour NCEP1. Or il est crucial pour la représentation du bilan de masse de modéliser les bonnes occurences de chutes de neige car celles-ci ont un impact direct sur l'albédo. Ne pas modéliser une petite chute de neige ayant eu lieu (cas 2) ou au contraire modéliser une chute de neige qui n'a pas réellement eu lieu (cas 3) peut avoir des conséquences importantes sur l'albédo de surface et donc sur la représentation du bilan de masse final.

Par contre, les Figures 3.4, 3.5 b et H.5 nous indiquent que les cumuls de précipitations simulés semblent bien trop faibles par rapport aux quantités mesurées, surtout sur la partie ouest des îles Kerguelen (Port Christmas et la Mortadelle). Ce déficit de précipitation semble lié à une sous-estimation des forts événements par rapport aux petits événements (Figure H.6) Le MAR simule généralement trop d'événements au total, mais représente mal les événements de plus de 10 mm par jour, qui représentent une part importante des quantités totales de précipitations (Figure H.6), surtout pour les sites occidentaux de la Mortadelle et de Port-Christmas (plus de 60%). A Port-Christmas, un biais dans les mesures est possible car la station a été installée en aval d'une lagune. Par grand vent, une partie de l'eau collectée dans le pluviomètre pourrait donc provenir de cette lagune plutôt que des précipitations. La surestimation des petits événements par le MAR par rapport aux observations est en partie due aux seuils de détection des évéments pluvieux par les pluviomètres. En effet, les pluviomètres installés sur l'archipel des Kerguelen sont des systèmes à augets, qui ne se déclenchent qu'à partir d'une certaine quantité de liquide présente dans l'auget (0,5 mm pour la Mortadelle, 0,2 mm pour les stations Kcrumble et 0,1 mm pour la station de Port-aux-Français). Cela signifie que certains événements sont situés sous ces seuils de détection des pluviomètres et vont donc être simulés par le MAR mais pas observés. Ces événements simulés mais non observés représentent entre 22% et 59% du nombre total d'événements simulés par le MAR selon les sites de mesure. La répartition spatiale des précipitations sur l'archipel est par ailleurs très similaire entre les deux simulations, à part à Port-aux-Français où le MAR forcé par NCEP1 représente plus fidèlement les cumuls de précipitations observés (Figures 3.4, 3.5 b et H.5).

3.6.2.2 Prise en compte d'une humidité plus importante

Le déficit de précipitation en sortie du MAR peut provenir de différents problèmes, propres au MAR lui-même ou propres à ERA-Interim et NCEP1. En effet, les modèles régionaux sont fortement influencés par le modèle utilisé pour le forcer à ses frontières (Giorgi and Mearns, 1999; Agosta, 2012; Fettweis et al., 2013), et ce d'autant plus que la taille du domaine est petite (dans ce cas-ci 800 x 800 km).
Le déficit de précipitation peut être causé par :

1. une représentation insuffisante de la microphysique nuageuse dans le modèle MAR, qui produit alors un couvert nuageux trop faible et des précipitations réduites.
2. la descente d'échelle importante entre les réanalyses ($\sim$ 210 km pour NCEP1, $\sim$ 80 km pour ERA-Interim) et le MAR (10 km), qui nécessite une adaptation de l'humidité entre la zone tampon du modèle MAR (proche de ses frontières) et le centre du domaine, qui conduit à des variations d'humidité.
3. le fait que l'humidité aux îles Kerguelen dans ERA-Interim et NCEP1 est basée sur les radiosondages de Port-aux-Français (voir Figure 1), qui sont effectués dans une zone où l'effet de foehn est très important, et où la sécheresse de l'air n'est donc pas forcément représentative de cette région océanique.

Une manière de voir si le MAR simule un couvert nuageux suffisant consiste à comparer le rayonnement de grandes longueurs d'onde incident en surface (servant d'indicateur de la couverture nuageuse) dans les sorties du modèle et dans les observations. Cette comparaison, réalisée à la station de la Mortadelle en 2011 (Figure 3.6), montre que le rayonnement de grandes longueurs d'onde incident dans le modèle MAR forcé par ERA-Interim est effectivement sous-estimé par rapport aux observations, indiquant une sous-estimation du couvert nuageux par le modèle. Le déficit de précipitation en sortie du MAR est donc probablement partiellement causé par l'effet (1) décrit ci-dessus.

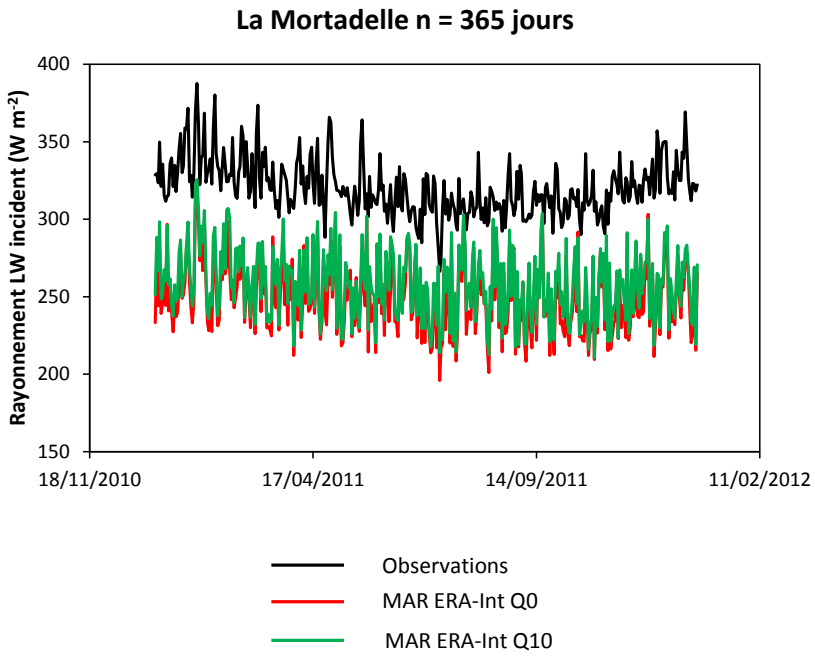

FIGURE 3.6 – Séries temporelles du rayonnement de grandes longueurs d'onde (LW) incident en surface simulé par le MAR forcé par ERA-Interim avec et sans augmentation de l'humidité au point de grille contenant la station de la Mortadelle et du rayonnement de grandes longueurs d'onde (LW) incident en surface mesuré à cette station. Les résultats sont similaires pour le forçage par NCEP1.

La Figure 3.7 compare l'humidité spécifique simulée par le MAR forcé par ERA-Interim avec celle calculée à partir de l'humidité relative mesurée à la station de la Mortadelle (seule la station de la Mortadelle dispose de mesures de pression de surface nécessaires pour convertir l'humidité relative en humidité spécifique). L'humidité spécifique simulée par le MAR forcé par ERA-Interim est généralement trop faible par rapport aux mesures (Figure 3.7), ce qui laisse penser que les effets (2) et/ou (3) ci-dessus ont lieu. Par contre, le forçage par NCEP1 donne une humidité spécifique parfois plus élevée et parfois plus faible que celle des mesures (non montré), ce qui indique que plusieurs des effets listés ci-dessus ont probablement lieu.

Pour tenter de représenter plus fidèlement les précipitations de l'archipel, une correction de l'humidité spécifique du modèle hôte (les réanalyses) peut être effectuée dans NESTOR. Ce type de correction a déjà été réalisé dans le cadre de simulations MAR à Ellesmere (Watelet,

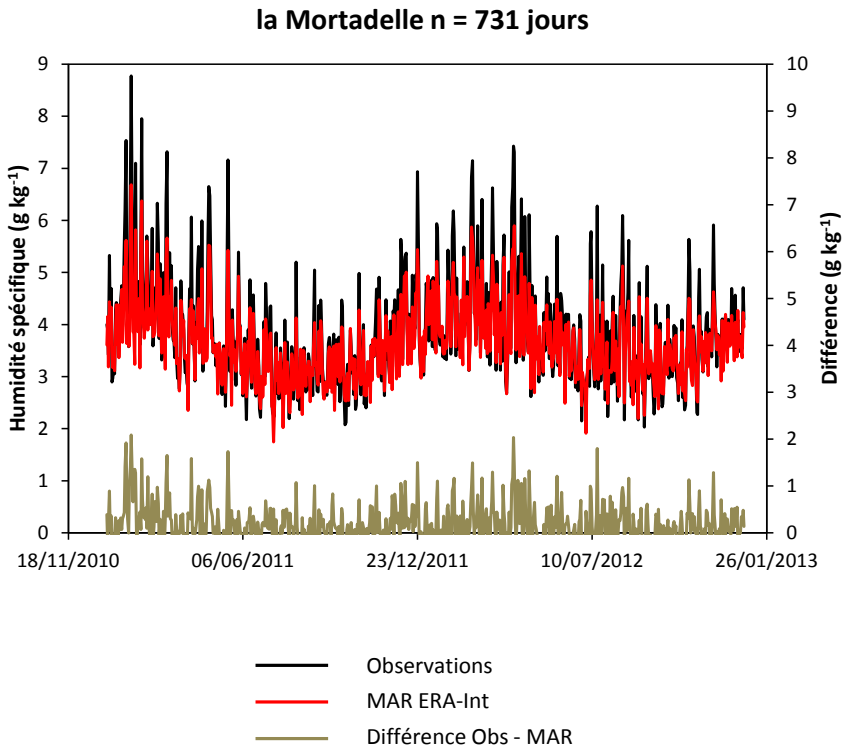

FIGURE 3.7 – Séries temporelles de l'humidité spécifique journalière en surface simulée par le MAR forcé par ERA-Interim au point de grille contenant la station de la Mortadelle et de l'humidité spécifique journalière en surface mesurée à cette station. La différence entre observation et simulation est également indiquée.

2013). J'ai testé plusieurs corrections d'humidité, en prenant comme référence les mesures de précipitation à la Mortadelle en 2011, tout en vérifiant que la correction d'humidité n'affecte pas trop les autres variables en sortie du MAR. Pour le forçage par ERA-Interim tout comme celui par NCEP1, la correction d'humidité la plus adaptée est de + 10%. La Figure 3.8 représente les mêmes sorties que la Figure 3.4, mais pour une humidité spécifique initiale augmentée de 10%. On remarque que les températures de surface sont effectivement très peu affectées par la correction d'humidité, tout comme les vitesses de vent (non montré). Par contre, le cumul de précipitation sur la période considérée est grandement améliorée par rapport à la version sans correction d'humidité. Le rayonnement de grandes longueurs d'onde incident en surface est par ailleurs légèrement augmenté (Figure 3.6), reflétant la présence un peu plus importante de nuages dans le modèle lorsque l'humidité est augmentée. Dans les Figures H.5 et H.6 et les Tableaux H.4 et H.5 sont reprises les mêmes sorties que précédemment, mais après augmentation de l'humidité spécifique d'ERA-Interim de 10%. Un résumé est fourni en Figure 3.9 et dans le Tableau 3.2 pour la station de la Mortadelle. On remarque que les cumuls de précipitations sont grandement améliorés, et que le MAR simule plus d'événements intenses (et généralement moins de petits événements) qu'initialement (Figures 3.9, H.5 et H.6). La représentativité des événements observés est cependant peu améliorée par rapport aux versions sans changement de

l'humidité spécifique (Tableaux 3.1 et H.5, amélioration ou détérioration légères selon les sites) car le fait d'augmenter l'humidité diminue le nombre d'événements observés mais non simulés (cas 2) mais augmente en contrepartie le nombre d'événements non observés mais simulés (cas 3) en raison de l'augmentation du nombre total d'événements de précipitations. Par ailleurs, les biais de précipitation sont fortement réduits, tandis que les coefficients de corrélation ne varient effectivement que très peu (Tableaux 3.1 et H.4).

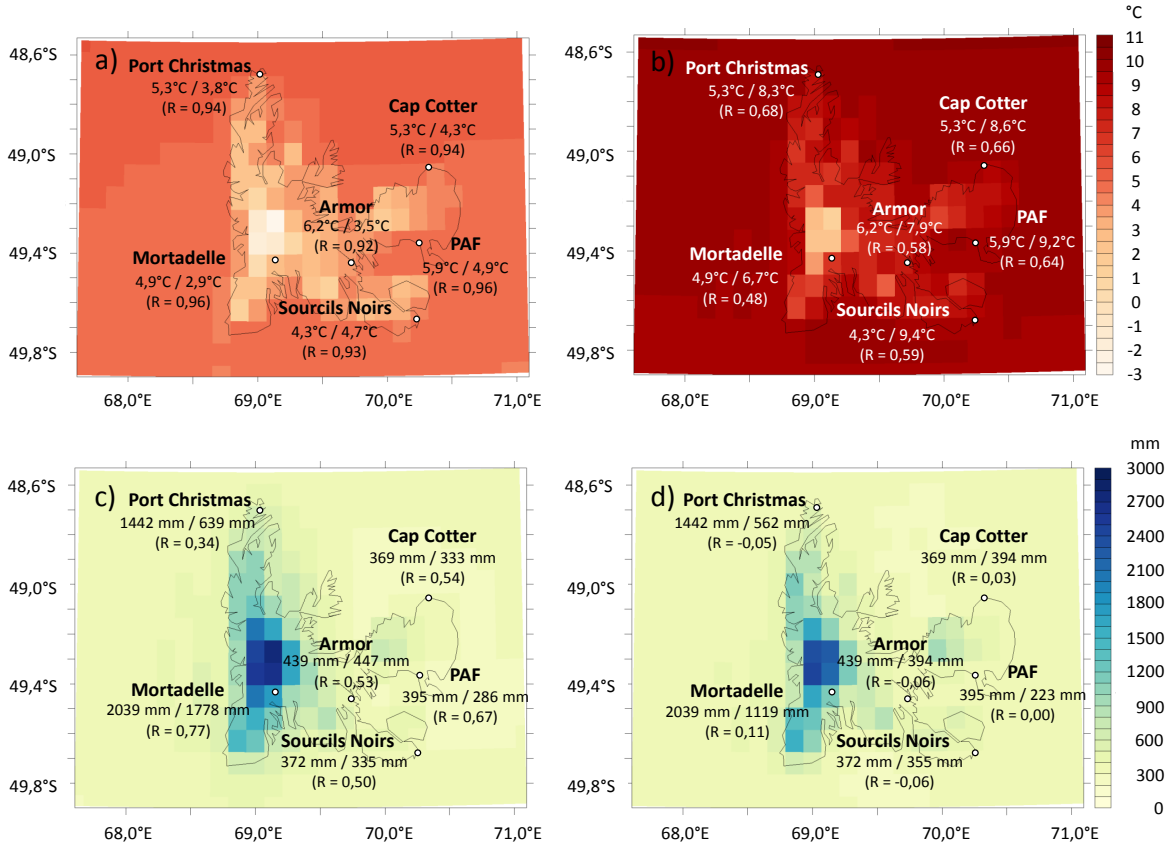

FIGURE 3.8 – Cartes de température moyenne (a & b) et précipitations cumulées (c & d) aux îles Kerguelen entre le 15/02/2012 et le 09/07/2012 simulées par le MAR lorsqu'il est forcé par ERA-Interim (a & c) et par NCEP1 (b & d) avec une humidité spécifique augmentée de 10%. Les valeurs indiquées correspondent à la valeur mesurée suivie de la valeur modélisée, ainsi que le coefficient de corrélation (R) entre parenthèse.

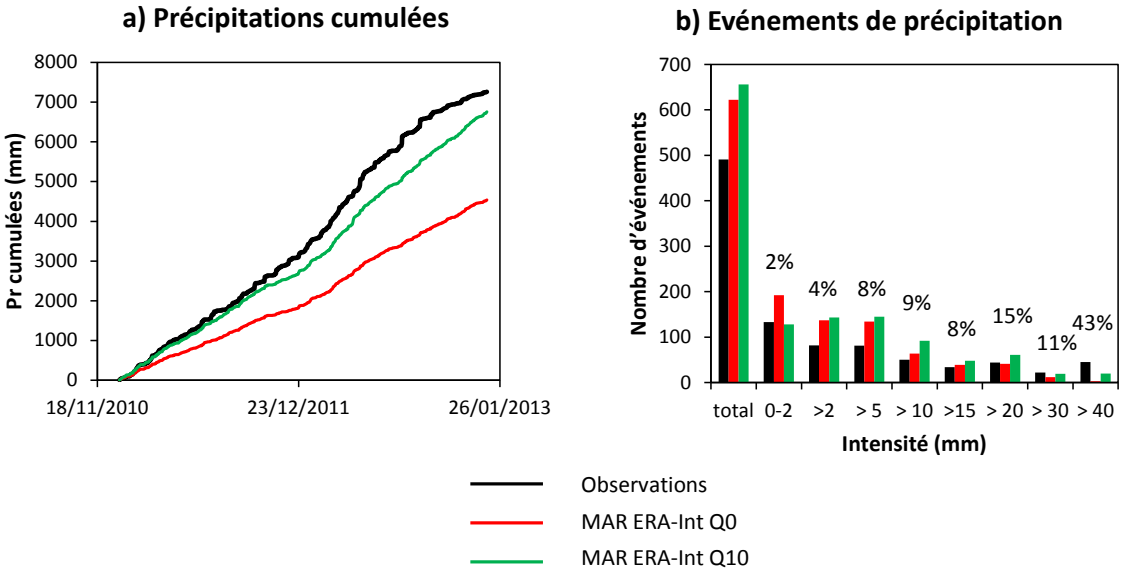

FIGURE 3.9 – a) Séries temporelles des cumuls de précipitations (liquides et solides) journalières simulées par le MAR forcé par ERA-Interim sans changement de l'humidité relative (Q0) et avec augmentation de 10% de l'humidité relative (Q10) au point de grille contenant la station météorologique de la Mortadelle et des précipitations journalières mesurées à cette station. b) Comparaison entre le nombre d'événements de précipitations par classes d'intensité simulés par le MAR forcé par ERA-Interim avec (Q10) et sans (Q0) augmentation de l'humidité relative et mesurés à la station de la Mortadelle. Les pourcentages indiqués au-dessus des histogrammes représentent la part de chaque classe d'intensité par rapport au cumul total de précipitations observées. Les résultats sont similaires pour la simulation forcée par NCEP1.

TABLE 3.2 – Evaluation des précipitations journalières simulées par le MAR forcé par ERA-Interim sans (Q0) et avec (Q10) augmentation de l'humidité par rapport aux observations à la station de la Mortadelle (n=731) : valeur moyenne mesurée à la station sur la période étudiée (Moy), RMSE (Root-Mean-Square Error[1]), coefficient de corrélation (R, les valeurs en gras sont significatives à 95% selon un test de Student ($p < 0{,}05$)) et biais moyen annuel, en été (DJFMAM) et en hiver (JJASON). Le pourcentage d'événements de précipitation 1) observés et simulés, 2) observés mais non simulés, 3) non observés mais simulés, et 4) ni observés ni simulés pour le MAR forcé par ERA-Interim Q0 et Q10 est également indiqué. Les sommes 1+4 (accord entre simulations et observations) et 2+3 (désaccord entre simulations et observations) sont aussi renseignées.

Forçage		ERA-Int Q0 (mm jour^{-1})	ERA-Int Q10 (mm jour^{-1})
Moy		10,0	10,0
RMSE		14,9	13,6
R	(s.u.)	**0,72**	**0,74**
biais	annuel	-3,7	-0,7
	été	-4,5	-1,3
	hiver	-3,0	-0,1
Cas	1	63	65
(%)	2	5	2
	3	22	25
	4	10	8
Cas	1+4	73	73
(%)	2+3	27	27

3.6.2.3 Conclusions sur la validation du MAR forcé par les réanalyses

En conclusion de ces analyses, les simulations forcées par ERA-Interim sont beaucoup plus proches des observations de température, précipitations, vent et humidité que celles forcées par NCEP1. La différence ne peut pas provenir des données assimilées dans chaque réanalyse, car les données de la station météorologique de Port-aux-Français sont assimilées depuis 1967 dans NCEP1 et depuis 1979 (le début des réanalyses) dans ERA-Interim, et les radiosondages à Port-aux-Français depuis 1970 dans NCEP1 et depuis 1979 dans ERA-Interim (idem). Par contre, elle provient probablement en partie de physiques différentes entre les deux réanalyses, mais aussi très certainement de leur différences de résolution. En effet, ERA-Interim, qui a une résolution d'environ 80 km, est plus adapté pour forcer des simulations MAR à 10 km de résolution que NCEP1 qui a une résolution d'environ 210 km. On considère généralement que la résolution du modèle régional ne doit pas être plus de 8 fois inférieure à celle du modèle-hôte (les réanalyses dans notre cas), afin d'éviter les erreurs d'interpolation et la génération de bruit aux frontières du modèle (Giorgi and Mearns, 1999). La taille du domaine d'intégration du MAR joue probablement également un rôle, et il serait judicieux par la suite d'effectuer des tests de sensibilité pour déterminer dans quel mesure elle intervient pour le forçage par NCEP. ERA-Interim convient donc tout juste, mais NCEP1 est beaucoup trop grossier pour servir de forçage dircet au MAR à 10 km de résolution (avec le domaine actuel de 80x80 points de grille). La solution probable pour utiliser NCEP1 efficacement serait de passer par une échelle intermédiaire, c'est-à-dire de réaliser des simulations MAR à $\sim$50 km de résolution forcées par NCEP1 (à 210 km), puis dans un deuxième temps de réaliser des simulations MAR à 10 km forcées par les sorties du modèle MAR à 50 km.

3.6.3 Comparaison entre simulations SMHiL et MAR sur l'année 2011

Les Figures 3.10 et 3.11 comparent les cumuls annuels de précipitations liquides et solides simulées par le MAR et SMHiL à différentes résolutions (20 km, 10 km et 5 km). Les deux modèles simulent de plus grandes quantités de précipitation lorsque la résolution augmente, ainsi qu'une répartition spatiale des précipitations qui semble plus réaliste au vu des effets orographiques (apparition notamment de pluies plus fortes au niveau du Mont Ross dans les simulations à 5 km de résolution). SMHiL simule plus de précipitations liquides et solides que le MAR à la même résolution, en raison de la prise en compte des précipitations orographiques de fine échelle (voir Section 2.4.4). La simulation SMHiL à 5 km de résolution obtenue à partir des sorties MAR à 20 km de résolution produit des précipitations solides et liquides sur une zone plus étendue que celle obtenue à partir des sorties MAR à 10 km, en raison du saut de résolution plus important qui perturbe l'interpolation des champs de grande échelle.

La répartition spatiale des précipitations liquides diffère par ailleurs fortement entre le MAR et SMHiL. Dans le MAR, les pluies sont concentrées sur la face ouest de l'archipel (face exposée aux westerlies) principalement ainsi que sur les reliefs (Mont Ross, calotte Cook et Péninsule Rallier du Baty, voir Figure 1.1). Dans SMHiL, au contraire, les précipitations sont réparties plus uniformément sur l'ensemble de l'archipel, avec une zone plus sèche sur la Péninsule Courbet (péninsule sur laquelle se situe Port-aux-Français). Cette différence entre les deux modèles ne peut pas être liée à une différence topographique. En effet, la Figure 3.10 indique des topographies très similaires entre simulations de même résolution, malgré l'utilisation de deux jeux de données topographiques différents (ETOPO1 et SRTM). La principale raison de cette différence de répartition des précipitations entre MAR et SMHiL réside dans la prise en compte de l'advection d'humidité dans le premier, alors que ce processus n'est pas pris en compte dans le

second. Le MAR est par conséquent capable de représenter le fort effet de foehn qui a lieu aux îles Kerguelen et l'assèchement des masses d'air après leur passage au-dessus de la calotte Cook et des reliefs occidentaux, ce que SMHiL ne peut représenter correctement. La sécheresse plus marquée sur la Péninsule Courbet par rapport aux autres régions dans SMHiL est simplement liée au fait que cette zone est extrêmement plate, et qu'elle reçoit donc peu de précipitations orographiques. La répartition spatiale des précipitations solides est par ailleurs assez similaire dans le MAR et dans SMHiL, contrairement à celle des pluies, car la formation de neige est fonction de l'altitude, et est donc principalement contrainte par la topographie (très similaire dans les deux modèles). Le problème de l'advection d'humidité avait déjà été soulevé dans le cadre des travaux de Agosta (2012) en Antarctique. Notre analyse sur les îles Kerguelen confirme la nécessité d'intégrer un tel schéma dans SMHiL afin de représenter correctement les précipitations. Cependant l'implantation d'un schéma d'advection dans SMHiL, initialement prévue dans le cadre de ma thèse, a été reportée car nous avons préféré nous pencher sur d'autres questions importantes telles que l'analyse des causes de grande échelle du recul de la calotte présentée plus haut.

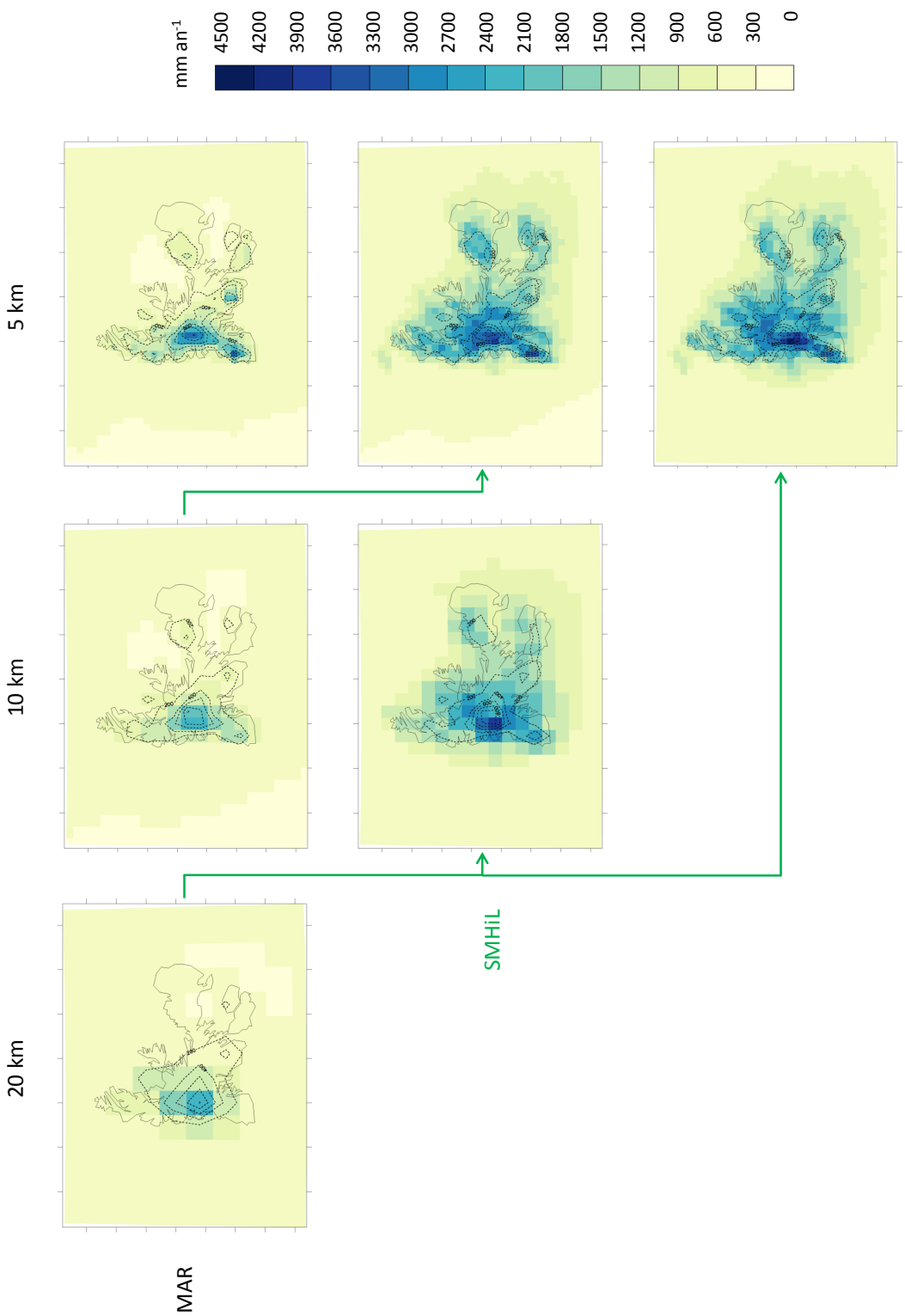

FIGURE 3.10 – Cumuls annuels de précipitations liquides simulées par le MAR forcé par ERA-Interim (sans changement de l'humidité spécifique) et par SMHiL forcé par les sorties MAR. Les courbes de niveaux sont indiquées en traits pointillés.

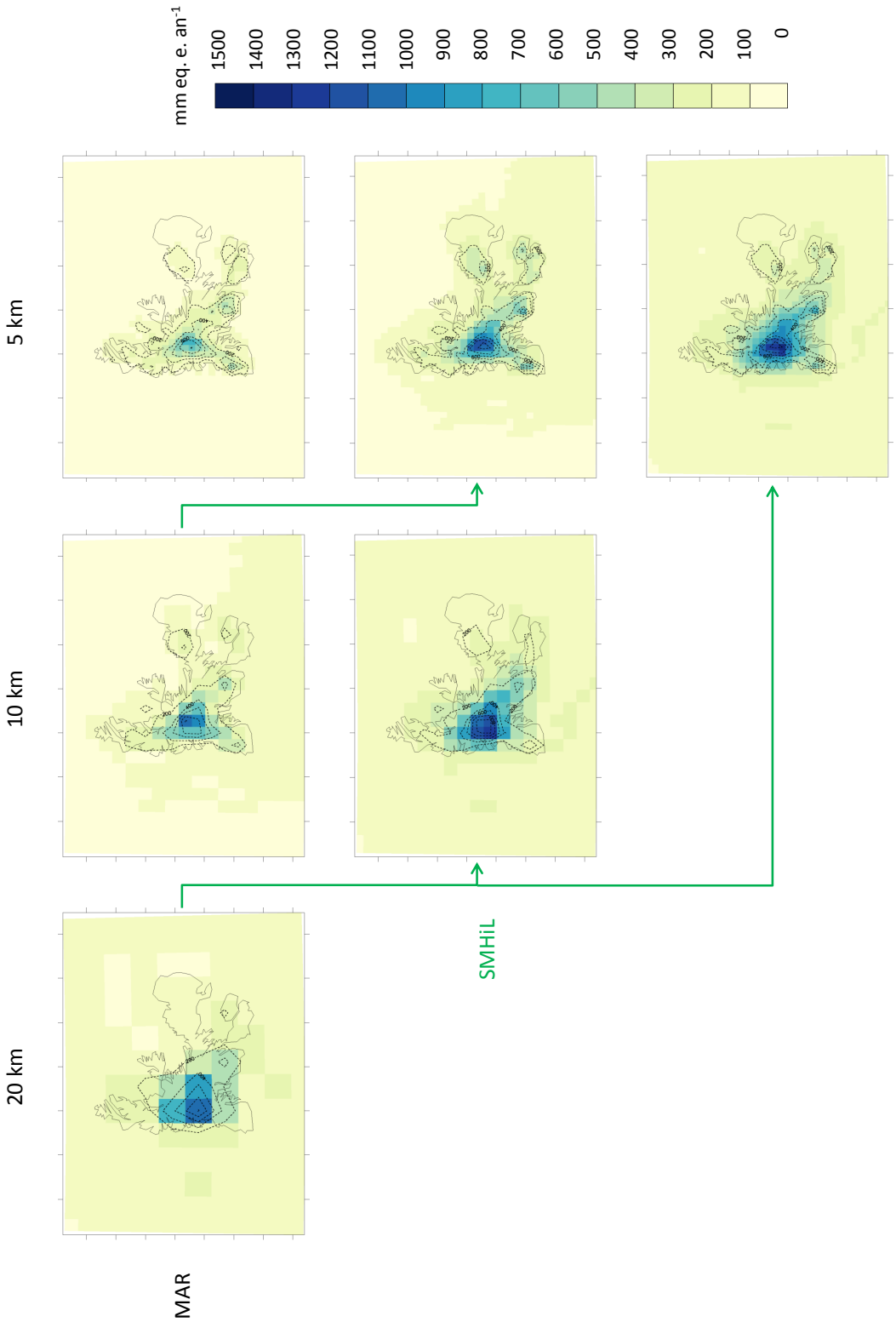

FIGURE 3.11 – Cumuls annuels de précipitations solides (en mm eq. e. an^{-1}) simulées par le MAR forcé par ERA-Interim (sans changement de l'humidité spécifique) et par SMHiL forcé par les sorties MAR. Les courbes de niveaux sont indiquées en traits pointillés.

3.7 Evolution future à l'échelle régionale

3.7.1 Motivations et principaux résultats

Après avoir évalué les tendances climatiques dans les réanalyses et les différents modèles de l'exercice CMIP5 (Section 3.5.2), sélectionné et évalué les modèles CMIP5 les plus adéquats (Section 3.5.3), et évalué les résultats de la régionalisation, nous nous intéressons à présent à l'évolution future du bilan de masse de surface régionalisé.

Les sorties de bilan de masse du modèle MAR forcé par ERA-Interim avec augmentation de l'humidité sont tout d'abord analysées, révélant des valeurs trop négatives par rapport à la valeur mesurée sur la dernière décennie dans la Section 3.3. L'analyse ci-dessous révèle que les gradients de bilan de masse avec l'altitude sont en fait trop élevés par rapport aux observations, et l'ablation au front trop importante. Nous montrons que cela n'est pas lié à un gradient trop important de température, mais à la définition de l'albédo de la glace dans le modèle MAR, qui est sous-estimé par rapport aux observations. Ce constat confirme l'importance de l'albédo dans le bilan de masse de surface déjà mentionnée dans la Section 3.2. L'ensemble des simulations réalisées avec le MAR présente donc un biais négatif lié à l'albédo. L'intercomparison des simulations forcées par ERA-Interim et les modèles CMIP5, ainsi qu'une analyse des anomalies de bilan de masse entre la période récente et future sont cependant intéressantes.

Dans un second temps, les sorties du modèle MAR forcé par les modèles CMIP5 sélectionnés sont évaluées par rapport aux sorties forcées par ERA-Interim, révèlant une sous-estimation du bilan de masse de surface par le modèle central (ACCESS1-3) liée à des températures trop importantes par rapport à ERA-Interim malgré des précipitations plus marquées. Le choix des modèles extrêmes est par ailleurs remis en cause. En effet, le modèle MRI-CGCM3 produit effectivement un bilan de masse moyen très négatif sur la période récente, mais le modèle GFDL-CM3, initialement choisi pour représenter les bilans de masse les plus élevés de la gamme CMIP5, fournit des valeurs moyennes très négatives sur la période 1980-2005 et plus faibles que celles d'ACCESS1-3.

Ensuite, l'évolution future du bilan de masse régionalisé grâce au modèle MAR au cours du 21 ^{e}siècle pour le scénario RCP8.5 est présentée. Le forçage par le modèle ACCESS1-3 simule un bilan de masse moyen sur la période 2006-2100 plus négatif que sur la période récente, légèrement moins marqué si l'on augmente l'humidité initiale de 5%. Le modèle extrême MRI-CGCM3 représente le bilan de masse le plus faible pouvant être simulé lors du forçage par un modèle CMIP5, avec une valeur de l'ordre de -19 m eq. e. an^{-1} sur la période 2006-2100, peu réaliste car cela signifierait une disparition extrêmement rapide de la calotte. Le modèle GFDL-CM3, quant à lui, présente un bilan de masse futur moins négatif que son bilan récent, pouvant signifier un problème de représentation des précipitations dans les simulations futures. L'ensemble des modèles CMIP5 sélectionnés prédit une perte de masse significative à l'horizon 2100, qui conduira très certainement à la disparition progressive de la calotte Cook au cours du prochain siècle.

Finalement, une méthode est proposée permettant d'estimer efficacement le bilan de masse de chaque modèle CMIP5 sans devoir passer par le modèle MAR, grâce au modèle degré-jour présenté précédemment. Celle-ci devrait permettre d'estimer rapidement l'enveloppe des bilans de masses récents et futurs des modèles CMIP5.

3.7.2 Evaluation préliminaire des résultats sur la période récente

Les modèles de circulation générale ne sont pas capables de représenter la variabilité inter-annuelle du climat. Afin d'évaluer leurs performances, seule une comparaison de leurs moyennes climatiques (> 10 ans) avec celles d'ERA-Interim sur la période historique est donc possible. Afin de comparer des moyennes climatiques les plus longues possibles, la période 1980-2005 a été choisie. Dans un premier temps, nous analyserons de manière critique le bilan de masse simulé par le modèle MAR lorsqu'il est forcé par ERA-Interim avec augmentation de l'humidité (Q10). Dans un second temps, nous évaluerons les performances du MAR forcé par le modèle le plus proche d'ERA-Interim, ACCESS1-3, par rapport à celles d'ERA-Interim. Dans un troisème temps, nous testerons le fait d'augmenter l'humidité dans ACCESS1-3 de 5%. Pour finir, nous évaluerons les sorties du MAR forcé par les deux modèles extrêmes sélectionnés, GFDL-CM3 et MRI-CGCM3.

Des comparaisons seront également effectuées ponctuellement entre les sorties moyennes de température et de vitesse du vent du MAR forcé par ces différents modèles sur la période 1980-2005 et les valeurs brutes de chaque modèle présentées dans la Section 3.5.3.2, Figures 3.2 et 3.3. Des incertitudes résultent cependant de cette approche en raison de (1) la différence de période considérée : 1980-1999 pour les valeurs brutes contre 1980-2005 pour les sorties du MAR, (2) la différence de niveaux de pression considérés : 850 hPa pour les températures et 700 hPa pour les vitesses de vent brutes contre la pression du dernier niveau avant la surface (k=23) pour les sorties du MAR, (3) pour les températures, la saison considérée : uniquement l'été pour les températures brutes contre l'année entière pour les sorties du MAR.

La Figure 3.12 compare les moyennes 1980-2005 de température de l'air, précipitations, vitesse du vent et humidité spécifique en surface des sorties du MAR forcé par les modèles ACCESS1-3, GFDL-CM3, MRI-CGCM3 et par ERA-Interim au point de grille correspondant au site de la Mortadelle (voir Figure 2.8 pour la localisation de ce site). Le bilan de masse de surface moyen sur la calotte Cook sur la période 1980-2005 modélisé par le MAR forcé par les mêmes modèles et réanalyse, ainsi que les pertes de surface engendrées sont présentés dans le Tableau 3.3. Le bilan de masse moyen a été calculé en déterminant la relation entre le bilan de masse de surface de chaque point de grille et l'altitude, puis en prenant en compte l'hypsométrie de la calotte en 2009 présentée dans Verfaillie et al. (submitted). Les pertes de masse sont calculées en considérant la surface de la calotte en 2009 (385 km^2).

TABLE 3.3 – Valeurs des bilans de masse de surface (SMB, en m eq. e. an^{-1}) et des pertes de masse (en Gt an^{-1}) moyens annuels sur la calotte Cook pour la période 1980-2005 simulés par le MAR forcé par les réanalyses ERA-Interim Q0 (ERA Q0) et ERA-Interim Q10 (ERA Q10) et les modèles ACCESS1-3 Q0 (AC3 Q0), ACCESS1-3 Q5 (AC3 Q5), GFDL-CM3 (GF3) et MRI-CGCM3 (MRI).

	ERA Q0	ERA Q10	AC3 Q0	AC3 Q5	GF3	MRI
SMB	-2,82	-2,01	-4,91	-4,46	-7,01	-14,06
Pertes	-1,08	-0,78	-1,89	-1,72	-2,70	-5,41

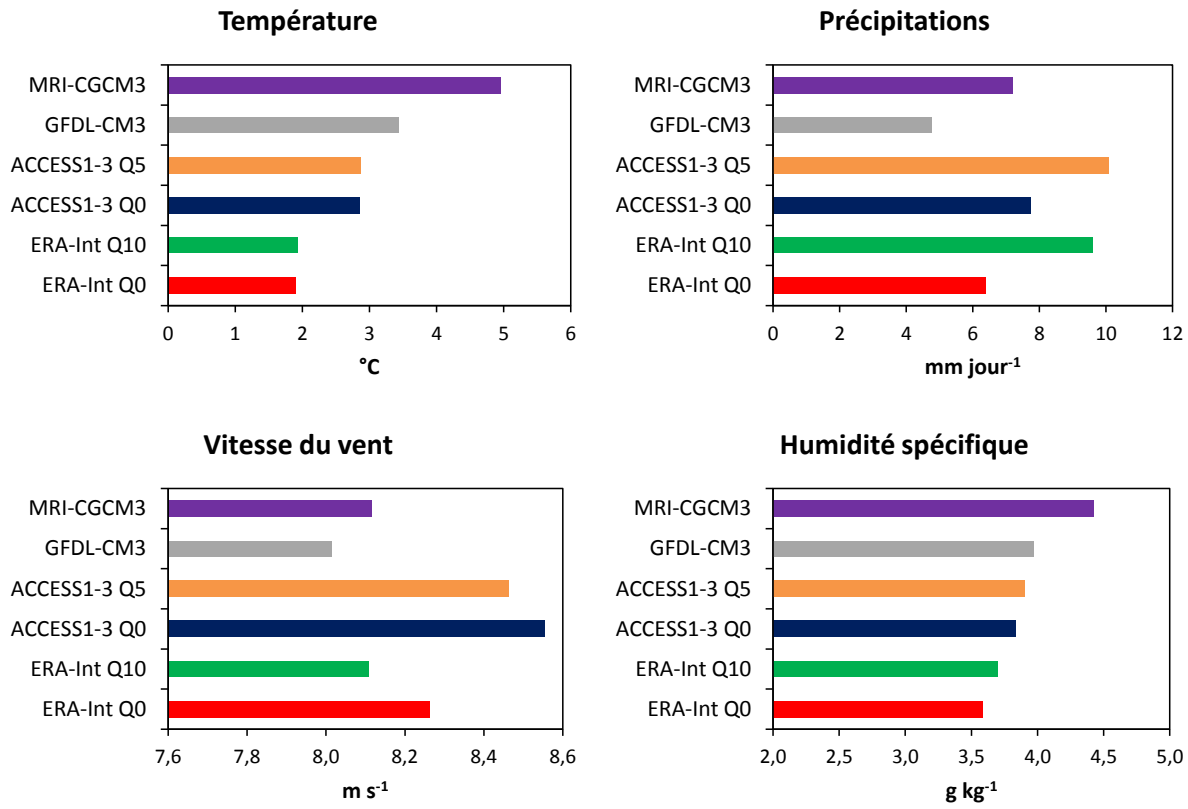

FIGURE 3.12 – Comparaison des moyennes 1980-2005 des valeurs journalières de température de l'air, précipitations, vitesse du vent et humidité spécifique simulées au site de la Mortadelle par le MAR forcé par ERA-Interim (avec et sans augmentation de l'humidité) et par les modèles CMIP5 sélectionnés (ACCESS1-3, GFDL-CM3 et MRI-CGCM3). Un cas avec augmentation de 5% de l'humidité spécifique du modèle ACCESS1-3 est également présenté. Les résultats aux autres sites d'étude sont similaires.

3.7.2.1 Analyse du bilan de masse de surface simulé par le MAR forcé par ERA-Interim

Les précipitations et températures des simulations forcées par ERA-Interim Q10 étant les plus proches de celles observées dans les mesures de terrain, on s'attend à ce que le bilan de masse de surface résultant soit relativement proche de la valeur mesurée précédemment (-1,51 $\pm$ 0,19 m eq. e. an^{-1} sur la période 2000-2009, Section 3.3). Pourtant, la valeur moyenne de bilan de masse de surface obtenue sur la période 1980-2005 est trop négative (-2,01 m eq. e. an^{-1}, Tableau 3.3). Cela se traduit par des pertes de masse à l'échelle de la calotte de l'ordre de -1 Gt an^{-1}, ce qui n'est pas négligeable comparé aux pertes de masse mesurées sur des calottes beaucoup plus grandes telles que les champs de glace patagoniens (pertes de l'ordre de -20 Gt an^{-1} mesurées sur le champ de glace sud de Patagonie sur la dernière décennie, Willis et al. (2012b)). Lorsqu'on regarde la distribution du bilan de masse ponctuel en fonction de l'altitude dans la simulation forcée par ERA-Interim Q10, on se rend compte que la pente du bilan de masse en fonction de l'altitude est trop élevée (21 mm eq. e. m^{-1}) par rapport à ce qui était observé par Vallon (1977a)

dans les années 70 (16 mm eq. e. m^{-1}) ou le gradient issu des mesures réalisées aux balises en 2011 (8 mm eq. e. m^{-1}). Au premier ordre, cela pourrait être lié à un gradient de température avec l'altitude trop élevé, et au second ordre à une durée d'ablation plus importante (mais les pentes futures sont similaires alors que la durée d'ablation est sensée augmenter dans le futur, donc cet effet est sans doute mineur). Cependant, on a observé dans la Section 3.6.2.1 qu'ERA-Interim présente un biais froid sur l'ensemble de l'archipel. Malgré cela, l'ablation à faible altitude dans la simulation forcée par ERA-Interim Q10 est beaucoup trop forte (environ -13 m eq. e. an^{-1} à 200 m d'altitude au lieu de -9 m eq. e. an^{-1} dans les observations (Section 3.2)). Cela signifie que ces valeurs d'ablation et de bilan de masse trop négatifs sont imputables à quelque chose d'autre qu'un processus lié à la température. Après analyse, il s'avère que l'albédo prescrit pour la glace dans le modèle MAR (0,25) est trop faible comparé aux valeurs mesurées sur les images issues de MODIS (de l'ordre de 0,5) dans la Section 3.2. En effet, l'albédo de la glace et de la neige aux îles Kerguelen est plus fort que les albédos habituellement rencontrés dans les Alpes par exemple, ce qui est principalement dû à la présence réduite d'impuretés aux îles Kerguelen, comme discuté précédemment dans la Section 3.2. Ce problème d'albédo de la glace a récemment été mis en évidence dans des simulations du bilan de masse au Groenland (Xavier Fettweis, communication personnelle). Ce constat confirme le rôle majeur joué par l'albédo dans le bilan de masse de surface, qui justifiait le fait que l'on mesure des bilans de masse déjà très négatifs proche du sommet de la calotte en 2011 comparé aux mesures réalisées dans les années 70 (discuté dans la Section 3.2). Le problème de l'albédo du modèle MAR impacte donc (avec un biais systématique négatif) l'ensemble des simulations récentes et futures réalisées. Cependant, il est judicieux de comparer les sorties forcées par les différents modèles CMIP5 par rapport à ERA-Interim afin d'évaluer leurs performances relatives.

3.7.2.2 Evaluation du forçage par ACCESS1-3 par rapport à celui d'ERA-Interim

Le forçage du modèle MAR par le modèle ACCESS1-3 produit des températures plus fortes d'environ 1 °C en moyenne sur la période 1980-2005 par rapport au forçage par ERA-Interim Q0. C'est un peu plus que la différence observée précédemment (environ 0 °C de différence aux îles Kerguelen, Figure 3.2) entre les valeurs brutes de températures estivales d'ACCESS1-3 et ERA-Interim sur la période 1980-1999, ce qui veut dire (1) que les températures hivernales d'ACCESS1-3 sont plus élevées que celles d'ERA-Interim, et/ou (2) que les températures (estivales ou annuelles) depuis 2000 dans ACCESS1-3 sont plus élevées que celles d'ERA-Interim, et/ou (3) que l'évolution de la température entre la surface et 850 hPa dans ACCESS1-3 est légèrement différente de celle d'ERA-Interim.

Les précipitations sont également légèrement plus fortes (d'environ 1,5 mm $jour^{-1}$ en moyenne sur la période d'étude) lors du forçage par ACCESS1-3 que par ERA-Interim Q0. Cette différence est principalement liée au fait que l'humidité spécifique du MAR forcé par ACCESS1-3 est plus élevée (d'environ 0,3 g kg^{-1} en moyenne) que pour le forçage par ERA-Interim.

Pour la vitesse du vent, ACCESS1-3 est le modèle-hôte qui donne les valeurs les plus élevées en sortie du MAR sur la période 1980-2005. Une différence d'environ 0,3 m s^{-1} en moyenne par rapport au forçage par ERA-Interim est simulée, ce qui correspond aux différences observées dans les valeurs brutes de vitesse du vent sur la période 1980-1999 (Figure 3.3).

Malgré les précipitations plus élevées dans ACCESS1-3 que dans ERA-Interim Q0, le bilan de masse de surface modélisé par le MAR lorsqu'il est forcé par ACCESS1-3 (-4,91 m eq. e. an^{-1}, Tableau 3.3) est plus négatif que celui modélisé lors du forçage par ERA-Interim Q0 (-2,82 m eq. e. an^{-1}). L'impact de la différence de température entre les deux modèles-hôtes sur

l'ablation semble en effet plus important que l'impact de leur différence de précipitations sur l'accumulation de la calotte Cook.

3.7.2.3 Prise en compte d'une humidité plus importante dans ACCESS1-3

Tout comme pour les réanalyses, il est possible d'augmenter artificiellement l'humidité spécifique des modèles-hôtes dans NESTOR afin d'augmenter les précipitations en sortie du MAR. Bien sûr, il n'y a pas d'assimilation des données de radiosondages dans les modèles CMIP5 qui puisse expliquer un déficit d'humidité spécifique dans ceux-ci comme c'était le cas pour les réanalyses. Par contre, les deux autres arguments permettant d'expliquer un déficit d'humidité restent valables, à savoir (1) une représentation insuffisante de la microphysique nuageuse dans le modèle MAR, et/ou (2) le problème de la descente d'échelle importante entre le modèle-hôte ($\sim$150 km pour ACCESS1-3) et le modèle régional (10 km) (Section 3.6.2.2). Des tests préliminaires sur l'année 2001 (non montrés), réalisés avant les simulations MAR complètes, ont révélé qu'une augmentation de l'humidité spécifique de 5% environ dans ACCESS1-3 permet de modéliser des précipitations en 2001 similaires à celles modélisées lors du forçage par ERA-Interim Q10, qui présente les valeurs se rapprochant le plus des observations (Section 3.6.2.2).

Effectivement, sur la période 1980-2005, le modèle ACCESS1-3 Q5 (augmentation de l'humidité de 5%) permet au MAR de simuler des précipitations plus importantes (de l'ordre de +2 mm jour^{-1} en moyenne, Figure 3.12) que le modèle ACCESS1-3 Q0 (sans augmentation de l'humidité). Les précipitations sont également plus importantes dans le cas d'ACCESS1-3 Q5 que celui d'ERA-Interim Q10, tout comme dans le cas d'ACCESS1-3 Q0 et ERA-Interim Q0. Les températures restent identiques entre les deux expériences ACCESS1-3, tandis que la vitesse du vent diminue très légèrement (-0,1 m s^{-1} en moyenne) dans ACCESS1-3 Q5 par rapport à ACCESS1-3 Q0 (cette différence est probablement due à la variabilité intrinsèque du modèle MAR). Le BMS de la calotte modélisé lors du forçage par ACCESS1-3 Q5 (-4,46 m eq. e. an^{-1}, Tableau 3.3) est plus élevé que celui du forçage sans augmentation d'humidité, mais reste tout de même très négatif, ce qui signifie que l'effet de la température sur le BMS dans ce modèle est vraiment important.

3.7.2.4 Evaluation du forçage par les modèles extrêmes

Dans la Section 3.5.3.2, deux modèles extrêmes en terme de température estivale sur la période 1980-1999 ont été choisis. Il s'agit de GFDL-CM3 (le plus froid) et MRI-CGCM3 (le plus chaud). Après forçage du MAR (Figure 3.12), il s'avère que MRI-CGCM3 est effectivement beaucoup plus chaud (plus de 2 °C de plus que les températures issues du forçage par ACCESS1-3) en moyenne sur la période 1980-2005 que les autres modèles. La différence par rapport à ERA-Interim est similaire à celle observée dans la Figure 3.2. Par contre, le forçage par GFDL-CM3 s'avère également plus chaud (+0,6 °C) que celui d'ACCESS1-3 sur cette période, alors que c'était le modèle qui présentait les biais bruts estivaux les plus froids par rapport à ERA-Interim sur la période 1980-1999 dans la Figure 3.2 (environ -5 °C). Cette différence pourrait être expliquée par le fait (1) que les températures hivernales de GFDL-CM3 sont beaucoup plus élevées que celles d'ERA-Interim (i.e., GFDL-CM3 présente une amplitude saisonnière beaucoup plus faible qu'ERA-Interim), et/ou (2) que les températures (estivales ou annuelles) depuis 2000 dans GFDL-CM3 sont beaucoup plus élevées que celles d'ERA-Interim, et/ou (3) que les évolutions de la température entre la surface et 850 hPa dans GFDL-CM3 et dans ERA-Interim sont très différentes.

En terme de précipitations, le forçage par MRI-CGCM3 produit légèrement moins de précipitations que le forçage par ACCESS1-3, mais légèrement plus que le forçage par ERA-Interim, en raison de la combinaison d'une humidité spécifique élevée (la plus élevée de tous le forçages, avec une valeur moyenne de 4,5 g kg^{-1} environ) avec des températures très élevées discutées ci-dessus. Le forçage par GFDL-CM3 en revanche produit très peu de précipitations (les plus faibles parmi tous les forçages, moins de 5 mm $jour^{-1}$ en moyenne), bien que son humidité spécifique soit relativement élevée (environ 4 g kg^{-1} en moyenne), car sa température moyenne est également élevée. La vitesse moyenne du vent modélisée par le MAR forcé par les deux modèles extrêmes est relativement faible, avec des différences par rapport au forçage par ERA-Interim similaires à celles observées sur le valeurs brutes de ces modèles dans la Figure 3.3.

Les températures très élevées modélisées par le MAR forcé par MRI-CGCM3 conduisent à un bilan de masse de surface moyen extrêmement négatif (-14,06 m eq. e. an^{-1}, Tableau 3.3), malgré les précipitations similaires à celles d'ACCESS1-3. Cette valeur de SMB constitue très probablement la valeur minimale que l'on puisse obtenir parmi les différentes simulations possibles avec le modèle MAR forcé par les modèles de l'exercice CMIP5. En ce qui concerne le forçage par GFDL-CM3, en revanche, le bilan de masse obtenu ne représente pas la valeur la plus positive que l'on puisse obtenir, en raison des températures trop élevées dans la Figure 3.12 par rapport à ce à quoi l'on s'attendait, et de précipitations trop faibles. Le SMB issu du MAR forcé par GFDL-CM3 (-7,01 m eq. e. an^{-1}, Tableau 3.3) présente même une valeur plus négative que celle du forçage par ACCESS1-3. On se rend compte que l'humidité est en fait un facteur clé de par la position de l'archipel des Kerguelen : une mauvaise représentation de l'humidité dans le modèle-hôte (i.e. une mauvaise représentation de la localisation de l'archipel par rapport aux zones dépressionnaires) se traduira pas des erreurs de bilan de masse importantes.

3.7.2.5 Discussion sur l'évaluation des résultats des modèles CMIP5 sélectionnés sur la période récente

En raison du problème de sous-estimation de l'albédo de la glace discuté précédemment, l'ensemble des simulations présente des valeurs de bilan de masse trop négatives par rapport à la réalité. Dans un futur proche, nous prévoyons donc de refaire ces simulations en augmentant l'albédo. La comparaison entre les sorties forcées par les différents modèles CMIP5 choisis et celles issues du forçage par ERA-Interim est cependant intéressante.

Le forçage du MAR par ACCESS1-3 produit un bilan de masse moyen de la calotte très négatif sur la période 1980-2005. Ce bilan résulte de simulations comportant un biais chaud (contrairement à ce qui avait été observé sur les températures estivales brutes à 850 hPa dans la Section 3.5.3.2, Figure 3.2), et un excès de précipitations par rapport à ERA-Interim. L'augmentation de l'humidité spécifique de 5% dans ACCESS1-3 donne un BMS moyen légèrement plus élevé, mais toujours négatif, ce qui permet de penser que l'excès de précipitations a peu d'influence car les précipitations ont déjà atteint des valeurs très élevées, et que le biais chaud engendrera une majorité de précipitations sous forme liquide.

L'analyse des modèles extrêmes avait initialement pour but de représenter les valeurs extrêmes du bilan de masse de surface modélisé (enveloppe du bilan de masse). Dans la Section 3.5.3.2 nous avions donc sélectionné le modèle le plus chaud (MRI-CGCM3) et le plus froid (GFDL-CM3) pendant les mois d'ablation maximale (en été, i.e. DJF aux îles Kerguelen). Après analyse des sorties du MAR forcé par ces deux modèles extrêmes, MRI-CGCM3 semble a priori avoir été bien choisi pour représenter la limite inférieure de SMB que l'on puisse obtenir par la modélisation régionale forcée par les modèles CMIP5. Sa température moyenne beaucoup

plus élevée que les autres modèles engendre en effet un SMB modélisé extrêmement négatif et peu réaliste de -14,06 m eq. e. an^{-1} sur la période 1980-2005. Le choix du modèle GFDL-CM3 s'avère par contre peu concluant. En effet, l'analyse réalisée sur les températures estivales à 850 hPa dans la Section 3.5.3.2 (Figure 3.2) semblait indiquer que ses faibles valeurs de température produiraient le bilan de masse de surface le plus élevé possible parmi les simulations réalisables avec les différents modèles CMIP5. Cependant, les résultats présentés ci-dessus révèlent des températures moyennes modélisées beaucoup plus élevées que celles attendues, ainsi que de faibles précipitations modélisées, qui engendrent un BMS négatif en sortie du MAR, de -7,01 m eq. e. an^{-1}. Cette valeur, fortement négative, est même inférieure à celle des sorties MAR forcées par ACCESS1-3. Nous constatons donc que ces modèles ne permettent sûrement pas de décrire l'enveloppe des bilans de masse de surface possibles.

Cela indique qu'une évaluation plus poussée des modèles CMIP5, faisant intervenir les températures à différents niveaux entre la surface et 850 hPa, et à différentes saisons, voire une analyse plus approfondie de l'humidité, serait sans doute nécessaire afin de choisir les modèles extrêmes les plus appropriés. En effet, la bonne représentation de l'humidité est cruciale car les îles Kerguelen doivent être correctement localisées par rapport aux zones dépressionnaires dans les modèles afin de représenter des bilans de masse corrects. Alternativement, nous proposons dans la Section 3.7.3.2 une méthode complémentaire permettant d'estimer rapidement le bilan de masse de l'ensemble des modèles CMIP5 grâce au modèle degré-jour utilisé en Sections 3.2, 3.3 et 3.4.

3.7.3 Evolution future du bilan de masse de surface

3.7.3.1 Bilan de masse futur modélisé par le MAR

Une fois les différents modèles évalués sur la période récente, nous analysons les prévisions de bilan de masse de surface pour le 21 ^{e}siècle. Des simulations futures avec le modèle MAR forcé par les modèles ACCESS1-3, GFDL-CM3 et MRI-CGCM3 ont été réalisées avec le scénario RCP8.5 afin d'évaluer quel serait le bilan de masse de la calotte Cook dans un contexte futur de concentrations en gaz à effet de serre élevées. Les résultats pour chaque modèle sur la période 1980-2100 et 2006-2100 sont présentés dans le Tableau 3.4. A nouveau, les bilans de masse présentés sont calculés pour l'ensemble de la calotte en se servant de la relation entre le bilan de masse de surface et l'altitude en chaque point de grille et de l'hypsométrie de la calotte en 2009.

TABLE 3.4 – Valeurs de bilan de masse de surface (SMB, en m eq. e. an^{-1}) et des pertes de masse (en Gt an^{-1}) moyens annuels sur la calotte Cook pour la période 1980-2100 et 2006-2100 simulés par le MAR forcé par les modèles ACCESS1-3 Q0 (AC3 Q0), ACCESS1-3 Q5 (AC3 Q5), GFDL-CM3 (GF3) et MRI-CGCM3 (MRI).

	Période	AC3 Q0	AC3 Q5	GF3	MRI
SMB	1980–2100	-8,45	-8,27	-5,10	-18,07
	2006–2100	-9,42	-9,31	-4,58	-19,17
Pertes	1980–2100	-3,25	-3,18	-1,96	-6,96
	2006–2100	-3,63	-3,59	-1,76	-7,38

On remarque tout d'abord les valeurs extrêmement négatives de bilans de masse simulés. Les simulations futures sont, tout comme les simulations récentes, affectées par un biais systématique

lié à la définition de l'albédo de la glace dans le MAR (Section 3.7.2.1), qui explique en partie ces valeurs très négatives. Cependant, si l'on travaille en anomalie par rapport à la période récente, on remarque que les bilans prédits dans un contexte futur d'augmentation des gaz à effet de serre (RCP 8.5) sont logiquement beaucoup plus négatifs (anomalies de l'ordre de 5 m eq. e. an^{-1}) que les bilans actuellement simulés.

Les valeurs de bilan de masse modélisé par le MAR forcé par ACCESS1-3 restent négatives après 2005, avec un bilan de masse de surface moyen entre 2006 et 2100 de -9,42 m eq. e. an^{-1} pour ACCESS1-3 Q0 et de -9,31 m eq. e. an^{-1} pour ACCESS1-3 Q5. Ces bilans de masse représentent des pertes de masse d'environ -3,8 Gt an^{-1} entre 2006 et 2100, ce qui est considérablement plus que la valeur simulée sur la période récente (-2 Gt an^{-1} environ). Ces valeurs sont en accord avec les résultats issus du modèle degré-jour présenté dans Favier et al. (in review). Bien sûr ces pertes sont surestimées car elles prennent en compte une surface de la calotte constante (valeur de 2009). Le forçage par MRI-CGCM3, quant à lui, produit un bilan de masse toujours très négatif après 2005, avec une perte estimée à -7,9 Gt an^{-1}, confirmant son choix en tant que modèle extrême parmi les modèles CMIP5. Pour GFDL-CM3, les résultats obtenus sont plus étranges. En effet, sur la période 1980-2005, ce modèle produit des bilans de masse négatifs (-5,10 m eq. e. an^{-1}) inattendus a priori, comme expliqué dans la section précédente (Section 3.7.2). A partir de 2006, cependant, le bilan de masse est moins négatif (-4,58 m eq. e. an^{-1}). Cela est très certainement dû à un problème de représentation des précipitations dans le modèle. En effet, on avait noté à la Section 3.3 que la limite entre assèchement et humidification future varie grandement selon les modèles CMIP5. La réponse future de ce modèle en terme d'humidité a probablement changé par rapport à sa réponse sur la période historique. L'ensemble des modèles CMIP5 sélectionnés pour forcer le MAR prédit cependant une perte de masse moyenne sur la période 2006-2100 de -7,86 Gt an^{-1} à -1,88 Gt an^{-1} selon les modèles, qui se traduira par sa disparition à court ou moyen terme.

3.7.3.2 Estimation du bilan de masse pour l'ensemble des modèles CMIP5 grâce au modèle degré-jour

Nous avons discuté à la Section 3.5.3 de l'impossibilité de réaliser des simulations régionales forcées par chaque modèle CMIP5 en raison des temps de calcul du MAR. Nous avons alors sélectionné le modèle CMIP5 se rapprochant le plus d'ERA-Interim sur la période récente, ainsi que deux modèles extrêmes en terme de température afin de représenter l'ensemble de la gamme de bilans de masse possibles au 21 ^{e}siècle. Cependant, il s'est avéré que le modèle GFDL-CM3, initialement choisi pour représenter les valeurs de bilan de masse les plus élevées possibles, n'est peut-être pas le modèle le plus extrême que nous ayons à disposition. En effet, les bilans de masse simulés sur la période 1980-2005 (Section 3.7.2) sont plus négatifs que ceux du modèle central (ACCESS1-3). Le bilan de masse futur simulé par le MAR forcé par GFDL-CM3, quant à lui, est bien le plus élevé parmi les modèles CMIP5 sélectionnés (Section 3.7.3.1), mais le changement de bilan de masse après 2006 laisse penser qu'il est dû à une mauvaise représentation de l'humidité sur la période future. La très grande variabilité de la limite future entre zone d'assèchement et d'humidification entre les différents modèles CMIP5 rend par ailleurs hasardeuse l'utilisation de trois modèles seulement.

Afin de pouvoir estimer rapidement les bilans de masse de chaque modèle CMIP5 sur les périodes récentes et futures, nous proposons une méthode se basant sur l'utilisation du modèle degré-jour employé précédemment (Sections 3.2, 3.3 et 3.4). Pour l'estimation du bilan de masse récent, les valeurs journalières de précipitations et température modélisées par le MAR forcé par

ACCESS1-3 aux pixels correspondant à la calotte Cook ($P_{MAR-ACCESS1-3}$, $T_{MAR-ACCESS1-3}$) sont utilisées en entrée du modèle degré-jour. Celui-ci produit alors un bilan de masse de surface ($SMB_{PDD-ACCESS1-3}$)qui peut être comparé au bilan de masse modélisé par le MAR forcé par ACCESS1-3 ($SMB_{MAR-ACCESS1-3}$).

Les précipitations et températures du modèle régional $P_{MAR-ACCESS1-3}$, $T_{MAR-ACCESS1-3}$ sont ensuite comparées aux valeurs brutes (sans régionalisation) de précipitations et températures du modèle ACCESS1-3 ($P_{ACCESS1-3}$, $T_{ACCESS1-3}$), afin d'établir les anomalies entre $P_{MAR-ACCESS1-3}$ et $P_{ACCESS1-3}$ et entre $T_{MAR-ACCESS1-3}$ et $T_{ACCESS1-3}$. Ces anomalies peuvent par la suite être appliquées aux valeurs brutes de chaque modèle CMIP5 (P_{CMIP5}, T_{CMIP5}), afin d'obtenir des champs $P_{MAR-CMIP5}$, $T_{MAR-CMIP5}$ utilisables en entrée du modèle degré-jour, via lequel leur bilan de masse peut alors être estimé. En réalisant ce travail sur l'ensemble des modèles CMIP5, on pourrait obtenir une idée de l'enveloppe des bilans de masse simulés par les modèles de l'exercice CMIP5 sur la période historique (pré-2005).

Pour évaluer l'ampleur de la gamme de bilan de masse simulé par les modèles CMIP5 au cours du 21 ^{e}siècle, il suffirait alors d'estimer l'anomalie de précipitations et de température brutes entre 2100 et le présent pour chaque modèle, puis d'ajouter ces différences aux valeurs $P_{MAR-CMIP5}$, $T_{MAR-CMIP5}$ utilisées en entrée du modèle degré-jour afin d'obtenir une estimation du bilan de masse à l'horizon 2100. Cette méthode sera appliquée prochainement.

Chapitre 4

Conclusions et perspectives

4.1 Conclusions

Les glaciers des régions sub-polaires ont reculé dramatiquement au cours du dernier siècle. Dans ces régions où les observations permettant de comprendre le recul glaciaire manquent cruellement, la présence de l'archipel des Kerguelen représente une occasion unique d'étudier la déglaciation depuis le dernier maximum glaciaire ainsi que le recul récent de ces glaciers. Situés à faible altitude et proches de l'océan, les glaciers de l'archipel ont montré une sensibilité particulière aux variations atmosphériques et océaniques depuis le dernier maximum glaciaire. Une analyse de l'étendue passée des glaciers sur l'archipel des Kerguelen (Hodgson et al., 2014) révèle que leurs positions au Petit Age Glaciaire étaient fortement avancées par rapport à leurs positions antérieures, probablement sur un grande partie de l'Holocène, mais des datations précises des moraines disponibles sur l'archipel des Kerguelen devront prochainement nous permettre de répondre à cette question. Depuis les années 60, la calotte Cook a cependant reculé de manière spectaculaire, perdant 20% de sa surface en 40 ans. L'objectif de mon travail de thèse était d'évaluer l'état actuel et futur de la calotte, et de comprendre les causes de son recul, au niveau local, mais également dans le contexte du changement climatique global. Pour ce faire, nous avons développé une approche globale s'appuyant sur un jeu de données complet mêlant observations de terrain et de satellites et modélisations à l'échelle globale et régionale.

Une analyse du retrait récent de la calotte Cook grâce à l'étude de ses variations d'albédo, d'étendue et de ligne de neige (Verfaillie et al., submitted) a tout d'abord révélé que le retrait important de la calotte au cours des dernières décennies est principalement lié à une sécheresse marquée sur l'archipel des Kerguelen depuis les années 70. La diminution des précipitations (environ 25% depuis les années 70), couplée à une légère augmentation de température atmosphérique, a engendré une disparition presque totale d'accumulation sur la calotte, limitée à présent au sommet et à certaines zones sujettes à une suraccumulation de neige liée au vent. De plus, en raison de la rétroaction importante de la disparition du couvert neigeux sur la fonte en surface au travers de la dégradation de l'albédo, l'ablation en surface a augmenté, aggravant le bilan de masse de la calotte. Les pertes d'altitude ont également amplifié l'ablation en augmentant localement les températures en surface de la calotte.

Les causes de cet assèchement observé aux îles Kerguelen ont ensuite été investiguées au travers de l'étude des variations climatiques régionales depuis les années 50 dans une large région centrée sur l'archipel (Favier et al., in review). Elle a mis en lumière le rôle de l'intensification du mode annulaire austral depuis les années 70 environ, qui a causé le déplacement vers le sud des zones dépressionnaires alimentant auparavant l'archipel des Kerguelen en précipitations.

Ce mode de variabilité atmosphérique, qui se situe actuellement dans sa phase la plus positive depuis le dernier millénaire (Abram et al., 2014), est lié principalement à la disparition de l'ozone stratosphérique et dans une moindre mesure à l'augmentation en gaz à effet de serre (Thompson et al., 2011).

En raison du caractère hémisphérique du mode annulaire austral, on s'attend à ce que d'autres régions glaciaires des zones subpolaires de l'hémisphère sud, telles que les champs de glace patagoniens, aient également été impactées par son intensification. Notre analyse combinant étude du changement climatique et du retrait glaciaire récent dans l'ensemble de la bande latitudinale 30° S - 60° S (Verfaillie et al., in prep.) montre effectivement que la Patagonie, ainsi que la Nouvelle-Zélande et sans doute la Géorgie du Sud ont été impactées par l'intensification du mode annulaire austral, avec des conséquences importantes sur le retrait glaciaire dans ces régions. Notre analyse révèle également une tendance au réchauffement océanique sur la face ouest de la péninsule antarctique et des plateformes de glace de l'Antarctique de l'ouest, sujettes à un retrait glaciaire très important lié à des changements de circulation océaniques et à l'instabilité basale des glaciers de cette région (Pritchard et al., 2012; Favier et al., 2014; Rignot et al., 2014; Scambos et al., 2014).

Au cours des siècles prochains, on s'attend à ce que le mode annulaire austral continue de s'amplifier, car l'effet bénéfique de la disparition progressive du trou d'ozone devrait être compensé par l'augmentation attendue des gaz à effet de serre (Thompson et al., 2011; Purich et al., 2013). Aux îles Kerguelen, l'atmosphère et l'océan devrait donc continuer à se réchauffer, tandis que les précipitations sur l'archipel ne devraient pas retrouver leur niveau d'avant 1960. L'accélération du retrait de la calotte Cook observé au cours des dernières décennies devrait donc se poursuivre, car la disparition presque totale d'accumulation engendre un ralentissement très marqué de la dynamique glaciaire qui ne compense plus les pertes à faible altitude. L'ablation n'est alors plus compensée, résultant en des pertes d'altitude de la surface très importantes (de l'ordre de 10 à 15 m par an), qui soumettent la surface à une ablation encore plus marquée liée à l'augmentation de la température locale. La calotte Cook est donc vouée à disparaître rapidement au cours des prochains siècles.

La régionalisation climatique mise en oeuvre grâce au modèle MAR sur la calotte Cook des îles Kerguelen (Sections 3.6 et 3.7) a confirmé la nécessité de prendre en compte l'advection d'humidité dans le modèle régional ainsi que dans le désagrégateur de précipitations. L'analyse des bilans de masse récent et futur issus de la simulation forcée par ERA-Interim a par ailleurs révélé l'impact de la sous-estimation de l'albédo de la glace dans le modèle MAR, qui induit un biais négatif sur les bilans de masse de l'ensemble des simulations réalisées. Cette étude a également mis en avant la nécessité de choisir certains modèles pour réaliser le forçage du MAR en raison de simulations coûteuses en temps de calcul. La méthode du choix de ces modèles, qui avait été préalablement validée au Groenland (Fettweis et al., 2013), ne s'est cependant pas révélée suffisante dans cette région, en raison de la forte saisonnalité des températures dans les modèles, des différences d'évolution des variables climatiques entre la surface et les couches atmosphériques au-dessus de la surface, mais surtout du choix des variables sur lesquelles se sont appuyées cette sélection des modèles-hôtes. En effet, la position de l'archipel des Kerguelen sous les zones dépressionnaires le rend extrêmement sensible au mode annulaire austral. Celui-ci résultant de différences de pression entre les moyennes et hautes latitudes sud, le meilleur moyen d'évaluer sa représentation dans les modèles-hôtes serait d'évaluer leur représentation du géopotentiel. Initialement, le vent avait été choisi pour représenter le géopotentiel, mais notre analyse révèle que ce n'est pas suffisant. Alternativement, nous proposons une méthode complémentaire, utilisant le modèle degré-jour présenté dans cette étude pour estimer le bilan

de masse récent et futur de l'ensemble des modèles CMIP5, afin d'estimer ses incertitudes liées à l'utilisation d'une moyenne multi-modèles CMIP5.

4.2 Perspectives

En premier lieu, la priorité serait d'améliorer la modélisation du bilan de masse par le modèle MAR et l'évaluation des incertitudes. Pour se faire, à court terme, nous prévoyons d'augmenter la valeur de l'albédo de la glace dans le modèle MAR afin de s'affranchir du biais sur le bilan de masse de surface lié à sa sous-estimation. Ensuite, il serait bon de réévaluer les modèles les plus adaptés au forçage du MAR sur base de l'analyse du géopotentiel, même si ACCESS1-3 a de fortes chances d'être le plus adapté car sa représentation du géopotentiel semble adaptée au vu de la qualité des vents modélisés. Il serait finalement intéressant d'estimer les incertitudes de bilan de masse lorsque l'ensemble des modèles CMIP5 est utilisé grâce au modèle degré-jour. En effet, on se rend compte que la position future de la limite entre zone d'assèchement et d'humidification dans les modèles CMIP5 varie grandement selon les modèles. L'archipel des Kerguelen est parfois situé sous les zones dépressionnaires, parfois en dehors selon le modèle utilisé. Or l'analyse récente des corrélations entre précipitations et index du mode annulaire austral révèle que la position de l'archipel par rapport aux zones dépressionnaires est crucial. L'utilisation de quelques modèles CMIP5 pour estimer le bilan de masse futur de la calotte Cook n'est donc pas suffisante, et il est nécessaire d'évaluer la gamme d'incertitudes liée à l'utilisation de l'ensemble des modèles.

En second lieu, il serait utile, afin d'estimer le bilan de masse totale (et non pas seulement le bilan de masse de surface) de la calotte, de prendre en compte la dynamique glaciaire. Dans un premier temps, nous pourrions coupler le MAR à un automate cellulaire comme nous l'avons fait avec le modèle degré-jour. Un couplage dynamique plus approfondi pourrait être envisagé avec le modèle dynamique GRISLI (Ritz et al., 2001). Cependant, GRISLI n'est pas utilisable aux îles Kerguelen, en raison de l'approximation shallow ice shelf utilisée qui n'est pas adaptée à la calotte Cook. A long terme, l'idéal serait d'utiliser le modèle ELMER-ICE (Zwinger et al., 2007), mais celui-ci nécessite une connaissance de la profondeur du lit rocheux ainsi que du frottement basal. Une campagne radar a été tentée en 2013-2014, mais la calotte comporte trop d'eau liquide en surface et sub-surface pour permettre la pénétration des ondes radar. Il faudrait alors envisager d'autres méthodes telles que les méthodes sismiques, ou utiliser un radar plus puissant. En ce qui concerne la connaissance du frottement basal, nous ne disposons pas actuellement de vitesses de surface distribuées permettant la réalisation de méthodes inverses pour déterminer le frottement basal. La réalisation et la corrélation d'images de surface devrait être mises en place pour pouvoir déterminer ces vitesses de surface distribuées.

En troisième lieu, il serait intéressant d'utiliser le modèle degré-jour, qui s'est montré utile sur la période récente, pour des applications paléoglaciologiques. En effet, des datations des paléo-stades du glacier Gentil aux îles Kerguelen à l'aide de datations cosmogéniques (Jomelli et al., 2014) sont actuellement en cours d'analyse. A partir de ces datations, le modèle degré-jour devrait permettre de déterminer les conditions climatiques (de température et précipitations) ayant conduit aux retraits et avancées glaciaires (e.g., Blard et al. (2007); Jomelli et al. (2011)). Cela permettrait en particulier d'étudier l'influence du mode annulaire austral sur les températures et précipitations au cours de l'Holocène, voire depuis le dernier maximum glaciaire.

En dernier lieu, en ce qui concerne les outils de régionalisation utilisés, nous avons montré dans cette étude que SMHiL n'est pas performant aux îles Kerguelen dans sa version actuelle.

Pour le moment, il est plutôt recommandé d'utiliser les modèles régionaux tels que le MAR, RACMO2 (Ettema et al., 2009; Lenaerts et al., 2010) ou WRF (Michalakes et al., 1998), couplés à une estimation des incertitudes de bilan de masse futurs, telle que la méthode utilisant le modèle degré-jour que nous proposons ci-dessus. Cependant, pour l'analyse d'objets plus grands tels que la péninsule antarctique ou les champs de glace patagoniens, une désagrégation grâce à SMHiL serait utile, et l'introduction d'un schéma d'advection de l'humidité dans le désagrégateur est cruciale. L'étude du lien entre le mode annulaire austral et la circulation atmosphérique et océanique en Patagonie ou en péninsule antarctique serait intéressante à mettre en oeuvre. Par exemple, de nombreuses études sur le mode annulaire austral montrent que son intensification devrait conduire à une intensification des vents d'ouest (Yin, 2005; Sallée et al., 2008; Thompson et al., 2011), en raison de la différence de pression plus marquée entre les moyennes et hautes latitudes sud. Ce processus a été peu étudié dans le cadre de cette thèse. Pourtant, il serait intéressant de l'étudier plus en détail, car il pourrait se traduire par un gradient de précipitations plus marqué entre la face ouest et la face est des glaciers de la péninsule (Pettit et al., 2014). Il est important de remarquer que ce processus pourrait aussi avoir un impact sur les glaciers et calottes patagoniens (Garreaud et al., 2013), pour autant que ceux-ci soient encore sous l'influence des zones dépressionnaires associées aux vents d'ouest. Le devenir des grandes plateformes et glaciers côtiers d'Antarctique pourrait également être investigué, au travers de l'étude des liens entre l'intensification du mode annulaire austral, le réchauffement possible des océans dans cette région et d'éventuels changements atmosphériques. En effet, ces processus ont certainement accéléré les pertes des glaciers côtiers (Pritchard et al., 2012; Favier et al., 2014; Rignot et al., 2014; Scambos et al., 2014), la fonte de surface ayant aussi probablement favorisé les processus de fracturation hydraulique précurseurs de la désintégration des plateformes (Kuipers Munneke et al., 2014). Finalement, l'impact possible du mode annulaire austral sur la banquise mériterait également d'être étudié. Quelques études ont été menées à ce jour montrant l'impact du mode annulaire austral sur l'environnement, et l'influence majeure que cette résultante indirecte des effets anthropiques a sur l'atmosphère. Le recul très marqué aux îles Kerguelen rappelle que ces effets climatiques a priori inattendus et mal connus sous nos latitudes sont en fait de tout premier ordre et méritent plus ample attention.

Remerciements

Une thèse de doctorat, ça ne se réalise pas toute seule ! J'aimerais remercier l'ensemble des personnes qui m'ont soutenue au cours de ces trois années de thèse, que ce soit au laboratoire, sur le terrain, ou en dehors du cadre de travail.

Tout d'abord, je voudrais remercier les deux rapporteurs de ma thèse, Michiel van den Broeke et Pierre Ribstein, d'avoir accepté de lire et d'évaluer ce manuscrit. Merci également par avance aux examinatrices Sandrine Anquetin, Masa Kageyama et Françoise Vimeux pour l'analyse critique et les nombreux conseils qu'elles pourront m'apporter lors de ma soutenance de thèse.

Je tiens ensuite à remercier mes co-directeurs de thèse, Hubert et Vincent, pour leur soutien tout au long de cette thèse. Ils ont toujours été présents pour m'épauler lorsque j'ai eu besoin d'aide, et les discussions scientifiques (mais également informelles !) que nous avons eu ont été extrêmement enrichissantes.

Un grand merci également à Xavier Fettweis et à Cécile Agosta, de l'Université de Liège, pour leur aide précieuse concernant le modèle MAR. Les innombrables emails que je leur ai envoyés ont toujours trouvé réponse très rapidement, et les deux séjours que j'ai effectués dans leur laboratoire m'ont réellement permis de prendre en main le modèle de manière efficace. Je voudrais également remercier les co-auteurs des articles auxquels j'ai participé, ainsi que les programmes IPEV-1048 GLACIOCLIM-KESAACO and LEFE-INSU KCRuMBLE ayant financé nos travaux de recherche et missions de terrain.

Merci par ailleurs à ceux qui m'ont accompagnée sur l'archipel des Kerguelen au cours des campagnes 2011-2012 et 2012-2013 : Vincent (Jomelli) et Adri, et Vincent (Favier) et Daniel ainsi que Sylvia, Matthieu, Franck et Paul, qui nous ont épaulés lors de mon deuxième séjour sur le glacier Ampère. Merci également aux courageux de la campagne 2010-2011 et 2013-2014, pour leurs nombreuses observations et résultats. Je tiens aussi à remercier l'équipe logistique de l'IPEV présente à Ker durant les campagnes (Yann, Nina, Romu, Flo, Bapt', Nico, ...) ainsi que tous les hivernants et campagnards d'été que j'ai côtoyés sur place et qui m'ont accompagnée durant mes missions de terrain aux quatre coins de l'archipel.

Je voudrais également remercier l'ensemble du personnel du LGGE, mes amis doctorants, post-docs, CDDs qui m'ont accompagnés depuis le master 2. Pour finir, merci à Arsène et à ma famille pour leur soutien sans faille au cours de ces trois années passionnantes.

Annexe A

Article Verfaillie et al. (2012)

The Cryosphere, 6, 1345–1358, 2012
www.the-cryosphere.net/6/1345/2012/
doi:10.5194/tc-6-1345-2012

The Cryosphere

Snow accumulation variability derived from radar and firn core data along a 600 km transect in Adelie Land, East Antarctic plateau

D. Verfaillie, M. Fily, E. Le Meur, O. Magand, B. Jourdain, L. Arnaud, and V. Favier

Laboratoire de Glaciologie et Géophysique de l'Environnement, UMR5183, Saint-Martin-d'Hères, France

Correspondence to: D. Verfaillie (dverfaillie@lgge.obs.ujf-grenoble.fr)

Received: 12 June 2012 – Published in The Cryosphere Discuss.: 24 July 2012
Revised: 25 October 2012 – Accepted: 26 October 2012 – Published: 16 November 2012

Abstract. The mass balance of ice sheets is an intensively studied topic in the context of global change and sea-level rise. However – particularly in Antarctica – obtaining mass balance estimates remains difficult due to various logistical problems. In the framework of the TASTE-IDEA (Trans-Antarctic Scientific Traverses Expeditions – Ice Divide of East Antarctica) program, an International Polar Year project, continuous ground penetrating radar (GPR) measurements were carried out during a traverse in Adelie Land (East Antarctica) during the 2008–2009 austral summer between the Italian–French Dome C (DC) polar plateau site and French Dumont D'Urville (DdU) coastal station. The aim of this study was to process and interpret GPR data in terms of snow accumulation, to analyse its spatial and temporal variability and compare it with historical data and modelling. The focus was on the last 300 yr, from the pre-industrial period to recent times. Beta-radioactivity counting and gamma spectrometry were applied to cores at the LGGE laboratory, providing a depth–age calibration for radar measurements. Over the 600 km of usable GPR data, depth and snow accumulation were determined with the help of three distinct layers visible on the radargrams ($\approx$1730, 1799 and 1941 AD). Preliminary results reveal a gradual increase in accumulation towards the coast (from ≈ 3 cm w.e. a^{-1} at Dome C to ≈ 17 cm w.e. a^{-1} at the end of the transect) and previously undocumented undulating structures between 300 and 600 km from DC. Results agree fairly well with data from previous studies and modelling. Drawing final conclusions on temporal variations is difficult because of the margin of error introduced by density estimation. This study should have various applications, including model validation.

1 Introduction

Polar regions play a significant role in the climate system. Large ice sheets located over Greenland and Antarctica influence the water cycle and thermohaline circulation through the capture or release of freshwater. These regions also are crucial for Earth radiation budget due to high snow and ice albedos. Hence, in the context of global climate change (Solomon et al., 2007), particular attention is being paid to the mass balance of Polar ice sheets.

In order to predict the behaviour of ice sheets under future climate conditions (i.e. their contribution to future sea-level rise), it is necessary (1) to assess their past and current state and (2) to understand the physical processes linking climate to the ice sheet mass balance. To this end, ice cores provide precious information on quaternary climate and atmospheric composition. However, obtaining the accurate Antarctic mass balance remains difficult, but can mainly be achieved through field measurements, which are generally interpolated by the use of remote sensing data. The resulting SMB maps are used to validate model outputs. Mass balance is the algebraic sum of two terms: the accumulation of snow on the surface of the ice sheet (through precipitation, hoar formation and wind deposition), which can be complemented by some refreezing at its base; and its ablation (through sublimation, surface and basal melting, wind scouring and iceberg calving). Surface mass balance (SMB) only refers to processes occurring at the surface of the ice sheet.

However, in Antarctica SMB remains poorly known. Its high variability and the shortness of the studied time periods make the observation of SMB trends difficult. Trends often appear inexistent, which seems to be the case for example in the coastal part of Adelie Land (Agosta et al., 2011). Another

example is the slight increase in surface elevation that has been observed in the interior of the continent, suggesting a recent gain in mass (e.g. Helsen et al., 2008), whereas precipitation appears not to have undergone any significant change since the 1950s (Monaghan et al., 2006a). This contradiction highlights the uncertainty of SMB measurements and interpretations, which result in a high level of incertitude concerning the future contribution of Antarctic SMB to sea level rise (Meehl et al., 2007).

Various ground-based techniques are used to determine SMB in Antarctica, such as stake farms or lines, ultrasonic sensors, snow pits and firn/ice cores (Eisen et al., 2008). Density is an important parameter which has to be known accurately, as well as the depth vs. age relationship. The latter can be determined by layer counting, radiochronology (decay of natural radioactive isotopes such as ^{210}Pb) or the determination of reference horizons (volcanic layers or radioactive horizons resulting from the atmospheric nuclear weapon tests carried out between the 1950s and the 1980s) (Eisen et al., 2008; Magand, 2009).

However, all these methods yield localised data and thus suffer from poor spatial representativeness. On the other hand, ground penetrating radar (GPR), offers the possibility to determine accumulation continuously over several hundreds of kilometres. GPR has been used previously in specific areas in East Antarctica, among others in Dronning Maud Land (e.g. Richardson et al., 1997; Richardson and Holmlund, 1999), along the Norwegian–US scientific traverse (Muller et al., 2010), or close to South Pole Station (Arcone et al., 2005a), providing precious information on snow accumulation in these areas. It is thus a powerful tool to assess its spatial (and temporal) variability and can be used to link firn/ice cores and stakes SMB measurements. However, such GPR studies are sparse and large regions in East Antarctica – especially in the interior of the continent – remain uncovered.

The aim of the present study was thus to improve our knowledge of East-Antarctic SMB by analysing new data (radar and firn cores) obtained along a transect between the Italian–French Concordia Dome C polar station (DC) and the French Dumont-Durville station (DdU) (Fig. 1). This round-trip traverse was made from 20 January to 10 February 2009 as part of the ANR-VANISH (Vulnerability of the ANtarctic Ice-SHeet) and IPEV-TASTE-IDEA (Trans-Antarctic Scientific Traverses Expeditions – Ice Divide of East Antarctica) scientific programs. During this traverse, (nearly) continuous radar measurements were made and 6 firn cores (16.5 to 21 m deep) were drilled (Fig. 1). Beta-radioactivity measurements and gamma spectrometry analysis of the cores at LGGE laboratory (Laboratoire de Glaciologie et Géophysique de l'Environnement) provided a depth–age calibration for radar measurements.

This transect is among the most documented ones in East Antarctica and has been followed regularly and studied since the 1970s (see for example the works of Pourchet et al., 1983;

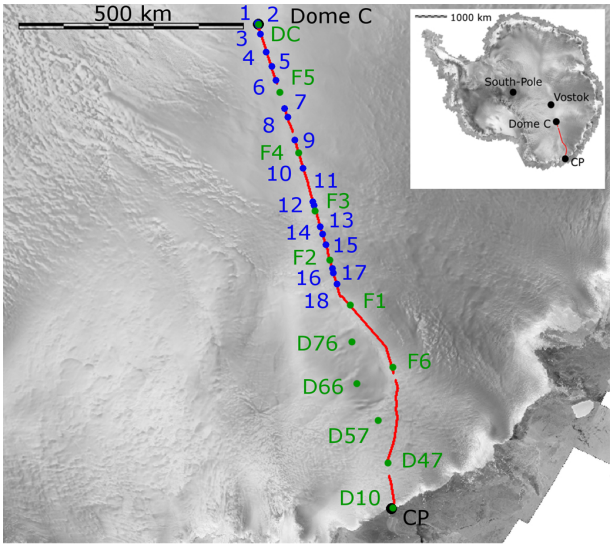

Fig. 1. Map of Antarctica showing the location of the radar section analysed (numbered 1 to 18, in blue) and cores (in green). Each blue number corresponds to the beginning of a radargram. A general map of Antarctica is inserted in the top right corner to show the location of the main scientific stations on the Antarctic plateau and East Antarctica, as well as the transect between DC and Dumont-d'Urville (Cap Prud'Homme is indicated on the map instead of Dumont-d'Urville, the latter being located on an island 5 km offshore).

Pettré et al., 1986). However, the data in this region are not evenly distributed. SMB measurements have been carried out regularly in the coastal area since 2004 (Genthon et al., 2007; Agosta et al., 2011; Favier et al., 2011). Other studies focused on the DC sector (Petit et al., 1982; Urbini et al., 2008). Frezzotti et al. (2004, 2005) used snow radar as well as stake farms, ice cores, surface morphology and remote sensing to estimate spatial and temporal variability of the SMB along a transect from Terra Nova Bay to DC, and from D66 to Talos Dome (Magand et al., 2004). However, SMB measurements between DC and the coast are sparse and no SMB radar measurements had ever been made along the DC-DdU traverse.

In the current study, the radar data was processed and interpreted in terms of SMB to analyse its spatial and temporal variability along the DC-DdU traverse. Results were compared with historical data in the region (Pettré et al., 1986; Mulvaney and Wolff, 1994; Pourchet et al., 2003; Frezzotti et al., 2004; Urbini et al., 2008) and to four SMB climatologies (Arthern et al., 2006; van de Berg et al., 2006, ERA-Interim and LMDZ4). We focused on the pre-industrial to the industrial period, which spans the last 300 yr (approximately the top 70 m of snow, or the first 750 ns of the radargrams).

Section 2 deals with the available radar and firn core data and the various methods used in this study. The results are subsequently displayed in Sect. 3, and discussed in Sect. 4.

2 Data and methods

2.1 Radar

Ground penetrating radar (GPR), also referred to as ice-penetrating radar, snow radar or radio echo sounding, is widely used in different fields, including engineering, archeology, seismic exploration, glaciology. It is used for mapping the internal structures of a substrate, or locating objects in cases of archeology and construction engineering (Daniels, 2000; Eisen et al., 2008). The main advantage of this method is that it provides a continuous measurement, in contrast with other widely used glaciological SMB measurements such as stakes or firn/ice cores. However, the main problem of GPR is that – unlike stake measurements, for example – it is an indirect measurement of SMB, and thus requires an interpretation which could lead to errors. Difficulties in signal processing or in signal interpretation and picking of the reflectors are the main possible sources of error.

A transmitter and receiver antenna, separated by a constant distance (common offset), are trailed behind the vehicle along the survey transect. It is usually combined with GPS measurements to obtain the geographical position. At fixed time intervals (in our case every second), the transmitting antenna emits an electromagnetic pulse, which penetrates the snow. When the electromagnetic wave reaches a layer with a different complex dielectric constant ϵ^*, it is partly reflected. This reflected signal is then received by the second antenna at the surface, and the two-way travel time (TWT) of the signal (from the surface to the interface and back) is recorded (Eisen et al., 2008). Several authors have investigated the origin of reflections in firn (e.g. Hempel et al., 2000; Eisen et al., 2003a,b; Kohler et al., 2003; Arcone et al., 2005b), but it is still unclear how continuous reflecting horizons are produced in firn and ice. In particular, "there remains some uncertainty about how the material properties in firn combine to form the continuous reflecting horizons" (Eisen et al., 2008). However, reflecting horizons have been shown by different authors and methods to be isochronous (Eisen et al., 2008 and references therein).

During the traverse, a MalåRTA (Rough Terrain Antenna) 100 MHz-frequency emitting antenna was used, with a common offset of 2 m. This frequency is a good compromise between the ideal resolution of reflecting horizons and the desired penetration depth in the firn (here at least 100 m).

The GPR produces radargrams, which are a representation of all the traces recorded along a section, with the horizontal axis representing the horizontal position and the vertical axis the two-way travel time (TWT) of the wave. Radargrams were processed with a dedicated software called ReflexW™. Time cut, time zero correction and signal processing (gain and filters) were carried out.

Unfortunately, the quality of the radar measurements declined from 7 to 9 February 2009, probably due to a deterioration of the antenna. On 10 February, the antenna was replaced and the resulting radargrams again became visible. But the reflectors could not be followed across this blind passage, meaning the radargrams from 7 February to the end of the transect were unusable. Consequently, we decided to analyse the profiles by starting from DC and continuing on as far as possible (i.e. until 6 February, 01:07 UTC). Table 1 summarises the radar data and Fig. 1 shows the radar section analysed.

Several steps are necessary to obtain accumulation values from a radargram:

1. The radargram requires processing to enhance the visibility of the reflecting horizons and two corrections (time zero and geometrical corrections) have to be made.
2. The vertical scale of the radargram has to be converted from time (TWT) to depth (see Sect. 2.4.2).
3. Several visible reflectors along the profile have to be selected as close as possible to dated layers of interest (i.e. volcanic or radioactive layers, see Sect. 2.3).
4. These reflectors have to be dated from firn core interpretation.
5. The snow thickness between two isochrones (or between one and the surface) has to be transformed in water equivalent depth and the latter divided by the time interval between the two isochrones (or the isochrone and the surface), as explained in Sect. 2.4.3.

A yearly averaged snow accumulation value is thus obtained.

The radar vertical resolution is given by the worst value calculated from two criteria. The first is the Rayleigh criterion (Eisen et al., 2008), which gives the resolution as one fourth of the nominal wavelength (0.75 m with a 100 MHz antenna). The second is the Ricker criterion (Eisen et al., 2008), mainly depending on the pulse length. The latter has been inferred from a later CMP measurement, and appears to be around 12 ns, which, given a velocity in the firn of $\approx 0.2\,\mathrm{m\,ns^{-1}}$, finally yields an actual resolution of 1.2 m. This means that we were able to distinguish two reflectors if they were separated by a distance of at least 1.2 m.

2.2 Firn cores

Six firn cores were drilled along the transect to calibrate radar measurements with a depth–age relationship at specific points. This depth vs. age relationship is obtained by beta radioactivity measurements to detect the radioactive layers of 1955 ± 1 and 1965 ± 1 corresponding to the fallout of the atmospheric nuclear weapon tests carried out in the 1950s and 1960s (Magand, 2009). Additional deeper core data (D47 and DC) were also used for density analysis (described below in Sect. 2.4.2). Table 2 summarises the main core characteristics and the depth of the radioactive layers.

Table 1. Summary of the radar data from DC to the coast. Gaps in the data are due to technical problems encountered during the transect. The fact that data starting at 597 km from DC is unusable was due to a deterioration of the antenna, as explained in the text. See Fig. 1 for explanation of the numbering of the profiles.

Distance from DC	Date and time interval (UTC)	Comments
0 to 138 km	2009/02/02 22:58–2009/02/02 23:26	radargrams 1–6
138 to 194 km	2009/02/02 23:26–2009/02/03 05:09	no data
194 to 250 km	2009/02/03 05:09–2009/02/03 09:00	radargrams 7–8
250 to 270 km	2009/02/03 09:00–2009/02/03 22:35	no data
270 to 597 km	2009/02/03 22:35–2009/02/06 01:07	radargrams 9–17
597 to 1100 km	2009/02/06 01:07–2009/02/10 11:37	data unusable

Table 2. Firn and ice cores used in this study: name, drilling year, coordinates, altitude in m above sea level (a.s.l.), distance from DC station, total drilling depth, depth of 1955 and 1965 radioactive layers in 2009. DC data is a compilation of different datasets. The 1955 and 1965 depths at DC are based on the 2004 EPICA Dome C core depths. Corresponding depths in 2009 were estimated using stake measurements from GLACIOCLIM-SAMBA observatory, as explained in Sect. 2.5.

Name	Year	Coordinates		Altitude	Distance from DC	Total depth	1955 depth	1965 depth
		(lat. S)	(long. E)	(m a.s.l.)	(km)	(m)	(m)	(m)
D47	1987–1989	67°23′00	138°43′00	1548	999	897	–	–
F6	2008–2009	68°44′70	134°54′53	2430	788	21	–	18–18.5
F1	2008–2009	70°08′32	134°08′01	2630	650	20.4	–	18–18.5
F2	2008–2009	71°02′50	133°01′17	2830	551	19.38	14–14.5	12–12.5
F3	2008–2009	71°56′13	131°17′42	3030	433	18.35	–	7.5–8
F4	2008–2009	72°54′17	129°10′17	3178	304	10	7–7.2	6–6.2
F5	2008–2009	73°58′27	126°34′51	3204	164	10.1	6.1–6.2	5–5.2
DC	1999–2008	75°06′00	123°21′00	3233	0	–	5.0	4.4

2.3 Selecting reflectors

Three visible reflecting horizons were selected for each profile (labeled R1 to R3). Each one was manually selected and tracked along the first profile (starting from DC) and from one profile to the next. It was possible to merge two consecutive radargrams to ensure the continuity of a reflector from one profile to the next. Depths were then calculated from the TWT, as explained below in Sect. 2.4.2. The selected reflectors are shown in Fig. 2.

Tracking the reflectors was possible until the end of radargram 17, approximately 600 km from DC (as explained above). However, tracking of reflectors R2 and R3 turned out to be difficult at the end of radargram 12 ($\sim$ 465 km from DC) due to very bad visibility of the radargram occurring there, and additional signal processing was applied to this radargram (dilatation and deconvolution filters) to enhance visibility. Hence, by using a deeper reflector visible before and after the blind gap as a marker, we were able to track these two horizons at the end of the profile. Nevertheless, R2 and R3 depths (and consequently accumulation) located at a distance of more than 470 km from DC remain uncertain.

2.4 Density

2.4.1 Density estimates

Density influences both the wave propagation speed in the snow and thus the conversion from TWT to depth (Sect. 2.4.2) and the final accumulation (Sect. 2.4.3). Although the influence of density on depth estimates is moderate, its impact on accumulation is more drastic. Depths of our reflectors go down to 70 m. As a result, we needed to estimate density beyond maximum depths of cores F2 to F4 (10 to 20 m). To estimate density as a function of depth and distance from DC, we thus chose to make use of two deep cores drilled at DC and D47 (Table 2). DC and D47 density measurements were fitted (third order polynomial fit) and density at each point along the transect was interpolated as a function of distance between the two sites concerned.

Figure 3 shows computed and measured density at DC, D47 and F2 to F4. Our method of fitting does not allow us to reproduce exactly the density values measured close to the surface due to extreme density variability in the top layers of snow. However, fitted values remained close to measured values in the top layers of snow (inside the measurements error bars), and reproduce measured values beyond a depth of 4 to 5 m well.

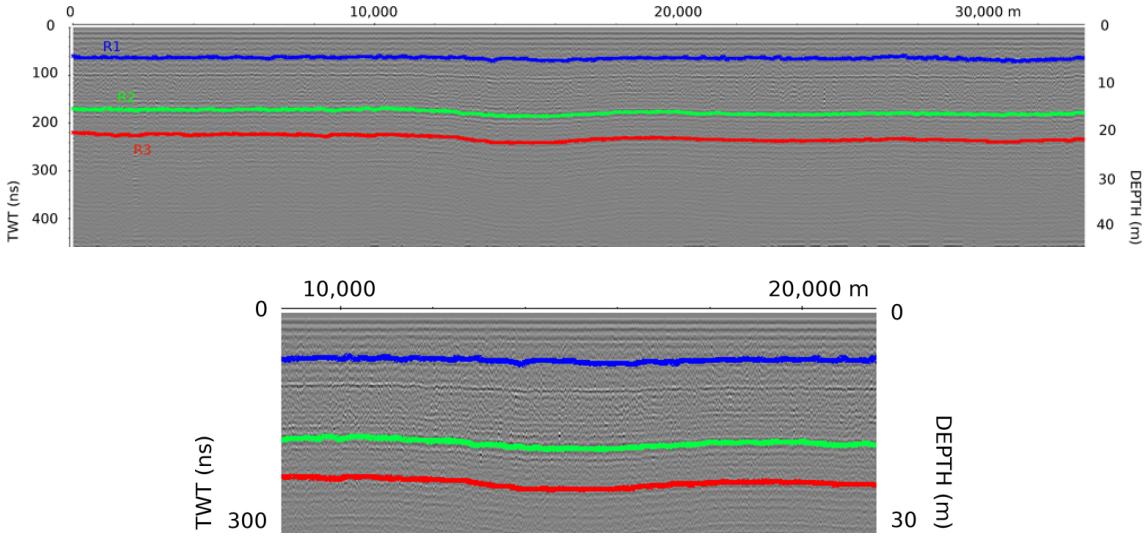

Fig. 2. Selected reflectors labeled R1 to R3 shown on radargram 5. Distance is in metres. The lower panel gives a detail of the reflectors in the middle of the radargram.

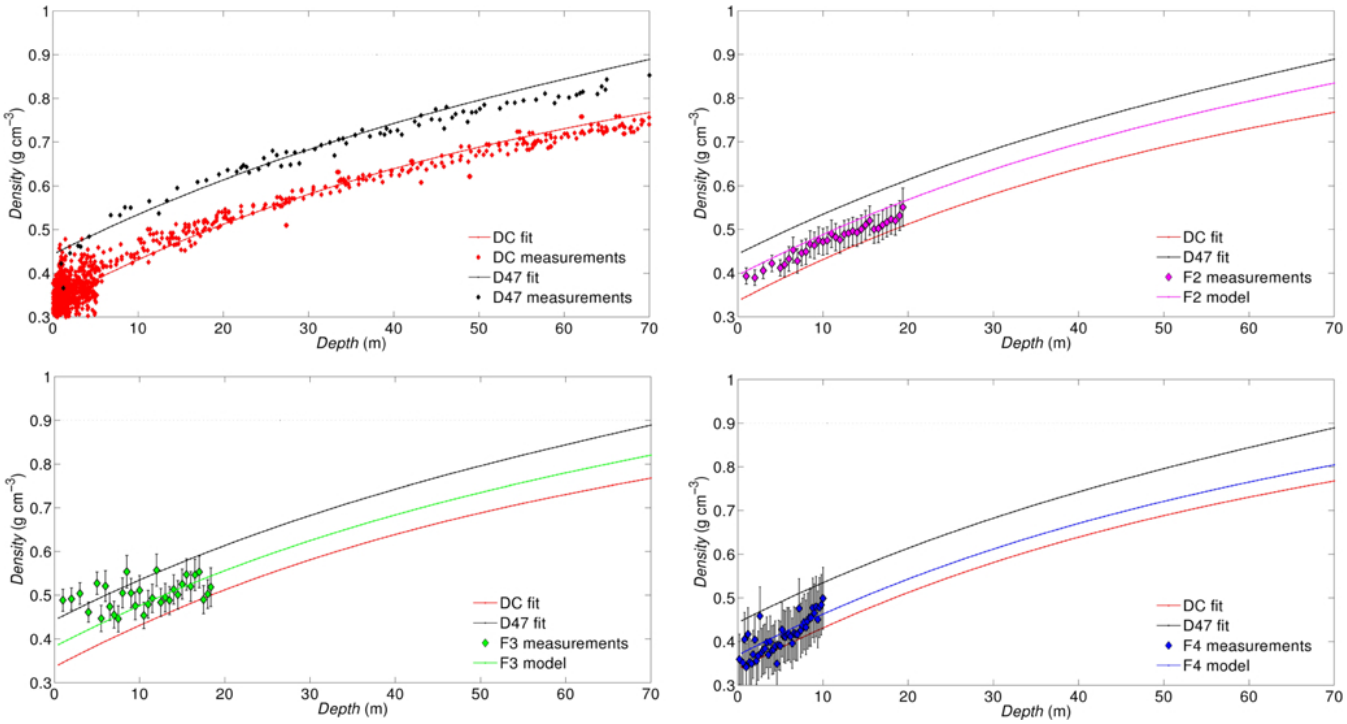

Fig. 3. Density as a function of depth. Density measurements up to 70 m in depth and their fits are represented at DC and D47 (top left panel). Measured and computed density at F2 (top right), F3 (lower left) and F4 (lower right) are also displayed. Error bars for DC and D47 measurements are not represented for reasons of clarity, but are of the same order of magnitude as for shallower cores F2 to F4 ($\sim 10\,\%$ error).

2.4.2 From density to wave speed and resulting conversion from TWT to depth

In order to convert TWT into depth, the knowledge of the radar wave speed is necessary. The latter is mainly controlled by snow density.

The electromagnetic wave propagation in a media is described as

$$c = c_v/\sqrt{\epsilon^*}, \quad (1)$$

where c is wave speed in the media, c_v is wave speed in the vacuum ($= 0.3\,\mathrm{m\,ns^{-1}}$) and ϵ^* is complex media dielectric

constant. The latter is defined by

$$\epsilon^* = \epsilon' - i\epsilon'', \tag{2}$$

where ϵ' is the real part, called complex permittivity, which is mainly influenced by density, and ϵ'' is the imaginary part, which is mainly controlled by conductivity (Eisen et al., 2008). The imaginary part of the dielectric constant is mainly affected by the presence of liquid water (Urbini et al., 2001) and by snow chemistry. Hence, in our study, this term can be left out because the Antarctic plateau is considered to be dry and "clean". Thus, in this case

$$\epsilon^* = \epsilon' \tag{3}$$

and, by combining Eqs. (1) and (3), we obtain

$$c = c_v/\sqrt{\epsilon'}. \tag{4}$$

Kovacs et al. (1995) proposed the following empirical approximation based on the comparison of permittivity and density measurements:

$$\epsilon' = (1 + 0.845 \times \rho)^2. \tag{5}$$

Finally, by introducing Eq. (5) into Eq. (4), we obtain the following expression:

$$c = \frac{c_v}{1 + 0.845 \times \rho}. \tag{6}$$

The latter expression was then used to determine wave speed vs. depth at the cores on the basis of density. Wave speed was then used to transform TWT into depth. A geometrical correction was necessary in the upper part of the profile to account for the fact that the emitter and receiver antennas were separated by a common-offset of 2 m.

Different sources of error can affect depth estimates, mainly wave speed estimates (density uncertainties, firn depth correction), time-zero correction and selection of the reflectors. Considering these error sources, we estimated a depth uncertainty of about 1 m.

2.4.3 From density to accumulation

Density values were used to transform accumulation in centimetres of snow into accumulation in cm water equivalent (w.e.) as follows:

$$a = \int_{z_{n-1}}^{z_n} \frac{s \times \rho(z)}{z_n - z_{n-1}} \mathrm{d}z \tag{7}$$

where n is the number of the reflector concerned R, z is depth, s is accumulation in cm of snow, a is accumulation in cm w.e., and ρ is density.

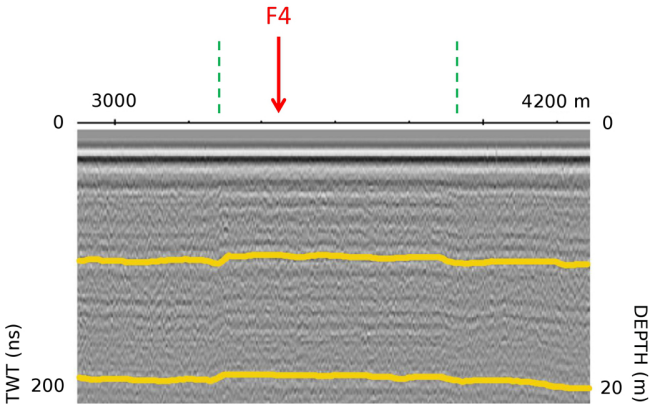

Fig. 4. Transition between the "real" and "natural" snow surface visible on radargram 9 in the vicinity of core F4. The first dotted line corresponds to the point where the radar vehicle left the transect route and the second one to the point where it got back on the route.

2.5 Dating reflectors

Dating of the selected reflectors by direct interpolation between two layers of known age at DC was not possible. Indeed, the snow surface in the vicinity of the station as well as on the transect route is constantly modified by the passage of vehicles and maintenance work, and so the "real" surface does not correspond to what would have been the "natural" undisturbed surface in 2009. Depths measured using radar thus refer to the disturbed real surface and not to the natural one, hence preventing the simple dating of the reflectors. The surface was intact only in the vicinity of firn core sites and, as the radar vehicle had to leave the transect route to get close to those sites, the surface displayed on the radargrams is natural for only a short distance. This is clearly visible on the radargram close to the F4 firn core (Fig. 4). Consequently, to date the reflectors, we had to use in a complementary way the F4 site where the surface was natural and the DC core where some layers are well dated.

At DC, as explained above, the absolute depths of the selected reflectors are not correct but the depth intervals between reflectors (R1–R2 and R2–R3) make sense. Besides, well dated volcanic layers (Table 3) in the 2004 EPICA Dome C ice core provide a depth–age scale at DC. Depths were determined for 2004, the year the EPICA ice core was drilled. Then data from GLACIOCLIM-SAMBA observatory stakes measurements[1] at DC were used to account for the 43 cm of snow that accumulated between 2004 and 2009. Knowing the depth–age relationship at DC (Fig. 5), it was possible to calculate the age interval between the reflectors. As the curve is non-linear, the uncertainty in the absolute depths led to uncertainty in the age interval but the error was only small, i.e. an error of 1 m in the location of the reflectors led to a 3 % difference in the age intervals. We then obtained

[1] Website: http://www-lgge.ujf-grenoble.fr/ServiceObs/SiteWebAntarc/dc.php

Table 3. Characteristic volcanic layers in the EPICA Dome C core: name, age, depth at DC in 2004 (adapted from Castellano et al., 2005) and estimated depth at DC in 2009 (for an undisturbed surface).

Name of layer	Age	Depth at DC in 2004 (m)	Estim. depth at DC in 2009 (m)
Agung	1964 ± 1	3.9	4.4
Tambora	1816 ± 4	12.5	12.9
Jorullo-Taal	1758 ± 6	15.36	15.8
Serua	1696 ± 4	18.62	19.05

a time interval of 142 ± 4 yr between reflectors R1 and R2, and of 69 ± 2 yr between R2 and R3.

At F4, a 10 m core was drilled, and the 1955 and 1965 radioactive horizons were identified. The density profile was measured and the 2009–1955 snow accumulation then computed (Table 4). The R1, R2 and R3 depths were obtained from radargrams and the R1–R2 and R2–R3 snow accumulation rate in cm a^{-1} (Table 4) was calculated.

The 1955–R1 snow accumulation rate at F4 was not known a priori, but was interpolated between the 1955–2009 (15.0 cm snow a^{-1}) and the R1–R2 (11.7 cm snow a^{-1}) rates, which makes sense because the values are relatively close. From this snow accumulation rate, we obtained the R1-1955 time interval and, finally, the age of the R1, R2, R3 layers, respectively 1941 ± 1, 1799 ± 5 and 1730 ± 7 AD.

3 Results

3.1 Undulating structures

The East Antarctic plateau is usually considered to be flat up to the break in slope, which, in the study's area, is located $\sim$230 km from the coast (i.e. 870 km from DC), and accumulation is assumed almost uniform up to that point (Pettré et al., 1986). However, GPS data (Fig. 6) revealed that there is a first change in slope around 300 km from DC. Radargrams then showed some undulating structures located between 300 and 600 km from DC (Fig. 7). In the middle of the plateau, 10 km wavelength undulations appeared with vertical amplitudes ranging from 5 to 20 m (Fig. 7), which seemed to be amplified with depth. These structures are also visible in Fig. 6, which illustrates changes in the surface elevation and in depth of the reflectors with increasing distance from DC.

3.2 Snow accumulation

Snow accumulation between DC and a point at 600 km from DC was plotted against core data and accumulation values from previous studies (Fig. 8) and model results (Fig. 9). Only our 1730–1799 and 1799–1941 values are shown, along

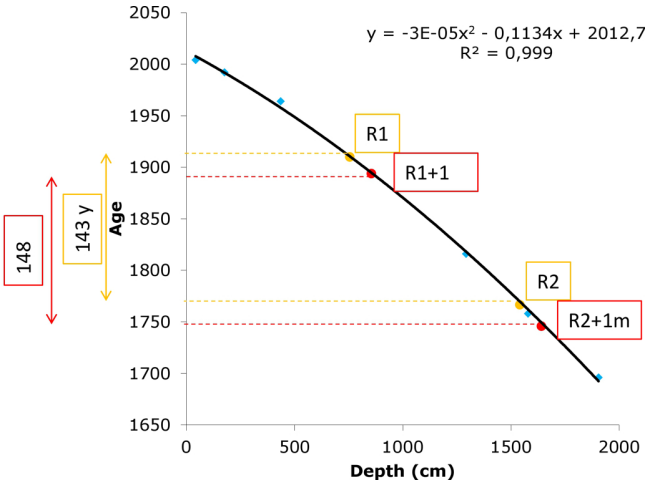

Fig. 5. 2009 Depth–age relationship at DC (black curve) based on dating of EPICA Dome C volcanic layers (blue dots). The age interval between reflectors R1 and R2 is shown, as well as the age interval between those two reflectors if a 1 m-shift in depth is applied.

with core values for the period 1965–2009. Radar values for 1941–2009 were left out because the surface of the transect route is no longer "natural" (Sect. 2.5), leading to a greater margin of error for reflectors close to the surface. For example, on the transect route close to core F4, a surface-induced accumulation error of $\sim +11$ % was estimated for the period 1941–2009, while the error was less than +5 % and +3 % for 1799–1941 and 1730–1799 periods, respectively. We consequently decided not to take the 1941–2009 accumulation values into consideration.

It should be noted that the accumulation ratio (in cm of snow, not shown) between 1965–2009 core estimates and 1730–1799 or 1799–1941 radar estimates was almost the same from DC to around 450 km from DC, but was greater at F2. For example, calculating the ratio $(a_1 - a_3)/a_1$ between 1965–2009 (a_1) and 1730–1799 (a_3) time periods yielded values of 0.22 to 0.27 for DC to F3, while the F2 value was 0.36. This could indicate an error in the selection of the reflectors at distances of more than 470 km from DC, as explained in Sect. 2.3. Accumulation estimates beyond this point should thus be considered with caution.

Accumulation data were compared to four SMB climatologies (Fig. 9):

– We first compared our results to those of Arthern et al. (2006) and van de Berg et al. (2006), which are currently assumed to be among the most reliable estimates of broad-scale patterns of SMB across Antarctica. The results of Arthern et al. (2006) were obtained by continuous-part universal kriging of SMB field measurements over the period 1950–1990 (Vaughan and Russell, 1997) with a background model based on passive microwaves data, whereas the SMB values of

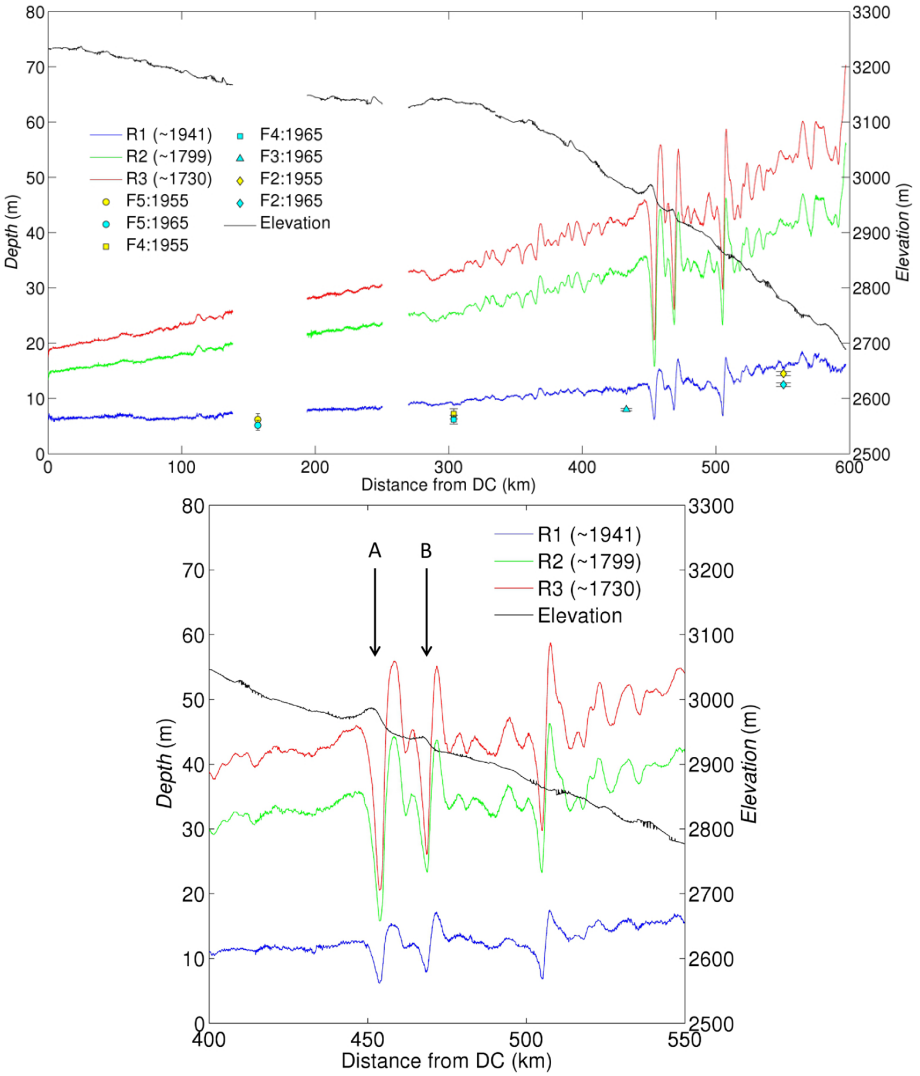

Fig. 6. Depth of reflectors and surface elevation vs. distance from DC. Couloured symbols represent depths of the 1955 and 1965 layers measured on the cores for the purpose of comparison, and their associated error bars. The lower panel focuses on undulations located between 400 and 550 km from DC, with A and B refering to two local elevation peaks that link with undulations, as discussed in the text.

Table 4. Summary of the parameters which were measured or computed at F4 to calculate ages, and ensuing computed age for each reflector.

Layers	Intervals	Measured depth (cm)	Depth interval (cm)	Snow accu (cm a^{-1})	Time interval (yr)	Computed age
	1955–2009		700–720	15.00 (measured)	54	
1955		700–720				
	R1–1955		173–193	13.33 (interpolated)	14 ± 1 (computed)	
R1		893				1941 ± 1
	R1–R2		1655	11.65 (measured)	142 ± 4 (from DC core)	
R2		2548				1799 ± 5
	R2–R3		746	10.82 (measured)	69 ± 2 (from DC core)	
R3		3294				1730 ± 7

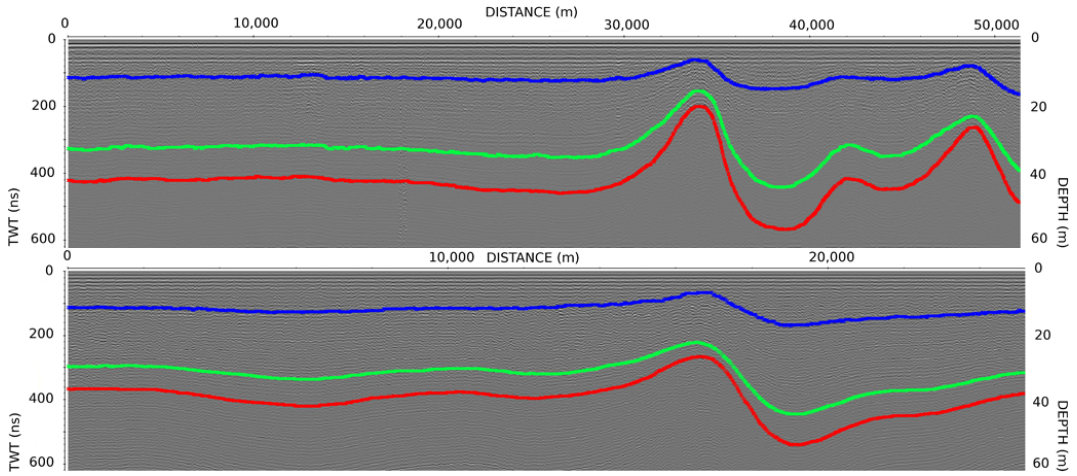

Fig. 7. Undulating structures visible on radargram 12 (4 February, 22:35 UTC to 5 February, 02:09 UTC, between 450 and 470 km from DC) and radargram 14 (5 February, 04:41 UTC to 06:39 UTC, between 495 and 510 km from DC).

van de Berg et al. (2006) were the results of the Regional Atmospheric Climate Model v.2 (RACMO2), which were calibrated with SMB field observations from the database of Vaughan and Russell (1997). In the latter model, RACMO2 was run at a resolution of 55 km without snowdrift with lateral boundary conditions from ERA-40 (Uppala et al., 2005) for the period 1980 to 2004.

– We also compared our SMB data to ERA-Interim values. ERA-Interim is the most recent reanalysis (Simmons et al., 2006) from the European Centre for Medium-Range Weather Forecasts (ECMWF), and covers the period 1989 to present. A reanalysis is the result of complex data assimilation to produce an optimal combination of observations and meteorological model results. The main advances of ERA-Interim over ERA-40 are a finer spectral truncation, improved model physics and a more efficient data assimilation system.

– Finally we compared our results to the SMB produced from an atmospheric global circulation model, LMDZ4 (Hourdin et al., 2006), which is the atmospheric component of the IPSL-CM4 climate system model (Marti et al., 2006) that participated in the World Climate Research Programme's Coupled Model Inter-Comparison Project phase 3 (CMIP3) exercise to build the IPCC 4th assessment report (Meehl et al., 2007). The model used in the present study includes several improvements for the simulation of polar climates suggested by Krinner et al. (1997).

4 Discussion

4.1 Undulating structures

The undulating structures visible in Figs. 6 and 7 are probably caused by redistribution of snow by the wind due to gravity waves that are triggered at breaks in a slope (Gallée and Pettré, 1998). This phenomenon was described in Adelie Land coastal areas by Pettré et al. (1986), where 40 km wavelength isochronal undulations were observed below the break point at 230 km from the coast. However, Pettré et al. (1986) did not find undulations further inland, and suggested that accumulation on the plateau was relatively uniform. However, it should be noted that their observations result from a 10 km spaced stake network until 430 km from the coast (670 km from DC), and three core measurements between DC and 670 km from DC. Consequently, they were not able to capture structures with wavelengths of around 10 km like the ones visible on our radargrams. As noted earlier, another break in the slope is also visible around 300 km from DC (Fig. 6). It is interesting to note that, like in Pettré's study, the undulations start just after that break in slope.

The undulations' link with local topography is clearly visible in Figs. 6, 8 and 9. Low accumulation intervals between 450 and 470 km from DC are located in the lee of local elevation peaks (labelled A and B in Fig. 6), where the surface slope is the steepest, reflecting local strong ablation conditions due to high snow erosion rates caused by divergence in the katabatic wind field (e.g. van den Broeke et al., 2006; Favier et al., 2011). The crest of deep undulations is located downwind from the surface crest, where the slope is closer to zero. Regarding undulations variations with time, the progressive steepening of fold limbs visible in Fig. 7 is a well-known feature caused by spatial variations in accumulation rates (see e.g. Arcone et al., 2005b).

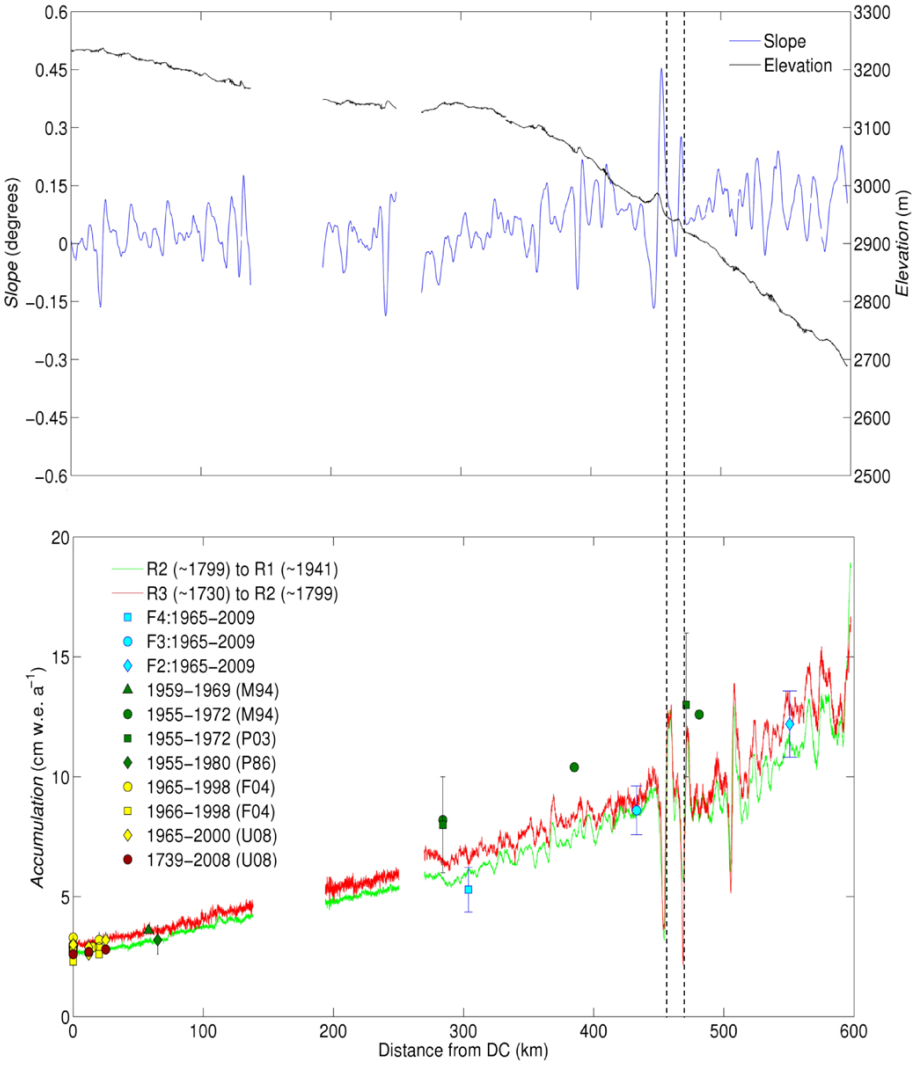

Fig. 8. Comparison of our accumulation results (radar and core measurements) and of previous studies along the transect. M94 = Mulvaney et al. (1994); P03 = Pourchet et al. (2003); P86 = Pettré et al. (1986); F04 = Frezzotti et al. (2004); U08 = Urbini et al. (2008). Upper panel shows elevation and slope.

To conclude, the undulations we observe would be the result of accumulation variations caused by interactions between katabatic wind and local topography. These processes are described in Arcone et al. (2005b).

4.2 Spatial variations in accumulation

A gradual increase in accumulation from DC to the end of the transect was observed (Figs. 8 and 9). This is consistent with previous observations in the region (see e.g. Pourchet et al., 1983; Pettré et al., 1986) along with a gradual increase in humidity from DC to the coast (Bromwich et al., 2004). Moreover, major variations in accumulation are reflected by the undulating structures described above (Figs. 8 and 9).

Radar and core accumulation values matched most historical measurements (Fig. 8), although the time periods studied were not the same. Several observations can be made:

– Our radar accumulation results agree fairly well with measurements made within 25 km of DC by Frezzotti et al. (2004) and Urbini et al. (2008) for the period 1965–"recent", and with estimates made by Urbini et al. (2008) for the period 1739–2008. Differences remained within less than 1 cm w.e. a^{-1}, i.e. less than 25 %. Changes in accumulation in the past 20 yr observed by Urbini et al. (2008) could not be checked here as radar data only allow estimations for older periods.

– Accumulation estimates made for the period 1955–1972 by Mulvaney and Wolff (1994) and Pourchet et al. (2003) are systematically higher than our radar and core

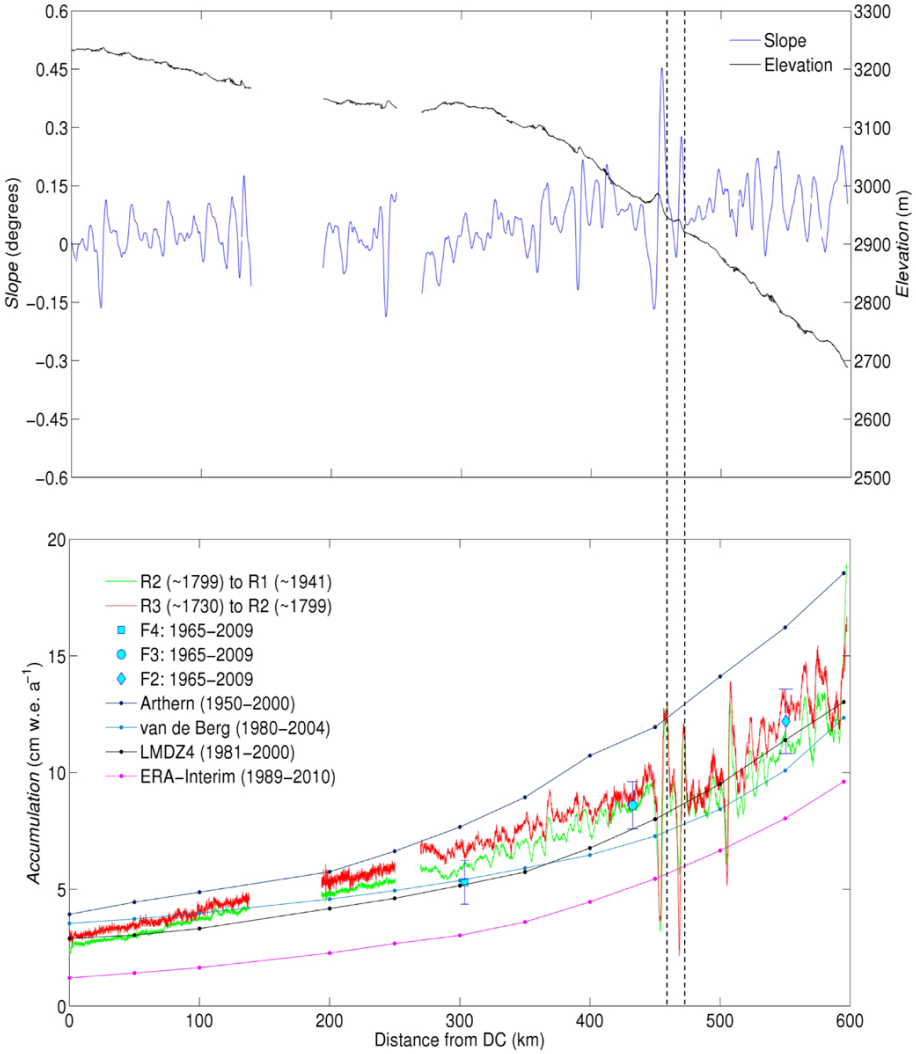

Fig. 9. Comparison of our accumulation results (radar and core measurements) and modelling results along the transect. Upper panel shows elevation and slope.

estimates. On the contrary, estimates by Mulvaney and Wolff (1994) and Pettré et al. (1986) for the periods 1959–1969 and 1955–1980, respectively, are in good agreement with our results. In addition, Agosta et al. (2011) found little change in coastal SMB after the 1970s. This could lead to the conclusion that 1955–1972 was an abnormally wet period compared to the last centuries, although this conclusion should be considered with caution because of the uncertainties linked to historical data for the period 1955–1972 and our estimates. Further analysis of this particular period would be required.

Regarding model validation, all four SMB climatologies are close to our accumulation results (Fig. 9). However, some differences between models can be noted:

– Accumulation modelled by Arthern is systematically higher than our results, indicating a wetter modelled climate. This is probably due to the fact that Arthern's accumulation map is based on available accumulation measurements. Between 200 and 500 km from DC, these correspond to data from Mulvaney and Wolff (1994) and Pourchet et al. (2003), which display higher accumulation values than our own (Fig. 8). Moreover, Pourchet's measurement made around 470 km from DC could have been made on one of the undulations described earlier.

– ERA-INTERIM reanalysis, on the contrary, yield much drier results than our own. This situation contrasts with the coastal area of Adelie Land where data of Agosta et al. (2011) were in good agreement with ERA-Interim results, whereas ERA-40 yields slightly too humid values due to larger sublimation

in ERA-Interim. Nevertheless, our conclusions confirm that ERA-Interim generally yield too dry values over plateaus, as observed by Agosta (2012). This is also the reason why ERA-40 SMB integrated over the whole of Antarctica represents the lower limit of SMB values in the litterature (e.g. Monaghan et al., 2006b).

– van de Berg model results are in good agreement with our accumulation estimates. Their climatology is refitted by altitude intervals on Vaughan and Russell (1997) data, thus it does not correspond to kriging. As a result, unlike Arthern et al. (2006), their method does not introduce local biases due to old measurements made in our study region. This points to the biases introduced by doubtful measurements in SMB extra- and interpolations, and confirms the need for data quality control, such as proposed by Magand et al. (2007).

– The LMDZ4 model is "*free from any meteorological observational constraint*" (Agosta et al., 2011). However, it is the model which agrees the best with our accumulation values, remaining within the margin of uncertainty of our 1965–2009 core estimates. It reacts particularly well in the study region, as observed previously in the coastal area (Agosta et al., 2011). This is surprising because "models that use observed sea ice, such as ERA, are expected to do better in depicting the absolute amount of precipitation than climatic models, since precipitation and evaporation rates depend on the extent of sea ice" (Agosta et al., 2011).

4.3 Temporal variations in accumulation

Temporal variations should be interpreted with caution. Indeed, density is used to convert accumulation in cm into cm w.e. (as explained in Sect. 2.4.3). Accumulation in cm of snow (not shown) and in cm w.e. (Figs. 8 and 9) evolve very differently with time due to snow densification. Considering the uncertainty margin on our accumulation results (which can be considered at least equal to uncertainties in core estimates, i.e. 11 to 17 %), accumulation in cm w.e. did not significantly increase with time. Indeed, if (1) dating of layers at DC based on the EPICA Dome C ice core and (2) our density estimates are valid, there was no difference in accumulation between the three study periods (radar 1730–1799, radar 1799–1941 and firn cores 1965–2009). However, because of the difficulty involved in estimating density, it is risky to draw conclusions variability of accumulation with time.

5 Conclusions and outlook

A radar transect was conducted in Adelie Land (East Antarctica) in 2008–2009, between DC station and the coast and six complementary firn cores were drilled. This long continuous radar dataset is one of the few obtained in the region.

Study of the 600 km-long usable dataset yielded three major results:

1. Accumulation increases gradually with an increase in the distance from DC, which is consistent with findings from previous studies in this region. Regarding spatial variations in accumulation, historical accumulation data and results from modelling studies along the transect are in good agreement with our results.

2. Previously undocumented 10 km wavelength undulations exist in a region located between 300 and 600 km from DC. These require further analyses in future studies, notably via atmospheric modelling (MAR model, Gallée and Schayes, 1994), assuming that the model can capture such a fine resolution. It also provides information that is useful for the search of new drilling sites. We now know that the section from 450 to 500 km from DC would not be suitable for drilling a new core because of the high variability of accumulation.

3. There is no significant change in accumulation with time, if dating of layers at DC based on the EPICA Dome C ice core and our density estimates are considered valid. Indeed, accumulation results rely heavily on density estimates, and consequently, drawing conclusions regarding changes in accumulation with time is difficult. Density is only measured occasionally and measurements are often not deep enough. We took advantage of two deep cores drilled at DC and D47 (1000 km apart) to estimate density along the transect, as an interpolation in function of the distance to those two sites.

In the long term, a more rapid method of measuring density is needed to ensure more frequent density measurements. This would be useful for all studies that require accurate density estimates.

New radar and firn core measurements were obtained during a transect between DC and Vostok stations in 2011–2012. Upcoming analysis of these new data should provide complementary knowledge about East-Antarctic SMB.

Acknowledgements. We would like to thank M. Frezzotti, and S. Urbini for the advice they gave at the start of this study. We also thank Cécile Agosta for her help with model accumulation results, the GLACIOCLIM-SAMBA observatory for providing stake data at DC, and Paul Duval and Hubert Gallée for the advice they gave on specific topics related to this study. This study was made possible thanks to IPEV and ANR funding ("VANISH" project no. ANR-07-VULN-013 and "Dome A" project no. ANR-07-BLAN-0125).

Edited by: M. Schneebeli

The publication of this article is financed by CNRS-INSU.

References

Agosta, C., Favier, V., Genthon, C., Gallée, H., Krinner, G., Lenaerts, J., and van den Broeke, M.: A 40-year accumulation dataset for Adelie Land, Antarctica and its application for model validation, Clim. Dynam., 38, 75–86, doi:10.1007/s00382-011-1103-4, 2011.

Agosta, C.: Evolution du bilan de masse de surface Antarctique par régionalisation physique et conséquences sur les variations du niveau des mers, Ph.D. thesis, Université Joseph Fourier, Grenoble, 2012.

Arcone, S., Spikes, V., and Hamilton, G.: Phase structure of radar stratigraphic horizons within Antarctic firn, Ann. Glaciol., 41, 10–16, 2005a.

Arcone, S., Spikes, V., and Hamilton, G.: Stratigraphic variation within polar firn caused by differential accumulation and ice flow: interpretation of a 400 MHz short-pulse radar profile from West Antarctica, J. Glaciol., 51, 407–422, 2005b.

Arthern, R., Winebrenner, D., and Vaughan, D.: Antarctic snow accumulation mapped using polarization of 4.3-cm wavelength microwave emission, J. Geophys. Res., 111, D06107, doi:10.1029/2004JD005667, 2006.

Bromwich, D., Guo, Z., Bai, L., and Chen, Q.: Modeled antarctic precipitation. Part I: Spatial and temporal variability, J. Climate, 17, 427–447, 2004.

Castellano, E., Becagli, S., Hansson, M., Hutterli, M., Petit, J. R., Rampino, M. R., Severi, M., Steffensen, J. P., Traversi, R., and Udisti, R.: Holocene volcanic history as recorded in the sulfate stratigraphy of the European Project for Ice Coring in Antarctica Dome C (EDC96) ice core, J. Geophys. Res., 110, D06114, doi:10.1029/2004JD005259, 2005.

Daniels, J.: Ground Penetrating Radar Fundamentals, prepared as an appendix to a report to the US EPA, Region V, Department of Geological Sciences, The Ohio State University, 2000.

Eisen, O., Wilhelms, F., Nixdorf, U., and Miller, H.: Identifying isochrones in GPR profiles from DEP-based forward modeling, Ann. Glaciol., 37, 344–350, 2003a.

Eisen, O., Wilhelms, F., Nixdorf, U., and Miller, H.: Revealing the nature of radar reflections in ice: DEP-based FDTD forward modeling, Geophys. Res. Lett., 30, 1218, doi:10.1029/2002GL016403, 2003b.

Eisen, O., Frezzotti, M., Genthon, C., Isaksson, E., Magand, O., Broeke, M., Dixon, D., Ekaykin, A., Holmlund, P., Kameda, T., Karlöf, L., Kaspari, S., Lipenkov, V., Oerter, H., Takahashi, S., and Vaughan, D.: Ground-based measurements of spatial and temporal variability of snow accumulation in East Antarctica, Rev. Geophys., 46, RG2001, doi:10.1029/2006RG000218, 2008.

Favier, V., Agosta, C., Genthon, C., Arnaud, L., Trouvillez, A., and Gallée, H.: Modeling the mass and surface heat budgets in a coastal blue ice area of Adelie Land, Antarctica, J. Geophys. Res., 116, F03017, doi:10.1029/2010JF001939, 2011.

Frezzotti, M., Pourchet, M., Flora, O., Gandolfi, S., Gay, M., Urbini, S., Vincent, C., Becagli, S., Gragnani, R., Proposito, M., Severi, M., Traversi, R., Udisti, R., and Fily, M.: New estimations of precipitation and surface sublimation in East Antarctica from snow accumulation measurements, Clim. Dynam., 23, 803–813, 2004.

Frezzotti, M., Pourchet, M., Flora, O., Gandolfi, S., Gay, M., Urbini, S., Vincent, C., Becagli, S., Gragnani, R., Proposito, M., Severi, M., Traversi, R., Udisti, R., and Fily, M.: Spatial and temporal variability of snow accumulation in East Antarctica from traverse data, J. Glaciol., 51, 113–124, 2005.

Gallée, H. and Pettré, P.: Dynamical constraints on katabatic wind cessation in Adélie Land, Antarctica, J. Atmos. Sci., 55, 1755–1770, 1998.

Gallée, H. and Schayes, G.: Development of a 3-dimensional meso-gamma primitive equation model – katabatic winds simulation in the area of terra-nova bay, Antarctica, Mon. Weather Rev., 122, 671–685, 1994.

Genthon, C., Lardeux, P., and Krinner, G.: The surface accumulation and ablation of a blue ice area near Cap Prudhomme, Adélie Land, Antarctica, J. Glaciol., 53, 635–645, 2007.

Helsen, M., van den Broeke, van de Wal, R., van de Berg, W., van Meijgaard, E., Davis, C., Li, Y., and Goodwin, I.: Elevation changes in Antarctica mainly determined by accumulation variability, Science, 320, 1626–1629, 2008.

Hempel, L., Thyssen, F., Gundestrup, N., Clausen, H., and Miller, H.: A comparison of radio-echo sounding data and electrical conductivity of the GRIP ice core, J. Glaciol., 46, 369–374, 2000.

Hourdin, F., Musat, I., Bony, S., Braconnot, P., Codron, F., Dufresne, J.-L., Fairhead, L., Filiberti, M.-A., Friedlingstein, P., Grandpeix, J.-Y., Krinner, G., LeVan, P., Li, Z.-X., and Lott, F.: The LMDZ4 general circulation model: climate performance and sensitivity to parametrized physics with emphasis on tropical convection, Clim. Dynam., 27, 787–813, 2006.

Kohler, J., Moore, J., and Isaksson, E.: Comparison of modelled and observed responses of a glacier snowpack to ground-penetrating radar, Ann. Glaciol., 37, 293–297, 2003.

Kovacs, A., Gow, A., and Morey, R.: The in-situ dielectric constant of polar firn revisited, Cold Reg. Sci. Technol., 23, 245–256, 1995.

Krinner, G., Genthon, C., Li, Z., and Le Van, P.: Studies of the Antarctic climate with a stretched-grid general circulation model, J. Geophys. Res., 102, 13731–13745, 1997.

Magand, O.: Bilan de masse de surface Antarctique: techniques de mesure et analyse critique, Ph.D. thesis, Université Joseph Fourier, Grenoble, 2009.

Magand, O., Frezzotti, M., Pourchet, M., Stenni, B., Genoni, L., and Fily, M.: Climate variability along latitudinal and longitudinal transects in East Antarctica, Ann. Glaciol., 39, 351–358, 2004.

Magand, O., Genthon, C., Fily, M., Krinner, G., Picard, G., Frezzotti, M., and Ekaykin, A.: An up-to-date quality-controlled surface mass balance data set for the 90°–180° E Antarctica sector and 1950–2005 period, J. Geophys. Res., 112, D12106, doi:10.1029/2006JD007691, 2007.

Marti, O., Braconnot, P., Bellier, J., Benshila, R., Bony, S., Brockmann, P., Cadule, P., Caubel, A., Denvil, S., Dufresne,

J.-L., Fairhead, L., Filiberti M.-A., Fichefet, T., Foujols, M.-A., Friedlingstein, P., Grandpeix, J.-Y., Hourdin, F., Krinner, G., Lévy, C., Madec, G., Musat, I., De Noblet, N., Polcher, J., and Talandier, C.: The new IPSL climate system model: IPSL-CM4, Note du Pôle de Modélisation 26, ISSN 1288-1619, 88 pp., 2006.

Meehl, G., Stocker, T., Collins, W., Friedlingstein, A., Gaye, A., Gregory, J., Kitoh, A., Knutti, R., Murphy, J., Noda, A., Raper, S. C. B., Watterson, I. G., Weaver, A. J., and Zhao, Z.-C.: Global climate projections, in: Climate Change 2007: The Physical Science Basis. Contribution of Working Group I to the Fourth Assessment Report of the Intergovernmental Panel on Climate Change, edited by: Solomon, S., Qin, D., Manning, M., Chen, Z., Marquis, M., Averyt, K., Tignor, M., and Miller, H., Cambridge University Press, 2007.

Monaghan, A., Bromwich, D., Fogt, R., Wang, S., Mayewski, P., Dixon, D., Ekaykin, A., Frezzotti, M., Goodwin, I., Isaksson, E., Kaspari, S., Morgan, V., Oerter, H., Van Ommen, T., Van der Veen, C., and Wen, J.: Insignificant change in Antarctic snowfall since the International Geophysical Year, Science, 313, 827–831, doi:10.1126/science.1128243, 2006a.

Monaghan, A., Bromwich, D., and Wang, S.: Recent trends in Antarctic snow accumulation from Polar MM5 simulations, Philos. T. R. Soc. A, 364, 1683–1708, 2006b.

Muller, K., Sinisalo, A., Anschutz, H., Hamran, S., Hagen, J., McConnell, J., and Pasteris, D.: An 860 km surface mass-balance profile on the East Antarctic plateau derived by GPR, Ann. Glaciol., 51, 1–8, 2010.

Mulvaney, R. and Wolff, E.: Spatial variability of the major chemistry of the Antarctic ice sheet, Ann. Glaciol., 20, 440–447, 1994.

Petit, J., Jouzel, J., Pourchet, M., and Merlivat, L.: A detailed study of snow accumulation and stable isotope content in Dome C (Antarctica), J. Geophys. Res., 87, 4301–4308, 1982.

Pettré, P., Pinglot, J., Pourchet, M., and Reynaud, L.: Accumulation distribution in Terre Adélie, Antarctica: effect of meteorological parameters, J. Glaciol., 32, 486–500, 1986.

Pourchet, M., Pinglot, F., and Lorius, C.: Some meteorological applications of radioactive fallout measurements in Antarctic snows, J. Geophys. Res., 88, 6013–6020, 1983.

Pourchet, M., Magand, O., Frezzotti, M., Ekaykin, A., and Winther, J.: Radionuclides deposition over Antarctica, J. Environ. Radioactiv., 68, 137–158, 2003.

Richardson, C. and Holmlund, P.: Spatial variability at shallow snow-layer depths in central Dronning Maud Land, East Antarctica, Ann. Glaciol., 29, 10–16, 1999.

Richardson, C., Aarholt, E., Hamran, S., Holmlund, P., and Isaksson, E. : Spatial distribution of snow in western Dronning Maud Land, East Antarctica, mapped by a ground-based snow radar, J. Geophys. Res., 102, 20343–20353, 1997.

Simmons, A., Uppala, S., Dee, D., and Kobayashi, S.: ERA-Interim: new ECMWF reanalysis products from 1989 onwards, ECMWF Newsl., 110, 25–35, 2006.

Solomon, S., Qin, D., Manning, M., Chen, Z., Marquis, M., Averyt, K., Tignor, M., and Miller, H.: IPCC, 2007: Climate Change 2007: The Physical Science Basis. Contribution of Working Group I to the Fourth Assessment Report of the Intergovernmental Panel on Climate Change, 2007.

Uppala, S., Kallberg, P., Simmons, A., and collaborators: The ERA-40 re-analysis, Q. J. Roy. Meteor. Soc., 131, 2961–3012, 2005.

Urbini, S., Vittuari, L., and Gandolfi, S. A.: GPR and GPS data integration: examples of application in Antarctica, Ann. Geofis., 44, 687–702, 2001.

Urbini, S., Frezzotti, M., Gandolfi, S., Vincent, C., Scarchilli, C., Vittuari, L., and Fily, M.: Historical behaviour of Dome C and Talos Dome (East Antarctica) as investigated by snow accumulation and ice velocity measurements, Global Planet. Change, 60, 576–588, 2008.

van de Berg, W., van den Broeke, M., Reijmer, C., and van Meijgaard, E.: Reassessment of the Antarctic surface mass balance using calibrated output of a regional atmospheric climate model, J. Geophys. Res., 111, D11104, doi:10.1029/2005JD006495, 2006.

van den Broeke, M., van de Berg, W. J., van Meijgaard, E., and Reijmer, C.: Identification of Antarctic ablation areas using a regional climate model, J. Geophys. Res., 111, D18110, doi:10.1029/2006JD007127, 2006.

Vaughan, D. and Russell, J.: Compilation of Surface Mass Balance Measurements in Antarctica, Internal Rep. ES4/8/1/1997/1, British Antarctic Survey, Cambridge, UK, 1997.

Annexe B

Modèles CMIP5 utilisés dans cette étude

TABLE B.1 – Description des différents modèles CMIP5 analysés dans le cadre de ma thèse. Les types de simulations utilisées (historique = "Histo", RCP 2.6 ou RCP 8.5) sont indiquées.

Modèle	Groupe	Pays	Histo	RCP 2.6	RCP 8.5
ACCESS1-0	Commonwealth Scientific and Industrial Research Organisation, and Bureau of Meteorology	AU	oui	non	oui
ACCESS1-3	Commonwealth Scientific and Industrial Research Organisation, and Bureau of Meteorology	AU	oui	non	oui
bcc-csm1-1	Beijing Climate Center, China Meteorological Administration	CN	oui	oui	oui
bcc-csm1-1-m	Beijing Climate Center, China Meteorological Administration	CN	oui	oui	oui
BNU-ESM	College of Global Change and Earth System Science, Beijing Normal University	CN	oui	oui	oui
CanCM4	Canadian Centre for Climate Modelling and Analysis	CA	oui	non	non
CanESM2	Canadian Centre for Climate Modelling and Analysis	CA	oui	oui	oui
CCSM4	National Center for Atmospheric Research	US	oui	oui	oui

Suite à la page suivante

TABLE B.1 – *Suite de la page précédente*

Modèle	Groupe	Pays	Histo	RCP 2.6	RCP 8.5
CESM1-BGC	National Science Foundation, Department of Energy, National Center for Atmospheric Research	US	oui	non	oui
CESM1-CAM5	National Science Foundation, Department of Energy, National Center for Atmospheric Research	US	oui	oui	oui
CESM1-CAM5-1-FV2	National Science Foundation, Department of Energy, National Center for Atmospheric Research	US	oui	non	non
CESM1- FASTCHEM	National Science Foundation, Department of Energy, National Center for Atmospheric Research	US	oui	non	non
CESM1-WACCM	National Science Foundation, Department of Energy, National Center for Atmospheric Research	US	oui	non	non
CMCC-CESM	Centro Euro-Mediterraneo per I Cambiamenti Climatici	IT	oui	non	oui
CMCC-CM	Centro Euro-Mediterraneo per I Cambiamenti Climatici	IT	oui	non	oui
CMCC-CMS	Centro Euro-Mediterraneo per I Cambiamenti Climatici	IT	oui	non	oui
CNRM-CM5	Centre National de Recherches Meteorologiques, Centre Européen de Recherche et Formation Avancée en Calcul Scientifique	FR	oui	oui	oui
CSIRO-Mk3-6-0	Commonwealth Scientific and Industrial Research Organisation, and Queensland Climate Change Centre of Excellence	AU	oui	oui	oui
EC-EARTH	EC-EARTH consortium	Europe	oui	non	oui
FGOALS-g2	Institute of Atmospheric Physics, Chinese Academy of Sciences, and Tsinghua University	CN	oui	oui	oui

Suite à la page suivante

TABLE B.1 – *Suite de la page précédente*

Modèle	Groupe	Pays	Histo	RCP 2.6	RCP 8.5
FGOALS-s2	Institute of Atmospheric Physics, Chinese Academy of Sciences	CN	oui	non	non
FIO-ESM	The First Institute of Oceanography, SOA	CN	oui	oui	oui
GFDL-CM2.1	National Oceanic and Atmospheric Administration Geophysical Fluid Dynamics Laboratory	US	oui	non	non
GFDL-CM3	National Oceanic and Atmospheric Administration Geophysical Fluid Dynamics Laboratory	US	oui	oui	oui
GFDL-ESM2G	National Oceanic and Atmospheric Administration Geophysical Fluid Dynamics Laboratory	US	oui	oui	oui
GFDL-ESM2M	National Oceanic and Atmospheric Administration Geophysical Fluid Dynamics Laboratory	US	oui	oui	oui
GISS-E2-H	National Aeronautics and Space Administration Goddard Institute for Space Studies	US	oui	oui	oui
GISS-E2-H-CC	National Aeronautics and Space Administration Goddard Institute for Space Studies	US	oui	non	non
GISS-E2-R	National Aeronautics and Space Administration Goddard Institute for Space Studies	US	oui	oui	oui
GISS-E2-R-CC	National Aeronautics and Space Administration Goddard Institute for Space Studies	US	oui	non	non
HadCM3	Met Office Hadley Centre	GB	oui	non	non
HadGEM2-AO	National Institute of Meteorological Research/Korea Meteorological Administration	KR	oui	oui	oui
HadGEM2-CC	Met Office Hadley Centre	GB	oui	non	oui

Suite à la page suivante

TABLE B.1 – *Suite de la page précédente*

Modèle	Groupe	Pays	Histo	RCP 2.6	RCP 8.5
HadGEM2-ES	Met Office Hadley Centre, National Institute for Space Research (Brazil)	GB, BR	oui	oui	oui
INM-CM4	Institute for Numerical Mathematics	RU	oui	non	oui
IPSL-CM5A-LR	Institut Pierre-Simon Laplace	FR	oui	oui	oui
IPSL-CM5A-MR	Institut Pierre-Simon Laplace	FR	oui	oui	oui
IPSL-CM5B-LR	Institut Pierre-Simon Laplace	FR	oui	non	oui
MIROC-ESM	Japan Agency for Marine-Earth Science and Technology, Atmosphere and Ocean Research Institute (The University of Tokyo), and National Institute for Environmental Studies	JP	oui	oui	oui
MIROC-ESM-CHEM	Japan Agency for Marine-Earth Science and Technology, Atmosphere and Ocean Research Institute (The University of Tokyo), and National Institute for Environmental Studies	JP	oui	oui	oui

Suite à la page suivante

TABLE B.1 – *Suite de la page précédente*

Modèle	Groupe	Pays	Histo	RCP 2.6	RCP 8.5
MIROC4h	Atmosphere and Ocean Research Institute (The University of Tokyo), National Institute for Environmental Studies, and Japan Agency for Marine-Earth Science and Technology	JP	oui	non	non
MIROC5	Atmosphere and Ocean Research Institute (The University of Tokyo), National Institute for Environmental Studies, and Japan Agency for Marine-Earth Science and Technology	JP	oui	oui	oui
MPI-ESM-LR	Max Planck Institute for Meteorology	DE	oui	oui	oui
MPI-ESM-MR	Max Planck Institute for Meteorology	DE	oui	oui	oui
MPI-ESM-P	Max Planck Institute for Meteorology	DE	oui	non	non
MRI-CGCM3	Meteorological Research Institute	JP	oui	oui	oui
MRI-ESM1	Meteorological Research Institute	JP	oui	non	non
NorESM1-M	Norwegian Climate Centre	NO	oui	oui	oui
NorESMl-ME	Norwegian Climate Centre	NO	oui	oui	oui

Annexe C

Article Hodgson et al. (2014)

Quaternary Science Reviews 100 (2014) 137–158

Contents lists available at ScienceDirect

Quaternary Science Reviews

journal homepage: www.elsevier.com/locate/quascirev

Terrestrial and submarine evidence for the extent and timing of the Last Glacial Maximum and the onset of deglaciation on the maritime-Antarctic and sub-Antarctic islands☆

Dominic A. Hodgson [a,c,*,1], Alastair G.C. Graham [b,1], Stephen J. Roberts [a], Michael J. Bentley [c], Colm Ó Cofaigh [c], Elie Verleyen [d], Wim Vyverman [d], Vincent Jomelli [e], Vincent Favier [f], Daniel Brunstein [e], Deborah Verfaillie [f], Eric A. Colhoun [g], Krystyna M. Saunders [h], Patricia M. Selkirk [i], Andrew Mackintosh [j], David W. Hedding [k], Werner Nel [l], Kevin Hall [m], Matt S. McGlone [n], Nathalie Van der Putten [o], William A. Dickens [a], James A. Smith [a]

[a] British Antarctic Survey, Natural Environment Research Council, High Cross, Madingley Road, Cambridge CB3 0ET, UK
[b] Department of Geography, College of Life and Environmental Sciences, University of Exeter, Amory Building, Rennes Drive, Exeter EX4 4RJ, UK
[c] Department of Geography, Durham University, South Rd, Durham DH1 3LE, UK
[d] Laboratory for Protistology and Aquatic Ecology, Biology Department, Ghent University, Krijgslaan 281-S8, 9000 Ghent, Belgium
[e] Université Paris 1 Panthéon Sorbonne – CNRS, Laboratoire de géographie physique, 1 Place A. Briand, 92195 Meudon, France
[f] Laboratoire de Glaciologie et de Géophysique de l'Environnement, LGGE, UJF–CNRS, UMR5183, 54 rue Molière, 38402 St Martin d'Hères, France
[g] School of Environmental and Life Sciences, The University of Newcastle, NSW 2308, Australia
[h] Institute of Geography and the Oeschger Centre for Climate Change Research, University of Bern, Erlachstrasse 9, Trakt 3,Bern 3012 Switzerland
[i] Department of Biological Sciences, Macquarie University, Sydney, NSW 2109, Australia
[j] Antarctic Research Centre, Victoria University of Wellington, Wellington 6012, New Zealand
[k] Department of Geography, University of South Africa, Florida Campus, Private Bag X6, Florida 1710, South Africa
[l] Department of Geography and Environmental Science, University of Fort Hare, Alice Campus, Private Bag X1314, Alice 5700, South Africa
[m] Geography Programme, University of Northern British Columbia, 3333 University Way, Prince George, BC V2N 479, Canada
[n] Landcare Research, PO Box 40, Lincoln 7640, New Zealand
[o] Department of Geology, Lund University, Sölvegatan 12, SE–223 62 Lund, Sweden

ARTICLE INFO

Article history:
Received 25 January 2013
Received in revised form
23 November 2013
Accepted 2 December 2013
Available online 13 March 2014

Keywords:
Antarctic ice sheet
Sub-Antarctica
Maritime Antarctica glaciation
Deglaciation
Quaternary
Climate

ABSTRACT

This paper is the maritime and sub–Antarctic contribution to the Scientific Committee for Antarctic Research (SCAR) Past Antarctic Ice Sheet Dynamics (PAIS) community Antarctic Ice Sheet reconstruction. The overarching aim for all sectors of Antarctica was to reconstruct the Last Glacial Maximum (LGM) ice sheet extent and thickness, and map the subsequent deglaciation in a series of 5000 year time slices. However, our review of the literature found surprisingly few high quality chronological constraints on changing glacier extents on these timescales in the maritime and sub–Antarctic sector. Therefore, in this paper we focus on an assessment of the terrestrial and offshore evidence for the LGM ice extent, establishing minimum ages for the onset of deglaciation, and separating evidence of deglaciation from LGM limits from those associated with later Holocene glacier fluctuations. Evidence included geomorphological descriptions of glacial landscapes, radiocarbon dated basal peat and lake sediment deposits, cosmogenic isotope ages of glacial features and molecular biological data. We propose a classification of the glacial history of the maritime and sub–Antarctic islands based on this assembled evidence. These include: (Type I) islands which accumulated little or no LGM ice; (Type II) islands with a limited LGM ice extent but evidence of extensive earlier continental shelf glaciations; (Type III) seamounts and volcanoes unlikely to have accumulated significant LGM ice cover; (Type IV) islands on shallow shelves with both

* Corresponding author. +44 1223 221635.
E-mail address: daho@bas.ac.uk (D.A. Hodgson).
[1] These authors contributed equally to this work.

http://dx.doi.org/10.1016/j.quascirev.2013.12.001

terrestrial and submarine evidence of LGM (and/or earlier) ice expansion; (Type V) Islands north of the Antarctic Polar Front with terrestrial evidence of LGM ice expansion; and (Type VI) islands with no data. Finally, we review the climatological and geomorphological settings that separate the glaciological history of the islands within this classification scheme.

1. Introduction

Reconstructing the Antarctic Ice Sheet through its Last Glacial Maximum (LGM) and post LGM deglacial history is important for a number of reasons. Firstly, ice sheet modellers require field data against which to constrain and test their models of ice sheet change. The recent development of a practical approach to modelling grounding line dynamics (Schoof, 2007) has led to a new generation of models (e.g., Pollard and DeConto, 2009) that require field constraints. Secondly, the most recent millennia and centuries of ice sheet history provide data on the 'trajectory' of the ice sheet, which are valuable for the initialisation of models. Thirdly, the use of recent satellite gravity measurements (e.g. GRACE), and other geodetic data such as GPS, for ice sheet mass balance estimates requires an understanding of glacial–isostatic adjustment (GIA). In the case of GRACE, the satellite-pair cannot distinguish between recent changes in the mass balance of the ice sheet, and those from the transfer of mass in the mantle resulting from past ice sheet melting. This means that robust ice sheet reconstructions are required to generate GIA corrections and it is these corrections that are regarded as the greatest limiting factors for ice mass measurements from satellite gravity (King et al., 2012). It has been suggested that some mass estimates may be in error by as much as 100% (Chen et al., 2006).

Several decades of study have produced an impressive body of work on Antarctic Ice Sheet history. There have been a number of attempts to synthesise the data but many of these have just focussed on the LGM. A notable reconstruction was produced by Ivins and James (2005) which attempted to provide time-slices of the ice sheet from the LGM to the present-day to use as the basis of their GIA modelling. This 'model', termed IJ05, has been widely adopted by the satellite gravity and GPS communities as the ice sheet reconstruction to underpin GIA assessments. The model, although a benchmark at the time, is now becoming a little out-of-date, with the proliferation of data since the early 2000s, and no longer includes all of the glacial geological data available.

As a result, the Antarctic Climate Evolution (ACE) and subsequent Past Antarctic Ice Sheet Dynamics (PAIS) programmes of the Scientific Committee for Antarctic Research (SCAR) proposed a co-ordinated effort by the glacial geology community to develop a synthesis of Antarctic Ice Sheet history. This paper covers the maritime and sub-Antarctic sectors. Other sectors of the Antarctic Ice Sheet, including the maritime Antarctic islands west of the Antarctic Peninsula, are described elsewhere in this Special Issue.

Although the combined volume of the maritime and sub-Antarctic LGM glaciers has had a very limited effect on global sea level, understanding past extent and timing of past glaciations in the sub-Antarctic is important for a number of reasons. First, the maritime and sub-Antarctic glaciers have been amongst the earliest ice masses to respond to recent rapid regional warming (e.g. Gordon et al., 2008; Cook et al., 2010) and, therefore, provide a sensitive indicator of interactions between Southern Hemisphere climate and ice sheet stability. This interaction can, in turn, be used to provide boundary conditions for various physical parameters in glaciological models, including those associated with abrupt climate change and the terminal phases of ice sheet decay. Second, the timing, thickness and extent of glacial maxima and subsequent glacier fluctuations in the maritime and sub-Antarctic region can be used to address questions regarding the relative pacing of climate changes between the hemispheres. For example, it is still not known if many of the maritime and sub-Antarctic islands have synchronous glaciations, follow an Antarctic pattern of glaciation, a South American or New Zealand pattern, or a Northern Hemisphere one. This has clear relevance to research aiming to determine if Southern Hemisphere glaciations precede those in the north (or vice versa), whether polar climates are in or out of phase between the hemispheres (Blunier et al., 1998), and in identifying the significant climate drivers. Third, the extent of glacial maxima on the maritime and sub-Antarctic Islands has determined how much of their terrestrial habitats and surrounding marine shelves have been available and suitable as biological refugia for local and Antarctic continental biota during glaciations (Clarke et al., 2005; Barnes et al., 2006; Convey et al., 2008). This knowledge helps explain evolutionary patterns in biodiversity and regional biogeography.

Whilst for some sectors of the Antarctic Ice Sheet it was possible to follow the original community aim of reconstructing the LGM and deglaciation in a series of 5000 year time slices, our review found surprisingly few high quality age constraints on changing glacier extents on these timescales in the maritime and sub-Antarctic sector. Thus, we limited ourselves to assessing the terrestrial and offshore evidence for the LGM ice extent, and establishing a minimum age for the onset of deglaciation. Specific aims for each of the maritime and sub-Antarctic islands were to:

1. Summarise evidence for LGM ice thickness and extent based on onshore geomorphological evidence, including evidence of glacial isostasy from relative sea level changes.
2. Summarise evidence for LGM ice extent and infer ice thickness using offshore geomorphological evidence from the continental shelf including regional bathymetric compilations.
3. Compile tables of minimum age constraints for glacial features relating to the local LGM (referred to hereon simply as 'LGM') and the onset of deglaciation.
4. Separate evidence of the LGM and onset of deglaciation from deglaciation associated with later Holocene glacier fluctuations

In the discussion we propose a classification of the sub-Antarctic islands based on their glacial history and consider the different climatic and topographic factors controlling glaciation.

1.1. Study area

The sub-Antarctic islands considered in this review are located between 35 and 70°S, but are mainly found within 10–15° of the Antarctic Polar Front (Fig. 1). We also include the South Orkney Islands, and Elephant Island and Clarence Island (the northernmost South Shetland Islands) which are in the maritime Antarctic region (Fig. 1). The remaining South Shetland Islands are covered in the review of Antarctic Peninsula glacial history elsewhere in this Special Issue. Together with the Falkland Islands these sub-Antarctic and maritime Antarctic islands cover an area of approximately c. 26,000 km^2, just under half the area of Tasmania, or 1.3 times the area of Wales. This figure does not take into account the now-submerged offshore portions of the islands, which considerably increase the total area available for accommodating past glaciation.

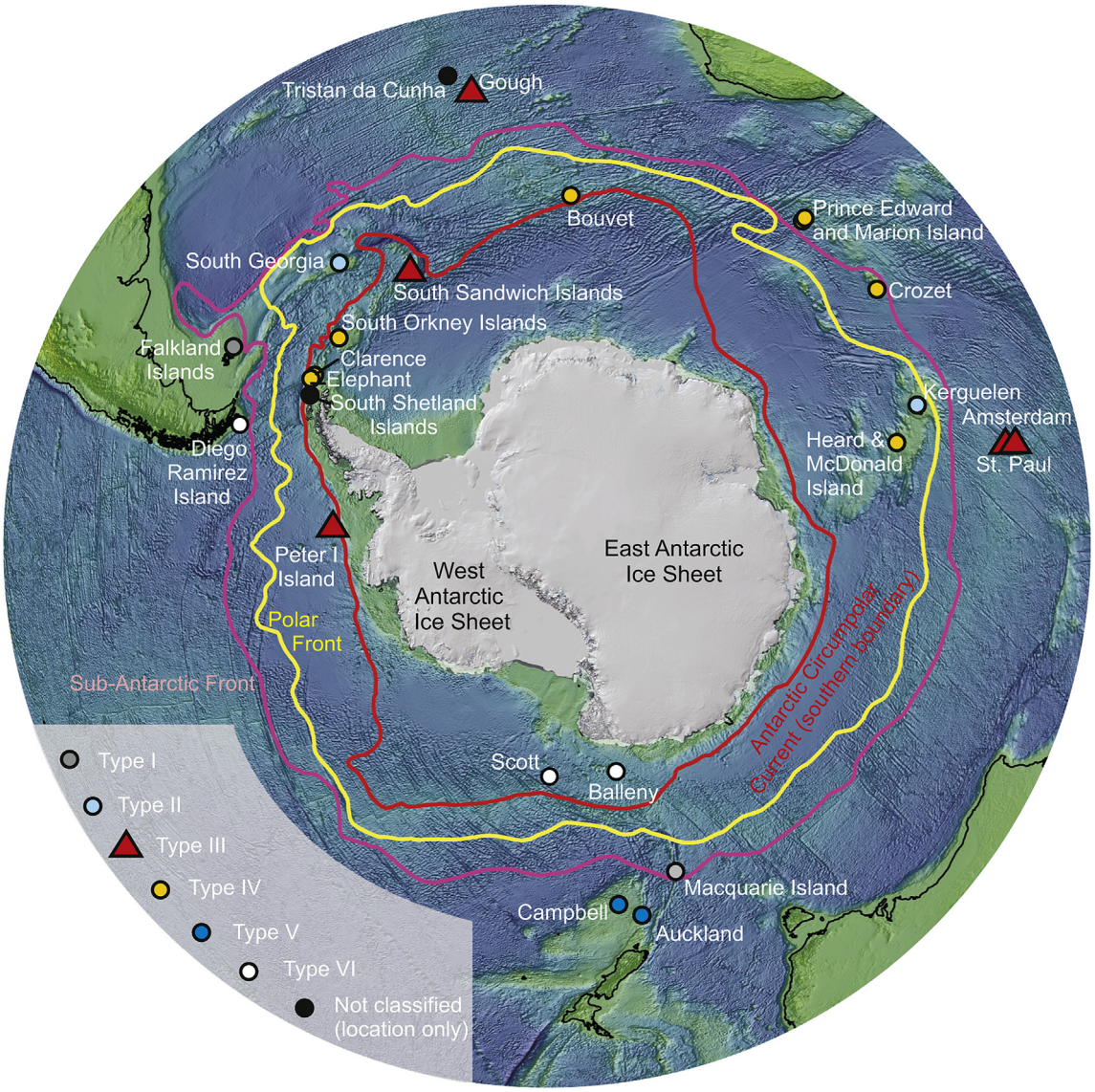

Fig. 1. Map and classification of the glacial history of the maritime and sub-Antarctic Islands included in this review, shown in relation to the position of the southern boundary of the Antarctic Circumpolar Current (red line), Antarctic Polar Front (yellow line), and sub-Antarctic Front (pink line).

We describe the sub-Antarctic and maritime Antarctic islands eastwards around the Southern Ocean, starting with the Atlantic sector then followed by the Indian Ocean and Pacific Ocean Sectors. Other approaches, such as latitudinal position relative to the Antarctic Polar Front, or mean altitude, would be equally valid from a glaciological perspective.

The geological origin of the sub-Antarctic islands has been described in detail by Quilty (2007). Their geological ages range from young volcanic islands such as Bouvet Island, Heard Island and the South Sandwich Islands, to islands composed of tectonically uplifted continental crust such as Macquarie Island or fragments of the continental crust of Gondwana, including islands on the Scotia Ridge such as South Georgia, the South Orkney Islands and Elephant and Clarence Islands.

The climates of the sub-Antarctic islands have been described by Pendlebury and Barnes-Keoghan (2007). However, these are based on measurements for a relatively short instrumental period, often at protected stations close to current sea level. Based on these datasets, mean temperatures of the coolest months range from −5 °C in the South Sandwich Islands to +11 °C at Amsterdam Island. Mean temperatures of the warmest month range from +1 °C in the South Sandwich Islands to +18 °C at Amsterdam Island. Mean annual precipitation ranges from 600 mm in the Falkland Islands to 3200 mm on Gough Island, although precipitation totals at high elevation (e.g., on South Georgia and Heard Island) are poorly constrained and could be considerably higher. The islands are influenced by a number of oceanic fronts including the Antarctic Polar Front, the sub-Antarctic Front and the South Subtropical Front (Fig. 1). All the islands are strongly influenced by the Southern Hemisphere Westerly Winds (mean wind speeds of 6–15 ms^{-1}), which mediate both the moisture supply required for snow accumulation and also the rate of evaporation and sublimation. Together, the temperature and moisture supply associated with the oceanic fronts, and the Southern Hemisphere Westerly Winds provide controls on the equilibrium line altitude and the thickness and extent of the region's glaciers.

While falling within the sub-polar belt, several New Zealand sub-Antarctic islands (Snares, Antipodes, Chatham, Bounty), were not considered in this review because they are of low mean altitude and no glacial deposits from the last glaciation have yet been

Table 1
Selected radiocarbon ages of peat and lake sediment deposits on the sub-Antarctic islands used here as minimum age constraints for deglaciation. Calibration of radiocarbon dates was undertaken using the CALIB 6.01 and the SHcal04 Southern Hemisphere data set (McCormac et al., 2004). Where dates were beyond the SHcal04 calibration period then the intcal09.14c dataset was used (marked with*). Other superscript markers denote: [a] extrapolated age; [**] see stratigraphic comment in Selkirk et al. (1998); [R] Age rejected by the original authors; [V] represents an unreliable minimum age for deglaciation as accumulation of sediments follows a volcanic event; R^1 calibrated using the Marine 09 data set with a Delta R of 948 (based on a local reservoir correction of 1348 (Herron and Anderson, 1990: p.268) minus the global marine reservoir of 400); the small size of these samples, taken over 5 and 2.5 cm slices, means that the ages from core PC 85–23 are likely to carry significant error; R^2 calibrated using the Marine 09 data set with a Delta R of 2509 (based on a local core top reservoir correction of 2909 minus the global marine reservoir of 400).

Site name	Sample ID	Latitude	Longitude	Elevation (m a.s.l.)	Material dated/ Stratigrpahic depth	Reported ^{14}C age	Calibrated age range 2 sigma	Source publication
Falkland Islands								
Plaza Creek	SRR-3906	51°23′18″S	58°29′20″W	<5	Peat	35,970 ± 280	40,521–41,705*	Clark et al., 1998
Hooker Point	–	51°42′00″S	57°46′49″W	0	Peat	–	c. 17,000	Long et al., 2005
Lake Sullivan	SRR-3898	51°49′57″S	60°11′27″W	–	Peat	13,610 ± 45	16,573–16,950*	Wilson et al., 2002
Beauchene Island	–	52°54′00″S	59°11′00″W	–	Peat	–	c. 12,500	Lewis Smith and Clymo, 1984
Port Howard, Site 9						9280 ± 260	9765–[11,000*]	Barrow, 1978
Elephant and Clarence Islands								
Walker Point, Elephant Island	LU-2952	61°08′35″S	54°42‘ 01′W	200–220	Moss peat	5350 ± 60	5927–6211	Björck et al., 1991
South Orkney Islands								
S. Orkney Plateau, Site PC85-23		60°49.10″S	45°44.70″W	304(–)	Marine pelecypods, 264–269 cm	11,535 ± 900	9442–13,848^{R1}	Herron and Anderson, 1990
S. Orkney Plateau, Site PC85-23		60°49.10″S	45°44.70″W	304(–)	Marine pelecypods, 83.5–86 cm	9570 ± 2180	4177–15,099^{R1}	Herron and Anderson, 1990
S. Orkney Plateau, GC02-SOI03	NZA 18576	60°22′S	47°00′W	786(–)	Marine sediment, 502 cm	10,542 ± 70	8348–8660^{R2}	Lee et al., 2010
Sombre Lake, Signy Island	AA-10691	60°41′12″S	45°37′00″W	5	Lake sediment, 250–252 cm	6570 ± 60	7292–7517	Jones et al., 2000
Heywood Lake, Signy Island	AA-10704	60°41′24″S	45°36′31″W	4	Moss fragment, 238–240 cm	5890 ± 60	6484–6791	Jones et al., 2000
Site ‘C’, Signy Island	SRR-1089				Moss bank, 125 cm	4801 ± 300	4799–6183	Fenton and Smth, 1983; Fenton, 1982
Site ‘D’, Moss Braes Signy Island	BETA-281,618	60°68′S	45°62′W	112	Moss bank, 178 cm	2860 ± 40	2784–3006	Royles et al., 2012
South Georgia								
Tønsberg Point, Lake 1	UA-2991	54°10′02″S	36°41′30″W	–	Lake sediment, 499 cm	15,715 ± 150	18,621–19,329*	Rosqvist et al., 1999
Gun Hut Valley, Site 4	SRR-736				Peat, 258 cm	9493 ± 370	9650–12150	Barrow, 1978
Gun Hut Valley	SRR-1979				Peat, 350 cm	9700 ± 50	10,550–11600	in Van der Putten and Verbruggen, 2005
Tønsberg Point, Tønsberg sequence	UtC-4179	54°10′S	36°39′W	–	Peat, 308 cm	9520 ± 80	10,512–10893	Van der Putten et al., 2004
Dartmouth Point	SRR-1165	54°19″S	36°26′W	–	Peat	9433 ± 120	10,264–10,869	Smith, 1981
Husdal, Sink Hole sequence	UtC-3307	54°11′24″ S	36° 42′ 12″ W	–	Peat, 460 cm	9160 ± 110	10,113–10,570	Van der Putten et al., 2012
Tønsberg Point Lake 10	UtC-6232	54°10′09″S	36°39′54″W	–	Lake sediment, 447 cm	9060 ± 50	10,116–10249	Van der Putten and Verbruggen, 2005
Grytviken	SRR-1168			–	Peat, 460 cm	8737 ± 50	9536–9795	Smith, 1981
Maiviken	SRR-1162	54°15″S	36°29′W	–	Peat, 180 cm	8657 ± 45	9495–9680	Smith, 1981
Gun Hut Valley, Site 3					Peat, 160 cm	8537 ± 65	9396–9553	Barrow, 1978
Husvik Harbour, Kanin Point	UtC-6866	54°11′09″S	36°41′44″W	–	Peat, 312 cm	8225 ± 45	9009–9270	Van der Putten et al., 2009
Black Head bog	Beta-271,303	54°04′07″S	37°08′41″W	43	Peat, 373 cm	8110 ± 50	8723–9123	Hodgson, D.A. (unpublished data)
Prince Olav Harbour Lake 1	Beta-271,300	54°04′24″S	37°08′08″W	335	Lake sediment, 197 cm	7110 ± 40	7788–7969	Hodgson, D.A. (unpublished data)
Fan Lake, Annenkov Island	SUERC-12584	54°29′55″S	37°03′03″W	90	Lake sediment, 584 cm	6953 ± 37	7656–7839	Hodgson, D.A. (unpublished data)
Husdal River site	UtC-6869	54°11′51″ S	36°42′12″ W	–	Peat, 300 cm	6840 ± 40	7571–7690	Van der Putten et al., 2013
Husdal	UtC-6867	54°11′63″ S	63°42′92″ W	–	Peat, 290 cm	6415 ± 40	7174–7418	Van der Putten et al., 2013
Gough Island								
					Peat	>43,000		Bennett et al., (1989)
Marion Island								
Macaroni Bay – extrapolated age	–			50	Peat, 300 cm	–	c. 17320[a]	Van der Putten et al., 2010
Macaroni Bay	K-1064			50	Peat, 175–185 cm	9500 ± 140	10,374–[11,000*]	Schalke and van Zinderen Bakker, 1971
Macaroni Bay	I-2278			50	Peat, 275–295 cm	10,600 ± 700	10,371–13841*	Schalke and van Zinderen Bakker, 1971^{R}
Kildakey Bay peat section	Pta-3208				Peat, 600 cm	7300 ± 70	7934–8198	Scott, 1985
Skua Ridge, First boring	Pta-3214				Peat, 130–140 cm	6930 ± 90	7574–7873	Scott, 1985

Table 1 (*continued*)

Site name	Sample ID	Latitude	Longitude	Elevation (m a.s.l.)	Material dated/ Stratigrpahic depth	Reported ^{14}C age	Calibrated age range 2 sigma	Source publication
Albatross Lakes, Third boring	Pta-3232				Peat, 353–363 cm	5990 ± 70	6601–6950	Scott, 1985
Albatross Lakes, Fourth boring	Pta-3231				Peat, 165–180 cm	4140 ± 70	4426–4744	Scott, 1985
Crozet – Ile de la Possession								
Base A. Faure, Baie du Marin	KIA-19231	46°25′49″S	51°51′31″E	110	Peat, 402 cm	9655 ± 60	10,750–[11,000*]^{V}	Van der Putten et al., 2010
Morne Rouge Volcano flank	KIA-31355	46°23′35.45″S	51°48′28.85″E	12	Peat, 197 cm	6110 ± 40	6779–7020^{V}	Ooms et al., 2011
Morne Rouge lake core	NZA-11510	46°23′26″S	51°48′45″E	50	Lake sediment, 405 cm	5750 ± 60	6389–6640^{V}	Van der Putten et al., 2008
Morne Rouge peat sequence	NZA-11509	46°23′26″S	51°48′45″E	50	Peat, 532 cm	5480 ± 60	6000–6316^{V}	Van der Putten et al., 2008
Kerguelen Islands								
Estacade	SacA 7753	49°16′ 03″S	70°32′29″E	7	Peat, 468 cm	13,190 ± 50	15,396–16,624*	Van der Putten et al., 2010
Golfe du Morbihan, Core 2					Peat 525 cm	11,010 ± 160	12,765–13,241*	Young and Schofield, 1973a,b
Ampère Glacier	2	49°23′50′S	69°10′14″E	265	Peat, sample 2	10,120 ± 90	11,336–12,054*	Frenot et al., 1997a
Ampère Glacier	1	49°23′50′S	69°10′14″E	260	Peat, sample 1	10,140 ± 120	11,264–12,151*	Frenot et al., 1997a
Ampère Glacier	3	49°23′42″S	69°10′55″E	280	Peat, sample 3	9930 ± 70	11,212–11,629*	Frenot et al., 1997a
Golfe du Morbihan, Core 1					Peat, 260 cm	8595 ± 125	9141–9912	Young and Schofield, 1973a,b
Ampère Glacier	4	49°23′ 47″S	69°09′55″E	240	Peat, sample 4	4590 ± 60	5054–5188	Frenot et al., 1997a
Ampère Glacier	5	49°24′ 15″S	69°10′23″E	30	Peat, sample 5	2220 ± 80	2098–2208	Frenot et al., 1997a
Ampère Glacier	6	49°24′ 15″S	69°10′23″E	30	Peat, sample 6	1960 ± 80	1732–1928	Frenot et al., 1997a
Ampère Glacier	7	49°23′ 47″S	69°09′55″E	240	Peat, sample 7	1670 ± 50	1384–1621	Frenot et al., 1997a
Ampère Glacier	8	49°24′ 15″S	69°10′23″E	30	Peat,, sample 8	1320 ± 70	1166–1282	Frenot et al., 1997a
Ampère Glacier	9	49°24′ 17″S	69°10′23″E	160	Peat, sample 9	900 ± 70	716–804	Frenot et al., 1997a
Heard Island								
Deacock Glacier moraine Long Beach	Wk 9485			4.2	Subfossil sedge, 250 cm	220±113	Modern–340	Kiernan and McConnell, 2008
Macquarie Island								
West Mt Eitel	SUA 3045	54°35′S	158°51′E	–	Freshwater diatom peat	Carbon dead	>40,000	Adamson et al., 1996
West Mt Eitel	Beta-57317	54°35′S	158°51′E	–	Freshwater diatom peat	Carbon dead	>40,000	Adamson et al., 1996
Emerald Lake	NZA 50,632	54°40′22″S	158°52′14″E	170	Lake sediment, 90 cm	13,659 ± 56	16,620–16,987*	Saunders, K (unpublished data)
Palaeolake Skua	SUA 2736	54°37′S	158°50′E	180	Lake sediment, 1360 cm	13,570 ± 150	15,975–17,034*	Selkirk et al., 1991
Palaeolake Skua	Beta-20165	54°37′S	158°50′E	180	Lake sediment, 900 cm	12,470 ± 140	14,063–15,119*	Selkirk et al., 1988
Palaeolake Toutcher	Beta-20162			200	Lake sediment	11,010 ± 200	12,579–13,276*	Selkirk et al., 1988
Finch Creek Ridge	Beta-1386	54°34′S	158°54′E	100	Peat, 182 cm	10,275 ± 230	11,284–12,581*	Selkirk et al., 1988**
Palaeolake Nuggets	SUA-1894			30	Lake sediment, 440 cm	9400 ± 220	10,146–[11,000*]	Selkirk et al., 1988
Palaeolake Sandell	Beta-20163			210	Lake sediment, >420 cm	7960 ± 110	8185–8639	Selkirk et al., 1988
Green Gorge Ridge	SUA-2164	54° 38′S,	158°54′E	100	Peat, 130 cm	7200 ± 130	7682–8203	Selkirk et al., 1988
Wireless Hill	Beta-1387			100	Sandy peat, 360 cm	5140 ± 140	5586–6200	Selkirk et al., 1982
Finch Creek Ridge	SUA-1845X	54°34′S,	158° 55′E	100	Peat, 190 cm	5930 ± 240	6206–7272	Selkirk et al., 1988
Campbell Island								
Homestead Scarp	Wk-19746	52°33′S	169°08′E	30	Peat	13,648 ± 73	16,577–16,997*	McGlone et al., 2010
Hooker Cliffs	NZ 6898	52°28′S	169°11′E	60	Peat	12,950 ± 200	14,845–16,629*	McGlone, 2002
Mt Honey	Wk-13466	52°34′S	169°08′E	120	Peat	12,445 ± 76	14,132–15,024*	McGlone et al., 2010
Rocky Bay	NZ 6984	52°33′S	169°04′E	130	Peat	11,700 ± 90	13,352–13,767*	McGlone, 2002
Auckland Island								
McCormick Peninsula	NZA 4509	50°32′S	166°13′E	25	Peat	15,170 ± 140	18,009–18,672*	McGlone, 2002
Deas Head	NZA 4607	50°32′S	166°13′E	20	Peat	11,951 ± 95	13,496–14,031*	McGlone et al., 2000
Hooker Hills	NZA 9293	50°33′S	166°10′E	275	Peat	10,859 ± 77	12,590–12,926*	McGlone et al., 2000

reported (McGlone, 2002). The sub-Antarctic islands of the Cape Horn archipelago are also excluded, but readers are referred to Sugden et al. (2005) for a recent review.

2. Methods

This review synthesises the existing literature on maritime and sub-Antarctic island glaciation incorporating earlier brief reviews of the regional glacial history by Hall (2004), Hall (2009) and Hall and Meiklejohn (2011), together with new and unpublished data from the contributing authors. We summarise evidence for late Quaternary (particularly post-LGM) glaciation on each of the islands, and where possible differentiate age constraints derived from robustly defined glacial features with age constraints from features whose provenance and age are less well established. Where age constraints for glacial features are unavailable we identify minimum ages for deglaciation based on, for example, the onset of peat formation and lake sediment deposition.

Where possible the standardised approach for the reporting of age constraints developed by the ACE/PAIS community ice sheet reconstruction team was applied (Tables 1and 2). For example, radiocarbon dates are reported as conventional ages (with errors) and as calibrated age ranges (2-sigma) and, where required, corrected for marine reservoir effects. Radiocarbon dates were

Table 2
Selected cosmogenic isotope exposure ages that can be used to provide constraints on glaciation in parts of the Falkland Islands (Prince's Street stone runs) and South Georgia (Husvik and Greene Peninsula). Cosmogenic ages were recalculated from Wilson et al. (2008) and Bentley et al. (2007) using the latest version of the CRONUS online calculator (Balco et al., 2008) (Wrapper script: 2.2; Main calculator: 2.1; Constants: 2.2.1; Muons: 1.1). We used a standard atmosphere flag for all samples, and South Georgia samples have an assumed density of 2.5 g/cm^3. We calculate mean and weighted mean ages of the samples along single moraines at Husvik and Greene Peninsula. [a]Model exposure age assuming no inheritance, zero erosion, density 2.65 g/cm^3, and a standard atmosphere using a constant production rate model and the scaling scheme for spallation of Lal (1991)/Stone (2000). This version of the CRONUS calculator uses a reference spallogenic ^{10}Be production rate of 4.49 ± atoms g^{-1} yr^{-1} (±1σ, SLHL) and muonogenic production after Heisinger et al. (2002a; 2002b).

Site name	Sample ID	Lat. (°S)	Long. (°W)	Elevation (m a.s.l.)	Elevation flag	Thickness of sample (cm)	Density (g cm^{-3}) Measured (italics), or assumed (normal)	Topographic shielding	Erosion rate	Isotope concentration	^{10}Be (atoms g^{-1})	^{10}Be Standard	^{26}Al (atoms g^{-1})	^{26}Al/^{10}Be ratio	^{26}Al Standard	Exposure age (yr)	Internal uncertainty (yr)	External uncertainty (yr)	Mean age (yr)	error (yr)	Weighted mean age (yr)	error (yr)
Falkland Islands																						
Prince's Street - stone runs (max)	PS/VAB-03	-51.61	-58.09	101	std	4.4	2.71	0.997	0	3.72E+06	1.48E+05	NIST_27900	1.87E+07	8.40E+05	Z92-0222	827366	40765	97892				
Prince's Street - stone runs (min)	PS/HSB-04	-51.62	-58.09	152	std	4.3	2.56	0.995	0	2.64E+05	1.30E+04	NIST_27900	1.81E+06	8.00E+04	Z92-0222	46275	2305	4674				
South Georgia																						
Husvik	HUS1	-54.1814	-36.7199	65	std	5	2.50	0.98	0	6.81E+04	1.00E+04	S555	0.00E+00	0.00E+00		11506	1695	1969				
Husvik	HUS2	-54.1814	-36.7191	65	std	5	2.50	0.98	0	8.33E+04	1.58E+04	S555	0.00E+00	0.00E+00		14084	2681	2948				
Husvik	HUS4	-54.1814	-36.7175	49	std	5	2.50	0.98	0	6.16E+04	2.80E+04	S555	0.00E+00	0.00E+00		10574	4819	4906	12055	5769	12107	1373
Greene Peninsula	GRE5	-54.3205	-36.4235	15	std	5	2.50	1	0	7.36E+04	4.45E+04	S555	0.00E+00	0.00E+00		12811	7771	7851				
Greene Peninsula	GRE1	-54.337	-36.6019	162	std	5	2.50	0.99	0	2.59E+04	1.41E+04	S555	0.00E+00	0.00E+00		3925	2139	2166				
Greene Peninsula	GRE2	-54.3349	-36.4525	150	std	5	2.50	0.99	0	2.23E+04	1.62E+04	S555	0.00E+00	0.00E+00		3419	2486	2503				
Greene Peninsula	GRE3	-54.3368	-36.4519	155	std	5	2.50	0.99	0	2.23E+04	1.67E+04	S555	0.00E+00	0.00E+00		3402	2550	2567				
Greene Peninsula	GRE4	-54.3335	-36.453	160	std	5	2.50	1	0	2.22E+04	1.17E+04	S555	0.00E+00	0.00E+00		3338	1761	1784	3521	4512	3515	1080

recalibrated with the calibration curves in CALIB 6.01. Where the data are available the type of organic material dated, its location and stratigraphic context are also reported.

Evidence of glaciation described in the paper includes: (1) geomorphological and geological evidence for ice presence such as glacial troughs and subglacial till; (2) ice marginal landforms including moraines, till deposits, polished rock and striae, proximal glacigenic deposits, and minimum ages for deglaciation from basal peat deposits and lake sediments; (3) ice thickness constraints taken from trimlines, drift limits and exposure age dates, along with indirect constraints from raised marine features and; (4) constraints based on molecular biological data that provide limits on the maximum extent of glaciers (Convey et al., 2008). Further details of data sources are provided within the individual case studies.

3. Results

3.1. Atlantic sector

3.1.1. Falkland Islands

The landscape of the Falkland Islands (51°45′S, 59°00′W, 12,173 km^2) is dominated by periglacial features. There is little evidence of LGM ice apart from the small cirques and short (max. 2.7 km) glacially eroded valleys described by Clapperton (1971a) and Clapperton and Sugden (1976). These occur on East Falkland at Mount Usborne and on West Falkland at Mount Adam and the Hornby Mountains. The minimum age of deglaciation of these cirques has not yet been determined, but chronological analyses of basal lake sediments in those occupied by tarns, or cosmogenic isotope analyses of moraines reported in some cirques, could provide this data.

The absence of widespread LGM glaciation at altitude is supported by cosmogenic isotope (^{10}Be and ^{26}Al) surface exposure dates on valley-axis and hillslope stone runs (relict periglacial block streams) which range from 827,366 to 46,275 yr BP (Wilson et al., 2008, Table 2). These old ages suggest not only an absence of large scale glaciation at the LGM, but also the persistence of periglacial weathering and erosion features, through multiple glacial-interglacial cycles. These features include coarse rock debris, silt and clay regoliths, and sand (Wilson et al., 2008). OSL dating of the sediments that underlie some stone runs suggest a period of enhanced periglacial activity between about 32,000 and 27,000 yr BP, and also confirms that parts of the stone runs may have been in existence from before 54,000 yr BP substantially pre-dating the LGM (Hansom et al., 2008).

Peat deposits as old as 40,521–41,705 cal yr BP have been found at Plaza Creek (Clark et al., 1998). Other peat sections, for example at Hookers Point (Long et al., 2005) and Lake Sullivan (Wilson et al., 2002) show peat accumulation commenced at c. 17,000 cal yr BP, and 16,573–16,950 cal yr BP respectively, presumably at a time of increased moisture supply (Table 1). Elsewhere the base of peat deposits has been dated to the Lateglacial/early Holocene, for example at 12,500 cal yr BP on Beauchêne Island (Lewis Smith and Clymo, 1984) and 9765–11,000 cal yr BP at Port Howard (Barrow, 1978). Studies of Quaternary environments (e.g., Clark et al., 1998; Wilson et al., 2002) provide no evidence of LGM glaciation beyond the cirques and small valley glaciers, and there are no studies, or bathymetric data that show evidence for LGM glaciers extending offshore.

3.1.2. Elephant Island and Clarence Island (maritime Antarctic)

Elephant Island (61°08′S, 55°07′W, 558 km^2) is a 47 × 27 km mountainous island at the northern limit of the South Shetland Islands (Figs. 1 and 2). It has a maximum elevation of 853 m at

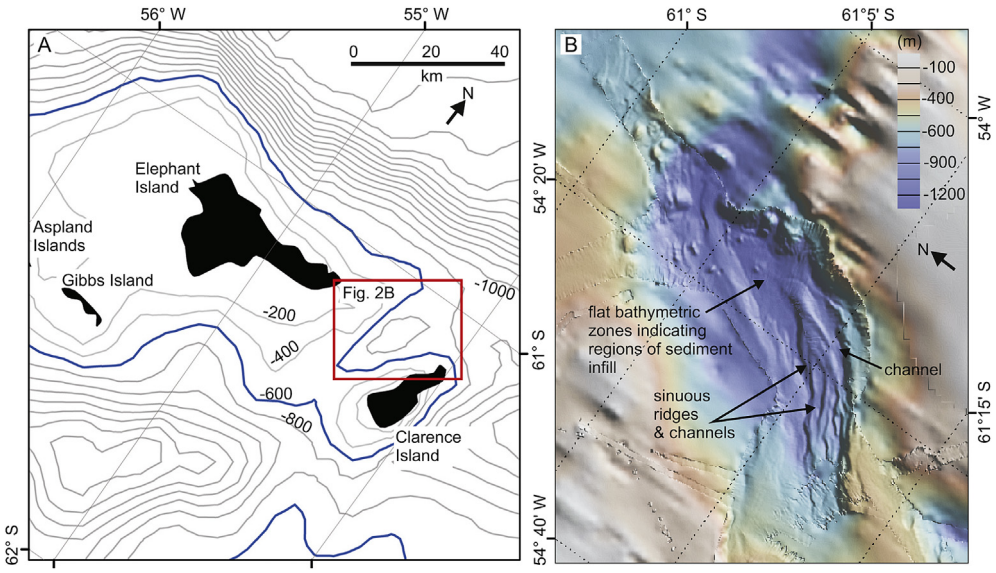

Fig. 2. (A) Regional bathymetric plot showing the large shallow continental shelf (<200 m depth) connecting Elephant Island, Gibbs Island and the Apsland Islands. In contrast, Clarence Island falls away steeply on all sides to ocean depths of at least 600 m. (B) Elephant Island and Clarence Island are separated by an over deepened trough in excess of 1300 m water depth with sinuous ridges and channels partially covered by a substantial sediment infill. Note the different orientations of the figures.

Pardo Ridge. Twenty km to the east, Clarence Island (61°12′S 054°05′W) is a 19.3 km long island that rises steeply to 2300 m at Mt Irving (Fig. 2). The islands are part of the Mesozoic Scotia metamorphic complex on the Scotia Ridge (Marsh and Thomson, 1985). Both are heavily glaciated today, with numerous tidewater glaciers. Offshore, bathymetry data show that Elephant Island shares a shallow continental shelf of ~200–600 m water depth with the two smaller outlying Gibbs and Aspland Islands 30–40 km to the south west (Fig. 2A). A significant proportion of this shelf is shallow (<200 m) suggesting the presence of a large area available for ice accumulation during glacial low stands, consistent with the majority of South Shetland Islands and the western Antarctic Peninsula.

In contrast, the bathymetry surrounding Clarence Island falls away steeply on all sides to ocean depths of at least 600 m. There are no clear glacial troughs radiating from Elephant Island in existing bathymetric datasets, but there appears to be an over deepening (a trough in excess of 1300 m water depth) in the breach between Elephant Island and Clarence Island to the east. Within this trough, there is no evidence of former ice grounding, for example in the form of streamlined bed forms as observed in troughs elsewhere along the west Antarctic Peninsula shelf (Fig. 2B). Instead, sets of sinuous ridges and channels are observed which are partially covered by a substantial sediment infill, forming flat and featureless bathymetric zones in the base of the trough. While we cannot rule out a glacial origin for these ridge/channel features (e.g., as subglacial eskers or meltwater channels), there is no indication in the surrounding valley sides for substantial glacial moulding of the landscape and thus former ice overriding. At the shelf break around Elephant Island, multibeam data are similarly inconclusive over the presence or absence of geomorphic features that might have formed at grounding line positions if local ice had extended towards the shelf break in the past.

No marine geochronological data constraining offshore ice extent or deglaciation have been reported. At Elephant Island a basal age from the deepest known moss bank in Antarctica at Walker Point provides a minimum age for local deglaciation onshore of 5927–6211 cal yr BP (Björck et al., 1991).

3.1.3. South Orkney Islands (maritime Antarctic)

The South Orkney Islands (60°35′S, 45°30′W, 620 km^2), an archipelago located 600 km north-east of the tip of the Antarctic Peninsula, comprises four main islands: Coronation Island which rises to 1266 m, Laurie Island, Powel Island and Signy Island. Their geology consists of folded metamorphic sediments (Matthews and Malling, 1967) forming part of the Scotia Ridge. Geomorphological mapping by Sugden and Clapperton (1977), together with seismic data and piston cores obtained from the South Orkney Islands plateau during DF-85 (USCGC *Glacier)* by Herron and Anderson (1990), provide the only published data constraining the offshore extent of grounded ice at the LGM. These studies described several offshore glacial troughs fed by glaciers draining an expanded ice cap. A seismic profile across the western plateau showed a prominent glacial unconformity between the 250–300 m isobaths, interpreted as marking the limit of grounded ice during the most recent phase of extensive glaciation (Herron and Anderson, 1990; Bentley and Anderson, 1998). To constrain the age of this unconformity, piston cores and sediment grabs were recovered from 35 locations. Only a handful of the cores penetrated glacier proximal/subglacial till but nevertheless confirmed that grounded ice reached to at least 246 m water depth (core 85–21) but possibly as deep as 311 m (core 85–30). Radiocarbon analyses of articulated pelecypod shells found within diatomaceous glacial marine sediment at South Orkney Plateau Site PC 85–23 indicated that the ice cap had retreated from the inner portion of the plateau and to within 15 km of Signy Island prior to 9442–13,848 cal yr BP (11,535 ^{14}C yr BP, Table 1) (Herron and Anderson, 1990); although this had previously been reported as c. 6000–7000 years BP based on calculated accumulation rates (Herron and Anderson, 1990; Bentley and Anderson, 1998). Consistent with this deglaciation age, diatom ooze layers were accumulating at another site on the plateau by at least 8348 to 8660 cal yr BP (Lee et al., 2010). Analyses of the ice rafted debris (IRD) assemblage in slope cores, which were composed predominantly of material derived from the South Orkney Islands, led Herron and Anderson (1990) to speculate that the outer shelf was covered by a large ice shelf at the LGM. The presence of a much more extensive regional ice shelf, connecting the

South Orkney Ice cap with the Antarctic Peninsula Ice Sheet at the LGM has also been suggested by Johnson and Andrews (1986). However, this hypothesis is based on limited geological data and, whilst ice sheet models imply a more extensive ice shelf (Golledge et al., 2012; Pollard & DeConto, 2009), they indicate it was not contiguous with the Antarctic Peninsula. Thus, the alternative interpretation that the Antarctic Peninsula Ice Sheet and South Orkney Ice Cap behaved as independent ice centres must still be considered. New marine geological and geophysical data acquired from the South Orkney shelf by RRS *James Clark Ross* in 2011 (JR244) will hopefully resolve this issue (W. Dickens, personal communication).

On-shore, a minimum age for deglaciation can be inferred from the onset of lake sediment accumulation which began at Signy Island between 7292 and 7517 cal yr BP (Sombre Lake) and 6484–6791 cal yr BP (Heywood Lake) (Jones et al., 2000). Moss banks accumulated on Signy Island from 4799 to 6183 cal yr BP (Fenton, 1982; Fenton and Smith, 1983) and 2784–3006 cal yr BP (Royles et al., 2012).

3.1.4. South Georgia

South Georgia (54°17′S, 36°30′W, 3755 km^2) is a large heavily glaciated island 170 km long and 39 km wide dominated by the continental rock of the Allardyce and Salvesen Ranges, with the highest peak at Mt Paget (2934 m). Glacial geomorphological research on South Georgia is more advanced than most islands of the sub-Antarctic and includes studies on both the terrestrial and submarine glacial geomorphology, together with age constraints from lake sediments, peat deposits and moraines. Compilations of bathymetric soundings from the continental shelf have revealed large cross shelf glacial troughs, moraines and trough mouth fans on the shelf and adjacent slope (Graham et al., 2008). These observations suggest that one or more glaciations have extended to the continental shelf break (Fig. 3A) with their isostatic signature recorded by the raised beaches found at onshore altitudes of 6–10 m, 52 and 124 m a.s.l. (Clapperton et al., 1978). Early work assumed that the LGM glaciers extended across the continental shelf, although there was no chronological control on these periods of extensive shelf glaciation (Clapperton, 1990). More recent evidence based on the submarine geomorphology of the coastal fjords (Hodgson et al., 2014), combined with age constraints on land (Bentley et al., 2007) suggest that these continental shelf glaciations probably pre-date the LGM and that the LGM glaciers were most likely restricted to the inner fjords. The possibility that cold-based, generally non-erosive glaciers, were present at the LGM has not yet been considered in the literature.

Further evidence that the LGM was restricted to the inner fjords includes geomorphological mapping and cosmogenic isotope and radiocarbon dating of the onshore Lateglacial to Holocene moraines (Clapperton, 1971b; Sugden and Clapperton, 1977; Clapperton and

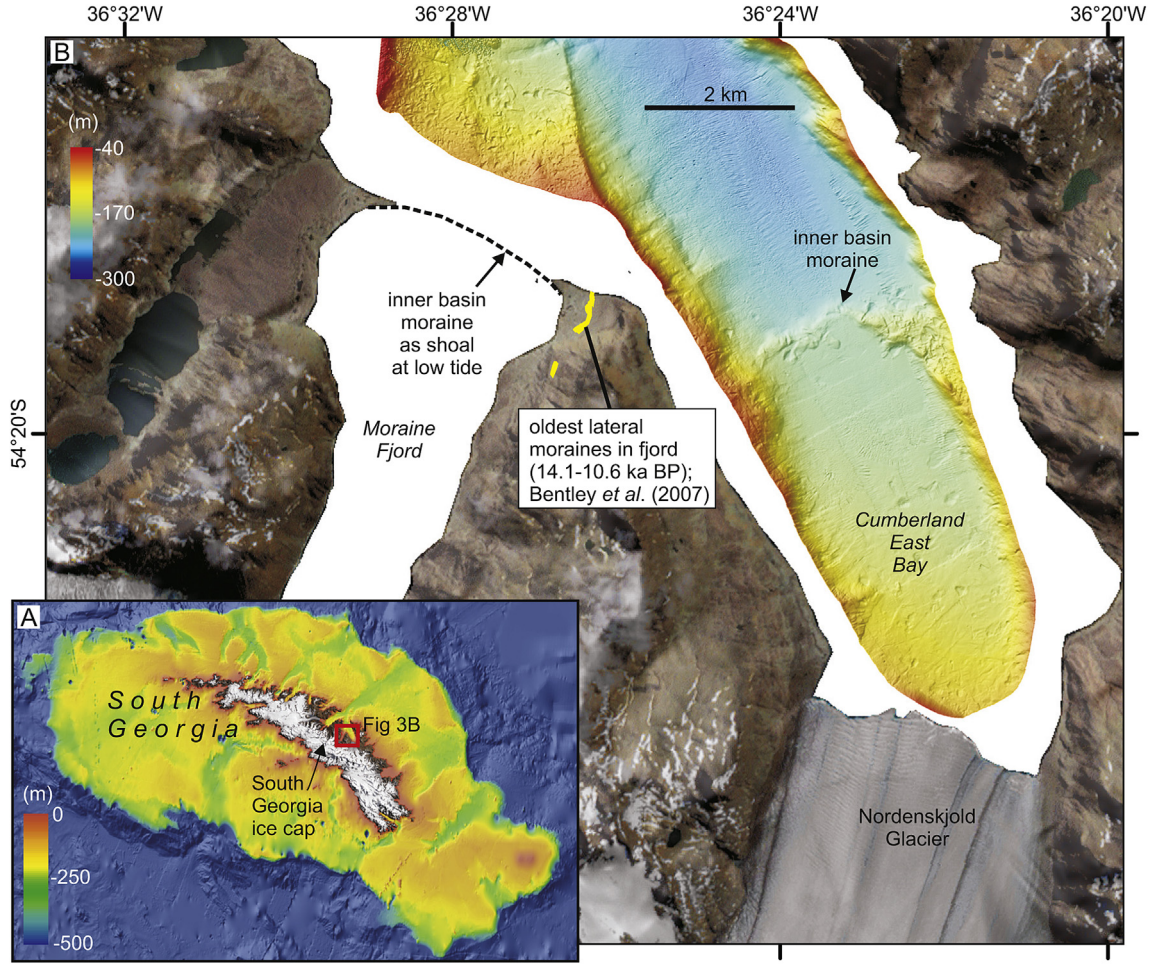

Fig. 3. (A) Map of the South Georgia continental block illustrating well-developed glacial cross-shelf troughs (bathymetric data from Fretwell et al. (2009). (B) Cumberland East Bay, South Georgia showing an example of the oldest dated terrestrial category 'a' moraines at the northern end of the Greene Peninsula east of Moraine Fjord (from Bentley et al. (2007)). These are shown, together with shipborne swath bathymetry data presented in Hodgson et al. (2014), illustrating the fjord-mouth ('inner basin') moraines in Moraine Fjord and Cumberland East Bay which are of presumed similar age. Bathymetry is shown at 5-m grid cell size.

Sugden, 1988; Clapperton et al., 1989; Bentley et al., 2007) which have been correlated with the submarine glacial geomorphology in the fjords (Hodgson et al., 2014). This evidence is supported by minimum deglaciation ages derived from the onset of lake sedimentation and peat formation (Clapperton et al., 1989; Wasell, 1993; Rosqvist et al., 1999; Rosqvist and Schuber, 2003; Van der Putten et al., 2004; Van der Putten, 2008). The oldest cosmogenic isotope dates on South Georgia range between 14,084 and 10,574 yr BP (Table 2). These mark the oldest mapped ice advance, estimated using an error-weighted mean to have occurred at 12,107 ± 1373 yr BP (Bentley et al., 2007). Evidence of this ice advance (which corresponds to Bentley et al.'s 'category 'a' moraines') is seen at Husvik and Greene Peninsula and can be correlated on geomorphological grounds with the oldest moraine ridges at Antarctic Bay, Possession Bay and Zenker Ridge. The clear offshore expression of these moraines can also be seen in the submarine glacial geomorphology. For example, in Moraine Fjord the ice advance is present as a bouldery shoal occupied by kelp beds visible at low tide, and in Cumberland East Bay, as a pronounced inner basin loop moraine spanning the entrance to the fjord (Fig. 3B).

Lake sedimentation in one inner fjord location on Tønsberg Point commenced as early as 18,621–19,329 cal yr BP (Rosqvist et al., 1999) but in other areas basal lake sediment dates are early Holocene in age. For example, Lake 10 on Tønsberg Point was deglaciated before 10,116–10,249 cal yr BP) (Van der Putten and Verbruggen, 2005), Fan Lake on Annenkov Island, situated off the south coast, was deglaciated before 7656–7839 cal yr BP and a lake adjacent to Prince Olav Harbour before 7788–7969 cal yr BP (Hodgson D.A. unpublished data) (Table 1). Glaciofluvial sediments were deposited at Husdal in Stromness Bay prior to 10,113–10,570 cal yr BP (Van der Putten et al., 2012) followed by the onset of peat formation. Elsewhere the earliest onset of peat formation ranges from 12,150–9650 cal yr BP to 11,600–10,550 cal yr BP at Gun Hut Valley (Barrow, 1978; Van der Putten and Verbruggen, 2005), 10,624–10,869 cal yr BP on Dartmouth Point (Smith, 1981), 10,512–10,893 cal yr BP on Tønsberg Point, 9009–9270 cal yr BP on Kanin Point (Van der Putten et al., 2009), 9495–9680 cal yr BP at Maiviken (Smith, 1981), a peat bog at Black Head in Prince Olav Harbour at 8723–9123 cal yr BP (Hodgson D.A. unpublished data), and 7571–7690 cal yr BP and 7174–7418 cal yr B.P at Husdal (Van der Putten et al., 2013) (Table 1). These dates are considered reliable as minimum age constraints for deglaciation as they are either based on plant macrofossils at the base of peat sequences or lake sediments, or on bulk basal lake sediments in which radiocarbon reservoirs are absent or well constrained. Raised marine features, interpreted as raised beaches, are also found at a relatively low level around the north east coast of South Georgia (2–3 m a.s.l. in Clapperton et al., 1978; <10 m a.s.l. in Bentley et al., 2007). Some of these features have been reinterpreted as being the result of fluvio-deltaic deposition at higher relative sea levels, such as the c. 9 m a.s.l. 'Line M' in Stromness Bay which may mark the inland position of a former coast line in Husdal (Van der Putten et al., 2013). Both interpretations imply a maximum of <10 m of post-glacial rebound since exposure of these areas by Holocene ice retreat, and in most cases just 2–3 m, although these features remain undated. The implication of these data taken together is that large parts of the South Georgia coastline, particularly the peninsulas along the north coast, were free of grounded ice very early on in the post-glacial interval—and possibly during the LGM – and that, contrary to previous suggestions (Clapperton et al., 1989), the LGM extent of the South Georgia ice cap was restricted to the inner fjords.

Late Holocene glacier fluctuations on South Georgia have also been identified and include lichen growth rate evidence from a series of ice-free moraine ridges down slope of two small mountain cirques in Prince Olav Harbour. These suggest ice retreat from the outermost moraines occurred between the end of the 'Little Ice Age' (post *c.* 1870) and the early 20th century, and from the innermost moraines during the second half of the 20th century (Roberts et al., 2010). The latter retreat has been linked to the well-documented warming trend since *c.* 1950 and can also be seen in the extensive photographic record the retreat of glacier fronts around South Georgia (Gordon et al., 2008; Cook et al., 2010).

Although our understanding of glaciation is relatively advanced for South Georgia, at least compared with other sub-Antarctic

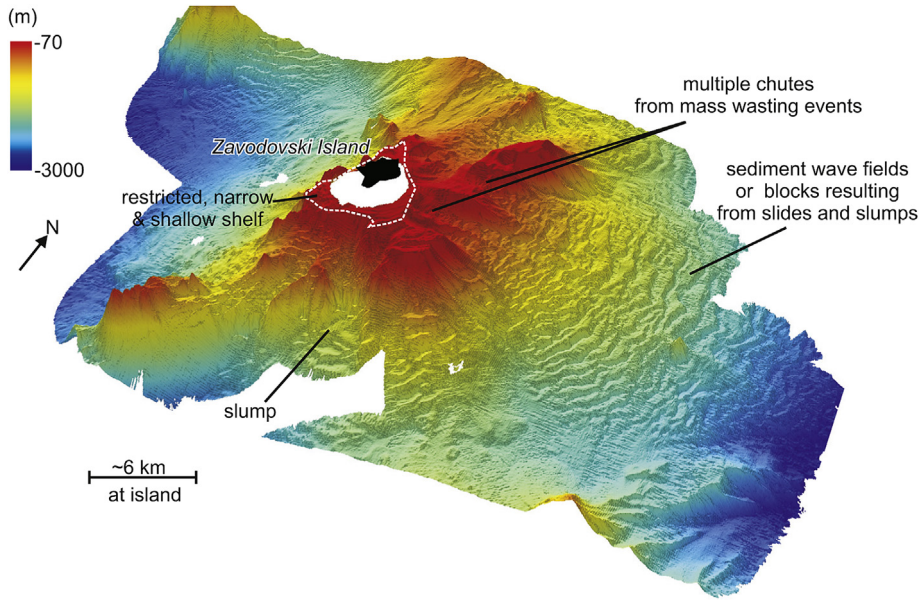

Fig. 4. Zavodovski Island, one of the South Sandwich Islands showing that the steep submerged slopes that flank these volcanic islands limit the potential for ice expansion offshore. The submarine geomorphology is dominated by features related to slope instability and volcanism and no distinct glacial features have been identified (Leat et al., 2010).

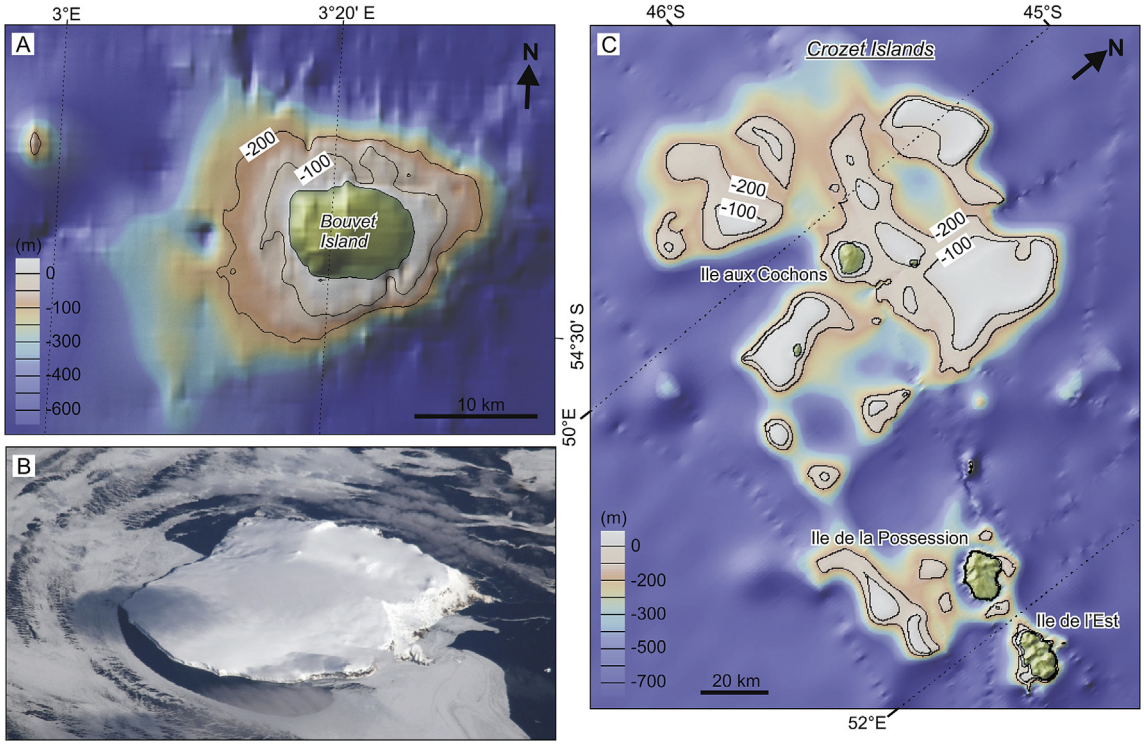

Fig. 5. Regional bathymetry around selected volcanic islands: (A) Bouvet Island, South Atlantic, and (C) the Crozet Islands, southern Indian Ocean, both drawn from the Global Multi-Resolution Topography (GMRT) synthesis (Ryan et al., 2009). Contours at −100 m and −200 m water depths illustrate shallow plateaus around Bouvet Island, as well as several of the islands of the Crozet archipelago. The satellite image (B) shows modern glacial cover on Bouvet Island, looking west from an altitude of 361 km; taken from the Image Science and Analysis Laboratory, NASA-Johnson Space Center. "The Gateway to Astronaut Photography of Earth." http://eol.jsc.nasa.gov/scripts/sseop/photo.pl?mission=ISS017&roll=E&frame=16161 last accessed 12/04/2012 12:48:51.

islands, there still remains a paucity of chronological control to constrain ice cap positions through the last deglaciation, particularly at ice-marginal positions offshore.

3.1.5. South Sandwich Islands

The South Sandwich Islands (56°20′S, 26°00′W to 59°20′S, 28°00′W, 618 km^2), comprise a 390 km long chain of submarine volcanic edifices that emerge as small volcanic islands at the eastern periphery of the Scotia Sea. The ten islands are strongly influenced by cold ocean currents from the Weddell Sea. They are up to 90% permanently ice covered (e.g., Montague Island) with variations in ice cover being the result of differences in altitude, and heat flow from the eruption of volcanoes. Areas of shallow shelf surrounding each edifice are limited, preventing widespread glaciation. The submerged slopes that flank the islands are mostly steep and fall away sharply into water depths >500 m depth (Leat et al., 2010) (Fig. 4) and many of the islands exhibit dynamic erosional coastlines (Allen and Smellie, 2008; Leat et al., 2010). Thus, any potential thicker ice cover at the LGM would have likely remained localised to the island summits and would have been restricted to extents very similar, if not identical, to those today. A close inspection of available multibeam bathymetric data for the South Sandwich arc confirms that no distinct glacial features are preserved in the sea-floor record, instead being dominated by features related to slope instability and volcanism (Leat et al., 2010) (Fig. 4). No studies have been carried out on the late Quaternary glacial history onshore, and there are no age constraints.

3.1.6. Bouvet Island

Bouvet Island or Bouvetøya (54°26′S, 3°25′E, 50 km^2) is located south of the Antarctic Convergence (Fig. 1). It consists of a single dominant active cone volcano (Fig. 5A). It is heavily ice-covered (~92%, Hall, 2004, Fig 5B) with many hanging glaciers discharging at the present coastline. A recent review (Hall, 2009) found that information on Quaternary glaciation is limited to observational data on glacier extent through the 20th century, with ice front variations in the order of 10–100 m (Mercer, 1967; Orheim, 1981). These were attributed to differences in aspect relative to the prevailing winds, as well as to local tidewater effects. The island consists of young oceanic crust, 4–5 Ma in age (Mitchell, 2003). On land, any record of Quaternary glaciations may have been obscured by continuing volcanism and tectonic activity, or remains covered today by extensive snow and ice. Offshore, the limited bathymetry data show a 3–4 km-wide shelf of <200 m water depth (Fig. 5A). Hence, even with extensive ice grounding onto the submarine shelf, any former ice cap on Bouvet Island probably had an aerial extent no larger than ~330 km^2. Even with complete ice cover, this would be comparable in size to some of the smaller glacier systems in Svalbard and the Southern Patagonian Ice Field today (World Glacier Monitoring Service, 1999, updated 2012; www.geo.uzh.ch/microsite/wgms/).

3.1.7. Gough Island

Gough Island (40°21′S, 9°55′W, 65 km^2) is a young (1 Ma) volcanic island. The island is not glaciated today, and appears to have no evidence of former glaciation. Bennett et al. (1989) dated a bedded, polleniferous peat sequence from the south-east of the island. They recovered an infinite radiocarbon age of >43,000 ^{14}C yr BP from the basal sediments, and argued for a continous occupation by the local flora through the last glacial-interglacial cycle. The well developed terraces around the coast (from −50 m below sea level to 75 m above sea level) are also considered to be the result of

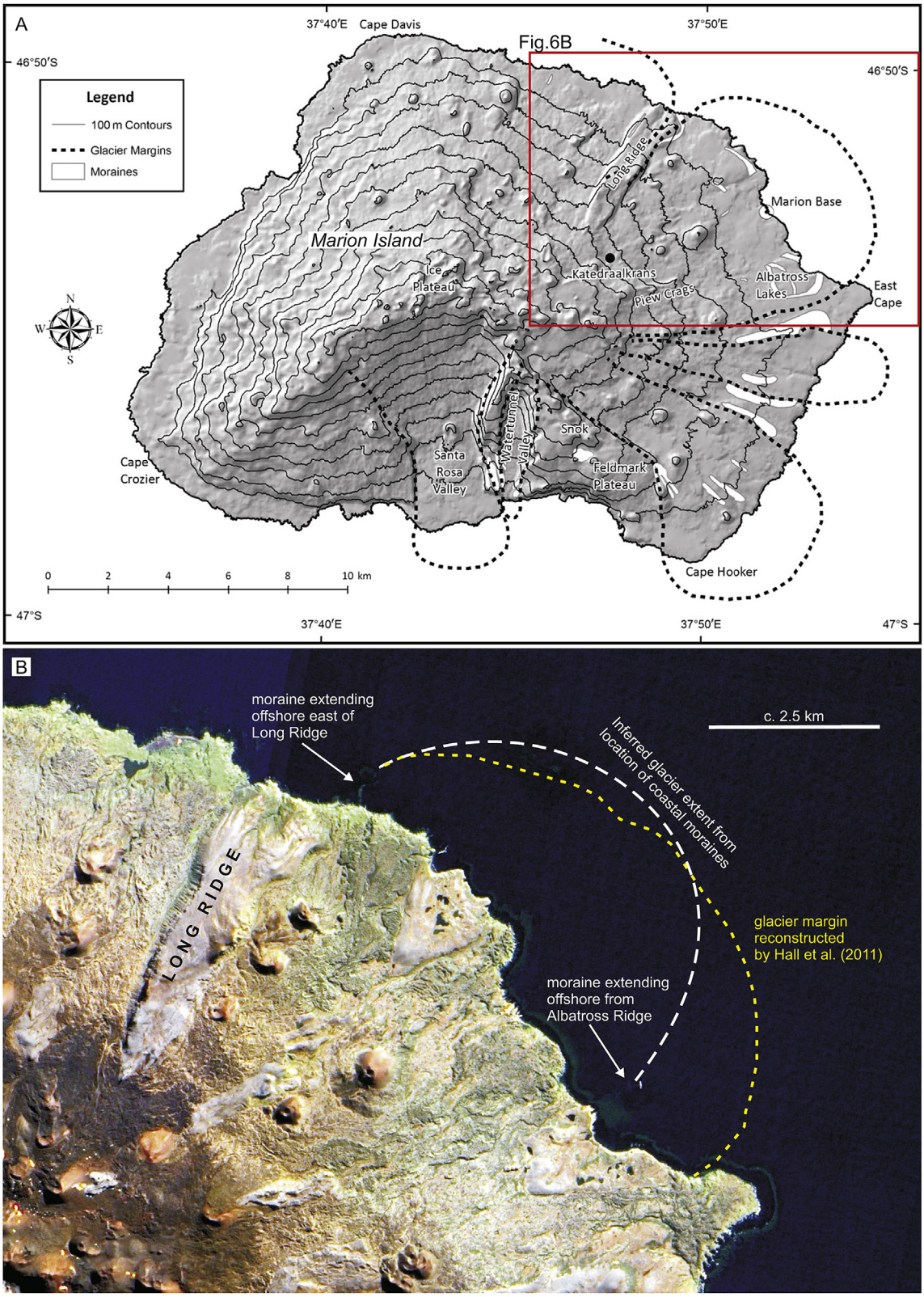

Fig. 6. (A) Reconstruction of palaeo-glaciers with limited offshore extent on sub-Antarctic Marion Island, based on glacial bedform evidence and landscape interpretations presented in Hall and Meiklejohn (2011). (B) Satellite image showing the position and orientation of some of the outer kelp beds, which may reveal the presence of offshore latero-frontal moraines from which former glacier positions can be inferred. An alternative hypothesis is that the kelp beds mark the termination of submarine lava flows.

progressive elevation during the evolution of the volcano, with those above sea level being related to coastal erosion at the last interglacial (3–4 m), Middle Pleistocene (12–15 m and 30 m) and earlier Pleistocene (55 m) and older (75 m). Those below sea level are thought to related to erosion during intervals of lower sea level during glaciation(s) (Quilty, 2007).

3.2. Indian Ocean Sector

3.2.1. Marion Island and Prince Edward Island

Marion Island (46°55′S, 37°45′E, 293 km^2) and Prince Edward Island (46°39′S, 37°57′E, 46 km^2) are young (0.45 Ma) active volcanic islands (McDougall et al., 2001; Boelhouwers et al., 2008) located on top of a small submarine plateau with a rapidly disappearing ice cap (Sumner et al., 2004). Up to eight volcanic, and five glacial episodes, have been inferred from K–Ar dating of striated outcrops, till, fluvioglacial deposits and glaciogenic deposits intercalated with lavas (McDougall et al., 2001). Some of the earlier volcanic episodes were correlated with glacial stages (Marine Isotope Stages 2, 4 10 and 12) and the four most recent episodes correlate or overlap with interglacials (Marine Isotope Stages 1, 3 5, 7). This data, together with recent geomorphological evidence (Boelhouwers et al., 2008), meant that the original hypothesis, that faulting and volcanic activity on Marion Island were periodically triggered by deglaciation (Hall, 1982), had to be reassessed (Hall et al., 2011).

The most recent advances in understanding the late Quaternary glacial and LGM glacial geomorphology of Marion Island are summarised by Boelhouwers et al. (2008) and Hall et al. (2011). These studies both suggest that the island was covered by a large LGM ice mass that separated into individual glaciers near their terminal margins (Fig. 6A). Raised beaches are also present which may be the result of isostatic rebound following deglaciation (Hall, 1977), or tectonic uplift. Thick tills at the present coastline, and the location and orientation of lateral moraines (e.g. flanking Long Ridge), suggest the likelihood of extensive seaward expansion of glaciers during times of lower glacial sea levels. Therefore, offshore evidence of the maximum extent of glaciers should be preserved on the continental shelf. Even though there are no high resolution bathymetric data for the coastal margins of the island, analysis of the present day coastline from aerial photographs and QuickBird satellite imagery (Fig. 6B) suggests that the position and orientation of some of the outer kelp beds (which indicate the presence of shallower water) may be revealing the presence of offshore terminal moraines from which the former position of glaciers could be inferred (Fig. 6B); similar to the kelp beds seen at the entrance to Moraine Fjord, South Georgia (Fig. 3B). Alternatively, the kelp beds could mark the termination of submarine lava flows. These different interpretations require further analysis through a programme of direct sampling and nearshore bathymetric survey.

Although the collective evidence suggests that glaciers extended beyond the coastline in many areas, phylogenetic studies of invertebrate communities (Chown and Froneman, 2008) and well-developed periglacial landforms, such as solifluction terraces and sorted patterned ground (e.g. Nel, 2001) show at least some inland areas remained exposed as nunataks during the last glacial period. For example, differences in phylogenetic substructure among populations of springtails (Myburgh et al., 2007), mites (Mortimer and van Vuuren, 2007; Mortimer et al., 2012) and the cushion plant *Azorella selago* (Mortimer et al., 2008) on the island are considered consistent with a hypothesis of within-island disjunction of populations by advancing glaciers, followed by population expansion from these refuges after glacial retreat (Fraser et al., 2012).

At present, there are few age constraints for the glacial features present on Marion Island. The base of one 3 m peat sequence from Albatross Ridge has been inferred at c. 17,320 years BP (Van der Putten et al., 2010) based on extrapolation from a date of 10,374–11,000 cal yr BP (9500 ± 140 ^{14}C yr BP, Table 1) reported at 175–185 cm within a 3 m long peat profile (Schalke and van Zinderen Bakker, 1971). This suggests the onset of deglaciation could be as early as c. 17,320 years BP in this area. However, this extrapolated date has been disputed as it assumes a uniform sedimentation rate which is questionable where tephra deposits are involved (Gribnitz et al., 1986), and because elsewhere on Albatross Ridge peat core basal ages of only 6601–6950 cal yr BP (depth: 353–363 cm) and 4426–4744 cal yr BP (depth: 165–180 cm) have been reported (Scott, 1985). On nearby Skua Ridge the oldest peat basal age is 7574–7873 cal yr BP and at Kildakey Bay it is 7934–8198 cal yr BP (Scott, 1985). As all these sites overlie old grey lavas they are considered reliable minimum ages for deglaciation. Other peat cores that have been taken on the island were dated at 3180 ± 20 ^{14}C yr BP (3316–3403 cal yr BP; Junior's Kop), 4020 ± 65 ^{14}C yr BP (4225–4587 cal yr BP; near the Marion Base Station), 2685 ± 130 ^{14}C yr BP (2351–3005 cal yr BP; Nellie Humps Valley) (Schalke and van Zinderen Bakker, 1971) and 4750 ± 40 ^{14}C yr BP (5316–5485 cal yr BP; near the Marion Base Station) (Yeloff et al., 2007), but as these overlie Holocene black lava flows they provide minimum age constraints on these volcanic episodes rather than deglaciation.

Some late Holocene (possibly Little Ice Age) ice advances have been inferred from striated basalt surfaces (Hall et al., 2011) and geomorphological evidence of Holocene ice is present in small cirque basins at Snok and the summit of the island (Boelhouwers et al., 2008). Similarly, perennial high altitude late Holocene snow cover and volcanic activity have been suggested from the absence of the large-scale relic periglacial landforms above 750 m a.s.l (Boelhouwers et al., 2008; Hedding, 2008). The last remnants of the Holocene ice cap had largely disappeared by the late 1990s (Sumner et al., 2004), presumably as a result of regional climate changes and/or geothermal activity (c. 1980 AD).

On nearby Prince Edward Island, Verwoerd (1971) found no geomorphological evidence of glacial activity. Whilst he attributed this to the lower altitude of the island, which rises to 672 m compared with Marion Island at 1240 m, he considered it unlikely that the island had entirely escaped Quaternary glaciation. From satellite images it may be possible to resolve glacial features similar to the moraines and other glacial features found on Marion Island, but further analysis and ground-truthing are required.

3.2.2. Crozet Islands

The Crozet Islands (46°25′S, 51°38′E, 400 km^2) consist of five main oceanic islands situated in the southern part of the Indian Ocean (Fig. 1). They are volcanic, built by several magmatic events which started about 8.1 Ma (Lebouvier and Frenot, 2007; Quilty, 2007). The islands are currently free of ice, but there is evidence of strong glacial erosion resulting in a series of radially arranged glacial valleys, a major cirque complex and related moraines on Île de l'Est, and three steep sided U-shaped valleys of likely glacial origin on Île de la Possession (Vallée des Branloires, Baie de la Hébé, Baie du Petit Caporal) (Lebouvier and Frenot, 2007; Quilty, 2007), together with mapped moraines and lakes formed by glacial activity (Chevallier, 1981). This suggests the presence of Quaternary glaciers (Camps et al., 2001; Giret et al., 2003), although earlier papers have suggested these may pre-date the LGM (Chevallier, 1981; Giret, 1987; Bougère, 1992; Hall, 2009) or were not glacial features (Bellair, 1965). Offshore, examination of bathymetric compilations shows no clear indication for past glaciations, although a significant portion of the surrounding sea-floor

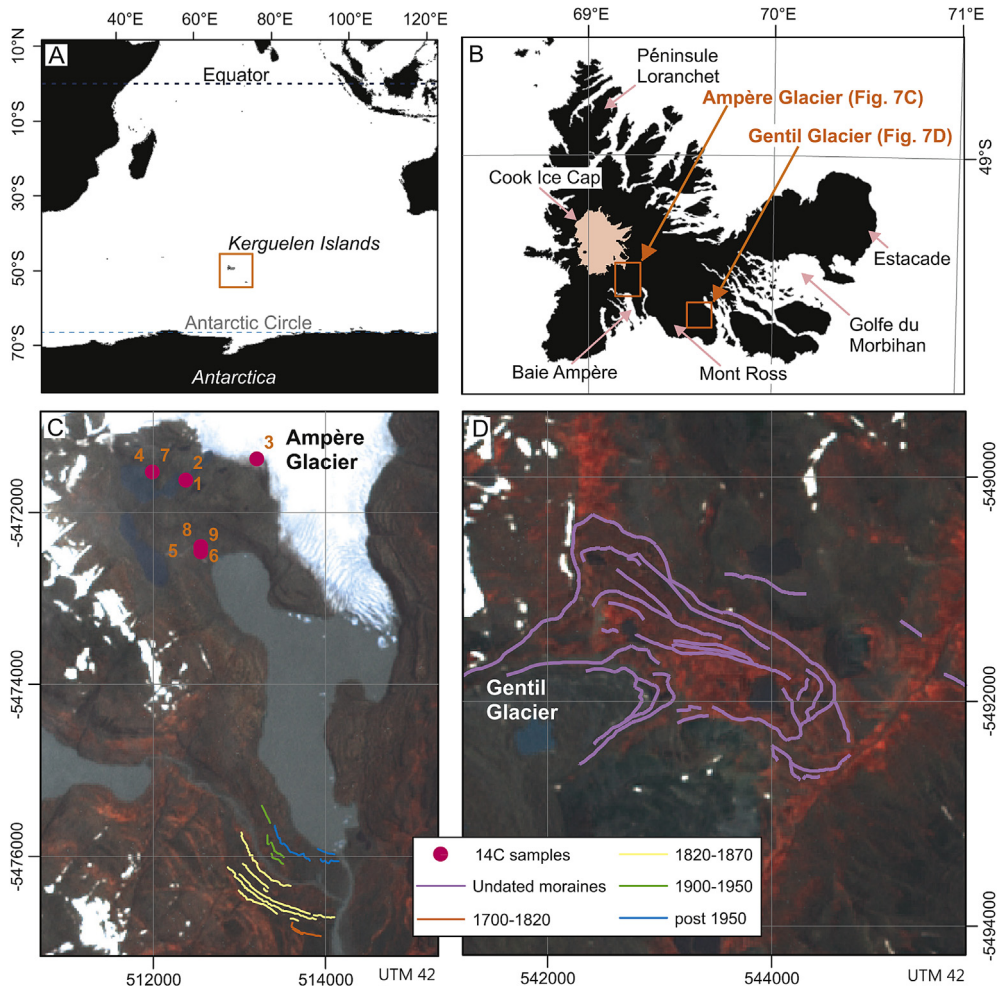

Fig. 7. (A) Location of the Kerguelen Islands. (B) Location of glaciological investigations at the Ampère Glacier and the Gentil Glacier. (C) The Baie d'Ampère showing the location of the 9 radiocarbon dated peat deposits listed in Table 1, and more recent moraines post AD 1700. (D) The Gentil Glacier frontal and lateral moraines at the base of Mont Ross that predate AD 934 ± 46 (1016 cal yr BP) based on the absence of a diagnostic ash layer from the Allouarn Volcano (Arnaud et al., 2009).

(~2500 km^2) lies at shallow depths, indicating the potential for more extensive ice accumulation during glacial lowstands (Fig. 5C). There is no chronology on glacial extents since the LGM, but palaeoenvironmental records suggest that Baie du Marin (close to the base Aflred Faure) must have been free of ice at 10,750–11,000 cal yr BP based on organic sediment layers in peat cores (Van der Putten et al., 2010) (Table 1). Additional dates from the Mourne Rouge flank in the Vallée des Branloires of 6779–7020 cal yr BP (Ooms et al., 2011) and basal dates from Mourne Rouge Lake of 6389–6640 cal yr BP and a peat sequence of 6000–6316 cal yr BP (Van der Putten et al., 2008) have also been published, but because these are from within the Morne Rouge volcano they are indicative of a minimum age for the eruption rather than a minimum age for deglaciation.

3.2.3. *The Kerguelen Islands*

The Kerguelen Islands (48°30′S, 68°27′E and 50°S, 70°35′E) consist of a main island (7200 km^2) surrounded by numerous smaller islands of mostly ancient (39–17 Ma) volcanic origin. The main island is characterised by mountains up to 1850 m (Mt Ross), the large 403 km^2 (in 2001) Cook Ice Cap on Le Dome (1049 m), and several glaciers on the western part of the island (Fig. 7). The eastern part of the island is generally of lower relief, but includes widespread evidence of glacial striations, glacial outwash and glacial moraines (Quilty, 2007).

Despite being one of the sub-Antarctic islands that remain partially glaciated, there is remarkably little information on the Quaternary glacial history of the Kerguelen Islands. Some studies have suggested that the main island may have been completely covered at the LGM (Hall, 1984); an interpretation at least partly supported by the presence of numerous ice-scoured lake basins (Heirman, 2011), U-shaped valleys radiating from the Cook Ice Cap, deeply-incised fjords and the lack of terminal moraines, which implies that ice may have extended offshore (Bellair, 1965). However, other studies have suggested that the LGM glaciation was limited (Nougier, 1972), and this is supported by the absence of present day isostatic rebound (Testut et al., 2005). This latter theory suggests that glaciers were restricted to the central plateau and to the east and south west where there are glacial erratics, aeolian sands, depressions filled with peat, gelifraction soils and moraine complexes, as well as residual valley glaciers and cirques. Conversely, in the north the highly degraded morphology of the moraines in the Loranchet Peninsula and the near absence of glacial erratics has been interpreted as evidence of more ancient glaciation (Nougier, 1972).

There are no chronological constraints on maximum glacier extent at the LGM. However, there are reliable minimum bulk

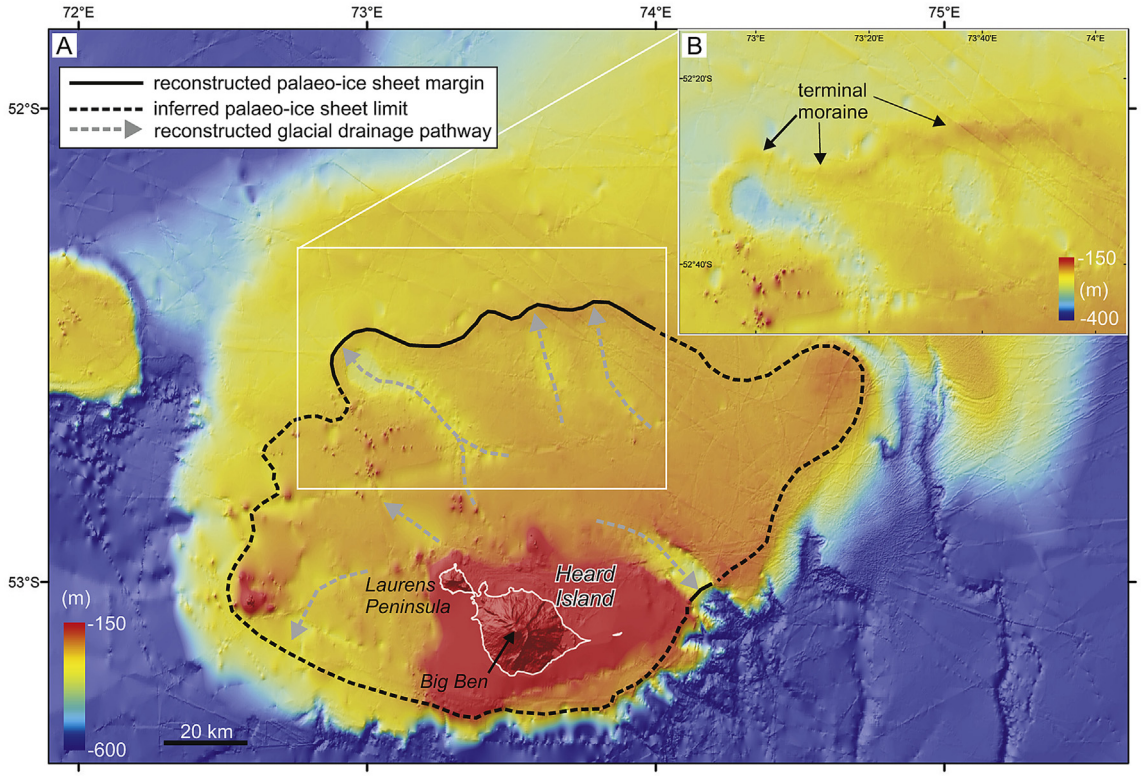

Fig. 8. (A) Regional bathymetric grid of Heard Island showing well-developed cross-shelf troughs and moraines extending as much as 50–80 km from the present shoreline. Data drawn from a compilation by Beaman and O'Brien (2011). (B) Inset showing higher resolution data at ~100 m grid cell size.

radiocarbon ages for deglaciation from peat deposits at Estacade, the Golf du Morbihan (Young and Schofield, 1973a), and the Baie d'Ampère (Fig. 7B), and geomorphological observations on the Gentil glacial moraines at the base of Mont Ross (Fig 7D). The oldest peat deposit at Estacade dates from 15,396–6,624 cal yr BP (Van der Putten et al., 2010) and at the Golfe du Morbihan from 12,765–13,241 and 9141–9912 cal yr BP (Young and Schofield, 1973a, 1973b). In the Baie d'Ampère the recent (post 1990 AD) retreat of the front of Ampère glacier has re-exposed a series of early Holocene peat deposits (Frenot et al., 1997b). One group provides minimum ages for deglaciation between 13,241 and 11,212 cal yr BP (Table 1, sample numbers 1–3, Fig 7C). These can be clearly separated from later periods of Holocene glacial retreat from 5054–5188 cal yr BP (Table 1, sample number 4, Fig. 7C), and 2208 to 716 cal yr BP (Table 1, sample numbers 5–9, Fig. 7C) that may correspond to warm periods inferred from peat deposits (e.g., Young and Schofield, 1973a). Other older frontal and lateral moraines associated with the Gentil Glacier have been identified at the base of Mont Ross (Fig 7D). It is not known if these date from the LGM, but they must predate AD 934 ± 46 (1016 cal yr BP) based on the absence of a diagnostic ash layer from the Allouarn Volcano (Arnaud et al., 2009). In terms of maximum ice thickness, erosional evidence produced by the ice flow on rock cliffs on both sides of the valley above Lac d'Ampère reveal that the surface of the glacier was about 150 m higher than today during the maximum Holocene extent. Whether this is equivalent to the LGM ice thickness is not known. The lack of remains of lateral or frontal moraines on the slopes of both sides of the valley may indicate that previous Holocene glacial extents were smaller than those of the last millennium or that at its maximum the glacier reached positions in the fjord that are submerged offshore today. The possibility that cold-based, generally non-erosive glaciers, were present at the LGM has not yet been considered in the literature.

Collectively, the evidence from the moraines suggests that the Kerguelen glaciers are highly sensitive to climate changes and that various Holocene ice advances may have approached LGM ice maxima. For example, various studies have shown that the Ampère Glacier has advanced and retreated up to 3.8 km from its 2010 front position on multiple occasions in the late Holocene (Frenot et al., 1993, 1997a; Arnaud et al., 2009).

Recent glacier retreat has been documented from the first half of the 20th century (Aubert de la Rue, 1967; Vallon, 1977) and the total ice extent on Kerguelen Islands declined from 703 to 552 km^2 between 1963 and 2001, with the Cook Ice Cap retreating from 501 to 403 km^2 in the same period (Berthier et al., 2009). Current rapid deglaciation at the Kerguelen Islands is exceptional (Cogley et al., 2010) and possibly linked to increased temperature (Frenot et al., 1993, 1997a; Jacka et al., 2004), and decreased precipitation since AD 1960 (e.g., Frenot et al., 1993, 1997a; Berthier et al., 2009). An alternative hypothesis is that the retreat is related to migration of the sub-Antarctic convergence from the north to the south of the Kerguelen Islands around AD 1950 (Vallon, 1977).

3.2.4. *Heard Island and McDonald Island*

Heard Island and McDonald Island (located at approximately 53°06'S, 73°31'E) are 380 km^2 in area. Heard Island consists of an active strato-volcano, Big Ben (2745 m), situated just south of the present day Polar Front. It is heavily glaciated with ice covering 70% or 257 km^2 of the island, with 12 major glaciers radiating towards the sea from the summit of Big Ben or the peaks of Laurens Peninsula (McIvor, 2007). The island is one of the few exposures of

the Kerguelen Plateau, the second largest submarine plateau on Earth. It comprises young volcanic material that has built on top of the Late Miocene – Early Pliocene Drygalski Formation, which today forms a flat 300 m high plateau off the northern coast of Heard Island (Kiernan and McConnell, 1999).

There are no published data on Heard Island's glacial history since the LGM, with the exception of descriptions of till and moraine formation (Lundqvist, 1988), and the Dovers Moraines; a series of lateral moraines and extensive hummocky moraines (Kiernan and McConnell, 1999), which are undated, but most likely of Holocene age (Hall, 2002).

Some of the glaciers reach sea level today. Offshore on the continental shelf a bathymetric grid compilation (Beaman and O'Brien, 2011) shows evidence of extensive glaciation with at least four, and possibly more, large cross-shelf troughs and moraines extending as much as 50–80 km from the present shoreline (Balco, 2007) (Fig. 8A), but the age of these features remains unknown. Based on their position and depth, these features would require grounded ice to a depth of at least 180 m and a palaeo-grounding line at 120 m below the LGM sea level (Hall et al., 2011). This observation suggests the ice was a minimum of 135 m thick at its margin and, hence, several hundred metres thick at its centre (Balco, 2007). New bathymetic data for the sea-floor plateau surrounding Heard Island now exist at a resolution that permits a closer analysis of these submerged glacial features (~100 m grid cell size; Fig. 8B). The moraine belt is well-resolved over a distance of ~80 km on the new bathymetric grids but is not resolved to the west, east and south of the plateau. Where it is well-resolved, the moraine belt is broadly symmetric in profile, 50–80 m high and up to 4 km in width. The size of the feature suggests it is a terminal moraine of a larger ice cap that covered significant portions of the island and its marine plateau in the past. Balco (2007) also observed over-deepened troughs, likely of glacial origin, that cut across the shelf inshore of the moraine. These are clearly represented in the new bathymetry (Fig. 8B) and suggest that the ice cap was organised into several discrete faster-flowing outlets, in common with most examples of ice caps and ice sheets today.

Sketches of more extensive glaciers by visiting sealers between 1850s–1870s AD, and photographic evidence, documents glacial retreat over the latter half of the 20th Century (Kiernan and McConnell, 1999, 2002; Ruddell, 2005; Thost and Truffer, 2008). This may be linked to a shift in the position of the Polar Front which now regularly migrates to the south of Heard Island. A radiocarbon date of modern to 340 cal yr BP (220 ± 113 ^{14}C yr BP; Wk 9485) from plant material buried beneath beach gravels at Long Beach provides a local minimum age for deglaciation at that site (Kiernan and McConnell, 2008), but is not related to the retreat of an LGM ice cap. Nevertheless, the relatively small area of the island that has periglacial features does suggest that onshore deglaciation has been relatively recent and this may also explain why glacioisostatic features such as raised beaches have not been described. Well formed vegetation banked terraces occur at Mt Andree possibly marking one of the longest exposed areas (Kiernan and McConnell, 2008), but these have not been dated. As Heard Island contains abundant volcanic deposits such as lava flows and tephra, there is potential to use these in future to help constrain the glacial history.

Nearby McDonald Island, approximately 40 km to the west, has undergone recent volcanic activity, notably in the AD 1990s when the main island was observed to have doubled in size (McIvor, 2007). There is no published information on its glacial history.

3.2.5. Amsterdam and St Paul Islands

Situated between South Africa and Australia, Amsterdam Island (37°50′S, 77°30′E, 55 km^2) and Saint-Paul Island (38°43′S, 77°31′E, 6 km^2) are volcanic islands dating from about 400 to 200 ka (Lebouvier and Frenot, 2007; Amsterdam Island) which have evidence of continued and recent volcanic activity. No glacial geomorphological data are published.

3.3. Pacific sector

3.3.1. Macquarie Island

Macquarie Island (54°37′S; 158°54′E, 200 km^2) is situated north of the Polar Front (Fig. 1). It is nearly 34 km long and up to 5 km wide and largely consists of a high plateau of between 150 and 300 m a.s.l with the highest point being Mt Hamilton (433 m). There are no permanent snowfields or glaciers. The island consists entirely of oceanic crust together with remnants of submarine volcanoes. These ocean-floor rocks belong to the Miocene Macquarie Ridge, which stretches from around 61°S to New Zealand (Carmichael, 2007). The island emerged 4000 m above the ocean floor about 600,000–700,000 years ago and the current tectonic uplift rate is somewhere between about 0.8 mm yr^{-1} (Adamson et al., 1996) and 1.5 mm yr^{-1} (Colhoun and Goede, 1973). Therefore the palaeobeaches, terraces and cobbles seen around the island are not interpreted as being the result of glacioisostatic uplift, but of marine erosion and deposition during the geological uplift of the island over the last six Quaternary glacial-interglacial cycles.

The scientific debate concerning the glacial history of Macquarie Island is summarised in Selkirk et al. (1990). In brief, early interpretations of glacial features such as erratics, polished and striated cobbles, moraines, kame terraces, over-deepened lakes, meltwater channels, glacial valleys and cirques on the island (Mawson, 1943; Colhoun and Goede, 1974; Löffler and Sullivan, 1980; Crohn, 1986) have now been explained as topographic expressions of faulting and non-glacial erosion associated with the tectonic uplift of the island, and as periglacial features (Ledingham and Peterson, 1984; Adamson et al., 1996). This is supported by the presence of multiple raised beaches with thermoluminescence ages of 340 ± 80 ka (at Hasselborough Bay, 263 m asl) and 172 ± 40 ka (at Wireless Hill, 100 m asl) attributed to Marine Isotope Stage 9 (340–330 ka) and Stage 5e (130–125 ka), respectively. Although the TL errors are very large, these dates imply that the island has not been subject to extensive glacial erosion (Adamson et al., 1996). A thermoluminescence date of 92 ± 120 ka from a lacustrine deposit exposed in a bank of North Bauer Creek suggests that lake sediments accumulated in the early half of the last glacial cycle between Oxygen Isotope Stage 4 and the middle of Stage 5 (Adamson et al., 1996). This deposit was subsequently overlain by periglacial mass flows that accumulated during the last glacial. Peats with infinite radiocarbon ages of >40,000 yr BP have also been found at West Mount Eitel (Adamson et al., 1996). These peats overlie rounded beach cobbles, and in turn are overlain by a thick deposit of sub-angular matrix-supported cobbles (the likely product of periglacial conditions), capped by a thick sandy peat with present-day vegetation.

A near island-wide periglacial environment most likely persisted until just after the peak of the LGM, following which radiocarbon evidence shows that periglacial conditions moderated sufficiently to permit the continuous deposition of lake sediment and terrestrial peat deposits. These date from 15,975–17,034 cal yr BP to 14,063–15,119 cal yr BP at Palaeolake Skua (Selkirk et al., 1991) and 11,284–12,581 cal yr BP at the Finch Creek Ridge peat deposit (Selkirk et al., 1988) (Table 1). Sediments in extant lakes date from 16,620–16,987 cal yr BP (Saunders, K. Unpublished data). These can only be considered minimum ages for the transition from perglacial conditions as basal ages have yet to be determined for some of the lakes, such as Palaeolake Toutcher (Selkirk et al., 1988). Younger deposits dated to 8185–8639 cal yr BP are found at Palaeolake Sandell. In addition, peat deposits dating to

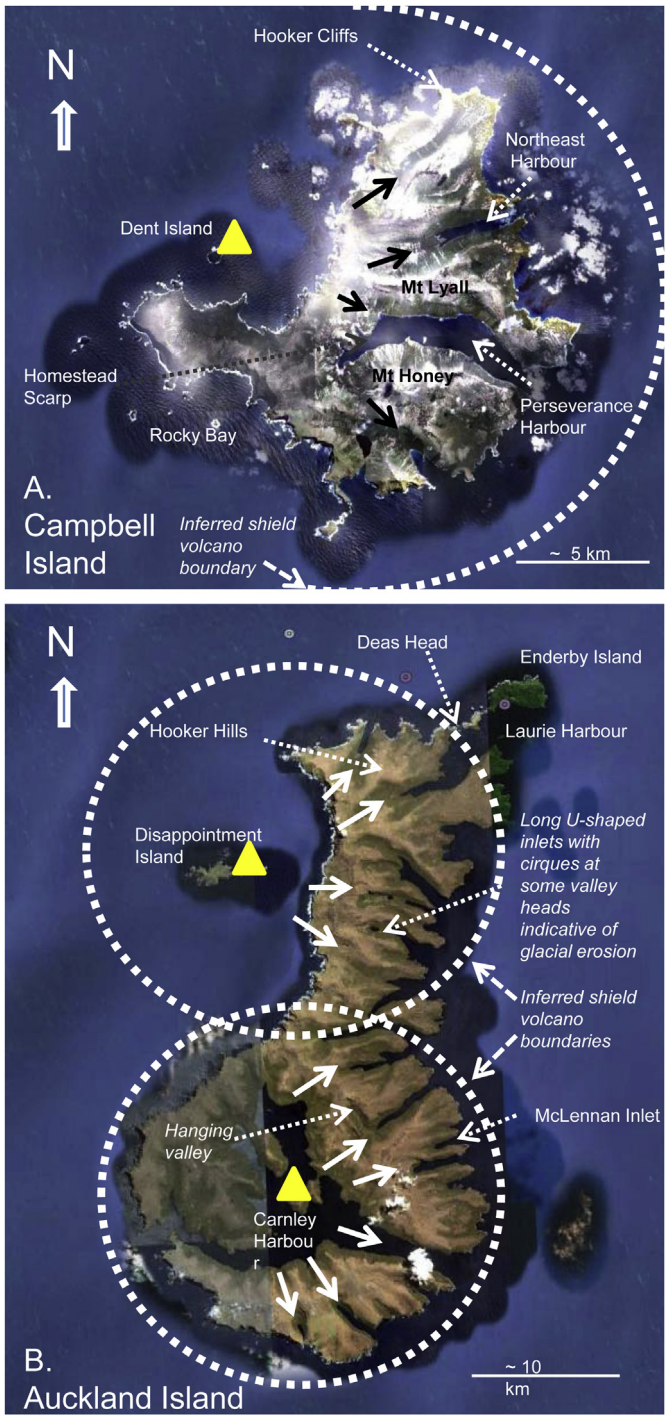

Fig. 9. (A) Satellite image of Campbell Island showing the approximately radial arrangement of the drainage system (black arrows) from the former centre of the shield volcano at Dent Island (triangle). This drainage system likely determined the orientation of the over-deepened glacial troughs including Perseverance Harbour and Northeast Harbour. (B) Satellite image of the Auckland Islands showing the approximately radial arrangement of the drainage system (white arrows) from the centres of the shield volcanoes at Carnley Harbour and Disappointment Island (triangles). The image clearly shows the deeply incised glacial troughs and hanging valleys on the east coast. The dashed white lines marking the former extent of the shield volcanoes are derived from Quilty (2007). Satellite images complied by Google Earth (2013) from SIO, NOAA, U.S. Navy, NGA and GEBCO sources.

7682–8203, 5586–6200 and 6206–7272 cal yr BP occur at Green Gorge, Wireless Hill and Finch Creek ridge (Selkirk et al., 1982; Selkirk et al., 1988) (Table 1).

Combined with evidence for tectonic uplift, geomorphological observations suggest extensive periglacial rather than glacial processes were the most important in fashioning the cold uplands of Macquarie Island. This has resulted in the formation of turf banked and stone banked terraces in several locations, mainly on the leeward eastern parts of the island (Selkirk et al., 1990; Selkirk, 1998; Selkirk-Bell and Selkirk, 2013). Whist there may have been small nivation cirques on some areas of the plateau during glaciations (Hall, 2004) there is no evidence for any former ice caps or glaciers (Ledingham and Peterson, 1984; Adamson et al., 1988). Similarly, early suggestions that the island's present biota arrived by long-distance dispersal following retreat of an overriding ice sheet (Taylor, 1955) have also subsequently been disproven (Van der Putten et al., 2010). On the basis of this evidence we concur with Selkirk et al. (1990) and Adamson et al. (1996) in concluding that there is no compelling evidence of LGM glaciation of Macquarie Island.

3.3.2. Campbell Island

Campbell Island (52°33′S, 166°35′E, 120 km^2) is the southernmost of the New Zealand sub-Antarctic Islands. It is of ancient volcanic origin (6–11 Ma), being a remnant of a shield volcano centered approximately on Dent Island (Fig. 9A). It is not currently glaciated.

There are no detailed studies on the glacial history of Campbell Island. However, there are several prominent U-shaped valleys including Perseverance Harbour and Northeast Harbour. These appear to be arranged in a more or less radial pattern, around the former volcanic centre at Dent Island (Fig. 9A). This suggests that the radial drainage pattern may have been established in the mid to late Miocene before the western part of the former shield volcano was eroded away by the sea, or experienced a flank collapse, leaving only the eastern part. This hypothesis would explain why the main U-shaped valleys, particularly Perseverance Harbour, now appear to lack a sufficient ice catchment area to explain their large scale relative to the remaining landmass of island (Fig. 9A).

Unequivocal evidence of LGM glaciation is not very obvious on the island (Quilty, 2007). Nevertheless, glacial features such a 'corrie and moraine' (most likely on Mt Honey) have been reported since at least 1896 (Marshall, 1909). Geomorphological features associated with glacial U-shaped valleys have also been described (Marshall, 1909; Quilty, 2007). These include early soundings from Perseverance Harbour that suggested that it was over deepened by ice derived from glaciers at Mount Honey and Mount Lyall, with a valley east of Mount Honey being interpreted as a hanging valley occupied by an ice tributary to a larger glacier (Marshall, 1909). A sill at the entrance of Perseverance Harbour has been variously interpreted as a glacial till, or debris associated with longshore currents (Quilty, 2007). Studies by McGlone et al. (1997) and McGlone (2002) also described cirque-like features at around 150 m a.s.l. on the higher mountains, diamictons interpreted as tills, and a possible lateral moraine composed of a bouldery sandy gravel, 2–3 m thick, exposed at the top of the 90 m high Hooker sea cliff in the north of the island. Possible kame terraces, terminal moraines, and erratic blocks have also been considered as evidence of extensive ice cover at the LGM.

Most, if not all, of the glacial features on the island remain undated and even those that are present are either covered by a deep blanket of overlying peat (McGlone, 2002), are heavily eroded, or unproven. In Perseverance Harbour for example the fjord walls are not steep sided with well-preserved glacial features compared with those described at some other sub-Antarctic Islands such as the

Auckland Islands and South Georgia. This raises the possibility that many of the glacial features described pre-date the LGM and that Quaternary glaciation has been both limited, and within the footprint of earlier glacial episodes. This interpretation is supported by the high number of endemic species on the island which excludes full LGM ice cover. Some researchers have even argued that the valley systems were formed by fluvial processes (Campbell, 1981), although most evidence supports at least partial glaciations during the Quaternary.

Following the last glaciation the earliest dates for peat accumulation range between 16,577–16,997 cal yr BP at Homestead Scarp and 14,132–15,024 cal yr BP at Mt Honey (McGlone et al., 2010). One coastal site at Hooker Cliffs has a minimum age for peat deposition of 14,845–16,629 cal yr BP, whilst peat accumulated at Rocky Bay from 13,352– 13,767 cal yr BP (McGlone, 2002).

3.3.3. Auckland Island

The Auckland Island archipelago (50°50′S, 166°05′E), with a combined area of 625 km^2, is the largest of the New Zealand sub-Antarctic islands, situated to the northwest of Campbell Island, 465 km south-southeast of the South Island of New Zealand. The islands are not currently glaciated. They are entirely volcanic in origin, the emergent parts of the Campbell Plateau basement continental crust, and are composed of basaltic volcanics of Oligocene-Miocene age (Wright, 1967).

Similar to Campbell Island, former shield volcanoes, formed between 25 and 10 Ma, appear to have had a strong influence on the drainage pattern established on the Auckland Islands. Many of the fjords are radially arranged around inferred former ice domes centred on Carnley Harbour in the South and Disappointment Island in the north (Fig. 9B); locations where Quilty (2007) identifies two former shield volcanoes (Fig. 9B). As at Campbell Island, evidence of glaciation is best preserved on the east coast with that on the western part of the island having been removed through marine erosion, or flank collapse (to the north) and marine erosion or explosive loss of the interior of the caldera (in the south). The presence of endemic plants and animals likely rules out complete glaciation during the LGM. However, there is extensive evidence of Quaternary glaciation, for example in the many deeply incised fjords, such as McLennan Inlet. This suggests that although the Auckland Islands are at a latitude 200 km north of Campbell Island the higher maximum attitude (705 m versus 569 m at Campbell Island) and larger land area has enabled extensive Quaternary ice accumulation.

Glacial features in the Auckland Islands were first described by Speight (1909). The eastern flank of the main Auckland Island has an impressive abundance of evidence of past glacial activity in the form of deeply cut wide U-shaped valleys with long coastal inlets and lateral moraines, hanging valleys, moraine-dammed lakes and cirques (Fig. 9B), and submarine terminal moraines (Speight, 1909); but there are currently no age constraints for these features. McGlone's (2002) interpretation is that at the LGM all the major inlets in the east were glacier-filled, with cirques forming between 250 and 300 m in altitude (Wright, 1967). Fleming et al. (1976) and McGlone (2002) described till on Enderby Island (a small low-lying island close to the northeastern extremity of the mainland, Fig. 9B) which was deposited during the last glaciation by an extended glacier flowing from the uplands (400–460 m high) north-eastwards, filling Laurie Harbour. The till is separated into two members by laminated lake silts suggesting that two distinct glacial advances, possibly within the LGM, are recorded. The oldest Auckland Island radiocarbon date is 18,009–18,672 cal yr BP from a sandy layer with fine organics from the base of a c. 4 m thick blanket peat from the northern lowland slopes of the Hooker Hills. As this area was overrun by the Laurie Harbour palaeoglacier, it provides a minimum age for deglaciation (McGlone, 2002). Peat deposits have also been dated at Deas Head (13,496–14,031 cal yr BP) and Hooker Hills (12,590–12,926 cal yr BP) (McGlone et al., 2000).

3.3.4. Balleny, Scott, and Peter I islands

Balleny Island (66°55′S, 163°20′E, 400 km^2) and Scott Island (67°24′S, 179°55′W, $>$ 1 km^2) are the subaerial expressions of a series of submarine ridges formed by volcanic activity on a timescale of $<$10 Ma. No glacial geomorphological data are published, although Scott Island is largely glaciated today.

Peter I Island (68°50′S, 90°35′W, 154 km^2) is the remnant of a former shield volcano formed 0.3–0.1 Ma and is heavily glaciated. No glacial geomorphological data are published. The well mapped bathymetry data around the island reveal that significant ice expansion is not possible due to steep flanks which fall away rapidly into the deep sea.

3.3.5. Diego Ramirez

The Diego Ramirez Islands (56°30′S, 68°42′W, c. 2 km^2) are a group of small islands at the southernmost tip of Chile, formed during subduction of the continental crust. No glacial geomorphological data are published.

4. Discussion

Although many of the sub-Antarctic and maritime Antarctic Islands have been visited for several decades, this review demonstrates that few systematic studies of their glacial geomorphology and geochronology have been undertaken. As a result, the position of the LGM ice limits are not well defined, and in most cases there are no LGM age constraints, or constraints on the onset of deglaciation. Nevertheless, existing cosmogenic isotope dating studies on moraines and the basal ages of peat and lake deposits permit minimum ages for deglaciation to be inferred for some islands.

In terms of maximum ice volumes at the LGM, the sub-Antarctic islands can be divided into the following groups:

4.1. Type I) Islands which accumulated little or no LGM ice

These include the Falkland Islands and Macquarie Island. Situated north of the Antarctic Polar Front (Fig. 1) they are characterised by periglacial features with little evidence of extensive glaciations except for upland tarns and nivation hollows (Falkland Islands). This suggests either an insufficient moisture supply during glacial periods, insufficient altitude and relief to develop significant glaciers, or stronger Westerly Winds and more wind-driven ablation preventing glacier initiation. In these environments, glaciation was very limited and periglacial landscapes prevailed, for example the stone runs in the Falkland Islands (Wilson et al., 2008), and stone stripes and polygons on Macquarie Island (Selkirk et al., 1990). Where glaciers accumulated on the Falkland Islands they appear to have been restricted to eastern slopes, suggesting an important role for preferential snow accumulation on the lee side of ridges sheltered from the prevailing Westerly Winds. Elsewhere, there is evidence of wind erosion through the LGM where wind-blown sand grains carried up to heights of a metre above ground level have eroded the lower faces of exposed rock, forming distinct rock pillars in some parts of West Falkland such as the Port Stephens Formation (Aldiss and Edwards, 1999). On Macquarie Island, the moderating effect of the maritime climate and the relatively low altitude of the plateau (c. 150–300 m) would have also played a role in limiting snow accumulation (Selkirk et al., 1990).

4.2. Type II) Islands with a limited LGM ice extent but evidence of extensive earlier continental shelf glaciations

These islands include South Georgia and possibly Kerguelen, although for the latter data are still limited. Current chronological data suggests that the LGM ice extent at these locations was limited to the fjords despite there being glacial geomorphological evidence of earlier glaciations that extended across their continental shelves. This is of interest because both islands retain permanent ice caps today on account of their high altitude (up to 2934 m on South Georgia, and 1049 m on Kerguelen) and would have had substantially lower equilibrium lines during the last glacial. One hypothesis is that glacier extent was limited at the LGM because they were deprived of moisture by the more extensive sea ice (Bentley et al., 2007; Allen et al., 2011; Collins et al., 2012), and stronger Westerly Winds. This is a common feature of this group of sub-Antarctic islands where the combination of more northerly sea ice and strong winds increased aridity; hence most peat and lake sequences only start to accumulate in the early to mid-Holocene (Van der Putten and Verbruggen, 2005; Van der Putten, 2008), with occasional exceptions dating from at or before the LGM (Rosqvist et al., 1999). Patagonian climate, east of the Andes was also more arid at this time (Recasens et al., 2011) due, in part, to the same factors, combined with the rain shadow effect of the mountains. These islands may therefore have followed a glacial history more similar to that of central Patagonia (46°S), the closest continental landmass at these latitudes, where a series of Pleistocene glaciations (of Marine Isotope Stage 20 and younger) extended beyond LGM limits (Singer et al., 2004) with the most extensive glacial advance occurring at c. 1.1 Ma (Rabassa, 2000), although the pattern of South American glaciation may be rooted in other drivers, such as glacial erosion (Kaplan et al., 2009), in addition to climate processes. An alternative hypothesis is that over many glacial cycles, the glacial erosion of the alpine valleys and fjords has been sufficient to reduce the length of glaciers in the most recent cycle because theoretically glacier length can scale linearly with erosion depth (Anderson et al., 2012). In such cases, there are often earlier moraines deposited well beyond the LGM limit, referred to by Anderson et al. (2012) as 'far-flung' moraines. This suggests that the glacially modified landscape, rather than a different climate, may be capable of explaining the earlier more extensive glacier extents.

In either case, this glacial history contrasts with much of the Antarctic continent, including the Antarctic Peninsula, where the LGM glaciation was amongst the most extensive in the Quaternary.

4.3. Type III) Seamounts and volcanoes unlikely to have accumulated significant LGM ice cover

These islands can be divided into two sub-groups. First those which are situated south of the Antarctic Polar Front including the South Sandwich Islands, Clarence Island and Peter I Island which are unlikely to have accumulated significant expansion of ice due to steep flanks which fall away rapidly into the deep sea. Second, islands to the north of the Antarctic Polar Front, including Amsterdam and St Paul Islands and Gough Island. These have no evidence of glaciation, low mean altitudes and also have steep flanks which fall away rapidly into the deep sea.

4.4. Type IV) Islands on shallow shelves with both terrestrial and submarine evidence of LGM (and/or earlier) ice expansion

These include volcanic islands such as Heard Island, Bouvet Island, Marion Island, Prince Edward Island and the Crozet Islands which are located on top of extensive submarine plateaux, and non-volcanic islands including the South Orkney Islands and Elephant Island which are located on the South Scotia Ridge and surrounded by shallow shelves. On some of the volcanic islands, such as Heard Island and possibly Marion Island, there is geomorphological evidence that the glaciers extended onto the adjacent shelf; and on Heard Island, perhaps as far as the shelf break in some areas. This expansion would have been facilitated by the glacial eustatic sea level fall. Glaciation of these volcanic islands may have been initiated by a northward shift of the Antarctic Polar Front during the last glacial resulting in cooler temperatures and increased precipitation as snow. Loss of ice by calving of tidewater glaciers may have also been diminished as a result of the expansion of Antarctic sea ice which would have acted to reduce wave energy (Balco, 2007). At the South Orkney Islands there is very good evidence that grounded ice reached to at least 246 m water depth, whilst on the Elephant Island archipelago the presence of a large shallow continental shelf also shows that a large area for ice accumulation was exposed during glacial low stands.

4.5. Type V) Islands north of the Antarctic Polar Front with terrestrial evidence of LGM ice expansion

These islands are separated from the Type IV islands only on the basis of their lower latitude and the absence of offshore bathymetric data. They include Campbell Island and the Auckland Islands. The Auckland Islands have terrestrial geomorphological evidence of extensive Quaternary glaciations, including the LGM, and minimum ages for post-LGM ice retreat based on the onset of peat accumulation. At Campbell Island the evidence of LGM ice expansion is less clear and it is likely that any LGM ice expansion was within the footprint of earlier Quaternary glaciations. In both cases the orientation of the fjords appears to have been influenced by radial drainage from former shield volcanoes. This radial drainage pattern is also seen in most of the volcanic Type IV islands.

4.6. Type VI) Islands with no data

Balleny Island, Scott Island and Diego Ramirez have no published glacial history that we are aware of.

In addition to the geomorphological evidence, biological and molecular biological data confirm that the majority of the sub-Antarctic islands were not completely ice-covered at the LGM. This is because various elements of the flora and fauna have survived on the islands intact throughout the LGM and possibly earlier glaciations, resulting in the development of distinct floral provinces in the South Atlantic Ocean, South Pacific Ocean, and South Indian Ocean (Van der Putten et al., 2010). The evolution of endemic species also points to the long term persistence of glacial refugia. For example, highly divergent mitochondrial DNA lineages within the endemic weevil group *Ectemnorhinus* have been found within and among sub-Antarctic islands, most of them estimated to have existed since long before the LGM (Grobler et al., 2011). Similarly, evidence of biotic persistence on sub-Antarctic islands is found in mites (Mortimer et al., 2011) and flowering plants (Van der Putten et al., 2010; Wagstaff et al., 2011; Fraser et al., 2012), birds (McCracken et al., 2013) and in limpets on the continental shelf (González-Wevar et al., 2013), from at least the beginning of the Quaternary, with some genera such as *Pleurophyllum* possibly being the last remnants of a once-diverse Antarctic flora that dispersed northward in response to Neogene glacial advance (Wagstaff et al., 2011).

The differences in glacial history in the sub-Antarctic region appear to be a result of both latitudinal changes in climate and topographic control on the glacial equilibrium line altitude. For example, islands south of the Polar Front are generally colder,

accumulate glaciers and typically retain ice cover today because the glacial equilibrium line altitude is low. On these islands, the eustatic sea level fall during the LGM would have been sufficient to enable glaciers to expand, particularly where this opened up new exposures of shallow sea-floor to accumulation. On other islands such as Macquarie Island and the Falkland Islands topographic control appears to be more important. In these cases, their low mean altitudes meant that they have never accumulated significant ice masses. In contrast, the high mean altitudes of both South Georgia and Kerguelen have resulted in ice caps that have persisted to the present but experienced limited expansion at the LGM relative to earlier Pleistocene glaciations. This may be the result of the impact of the earlier glacially modified landscape on maximum LGM ice extent (see Anderson et al., 2012), or moisture deprivation resulting from more extensive sea ice (as described above); a feature seen along the Antarctic coast where relatively low winter precipitation and cloudiness occurs when the sea ice extent is greater (King and Turner, 1997). In the case of South Georgia, Bentley et al. (2007) note that the extent of sea ice in the northern Weddell Sea and central Scotia Sea is critical in determining the moisture content of depressions reaching the island. In addition to changes in sea ice extent, reduced moisture delivery is a product of a northward shift of the Southern Hemisphere Westerly Winds during the glacial; reducing the moisture supply from subtropical air masses (Björck et al., 2012; Stager et al., 2012) and enhancing evaporation and sublimation rates. One simplified study with a general circulation model (Toggweiler et al., 2006) also suggests that the belt of the Southern Hemisphere Westerly Winds may move northward towards the Equator during cold periods (and vice versa). Other general circulation models have suggested no change in the latitudinal position of the Westerlies, but a general drying out at these latitudes (Rojas et al., 2009). Nevertheless, it seems likely that changing moisture supply was important in determining the mass balance of glaciers in the maritime and the sub-Antarctic regions (see discussion in Bentley et al., 2007), with altitude, temperature, insolation and aspect also being influential.

Although the sub-Antarctic islands' glaciers responded to different forcing at the LGM, and in particular have a regionally heterogeneous glaciation history that in some cases mirrors a South American pattern (see comments on Type II glacial histories) and others an Antarctic one (see comments on Elephant Island and the South Orkney Islands in the discussion of Type IV glacial histories), there is good evidence that those which have remaining ice cover are responding in the same way to the current warming trend. The majority of glaciers on these islands are showing evidence of recent retreat, which seems to have accelerated over the past three to five decades (e.g., Thost and Truffer, 2008; Berthier et al., 2009; Cook et al., 2010; Hall et al., 2011).

5. Conclusions

In the context of the ACE/PAIS community Antarctic Ice Sheet reconstruction (this Special Issue) the ice volume changes associated with the post-LGM deglaciation of the sub-Antarctic Islands are unlikely to have made a significant contribution to global sea level. However, being peripheral to the main Antarctic Ice Sheet, they are, and have been, very responsive to past climate changes and provide examples of later stages of deglaciation and the processes involved. For example, the deglaciation of the fjords of South Georgia in the early Holocene is remarkably similar to that occurring in the fjords of the western Antarctic Peninsula today. This early Holocene analogue serves as a useful gauge for determining the predictive accuracy of ice and climate models. Elsewhere the rapid recent deglaciation, and in some areas total loss of ice (e.g. Marion Island), provide examples of the final stages of deglaciation.

The lack of information on sub-Antarctic glaciation in this review highlights a need for future focus on the glacial history of the islands. Research priorities and future work should encompass:

- A greater emphasis on delimiting onshore and offshore limits of past glaciation, using glacial geomorphic, geophysical and sedimentary investigations and imaging and dating of submarine glacial features such as moraines and trough mouth fans.
- Targeted dating of glacial and postglacial sequences to increase understanding of the timing and pattern of post-LGM deglaciation.
- The use of volcanic markers to help constrain glacial history, given that many sub-Antarctic islands contain abundant lavas and tephras.
- Closer integration of ice-sheet modelling with climate and topographic forcing to reconstruct likely patterns of former glacial activity, especially where glacial geologic evidence is sparse or lacking.
- Glacier mass balance modelling, including sensitivity tests, to ascertain the key drivers of glacial change in the sub-polar belt.
- Examining patterns of Holocene glacier and ice-cap change in more detail to provide context to the widespread deglaciation occurring throughout the sub-Antarctic today.

Acknowledgements

We thank the field parties carrying out terrestrial glaciological studies in the sub-Antarctic Islands and the crews and scientific shipboard parties participating in marine geophysical surveys, and the logistics organisations for making all of this field work possible. Furthermore, we acknowledge financial support from the Antarctic Climate Evolution (ACE) and its successor Past Antarctic Ice Sheet Dynamics (PAIS) scientific research programmes of the Scientific Committee on Antarctic Research (SCAR) for a workshop held in 2011 in Edinburgh (UK) that kick-started the Antarctic Ice Sheet community reconstruction initiative. AGCG was supported by a Natural Environment Research Council (NERC) New Investigator Award, NE/K000527/1. We are most grateful to our reviewers for their constructive observations.

References

Adamson, D.A., Selkirk, P.M., Colhoun, E.A., 1988. Landforms of aeolian, tectonic and marine origin in the Bauer Bay-Sandy Bay region of subantarctic Macquarie Island. Pap. Proc. R. Soc. Tasmania. 122 (1), 65–82.

Adamson, D.A., Selkirk, P.M., Price, D.M., Ward, N., Selkirk, J.M., 1996. Pleistocene uplift and palaeoenvironments of Macquarie Island: evidence from palaeobeaches and sedimentary deposits. Pap. Proc. R. Soc. Tasmania. 130 (2), 25–32.

Anderson, R.S., Dühnforth, M., Colgan, W., Anderson, L., 2012. Far-flung moraines: exploring the feedback of glacial erosion on the evolution of glacier length. Geomorphology 179, 269–285.

Aldiss, D.T., Edwards, E.J., 1999. The Geology of the Falkland Islands. British Geological Survey Technical Report. WC/99/10.

Allen, C.S., Smellie, J.L., 2008. Volcanic features and hydrological setting of southern Thule, south Sandwich islands. Antarct. Sci. 20 (3), 301–308.

Allen, C.S., Pike, J., Pudsey, C.J., 2011. Last glacial-interglacial sea-ice cover in the SW Atlantic and its potential role in global deglaciation. Quat. Sci. Rev. 30 (19–20), 2446–2458.

Arnaud, F., Révillon, S., Poulenard, J., Boone, D., Heirman, K., 2009. First reconstruction of last millennium flooding activity on Kerguelen archipelago (50°S, sub-Antarctic Indian Ocean) from Lake Armor sediment: implications for southern hemisphere cyclonic circulation changes. Geophys. Res. Abs. 11, 10436.

Aubert de la Rue, E., 1967. Remarques sur la disparition des glaciers de la Peninsule Courbet (Archipel de Kerguelen). Terres Austr. Antarct. Franç. Paris 40, 3–19.

Balco, G., 2007. A surprisingly large marine ice cap at Heard Island during the Last Glacial Maximum? In: Cooper, A.K., Raymond, C.R. (Eds.), Antarctica: A

Keystone in a Changing World – Online Proceedings of the 10th ISAES. USGS Open-File Report 2007–1047.
Balco, G., Stone, J., Lifton, N., Dunai, T., 2008. A simple, internally consistent, and easily accessible means of calculating surface exposure ages and erosion rates from Be-10 and Al-26 measurements. Quat. Geochronol. 3, 174–195.
Barnes, D.K.A., Hodgson, D.A., Convey, P., Allen, C.S., Clarke, A., 2006. Incursion and excursion of Antarctic biota: past, present and future. Global Ecol. Biogeogr. 15, 121–142.
Barrow, C.J., 1978. Postglacial pollen diagrams from South Georgia (sub-Antarctic) and West Falkland Island (South Atlantic). J. Biogeogr. 5, 251–274.
Beaman, R.J., O'Brien, P.E., 2011. Kerguelen Plateau Bathymetric Grid, November 2010, Record 2011/22. Geoscience Australia, Canberra, Australia, p. 18.
Bellair, P., 1965. Un exemple de glaciation aberrante, les Îles Kerguelen. Com. Natl. Franc. Rech. Antarc. 11, 1–27.
Bennett, K.D., Gribnitz, K.H., Kent, L.E., 1989. Pollen analysis of a Quaternary peat sequence on Gough Island, South Atlantic. New. Phytol. 113, 417–422.
Bentley, M.J., Anderson, J.B., 1998. Glacial and marine geological evidence for the ice sheet configuration in the Weddell Sea-Antarctic Peninsula region during the last glacial maximum. Antarct. Sci. 10, 309–325.
Bentley, M.J., Evans, D.J.A., Fogwill, C.J., Hansom, J.D., Sugden, D.E., Kubik, P.W., 2007. Glacial geomorphology and chronology of deglaciation, South Georgia, sub-Antarctic. Quat. Sci. Rev. 26 (5–6), 644–677.
Berthier, E., Le Bris, R., Mabileau, L., Testut, L., Remy, F., 2009. Ice wastage on the Kerguelen Islands (49 degrees S, 69 degrees E) between 1963 and 2006. J. Geophys. Res. Earth Surface 114. http://dx.doi.org/10.1029/2008JF001192.
Björck, S., Malmer, N., Hjort, C., Sandgren, P., Ingólfsson, O., Wallen, B., Smith, R.I.L., Jonsson, B.L., 1991. Stratigraphic and paleoclimatic studies of a 5500-year-old moss bank on Elephant Island, Antarctica. Arct. Alp. Res. 23 (4), 361–374.
Björck, S., Rundgren, M., Ljung, K., Unkel, I., Wallin, Å., 2012. Multi-proxy analyses of a peatbog on Isla de los Estados, easternmost Tierra del Fuego: a unique record of the variable Southern Hemisphere Westerlies since the last deglaciation. Quat. Sci. Rev. 42, 1–14.
Blunier, T., Chappellaz, J., Schwander, J., Dallenbach, A., Stauffer, B., Stocker, T.F., Raynaud, D., Jouzel, J., Clausen, H.B., Hammer, C.U., Johnsen, S.J., 1998. Asynchrony of Antarctic and Greenland climate change during the last glacial period. Nature 394 (6695), 739–743.
Boelhouwers, K., Meiklejohn, K.I., Holness, S.D., Hedding, D.W., 2008. Geology, geomorphology and climate change. In: Chown, S.L., Froneman, P.W. (Eds.), The Prince Edward Islands. Land-sea Interactions in a Changing Ecosystem. Sun Press, Stellenbosch, South Africa, pp. 65–96.
Bougère, J., 1992. Dynamique actuelle à Île de la Possession (Archipel de Crozet): Substitution de processus geomorphologiques (PhD thesis). l'Univerisité de Nice Sophia Antipolis, Reúnion.
Campbell, I.B., 1981. Soil pattern of Campbell Island. N. Z. J. Sci. 24, 111–135.
Camps, P., Henry, B., Prévot, M., Faynot, L., 2001. Geomagnetic palaeosecular variation recorded in Plio-Pleistocene volcanic rocks from Possession Island (Crozet Archipelago, southern Indian Ocean). J. Geophys. Res. 106 (B2), 1961–1971.
Carmichael, N., 2007. Macquarie Island, its conservation and management. Pap. Proc. R. Soc. Tasmania. 141 (1), 11–17.
Chen, J.L., Wilson, C.R., Blankenship, D.D., Tapley, B.D., 2006. Antarctic mass rates from GRACE. Geophys. Res. Lett. 33, L11502.
Chevallier, L., 1981. Carte géologique au 1:50 000. Archipe! Crozet, Ile de la Possession. Com. Natl. Franç. Rech. Antarc. 50, 16.
Chown, S.L., Froneman, P.W., 2008. The Prince Edward Islands: Land Sea Interactions in a Changing Ecosystem. African Sun Media, Stellenbosch, South Africa, p. 470.
Clapperton, C.M., 1971a. Evidence of cirque glaciation in the Falkland Islands. J. Glaciol. 10 (58), 121–125.
Clapperton, C.M., 1971b. Geomorphology of the Stromness Bay-Cumberland Bay area, South Georgia. Br. Antarct. Surv. Sci. Rep 70.
Clapperton, C.M., Sugden, D.E., 1976. The maximum extent of glaciers in part of West Falkland. J. Glaciol. 17 (75), 73–77.
Clapperton, C.M., Sugden, D.E., Birnie, R.V., Hansom, J.D., Thom, G., 1978. Glacier fluctuations in South Georgia in comparison with other island groups in the Scotia Sea. In: Van Zinderen Bakker, E.M. (Ed.), Antarctic Glacial History and World Palaeoenvironments. A.A. Balkema, Rotterdam, pp. 95–104.
Clapperton, C.M., Sugden, D.E., 1988. Holocene glacier fluctuations in South America and Antarctica. Quat. Sci. Rev. 7, 185–198.
Clapperton, C.M., Sugden, D.E., Birnie, J., Wilson, M.J., 1989. Later-Glacial and Holocene glacier fluctuations and environmental change on South Georgia, Southern Ocean. Quat. Res. 31, 210–228.
Clapperton, C.M., 1990. Quaternary glaciations in the Southern Ocean and Antarctic Peninsula area. Quat. Sci. Rev. 9 (2–3), 229–252.
Clark, R., Huber, U.M., Wilson, P., 1998. Late Pleistocene sedments and environmental change at Plaza Creek, Falkland Islands, South Atlantic. J. Quat. Sci. 13, 95–105.
Clarke, A., Barnes, D.K.A., Hodgson, D.A., 2005. How isolated is Antarctica? Trends. Ecol. Evol. 20 (1), 1–3.
Cogley, G.J., Berthier, E., Donoghue, S., 2010. Glaciers of the Subantarctic Islands. Global Land Ice Measurements from Space. Chapter 37B.
Colhoun, E.A., Goede, A., 1973. Fossil Penguin Bones, ^{14}C dates and the raised marine terrace of Macquarie Island; some comments. Search 4 (11–12), 499–501.
Colhoun, E.A., Goede, A., 1974. A reconnaissance survey of the glaciation of Macquarie Island. Pap. Proc. R. Soc. Tasmania. 108, 1–19.
Collins, L.G., Pike, J., Allen, C.S., Hodgson, D.A., 2012. High resolution reconstruction of southwest Atlantic sea-ice and its role in the carbon cycle during marine isotope stages 3 and 2. Palaeoceanography 27, PA3217. http://dx.doi.org/10.1029/2011PA002264.
Convey, P., Gibson, J.A.E., Hillenbrand, C.-D., Hodgson, D.A., Pugh, P.J.A., Smellie, J.L., Stevens, M.I., 2008. Antarctic terrestrial life – challenging the history of the frozen continent? Biol. Rev. 83, 103–117.
Cook, A.J., Poncet, S., Cooper, A.P.R., Herbert, D.J., Christie, D., 2010. Glacier retreat on South Georgia and implications for the spread of rats. Antarct. Sci. 22 (3), 255–263.
Crohn, P.W., 1986. The geology and geomorphology of Macquarie Island with special emphasis on heavy metal trace element distribution. ANARE Res. Note 39, 28.
Fenton, J.H.C., 1982. The formation of vertical edges on Antarctic moss peat banks. Arctic Antar. Alp. Res. 14 (1), 21–26.
Fenton, J.H.C., Smith, R.I.L., 1983. Distribution, composition and general characteristics of the moss banks of the maritime Antarctic. Br. Antarct. Surv. Bull. 51, 215–236.
Fleming, C.A., Mildenhall, D.C., Moar, N.T., 1976. Quaternary sediments and plant microfossils from Enderby Islands, Auckland Islands. J. R. Soc. N. Z. 6, 433–458.
Fraser, C.I., Nikula, R., Ruzzante, D.E., Waters, J.M., 2012. Poleward bound: biological impacts of Southern Hemisphere glaciation. Trends. Ecol. Evol. 27 (8). http://dx.doi.org/10.1016/j.tree.2012.04.011.
Frenot, Y., Gloaguen, J.C., Picot, G., Bougère, J., Benjamin, D., 1993. *Azorella selago* Hook. used to estimate glacier fluctuations and climatic history in the Kerguelen Islands over the last two centuries. Oecologia 95, 140–144.
Frenot, Y., Gloaguen, J.C., Tréhen, P., 1997a. Climate change in Kerguelen islands and colonization of recently deglaciated areas by *Poa kerguelensis* and *Poa annua*. In: Battaglia, F., Valencia, J., Walton, D.W.H. (Eds.), Antarctic Communities: Species, Structure and Survival. Cambridge University Press, pp. 358–366.
Frenot, Y., Gloaguen, J.C., Van De Vijver, B., Beyens, L., 1997b. Datation de quelques sédiments tourbeux holocènes et oscillations glaciaires aux Iles Kerguelen. C. R. Acad. Sci. Paris 320, 567–573.
Fretwell, P.T., Tate, A.J., Deen, T.J., Belchier, M., 2009. Compilation of a new bathymetric dataset of South Georgia. Antarct. Sci. 21 (2), 171–174.
Giret, A., 1987. Notice de la Carte Géologique au 1/50 000 de l'Île de la Possession, Îles Crozet. Com. Natl. Franç. Rech. Arct. Antarct. 58, 17–41.
Giret, P.A., Weis, D., Zhou, X., Cottin, J.-Y., Tourpin, S., 2003. Les Îes Crozet. Géologues 137, 15–23.
Golledge, N.R., Fogwill, C.J., Mackintosh, A.M., Buckley, K.M., 2012. Dynamics of the Last Glacial Maximum Antarctic ice-sheet and its response to ocean forcing. Proc. Natl. Acad. Sci. U. S. A.. http://dx.doi.org/10.1073/pnas.1205385109.
González-Wevar, C.A., Saucède, T., Morley, S.A., Chown, S.L., Poulin, E., 2013. Extinction and recolonization of maritime Antarctica in the limpet *Nacella concinna* (Strebel, 1908) during the last glacial cycle: toward a model of Quaternary biogeography in shallow Antarctic invertebrates. Mol. Ecol. 22 (20), 5221–5236.
Gordon, J.E., Haynes, V.M., Hubbard, A., 2008. Recent glacier changes and climate trends on South Georgia. Global Planet Change 60 (1–2), 72–84.
Graham, A.G.C., Fretwell, P.T., Larter, R.D., Hodgson, D.A., Wilson, C.K., Tate, A.J., Morris, P., 2008. New bathymetric compilation highlights extensive paleo-ice sheet drainage on the continental shelf, South Georgia, sub-Antarctica. Geochem. Geophys. Geosyst. 9 (13). http://dx.doi.org/10.1029/2008GC001993.
Gribnitz, K.H., Kent, L.E., Dixon, R.D., 1986. Volcanic ash, ash soils and the inferred Quaternary climate of sub-Antarctic Marion Island. S-Afr. Tydskr. Wet. 82, 629–635.
Grobler, G.C., Bastos, A.D.S., Treasure, A.M., Chown, S.L., 2011. Cryptic species, biogeographic complexity and the evolutionary history of the *Ectemnorhinus* group in the subAntarctic, including a description of *Bothrometopus huntleyi*, n. sp. Antarct. Sci. 23 (3), 211–224.
Hall, B.L., 2009. Holocene glacial history of Antarctica and the sub-Antarctic islands. Quat. Sci. Rev. 28, 2213–2230.
Hall, K., 1977. Some observations on the former sea levels of Marion Island. S. Afr. J. Antarct. Res. 7, 19–22.
Hall, K., 2002. Review of present and Quaternary periglacial processes and landforms of the maritime and sub-Antarctic region. S. Afr. J. Sci. 98, 71–81.
Hall, K., 2004. Quaternary glaciation of the sub-Antarctic Islands. In: Ehlers, J.U., Gibbard, P.L. (Eds.), Quaternary Glaciations – Extent and Chronology. Part III. Elsevier, Amsterdam, pp. 339–352.
Hall, K., Meiklejohn, I., Bumby, A., 2011. Marion Island (sub-Antarctic) volcanism and glaciation new findings and reconstructions. Antarct. Sci. 23 (2), 155–163.
Hall, K., Meiklejohn, K.I., 2011. Glaciation in southern Africa and in the sub-Antarctic. In: Ehlers, J., Gibbard, P.L., Hughes, P.D. (Eds.), Quaternary Glaciations – Extent and Chronology: a Closer Look. Elsevier, Amsterdam, pp. 1081–1085.
Hall, K.J., 1982. Rapid deglaciation as an initiator of volcanic activity: an hypothesis. Earth Surf. Proces. Landf. 7, 45–51.
Hall, K.J., 1984. Evidence in favour of total ice cover on sub-Antarctic Kerguelen Island during the last glacial. Palaeogeogr. Palaeoclimatol. Palaeoecol. 47, 225–232.
Hansom, J.D., Evans, D.J.A., Sanderson, D.C.W., Bingham, R.G., Bentley, M.J., 2008. Constraining the age and formation of stone runs in the Falkland Islands using Optically Stimulated Luminescence. Geomorphology 94, 117–130.
Hedding, D.W., 2008. Spatial inventory of landforms in the recantly exposed central highland of sub-Antarctic Marion Island. S. Afr. Geogr. J. 90 (1), 11–21.

Heirman, K., 2011. A Wind of Change: Changes in Position and Intensity of the Southern Hemisphere Westerlies during Oxygen Isotope Stages 3. 2 and 1 (PhD thesis). Ghent University, Ghent, Belgium.
Heisinger, B., Lal, D., Jull, A.J.T., Kubik, P., Ivy-Ochs, S., Knie, K., Nolte, E., 2002a. Production of selected cosmogenic radionuclides by muons: 2. Capture of negative muons. Earth Planet. Sci. Lett. 200 (3–4), 357–369.
Heisinger, B., Lal, D., Jull, A.J.T., Kubik, P., Ivy-Ochs, S., Neumaier, S., Knie, K., Lazarev, V., Nolte, E., 2002b. Production of selected cosmogenic radionuclides by muons: 1. Fast muons. Earth Planet. Sci. Lett. 200 (3–4), 345–355.
Herron, M.J., Anderson, J.B., 1990. Late Quaternary glacial history of the south Orkney plateau, Antarctica. Quat. Res. 33, 265–275.
Hodgson, D.A., Graham, A.G.C., Griffiths, H.J., Roberts, S.J., Ó Cofaigh, C., Bentley, M.J., Evans, D.J.A., 2014. Glacial history of sub-Antarctic South Georgia based on the submarine geomorphology of its fjords Quat. Sci. Rev. 89, 129–147.
Ivins, E.R., James, T.S., 2005. Antarctic glacial isostatic adjustment: a new assessment. Antarct. Sci. 17 (4), 541–553.
Jacka, T.H., Budd, W.F., Holder, A., 2004. A further assessment of surface temperature changes at stations in the Antarctic and Southern Ocean, 1949-2002. Ann. Glaciol. 39, 331–338.
Johnson, R.G., Andrews, J.T., 1986. Glacial terminations in theoxygen isotope record of deep sea cores: hypothesis of massive Antarctic ice-shelf destruction. Palaeogeogr. Palaeoclimatol. Palaeoecol. 53, 107–138.
Jones, V.J., Hodgson, D.A., Chepstow-Lusty, A., 2000. Palaeolimnological evidence for marked Holocene environmental changes on Signy Island, Antarctica. Holocene 10 (1), 43–60.
Kaplan, M.R., Hein, A.S., Hubbard, A., 2009. Can glacial erosion limit the extent of glaciation? Geomorphology 103 (2), 172–179.
Kiernan, K., McConnell, A., 1999. Geomorphology of the sub-Antarctic Australian Territory of Heard Island-McDonald Island. Aust. Geogr. 30 (2), 159–195.
Kiernan, K., McConnell, A., 2002. Glacier retreat and melt-lake expansion at Stephenson Glacier, Heard Island World Heritage area. Polar. Rec. 38 (207), 297–308.
Kiernan, K., McConnell, A., 2008. Periglacial processes on Heard Island, southern Indian Ocean. Pap. Proc. R. Soc. Tasmania. 142 (2), 1–12.
King, J.C., Turner, J., 1997. Antarctic Meteorology and Climatology. Cambridge Atmospheric and Space Science Series. Cambridge University Press, Cambridge, p. 409.
King, M.A., Bingham, R.J., Moore, P., Whitehouse, P.L., Bentley, M.J., Milne, G.A., 2012. Lower satellite-gravimetry estimates of Antarctic sea-level contribution. Nature 491, 586–589. http://dx.doi.org/10.1038/nature11621.
Lal, D., 1991. Cosmic-ray labeling of erosion surfaces – in situ nuclide production-rates and erosion models. Earth Planet. Sci. Lett. 104 (2–4), 424–439.
Leat, P.T., Tate, A.J., Tappin, D.R., Day, S.J., Owen, M.J., 2010. Growth and mass wasting of volcanic centers in the northern South Sandwich arc, revealed by new multibeam mapping. Mar. Geol. 275, 110–126.
Lebouvier, M., Frenot, Y., 2007. Conservation and management in the French sub-Antarctic islands and surrounding seas. Pap. Proc. R. Soc. Tasmania. 141 (1), 23–28.
Ledingham, R., Peterson, J.A., 1984. Raised beach deposits and the distribution of structural lineaments on Macquarie Island. Pap. Proc. R. Soc. Tasmania. 118, 223–235.
Lee, J.I., Bak, Y.-S., Yoo, K.-C., Lim, H.S., Yoon, H.I., Yoon, S.H., 2010. Climate changes in the South Orkney Plateau during the last 8600 years. Holocene 20, 395–404.
Lewis Smith, R.I., Clymo, R.S., 1984. An extraordinary peat-forming community on the Falkland Islands. Nature 309, 617–620.
Löffler, E., Sullivan, M.E., 1980. The extent of former glaciation on Macquarie Island. Search 11, 246–247.
Long, A., Bentley, M., Scaife, R., 2005. Sea-level and Vegetation History of the Falkland Islands: An interim report for the Shackleton Fund. Department of Geography, University of Durham, UK.
Lundqvist, J., 1988. Notes on till and moraine formation at some Heard Island glaciers. Geogr. Anna. Ser. Phys. Geogr. 70 (3), 225–234.
Marsh, P.D., Thomson, J.W., 1985. Report on Antarctic fieldwork: the Scotia metamorphic complex on Elephant island and Clarence island, South Shetland Islands. Br. Antarct. Surv. Bull. 69, 71–75.
Marshall, P., 1909. Article XXIX. – the geology of Campbell island and the Snares. In: Chilton, C. (Ed.), The Subantarctic Islands of New Zealand. Reports on the geophysics, geology, zoology, and botany of the islands lying to the south of New Zealand, Based mainly on observations and collections made during an Expedition in the Government Steamer "Hinemoa" (Captain J. Bollons) in November, 1907. Philosophical Institute of Canterbury. John Mackay, Government Printer, Wellington N.Z, pp. 680–744.
Matthews, D.W., Malling, D.H., 1967. The geology of the south Orkney islands. I. Signy Island. Sci. Rep. Falkl. Islands Depend. Surv. 25, 0–32.
Mawson, D., 1943. Macquarie Island: Its Geography and Geology. Australas. Antarctic Expedition 1911–14. In: Scientific Reports Series A: 5.
McCormac, F., Hogg, A., Blackwell, P., Buck, C., Higham, T., Reimer, P., 2004. Shcal04 southern hemisphere calibration 0-11.0 cal Kyr BP. Radiocarbon 46, 1087–1092.
McCracken, K.G., Wilson, R.E., Peters, J.L., Winker, K., Martin, A.R., 2013. Late Pleistocene colonization of south Georgia by yellow-billed pintails pre-dates the Last Glacial Maximum. J. Biogeogr.. http://dx.doi.org/10.1111/jbi.12162. Published online: 26 JUN 2013.
McDougall, I., Verwoerd, W., Chevallier, L., 2001. K–Ar geochronology of Marion Island, southern Ocean. Geol. Mag. 138, 1–17.
McGlone, M.S., Moar, N.T., Wardle, P., Meurk, C.D., 1997. The lateglacial and Holocene vegetation and environmental history of Campbell Island, far southern New Zealand. Holocene 7, 1–12.
McGlone, M.S., Wilmshurst, J.M., Wiser, S.K., 2000. Lateglacial and Holocene vegetation and climatic change on Auckland island, subantarctic New Zealand. Holocene 10 (6), 719–728.
McGlone, M.S., 2002. The Late Quaternary peat, vegetation and climate history of the Southern Oceanic Islands of New Zealand. Quat. Sci. Rev. 21 (4–6), 683–707.
McGlone, M.S., Turney, C.S.M., Wilmshurst, J.M., Renwick, J., Pahnke, K., 2010. Divergent trends in land and ocean temperature in the Southern Ocean over the past 18,000 years. Nat. Geosci.. http://dx.doi.org/10.1038/NGEO931.
McIvor, E., 2007. Heard and McDonald islands. Pap. Proc. R. Soc. Tasmania. 141 (1), 7–10.
Mercer, J., 1967. Glaciers of the Antarctic. In: Antarctic Map Folio Series, vol. 7. American Geographical Society.
Mitchell, N.C., 2003. Susceptibility of mid-ocean ridge volcanic islands and seamounts to large-scale landsliding. J. Geophys. Res. 108 (B8), 2397. http://dx.doi.org/10.1029/2002JB001997.
Mortimer, E., van Vuuren, B.J., 2007. Phylogeography of *Eupodes minutus* (Acari: Prostigmata) on sub-Antarctic Marion Island reflects the impact of historical events. Polar. Biol. 30, 471–476.
Mortimer, E., McGeoch, M.A., Daniels, S.R., Jansen Van Vuuren, B., 2008. Growth form and population genetic structure of *Azorella selago* on subAntarctic Marion Island. Antarct. Sci. 20 (4), 381–390.
Mortimer, E., van Vuuren, B., Lee, J.E., Marshall, D.J., Convey, P., Chown, S.L., 2011. Mite dispersal among the Southern Ocean Islands and Antarctica before the last glacial maximum. Proc. R. S. Lond. B 278 (1709), 1247–1255. http://dx.doi.org/10.1098/rspb.2010.1779.
Mortimer, E., Jansen Van Vuuren, B., Meiklejohn, K.I., Chown, S.L., 2012. Phylogeography of a mite, *Halozetes fulvus*, reflects the landscape history of a young volcanic island in the sub-Antarctic. Biol. J. Linn. Soc. 105, 131–145.
Myburgh, M., Chown, S.L., Daniels, S.R., Jansen Van Vuuren, B., 2007. Population structure, propagule pressure, and conservation biogeography in the sub-Antarctic: lessons from indigenous and invasive springtails. Divers. Distrib. 13 (2), 143–154.
Nel, W., 2001. A Spatial Inventory of Glacial, Periglacial and Rapid Mass Movement Forms on Part of Marion Island: Implications for Quaternary Environmental Change. University of Pretoria, South Africa, Pretoria.
Nougier, J., 1972. Aspects de morpho-tectonique glaciaire aux Iles Kerguelen. Rev. Géogr. Phys. Géol. Dyn. 14, 499–505.
Ooms, M., Van de Vijver, B., Temmerman, S., Beyens, L., 2011. A Holocene palaeoenviromental study of a sediment core from Ile de la Possession, Iles Crozet, sub-Antarctica. Antarct. Sci. 23 (5), 431–441.
Orheim, O., 1981. The glaciers of Bouvetøya. Nor. Polarinst. Skr. 175, 79–84.
Pendlebury, S.F., Barnes-Keoghan, I.P., 2007. Climate and climate change in the Sub-Antarctic. Pap. Proc. R. Soc. Tasmania. 14 (1), 67–81.
Pollard, D., DeConto, R., 2009. Modelling West Antarctic ice sheet growth and collapse through the past five million years. Nature 458, 329–332.
Quilty, P.G., 2007. Origin and evolution of the sub-Antarctic islands: the foundation. Pap. Proc. R. Soc. Tasmania. 141 (1), 35–58.
Rabassa, J., 2000. Quaternary of Tierra del Fuego, southernmost South America: an updated review. Quat. Int. 68–71, 217–240.
Recasens, C., Ariztegui, D., Gebhardt, C., Gogorza, C., Haberzettl, T., Hahn, A., Kliem, P., Lisé-Pronovost, A., Lücke, A., Maidana, N.I., Mayr, C., Ohlendorf, C., Schäbitz, F., St-Onge, G., Wille, M., Zolitschka, B., ScienceTeam, P., 2011. New insights into paleoenvironmental changes in Laguna Potrok Aike, Southern Patagonia, since the Late Pleistocene: the PASADO multiproxy record. Holocene, 0959683611429833.
Roberts, S.J., Hodgson, D.A., Shelley, S., Royles, J., Griffiths, H.J., Thorne, M.A.S., Deen, T.J., 2010. Establishing age constraints for 19th and 20th century glacier fluctuations on South Georgia (South Atlantic) using lichenometry. Geogr. Ann. (A) 92A (1), 125–139.
Rojas, M., Moreno, P., Kageyama, M., Crucifix, M., Hewitt, C., Abe-Ouchi, A., Ohgaito, R., Brady, E.C., Hope, P., 2009. The Southern Westerlies during the last glacial maximum in PMIP2 simulations. Clim. Dyn. 32, 525–548. http://dx.doi.org/10.1007/s00382-008-0421-7.
Rosqvist, G.C., Rietti-Shati, M., Shemesh, A., 1999. Late glacial to middle Holocene climatic record of lacustrine biogenic silica oxygen isotopes from a Southern Ocean island. Geology 27 (11), 967–970.
Rosqvist, G.C., Schuber, P., 2003. Millennial-scale climate changes on South Georgia, Southern Ocean. Quat. Res. 59, 470–475.
Royles, J., Ogée, J., Wingate, L., Hodgson, D.A., Convey, P., Griffiths, H., 2012. Carbon isotope evidence for recent climate-related enhancement of CO_2 assimilation and peat accumulation rates in Antarctica. Global Change Biol. 18, 3112–3124. http://dx.doi.org/10.1111/j.1365-2486.2012.02750.x.
Ruddell, A., 2005. An inventory of present glaciers on Heard Island and their historical variation. In: Green, K., Woehler, E. (Eds.), Heard Island. Southern Ocean Sentinel. Surrey Beatty & Sons, Chipping Norton, pp. 28–51.
Ryan, W.B.F., Carbotte, S.M., Coplan, J.O., O'Hara, S., Melkonian, A., Arko, R., Weissel, R.A., Ferrini, V., Goodwillie, A., Nitsche, F., Bonczkowski, J., Zemsky, R., 2009. Global multi-resolution topography synthesis. Geochem. Geophys. Geosyst. 10 (3), Q03014. http://dx.doi.org/10.1029/2008GC002332.
Schalke, H.J.W.G., van Zinderen Bakker, E.M.S., 1971. History of the vegetation. In: Van Zinderen Bakker, E.M., Winterbottom, J.M., Dyer, R.A. (Eds.), Marion and

Prince Edward Islands. Report on the South African Biological and Geo-logical Expedition, 1965–1966. A.A. Balkema, Cape Town, pp. 89–97.
Schoof, C., 2007. Ice sheet grounding line dynamics: steady states, stability and hysteresis. J. Geophys. Res. Earth Surf. 112, F03S28.
Scott, L., 1985. Palynological indications of the Quaternary vegetation history of Marion Island (sub-Antarctic). J. Biogeogr. 12, 413–431.
Selkirk-Bell, J.M., Selkirk, P.M., 2013. Vegetation-banked terraces on subantarctic Macquarie Island: a reappraisal. Arct. Antarc. Alp. Res. 45 (2), 261–274.
Selkirk, D.R., Selkirk, P.M., Griffin, K., 1982. Palynological evidence for Holocene environmental change and uplift on Wireless Hill, Macquarie Island. Proc. Linn. Soc. N. S. W. 107 (1), 1–17.
Selkirk, D.R., Selkirk, P.M., Bergstrom, D.M., Adamson, D.A., 1988. Ridge top peats and palaeolake deposits on Macquarie Island. Pap. Proc. R. Soc. Tasmania 122 (1), 83–90.
Selkirk, J.M., 1998. Active vegetation-banked terraces on Macquarie Island. Zeitsschr. Geomorph. N. F. 42 (4), 243–496.
Selkirk, P.M., Seppelt, R.D., Selkirk, D.R., 1990. Subantarctic Macquarie Island: Environment and Biology. Cambridge University Press, Cambridge, p. 285.
Selkirk, P.M., McBride, T.P., Keenan, H.M., Adamson, D.A., 1991. Palaeolake deposits and cliff retreat on subantarctic Macquarie Island. In: Gillieson, D.S., Fitzsimons, S.J. (Eds.), Quaternary Research in Australian Antarctica: Future Directions. ADFA, Canberra, pp. 45–53.
Singer, B.S., Ackert, R.P.J., Guillou, H., 2004. 40Ar/39Ar and K–Ar chronology of Pleistocene glaciations in Patagonia. Geol. Soc. Am. Bull. 116, 434–450.
Smith, R.I.L., 1981. Types of peat and peat-forming vegetation on South Georgia. Br. Antarct. Surv. Bull. 53, 119–139.
Speight, R., 1909. Article XXX. – Physiography and geology of the Auckland, Bounty and Antipodes islands. In: Chilton, C. (Ed.), The Subantarctic Islands of New Zealand. Reports on the geo-physics, geology, zoology, and botany of the islands lying to the south of New Zealand, Based mainly on observations and collections made during an Expedition in the Government Steamer "Hinemoa" (Captain J. Bollons) in November, 1907. Philosophical Institute of Canterbury. John Mackay, Government Printer, Wellington N.Z, pp. 705–744.
Stager, J.C., Mayewski, P.A., White, J., Chase, B.M., Neumann, F.H., Meadows, M.E., King, C.D., Dixon, D.A., 2012. Precipitation variability in the winter rainfall zone of South Africa during the last 1400 yr linked to the austral westerlies. Clim. Past 8, 877–887.
Stone, J.O., 2000. Air pressure and cosmogenic isotope production. J. Geophys. Res. – Atmos. 105 (B10), 23753–23759.
Sugden, D.E., Clapperton, C.M., 1977. The maximum ice extent on island groups in the Scotia Sea, Antarctica. Quat. Res. 7, 268–282.
Sugden, D.E., Bentley, M.J., Fogwill, C.J., Hulton, N.R.J., McCulloch, R.D., Purves, R.S., 2005. Late-glacial glacier events in southernmost South America: a blend of 'northern' and 'southern' hemispheric climatic signals. Geogr. Ann.: Ser. A, Phys. Geogr. 87 (2), 273–288.
Sumner, P.D., Meiklejohn, K.I., Boelhouwers, J.C., Hedding, D.W., 2004. Climate change melts Marion Island snow and ice. S. Afr. J. Sci. 100, 395–398.
Taylor, B.W., 1955. The Flora, Vegetation and Soils of Macquarie Island. In: ANARE Reports, Series B, vol. II, p. 192. Botany.
Testut, L., Wöppelmann, G., Simon, B., Téchiné, P., 2005. The sea level at Port-aux-Français, Kerguelen Island, from 1950 to the present. Ocean Dyn.. http://dx.doi.org/10.1007/s10236-005-0056-8.
Thost, D.E., Truffer, M., 2008. Glacier recession on Heard Island, southern Indian ocean. Arctic Antarc. Alp. Res. 40, 199–214.
Toggweiler, J.R., Russell, J.L., Carson, S.R., 2006. Midlatitude westerlies, atmospheric CO2, and climate change during the ice ages. Palaeoceanography 21, PA2005. http://dx.doi.org/10.1029/2005PA001154.
Vallon, M., 1977. Bilan de masse et fluctuations récentes du Glacier Ampère (Iles Kerguelen, TAAF). Zeitschr. Gletscherkd. Glazialgeol. 13, 55–85.
Van der Putten, N., Stieperaere, H., Verbruggen, C., Ochyra, R., 2004. Holocene palaeoecology and climate history of South Georgia (sub-Antarctic) based on a macrofossil record of bryophytes and seeds. Holocene 14 (3), 382–392.
Van der Putten, N., Verbruggen, C., 2005. The onset of deglaciation of Cumberland Bay and Stromness Bay, South Georgia. Antarct. Sci. 17 (1), 29–32.
Van der Putten, N., 2008. Post-glacial Palaeoecology and Palaeoclimatology in the Sub-Antarctic. University of Ghent, Ghent, p. 266.
Van der Putten, N., Hébrard, J.P., Verbruggen, C., Van de Vijver, B., Disnar, J.R., Spassov, S., de Beaulieu, J.L., De Dapper, M., Keravis, D., Hus, J., Thouveny, N., Frenot, Y., 2008. An integrated palaeoenvironmental investigation of a 6200 year old peat sequence from Ile de la Possession, Iles Crozet, sub-Antarctica. Palaeogeogr. Palaeoclimatol. Palaeoecol. 270, 179–185.
Van der Putten, N., Verbruggen, C., Ochyra, R., Spassov, S., de Beaulieu, J.-L., Dapper, M.D., Hus, J., Thouveny, N., 2009. Peat bank growth, Holocene palaeoecology and climate history of South Georgia (sub-Antarctica), based on a botanical macrofossil record. Quat. Sci. Rev. 28, 65–79.
Van der Putten, N., Verbruggen, C., Ochyra, R., Verleyen, E., Frenot, Y., 2010. Subantarctic flowering plants: pre-glacial survivors or post-glacial immigrants? J. Biogeogr. 37 (3), 582–592.
Van der Putten, N., Mauquoy, D., Verbruggen, C., Björck, S., 2012. Subantarctic peatlands and their potential as palaeoenvironmental and palaeoclimatic archives. Quat. Int. 268, 65–76.
Van der Putten, N., Verbruggen, C., Alexanderson, H., Björck, S., Van de Vijver, B., 2013. Postglacial sedimentary and geomorphological evolution of a small sub-Antarctic fjord landscape, Stromness Bay, South Georgia. Antarct. Sci. 25 (03), 409–419.
Verwoerd, W.J., 1971. Geology. In: Van Zinderen Bakker, E.M., Winterbottom, J.M., Dyer, R.A. (Eds.), Marion and Prince Edward Islands. Balkema, Cape Town, pp. 40–53.
Wagstaff, S.J., Breitwieser, I., Ito, M., 2011. Evolution and biogeography of Pleurophyllum (Astereae, Asteraceae), a small genus of megaherbs endemic to the subantarctic islands. Am. J. Bot. 98 (1), 62–75. http://dx.doi.org/10.3732/ajb.1000238.
Wasell, A., 1993. Diatom Stratigraphy and Evidence of Environmental Changes in Selected Lake Basins in the Antarctic and South Georgia. Report 23. Stockholm University, Department of Quaternary Research, Stockholm.
Wilson, P., Clark, R., Birnie, J., Moore, D.M., 2002. Late Pleistocene and Holocene landscape evolution and environmental change in the Lake Sullivan area, Falkland Islands, South Atlantic. Quat. Sci. Rev. 21, 1821–1840.
Wilson, P., Bentley, M.J., Schnabel, C., Clark, R., Xu, S., 2008. Stone run (block stream) formation in the Falkland Islands over several cold stages, deduced from cosmogenic isotope (^{10}Be and ^{26}Al) surface exposure dating. J. Quat. Sci. 23 (5), 461–473.
Wright, J.B., 1967. Contributions to the volcanic succession and petrology of the Auckland Islands II. Upper parts of the Ross Volcano. Trans. R. Soc. N. Z. Geol. 5, 71–87.
Yeloff, D., Mauquoy, D., Barber, K., Way, S., van Geel, B., Turney, C.S.M., 2007. Volcanic ash deposition and long-term vegetation change on subantarctic Marion Island. Arct. Antarc. Alp. Res. 39 (3), 500–511. http://dx.doi.org/10.1657/1523-0430(06-040)[YELOFF]2.0.CO;2.
Young, S.B., Schofield, E.K., 1973a. Pollen evidence for late Quaternary climate changes on Kerguelen islands. Nature 245, 311–312.
Young, S.B., Schofield, E.K., 1973b. Palynological evidence for the Late Glacial occurrence of *Pringlea* and *Lyallia* on Kergulen Islands. Rhodora 75, 239–247.

Annexe D

Article Bentley et al. (2014)

Quaternary Science Reviews 100 (2014) 1–9

Contents lists available at ScienceDirect

Quaternary Science Reviews

journal homepage: www.elsevier.com/locate/quascirev

A community-based geological reconstruction of Antarctic Ice Sheet deglaciation since the Last Glacial Maximum

The RAISED Consortium[1], Michael J. Bentley [a, *], Colm Ó Cofaigh [a], John B. Anderson [b], Howard Conway [c], Bethan Davies [d], Alastair G.C. Graham [e], Claus-Dieter Hillenbrand [f], Dominic A. Hodgson [f], Stewart S.R. Jamieson [a], Robert D. Larter [f], Andrew Mackintosh [g], James A. Smith [f], Elie Verleyen [h], Robert P. Ackert [i], Philip J. Bart [j], Sonja Berg [k], Daniel Brunstein [l], Miquel Canals [m], Eric A. Colhoun [n], Xavier Crosta [o], William A. Dickens [f], Eugene Domack [p], Julian A. Dowdeswell [q], Robert Dunbar [r], Werner Ehrmann [s], Jeffrey Evans [t], Vincent Favier [u], David Fink [v], Christopher J. Fogwill [w], Neil F. Glasser [d], Karsten Gohl [x], Nicholas R. Golledge [g], Ian Goodwin [y], Damian B. Gore [y], Sarah L. Greenwood [z], Brenda L. Hall [aa], Kevin Hall [ab], David W. Hedding [ac], Andrew S. Hein [ad], Emma P. Hocking [ae], Martin Jakobsson [z], Joanne S. Johnson [f], Vincent Jomelli [l], R. Selwyn Jones [g], Johann P. Klages [x], Yngve Kristoffersen [af], Gerhard Kuhn [x], Amy Leventer [ag], Kathy Licht [ah], Katherine Lilly [ai], Julia Lindow [aj], Stephen J. Livingstone [ak], Guillaume Massé [al], Matt S. McGlone [am], Robert M. McKay [g], Martin Melles [k], Hideki Miura [an], Robert Mulvaney [f], Werner Nel [ao], Frank O. Nitsche [ap], Philip E. O'Brien [y], Alexandra L. Post [aq], Stephen J. Roberts [f], Krystyna M. Saunders [ar], Patricia M. Selkirk [as], Alexander R. Simms [at], Cornelia Spiegel [aj], Travis D. Stolldorf [b], David E. Sugden [ad], Nathalie van der Putten [au], Tas van Ommen [av], Deborah Verfaillie [u], Wim Vyverman [h], Bernd Wagner [k], Duanne A. White [aw], Alexandra E. Witus [b], Dan Zwartz [g]

[a] Department of Geography, Durham University, Science Laboratories, South Rd, Durham, DH1 3LE, UK
[b] Department of Earth Sciences, Rice University, 6100 Main Street, Houston, TX 77005, USA
[c] Department of Earth and Space Sciences, University of Washington, 4000 15th Avenue NE, Seattle, WA, USA
[d] Centre for Glaciology, Department of Geography and Earth Sciences, Aberystwyth University, Aberystwyth, Wales, SY23 3DB, UK
[e] College of Life and Environmental Sciences, University of Exeter, Exeter, EX4 4RJ, UK
[f] British Antarctic Survey, High Cross, Madingley Rd, Cambridge, CB3 0ET, UK
[g] Antarctic Research Centre, Victoria University of Wellington, PO Box 600, Wellington, New Zealand
[h] Laboratory for Protistology and Aquatic Ecology, Biology Department, Ghent University, Krijgslaan 281–S8, 9000, Ghent, Belgium
[i] Department of Earth and Planetary Science, Harvard University, Cambridge, MA, USA
[j] Department of Geology and Geophysics, Louisiana State University, Baton Rouge, LA, USA
[k] Institute of Geology and Mineralogy, University of Cologne, Zuelpicher Strasse 49a, 50674 Cologne, Germany
[l] Université Paris 1 Panthéon Sorbonne–CNRS, Laboratoire de Géographie Physique, 1 Place A. Briand, 92195, Meudon, France
[m] CRG Marine Geosciences, Department of Stratigraphy, Paleontology and Marine Geosciences, Faculty of Geology, University Barcelona, Campus de Pedralbes, C/Marti i Franques s/n, 08028, Barcelona, Spain
[n] School of Environmental and Life Sciences, The University of Newcastle, NSW, 2308, Australia
[o] Environnement et Paléoenvironnement Océaniques et Continentaux, UMR 5805, Université Bordeaux 1, Avenue des Facultés, 33405, Talence Cedex, France
[p] College of Marine Science, University of South Florida, 140 7th Avenue South, St. Petersburg, FL 33701-5016, USA
[q] Scott Polar Research Institute, University of Cambridge, Cambridge, CB2 1ER, UK
[r] Environmental Earth System Science, Stanford University, Stanford, CA, 94305, USA
[s] Institute of Geophysics and Geology, University of Leipzig, Talstraße 35, D-04103, Leipzig, Germany
[t] Department of Geography, University of Loughborough, Loughborough, LE11 3TU, UK
[u] Laboratoire de Glaciologie et de Géophysique de l'Environnement, LGGE, UJF–CNRS, UMR5183, 54 rue Molière, 38402, St Martin d'Hères, France
[v] Institute for Environmental Research, ANSTO, Menai, NSW, 2234, Australia
[w] Climate Change Research Centre, University of New South Wales, Sydney, Australia

* Corresponding author.
E-mail address: m.j.bentley@durham.ac.uk (M.J. Bentley).

[1] RAISED = Reconstruction of Antarctic Ice Sheet Deglaciation.

http://dx.doi.org/10.1016/j.quascirev.2014.06.025

[x] Alfred Wegener Institute, Helmholtz-Centre for Polar and Marine Research, Am Alten Hafen 26, D-27568, Bremerhaven, Germany
[y] Department of Environment and Geography, Macquarie University, NSW, 2109, Australia
[z] Department of Geological Sciences, Stockholm University, 106 91, Stockholm, Sweden
[aa] School of Earth and Climate Sciences, University of Maine, Orono, ME, USA
[ab] Geography Programme, University of Northern British Columbia, 3333 University Way, Prince George, BC, V2N 479, Canada
[ac] Department of Geography, University of South Africa, Florida Campus, Private Bag X6, Florida, 1710, South Africa
[ad] School of GeoSciences, University of Edinburgh, Drummond Street, Edinburgh, EH8 9XP, UK
[ae] Department of Geography, Northumbria University, Newcastle upon Tyne, NE1 8ST, UK
[af] Department of Earth Science, University of Bergen, Allegate 41, Bergen, N-5014, Norway
[ag] Department of Geology, Colgate University, Hamilton, NY, 13346, USA
[ah] Department of Earth Sciences, Indiana University-Purdue University Indianapolis, 723 West Michigan Street, SL118, Indianapolis, IN, USA
[ai] Department of Geology, University of Otago, PO Box 56, Dunedin, New Zealand
[aj] Department of Geosciences, University of Bremen, Bremen, Germany
[ak] Department of Geography, University of Sheffield, Sheffield, S10 2TN, UK
[al] LOCEAN, UMR7159 CNRS/UPMC/IRD/MNHN, Université Pierre et Marie Curie, 4 Place Jussieu, 75252, Paris, France
[am] Landcare Research, PO Box 40, Lincoln, 7640, New Zealand
[an] National Institute of Polar Research, 10-3 Midori-cho, Tachikawa, Tokyo, 190-8518, Japan
[ao] Department of Geography and Environmental Science, University of Fort Hare, Alice Campus, Private Bag X1314, Alice, 5700, South Africa
[ap] Lamont-Doherty Earth Observatory of Columbia University, Palisades, NY, USA
[aq] Geoscience Australia, GPO Box 378, Canberra, ACT, 2601, Australia
[ar] Institute of Geography and the Oeschger Centre for Climate Change Research, University of Bern, Bern, Erlachstrasse 9, Trakt 3, 3012, Switzerland
[as] Department of Biological Sciences, Macquarie University, Sydney, NSW, 2109, Australia
[at] Department of Earth Science, University of California, Santa Barbara, 1006 Webb Hall, Santa Barbara, CA, 93106, USA
[au] Department of Geology, Lund University, Sölvegatan 12, SE–223 62, Lund, Sweden
[av] Australian Antarctic Division and Antarctic Climate and Ecosystems Cooperative Research Centre, Private Bag 80, Hobart 7001, Tasmania, Australia
[aw] Institute for Applied Ecology, University of Canberra, ACT, 2601, Australia

ARTICLE INFO

Article history:
Received 4 December 2013
Received in revised form
11 June 2014
Accepted 18 June 2014
Available online 22 July 2014

Keywords:
Antarctic Ice Sheet
Glacial geology
Modelling
Quaternary

ABSTRACT

A robust understanding of Antarctic Ice Sheet deglacial history since the Last Glacial Maximum is important in order to constrain ice sheet and glacial-isostatic adjustment models, and to explore the forcing mechanisms responsible for ice sheet retreat. Such understanding can be derived from a broad range of geological and glaciological datasets and recent decades have seen an upsurge in such data gathering around the continent and Sub-Antarctic islands. Here, we report a new synthesis of those datasets, based on an accompanying series of reviews of the geological data, organised by sector. We present a series of timeslice maps for 20 ka, 15 ka, 10 ka and 5 ka, including grounding line position and ice sheet thickness changes, along with a clear assessment of levels of confidence. The reconstruction shows that the Antarctic Ice sheet did not everywhere reach the continental shelf edge at its maximum, that initial retreat was asynchronous, and that the spatial pattern of deglaciation was highly variable, particularly on the inner shelf. The deglacial reconstruction is consistent with a moderate overall excess ice volume and with a relatively small Antarctic contribution to meltwater pulse 1a. We discuss key areas of uncertainty both around the continent and by time interval, and we highlight potential priorities for future work. The synthesis is intended to be a resource for the modelling and glacial geological community.

1. Aim and rationale

This paper provides an overview of, and introduction to, a community-based reconstruction of the deglaciation of the Antarctic Ice Sheet. Reconstructing the Antarctic Ice Sheet through its most recent (post-Last Glacial Maximum; LGM) deglacial history is important for a number of reasons (Bentley, 2010). Firstly, ice sheet modellers require field data against which to constrain and test their models of ice sheet change. The development of a practical approach to modelling grounding line dynamics (Schoof, 2007) has led to a new generation of models (e.g. Pollard and DeConto, 2009; Pattyn et al., 2012) that require such field constraints. Secondly, the most recent millennia of Antarctic Ice Sheet history are important for evaluating the response of the ice sheet to various forcing agents (e.g. sea-level rise, atmospheric and oceanographic temperature influences) and constraining past rates of grounding-line retreat. Thirdly, the use of recent satellite gravity measurements (e.g. GRACE), and other geodetic data such as GPS, for estimating ice-sheet mass balance requires an understanding of Glacial-Isostatic Adjustment (GIA). In the case of GRACE, the satellite-pair cannot distinguish between changes in mass from ice, and those from transfer of mass in the mantle. This means that robust ice-sheet reconstructions are required to generate GIA corrections and it is these corrections that are regarded as the greatest limiting factors for gravimetric estimates of ice-sheet mass balance (Chen et al., 2006; Velicogna and Wahr, 2013). There have been notable attempts to develop models of ice-sheet extent and thickness as a basis of GIA corrections (Ivins and James, 2005; Whitehouse et al., 2012a; Ivins et al., 2013) but it is not clear if these are comprehensive in their inclusion of all available marine and terrestrial glacial geological data. In addition, ice-sheet reconstructions are also important for constraining the location of biological refugia during glaciation (Convey et al., 2008) and understanding climatic and oceanographic change during the glacial–interglacial transition.

Several decades of work have produced a large body of geological data constraining Antarctic Ice Sheet history. There have been a number of attempts to synthesise the data but many of these reconstructions have focussed only on LGM ice-sheet extent (Denton and Hughes, 1981; Anderson, 1999; Bentley, 1999; Anderson et al., 2002; Denton and Hughes, 2002; Wright et al., 2008; Livingstone et al., 2012) and in some places they have been

superseded by new datasets. Importantly, the period between the LGM and present has not seen similar attention. Moreover, significant progress has been made in developing and refining the methods used to acquire and analyse data needed for terrestrial and marine records of past ice-sheet thickness and extent (e.g. mapping of subglacial bedforms on the continental shelf using multibeam-swath bathymetry). Many of these new datasets that have been acquired have yet to be incorporated into continent-wide reconstructions of the ice sheet.

The glacial geological literature is widely dispersed across journals and reports ('grey' literature), covers a broad range of techniques, is presented in many different formats, and is subject to various uncertainties (especially dating) that may be subtle, and have changed over time as techniques and understanding have developed. Understandably, therefore, it can be difficult for modellers to penetrate and use this literature to constrain and test their models.

This volume contains results from a co-ordinated effort by the Antarctic glacial geology community to develop a synthesis of Antarctic ice-sheet history and to create a series of ice-sheet reconstructions that can be used by ice sheet and GIA modellers. It should also foster further research and debate within the geological community on the progress made in understanding Antarctic Ice Sheet history. Other ice sheet communities have already completed such syntheses, including the Laurentide (Dyke et al., 2002), the Fennoscandian (Gyllencreutz et al., 2007), and the British-Irish (Clark et al., 2012) ice sheets.

The RAISED consortium comprises a wide community of glacial and marine geologists and others working on ice sheet history. Collectively we have assembled a group of experts able to develop and document a series of reconstructions for each of the sectors around Antarctica, and drawn these together into a synthesis that we believe is comprehensive, provides realistic assessment of uncertainty and is broadly representative of the views of the whole community, and which can be used by modellers.

The detailed reviews are divided into six sectors: East Antarctica (Mackintosh et al., 2014), Ross Sea (Anderson et al., 2014), Amundsen-Bellingshausen Sea (Larter et al., 2014), Antarctic Peninsula (Ó Cofaigh et al., 2014), Weddell Sea (Hillenbrand et al., 2014) and sub-Antarctic Islands (Hodgson et al., 2014). The approximate sector boundaries are shown in Fig. 1. The divisions are based broadly on glaciological and topographic grounds. Most sectors are named by coastal sector because much of the data comes from the continental shelf or coastal nunataks, but sectors also extend inland to encompass relevant ice-core data, where available. The sector division we have used is also fairly compatible with earlier divisions of the continent by modellers, glaciologists, and field studies and so should facilitate broad comparison.

This overview paper summarises these sector-by-sector reviews and presents an Antarctic-wide reconstruction of deglaciation since the LGM. We also discuss the common themes that emerge, and identify key areas for further work. We emphasise that anyone wishing to utilise any part of the reconstruction is strongly advised to read the relevant sector papers, which include much more detail including extended discussions of where and why there are key uncertainties.

2. Approach and Methods

For all sectors we have attempted, where possible, to provide reconstructions of the ice sheet (with clear identification of the range of uncertainty) for a series of timeslices, namely 20 ka, 15 ka, 10 ka, and 5 ka. In some sectors the available data are not sufficient to allow this classification: these are discussed further below. In a few sectors data availability was sufficient to allow a further timeslice of 25 ka: these are discussed in the relevant papers. The timeslices were chosen to strike a balance between the reality of available data, and providing sufficient closely-spaced reconstructions for them to be useful to modellers, as well as to provide reconstructions of time periods other than the maximum. A spacing of 5 ka was chosen to provide a reasonable compromise between data availability and the needs of modellers. The use of *dated* timeslices also has the advantage of avoiding terms like 'the LGM', which has been used rather variably both to refer to local ice-sheet maxima, and as a global chronostratigraphic term to refer to the period c. 26.5–19 ka BP (see Clark et al., 2009 for discussion). This has led to some confusion in ice-sheet syntheses. Whilst the 20 ka timeslice can be a useful rough proxy for the global LGM, it is clear from Anderson et al. (2002) and this volume that the Antarctic Ice Sheets did not reach a synchronous maximum extent, and that Local Last Glacial Maximum (LLGM; (Clark et al., 2009)) positions differ widely in timing.

Each paper in this volume synthesises the available marine and terrestrial glacial geological datasets to determine the position of the ice-sheet grounding-line, the ice-sheet upper surface, and in some cases flow-directional features for that particular sector and timeslice. We have made considerable efforts to be clear about uncertainty in the position and timing of retreat of the grounding-line and, as such, it is intended to demonstrate where there are robust constraints for models as opposed to geographic areas or time intervals where the position of the grounding-line or ice-sheet surface is less certain. There are a number of challenges associated with dating the geological evidence of deglaciation around Antarctica: offshore this includes the marine-reservoir effect, and reworking of old carbon, and onshore the reworking of previously exposed erratics presents problems for cosmogenic dating. These uncertainties are assessed in full in each of the sector papers. The use of timeslices also allows future development of more closely-spaced reconstructions, as available datasets expand to address specific debates. In cases where there are time intervals that are unusually data-rich it will be possible to develop new timeslice reconstructions. This may be particularly appropriate for intervals during the immediate post-maximum deglaciation where there is often much more marine geological data available.

2.1. Availability of data

Each of the sector reviews provides substantial datasets identifying critical chronological data that have been used to constrain the reconstructions – these are available online as supplementary datasets. We also include here, as a supplementary dataset, the Antarctic-wide timeslice reconstructions of grounding-line and ice-sheet surface (Supplementary Information). We emphasise that any use of the data should rest on careful reading, and citation, of the appropriate individual sector paper(s): these are where critical issues of dating uncertainties and calibration, alternative models and other issues are discussed in detail.

3. Reconstructions

We show the combined reconstructions for each timeslice in Fig. 2. Around the West Antarctic margin and those parts of the East Antarctic Ice Sheet (EAIS) that flow into the Ross Sea and Weddell Sea the available data allow timeslice reconstructions of 20 ka, 15 ka, 10 ka, and 5 ka (Fig. 2a–d). Note that, due to a lack of constraining data around much of the East Antarctic margin and in particular a lack of dating control, we are unable yet to attempt a full time-slice reconstruction of the deglaciation of the largest part of the EAIS (Mackintosh et al., 2014). However, this does not mean

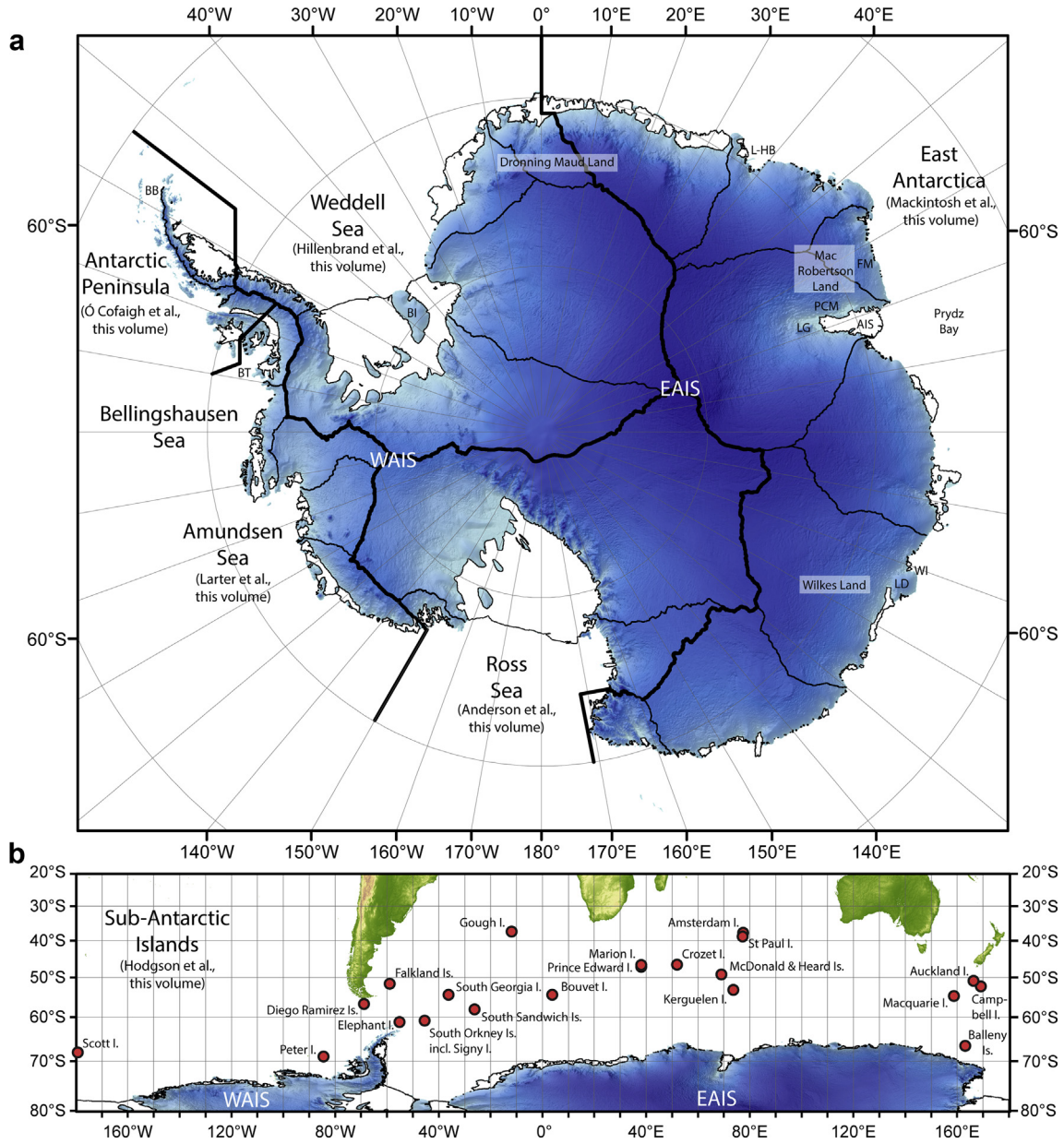

Fig. 1. Map of sector boundaries for the reconstructions presented in this volume. (a) Map of Antarctica. Blue shading indicates ice sheet elevation, ice shelves in white. Ice divides based on Zwally et al. (2012). EAIS = East Antarctic Ice Sheet; WAIS = West Antarctic Ice Sheet; L-HB = Lützow-Holm Bay; FM = Framnes Mountains; PCM = Prince Charles Mountains; LG = Lambert Glacier; AIS = Amery Ice Shelf; WI = Windmill Islands; LD = Law Dome; BT = Belgica Trough; BB = Bransfield Basin; BI = Berkner Island. (b) Map of sites (red dots) included in the review of sub-Antarctic islands (Hodgson et al., 2014).

that no constraints are possible. Accordingly, we include the EAIS in the 20 ka timeslice (Fig. 2a) with ice sheet thickness changes in this sector from Mackintosh et al. (2014), and a grounding line position based on Livingstone et al. (2012), but modified to be fully consistent with grounding-line features described by Mackintosh et al. (2014) in Prydz Bay and George V Shelf. Moreover, Mackintosh et al. (2014) discuss the data in great detail region-by-region around the East Antarctic margin, including areas such as Mac. Robertson Land and adjacent to the Lambert/Amery system where robust constraints do exist. For the sub-Antarctic islands there are data available for maximum configurations of the ice masses over some islands, but there are few data for subsequent periods and so we are not yet in a position to provide timeslice reconstructions for deglacial configurations (see Hodgson et al. (2014) for full discussion).

3.1. 20 ka timeslice

Around much of Antarctica the grounding line was close to the continental shelf break at 20 ka. However, there are important exceptions in the Ross Sea, Prydz Bay, and Weddell Sea regions. Moreover, in some areas the maximum extent was reached prior to 20 ka and retreat had begun by this time (e.g. Hillenbrand et al., 2014).

There is an ongoing debate about the extent of ice in the Weddell Sea at the LGM, and the post-LGM retreat history (Hillenbrand et al., 2014). In broad terms, the available marine geological data in the Weddell Sea have been interpreted as showing extensive ice on the continental shelf at 20 ka. However, data are sparse in the southern Weddell Sea where the confluence of ice flowing from the East Antarctic and West Antarctic Ice Sheets occurred. In this

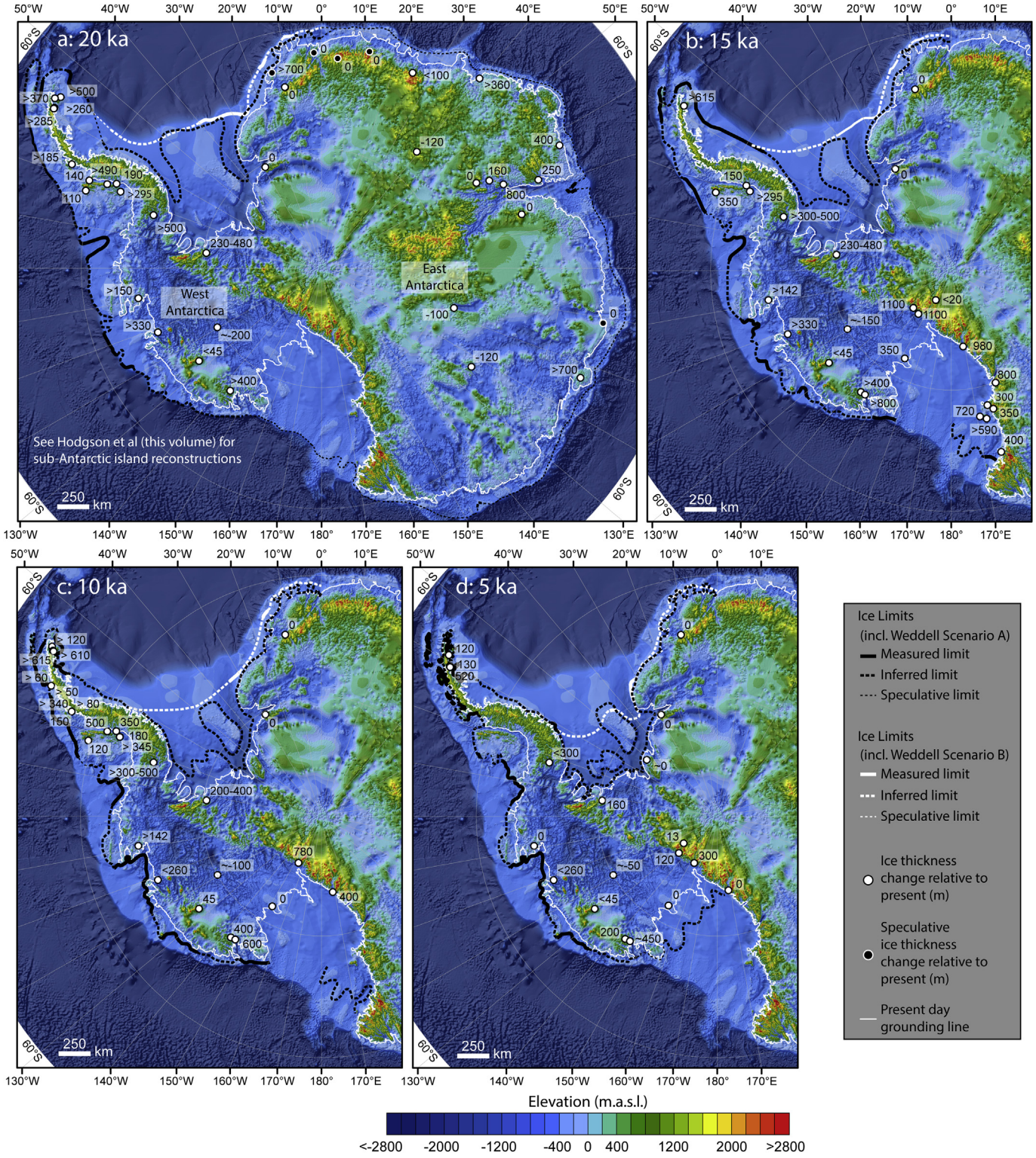

Fig. 2. Timeslice reconstructions for the Antarctic Ice Sheet. Bed topography from BEDMAP2 (Fretwell et al., 2013). (a) 20 ka; (b) 15 ka; (c) 10 ka; (d) 5 ka. In all cases we show grounding line position and ice sheet thickness change (in metres relative to present elevation) or reconstructed ice sheet elevation (Ross Sea only). For grounding line positions the level of uncertainty is indicated by line style. For most of the sub-Antarctic islands, only information on maximum extent is known, and so we do not show the full timeslice reconstruction (see Hodgson et al. (2014)). For the 20 ka timeslice there are portions of the East Antarctic sector and Ross Sea sector where we are unable to place a firm grounding line limit; in these areas we adopt the grounding line in Livingstone et al. (2012) but emphasise that the nature of the uncertainty in grounding line position in these areas are discussed in full in Mackintosh et al. (2014) and Anderson et al. (2014)

region, the retreat history of the EAIS is still open to debate and the retreat history of the West Antarctic Ice Sheet (WAIS) is virtually unconstrained by reliable radiocarbon dates (Hillenbrand et al., 2012; Stolldorf et al., 2012). Terrestrial glacial-geological data show very little change in elevation of the EAIS (e.g. Hein et al., 2011) and by use of ice sheet models the terrestrial data have been used to infer much less extensive grounded ice on the shelf than in the Hillenbrand et al. (2012) reconstruction (e.g. Bentley et al., 2010). The two scenarios imply very different spatial extent of the ice sheet in the Weddell Sea embayment and this is reflected in Fig. 2 by the use of an alternative, more extensive grounding line (Scenario B) in the Weddell Sea. So in this region the selection of a particular limit depends on the interpretation of the available data. Hillenbrand et al. (2014) discuss both scenarios in detail and following Hillenbrand et al. (2012) and Larter et al. (2012), suggest that one potential way to reconcile these conflicting reconstructions would be for thin, low-gradient, lightly-grounded ice sheets to have extended across the outer shelf.

In the Antarctic Peninsula sector the ice sheet was grounded to the outer shelf/shelf edge at the LGM until ~20 ka BP (O'Cofaigh et al., 2014). Based on the distribution of glacial landforms and subglacial sediments, palaeo-drainage of the ice sheet across the inner and middle shelf was partitioned into a series of ice streams flowing in cross-shelf bathymetric troughs.

In the Belgica Trough, Bellingshausen Sea the grounding line was deeply embayed and ice-sheet retreat had begun already (Larter et al., 2014). In the Amundsen Sea Embayment, geomorphological features and a small number of radiocarbon dates from the outer shelf indicate that the grounding line extended to, or close to, the shelf edge. However, data constraining the earliest stages of grounding-line retreat are sparse. Foraminifera-bearing layers of LGM age in one core near the shelf edge suggest that either retreat started before 20 ka or the grounding line position fluctuated across the outer shelf at around this time.

Anderson et al. (2014) demonstrate that over half of the ice that was grounded in the Ross Sea came from East Antarctica. In eastern Ross Sea, subglacial geomorphological features extend to the shelf margin, indicating that the WAIS extended across the continental shelf during the last ice-sheet expansion. However, the precise timing of this expansion remains unresolved and we are unable to constrain the limit at 20 ka. Marine radiocarbon ages, mainly acid insoluble organic (AIO) ages, indicate that the ice sheet probably retreated from the shelf prior to the LGM. Terrestrial and glaciological data from the margins of the Ross Sea embayment indicate that the ice sheet retreated during the Holocene. Ongoing research is focused on obtaining compound specific radiocarbon ages aimed at resolving this controversy.

Although large tracts of East Antarctica have not been studied in detail, Mackintosh et al. (2014) show that the ice sheet in Mac. Robertson Land reached close to the continental-shelf margin at this time. In contrast, in Prydz Bay the Lambert/Amery glacier did not extend beyond the inner continental shelf. Onshore, evidence from nunataks in the Prince Charles and Framnes Mountains indicate that the ice sheet thickened by hundreds of metres near the current coast or grounding lines. On the other hand, preservation of sediments from Marine Isotope Stage 3 or earlier indicates that many low-lying coastal oases remained ice-free during this period. Similarly, in Dronning Maud Land, a limited amount of evidence from nunataks suggests that modest or no thickening of the ice sheet occurred at this time. In the ice-sheet interior, ice-core evidence and ice-sheet models indicate that it is probable that the central domes of the ice sheet were around 100 m lower than present. Note that there are very few direct ages on glacial features from ~20 ka in East Antarctica and inferences of the position and thickness of the former ice sheet are largely based on relatively loose minimum or maximum age constraints.

There is evidence on Sub-Antarctic Heard Island, Bouvet Island, Marion Island, Prince Edward Island and Crozet Island, and maritime Antarctic South Orkney Islands and Elephant Island for glaciations extending well onto their continental shelves. However a lack of age constraints from marine sediment cores means these cannot be unequivocally dated to the LGM or to the 20 ka timeslice.

3.2. 15 ka timeslice

In the Antarctic Peninsula, initial retreat was underway by 18 cal ka BP in the east and by 17.5 cal ka BP in Bransfield Basin. Further south, however, along the western Peninsula margin, the timing of initial pull-back from the outer shelf decreased progressively. Retreat of individual ice streams appears to have been asynchronous with subglacial topography exerting a major control. In the western Weddell Sea, the interpretation underpinning the extensive scenario (B) suggests ice had withdrawn from the shelf edge, whereas in Scenario A the ice had retreated onto the mid-shelf in the western Weddell Sea. The grounding line in the western Ross Sea was little changed from the 20 ka position.

There is only one site in East Antarctica (north of Loewe Massif in the Prince Charles Mountains) where there is clear evidence of ice retreat on the continental shelf prior to 15 ka. At all other sites where direct constraints are available, it appears that the East Antarctic Ice Sheet remained close to its maximum position on the shelf at this time. However, exposure of some terrestrial sites (Mackintosh et al., 2014) suggests a thinned ice sheet in places, particularly along the present-day coast.

In the Belgica Trough, Bellingshausen Sea the retreat of an embayed grounding line continued. Similar embayments into outer-shelf troughs probably developed in the eastern Amundsen Sea area, but the only age constraints available from an inter-stream ridge in the area suggest retreat there must have followed shortly after retreat in the adjacent troughs. In the western part of the Amundsen Sea, the grounding line had already retreated across most of the narrow shelf by 15 ka.

The onset of peat formation and lake sedimentation shows that terrestrial deglaciation was occurring at least at one site on Sub-Antarctic South Georgia, Kerguelen, Auckland and Marion Island (though the latter is extrapolated) and at three sites on Campbell Island.

3.3. 10 ka timeslice

Along the western and eastern margin of the Antarctic Peninsula, the ice sheet underwent significant recession between 15 and 10 cal ka BP and had retreated towards its present configuration by the mid-Holocene. In the east, it may have approached its present configuration by 10 ka.

In the Weddell Sea the grounding line was either at the northern tip of Berkner Island (Scenario B) or close to the inner ice rises of the southwestern Weddell Sea, and close to present in the southeastern Weddell Sea (Scenario A).

In the Ross Sea, retreat of the East Antarctic Ice Sheet from the western continental shelf occurred mainly after 13 cal yr BP and was most rapid during the Holocene. At 10 ka retreat of the West Antarctic Ice Sheet in both the eastern Ross Sea and the western Weddell Sea was well underway.

Marine and onshore evidence indicate substantial ice sheet thinning and lateral retreat of the East Antarctic Ice Sheet had started prior to this timeslice and continued during and after. The marine margin of the East Antarctic Ice Sheet in Wilkes Land had retreated to within 35 km of its present grounding position. Ice

retreat had also begun by this time in the Windmill Islands adjacent to Law Dome, in Prydz Bay, and on the continental shelf in Mac.-Robertson Land and Lützow-Holm Bay. Terrestrial evidence from the Prince Charles and Framnes Mountains indicates that substantial thinning had already occurred by this time.

In those Sub-Antarctic Islands that were glaciated the majority show extensive accumulation of terrestrial deposits by 10 ka including South Georgia, Marion Island, Crozet, Kerguelen, and Auckland Island. One moraine has also been dated onshore by ^{10}Be at South Georgia delineating a still stand in ice retreat (or a minor advance), and at Signy Island marine sediment cores from the adjacent shelf show the onset of post-glacial marine sediments in this time slice.

In the Amundsen Sea Embayment, there was rapid grounding-line retreat from the middle and inner shelf after about 13 ka, so that the ice margin right across the Amundsen Sea was close to its modern limits by 10 ka.

3.4. 5 ka timeslice

Around all of Antarctica the ice-sheet grounding-line was on the innermost shelf by 5 ka, and in many regions was at or close to its present position. Notably the Ross Sea, and Weddell Sea (Scenario B) reconstructions still show grounding lines a significant distance outboard of their present locations. In the Framnes Mountains and at Lützow Holm Bay in East Antarctica, dated erratic boulders indicate that the ice-sheet profile had reached very close to its present configuration by this time, and that substantial thinning had occurred between the 10 and 5 ka timeslices. In the maritime and sub-Antarctic most currently ice-free terrestrial areas were exposed by 5 ka with some areas showing evidence of subsequent Holocene ice-front fluctuations.

4. Conclusions from the overview of sector reviews

A number of common themes emerge from the reconstruction and the constituent papers of this volume, and we highlight five of these here. Firstly, the Antarctic Ice sheet did not everywhere reach the continental shelf edge at 20 ka, or the grounding line had already retreated from the shelf edge by this time (Fig. 2a). This includes the western Ross Sea and Prydz Bay, and possibly the Amundsen Sea and eastern Weddell Sea.

Secondly, it is clear that the local LGM (cf. Clark et al., 2009) and retreat from it were not synchronous around the Antarctic margin. Specific examples include 'early' retreat of the ice sheet margin in the Bellingshausen Sea and parts of the western Amundsen Sea compared to 'late' retreat of the western Ross Sea and parts of the Antarctic Peninsula. Moreover, parts of the East Antarctic margin show a very different timing of retreat, with the onset of retreat in some areas occurring by ~18 ka and being near-complete by ~12 ka, but with retreat in other areas only beginning at ~12 ka (Mackintosh et al., 2014). This point has been emphasised before (Anderson et al., 2002; Livingstone et al., 2012) and shows that we should be cautious in interpreting synchronous behaviour of the circum-Antarctic ice margin (Weber et al., 2011). The apparent diachroneity in grounded ice-sheet advance and retreat also opens up the possibility that marine benthic fauna survived the Last Glacial period in-situ on the Antarctic shelf by moving from one continental shelf refuge to another (Thatje et al., 2005).

Thirdly, we do not quantify the volume of the ice sheet here but we note that the extent and thickness data are consistent with those summarised in an increasing number of recent ice-model reconstructions using different ice models (Mackintosh et al., 2011; Golledge et al., 2012; Whitehouse et al., 2012a; Golledge et al., 2013). These models all concluded that the total Antarctic contribution to post-glacial sea level rise was probably <10 m of equivalent eustatic sea level; smaller than previous model-based estimates. These more modest estimates of Antarctic Ice Sheet volume have implications for balancing the global LGM sea-level budget (see Andrews, 1992; Bentley, 1999 for discussion), and for GIA correction of contemporary mass balance (King et al., 2012; Shepherd et al., 2012; Ivins et al., 2013).

Fourthly, the contribution of the Antarctic Ice Sheet to Meltwater Pulse-1A (MWP-1A), an abrupt ~20 m rise in global sea level 14.65–14.31 ka (Deschamps et al., 2012), has been debated. Interpretation and modelling of far-field sea level records suggests a significant or dominant Antarctic contribution (Clark et al., 2002; Weaver et al., 2003), whereas, in contrast, interpretation of Antarctic glacial geology from around the continent suggests only a very minor contribution (Licht, 2004; Bentley et al., 2010; Mackintosh et al., 2011). MWP-1A occurred between our timeslices for 15 ka and 10 ka. Inspection of the difference between those timeslices and close inspection of the limiting ages for deglaciation around the continent do not show a major change at the time of MWP-1A. Even after taking dating uncertainties into account this is consistent with only a minor contribution of Antarctica to this melwater pulse. Fifthly, in some areas the spatial pattern of deglaciation of the shelf is highly variable. This is particularly the case during the Holocene when the ice sheet was grounded on the inner shelf. A number of factors might explain this diachronous retreat behaviour between individual troughs on the shelf including, perhaps most importantly, the effect of local topography/bathymetry on ice sheet dynamics and channelling of any inflow of relatively warm ocean water to the grounding line (Anderson et al., 2002; Heroy and Anderson, 2007; Ó Cofaigh et al., 2008; Livingstone et al., 2012; Jamieson et al., 2012). Other factors include variability in the area, elevation and climate conditions of glacial drainage basins that contributed to the expanded ice sheets around the continent; spatial differences in isostatic depression and rebound; and potential for intrusion of warm deep water onto the continental shelf (Anderson et al., 2013).

5. Recommendations for future work

It is clear from the reconstructions that the level of knowledge of Antarctic Ice Sheet history is extremely variable in time and space. Each of the sector reviews identifies suggestions for future work and we highlight some of those here. With the exception of Mac.-Robertson Land and the Lambert/Amery system where most work has been focussed, East Antarctica contains substantial regions where we still do not know the broad deglacial history, and these have prevented a full circum-Antarctic timeslice-based reconstruction. The acquisition of further terrestrial and marine data around the East Antarctic margin has to be a priority, and in particular we identify the need for robust geochronological information from onshore localities to constrain former East Antarctic Ice Sheet thickness (Mackintosh et al., 2014). In the Weddell Sea, obtaining targeted data to distinguish between the two alternative scenarios A and B would go a long way to helping resolve a significant debate about ice sheet extent in this region (Hillenbrand et al., 2014).

The glacial history of the sub-Antarctic islands is exceptionally poorly known – in many cases we do not even have a broad understanding of the maximum ice-sheet configuration at the LGM, let alone the subsequent deglacial history. Yet such islands can provide important information on sub-Antarctic environmental change and can be a useful test bed for understanding the mechanisms of ice-sheet retreat in the later phases of deglaciation (Hodgson et al., 2014).

In contrast to the Bellingshausen Sea, whose deglaciation history is poorly constrained because it is entirely based on AIO dates from marine cores, the amount of geological and geophysical data in the Amundsen Sea has multiplied rapidly in recent years. However, we still require further chronological control on the steps in retreat that are increasingly being identified in the geomorphological record of the region. This would aid efforts to better understand if the recent ice sheet change in this important area is exceptional (Larter et al., 2014). Although the ice-sheet retreat history of the Antarctic Peninsula sector, particularly along its western margin, is one of the best constrained in Antarctica, there remain major data gaps, most notably along the Weddell Sea margin. In line with several other sectors the constraints on the timing of ice-sheet retreat are poor, and even in comparatively well-studied areas of the Peninsula we still require further chronological control so as to assess the variability between different ice-stream catchments and retreat rate.

Whilst the 20 ka timeslice is relatively well known, at least around West Antarctica, the constraints on ice-sheet configuration reduce rapidly through the deglacial period, and in several areas we know surprisingly little about the Holocene configuration of the ice sheet. Whilst deglacial reconstructions have been published for the Ross Sea (Conway et al., 1999), the eastern Ross Sea is still poorly constrained. We lack radiocarbon age constraints for ice-sheet retreat from the continental shelf and must rely heavily on terrestrial glacial-geological and glaciological data from the inner shelf. Understanding the Holocene is particularly important both for providing the context for recent ice-sheet change (understanding if it is unusual or a part of Holocene variability), and because ongoing GIA is particularly sensitive to the most recent changes in ice loading (Ivins et al., 2000; Nield et al., 2012; Whitehouse et al., 2012b).

Acknowledgements

Our thanks go to the many individuals who have studied Antarctic deglaciation and the people who have supported them in the field and at sea over the last several decades – our understanding of ice-sheet behaviour and this volume would not exist without their dedicated hard work, often in demanding conditions. We also thank all of the national funding agencies who have supported the work described in this volume (MJB acknowledges NERC grant NE/F014260/1). We also thank the Editors of QSR for their helpful comments and editorial support and to Chris Clark and Mike Hambrey for reviews that helped improve the paper. Tim Horscroft was very helpful in keeping the various papers on schedule. The Scientific Committee on Antarctic Research (SCAR) research programme 2004–2011 'Antarctic Climate Evolution' (ACE) provided funding for an initial discussion workshop for which we are grateful. This Special Volume forms an output of the SCAR programme 'Past Antarctic Ice Sheet Dynamics' (PAIS).

Appendix A. Supplementary data

Supplementary data related to this article can be found at http://dx.doi.org/10.1016/j.quascirev.2014.06.025.

References

Anderson, J.B., 1999. Antarctic Marine Geology. Cambridge University Press, Cambridge.
Anderson, J.B., Shipp, S.S., Lowe, A.L., Wellner, J.S., Mosola, A.B., 2002. The Antarctic Ice Sheet during the Last Glacial Maximum and its subsequent retreat history: a review. Quat. Sci. Rev. 21, 49–70.
Anderson, J.B., Kirshner, A.E., Simms, A.R., 2013. Geological Constraints on Antarctica's Contribution to Post-LGM Sea-Level Rise. In: Hambrey, M.J., Barker, P.F., Barrett, P.J., Bowman, V., Davies, B., Smellie, J.L., Tranter, M. (Eds.), Antarctic Palaeoenvironments and Earth-Surface Processes, Geological Society, London, Special Publications, 381. http://dx.doi.org/10.1144/SP381.13.
Anderson, J.B., Conway, H., Bart, P.J., Witus, A.E., Greenwood, S.L., McKay, R.M., Hall, B.L., Ackert, R.P., Licht, K., Jakobsson, M., Stone, J.O., 2014. Ross Sea paleo-ice sheet drainage and deglacial history during and since the LGM. Quat. Sci. Rev. 100, 31–54. http://dx.doi.org/10.1016/j.quascirev.2013.08.020.
Andrews, J.T., 1992. Glaciation - a case of missing water. Nature 358, 281–291.
Bentley, M.J., 1999. Volume of Antarctic Ice at the Last Glacial Maximum, and its impact on global sea level change. Quat. Sci. Rev. 18, 1569–1595.
Bentley, M.J., 2010. The Antarctic palaeo record and its role in improving predictions of future Antarctic Ice Sheet change. J. Quat. Sci. 25, 5–18.
Bentley, M.J., Fogwill, C.J., Le Brocq, A.M., Hubbard, A.L., Sugden, D.E., Dunai, T.J., Freeman, S., 2010. Deglacial history of the West Antarctic Ice Sheet in the Weddell Sea embayment: constraints on past ice volume change. Geology 38, 411–414.
Chen, J.L., Wilson, C.R., Blankenship, D.D., Tapley, B.D., 2006. Antarctic mass rates from GRACE. Geophys. Res. Lett. 33, L11502.
Clark, C.D., Hughes, A.L.C., Greenwood, S.L., Jordan, C., Sejrup, H.P., 2012. Pattern and timing of retreat of the last British-Irish Ice Sheet. Quat. Sci. Rev. 44, 112–146.
Clark, P.U., Dyke, A.S., Shakun, J.D., Carlson, A.E., Clark, J., Wohlfarth, B., Mitrovica, J.X., Hostetler, S.W., McCabe, A.M., 2009. The Last Glacial maximum. Science 325, 710–714.
Clark, P.U., Mitrovica, J.X., Milne, G.A., Tamisiea, M.E., 2002. Sea-level fingerprinting as a direct test for the source of global meltwater pulse IA. Science 295, 2438–2441.
Convey, P., Gibson, J.A.E., Hillenbrand, C.-D., Hodgson, D.A., Pugh, P.J.A., Smellie, J.L., Stevens, M.I., 2008. Antarctic terrestrial life – challenging the history of the frozen continent? Biol. Rev. 83, 103–117.
Conway, H., Hall, B.L., Denton, G.H., Gades, A.M., Waddington, E.D., 1999. Past and future grounding-line retreat of the West Antarctic Ice Sheet. Science 286, 280–283.
Denton, G.H., Hughes, T.J., 1981. The Last Great Ice Sheets. Wiley, New York.
Denton, G.H., Hughes, T.J., 2002. Reconstructing the Antarctic Ice Sheet at the Last Glacial Maximum. Quat. Sci. Rev. 21, 193–202.
Deschamps, P., Durand, N., Bard, E., Hamelin, B., Camoin, G., Thomas, A.L., Henderson, G.M., Okuno, J.i., Yokoyama, Y., 2012. Ice-sheet collapse and sea-level rise at the Bolling warming 14,600[thinsp]years ago. Nature 483, 559–564.
Dyke, A.S., Andrews, J.T., Clark, P.U., England, J.H., Miller, G.H., Shaw, J., Veillette, J.J., 2002. The Laurentide and Innuitian ice sheets during the Last Glacial Maximum. Quat. Sci. Rev. 21, 9–31.
Fretwell, P., Pritchard, H.D., Vaughan, D.G., Bamber, J.L., Barrand, N.E., Bell, R., Bianchi, C., Bingham, R.G., Blankenship, D.D., Casassa, G., Catania, G., Callens, D., Conway, H., Cook, A.J., Corr, H.F., Damaske, D., Damm, V., Ferraccioli, F., Forsberg, R., Fujita, S., Gim, Y., Gogineni, P., Griggs, J.A., Hindmarsh, R.C.A., Holmlund, P., Holt, J.W., Jacobel, R.W., Jenkins, A., Jokat, W., Jordan, T., King, E.C., Kohler, J., Krabill, W., Riger-Kusk, M., Langley, K.A., Leitchenkov, G., Leuschen, C., Luyendyk, B.P., Matsuoka, K., Mouginot, J., Nitsche, F.O., Nogi, Y., Nost, O.A., Popov, S.V., Rignot, E., Rippin, D.M., Rivera, A., Roberts, J., Ross, N., Siegert, M.J., Smith, A.M., Steinhage, D., Studinger, M., Sun, B., Tinto, B.K., Welch, B.C., Wilson, D., Young, D.A., Xiangbin, C., Zirizzotti, A., 2013. Bedmap2: improved ice bed, surface and thickness datasets for Antarctica. Cryosphere 7, 375–393. http://dx.doi.org/10.5194/tc-7-375-2013.
Golledge, N., Fogwill, C.J., Mackintosh, A.N., Buckley, K.M., 2012. Dynamics of the Last Glacial maximum Antarctic ice-sheet and its response to ocean forcing. Proc. Natl. Acad. Sci. 109, 16052–16056.
Golledge, N.R., Levy, R.H., McKay, R.M., Fogwill, C.J., White, D.A., Graham, A.G.C., Smith, J.A., Hillenbrand, C.-D., Licht, K.J., Denton, G.H., Ackert Jr., R.P., Maas, S.M., Hall, B.L., 2013. Glaciology and geological signature of the Last Glacial Maximum Antarctic Ice Sheet. Quat. Sci. Rev. 78, 225–247.
Gyllencreutz, G., Mangerud, J., Svendsen, J.-I., Lohne, Ø., 2007. DATED - a GIS-based reconstruction and dating database of the Eurasian deglaciation. In: Johansson, P., Sarala, P. (Eds.), Applied Quaternary Research in the Central Part of Glaciated Terrain. Geological Survey of Finland, pp. 113–120.
Hein, A.S., Fogwill, C.J., Sugden, D.E., Xu, S., 2011. Glacial/interglacial ice-stream stability in the Weddell Sea embayment, Antarctica. Earth Planet. Sci. Lett. 307, 211–221.
Heroy, D.C., Anderson, J.B., 2007. Radiocarbon constraints on Antarctic Peninsula ice sheet retreat following the Last Glacial Maximum (LGM). Quat. Sci. Rev. 26, 3286–3297.
Hillenbrand, C.-D., Melles, M., Kuhn, G., Larter, R.D., 2012. Marine geological constraints for the grounding-line position of the Antarctic Ice Sheet on the southern Weddell Sea shelf at the Last Glacial Maximum. Quat. Sci. Rev. 32, 25–47.
Hillenbrand, C.-D., Bentley, M.J., Stolldorf, T.D., Hein, A.S., Kuhn, G., Graham, A.G.C., Fogwill, C.J., Kristoffersen, Y., Smith, J.A., Anderson, J.B., Larter, R.D., Melles, M., Hodgson, D.A., Mulvaney, R., Sugden, D.E., 2014. Reconstruction of changes in the Weddell Sea sector of the Antarctic Ice Sheet since the Last Glacial Maximum. Quat. Sci. Rev. 100, 111–136. http://dx.doi.org/10.1016/j.quascirev.2013.07.020.
Hodgson, D.A., Graham, A.G.C., Roberts, S.J., Bentley, M.J., Ó Cofaigh, C., Verleyen, E., Jomelli, V., Favier, V., Brunstein, D., Verfaillie, D., Colhoun, E.A., Saunders, K.,

Selkirk, P.M., Mackintosh, A., Hedding, D.W., Nel, W., Hall, K., McGlone, M.S., Van der Putten, N., 2014. Terrestrial and submarine evidence for the extent and timing of the Last Glacial Maximum and the onset of deglaciation on the sub-Antarctic islands. Quat. Sci. Rev. 100, 137–158.
Ivins, E.R., James, T.S., 2005. Antarctic glacial isostatic adjustment: a new assessment. Antarct. Sci. 17, 541–553.
Ivins, E.R., James, T.S., Wahr, J., O. Schrama, E.J., Landerer, F.W., Simon, K.M., 2013. Antarctic contribution to sea level rise observed by GRACE with improved GIA correction. J. Geophys. Res. Solid Earth 118, 3126–3141.
Ivins, E.R., Raymond, C.A., James, T.S., 2000. The influence of 5000 year-old and younger glacial mass variability on present-day crustal rebound in the Antarctic Peninsula. Earth Planets Space 52, 1023–1029.
Jamieson, S.S.R., Vieli, A., Livingstone, S.J., Cofaigh, C.O., Stokes, C., Hillenbrand, C.D., Dowdeswell, J.A., 2012. Ice-stream stability on a reverse bed slope. Nat. Geosci. 5, 799–802.
King, M.A., Bingham, R.J., Moore, P., Whitehouse, P.L., Bentley, M.J., Milne, G.A., 2012. Lower satellite-gravimetry estimates of Antarctic sea-level contribution. Nature 491, 586–+.
Larter, R.D., Graham, A.G.C., Hillenbrand, C.-D., Smith, J.A., Gales, J.A., 2012. Late Quaternary grounded ice extent in the Filchner Trough, Weddell Sea, Antarctica: new marine geophysical evidence. Quat. Sci. Rev. 53, 111–122.
Larter, R.D., Anderson, J.B., Graham, A.G.C., Gohl, K., Hillenbrand, C.-D., Jakobsson, M., Johnson, J.S., Kuhn, G., Nitsche, F.O., Smith, J.A., Witus, A.E., Bentley, M.J., Dowdeswell, J.A., Ehrmann, W., Klages, J.P., Lindow, J., Ó Cofaigh, C., Spiegel, C., 2014. Reconstruction of changes in the Amundsen Sea and Bellingshausen Sea sector of the West Antarctic Ice Sheet since the Last Glacial Maximum. Quat. Sci. Rev. 100, 55–86. http://dx.doi.org/10.1016/j.quascirev.2013.10.016.
Licht, K.J., 2004. The Ross Sea's contribution to eustatic sea level during meltwater pulse 1A. Sediment. Geol. 165, 343–353.
Livingstone, S.J., Cofaigh, C.O., Stokes, C.R., Hillenbrand, C.D., Vieli, A., Jamieson, S.S.R., 2012. Antarctic palaeo-ice streams. Earth-Science Rev. 111, 90–128.
Mackintosh, A., Golledge, N., Domack, E., Dunbar, R., Leventer, A., White, D., Pollard, D., DeConto, R., Fink, D., Zwartz, D., Gore, D., Lavoie, C., 2011. Retreat of the East Antarctic ice sheet during the Last Glacial termination. Nat. Geosci. 4, 195–202.
Mackintosh, A.N., Verleyen, E., O'Brien, P.E., White, D.A., Jones, R.S., McKay, R., Dunbar, R., Gore, D.B., Fink, D., Post, A.L., Miura, H., Leventer, A., Goodwin, I., Hodgson, D.A., Lilly, K., Crosta, X., Golledge, N.R., Wagner, B., Berg, S., van Ommen, T., Zwartz, D., Roberts, S.J., Vyverman, W., Massé, G., 2014. Retreat history of the East Antarctic Ice Sheet since the Last Glacial Maximum. Quat. Sci. Rev. 100, 10–30. http://dx.doi.org/10.1016/j.quascirev.2013.07.024.
Nield, G.A., Whitehouse, P.L., King, M.A., Clarke, P.J., Bentley, M.J., 2012. Increased ice loading in the Antarctic Peninsula since the 1850s and its effect on glacial isostatic adjustment. Geophys. Res. Lett. 39.
Ó Cofaigh, C., Dowdeswell, J.A., Evans, J., Larter, R.D., 2008. Geological constraints on Antarctic palaeo-ice-stream retreat. Earth Surf. Process. Landf. 33, 513–525.
Ó Cofaigh, C., Davies, B.J., Livingstone, S.J., Smith, J.A., Johnson, J.S., Hocking, E.P., Hodgson, D.A., Anderson, J.B., Bentley, M.J., Canals, M., Domack, E., Dowdeswell, J.A., Evans, J., Glasser, N.F., Hillenbrand, C.-D., Larter, R.D., Roberts, S.J., Simms, A.R., 2014. Reconstruction of Ice-Sheet Changes in the Antarctic Peninsula Since the Last Glacial Maximum. Quat. Sci. Rev. 100, 87–110.
Pattyn, F., Schoof, C., Perichon, L., Hindmarsh, R.C.A., Bueler, E., de Fleurian, B., Durand, G., Gagliardini, O., Gladstone, R., Goldberg, D., Gudmundsson, G.H., Huybrechts, P., Lee, V., Nick, F.M., Payne, A.J., Pollard, D., Rybak, O., Saito, F., Vieli, A., 2012. Results of the Marine Ice Sheet Model Intercomparison Project, MISMIP. Cryosphere 6, 573–588.
Pollard, D., DeConto, R., 2009. Modelling West Antarctic ice sheet growth and collapse through the past five million years. Nature 458, 329–332.
Schoof, C., 2007. Ice sheet grounding line dynamics: Steady states, stability, and hysteresis. J. Geophys. Res.-Earth Surf. 112.
Shepherd, A., Ivins, E.R., Geruo, A., Barletta, V.R., Bentley, M.J., Bettadpur, S., Briggs, K.H., Bromwich, D.H., Forsberg, R., Galin, N., Horwath, M., Jacobs, S., Joughin, I., King, M.A., Lenaerts, J.T.M., Li, J.L., Ligtenberg, S.R.M., Luckman, A., Luthcke, S.B., McMillan, M., Meister, R., Milne, G., Mouginot, J., Muir, A., Nicolas, J.P., Paden, J., Payne, A.J., Pritchard, H., Rignot, E., Rott, H., Sorensen, L.S., Scambos, T.A., Scheuchl, B., Schrama, E.J.O., Smith, B., Sundal, A.V., van Angelen, J.H., van de Berg, W.J., van den Broeke, M.R., Vaughan, D.G., Velicogna, I., Wahr, J., Whitehouse, P.L., Wingham, D.J., Yi, D.H., Young, D., Zwally, H.J., 2012. A Reconciled estimate of ice-sheet mass balance. Science 338, 1183–1189.
Stolldorf, T., Schenke, H.-W., Anderson, J.B., 2012. LGM ice sheet extent in the Weddell Sea: evidence for diachronous behavior of Antarctic Ice Sheets. Quat. Sci. Rev. 48, 20–31.
Thatje, S., Hillenbrand, C.-D., Larter, R., 2005. On the origin of Antarctic marine benthic community structure. Trends Ecol. Evol. 20, 534–540.
Velicogna, I., Wahr, J., 2013. Time-variable gravity observations of ice sheet mass balance: Precision and limitations of the GRACE satellite data. Geophys. Res. Lett. 40, 3055–3063.
Weaver, A.J., Saenko, O.A., Clark, P.U., Mitrovica, J.X., 2003. Meltwater pulse 1A from Antarctica as a trigger of the bolling- allerod warm interval. Science 299, 1709–1713.
Weber, M.E., Clark, P.U., Ricken, W., Mitrovica, J.X., Hostetler, S.W., Kuhn, G., 2011. Interhemispheric ice-sheet synchronicity during the Last Glacial Maximum. Science 334, 1265–1269.
Whitehouse, P.L., Bentley, M.J., Le Brocq, A.M., 2012a. A deglacial model for Antarctica: geological constraints and glaciological modelling as a basis for a new model of Antarctic glacial isostatic adjustment. Quat. Sci. Rev. 32, 1–24.
Whitehouse, P.L., Bentley, M.J., Milne, G.A., King, M.A., Thomas, I.D., 2012b. A new glacial isostatic adjustment model for Antarctica: calibrated and tested using observations of relative sea-level change and present-day uplift rates. Geophys. J. Int. 190, 1464–1482.
Wright, A.P., White, D.A., Gore, D.B., Siegert, M.J., 2008. Antarctica at the Last Glacial Maximum, deglaciation and the Holocene. In: Florindo, F., Siegert, M. (Eds.), Antarctic Climate Evolution, Advances in Antarctic Earth Sciences, Developments in Earth & Environmental Sciences, vol. 8. Elsevier, Amsterdam, pp. 531–570.
Zwally, H. Jay, Giovinetto, Mario B., Beckley, Matthew A., Saba, Jack L., 2012. Antarctic and Greenland Drainage Systems. GSFC Cryospheric Sciences Laboratory. http://icesat4.gsfc.nasa.gov/cryo_data/ant_grn_drainage_systems.php.

Annexe E

Article Verfaillie et al. (soumis)

Recent glacier decline in the Kerguelen Islands (49°S, 69°E) derived from modeling, field observations and satellite data

Deborah Verfaillie,[1,2] Vincent Favier,[1,2] Marie Dumont,[3] Vincent Jomelli,[4] Adrien Gilbert,[1,2] Daniel Brunstein,[4] Hubert Gallée,[1,2] Vincent Rinterknecht,[5] Martin Menegoz,[1,2] Yves Frenot[6]

Abstract.

The retreat of glaciers in the Kerguelen Islands (49°S, 69°E) was analyzed using field data and MODIS images to validate a positive degree-day (PDD) model forced by data from local meteorological stations. Mass balance measurements made during recent field campaigns on the largest glacier of the Cook Ice Cap were compared to data from the early 1970s, providing a 40-year view of the differences in the spatial distribution of surface mass balance (SMB). As these data depend to a great extent on specific years, our interpretation of climate-induced changes was limited. To obtain additional regional data for the validation of our models, we analyzed MODIS images (2000-2012) to determine if our model was capable of reproducing variations in the transient snow line. The PDD model correctly simulated the variations in the snow line, the spatial variations in the SMB and its trend with elevation. Yet, current SMB values diverge from their classic linear representation with elevation, and stake data at high altitudes now display much more negative SMB values than would be expected. By analyzing MODIS albedo values, we observed that these values are caused by the disappearance of snow and associated feedback on melt rates. In addition, we noticed that certain parts of Ampere Glacier could not be reproduced by the surface energy balance model, because overaccumulation appears to occur due to wind deposition. Finally, MODIS and field data and the models demonstrate the acceleration of glacier wastage in Kerguelen up to high altitudes due to reduced net accumulation.

1. Introduction

Southern sub-polar regions, located between 45 and 55°S, play a key role in global atmospheric circulation (e.g. *Garreaud et al.* [2009]; *Thompson et al.* [2011]; *Purich et al.* [2013]) because energy from the tropics is mixed with polar cold air masses, leading to significant cyclonic activity in the region. Due to the association of low temperature with high amount of humidity transported by the westerlies, large ice caps can form in Patagonia, New Zealand and Sub-Antarctic Islands despite the low elevation of the mountain ridges (e.g. *Fitzharris et al.* [1997]; *Takeuchi et al.* [1999]; *Fitzharris et al.* [2007]; *Garreaud et al.* [2009]). Like in many other regions, glaciers in the southern sub-polar regions are currently retreating. While glaciers in New Zealand retreated less and even advanced slightly from 1976 to the early 2000s, but have rapidly retreated since [*Fitzharris et al.*, 2007], glaciers in Patagonia retreated significantly throughout the period, with a surface area loss between 0.4% and 36% since 1945 [*Lopez et al.*, 2010; *Melkonian et al.*, 2013], and an acceleration of the retreat after the 1990s [*Rignot et al.*, 2003; *Willis et al.*, 2012a, b].

The rapid response of glaciers to global warming has been widely studied by remote sensing, mainly on the Patagonian ice fields, where the detailed mass loss data were obtained from satellite imagery (e.g., *Rignot et al.* [2003]; *Willis et al.* [2012a, b]). Glaciological modeling studies have also been performed in Patagonia [*Schaefer et al.*, 2013; *Lenaerts et al.*, 2014], but the models were forced by reanalysis data that contain serious biases (mainly concerning humidity) and calving processes were ignored even though they are not negligible in these ice fields. Only a few field data are available on the mass balance of southern sub-polar glaciers. Indeed, except for Brewster glacier (New Zealand) since 2005 [*Anderson et al.*, 2010], long term surface mass balance measurement programs have rarely continued for periods of more than a few years, and as a result, our knowledge of glaciological processes in the area is limited. In addition, the surface energy balance has only been analyzed for periods of less than one year (e.g., *Takeuchi et al.* [1999]; *Schneider et al.* [2007]) and data are too scarce to clearly depict the main climatic changes that have occurred in the sub-polar regions in recent decades.

The Kerguelen Islands (49°S, 69°E) are located in the southern Indian Ocean (Fig. 1 a) and form a unique sub-polar observation site due to the scarcity of glacier-covered zones in this area. As these glaciers are located at low altitudes and on islands, they are directly impacted by oceanic and associated atmospheric variations (e.g. *Poggi* [1977a, b]; *Vallon* [1987]), and they have been subject to marked fluctuations in the last two centuries [*Frenot et al.*, 1993]. After a relatively stable period from 1799 to 1965, the Cook Ice Cap then retreated extremely rapidly, losing 20% of its surface area in the last 40 years [*Berthier et al.*, 2009]. This acceleration has generally been attributed to warming, while

[1]CNRS, LGGE, UMR5183, F-38041 Grenoble, France
[2]Univ. Grenoble Alpes, LGGE, UMR5183, F-38041 Grenoble, France
[3]Météo France, CNRS/CNRM, CEN, GAME UMR 3589, F-38041 Grenoble, France
[4]CNRS, LGP, UMR8591, F-92195 Meudon, France
[5]Univ. St Andrews, DEES, St Andrews, UK
[6]Univ. Rennes 1/CNRS, ECOBIO, UMR6553, Rennes, France

0148-0227/14/$9.00

fluctuating precipitation has generally been assumed to be of less importance (e.g., *Frenot et al.* [1993, 1997]; *Berthier et al.* [2009]). However, due to our lack of knowledge of the relationship between the local climate, the glaciers and ice dynamics in the area, until recently it was difficult to conclude whether the recent significant drying trend had a serious impact on glacier wastage.

As part of a four-year glaciological program in the Kerguelen Islands, in 2010, a meteorological, glaciological and hydrological network was set up on and around Ampere Glacier - an outlet glacier of the Cook Ice Cap (Fig. 1 a) - to detect, monitor and understand climate and mass balance variability and change in the glacial environment of the ice cap. We used data from previous short term mass balance studies [*Vallon*, 1977a, b, 1987], and short term energy balance studies (e.g. *Poggi* [1977a, b]) conducted on Ampere Glacier between 1970 and 1974 for comparison with our new results.

The objective of the present study was to improve our knowledge of the relationship between the glaciers and climate in this sub-polar area. The field data (Section 2.1) analyzed in this study is the first step in understanding the recent rapid retreat of the cryosphere on Kerguelen, and was used to validate the surface mass balance and surface energy balance models. But in addition, collecting spatially distributed data on the surface characteristics and ablation from satellite images (Section 2.2) was crucial to validate our models.

Following *Lopez et al.* [2008], we produced our own images of the ice and snow cover from MODIS Level-1B images. We applied the method developed by *Sirguey et al.* [2009] and *Dumont et al.* [2012] to produce surface albedo maps from MODIS Level-1B images of the Cook Ice Cap to estimate the transient snow line and assess changes in the extent of the accumulation area of the ice cap since 2000. In addition, MODIS albedo values measured at the location of stakes enabled computation of the local surface mass balance through energy balance estimates from a surface energy balance model, as well as comparison with surface mass balance values measured in the year 2011. To identify the causes and processes involved in the retreat of the ice cap, the third method we used was analyzing climatic data (Section 2.3) over Kerguelen derived from measurements and reanalyses since the 1950s. Finally, we obtained an additional estimate of surface mass balance at the ice cap scale by implementing a simple positive degree-day model based on temperature and precipitation measured at the scientific station of Port-aux-Français. The model was validated using surface energy and mass balance measurements. The modeling results were then compared with previous estimates derived from field observations and satellite imagery.

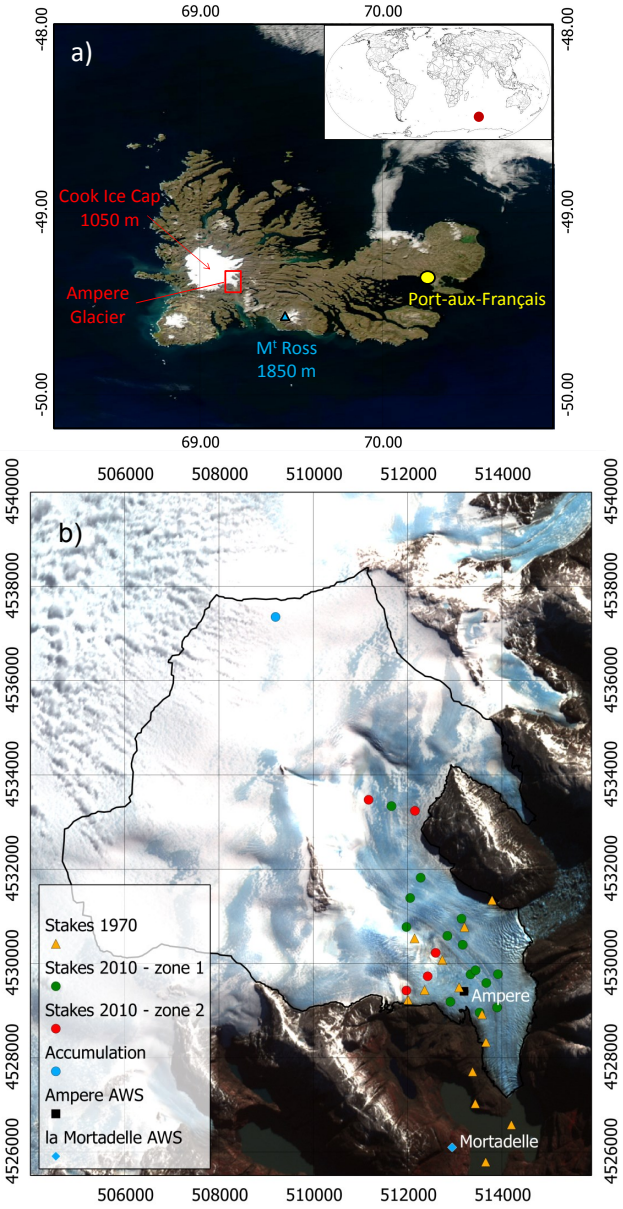

Figure 1. (a) MODIS© image of the Kerguelen Islands showing the main study sites (in red) and the location of Port-aux-Français scientific station. The location of the Kerguelen Islands is indicated by the red dot on the world map in the top right corner. (b) Field network set up in 2010 on and around Ampere Glacier. The positions of the ablation stakes in Vallon's 1970 study are also shown. Position of the accumulation point from Section 3.4 is also indicated (the latter does not correspond to a stake measurement). The background image is an ASTER image acquired on April 23, 2009. Coordinates are in UTM (Zone 42S).

2. Data

2.1. Field data on and around the glacier

Field data from a meteorological and glaciological network set up on and around Ampere Glacier (Fig. 1 b) were used in this study. These data came from :

• field campaigns conducted in 2010-2011 and 2011-2012, during which ablation stakes were measured to assess the glacier climatic mass balance [*Cogley et al.*, 2011]. The climatic mass balance is the sum of the surface mass balance and the internal mass balance. As internal ablation and accumulation are negligible compared to other terms in Ampere glacier, we hereafter only refer to surface mass balance (SMB). SMB is the sum of the accumulation at the surface of the ice sheet (through precipitation, hoar formation and wind deposition) and surface ablation (through sublimation, melting and wind scouring). Twenty ablation stakes were set up in December 2010 and January 2011 and measured one year later in December 2011 and January 2012 (stake height and location were measured). The stakes were separated into two categories (Fig. 1 b) : those located in the regular ablation area (zone 1), and those located at specific points where snow overaccumulates due to wind deposition (zone 2). An automatic weather station (AWS) was also set up on a rock outcrop close to the glacier (Fig. 1 b, la Mortadelle, 200 m above sea level (a.s.l.)) to record local meteorological

Table 1. Characteristics of sensors installed on the Mortadelle and Ampere AWS: Name, Data, Accuracy (according to the manufacturer) and Measurement height (la Mortadelle / Ampere).

Name of sensor	Data	Accuracy	Height
Young 05103 anemometer	Wind speed	± 0.3 m s^{-1}	5 m / 2.1 m
	Wind direction	$\pm 3°$	
Vaisala HMP45C	Air temperature	± 0.4 °C	5 m / 2.1 m
	Relative humidity	$\pm 3\%$	
Kipp & Zonen CG3 radiometer	Incoming LW radiation	$\pm 10\%$ [1]	2 m / -
Kipp & Zonen CMP3 radiometer	Incident & reflected SW radiation	$\pm 10\%$ [2]	- / 2 m
P. MECANIQUE 3029 pluviometer	Amount of precipitation	± 0.5 mm	0.85 m / -
Campbell Sc. SC100 pressure gauge	Pressure	± 1.5 mbar	2 m / -
Acoustic gauge Campbell Sc. SR50A	Surface height	± 1 cm	- / 1.6 m

[1] accuracy for daily totals.

conditions. The characteristics of the different AWS sensors are listed in Table 1. Thirty minute averaged data on air temperature and humidity, wind speed and direction, precipitation, and incoming and outgoing shortwave and longwave radiation (SW and LW respectively) were measured at the AWS. Additional surface short term heat budget measurements were recorded by a second AWS (Fig. 1 b, Ampere, 280 m a.s.l.) placed on the glacier surface during the field campaigns. A stake farm was also installed around this AWS. It consisted of four stakes that were measured daily, and used for calibration of the SMB model (Section 3.5).

• previous surface energy balance (SEB) studies [*Poggi*, 1977a] and SMB studies using stakes [*Vallon*, 1977a, b, 1987], conducted on Ampere Glacier in the 1970s (the positions of the stakes are shown in Fig. 1 b).

2.2. Satellite images

2.2.1. MODIS Terra sensor

The EOS/AM-1 TERRA platform was launched in December 1999, carrying, among others, the MODIS sensor, which started producing images of the Earth's surface in February 2000. The sensor is a multispectral radiometer, working in 36 bands from the visible to the thermal infrared. It produces images at three spatial resolutions: 250 m (band 1 and 2), 500 m (band 3 to 7) and 1 km (all remaining bands). We used MODIS images for our study because of its high temporal resolution (global coverage in less than 2 days, and more than 1 image per day over Kerguelen), which is required to study changes in the seasonal snow line on the Cook Ice Cap. The different MODIS products used in this study are described in the following sections.

2.2.2. MODIS Level-1B Products

For the production of albedo maps, we used MODIS Level-1B Swath images (MOD02QKM, MOD02HKM, MOD021KM and MOD03) distributed by the Level 1 and Atmosphere Archive and Distribution System (LAADS, http://ladsweb.nascom.nasa.gov/). We preferred these images to MOD10 and MCD43 products because of (1) their better resolution (250 m for MOD02QKM), (2) the possibility to retrieve different types of albedo from them (as explained in Section 3.1), (3) their high accuracy (root mean square deviation of about 0.05 between MODIS-retrieved albedo and field-measured albedo as shown in *Dumont et al.* [2012]) and (4) a misinterpretation of Kerguelen snow surfaces in MOD10, which, in those images, are mapped as clouds (also the case in some regions of New Zealand [*Hall et al.*, 2002; *Sirguey et al.*, 2009] and in Patagonia [*Lopez et al.*, 2008]). MODIS Level-1B Swath products contain radiance measurements at the top of atmosphere in different bands, and a geolocation file providing geometry and topography parameters (such as solar and sensor azimuths and zeniths).

The Cook Ice Cap behaves similarly to alpine glaciers, with an ablation season mainly during (austral) summer and an accumulation season mainly during (austral) winter [*Vallon*, 1977a]. Consequently, we analyzed images in three different periods between 2000 and 2012:

• November-December, which corresponds to the beginning of the ablation season

• March-April, which is the end of the ablation season

• July-August, in the middle of winter, hence the accumulation season.

Those periods were chosen to evaluate the seasonal variations in the location of the snow line and its highest position (in March-April), as well as any differences between 2000 and the present. A complementary analysis of the variations in the snow line of the Ampere Glacier was also carried out. We only used images of the Cook Ice Cap and the Ampere Glacier that were completely clear, and thus usable for glacier monitoring, which came to a total of only 57 images out of the 8,700 images available. In addition, between December 2010 and December 2011, one to three images per month of the Ampere Glacier (but not always the whole of Cook Ice Cap) were used to estimate variations in the surface albedo and hence to calculate the SW radiation budget for 2011 (see Section 3.4).

2.2.3. High-resolution images

Additional ASTER and Landsat images were used to draw a mask of the ice cap for each albedo map (using the image taken on the date closest to the date of the albedo map). To validate the albedo retrieval method (Section 3.1) and the threshold we chose for the albedo of snow (Section 3.2), we compared one of our albedo maps with an ASTER image taken on the exact same date. ASTER and Landsat images have a much better spatial resolution (15 m and 30 m respectively) than MODIS images, but are only rarely available. Complementary high-resolution images used in this study are described in Table 2. Two digital elevation models (DEM) were also used to assess the elevation of the ice cap: one generated from the February 2000 Shuttle Radar Topographic Mission (SRTM, *Farr et al.* [2007]) and the other from Satellite Pour l'Observation de la Terre (SPOT5) optical stereo imagery acquired in December 2009 [*Korona et al.*, 2009].

2.3. Meteorological and climatic data

Direct meteorological measurements have been performed routinely by Météo France at the station of Port-aux-Français (29 m a.s.l., see Fig. 1 a) since 1950. Measurements were also compared to model results using complementary reanalysis data.

We used ERA-40 and ERA-Interim data [*Uppala et al.*, 2005; *Dee et al.*, 2011] from the European Centre for Medium-Range Weather Forecasts (ECMWF), and Reanalysis 1 and 2 data [*Kalnay et al.*, 1996; *Kanamitsu et al.*, 2002] from the National Centers for Environmental Prediction, National Center for Atmospheric Research and Department of Energy (NCEP-NCAR, NCEP-DOE). Reanalyses correspond to outputs from models using data assimilation, i.e. combination - during a given cycle - of observations (from radiosondes, buoys, satellites, etc.) and prior forecast

Table 2. Description of high-resolution ASTER and Landsat images.

Satellite	Date	Product reference	Resolution
ASTER	April 23, 2009	SC:AST_L1A.003:2072780070	15 m
Landsat	January 11, 2001	LE71390942001011SGS00	30 m
Landsat	November 27, 2001	LE71390942001331SGS00	30 m
Landsat	March 11, 2005	LE71390942005070ASN00	30 m
Landsat	August 10, 2008	LE71390942008223SGS00	30 m
Landsat	February 24, 2011	LE71390942011055ASN00	30 m

model information, to obtain a physically coherent estimate of the state of the atmosphere that is as close to reality as possible. Each reanalysis is produced with a single version of a data assimilation system. Reanalyzed temperature and precipitation data are assumed to be reliable. Indeed, surface and radiosonde observations performed at Port-aux-Français have been assimilated in the reanalyses since 1967 and 1968 respectively for ERA and 1967 and 1970 respectively for NCEP.

As grids and resolutions differ between models (i.e. $\sim$ 210 km for NCEP 1 and NCEP 2, $\sim$ 125 km for ERA-40 and $\sim$ 80 km for ERA-Interim), reanalysis data for Kerguelen were retrieved for different grid cell locations depending on the reanalysis concerned. The location of the grid cells used in this study is 50°S, 70°E for ERA-40, 48°S, 69°E for ERA-Interim and 48.6°S, 69.4°E for NCEP 1 and 2.

3. Methods

3.1. Albedo retrieval method

An algorithm [*Sirguey et al.*, 2009; *Dumont et al.*, 2012] was performed to retrieve the subpixel snow cover and hemispherical-conical reflectance for seven spectral bands from MODIS images. This algorithm accounts for the correction of atmospheric effects and the multiple reflections that occur in rugged terrain. The pixels identified as snow or ice are then corrected using another algorithm to obtain directional-hemispherical reflectance, and then albedo. Blue sky albedo is obtained as well as white sky albedo, the latter being the albedo of the same surface under pure diffuse illumination. The albedo we used in this study was the white sky albedo, as it makes it possible to compare albedo maps obtained at different periods of the year when the solar zenith angle is not the same. Albedo maps (250 m resolution) were finally obtained from each processed MODIS image.

3.2. Determination of the transient snow line and accumulation area

The equilibrium line altitude (ELA) can generally be approximated to the altitude of the snow line (separation between the area covered by snow and the area where ice is visible) at the end of the ablation season (e.g. *Rabatel et al.* [2012]). Figure 2 shows the comparison between an albedo map derived from MODIS and an ASTER image taken on the same day, which helped us determine the albedo threshold between ice and snow. Figure 2 b shows that an albedo threshold of 0.65 appears to mark the limit between older, dirtier snow (dim area between the black and orange lines on the ASTER image) and more recent, brighter snow (area above the orange line). This is particularly visible in the NW part of the ice cap (Fig. 2 b). The older snow in this image probably corresponds to firn from previous years, making it possible to see the retreat of the snow cover in the year 2009, and the position of the transient snow line (i.e. the line separating snow surfaces from ice or firn surfaces at any instant, *Cogley et al.* [2011]). On the other hand, the 0.55 threshold quite satisfactorily reproduces the separation between ice- and firn covered areas visible on the ASTER image, and hence the transient firn line. The firn line is defined in *Cogley et al.* [2011] as "The set of points on the surface of a glacier delineating the firn area and, at the end of the mass-balance year, separating firn (usually above) from glacier ice (usually below)". In this study, we will refer to the firn line at any instant as "the transient firn line", by comparison with the transient snow line defined above. However, the transition from dirty ice to clean snow in Fig. 2 b appears to be progressive, meaning that the albedo limits of the transient firn and snow line present some uncertainty. Figure 2 c shows the location of the transient firn line in a close-up of the NW part of the ice cap for a threshold albedo value of 0.55 $\pm$ 0.05. It indicates that a transient firn line at 0.5 would be too low compared to the information in the ASTER image, while a value of 0.6 would miss some of the firn visible in the image.

These thresholds are slightly higher than the commonly measured albedo values. For example, the maximum albedo value of the ablation zone on Saint-Sorlin glacier (French Alps), derived from AWS measurements, terrestrial photographs and MODIS images is 0.5 [*Dumont et al.*, 2011, 2012]. There are three possible reasons for this difference in albedo, (1) fewer impurities in Kerguelen air masses than in the French Alps, (2) the relative small amount of rock outcrops (nunataks) on Ampere Glacier compared to alpine glaciers, which are generally surrounded by rock faces, and (3) very frequent snowfalls all year round on Kerguelen, which cause frequent increases in the snow albedo. Given the difference in resolution between the MODIS and ASTER images, the good visual correspondence between firn/snow areas in the two images gives us confidence in our method of albedo retrieval and our choice of albedo thresholds.

Pixels with an albedo exceeding 0.55 located inside the ice cap mask were counted to assess the firn- and snow-covered area for each albedo map. The total area of the ice cap was also estimated for each albedo map (albedo $>$ 0.3). The ratio of firn- and snow- covered areas to areas not covered with snow in the Cook Ice Cap was then calculated for each image.

3.3. Surface energy balance model

Punctual SEB computations were performed using data from la Mortadelle and Ampere AWS and compared to estimates of punctual energy budget in Section 3.4. Here we used data from December 14, 2011, to December 30, 2011. During this period, an AWS was placed on the surface of the glacier (Fig. 1 b) to measure albedo, air temperature and humidity and wind speed. The energy stored in the top layers of the glacier was calculated as (in W m^{-2}, fluxes toward the surface are positive)[*Oke*, 1987; *Favier et al.*, 2011]:

$$SW_i + SW_r + LW_i - ((1-\epsilon)LW_i + \epsilon\sigma T_s^4) + LE + H = F_{surface}, \quad (1)$$

where SW_i is incoming shortwave radiation and SW_r is reflected shortwave radiation that were directly measured on the glacier ; LW_i is incoming longwave radiation that was measured at la Mortadelle AWS, and the term in brackets is outgoing longwave radiation LW_r that was deduced form the modeled surface temperature T_s and Stefan-Boltzmann's equation. ϵ=0.99 is surface emissivity and

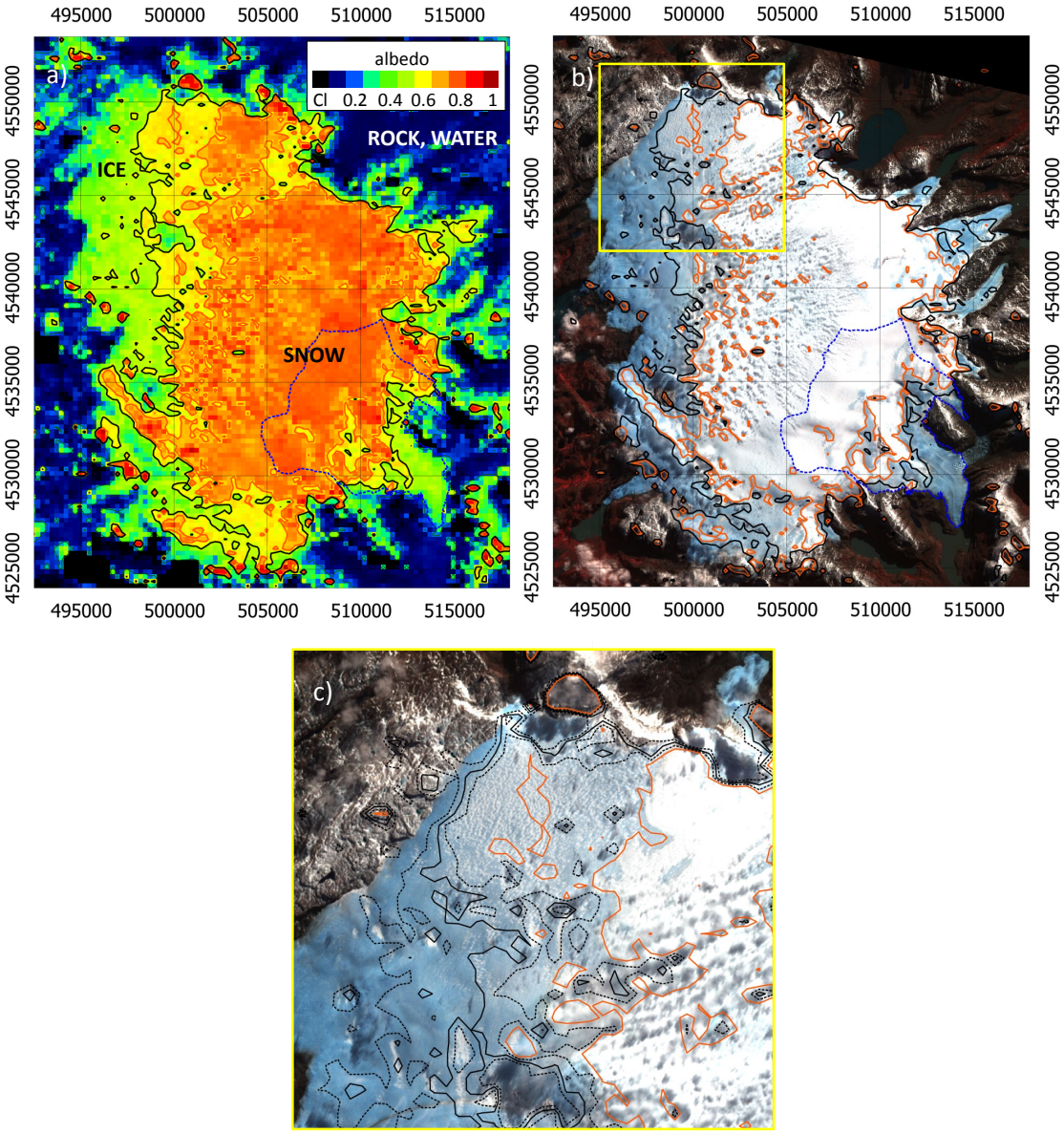

Figure 2. Comparison between a MODIS-derived albedo map (a) and an ASTER image (b) of the Cook Ice Cap, both produced on April 23, 2009. In images a and b, the black line represents an albedo threshold of 0.55, and the orange line a threshold of 0.65. The dotted blue line shows the limits of Ampere glacier. (c) Detail of the NW part of the ice cap showing the position of the firn line for a threshold of 0.55 (continuous black line) and uncertainty limits of 0.5 and 0.6 (dashed black lines). The orange line represents the snow line, at an albedo of 0.65. Clouds (Cl) are in black in (a). Coordinates are in UTM (Zone 42S).

σ=5.67 $10^{-8} Wm^2 K^{-4}$ is the Stefan-Boltzmann constant. H and LE are turbulent and sensible hat fluxes respectively, which were computed using the Bulk-method including stability corrections based on the bulk Richardson Number. Surface roughness lengths were taken from the literature [*Favier et al.*, 2011], to get agreement between the ablation measured at the stakes and modeled ablation. The heat flux supplied by precipitation was not taken into account because during precipitation, the temperature is always close to 0°C.

$F_{surface}$ is the energy available at the surface. Some shortwave radiation is not available for warming/cooling processes at the surface, or for melting, because the shortwave flux partly penetrates the ice. Hence, $F_{surface}$ is separated into two terms:

$$F_{surface} = G_0 + (1 - a)SW, \quad (2)$$

where G_0 is the energy excess or deficit at the surface. In this equation, a is the fractional amount of shortwave radiation that is absorbed in the top layer of the model (at the surface).

When the surface temperature is 0°C, positive G_0 values represent the energy available for melt. Otherwise, this amount is used to cool/warm the frozen surface and underlying snow/ice. For this task, heat conduction within the snow or ice was computed by solving the thermal diffusion

equation according to an explicit scheme to a depth of 2 m, with a 5 cm grid resolution and a 20 s time step.

As Ampere AWS data were only available during field campaigns, annual outputs from this SEB model have not been validated yet, but we are confident in the estimates provided by the model (presented below).

3.4. Estimation of punctual SMB using MODIS albedo and SEB estimates

Based on MODIS albedo estimates, we calculated punctual SMB at the location of the stakes on the basis of estimated solid precipitation and a simple computation of ablation, in which the SW radiation budget is calculated using MODIS albedo values (Section 3.2). In addition, we estimated SMB for a pixel located in the accumulation zone (see Fig. 1 b), at 990 m a.s.l., for which all the images used for computation of SMB at the ablation stakes were clear. Our method is similar to the one used by *Greuell et al.* [2007], except that we calculated punctual SMB values instead of glacier-averaged values.

The annual accumulation term at the location of each stake can be estimated as:

$$Accumulation = \sum_{i=1}^{n} P_S, \quad (3)$$

where P_S is the amount of solid precipitation (in mm), occurring during events i = 1 to n. Hoar formation and wind deposition are not taken into account.
$P_S = P$ if $T_{air} + \gamma \times z \leq 1°C$ (e.g. *Jóhannesson et al.* [1995]), and is equal to 0 otherwise. T_{air} is the temperature from the Mortadelle AWS data, z is stake altitude (in m a.s.l.), $\gamma = -0.8°C/100m$ is the lapse rate (determined from outputs from the regional model MAR [*Gallée and Schayes*, 1994] and from la Mortadelle and Ampere AWS), used to account for the effect of altitude on precipitation phase and P is the 30 minute precipitation amount calculated using outputs from the regional model MAR. Briefly, the relationship between modeled elevation and modeled total precipitation in the MAR model is:

$$P(z) = P_{PAF}(2.79z + 783)/783, \quad (4)$$

where P_{PAF} is the 30 minute precipitation amount measured at Port-aux-Français. This relationship was used to calculate total precipitation and then solid precipitation at stake altitude on Ampere Glacier.

Because of the high amount of humidity in the air, sublimation is low on the Cook Ice Cap (e.g. *Poggi* [1977a]). Since melting amounts are large (7 to 10 m water equivalent (w.e.) per year in the ablation area), the contribution of sublimation to the ablation term can be ignored (see Section 3.3). Similarly, we ignored the contribution of wind scouring. In addition, conduction through ice and snow (G) can also be ignored because the ice cap is temperate. Consequently, the annual ablation term can be estimated as:

$$Ablation \approx Melting = (SW + LW + LE + H + Pr)\frac{1}{L_f}, \quad (5)$$

where SW is the shortwave radiation budget, LW is the longwave radiation budget, LE and H represent the turbulent latent and sensible heat contributions and Pr is the contribution of precipitation. Pr is small compared to other terms [*Poggi*, 1977a] and can thus be ignored. Finally, L_f is the latent heat of fusion (= 0.334×10^6 J kg^{-1}). Contributions are annual energy amounts expressed in W m^{-2} a^{-1}.

We calculated the SW contribution to SMB at each stake location on Ampere Glacier as:

$$SW \sim \frac{1}{n}\sum_{m=1}^{n}[(1-\bar{\alpha}_m)SW_i^m], \quad (6)$$

where $n = 12$ (the number of months in a year), $\bar{\alpha}_m$ is the mean albedo obtained during month m from available clear-sky images (1 to 3 images per month), and SW_i^m is the monthly accumulated incoming SW radiation measured at la Mortadelle AWS during month m. For months with no clear-sky images, we used the albedo value from the closest date.

The incoming longwave radiation (LW_i) on the glacier was estimated from la Mortadelle AWS measurements assuming that there are no major variation in the mean flux (mean annual flux is 320 W m^{-2}) between 200 m a.s.l. and 600 m a.s.l. The outgoing longwave radiation flux was estimated using the Stefan-Boltzmann law, yielding a value of -311 ±5 W m^{-2} assuming a mean surface temperature between -2 °C and 0 °C. This surface temperature range was chosen given that (1) the Mortadelle AWS monthly air temperature in winter is usually above 0 °C and (2) some preliminary punctual SEB simulations (Section 3.3) yielded a mean annual surface temperature of -1 °C. These assumptions suggest a mean annual longwave radiation budget of 9 ±5 W m^{-2}. LE and H were not directly measured on our AWS. As the state and temperature of the glacier surface is not expected to vary much between 200 m a.s.l. and 600 m a.s.l. because of almost continuous melt rates, a fixed value for turbulent heat fluxes was chosen that does not depend on elevation. A rough estimate of the turbulent heat contribution was first assessed from *Poggi* [1977a] (50 W m^{-2}) and then compared to estimates from a punctual SEB model (34 W m^{-2}, Section 3.3).

Uncertainties on SMB due to albedo were roughly estimated as the highest error introduced when we used different

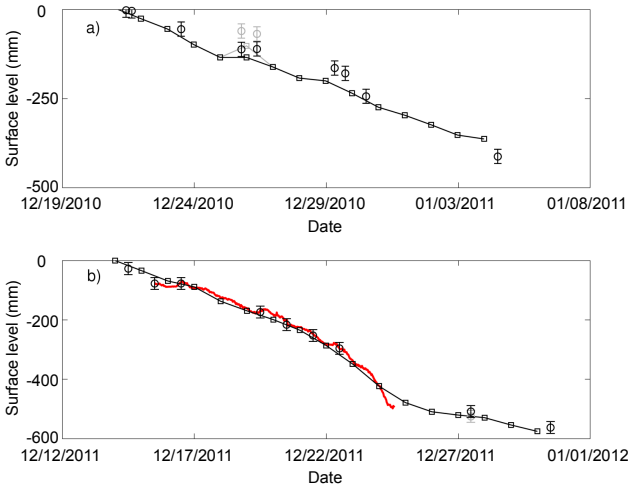

Figure 3. Computed and measured surface height in the ablation zone during the summer field campaigns in December 2010 (a) and December 2011 (b). Thin black and gray lines and squares are the ice and snow surface height (respectively) computed with the PDD approach. Black and gray circles are the mean measured ice and snow surface height (respectively) at a stake farm (4 stakes) located around the Ampere AWS on the ablation zone (280 m a.s.l., see Fig. 1 b). The red curve is the 30-minute surface elevation measured with an acoustic gauge at the same location. Error bars are ±20 mm, which represent the mean standard deviation between stake measurements.

pixels adjacent to the one in which the stake was located. This yielded uncertainties of 6% for the accumulation point, ± 10% for stakes located in zone 1, and between ± 10 % and ± 31% for stakes located in zone 2. In addition, because MODIS albedo estimates were only considered under clear sky conditions, a slight underestimation of the mean annual albedo occurs. Indeed, (1) albedo in clear-sky conditions is lower than when some cloud cover is present because there is less absorption of near-infrared radiations (i.e. a part of the solar spectrum for which the albedo is lower) and (2) fresh snow may already have melted in clear sky images. A rough estimate of the resulting uncertainty suggests that albedo values should be increased by +0.05, leading to a systematic bias on SMB values of +0.5 m w.e. a^{-1}.

3.5. Positive degree-day model

We computed the snow line and SMB with a simple positive degree-day (PDD) model based on *Hock* [1999] and fully described in *Maisincho et al.* [2014]. Solid precipitation on the ice cap was estimated using the same method as described in Section 3.4, with precipitation data from Port-aux-Français available since 1951.

Figure 3 shows the comparison of computed and measured surface height on the ablation area (280 m a.s.l.) using meteorological data from Ampere AWS (and precipitation from la Mortadelle AWS), which was used to calibrate the ice and snow melting coefficients. In December 2010 (Fig. 3 a), a lot of minor snowfall events influenced measurements as well as modeling. As a result, the melting coefficient for ice was calibrated using measurements made in December 2011 (Fig. 3 b). However, the lack of situations with long-term snow cover led us to use a snow coefficient from the literature, which is the average of values from *Radic and Hock* [2011] (4.9 mm w.e.$^{\circ}C^{-1}d^{-1}$). For ice, the value in this study (7.4 mm w.e.$^{\circ}C^{-1}d^{-1}$) is close to the average value from *Radic and Hock* [2011] (7.2 mm w.e.$^{\circ}C^{-1}d^{-1}$).

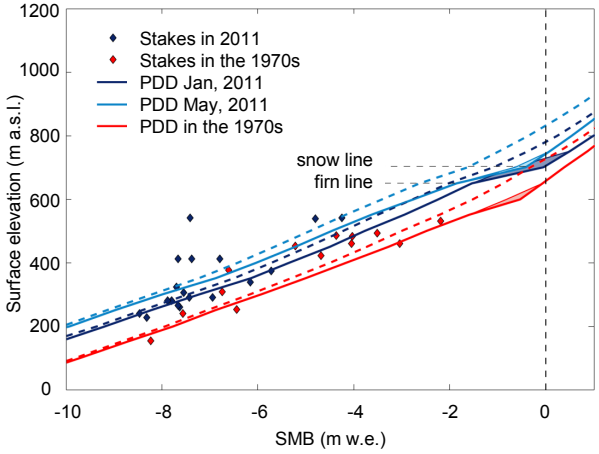

Figure 4. 2011 Ampere Glacier SMB values (m water equivalent, diamonds) at stake locations (see Fig. 1 b) plotted against surface elevation (m above sea level). Values obtained between 1970 and 1974 by *Vallon* [1977a, b, 1987] are also given for the purpose of comparison. Lines represent ice cap SMB derived from our PDD model, for the early 1970s (red line, average of 1970-1974) and 2011 (blue lines). The PDD SMB for 2011 is calculated from January to January (light blue line) and from May to May (dark blue line). The dotted lines represent the version of the model with no initial firn cover, while the solid lines represent the version with an initial firn cover. Uncertainty intervals (± 10 m w.e.) in the initial firn accumulation are also given.

Modeling should reproduce the reduction in size of the area covered by firn. To account for this process, an initial firn thickness from 1951 was used on which a PDD run was performed over 20 years (spin-up) to assess the initial firn cover in 1971, and the PDD run was then extended to the present. We assumed different cases with firn layers ranging from 5 to 15 m w.e., which are discussed in Section 4.1.

In addition, a second run was performed without an initial firn cover, assuming that the firn layer at the beginning of the 1970s resulted only from the mean annual accumulation and ablation from the previous years.

4. Results

4.1. PDD validation using field data

SMB at the ice cap scale was modeled with a simple PDD model based on meteorological measurements and reanalysis data (Section 3.5). Results are shown in Fig. 4 for comparison with stake measurements (presented in Section 4.3). Our PDD model results are in agreement with SMB measurements (Fig. 4) for the recent period (medium correlation (R) of 0.58 discussed below, p-value <0.001 according to a Student's t test) and the 1970s (excellent correlation of 0.99, p-value <0.001). This shows that the PDD model initiated with a 20 year spin-up and a firn cover is capable of reproducing the SMB distribution with elevation and the SMB changes between the 1970s and 2011. However, Fig. 4 shows that the initial amount of firn does not have much impact on modeled SMB. Indeed, a slight difference in SMB (only concerning elevations close to the firn and snow lines) can be observed between 5 m and 15 m firn experiments, but higher amounts of initial firn yielded the same final SMB as the 15 m firn experiment.

4.2. Recent variations in the snow line and accumulation area derived from MODIS albedo maps

Figure 5 b, c shows changes in the ratio between areas covered by firn and snow (albedo > 0.55) on the ice cap and the entire ice cap surface between 2001 and 2012 calculated from albedo maps (Section 3.2). This ratio may be considered equivalent to the accumulation area ratio (AAR) at the end of the ablation season, if we assume that the snow line elevation is similar to the ELA at the end of summer. In Fig. 5, we use the term "AAR", even though we acknowledge that winter values of this ratio are different from the strict sense AAR which should be based on annual values. Despite the marked scattering of the results and the limited number of good quality images, the ratio decreased between 2001 and 2012. A low firn line appeared on April 5, 2012 followed by a rapid increase that was revealed on April 25, 2012, suggesting that estimates may not reflect the highest annual firn line position, and the trends obtained may not be very accurate due to the small number of images available. However, the same trend was observed in each season, showing that the ratio had decreased by ∼ 20 % at the end of the ablation season from 2001 to 2012 (which corresponds to a decrease of ∼ 90 km^2 in the firn and snow covered areas). Values for March-April 2008 and 2009 are, however, the highest of the March-April period. The ratio between the area covered by fresh snow (albedo > 0.65) and the entire ice cap (not shown) was about 1.5 times lower than the same ratio for firn- and snow-covered surfaces, showing the potential extent of firn disappearance, while the rate of retreat for the snow line was about the same as that of the firn line in the last decade.

Figure 6 shows two albedo maps obtained for the period March-April (end of the ablation season), in 2001 and in 2012. The difference in the firn line (black line) and snow line (orange line) between the two images is striking. In

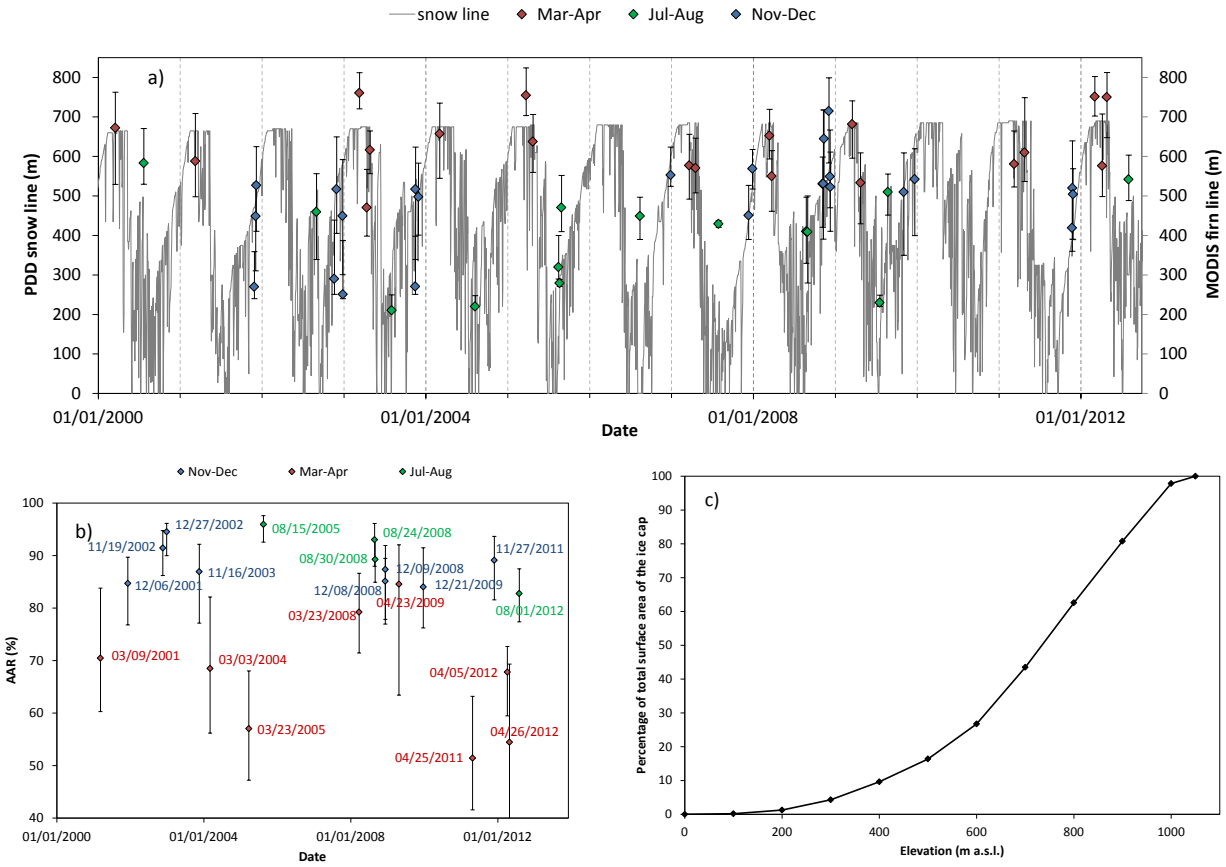

Figure 5. (a) Comparison between Ampere Glacier snow line computed with the PDD model and discrete firn line elevations for the Ampere Glacier obtained from albedo maps derived from MODIS images. Error bars are given for a firn albedo limit between 0.5 and 0.6 on the MODIS images. (b) Changes in the ratio of the accumulation area (firn- and snow-covered area) to the surface area of the entire ice cap between January 2000 and August 2012, for three periods: November-December (blue), March-April (red) and July-August (green) derived from clear-sky MODIS images. Error bars are also indicated for a firn albedo limit between 0.5 and 0.6 on the MODIS images. (c) Hypsometry of the Cook Ice Cap in 2009, i.e. the percentage of the surface area of ice cap below a given elevation.

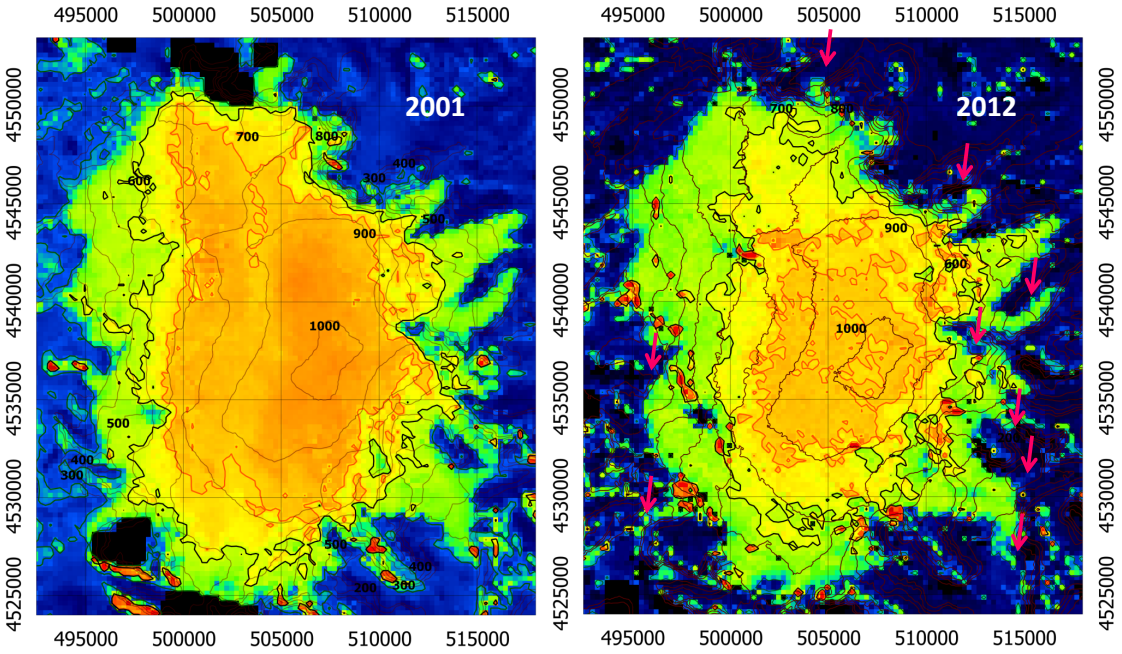

Figure 6. Comparison between albedo maps for March 9, 2001 (left) and April 26, 2012 (right). For key to pixel colours, see Fig. 2, panel a. The firn line is represented by a black line, the snow line is in orange, and contour lines in 2000 (SRTM DEM) and 2009 (SPOT DEM) respectively are in burgundy (numbers indicate contour line elevations in m a.s.l.). The pink arrows in the 2012 image point to sites where ice tongues or termini disappeared between 2001 and 2012. Coordinates are in UTM (Zone 42S).

were not acquired at the exact same date, but about six weeks apart, due to the scarcity of clear-sky images, and the disappearance of the snow cover could thus be partly linked to the time lag between the images, PDD modeling showed that this reduction is consistent (Section 4.4), and that the estimated snow line in 2001 was close to its maximum. Moreover, the MODIS images also showed a retreat of the ice cap between 2001 and 2012. Indeed, the disappearance of ice, unlike that of snow, does not depend on the time of year, and Fig. 6 shows that some glacier snouts and termini have disappeared in 2012, especially on the eastern flank of the ice cap (sites are indicated by pink arrows). The glacier retreat was confirmed by comparing Landsat images acquired in 2001 and 2011 (not shown here).

4.3. Current SMB and snow line estimates from stake measurements and comparison with the 1970s

Figure 4 also shows Ampere Glacier SMB values at stake locations in 1970-1974 and 2011 plotted against surface elevation. Despite the marked scattering in the distribution of SMB with elevation, a simple linear extrapolation of stake measurements suggests that, in 2011, the snow line was located at about 800-1000 m a.s.l., in agreement with the transient snow line value obtained for Ampere Glacier from MODIS images in 2012 (Fig. 6). However, the data display marked scattering caused by five values from stakes located at the border of the glacier where snow can accumulate (Fig. 1 b, zone 2).

Despite the two short observation periods, we were able to compare SMB and snow line elevation values on Ampere Glacier between 1970 and 1974 [*Vallon*, 1977a, b, 1987] with our values for 2011 (Fig. 4). The comparison revealed that the spatial distribution of SMB has changed significantly in 40 years:

1. SMB is more negative at the same elevation

2. SMB extrapolation suggests that the snow line was above 800 m a.s.l. in 2011 (this was confirmed by field observations in 2012 and 2013), whereas it was located around 650 m a.s.l. in the early 1970s. Even if the snow line elevation was computed only using data from one year, the PDD model shows that it was similar between 2008 and 2012, suggesting that this difference makes sense.

3. SMB gradient above 400 m a.s.l. is lower than in the early 1970s.

4.4. Comparison between the PDD snow line and the MODIS transient firn line

PDD model results showed a difference of about 50-100 m between the snow line and the firn line elevations for 2011, in good agreement with MODIS estimates in 2012 (around 100 m, see Section 4.2). Figure 5 a compares the modeled snow line and the transient firn line elevation obtained from MODIS images on Ampere Glacier. Despite its high variability, the modeled snow line agrees well with transient firn line variations in MODIS images (correlation of 0.67 for a transient firn line at an albedo of 0.55, p-value <0.001). The mean difference between the PDD-modeled snow line and MODIS-derived transient firn line ($\overline{x}_{PDD} - \overline{x}_{MODIS}$) was 46 m for a transient firn line threshold of 0.5 and -31 m for a threshold of 0.55. This means that the actual threshold should be close to 0.53, and gives us further confidence in our PDD estimates. The annual maximum PDD-modeled snow line elevation (corresponding to the ELA) of the Ampere Glacier increased by $\sim$ 30 m between 2000 and 2012.

4.5. Information provided by SEB modeling and albedo estimates from MODIS

We calculated punctual SMB values at stake locations (see Fig. 1 b for locations) for 2011 and compared them to values measured at the stakes in 2011, as illustrated in Fig. 7.

The poor quality of the information concerning turbulent heat fluxes and precipitation constitutes the main uncertainty in SEB and SMB computation. High $LE + H$ values tend to decrease the local mass balance. Conversely, high precipitation tends to limit negative SMB values. We observed that field SMB data cannot be reproduced if we assume a value of 50 W m^{-2} for turbulent heat fluxes (as measured by *Poggi* [1977a]) even if we assume a P twice as large as the one calculated from the relationship described in Section 3.4 (Fig. 7 a). On the other hand, we observed that SMB is correctly computed assuming calculated precipitation and turbulent heat fluxes $\sim$ 30 W m^{-2} (Fig. 7 b). Preliminary results from our SEB model during 2011 yielded a similar mean value of punctual $LE + H$ of 34 W m^{-2}.

However, even for the case with turbulent heat fluxes of 30 W m^{-2}, points located in overaccumulation areas (zone 2) yield SMB estimates too negative compared to measurements (they fall under the x = y curve), while the ones located in zone 1 agree well with measurements. About three times the amount of P (which is mostly liquid) have to be considered for the computed SMB in zone 2 to agree with measurements, suggesting that they are located in large corniches.

Finally we observed that the point chosen at 990 m a.s.l., where accumulation is expected to occur, displays a negative estimated SMB value (approximately -3200 mm w.e. for the case with turbulent heat fluxes of 30 W m^{-2} at an elevation of 990 m a.s.l.). In the case of $LE + H = 30$ W m^{-2}, accumulation calculated from the relationship described in Section 3.4 (approximately +3350 mm w.e.) compensates the SW contribution to SMB (approximately -3140 mm w.e.). This demonstrates that $LE + H$ and LW must decrease with elevation in order to have a slight accumulation at the top of the ice cap, and that constant values used in the ablation zone are not appropriate at such high elevations.

4.6. Long term variations in the snow line and link with climate variability

Measured and reanalyzed temperature and precipitation data over Kerguelen since 1948 are presented in Fig. 8.

Météo France measurements revealed a marked decrease in temperature of about -0.06 °C a^{-1} from 1952 to 1964, followed by a sharp increase of about +0.06 °C a^{-1} from 1964 to 1982. Reanalyses and measurements after 1982 revealed a slight increase (not significant at the 95% confidence level) in temperature of about +0.002 °C a^{-1} to +0.01 °C a^{-1}.

Precipitation measured at Port-aux-Français before 1973 presented a very different variability than precipitation measured after 1973. Measurements after 1973 displayed a significant (at the 95% confidence level) decrease in precipitation of about 25% in the last 40 years, slightly higher than in reanalysis data, which suggest a decrease of 5% to 20%. Analysis of daily precipitation revealed that this decrease is not linked to a decrease in the intensity of precipitation, but rather to a decrease in the frequency of precipitation events (Table 3). However, it should be kept in mind that precipitation measurements using rain gauges are negatively biased in strong wind conditions [*Larson and Peck*, 1974], which is often the case on the Kerguelen Islands, implying that actual precipitation amounts are probably larger than measured but such a bias was also likely present in past measurements.

Table 4 compares mean ELA values from the PDD model and from MODIS images during the 1950s and the 2000s. The mean modeled ELA for the period 2000-2009 was 127 m higher than the mean ELA for the period 1958-1963 (last

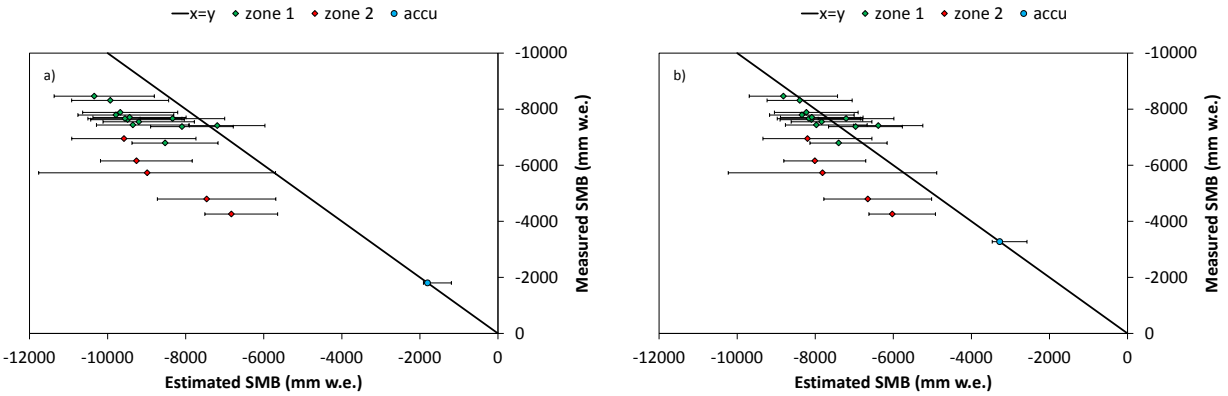

Figure 7. Comparison between field annual SMB measured at stake locations (see Fig. 1 b for locations) and annual SMB estimates. Two cases were used for the computation of SMB: (a) turbulent heat fluxes of 50 W m^{-2} and doubled precipitation compared to estimates, and (b) turbulent heat fluxes of 30 W m^{-2} and estimated precipitation. Values are separated into zone 1 and zone 2 (see Section 2.1 for explanations). The point named "accu" corresponds to the x = y SMB value calculated with the albedo of a pixel situated in the accumulation zone of the glacier (990 m a.s.l.). Error bars were estimated by calculating the error introduced when selecting different pixels adjacent to the one in which the stake is located, plus the systematic bias introduced by using clear-sky images.

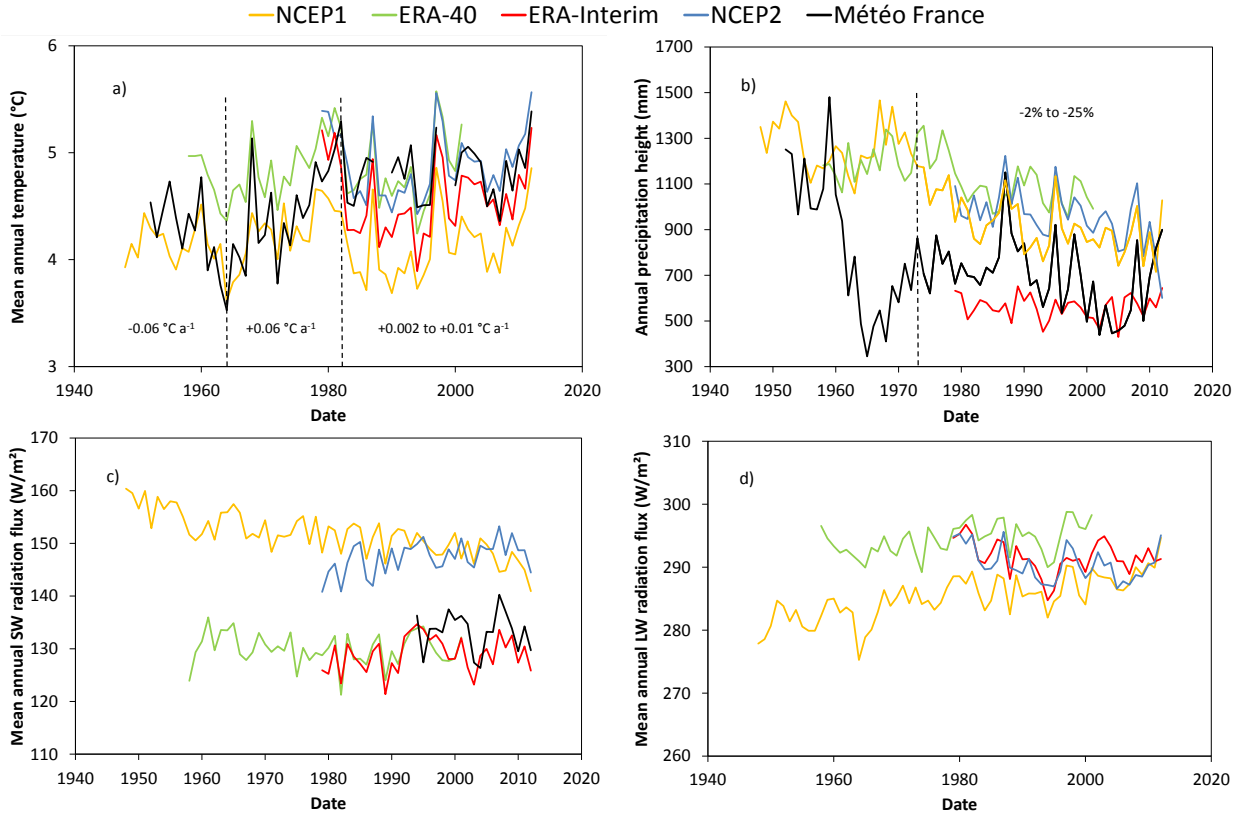

Figure 8. Meteorological (Météo France measurements at Port-aux-Français) and climatic (NCEP Reanalysis 1 and 2, ERA-40 and ERA-Interim reanalysis) data for the Kerguelen Islands since 1948: (a) temperature 2 m above the surface, (b) precipitation, (c) shortwave (SW) radiation flux and (d) longwave (LW) radiation flux. Temperature and precipitation trends for different periods (delimited by vertical dashed lines) are also shown.

Table 3. Characteristics of precipitation events from Météo France measurements at Port-aux-Français. Total annual amount of precipitation, total number of precipitation events and number of events with less than 20 mm d^{-1} are shown for 10 year-periods since 1953.

	Mean annual precipitation (mm a^{-1})	Total number of precipitation events	Precipitation events < 20 mm d^{-1}	Ratio of events < 20 mm d^{-1} compared to total number of events (%)
1953 - 1962	1055	2402	2298	95.7
1963 - 1972	567	2113	2083	98.6
1973 - 1982	743	2102	2051	97.6
1983 - 1992	789	2013	1947	96.7
1993 - 2002	649	1928	1888	97.9
2003 - 2012	626	1814	1764	97.2

Table 4. Comparison of mean ELA values calculated by the PDD model and estimated from MODIS images over the periods 1958-1963 and 2000-2009. PDD values are calculated with measured precipitation and temperature from Port-aux-Français (Measured), with normal precipitation but temperature from the 1950s repeated until the 2000s (T50s) and with normal temperature but precipitation from the 1950s repeated every decade until the 2000s (P50s). Uncertainty estimates for 2000-2009 mean ELA correspond to the standard deviations of centered snow line values.

Climate forcing	Measured		T50s	P50s
Time period	1958–63	2000–09	2000–09	2000–09
PDD ELA (m)	549	677±182	638±196	578±175
MODIS ELA (m)		668±142		

cipitation from the 1950s repeated during the next decades, labeled P50s) yielded a mean ELA for 2000-2009 ∼100 m lower than the actual modeled ELA, while the same ELA for unchanged temperature (labeled T50s) was only ∼40 m lower. This indicates that precipitation decrease has contributed for about 70% to the rise in ELA from the 1950s to date, while temperature has had a much smaller contribution. The agreement between modeled and measured mean ELA for the period 2000-2009 (compared to the P50s and T50s hypothetical cases) should be noted anew, although standard deviation of the measured ELA is smaller than the ones for modeled values, indicating that the model could be slightly too sensitive compared to measurements. A similar analysis was carried out on mass balance measurements (obtained from the difference between two digital elevation models) and estimates using the same PDD. The PDD forced with measured values from Port-aux-Français indicates an equilibrium in 1960 [*Frenot et al.*, 1993] and a similar modeled mass balance between 1963 and 2000 (-1.13 ± 0.13 m w.e. a^{-1}) as the one measured by *Berthier et al.* [2009] (-1.33 ± 0.90 m w.e. a^{-1}). When comparing these values with the ones modeled for 2000-2009 using measured values and hypothetical cases P50s and T50s, we find that, similarly to ELA, 77% of the differences in surface mass balance can be explained by the decrease in precipitation.

Changes in precipitation occurrence were likely associated to variations in other climatic settings which may have had significant impact on glaciers, as for instance cloudiness. We analyzed the variations of this variable, which may have changed significantly during the last 50 years. Figure 8, panels c and d show incident shortwave and incoming longwave radiation trends that differ depending on the reanalysis. Recent reanalyses show a slight increase in incident SW radiation and a slight decrease in incoming LW radiation in recent decades. This indicates a decrease in cloud cover which certainly played a role in the ice cap wastage, although this result should be interpreted with caution because (1) previous generation reanalyses displayed opposite trends and (2) there are no available long term field measurements in this area to enable us to confirm this result.

5. Discussion and Conclusions

The PDD model reproduced current and past SMB (in the early 1970s) reasonably well, showing that temperature and precipitation were the first order variables that explained the SMB variations. PDD results indicated that the mean firn limit was about 100 m lower in the early 1970s than today. Nevertheless, an acceleration in punctual ablation up to high elevations and a resulting decrease in SMB gradient with elevation have been observed, which are not fully reproduced by the PDD model. Our rough estimates of SEB based on MODIS albedo showed that they result from feedback including albedo and spatial reduction in snow corniches due to lower amounts of solid precipitation. Including wind drift and snow accumulation processes is necessary for the study of fine scale (about 10-100 m) corniche formation. However, at larger scales (1-10 km), a distributed surface heat budget would be enough to model most processes and feedback that occur at the ice cap scale.

Modeling the punctual SMB for 2011 using albedo estimates from MODIS imagery showed that the LW radiation budget represents 4% to 13% of the available energy for melting, while the SW radiation budget represents 58% to 64%. Consequently, turbulent heat fluxes contribute 29% to 32% to ablation, which is lower than on Patagonian glaciers (i.e. *Schneider et al.* [2007]), and less than estimates based on the measurements (42%) made in summer by *Poggi* [1977a]. These estimates were confirmed by a one-year (2011) SEB model, yielding mean contributions of 68% for SW, 1% for LW and 31% for turbulent heat fluxes. Albedo thus plays an important role in ablation through the SW radiation budget, which motivated us to undertake a thorough study of changes in the snow line using MODIS data and modeling.

MODIS imagery also revealed a change in the location of the snow line between 2000 and 2012. The current snow line is above 800 m a.s.l. (Fig. 4), but slightly lower on the ice cap's western flank than on its eastern flank (Fig. 6), due to dominant eastward moisture transport [*Garreaud et al.*, 2009]. MODIS also showed a decrease in the accumulation area ratio since 2000 (Figs. 5 and 6), despite the larger accumulation area and lower firn line altitude values in March-April 2008 and 2009 compared to other years, that were probably due to the occurrence of large precipitation amounts and relatively low temperatures in 2008 and 2009 (Fig. 8). As the ice cap is very flat between ∼ 600 m a.s.l. and its summit (1,030 m a.s.l.), even a small rise in the snow line has dramatic consequences for the reduction of the accumulation area (Fig. 5). The extent of the current accumulation area *sensu stricto* is small and negative SMB can probably be found at high altitudes.

In fact, comparison with field data from the 1970s indicates that the snow line has risen more than 150 m in 40 years. Moreover, the SMB gradient with elevation is lower today than it was in the early 1970s. Indeed, since snow cover is almost continuously absent up to high elevations, the albedo at stakes with distinct elevations is more uniform (as it remains in the albedo range of ice almost all through the entire ablation season), leading to a lower SMB gradient with elevation.

To sum up, the snow line has risen with time, the accumulation area is now reduced and the mean albedo of the ice cap is lower. These processes led to a retreat of the ice cap. Climatic forcings that explain this retreat were investigated using meteorological measurements and reanalysis data (Fig. 8), and showed that changes in precipitation represent the initial first order process that explains the marked increase in ablation and decrease in accumulation since the 1970s. An analysis of the ELA (Table 4) revealed that about 70% of the rise in ELA since the 1950s was due to the decrease in precipitation. We are aware that the analysis of such hypothetical series is rather simplistic and that further analysis should be needed. For instance, a study of the long term trends in incoming SW and LW radiation using reanalysis data (Fig. 8 c, d) revealed that a decreasing trend of the cloud cover was likely, and may have played a significant role in glacier retreat, even though long term field measurements are lacking to definitely conclude on such a trend. In addition, a similar analysis, but concerning mass balance values, was carried out, also indicating a significant contribution from precipitation (77%) compared to temperature. The decrease in precipitation was due to a reduction in the frequency of precipitation events (Table 3). This was probably linked to a southward shift of the storm tracks due to

more frequent positive phases of the Southern Annual Mode (SAM) in recent decades, which has had important impacts on the environment [*Villalba et al.*, 2012; *Manatsa et al.*, 2013; *Delworth and Zeng*, 2014]. Combined with a more moderate increase in temperature, this resulted in a rise in the 0 °C level, leading to a decrease in the occurrence of solid precipitation at low to intermediate elevations. The latter caused an albedo feedback, which, combined with the slight increase in SW radiation (+2% to +4% according to data from ERA-Interim and NCEP 2 reanalysis), led to more ablation and a rapid rise in the snow line. The subsequent decrease in elevation caused additional positive feedback on ablation due to the local increase in temperature.

However, different behaviors were observed between two zones of the glacier (zone 1 and zone 2, see Fig. 1 b), which are visible as large snow corniches or dunes in the lee of crests. As can be seen in Fig. 1 b, the spatial distribution of these zones is not related to elevation but to the distance to the crests. Because rough estimates of SMB using MODIS albedo suggest that large negative SMB should be observed, it is very likely that these zones only exist because of overaccumulation. The limited extent of these local accumulation zones is visible on the MODIS images as well as in the field. These different zones were not fully reproduced by a simple approach based on changes in fluxes with elevation and overaccumulation processes must thereby be accounted for.

As a consequence, a full modeling approach would be useful. To this end, recently initiated regional scale simulations of mass balance processes over the Kerguelen Islands with a downscaling scheme (SMHiL, *Agosta* [2012]) and the regional climate model MAR (Modèle Atmosphérique Régional, *Gallée and Schayes* [1994]) should provide new insights into changes in its ice bodies.

Acknowledgments. We would like to thank Julie Gardelle, Etienne Berthier and Yves Arnaud for their help with satellite imagery, and the Météo France team at Port-aux-Français for providing meteorological data and information about the meteorological station. Special thanks to the IPEV logistics team and all the people who helped us during the field campaigns, without whose help this study would not have been possible. We also thank the French Austral and Antarctic Territories (TAAF). NCEP 1 and 2 reanalysis data were provided by the NOAA/OAR/ESRL PSD, Boulder, Colorado, USA, from their Web site at http://www.esrl.noaa.gov/psd/. ERA-40 and ERA-Interim reanalysis data were downloaded from the ECMWF data portal at http://data-portal.ecmwf.int/. MODIS Level-1B Swath images were retrieved from the LAADS at http://ladsweb.nascom.nasa.gov/, and the Landsat images from the USGS at http://glovis.usgs.gov/. The ASTER image is courtesy of the GLIMS project. Field measurements and research were funded by IPEV program n° 1048 (GLACIOCLIM-KESAACO) and by INSU program LEFE-KCRuMBLE.

References

Agosta, C. (2012), Evolution du bilan de masse de surface Antarctique par régionalisation physique et conséquences sur les variations du niveau des mers. PhD thesis, Université de Grenoble, France.

Anderson, B., A. Mackintosh, D. Stumm, L. George, T. Kerr, A. Winter-Billington, and S. Fitzsimons (2010), Climate sensitivity of a high-precipitation glacier in New Zealand, *J. Glaciol.*, *56*(195), 114–128, doi:10.3189/002214310791190929.

Berthier, E., R. Le Bris, L. Mabileau, L. Testut, and F. Remy (2009), Ice wastage on the Kerguelen Islands (49 degrees S, 69 degrees E) between 1963 and 2006, *J. Geophys. Res.*, *114*, F03005, doi:10.1029/2008JF001192.

Cogley, J.G., R. Hock, L.A. Rasmussen, A.A. Arendt, A. Bauder, R.J. Braithwaite, P. Jansson, G. Kaser, M. Möller, L. Nicholson and M. Zemp (2011), Glossary of Glacier Mass Balance and Related Terms, *IHP-VII Technical Documents in Hydrology*, *86*, IACS Contribution No. 2, UNESCO-IHP, Paris.

Dee, D.P., S.M. Uppala, A.J. Simmons, P. Berrisford, P. Poli, S. Kobayashi, U. Andrae, M.A. Balmaseda, G. Balsamo, P. Bauer, P. Bechtold, A.C.M. Beljaars, L. van de Berg, J. Bidlot, N. Bormann, C. Delsol, R. Dragani, M. Fuentes, A.J. Geer, L. Haimberger, S.B. Healy, H. Hersbach, E.V. Hólm, L. Isaksen, P. Kållberg, M. Köhler, M. Matricardi, A.P. McNally, B.M. Monge-Sanz, J.-J. Morcrette, B.-K. Park, C. Peubey, P. de Rosnay, C. Tavolato, J.-N. Thépaut, and F. Vitart (2011), The ERA-Interim reanalysis: configuration and performance of the data assimilation system, *Q. J. Roy. Meteorol. Soc.*, *137*, 553–597, doi:10.1002/qj.828.

Delworth, T.L. and F. Zeng (2014), Regional rainfall decline in Australia attributed to anthropogenic greenhouse gases and ozone levels, *Nature Geosci.*, *7*, 583–587, doi:10.1038/ngeo2201.

Dumont, M., P. Sirguey, Y. Arnaud, and D. Six (2011), Monitoring spatial and temporal variations of surface albedo on Saint Sorlin Glacier (French Alps) using terrestrial photography, *The Cryosphere*, *5*, 759–771, doi:10.5194/tc-5-759-2011.

Dumont, M., J. Gardelle, P. Sirguey, A. Guillot, D. Six, A. Rabatel, and Y. Arnaud (2012), Linking glacier annual mass balance and glacier albedo retrieved from MODIS data, *The Cryosphere*, *6*, 1527–1539, doi:10.5194/tcd-6-2363-2012.

Farr, T.G., P.A. Rosen, E. Caro, R. Crippen, R. Duren, S. Hensley, M. Kobrick, M. Paller, E. Rodriguez, L. Roth, D. Seal, S. Shaffer, J. Shimada, J. Umland, M. Werner, M. Oskin, D. Burbank, and D. Alsdorf (2007), The Shuttle Radar Topography Mission, *Rev. Geophys.*, *45*, RG2004, doi:10.1029/2005RG000183.

Favier, V., C. Agosta, C. Genthon, L. Arnaud, A. Trouvillez, and H. Galle (2011), Modeling the mass and surface heat budgets in a coastal blue ice area of Adelie Land, Antarctica, *J. Geophys. Res.*, *116*, F03017, doi:10.1029/2010JF001939.

Fitzharris, B.B., T.J. Chinn, and G.N. Lamont (1997), Glacier balance fluctuations an atmospheric circulation patterns over the Southern Alps, New Zealand, *Int. J. Clim.*, *17*(7), 745–763, doi:10.1002/(SICI)1097-0088(19970615)17:7¡745::AID-JOC160¿3.0.CO;2-Y.

Fitzharris, B.B., G.R. Clare, and J. Renwick (2007), Teleconnections between Andean and New Zealand glaciers, *Glob. Plan. Change*, *59*(1-4), 159–174, doi:10.1016/j.gloplacha.2006.11.022.

Frenot, Y., J.-C. Gloaguen, G. Picot, J. Bougère, and D. Benjamin (1993), Azorella selago Hook. used to estimate glacier fluctuations and climatic history in the Kerguelen Islands over the last two centuries, *Oecologia*, *95*, 140-144, doi:10.1007/BF00649517.

Frenot, Y., J.-C. Gloaguen, B. Van de Vijver, and L. Beyens (1997), Datation of some Holocene peat sediments and glacier fluctuations in the Kerguelen Islands, *Comptes Rendus de l'Académie des Sciences, Série III-Sciences de la Vie - Life Sciences*, *320*(7), 567–573, doi:10.1016/S0764-4469(97)84712-9.

Gallée, H., and G. Schayes (1994), Development of a three-dimensional meso-γ primitive equation model: katabatic winds simulation in the area of Terra Nova Bay, Antarctica, *Mon. Weather Rev.*, *122*, 671–685, doi:10.1175/1520-0493(1994)122¡0671:DOATDM¿2.0.CO;2

Garreaud, R.D., M. Vuille, R. Compagnucci, and J. Marengo (2009), Present-day South American climate, *Palaeog. Palaeocl. Palaeoecol.*, *281*, 180–195, doi:10.1016/j.palaeo.2007.10.032.

Greuell, W., J. Kohler, F. Obleitner, P. Glowacki, K. Melvold, E. Bernsen, and J. Oerlemans (2007), Assessment of interannual variations in the surface mass balance of 18 Svalbard glaciers from the Moderate Resolution Imaging Spectroradiometer/Terra albedo product, *J. Geophys. Res.*, *112*, D07105, doi:10.1029/2006JD007245.

Hall, D.K., G.A. Riggs, V.V. Salomonson, N.E. DiGirolamo, and K.J. Bayr (2002), MODIS snow-cover products, *Rem. Sens. Env.*, *83*(1–2), 181–194, doi:10.1016/S0034-4257(02)00095-0.

Hock, R. (1999), A distributed temperature-index ice- and snowmelt model including potentiel direct solar radiation, *J. Glaciol.*, *45*(149), 101–111.

Jóhannesson, T., T. Laumann, and M. Kennett (1995), Degree-day glacier mass-balance modelling with applications to glaciers in Iceland, Norway and Greenland, *J. Glaciol.*, *41*(138), 345–358.

Kalnay, E., M. Kanamitsu, R. Kistler, W. Collins, D. Deaven, L. Gandin, M. Iredell, S. Saha, G. White, J. Woollen, Y. Zhu, A. Leetmaa, R. Reynolds, M. Chelliah, W. Ebisuzaki, W. Higgins, J. Janowiak, K.C. Mo, C. Ropelewski, J. Wang, J. Roy, and J. Dennis (1996), The NCEP/NCAR 40-Year Reanalysis Project, *B. Am. Meteorol. Soc.*, *77*(3), 437–471, doi:10.1175/1520-0477(1996)077¡0437:TNYRP¿2.0.CO;2.

Kanamitsu, M., W. Ebisuzaki, J. Woollen, S.K. Yang, J.J. Hnilo, M. Fiorino, G.L. and Potter (2002), NCEP-DOE AMIP-II Reanalysis (R-2), *B. Am. Meteorol. Soc.*, *83*(11), 1631–1643, doi:10.1175/BAMS-83-11-1631

Korona, J., E. Berthier, M. Bernard, F. Remy, and E. Thouvenot (2009), SPIRIT. SPOT 5 stereoscopic survey of Polar Ice: Reference Images and Topographies during the fourth International Polar Year (2007-2009), *ISPRS J. Photogramm.*, *64*, 204–212, doi:10.1016/j.isprsjprs.2008.10.005.

Larson, L.W., and E.L. Peck (1974), Accuracy of precipitation measurement for hydrological modelling, *Water Res. Res.*, *10*, 857–863, doi:10.1029/WR010i004p00857.

Lenaerts, J., M. van den Broeke, J. van Wessem, W. van de Berg, E. van Meijgaard, L. van Ulft, and M. Schaefer (2014), Extreme precipitation and climate gradients in Patagonia revealed by high-resolution regional atmospheric climate modelling. *J. Clim.*, *27*, 4607–4621, doi:10.1175/JCLI-D-13-00579.1.

Lopez, P., P. Sirguey, Y. Arnaud, B. Pouyaud, and P. Chevallier (2008), Snow cover monitoring in the Northern Patagonia Icefield using MODIS satellite images (2000-2006), *Glob. Plan. Ch.*, *61*, 103–116, doi:10.1016/j.gloplacha.2007.07.005.

Lopez, P., P. Chevallier, V. Favier, B. Pouyaud, F. Ordenes, and J. Oerlemans (2010), A regional view of fluctuations in glacier length in southern South America, *Glob. Plan. Ch.*, *71*, 85–108, doi:10.1016/j.gloplacha.2009.12.009.

Maisincho, L., V. Favier, P. Wagnon, R. Basantes Serrano, B. Francou, M. Villacis, A. Rabatel, L. Mourre, V. Jomelli, and B. Cáceres (2014), On the interest of positive degree day models for mass balance modeling in the inner tropics, *The Cryosphere Discuss.*, *8*, 2637-2684, doi:10.5194/tcd-8-2637-2014.

Manatsa, D., Y. Morioka, S.K. Behera, T. Yamagata, and C.H. Matarira (2013), Link between Antarctic ozone depletion and summer warming over southern Africa. *Nature Geosci.*, *6*, 934–939, doi:10.1038/ngeo1968.

Melkonian, A.K., M.J. Willis, M.E. Pritchard, A. Rivera, F. Bown, and S.A. Bernstein (2013), Satellite-derived Volume Loss Rates and Glacier Speeds for the Cordillera Darwin Icefield, Chile, *The Cryosphere*, *7*, 823–839, doi:10.5194/tc-7-823-2013.

Oke, T.R. (1987), Boundary Layer Climates, 2nd ed., 435 pp., Routledge, New York.

Poggi, A. (1977a), Heat Balance in ablation area of Ampere Glacier (Kerguelen Islands), *J. Appl. Meteorol.*, *16*, 48–55, doi:10.1175/1520-0450(1977)016¡0048:HBITAA¿2.0.CO;2.

Poggi, A. (1977b), Etude comparative du bilan thermique en deux stations du glacier Ampère Iles Kerguelen, *Zeitschrift für Gletscherkunde und Glazialgeologie*, *13*, 87–97.

Purich, A., T. Cowan, S.-K. Min, and W. Cai (2013), Autumn precipitation trends over Southern Hemisphere midlatitudes as simulated by CMIP5 models, *J. Climate*, *26*(21), 8341–8356, doi:10.1175/JCLI-D-13-00007.1.

Rabatel, A., A. Bermejo, E. Loarte, A. Soruco, J. Gomez, G. Leonardini, C. Vincent, and J.E. Sicart (2012), Can the snowline be used as an indicator of the equilibrium line and mass balance for glaciers in the outer tropics?, *J. Glaciol.*, *58*(212), 1027–1036, doi:10.3189/2012JoG12J027.

Radic, V., and R. Hock (2011), Regionally differentiated contribution of mountain glaciers and ice caps to future sea-level rise, *Nat. Geosci.*, *4*(2), 91–94, doi:10.1038/ngeo1052.

Rignot, E., A. Rivera, and G. Casassa (2003), Contribution of the Patagonia Icefields of South America to sea level rise, *Science*, *302*(5644), 434–437, doi:10.1126/science.1087393.

Schaefer, M., H. Machguth, M. Falvey, and G. Casassa (2013), Modeling past and future surface mass balance of the Northern Patagonia Icefield, *J. Geophys. Res. Earth Surf.*, *118*, 571–588, doi:10.1002/jgrf.20038.

Schneider, C., R. Kilian, and M. Glaser (2007), Energy balance in the ablation zone during the summer season at the Gran Campo Nevado Ice Cap in the Southern Andes, *Glob. Plan. Change*, *59*(1–4), 175–188, doi:10.1016/j.gloplacha.2006.11.033.

Sirguey, P., R. Mathieu, and Y. Arnaud (2009), Subpixel monitoring of the seasonal snow cover with MODIS at 250 m spatial resolution in the Southern Alps of New Zealand: Methodology and accuracy assessment, *Rem. Sens. Env.*, *113*, 160–181, doi:10.1016/j.rse.2008.09.008.

Takeuchi, Y., R. Naruse, K. Satow, and N. Ishikawa (1999), Comparison of heat balance characteristics at five glaciers in the southern hemisphere, *Glob. Plan. Change*, *22*(1), 201–208, doi:10.1016/S0921-8181(99)00037-5.

Thompson, W.J., S. Solomon, P.J. Kushner, M.H. England, K.M. Grise, and D.J. Karoly (2011), Signatures of the Antarctic ozone hole in Southern Hemisphere surface climate change, *Nature Geosci.*, *4*, 741–749, doi:10.1038/ngeo1296.

Uppala, S.M., P.W. Kållberg, A.J. Simmons, U. Andrae, V. Bechtold, M. Fiorino, J.K. Gibson, J. Haseler, A. Hernandez, G.A. Kelly, X. Li, K. Onogi, S. Saarinen, N. Sokka, R.P. Allan, E. Andersson, K. Arpe, M.A. Balmaseda, A.C.M. Beljaars, L. Van De Berg, J. Bidlot, N. Bormann, S. Caires, F. Chevallier, A. Dethof, M. Dragosavac, M. Fisher, M. Fuentes, S. Hagemann, E. Hólm, B.J. Hoskins, L. Isaksen, P.A.E.M. Janssen, R. Jenne, A.P. Mcnally, J.-F. Mahfouf, J.-J. Morcrette, N.A. Rayner, R.W. Saunders, P. Simon, A. Sterl, K.E. Trenberth, A. Untch, D. Vasiljevic, P. Viterbo and J. Woollen (2005), The ERA-40 re-analysis, *Q. J. Roy. Meteor. Soc.*, *131*, 2961–3012, doi:10.1256/qj.04.176.

Vallon, M (1977a), Bilan de masse et fluctuations récentes du Glacier Ampère (Iles Kerguelen, TAAF), *Zeitschrift für Gletscherkunde und Glazialgeologie*, *13*, 55–85.

Vallon, M. (1977b), Topographie sous glaciaire du Glacier Ampère (Iles Kerguelen, TAAF), *Zeitschrift für Gletscherkunde und Glazialgeologie*, *13*, 37–55.

Vallon, M (1987), Glaciologie à Kerguelen, *Proceedings of the Colloque C.N.F.R.A. sur la Recherche Françaises dans les Terres Australes*, Strasbourg, 11–17 September 1987.

Villalba, R., A. Lara, M.H. Masiokas, R. Urrutia, B.H. Luckman, G.J. Marshall, I.A. Mundo, D.A. Christie, E.R. Cook, R. Neukom, K. Allen, P. Fenwick, J.A. Boninsegna, A.M. Srur, M.S. Morales, D. Araneo, J.G. Palmer, E. Cuq, J.C. Aravena, A. Holz and C. LeQuesne (2012), Unusual Southern Hemisphere tree growth patterns induced by changes in the Southern Annular Mode. *Nature Geoscience*, *5*, 793–798, doi:10.1038/ngeo1613.

Willis, M.J., A.K. Melkonian, M.E. Pritchard, and J.M. Ramage (2012a), Ice loss rates at the Northern Patagonian Icefield derived using a decade of satellite remote sensing, *Rem. Sens. Env.*, *117*, 184–198, doi:10.1016/j.rse.2011.09.017.

Willis, M.J., A.K. Melkonian, M.E. Pritchard, and A. Rivera (2012b), Ice loss from the Southern Patagonian Ice Field, South America, between 2000 and 2012, *J. Geophys. Res.*, *39*, L17501, doi:10.1029/2012GL053136.

Corresponding author: D. Verfaillie, Laboratoire de Glaciologie et Géophysique de l'Environnement, 54 rue Molière, BP 96, 38402 Saint-Martin-d'Hères cedex, France. (deborah.verfaillie@ujf-grenoble.fr)

Annexe F

Informations supplémentaires de l'article Favier et al. (en révision)

Supplementary Information

The ozone hole as the main driver of dramatic glacier wastage in the sub-Antarctic region

V. Favier[1,2], D. Verfaillie[1,2], E. Berthier[3], M. Menegoz[1,2], V. Jomelli[4], J.E. Kay[5], L. Ducret[3], Y. Malbéteau[3], D. Brunstein[5], H. Gallée [1,2], Y.-H. Park[6]

(1) Univ. Grenoble Alpes, LGGE, F-38041 Grenoble, France
(2) CNRS, LGGE, F-38041 Grenoble, France
(3) LEGOS, CNRS, Université de Toulouse, 14 av. Edouard Belin, F-31400 Toulouse CEDEX, France
(4) Université Paris 1 Pantheon-Sorbonne, CNRS Laboratoire de Géographie Physique, 92195 Meudon, France
(5) Cooperative Institute for Research in Environmental Sciences University of Colorado at Boulder 216 UCB Boulder, CO 80309
(6) LOCEAN/DMPA, Muséum National d'Histoire Naturelle, Paris, France

The following pages include:

S.1. Supplementary Methods

1.1. Remotely-sensed mass balance estimation

We measured ice elevation on the Cook Ice Cap by differencing two digital elevation models (DEMs) generated during the February 2000 Shuttle Radar Topographic Mission (SRTM)[34] and from Satellite Pour l'Observation de la Terre (SPOT5) optical stereo imagery acquired in December 2009[35]. Systematic horizontal and vertical biases potentially affecting the DEMs have been modelled and removed before computing the glacier mass balance. A detailed description of the processing steps can be found elsewhere[36] and are only briefly summarized here.

First, the SRTM is bilinearly resampled to 40 m, to match the resolution of the SPOT5 DEM. Horizontal shifts between the DEMs must be corrected to avoid systematic biases according to terrain aspect[37]. The planimetric adjustment is done by minimizing the root mean square error of elevation differences between the two DEMs on stable areas[36,38]. In our case, the shift applied to coregister the SRTM DEM to the SPOT5 DEM was − 10.4 m and −6.4 m, respectively, in easting and northing. To account for the difference in spatial resolution of the two DEMs, we applied a correction derived from the relation off-glacier between elevation differences and the terrain maximum curvature[39]. No significant bias related to the SPOT5 acquisition geometry in the cross-track and along-track direction was observed. Given that the SAR images used to generate the SRTM DEM were acquired around mid-February 2000, the heart of the melt season on Kerguelen Islands, we assumed no penetration of the SRTM C-band signal given the likely occurrence of liquid water in the snow, firn and ice[3].

Pixels interpolated in at least one of the DEMs (40% of the ice-covered areas) are excluded as well as the pixels where elevation difference exceeds ±150 m. Glacier volume changes over void-filled regions of the DEMs were estimated assuming that void-filled pixels experienced the mean elevation change of measurable pixels in the same altitude interval. This value was added to the measured changes to obtain a total volume change in each altitude interval.

Mean volume changes are then converted into glacier-wide mass balance by assuming a density of 850 kg m^{-3} (ref 40).

Errors on the elevation changes are estimated on the ice free terrain where, by construction, the average elevation difference between the SRTM and SPOT5 DEM is null, the standard deviation of the elevation difference being 4.6 m. A novel approach has been developed here so that our error estimate captures the spatially-varying vertical biases in the DEMs[37,41]. The ice-free region surrounding the Cook Ice Cap is split into 25 quadrants (5 by 5, we found little sensitivity of the error estimate to the number of quadrants). Within each quadrant, N measurements of elevation changes are randomly drawn and averaged, leading to the average elevation difference $\mu_{dh(i)}$. N is chosen to "simulate" hypothetical glaciated areas of 410 km² (the size of the entire Cook Ice Cap in 2000) and, respectively, 67 km² (the size of Ampère Glacier). $\mu_{dh(i)}$ represents the error on the elevation changes for an ice body of the size of the Cook Ice Cap (respectively Ampère Glacier) located within this quadrant i. Then, the absolute value $|\mu_{dh(i)}|$ is computed in each quadrant. Finally, the mean of those 25 values (one for each quadrant) of $|\mu_{dh(i)}|$ is calculated and is considered as our error on the elevation

difference. This error is ±0.7 m for the entire Cook Ice Cap and ±1.0 m for Ampère Glacier. Those errors are likely conservative given that the mean slope off glacier (12.5°) is more than twice larger than the average slope on the Cook Ice Cap (5.3°) and errors on DEMs are known to increase almost linearly with slope[42]

During the conversion from volume to mass, we assumed an additional ±60 kg m^{-3} error on the density conversion factor[40].

1.2.PDD modeling

A glacier modeling was performed to reproduce the ice cap mass balance variations. Running a full surface energy balance model was not sufficiently accurate to understand the causes of Cook Ice Cap wastage since the 1950s, because 1) long term radiation and wind speed measurements are only available at Kerguelen since the 1990s, and 2) the reanalyzed (ERA40 and NCEP1) radiation and cloudiness data at Kerguelen do not significantly correlate with measurements performed at Kerguelen since 1990 (not shown).

Conversely, daily temperature and precipitation amounts are available since 1951, and based strictly on WMO protocols (Météo-France station) offering unique consistent long-term observations. A simple PDD model was applied, that allows calculation of daily snow or ice melting Aj(z) at a given elevation z, and at time step j[43,44]:

$$Aj(z) = - F\,(Tj(z_{ref}) + LR\,(z - z_{ref})) \quad \text{if} \quad Tj(z_{ref}) + LR\,.\,(z - z_{ref}) > 0 \qquad (2)$$

$$Aj(z) = 0 \quad \text{if} \quad Tj(z_{ref}) + LR\,.\,(z - z_{ref}) \leq 0 \qquad (3)$$

where F is degree day factor, z_{ref} is altitude of the reference meteorological data and Tj(z) is mean daily temperature at elevation *z*. Modeled ablation was considered similar as melting, because sublimation is expected to be low at Kerguelen due to the high humidity[10].The snow depth at previous time step is $S_{j-1}(z)$. The model assumes distinct degree day factors according to the presence (or not) of snow at the surface. Snow is present if $S_{j-1}(z) > 0$.

Snow cover results from the difference between ablation and snow accumulation at a given elevation *z*. Solid precipitation is assumed if air temperature is below a threshold (Tsnow/rain = 1.0°C (ref 45)), otherwise solid precipitation is zero. Temperature at distinct elevations is computed assuming a constant lapse rate (*LR*) with elevation but varying according to the glacier orientation (see Section S1.5) between the reference elevation (z_{ref}), where meteorological data are available and a given elevation (z).

In the model, we account for firn disappearance. This phenomenon provoked an albedo feedback and thus, slightly accelerated the glacier retreat. In terms of ablation, the firn is treated as snow, but to represent a maximum firn layer, the layer depth is limited to a maximum value of 15 m w.e. (If $S_j(z)$ exceeds this limit, the excess is considered to change into ice).

A spin up was applied to the PDD model, assuming that the climatic conditions observed during the 1950s were present during the preceding decade, which is justified by the front stability at the end of the 1950s. This allowed an initial 15 m w.e. thick firn cover to build up above 600 m asl on the glacier in the early 1970s, in agreement with field observations[10]. Sensitivity tests were performed on the impact of the firn layer thickness on the final vertical balance profile showing that the equilibrium line elevation only decreases by about 30 meters in elevation when a firn layer of 50 m w.e. depth is accounted for. This suggests that this additional parameterization does not highly impact the final mass balance.

Degree day factors calibration

The degree day factors were calibrated with ablation measurements performed on stakes and with a sonic gauge. Modeled ablation was also compared to ablation estimates from surface energy balance computations, performed with data from two automatic weather stations (AWS) installed close to and on the glacier (Supplementary Table 1) and the Mortadelle Hut (Supplementary Fig. 3). Here we used data from December 21, 2010 to January 4, 2011, and from December 14, 2011 to December 30, 2011. During those two periods, an AWS was located on the glacier, measuring albedo, air temperature and humidity and wind speed. Daily ablation from the PDD model was compared to surface energy balance results.

The energy stored into the top layers of the glacier ΔQ was calculated as (fluxes toward the surface are positive)[46,47]:

$$S\downarrow + S\uparrow + L\downarrow - ((1- \varepsilon)\, L\downarrow + \varepsilon\, \sigma\, T_s^4) + LE + H = F_{surface} \quad (\text{in W m}^{-2}) \qquad (4)$$

where S↓ is incoming solar radiation, S↑ is reflected short-wave radiation that were directly measured on the glacier ; L↓ is incoming long-wave radiation that was measured at la Mortadelle hut, and the term in brackets is outgoing longwave radiation L↑ that was deduced form the modeled surface temperature T_s and Stefan-Boltzmann's equation. $\varepsilon = 0.99$ is surface emissivity and $\sigma = 5.67\ 10\text{–}8$ W m^{-2} K^{-4} is the Stefan-Boltzmann constant, H and LE are turbulent sensible and latent heat fluxes respectively, which were computed using **the Bulk-method including stability corrections based on the bulk Richardson N**umber. Surface roughness lengths were taken from the literature[46], to get agreement between measured ablation at stakes and modeled ablation. The heat flux supplied by precipitation was not taken into account because temperature during precipitation is always close to 0°C.

$F_{surface}$ is the energy available at the surface. Part of the shortwave radiation is actually not available for warming/cooling processes at the surface or for melting, because shortwave flux partly penetrates the ice. Hence, $F_{surface}$ is separated into two terms:

$$F_{surface} = G_0 + (1 - a)\, S \qquad (\text{in W m}^{-2}) \qquad (5)$$

where G_0 is energy excess or deficit at the surface. In this equation, a is fractional amount of shortwave radiation that is absorbed in the top layer of the model (at the surface).

When the surface temperature is 0 °C, the positive G_0 values represent the energy available for melt. Otherwise, this amount is used to cool/warm the frozen surface and underlying snow/ice. For this task, heat conduction within the snow or ice was computed by solving the thermal diffusion equation according to an explicit scheme to a depth of 2 m, with a 5 cm grid resolution and a 20 s time step.

Surface energy balance modeling allows reproducing the measured ablation (Supplementary Fig. 1). Comparison between the ablation values computed with the PDD and the SEB approaches were performed to calibrate the degree day factors F for snow and ice. Calibration of F suggests that:

$$F = F_{ice} = 7.4 \text{ mm } °C^{-1}day^{-1} \quad \text{if} \quad S_{j-1}(z) = 0 \qquad (6)$$

The calibrated F_{ice} is very close from the mean values at a global scale from ref.26, i.e. F_{ice} = 7.2 mm $°C^{-1}day^{-1}$. For snow, the calibration was performed on only 5 days with marked snow cover, leading to a value close to 5 mm $°C^{-1}day^{-1}$. Due to the low number of ablation data used for this calibration, a low accuracy on this parameter is expected. However, this value is in good agreement with the mean F_{snow} given by ref 26 at a global scale. Hence, we used the mean value from ref 26 for snow covered situations (see Supplementary Fig. 1):

.

$$F = F_{snow} = 4.9 \text{ mm } °C^{-1}day^{-1} \quad \text{if} \quad S_{j-1}(z) > 0 \qquad (7)$$

1.3.Distributed modeling with cellular Automaton

A cellular automaton[48] was coupled to the latter PDD modeling to produce ice motion from high elevations to the glacier snout. This method was largely used in many paleo-climatic studies[27,49]. The model considers that ice is a plastic material moving through avalanches and deformation/sliding. Glacier motion was conducted assuming that the basal shear stress was maintained to a constant value of 1 bar[50]. It operates discrete ice movement on a hexagonal grid, allowing six possible cardinal directions of movement. The flow is then largely controlled by the local slope. If the depth-slope product of the accumulated ice exceeds a threshold basal shear stress, deformation/sliding is simulated by moving sufficient ice to the lowest adjacent nodes to reduce the slope and depth. The ice flux field is determined by mass conservation and ice velocities are derived from this flux and are therefore closely related to the idea of balance velocities. The model poorly reproduces ice velocities, and is not appropriate to analyze glacier response times or transient glacier regimes. The simulations were performed over a period of 200 years, ensuring that the glacier reached an equilibrium with the climatic conditions.

The ice flow model allowed reproducing the maximum CIC extent in the early 1960s and the quick retreat since then (Supplementary Fig. 2b), demonstrating that the glacier model correctly reproduces the main glaciological processes on CIC. The modeled CIC extent was compared to the glacier outlines drawn on an April 2009 ASTER image. This suggests that current observed ice cap extent largely exceeds the modeled equilibrium state extent under current climate, justifying that ice flow will continue to decline and the glacier will continue to shrink, as suggested by the present Ampere glacier dynamics.

Indeed, surface ice velocities estimations from successive positioning of stakes in the 1970s (with theodolite) and in 2010-11 (with differential GPS) demonstrate a reduction of velocities between the 1970s and present-day. This is particularly important in the low elevation areas (below 400 m asl). This decreasing flow explains that surface elevation changes are almost equal to the surface mass balance. Thus, ice dynamics only have a limited impact on elevation changes, signifying that ice flow from upstream regions is no more compensating for the very negative SMB in the ablation area.

1.4.Temperature lapse rate and Precipitation change with elevation

Field data and results from the regional circulation model MAR (Modèle Atmosphérique Régional) were used to get the regional distribution of temperature and precipitation. MAR presents the atmospheric scheme described in (51), coupled to a physically-based model of the snow pack[52,53]. The simulation is run at 10 km resolution on a stereographic grid for the year 2011. The model was forced with ERA-Interim reanalysis data, which is the most recent ECMWF reanalysis[54]. ERA-Interim[54] covers the period 1989 to the present. The main advances of ERA-Interim over ERA-40 are a finer spectral truncation (T255, nominal resolution of 80 km), improved model physics and a more efficient data assimilation system (4D-Var instead of 3D-Var). Surface elevation of each 10x10 km cell was assessed using the ETOPO1 global relief model[55] to get accurate representation of orographic impact on precipitation. Precipitation, temperature and elevation from each 10x10 km cell were extracted and compared to the cell elevation. Precipitation amounts at different

elevations and temperature vertical lapse rate from MAR model were computed (Supplementary Fig. 3). The lapse rate was assessed from data on points with more than 500 m elevation difference to allow accurate computations. Results were compared to field data.

Field temperature measurements performed during years 2011 and 2012 at la Mortadelle (165 m above sea level (asl), Supplementary Fig. 3a) and close to the glacier (242 m asl) allowed calculation of a mean lapse rate of -9.1°C km^{-1}. The lapse rate between la Mortadelle and Port-Aux-Français (PAF, 25 m asl) was -8.6°C km^{-1} in 2011 and 2012. Results from MAR model also give a lapse rate of -8.0°C m^{-1} along the same azimuth (South-East) while a lapse rate of about -6.7°C km^{-1} is modelled upwind of the ice cap. In our modeling, we accounted for the mean lapse rate given by MAR for the different azimuths of glaciers according to the summit of the ice cap.

The MAR model is also used to assess the spatial pattern of precipitation. There is a significant correlation between precipitation and elevation (Supplementary Fig. 3b). The relationship agrees with precipitation data at PAF (Supplementary Fig. 3b) even if this relationship underestimates the precipitation amounts at the Mortadelle Hut, because this latter site is located in a small corridor and seems to present site specific precipitation amounts. The relationship between elevation and precipitation was used to force the PDD model at different elevations.

S.2. Supplementary Discussion

2.1.Climatic trends from field, CMIP5 and Reanalysis data

We analyzed Reanalyses and CMIP5 models data confirming results from (32).

a. Recent past trends

Additionally to temperature and precipitation data from the meteorological station at Port-aux-Français (Fig. 2), the ERA-40 from the ECMWF and NCEP-NCAR Reanalysis1 (NCEP1) were also analyzed here.

ERA-40 fully covers the 1958–2001 period[56], and is run on a reduced Gaussian grid with T159 spectral truncation that has a nominal resolution of 125 km. NCEP-NCAR Reanalysis1 (NCEP1) are global atmospheric reanalyses available from 1948 to the present[57]. NCEP1 model produces 6-hourly data at a T62 spectral resolution (210 km) and for 28 vertical levels extending from 5hPa from the surface to a top level at 3hPa. It uses a sequential 6h-cycle data assimilation (3D-variational) scheme.

Outputs from models from the Coupled Model Intercomparison Project 5 (CMIP5) were also used to derive current climatic trends. CMIP5[58] involves 20 climatic groups, which performed different experiments divided into two categories: (1) near-term simulations (10 to

30 years), some forced by observed ocean state and sea-ice and (2) long-term simulations (on a century time-scale) using atmosphere-ocean global climate models (AOGCMs, sometimes coupled to a carbon cycle model) initialized from the end of freely evolving simulations of the historical period[58]. For the second half of the 20th century, we used outputs from historical simulations (from the long-term experiment), and a multi-model mean (MMM) was computed from 49 different versions of different models (interpolated on ERA-40 grid) (Supplementary Table 2).

Precipitation and 850 hPa temperature linear trends from 1957 to 2002 for ERA-40, NCEP1 and the CMIP5 MMM are presented in Supplementary Fig. 4. A Spearman test was applied to detect trends significant at the 95% confidence interval (non-shaded areas in Supplementary Fig. 4). Reanalysis data clearly suggest a temperature increase and a precipitation decrease as a consequence of a poleward shift of storm tracks that was associated with the increase of the SAM[15,18-23].

The CMIP5 MMM also suggests a significant warming, and reproduces the current observed dryness area, even though precipitation decrease area is less significant and the localization of this area is slightly shifted northward in the models. The limit between precipitation decrease and precipitation increase is different according to models, but all the models agree in describing a large area with precipitation decrease around Kerguelen or just a few degrees north from the Kerguelen Islands.

b. Projection for the 21st century

To estimate future climatic trends, we used outputs from the CMIP5 long-term experiment projection simulations[58]. The latter are produced by forcing the different AOGCMs with specified greenhouse gases concentrations corresponding to different scenarios, called representative concentration pathways (RCPs). There are four different RCPs (RCP 2.6, 4.5, 6 and 8.5), which refer to the target radiative forcing at the end of the 21st century. A multi-model mean (MMM) was also computed from the various model outputs (Supplementary Table 2).

Projected precipitation and 850 hPa temperature linear trends from 2006 to 2100 for the CMIP5 MMM under the lowest (RCP 2.6) and the highest (RCP 8.5) scenarios are presented in Supplementary Fig. 5. A Spearman test was applied to detect trends with significance at the 95% confidence interval (non-shaded areas in Supplementary Fig. 5).

CMIP5 MMM clearly suggests an important warming (+0.0073 ± 0.0115 °C a^{-1} for RCP2.6 scenario and +0.0296 ± 0.0200 °C a^{-1} for RCP8.5 scenario) and a slightly increasing precipitation trend (+0.51 ± 1.35 mm a^{-1} for RCP2.6 scenario and +1.92 ± 1.86 mm a^{-1} for RCP8.5 scenario) at Kerguelen as a consequence of global warming. Regarding the CMIP5 MMM, as a consequence of the +SAM increase[15,32], MMM suggest an intensification of the dryness North of the Kerguelen, and a significant moistening over a large band around the Antarctic continent. Due to the coarse resolution of the CMIP5 models, to the possible future shift of the border between these drying and moistening areas, and to the proximity of the

Kerguelen Islands with this border, it is difficult to say whether the Kerguelen area will keep drying in the future. In our modeling we assumed however that precipitation will progressively increase and reach the 1950s amount around the end of the 21st century. This assumption supposes severely more humid conditions at the end of the century than projected by CMIP5 models. However, it allows accounting for conditions that should limit glacier wastage at the end of the 21st century so that our projected mass loss for the ice cap is a maximum estimate.

2.2.Climatic trends from Kerguelen Islands Radiosonde

Using radiosonde data from Kerguelen Islands (WMO ID 61998, 1973-2011), we analyzed vertical, seasonal, and temporal variability in temperature and relative humidity at standard pressure levels (1000 mb, 850 mb, 700 mb and 500 mb). Supplementary Figure 6 compares annual mean temperature and relative humidity histograms from the first decade of record (1973-1982) with the last decade of record (2002-2011). Histograms provide confidence in analysis because unlike averaged time-series, spurious values do not influence the results. Supplementary Figure 7 shows annual mean time series of temperature and humidity and the corresponding number of available observations available in each year. Over the period of record (1973-2011), there are negligible changes in air temperature aloft, but evidence for slight warming at 1000 mb (Supplementary Fig. 6, 7). In contrast to the modest temperature changes, large reductions in relative humidity at all pressure levels are measured.

2.3.Important climatic changes due to the internal natural variability of the ocean

A significant correlation (r^2 = 0.95, n = 227) between monthly ocean surface temperatures from a buoy at Port-Aux-Français, in the Golfe du Morbihan (ROSAME network) and monthly mean air temperature at PAF between 1993 and 2013, confirms that air and ocean surface temperatures are very closely related in this area. To test whether air temperature changed before 1950, we analyzed the ERSST.v2 historical ocean surface data because they offer an extended image of possible ocean surface temperature change since 1854 in the area. These data are based on the Comprehensive Ocean-Atmosphere Data Set (COADS) dataset, which consists in quality controlled marine surface observations from ships, moored environmental buoys, drifting buoys, and near-surface measurements from oceanographic profiles[28]. The dataset begins in 1854 and ends in 2009 and offers monthly statistics of basic marine variables for each year using observed data falling within 2° latitude × 2° longitude boxes. The ERSST analysis is generated using in situ SST data and improved statistical methods that allow stable reconstruction using sparse data. We did not consider ERSST.v3b database because it accounts for near land–near-surface temperature and may be biased by air temperature at PAF. . We are aware that before 1970, ERSST.2 relies on only sparse data.

Air temperature at PAF and the ERSST.v2 presented similar oscillations from 1950 to 2009 (Fig. 2a). Cold period at PAF during the 1960s was very likely due to a short and strong oscillation in the SST. SST also likely performed big oscillations before the 70s,

suggesting that natural variability of the system is very high. Finally, the historical SST suggests the occurrence of a cold period from 1890 to 1905 and between 1925 and 1935.

2.4.Climate variability in the Kerguelen area over the last decades

In Fig. 2b we presented the time variations of the logarithm of precipitation and of temperature. Variations are almost synchronous and the trends are almost similar until 1975. However, after 1975, the two variables show opposite trends as the temperature increases while precipitation decreases. HadSST2[29] data and AVHRR satellite data form the Group for High Resolution Sea Surface Temperature (GHRSST)[59], offering information until 2013, confirm that atmospheric warming was consistent with sea surface warming in recent decades (over 1982-2012) around Kerguelen archipelago (Supplementary Fig. 8).

The relationship between spatial distribution of HadSST2 data and the mean air temperature measured at Kerguelen Islands was also analyzed to assess whether the signal observed at Kerguelen was only local. We performed correlation maps between measured temperature (or precipitation) and the distributed SST information (Fig. 3). The analysis described hereafter was also performed with ERSSTv2 data, yielding similar results as with HadSST2, but figures were not reproduced here to avoid redundancy and improve readability. The analysis was performed with December-January-February-March (DJFM) means before and after 1975. As observed by (31), before 1975, a dipole-like correlation exists between air temperature at Kerguelen and SST over hundreds of kilometers with significant correlation

ranging between r = 0.4 and r = 0.8 (Fig. 3a). This dipole presents a south-west to north-east direction as the typical pattern of the positive phases of the Subtropical Indian Ocean Dipole[31,60]. Focusing on the 1979-1998 period, (31) suggested such positive phases are associated with an increase of precipitation rates over Southern Africa and in some place of the Southern Indian Ocean, in particular north from Kerguelen area, in close relationship with warm anomalies in the Agulhas current. Correlation map made for precipitation before 1975 in the Kerguelen area confirms that precipitation was largely driven by SST variability along the Agulhas and Antarctic Circumpolar oceanic currents systems (Fig. 3b). The variability of these currents controls the contribution of warm water input within the track of the low pressure systems, inducing higher or lower evaporation rates, which are related to depression intensity before they reach the Kerguelen archipelago, as suggested by the correlation existing between precipitation at Kerguelen and the latent heat flux from ERA40 before 1975 (Fig. 3c). This also is in agreement with a previous study[61], which already suspected that Agulhas current may have an important impact on the Southern mid-latitude Indian Ocean variability and may have intensified the recent warming there.

Here we additionally show that the relationship was different before and after 1975 (Fig. 3). The link with Agulhas current fully disappears after 1975 (Fig. 3e). We suspect this resulted from the positive phase of the Southern Annular Model +SAM, resulting in a progressive southward shift of the precipitation belt[15]. Indeed, after 1975, the Kerguelen climate was increasingly affected by the more frequent high atmospheric pressure systems that dramatically limited the potential intrusion of precipitation in the area. The correlation map between ERA40 precipitation from the pixel including Kerguelen and latent heat flux confirms that precipitation is no more related to the Agulhas and to the Circumpolar oceanic

currents (Fig. 3f). However, this relationship is now observed if we use ERA40 precipitation from a pixel located 350km south from Kerguelen (Supplementary Fig. 9b). Since this point was not located within the storm track before 1975 (Supplementary Fig. 9a), this suggests that the storm track shifted approximately 2.5° southward. Thus, in spite of occurrence of positive anomalies in the latter currents and in large scale SST values around Kerguelen, we observe a highly significant precipitation decrease.

As a conclusion, before 1975 we suspect the atmospheric inter-annual variability was mainly driven by the Subtropical Indian Ocean Dipole; leading to a significant relationship between precipitation at Kerguelen and the SSTs along the Agulhas and the Antarctic Circumpolar oceanic currents. However, after 1975, Kerguelen climate was more deeply affected by a new dipole-like pattern, centered over the Indian Ocean, because more frequent occurrence of the positive phase of the +SAM was associated to a southward shift of the storm track, which is now located south from Kerguelen.

2.5.Climate variability in the 30°S-60°S region

Beyond the intrinsic potential inaccuracy and biases of the modeling, reanalysis data are particularly influenced by new data assimilation, such as buoys and satellite information included after 1980. Reanalysis data may thus include several biases, which are not present in the original field observations. To get a more accurate picture of large scale land surface precipitation changes it is thus necessary to focus on observations rather than on models. Here, we analyzed the CRU TS 3.21 precipitation data[62] (Supplementary Figure 10a&b) to display precipitation trends in Patagonia (northern and Southern Patagonian Icefields, NPI

and SPI respectively), Darwin Cordillera, and New Zealand. The CRU precipitation is a 0.5° gridded observational dataset obtained from meteorological stations distributed worldwide[62].

A precipitation decrease is observed since 1950 in Patagonia[63] whereas in Darwin Cordillera and New Zealand the decrease was more likely restricted to the last two decades. This is in agreement with acceleration of glacier wastage in the latter regions during the last decade, and confirms that semi-hemispheric SAM-induced precipitation decrease affected these regions and likely had a significant impact on the glacier retreat in these regions.

Supplementary references

(34) Farr, T.G. *et al*. The Shuttle Radar Topography Mission. *Rev. Geophys*. **45**, RG2004, doi:10.1029/2005RG000183 (2007).

(35) Korona, J., Berthier, E., Bernard, M., Remy, F. & Thouvenot, E. SPIRIT. SPOT 5 stereoscopic survey of Polar Ice: Reference Images and Topographies during the fourth International Polar Year (2007-2009). *ISPRS J. Photogramm.* **64**, 204-212 (2009).

(36) Gardelle, J., Berthier, E., Arnaud, Y. & Kääb, A. Region-wide glacier mass balances over the Pamir-Karakoram-Himalaya during 1999–2011. *The Cryosphere* **7**, 1263–1286 (2013).

(37) Nuth, C. & Kääb, A. Co-registration and bias corrections of satellite elevation data sets for quantifying glacier thickness change. *The Cryosphere* **5**, 271–290 (2011).

(38) Berthier, E. *et al*. Remote sensing estimates of glacier mass balances in the Himachal Pradesh (Western Himalaya, India). *Remote Sens. Environ.* **108**, 327-338 (2007).

(39) Gardelle, J., Berthier, E. & Arnaud, Y. Impact of resolution and radar penetration on glacier elevation changes computed from multi-temporal DEMs. *Journal of Glaciology* **58**, 419–422 (2012).

(40) Huss, M. Density assumptions for converting geodetic glacier volume change to mass change. *Cryosphere* **7**, 877-887 (2013).

(41) Berthier, E., Scambos, T.A. & Shuman, C.A. Mass loss of Larsen B tributary glaciers (Antarctic Peninsula) unabated since 2002. *Geoph. Res. Lett*. **39**, (2012).

(42) Toutin, T. Three-dimensional topographic mapping with ASTER stereo data in rugged topography. IEEE T. Geosci. Remote **40**, 2241-2247 (2002).

(43) Braithwaite, R.J. Positive degree-day factors for ablation on the Greenland ice sheet studied by energy-balance modeling. *J. Glaciol*. **41**, 153-160 (1995).

(44) Hock, R. Temperature index melt modelling in mountain areas. *J. Hydrol*. **282**, 104-115 (2003).

(45) Azam, M. F., Wagnon, P., Vincent, C., Ramanathan, A., Linda, A., Singh, V. B., Reconstruction of the annual mass balance of Chhota Shigri glacier, Western Himalaya, India, since 1969. *Ann. Glaciol*. **55** (66), doi: 10.3189/2014AoG66A104 (2014).

(46) Favier, V., Agosta, C., Genthon, C., Arnaud, L., Trouvillez, A. & Gallée, H. Modeling the mass and surface heat budgets in a coastal blue ice area of Adelie Land, Antarctica, J. Geophys. Res., **116**, F03017, doi:10.1029/2010JF001939, (2011).

(47) Oke, T. R. Boundary Layer Climates, 2nd ed., 435 pp., Routledge, New York (1987).

(48) Harper, J.T. & Humphrey, N.F. High altitude Himalayan climate inferred from glacial ice flux. Geoph. Res. Lett. 30 (14), 1764, doi:10.1029/2003GL017329 (2003).

(49) Blard, P.-H., Lavé, J., Pik, R., Wagnon, P. & Bourlès, D. Persistence of full glacial conditions in the central Pacific until 15,000 years ago. *Nature* **449**, 591-594 (2007).

(50) Nye, J.F. The Flow of Glaciers and Ice-Sheets as a Problem in Plasticity. *Proc. R. Soc. Lon. Ser. A* **207** (1091), 554-572 (1951).

(51) Gallée, H. & Schayes, G. Development of a three-dimensional meso-γ primitive equation model: katabatic winds simulation in the area of Terra Nova Bay, Antarctica. *Mon. Weather. Rev*. **122**, 671-685 (1994).

(52) Gallée, H. & Duynkerke, P.G. Air-snow interactions and the surface energy and mass balance over the melting zone of west Greenland during the Greenland Ice Margin Experiment. *J. Geophys. Res*. **102** (D12), 13813–13824 (1997).

(53) Gallée, H., Guyomarc'h, G. & Brun, E. Impact of snowdrift on the Antarctic ice sheet surface mass balance: possible sensitivity to snow-surface properties. *Bound.-Lay. Meteorol*. **99**, 1-19 (2001).

(54) Simmons, A., Uppala, S., Dee, D. & Kobayashi, S. ERAInterim: new ECMWF reanalysis products from 1989 onwards. *ECMWF Newsl*. **110**, 25-35 (2006).

(55) Amante, C. & Eakins, B.W. ETOPO1 1 Arc-Minute Global Relief Model: Procedures, Data Sources and Analysis. *NOAA Technical Memorandum NESDIS NGDC-24*, 19 pp, March 2009.

(56) Uppala, S. *et al*. The ERA-40 re-analysis, *Q. J. Roy. Meteor. Soc*. **131**, 2961-3012 (2005).

(57) Kalnay, E. *et al*. The NCEP/NCAR 40-Year Reanalysis Project, *B. Am. Meteorol. Soc*. **77** (3), 437-471 (1996).

(58) Taylor, K.E., Stouffer, R.J. & Meehl, G.A. An Overview of CMIP5 and the Experiment Design. *Bull. Amer. Meteor. Soc*. **93**, 485-498 (2012).

(59) Reynolds, R.W. *et al.* Daily High-resolution Blended Analyses for sea surface temperature, *J. Climate* **20**, 5473-5496 (2007).

(60) Hermes, J.C. & Reason, C.J.C. Ocean model diagnosis of interannual co-evolving SST variability in the South Indian and Atlantic Oceans. *J. Climate* **18**, 2864-2882 (2005).

(61) Richard, Y. et al. Temperature changes in the mid- and high-latitudes of the Southern Hemisphere. *Int. J. Climatol.* **33**, 1948-1963 (2013).

(62) Harris, I. *et al*. Updated high-resolution grids of monthly climatic observations the CRU TS3.10 Dataset, *Int. J. Climatology* **34**, 623-642 (2014).

(63) Garreaud *et al.* Large-Scale Control on the Patagonian Climate, *J. Climate* **26***,* 215-230 (2013).

Supplementary Tables

Supplementary Table 1. List of equipment installed on the AWS. sensors with their specificity, installed on the glacier and on the rocky surface close to la Mortadelle Hut.

Quantity[i], location	Type of Sensor	Height[ii], cm	Accuracy (s) according to the manufacturer
Air temperature, °C, Glacier	Vaisala HMP 45, aspirated[iii]	200	±0.4°C
Relative humidity, %, Glacier	Vaisala HMP 45, aspirated[iii]	200	±3 %
Wind speed, m s^{-1}, Glacier	Young 05103	210	±0.3 m s^{-1}
Wind direction, deg, Glacier	Young 05103	210	±3 deg
Incident and reflected short-wave radiation, W m^{-2}, Glacier	Kipp&Zonen CMP3*, 0.305<□<2.8µm	85	±10 %[iv]
Incoming long-wave radiation, W m^{-2}, la Mortadelle Hut	Kipp&Zonen CG3*, 5<□<50 µm	85	±10 %[iv]
Surface elevation, m, Glacier	Campbell acoustic gauge, SR50A	160	±1 cm
Precipitation, mm (half-hourly), la Mortadelle Hut	Precis mecanique 3029-	85	±0.5mm

[i]Quantities are recorded as half-hourly means over 10-s time-intervals except for wind direction which is an instantaneous value measured every 30 minutes.
[ii]Heights are variable but known with reasonable accuracy in summer thanks to manual measurements made every day, and sensor height is corrected assuming acoustic gauge measurements made during the rest of the year.
[iii]To prevent measurement errors due to radiation, Vaisala thermohygrometers are adequately shielded.
[iv]Expected accuracy for daily sums

Supplementary Table 2. CMIP5 models and simulations used in this study. Outputs are from the historical (Hist), and forecasted RCP2.6 and RCP8.5 experiments used in this study.

Model	*Modelling group*	*Country*	*Hist*	*RCP2.6*	*RCP8.5*
ACCESS1-0	Commonwealth Scientific and Industrial Research Organisation, and Bureau of Meteorology	Australia	y	n	y
ACCESS1-3	Commonwealth Scientific and Industrial Research Organisation, and Bureau of Meteorology	Australia	y	n	y
bcc-csm1-1	Beijing Climate Center, China Meteorological Administration	China	y	y	y
bcc-csm1-1-m	Beijing Climate Center, China Meteorological Administration	China	y	y	y
BNU-ESM	College of Global Change and Earth System Science, Beijing Normal University	China	y	y	y
CanCM4	Canadian Centre for Climate Modelling and Analysis	Canada	y	n	n
CanESM2	Canadian Centre for Climate Modelling and Analysis	Canada	y	y	y
CCSM4	National Center for Atmospheric Research	United	y	y	y
CESM1-BGC	National Science Foundation, Department of Energy, National Center for Atmospheric Research	United States	y	n	y
CESM1-CAM5	National Science Foundation, Department of Energy, National Center for Atmospheric Research	United States	y	y	y
CESM1-CAM5-1-FV2	National Science Foundation, Department of Energy, National Center for Atmospheric Research	United States	y	n	n
CESM1- FASTCHEM	National Science Foundation, Department of Energy, National Center for Atmospheric Research	United States	y	n	n
CESM1-WACCM	National Science Foundation, Department of Energy, National Center for Atmospheric Research	United States	y	n	n
CMCC-CESM	Centro Euro-Mediterraneo per I Cambiamenti Climatici	Italy	y	n	y
CMCC-CM	Centro Euro-Mediterraneo per I Cambiamenti Climatici	Italy	y	n	y
CMCC-CMS	Centro Euro-Mediterraneo per I Cambiamenti Climatici	Italy	y	n	y
CNRM-CM5	Centre National de Recherches Meteorologiques, Centre Européen de Recherche et Formation Avancée en Calcul Scientifique	France	y	y	y
CSIRO-Mk3-6-0	Commonwealth Scientific and Industrial Research Organisation, and Queensland Climate Change Centre of Excellence	Australia	y	y	y
EC-EARTH	EC-EARTH consortium	Europe	y	n	y
FGOALS-g2	Institute of Atmospheric Physics, Chinese Academy of Sciences, and Tsinghua University	China	y	y	y
FGOALS-s2	Institute of Atmospheric Physics, Chinese Academy of Sciences	China	y	n	n
FIO-ESM	The First Institute of Oceanography, SOA	China	y	y	y
GFDL-CM2.1	National Oceanic and Atmospheric Administration Geophysical Fluid Dynamics Laboratory	United States	y	n	n
GFDL-CM3	National Oceanic and Atmospheric Administration Geophysical Fluid Dynamics Laboratory	United States	y	y	y
GFDL-ESM2G	National Oceanic and Atmospheric Administration Geophysical Fluid Dynamics Laboratory	United States	y	y	y
GFDL-ESM2M	National Oceanic and Atmospheric Administration Geophysical Fluid Dynamics Laboratory	United States	y	y	y
GISS-E2-H	National Aeronautics and Space Administration Goddard Institute for Space Studies	United States	y	y	y
GISS-E2-H-CC	National Aeronautics and Space Administration Goddard Institute for Space Studies	United States	y	n	n
GISS-E2-R	National Aeronautics and Space Administration Goddard Institute for Space Studies	United States	y	y	y
GISS-E2-R-CC	National Aeronautics and Space Administration Goddard Institute for Space Studies	United States	y	n	n
HadCM3	Met Office Hadley Centre	UK	y	n	n
HadGEM2-AO	National Institute of Meteorological Research/Korea Meteorological Administration	Korea	y	y	y
HadGEM2-CC	Met Office Hadley Centre	UK	y	n	y
HadGEM2-ES	Met Office Hadley Centre, National Institute for Space Research (Brazil)	UK, Brazil	y	y	y
INM-CM4	Institute for Numerical Mathematics	Russia	y	n	y
IPSL-CM5A-LR	Institut Pierre-Simon Laplace	France	y	y	y
IPSL-CM5A- MR	Institut Pierre-Simon Laplace	France	y	y	y
IPSL-CM5B-LR	Institut Pierre-Simon Laplace	France	y	n	y
MIROC-ESM	Japan Agency for Marine-Earth Science and Technology, Atmosphere and Ocean Research Institute (The University of Tokyo), and National Institute for Environmental Studies	Japan	y	y	y
MIROC-ESM- CHEM	Japan Agency for Marine-Earth Science and Technology, Atmosphere and Ocean Research Institute (The University of Tokyo), and National Institute for Environmental Studies	Japan	y	y	y
MIROC4h	Atmosphere and Ocean Research Institute (The University of Tokyo), National Institute for Environmental Studies, and Japan Agency for Marine-Earth Science and Technology	Japan	y	n	n
MIROC5	Atmosphere and Ocean Research Institute (The University of Tokyo), National Institute for Environmental Studies, and Japan Agency for Marine-Earth Science and Technology	Japan	y	y	y
MPI-ESM-LR	Max Planck Institute for Meteorology	Germany	y	y	y
MPI-ESM-MR	Max Planck Institute for Meteorology	Germany	y	y	y
MPI-ESM-P	Max Planck Institute for Meteorology	Germany	y	n	n
MRI-CGCM3	Meteorological Research Institute	Japan	y	y	y
MRI-ESM1	Meteorological Research Institute	Japan	y	n	n
NorESM1-M	Norwegian Climate Centre	Norway	y	y	y
NorESMl-ME	Norwegian Climate Centre	Norway	y	y	y

Supplementary Figure captions

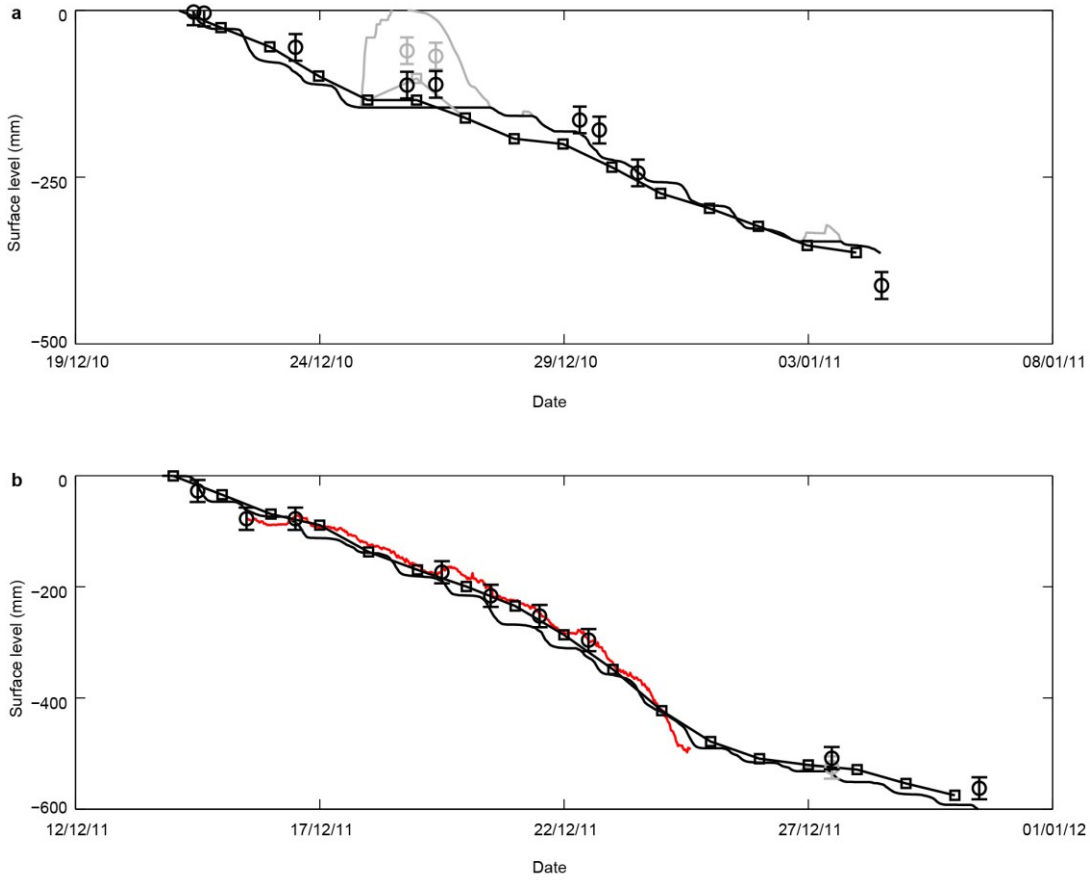

Supplementary Figure 1. Punctual validation of the PDD model. Computed and measured surface height at the AWS during summer field campaigns in December 2010 (a) and December 2011 (b). Thick black and gray lines are the computed ice and snow surface height (respectively) computed with the full SEB approach. Thin black and gray lines and squares are the computed ice and snow surface height (respectively) computed with PDD approach. Black and gray circles are the mean measured ice and snow surface height (respectively) at 4 stakes around the AWS. Red curve is the 30-minute surface elevation measured with an acoustic gauge at the AWS in 2011. Error bars are ±20 mm, which represent the mean standard deviation between stake measurements.

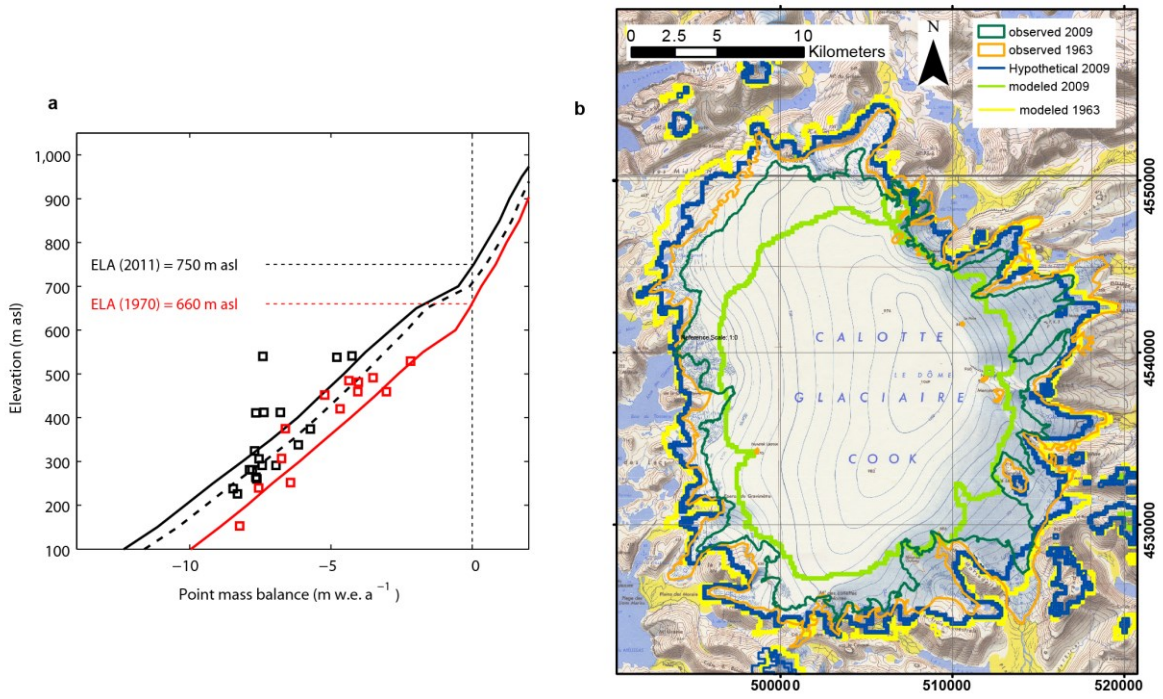

Supplementary Figure 2. **Distributed validation of the PDD model.** Mass balance validation. a) Measured (squares) and modeled (lines) surface mass balance of Ampere glacier during the 1970-1974 period (red) and during the year 2011 (black). Continuous lines are the surface mass balance computed over March 15 to March 14 period. This period corresponds to the occurrence of stake measurements in the 1970s. Discontinuous line is the modelled surface mass balance from January 1, 2011 to December 31, 2011, to compare with the stake measurements from December 31, 2011. b) Modeled glacier extent in 1963 (yellow) and 2009 (green) compared to the observations (in 1963 (orange) and 2009 (dark green)). The hypothetical glacier extent shown in blue corresponds to the glacier extent in 2009 computed with the measured temperature time series, but assuming that precipitation chronology from the 1950s was repeated during the following decades. Background is the 1:200,000 map published by Institut Géographique National (IGN). Coordinate system is UTM42S.

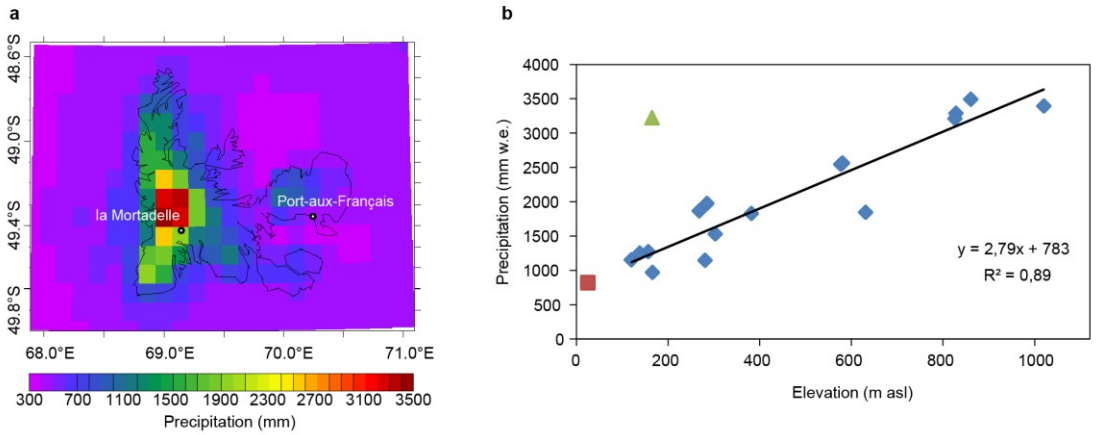

Supplementary Figure 3. **Modeled distribution of precipitation on CIC with MAR model.** a) Map of 2011 modeled cumulative precipitation at Kerguelen with the MAR model. b) Precipitation amounts from MAR model as a function of elevation (blue points). Red square and green triangle are precipitation at PAF and at la Mortadelle respectively.

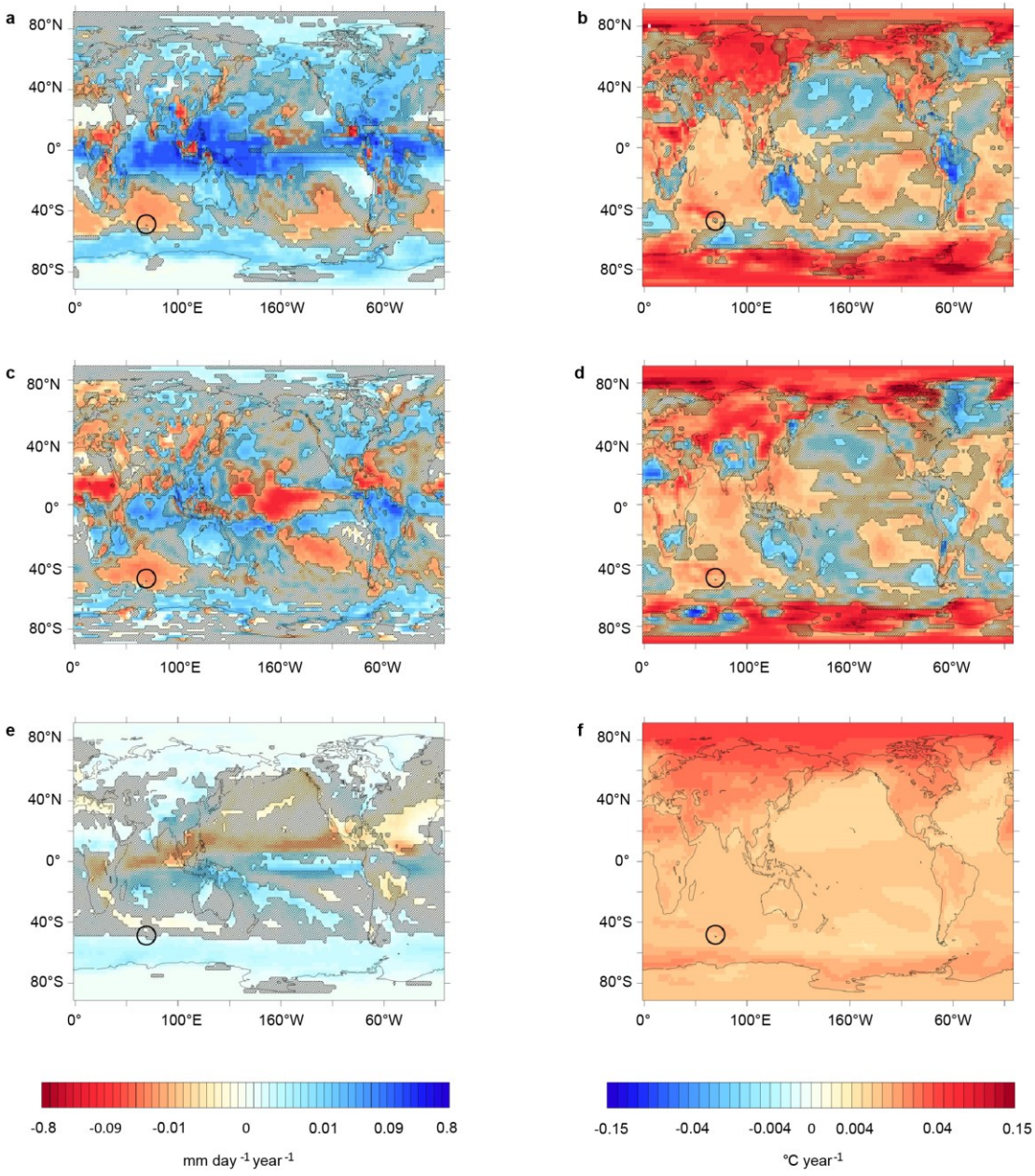

Supplementary Figure 4. Recent large scale precipitation and temperature trends. (left) Precipitation and (right) 850hPa temperature trends for 1957-2002 in ERA-40 (a&b), NCEP1 (c&d) and CMIP5 (e&f) multi-model mean (MMM). Shading indicates areas where the trend is not significant at the 95% confidence interval (Spearman test). Kerguelen's location is indicated by the black circle.

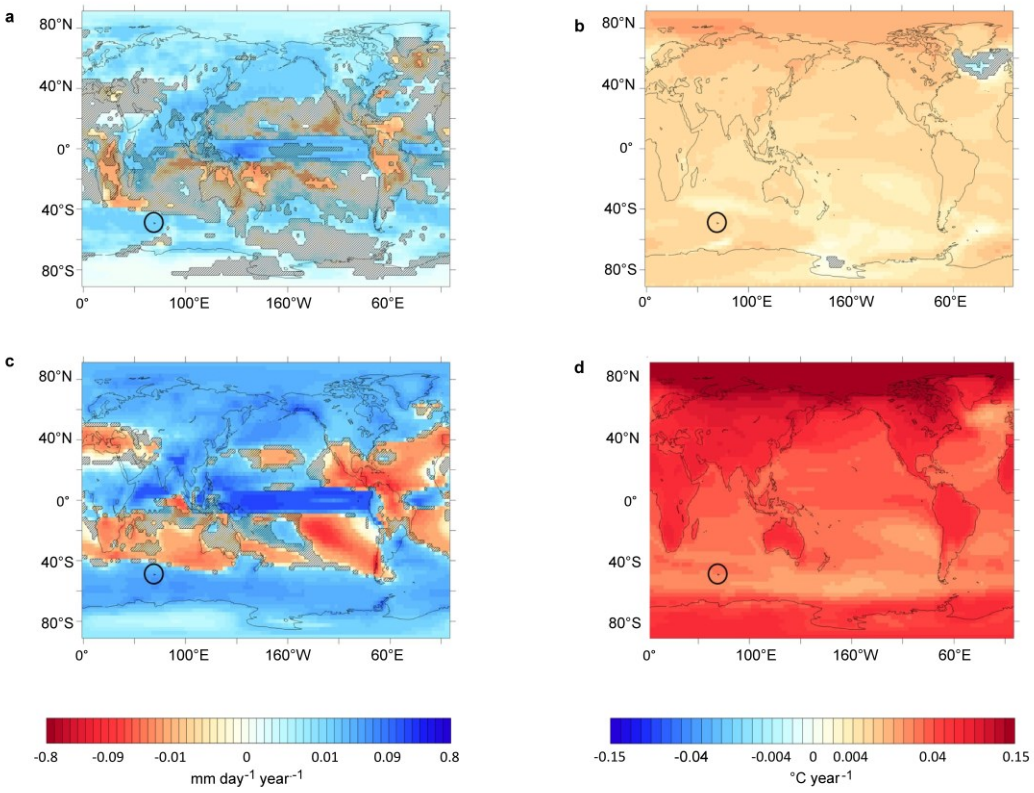

Supplementary Figure 5. Future forecasted large scale precipitation and temperature trends. (left) Precipitation and (right) surface temperature projected trends for 2006-2100 in the CMIP5 multi-model mean (MMM) for RCP 2.6 scenario (a&b) and RCP 8.5 scenario (c&d). Shading indicates areas where the trend is not significant at the 95% confidence interval (Spearman test). Kerguelen's location is indicated by the black circle. Please note the one-order of magnitude difference between current (Supplementary Fig. 5) and projected (this Figure) precipitation trends scale.

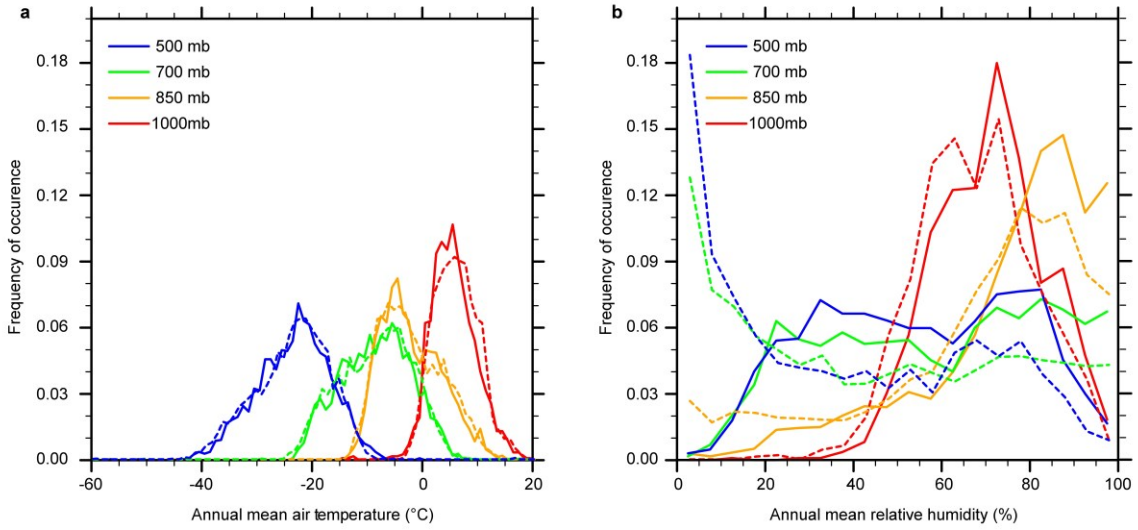

Supplementary Figure 6. Temperature and humidity histograms from Kerguelen Islands radiosonde (WMO ID 61998). Temperature (a) and relative humidity (b) histograms are presented for 1973-1982 (solid line), and 2002-2011 (dash). Data are represented at 500mb (blue), 700mb (green), 850mb (orange) and 1000mb (red).

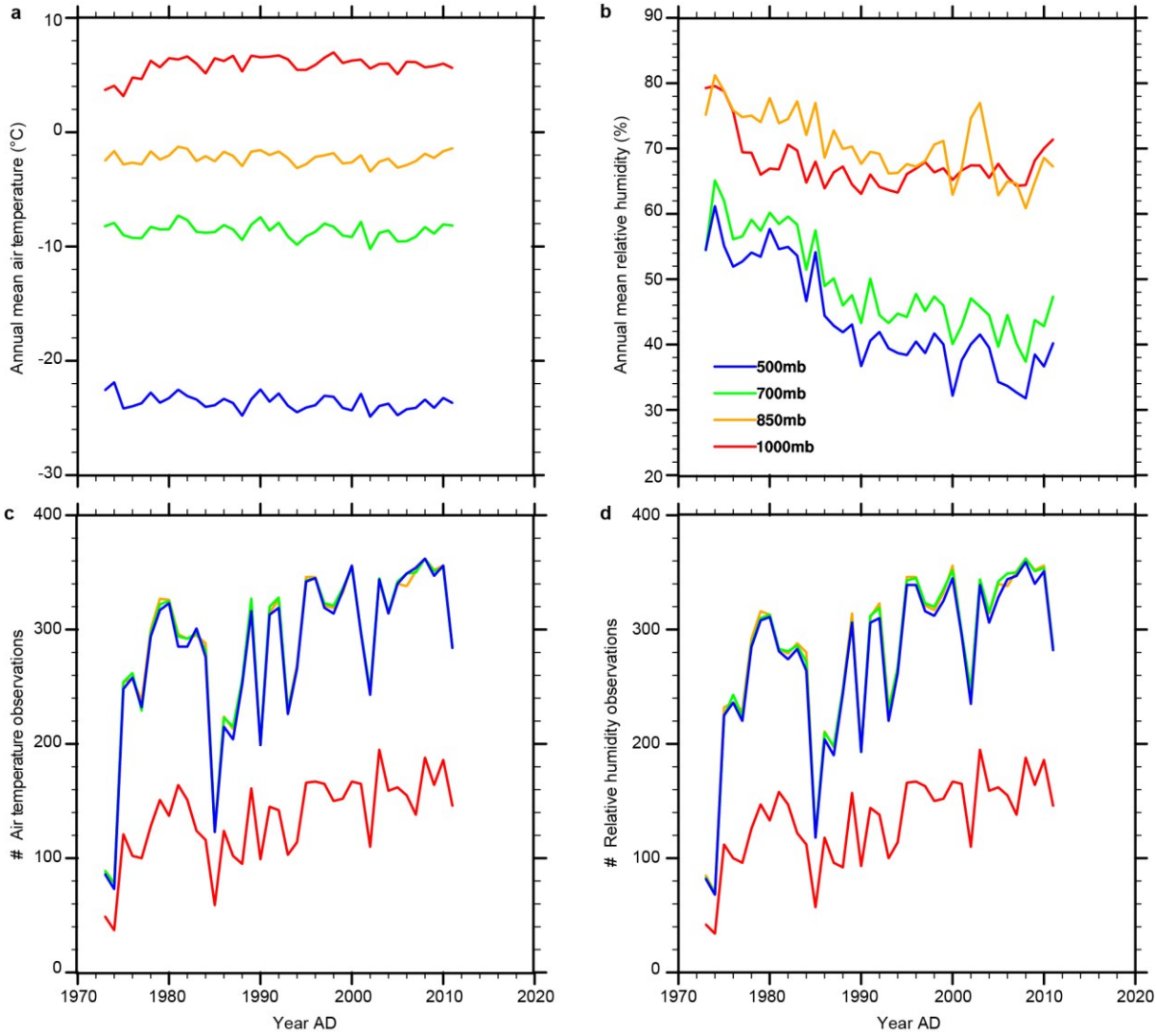

Supplementary Figure 7. Temperature and humidity Timeseries from Kerguelen Islands radiosonde (WMO ID 61998). Timeseries are for a) annual mean air temperature at 500mb (blue), 700mb (green), 850mb (orange) and 1000mb (red), b) annual mean relative humidity at 500mb, 700mb, 850mb and 1000mb, c) number of air temperature observations per year at each elevation, d) number of relative humidity observations at each elevation.

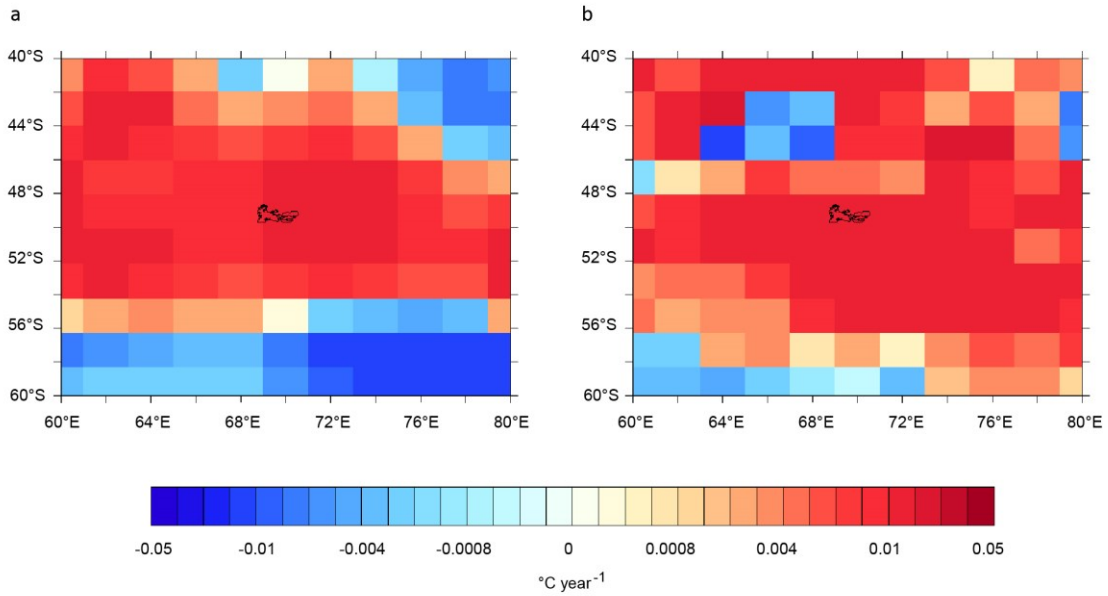

Supplementary Figure 8. Sea Surface Temperature linear trends over 1982-2012. a) HadSST2 data, b) AVHRR data. Each dataset has been re-gridded on the same 2°x2° regular grid.

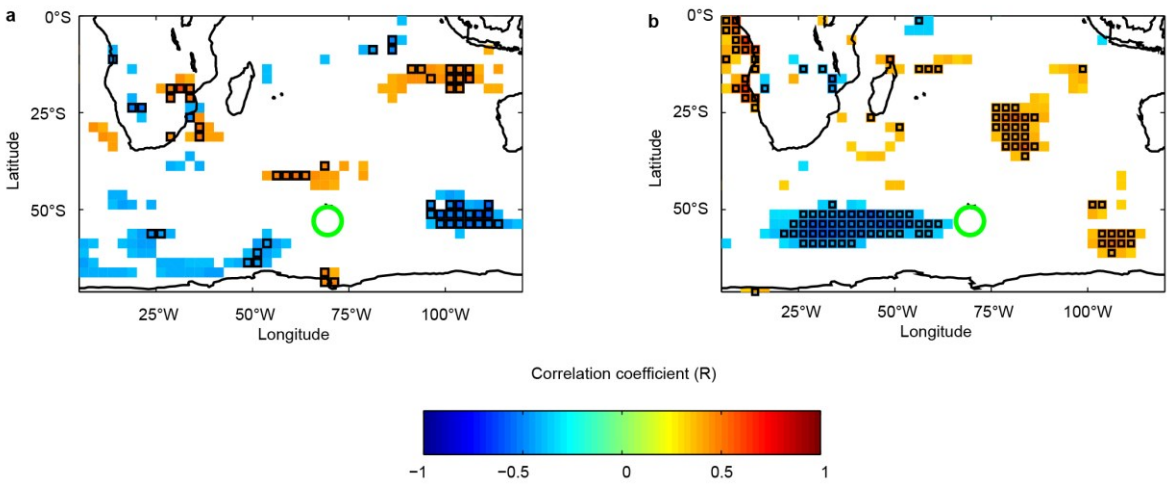

Supplementary Figure 9. Present location of the storm track. Correlation coefficient (*R*) between December to March (DJFM) ERA40 precipitation from the pixel located 350 km south from Kerguelen and ERA40 surface latent heat flux during DJFM. Surface latent heat flux is negative when evaporation occurs. Correlation maps are made before 1975 (a) and after 1975 (b). All time-series are detrended. Pixels where correlation is significant at 95% are in squared areas, at 90% are in colored areas. Pixels where correlation significance is lower than 90% are not shown. The point used for correlations is located inside the green circle.

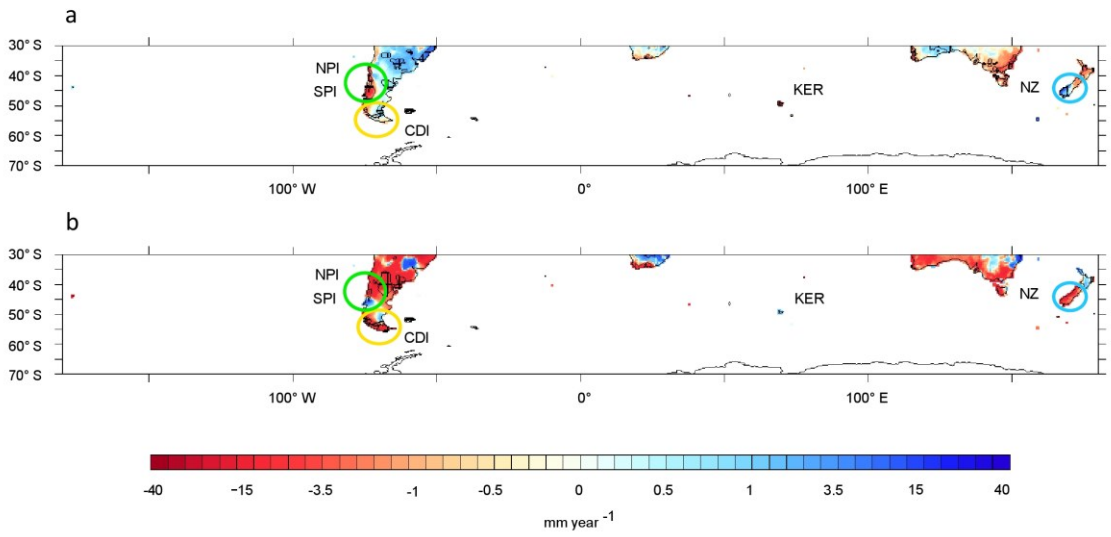

Supplementary Figure 10. 30°S-60°S maps of precipitation trends since 1950 and since 1992. The precipitation trends are computed from the CRU land precipitation product over a) 1950-2012 and b) 1992-2012. Circles are centered on NPI and SPI (green), CDI (orange) and New Zealand southern island (NZ, blue). KER means Kerguelen Islands.

Annexe G

Evaluation des modèles CMIP5

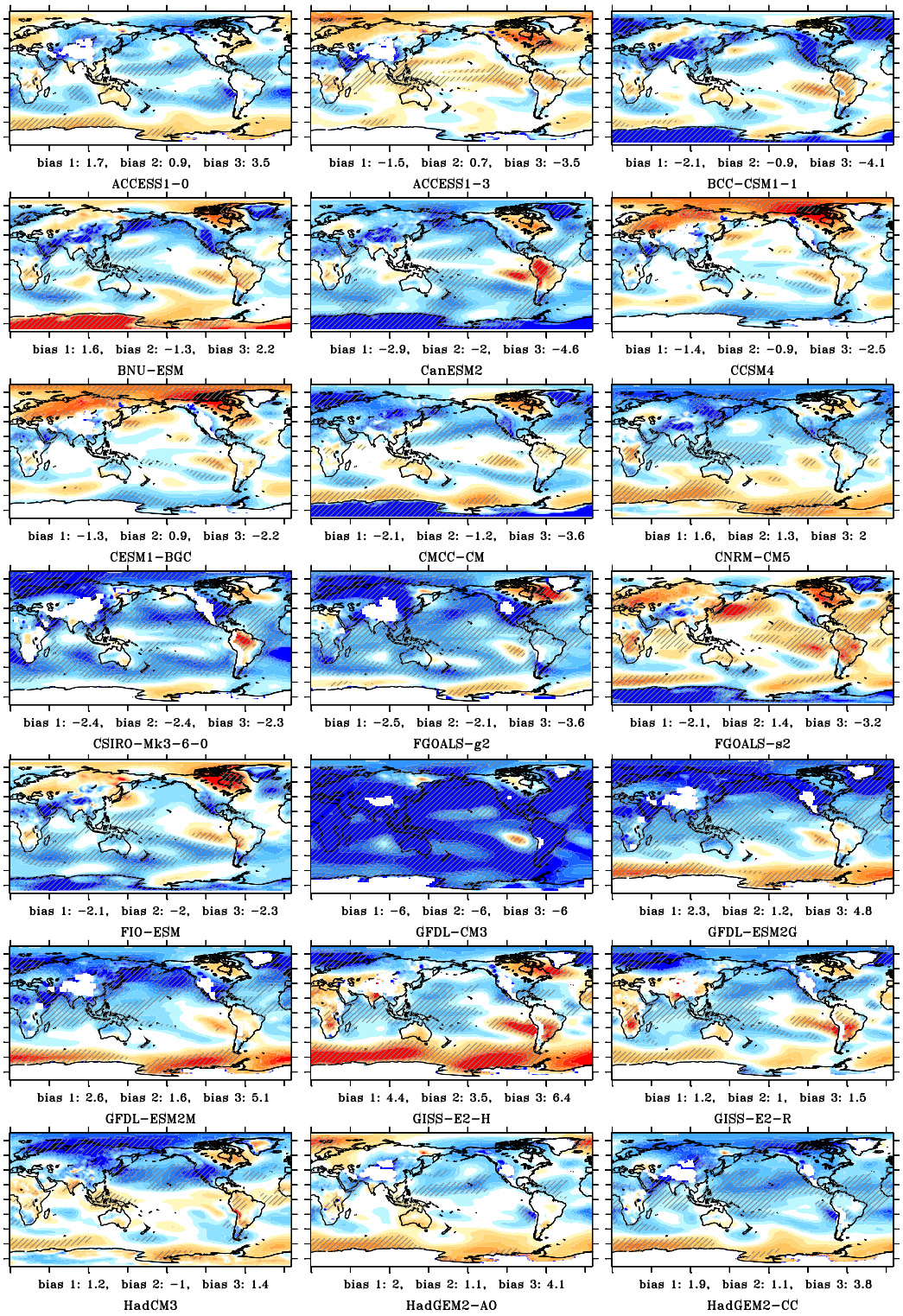

FIGURE G.1 – Anomalie moyenne ($\overline{T}_{CMIP5} - \overline{T}_{ERA-Int}$) de température estivale (DJF) à 850hPa par rapport à ERA-Interim sur la période 1980-1999, tracée sur la grille d'ERA-Interim. Les biais indiqués sont calculés de la manière suivante : $(\overline{T}_{CMIP5} - \overline{T}_{ERA-Int})/\sigma(T_{ERA-Int})$, où σ représente l'écart-type. Le biais 1 est calculé sur l'ensemble de la zone 40° S - 90° S, le biais 2 sur la zone 40° S - 60° S et le biais 3 sur la zone 60° S - 90° S. Les zones hâchurées représentent les endroits où l'anomalie de température est plus de deux fois supérieure à l'écart-type de la température dans le modèle CMIP5.

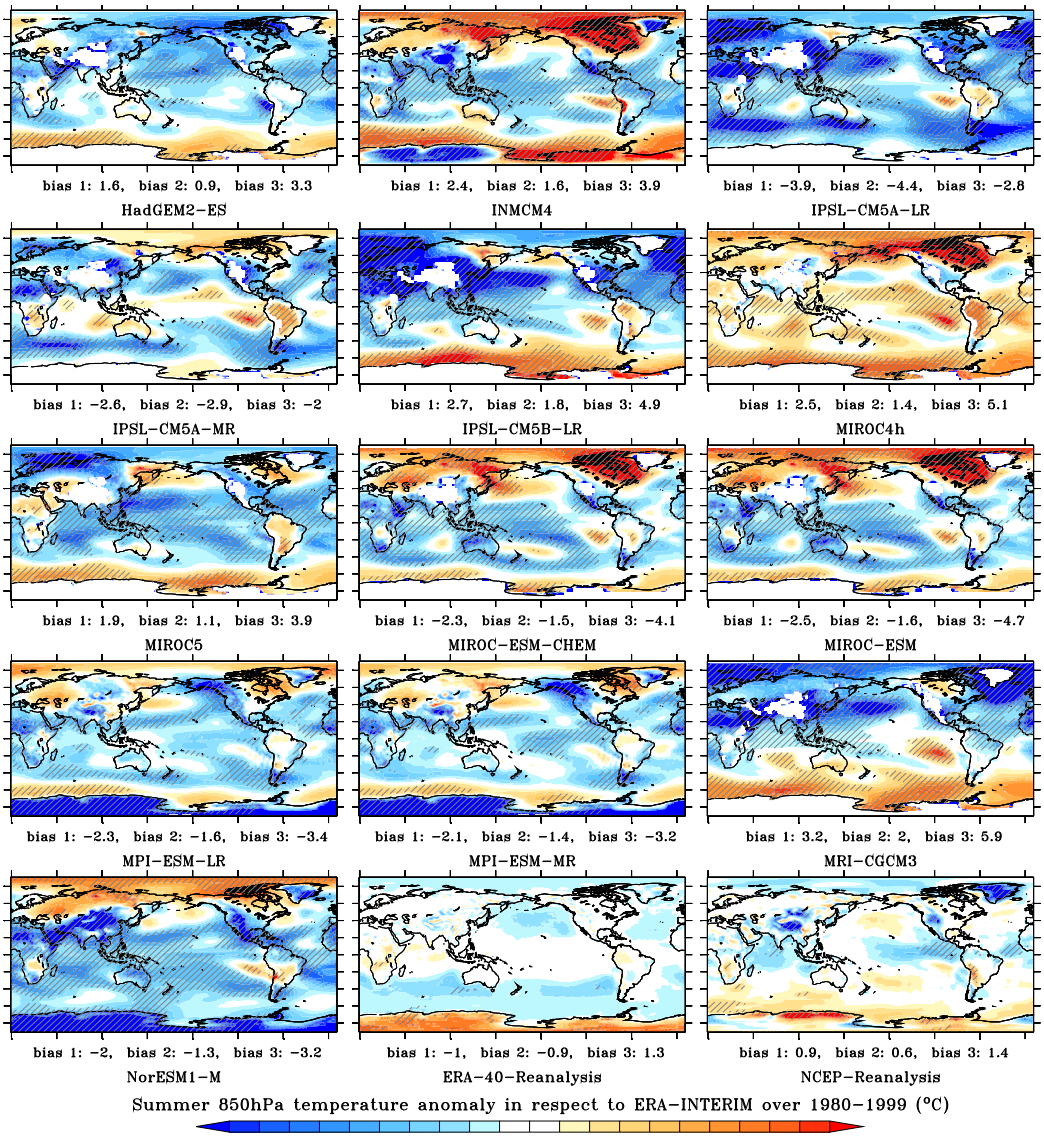

FIGURE G.1 – Anomalie moyenne ($\overline{T}_{CMIP5} - \overline{T}_{ERA-Int}$) de température estivale (DJF) à 850hPa par rapport à ERA-Interim sur la période 1980-1999, tracée sur la grille d'ERA-Interim. Les biais indiqués sont calculés de la manière suivante : $(\overline{T}_{CMIP5} - \overline{T}_{ERA-Int})/\sigma(T_{ERA-Int})$, où σ représente l'écart-type. Le biais 1 est calculé sur l'ensemble de la zone 40° S - 90° S, le biais 2 sur la zone 40° S - 60° S et le biais 3 sur la zone 60° S - 90° S. Les zones hâchurées représentent les endroits où l'anomalie de température est plus de deux fois supérieure à l'écart-type de la température dans le modèle CMIP5.

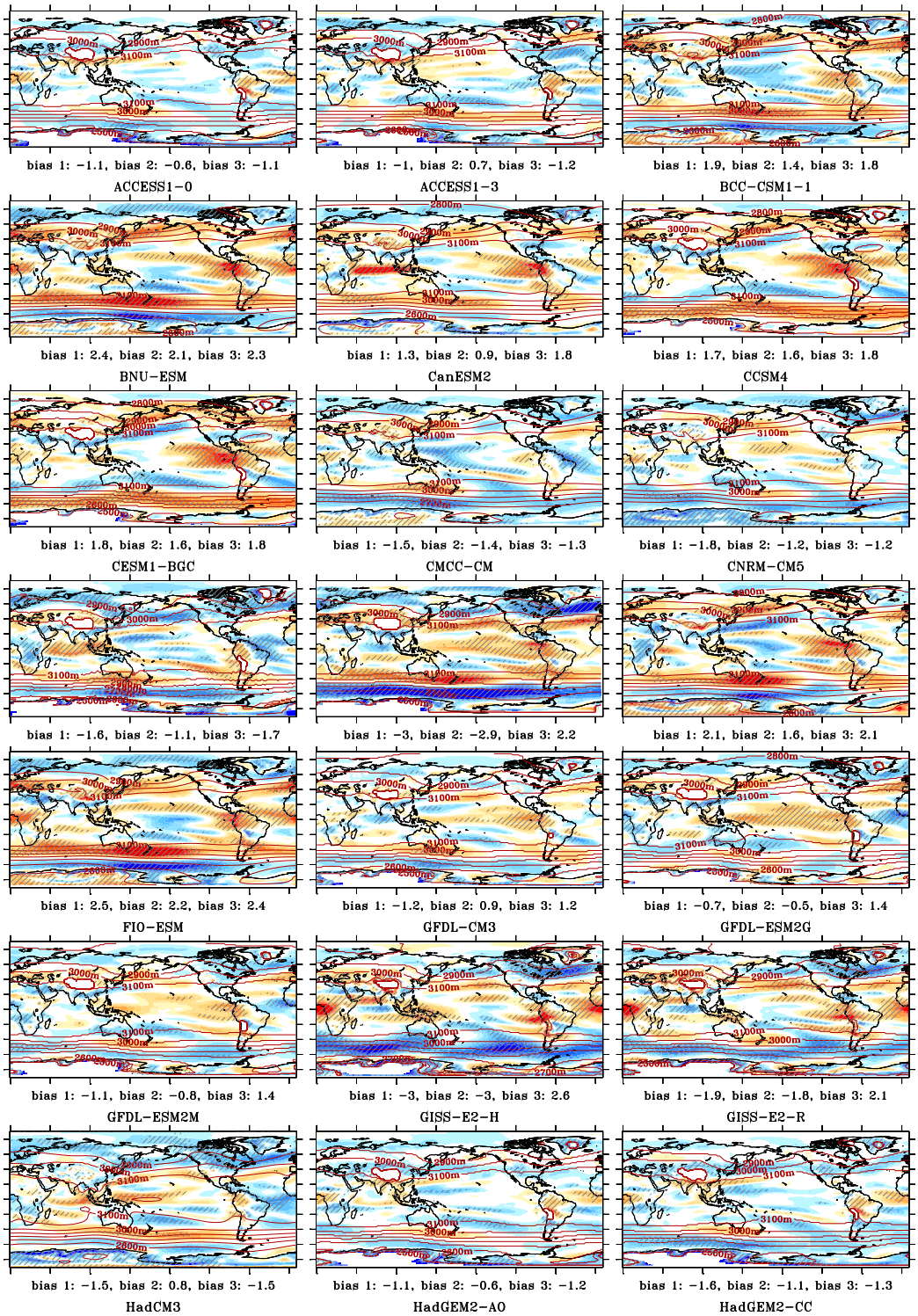

FIGURE G.2 – Anomalie moyenne ($\overline{WS}_{CMIP5} - \overline{WS}_{ERA-Int}$) de vitesse du vent annuelle à 700hPa par rapport à ERA-Interim sur la période 1980-1999, tracée sur la grille d'ERA-Interim. Les biais indiqués sont calculés de la manière suivante : $(\overline{WS}_{CMIP5} - \overline{WS}_{ERA-Int})/\sigma(WS_{ERA-Int})$, où σ représente l'écart-type. Le biais 1 est calculé sur l'ensemble de la zone 40° S - 90° S, le biais 2 sur la zone 40° S - 60° S et le biais 3 sur la zone 60° S - 90° S. Les contours correspondent à la hauteur du géopotentiel 700 hPa. Les zones hâchurées représentent les endroits où l'anomalie de vitesse du vent est plus de deux fois supérieure à l'écart-type de la vitesse du vent dans le modèle CMIP5.

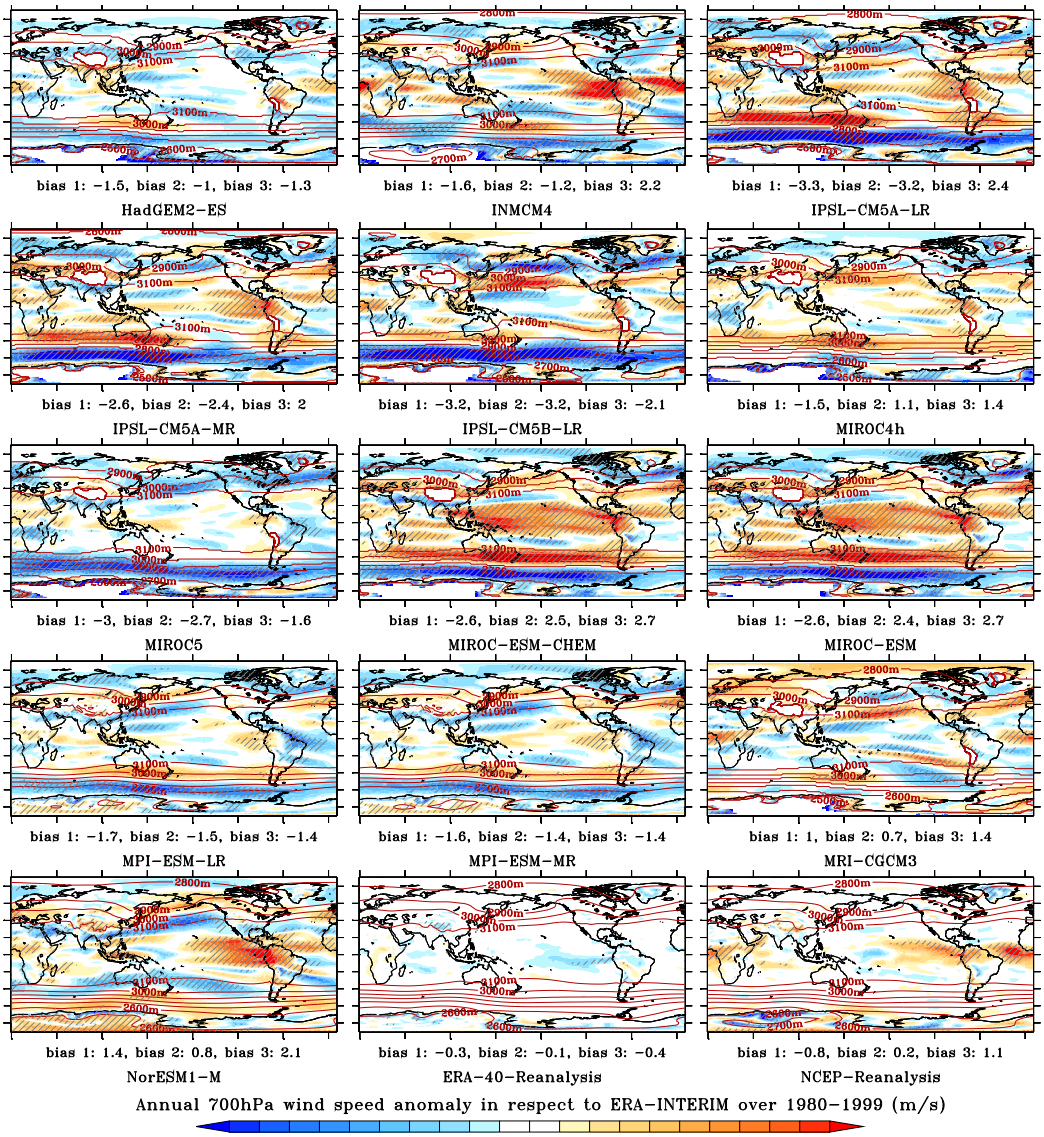

FIGURE G.2 – Anomalie moyenne ($\overline{WS}_{CMIP5} - \overline{WS}_{ERA-Int}$) de vitesse du vent annuelle à 700hPa par rapport à ERA-Interim sur la période 1980-1999, tracée sur la grille d'ERA-Interim. Les biais indiqués sont calculés de la manière suivante : $(\overline{WS}_{CMIP5} - \overline{WS}_{ERA-Int})/\sigma(WS_{ERA-Int})$, où σ représente l'écart-type. Le biais 1 est calculé sur l'ensemble de la zone 40° S - 90° S, le biais 2 sur la zone 40° S - 60° S et le biais 3 sur la zone 60° S - 90° S. Les contours correspondent à la hauteur du géopotentiel 700 hPa. Les zones hâchurées représentent les endroits où l'anomalie de vitesse du vent est plus de deux fois supérieure à l'écart-type de la vitesse du vent dans le modèle CMIP5.

Annexe H

Analyse des sorties du MAR forcé par les réanalyses

TABLE H.1 – Evaluation de la température journalière simulée par le MAR par rapport aux observations aux 6 stations météorologiques : nombre d'observations (n), valeur moyenne mesurée à la station sur la période étudiée (Moy), RMSE (Root-Mean-Square Error[1]), coefficient de corrélation (R, les valeurs en gras sont significatives à 95% selon un test de Student ($p < 0{,}05$)) et biais moyen annuel, en été (DJFMAM) et en hiver (JJASON).

Forçage	Station	n	Moy (°C)	RMSE (°C)	R	biais annuel (°C)	biais été (°C)	biais hiver (°C)
ERA-Int	Armor	297	5,07	1,48	**0,90**	-2,30	-2,37	-2,25
	Cotter	298	4,31	1,14	**0,91**	-0,92	-0,85	-0,99
	P. Christmas	168	5,15	0,89	**0,93**	-1,48	-1,34	-1,72
	S. Noirs	336	3,35	0,76	**0,93**	0,56	0,32	0,76
	Mortadelle	731	3,89	1,10	**0,94**	-1,70	-1,65	-1,74
	PAF	11470	4,84	1,04	**0,95**	-0,81	-0,79	-0,84
NCEP1	Armor	297		3,33	**0,47**	1,86	2,05	1,73
	Cotter	298		2,30	**0,57**	3,33	3,60	3,04
	P. Christmas	168		2,21	**0,66**	3,13	3,86	1,9
	S. Noirs	336		1,56	**0,50**	5,40	5,56	5,26
	Mortadelle	731		3,31	**0,39**	2,91	3,01	2,80
	PAF	22611		3,15	**0,52**	4,40	4,68	4,12

[1]La RMSE est calculée de la manière suivante : $RMSE = \sqrt{\frac{\sum_{i=1}^{n}(X_{obs,i} - X_{MAR,i})^2}{n}}$

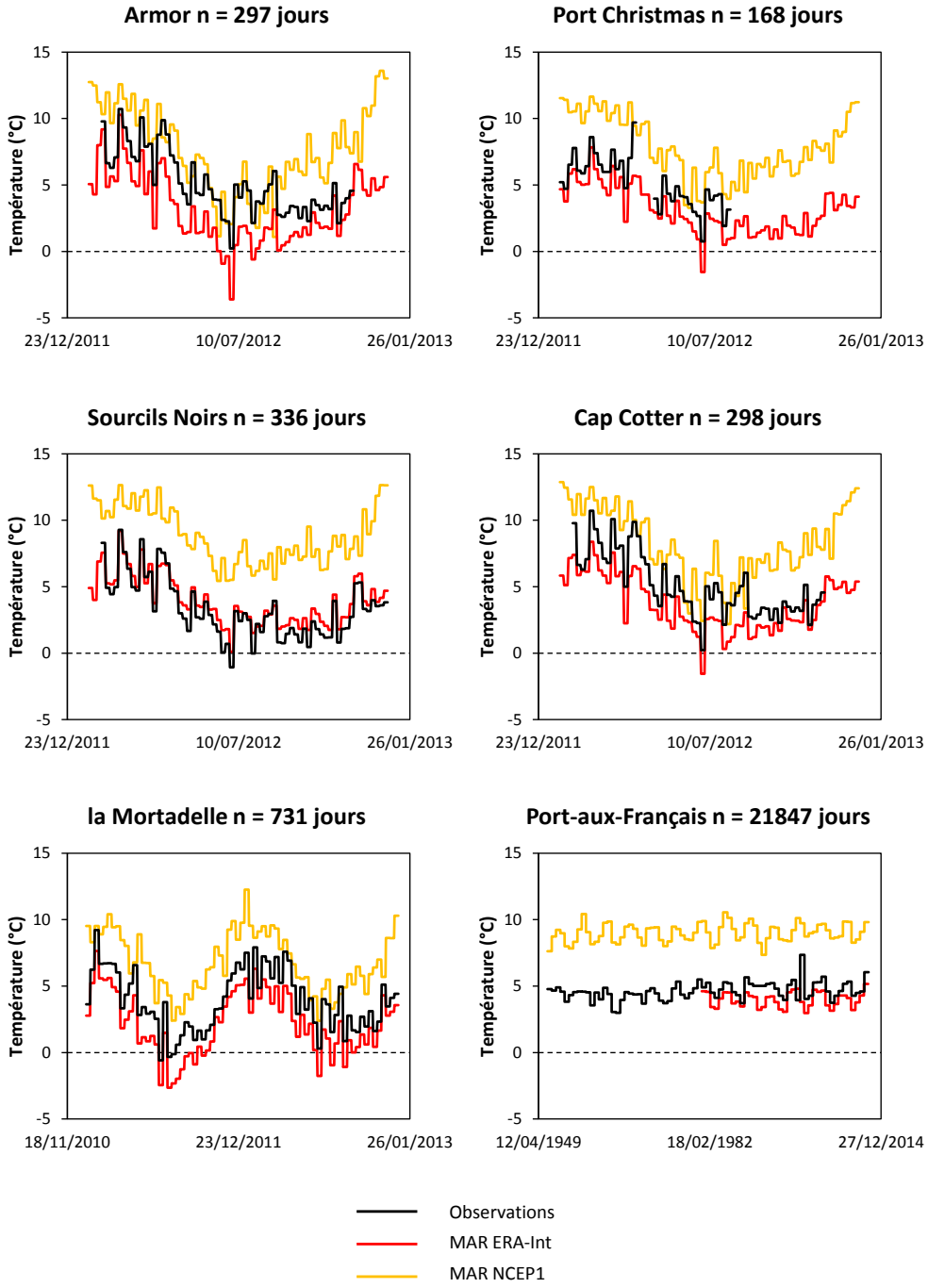

FIGURE H.1 – Séries temporelles de la température journalière de l'air en surface simulée par le MAR forcé par ERA-Interim et par NCEP1 en chaque point de grille contenant une station météorologique et de la température journalière de l'air en surface mesurée à cette station. Par souci de lisibilité, les mesures du réseau Kcrumble sont moyennées sur 5 jours, celles de la Mortadelle sur 10 jours et celles de PAF sur 300 jours.

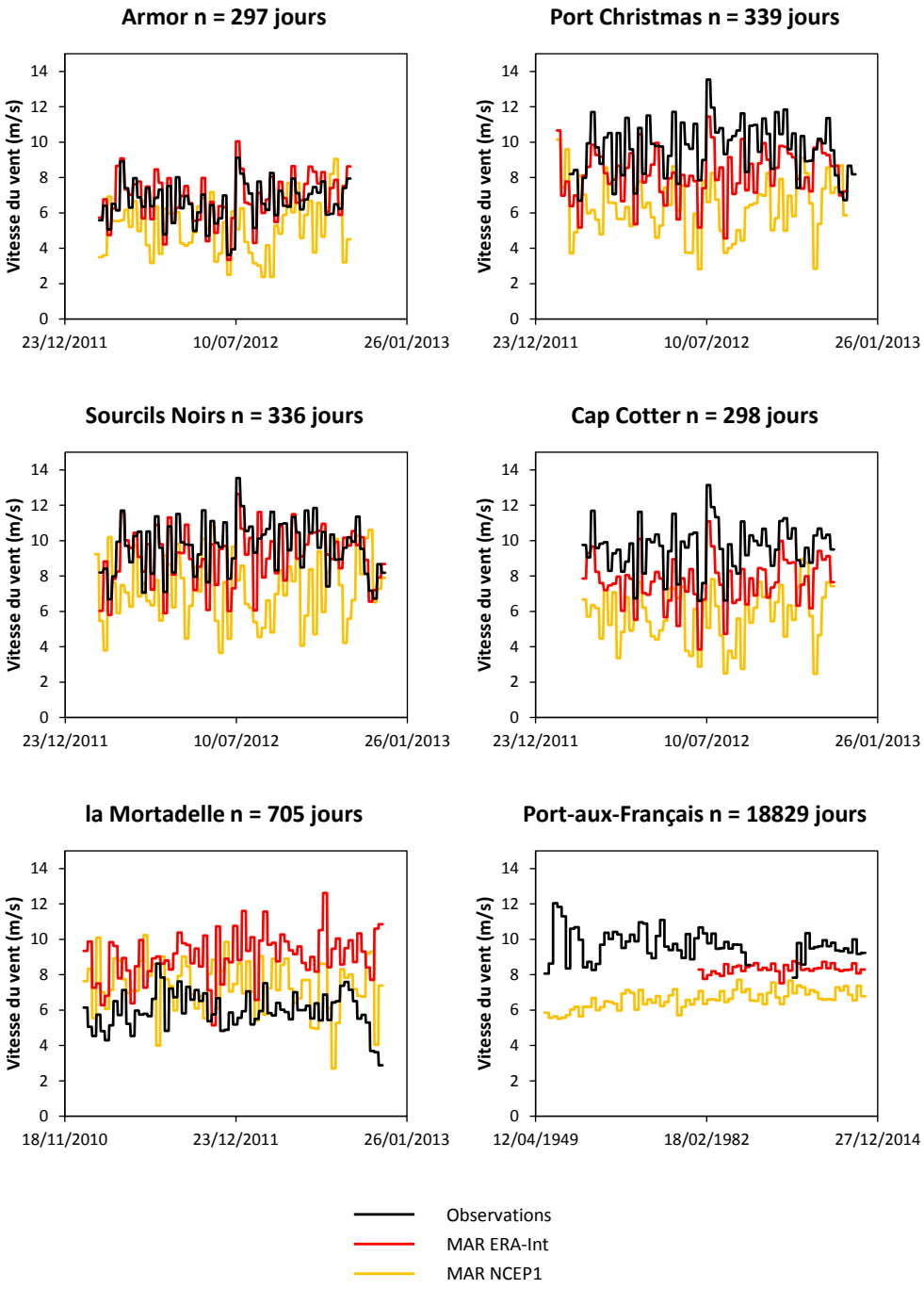

FIGURE H.2 – Séries temporelles de la vitesse du vent journalière en surface simulée par le MAR forcé par ERA-Interim et par NCEP1 en chaque point de grille contenant une station météorologique et de la vitesse du vent journalière en surface mesurée à cette station. Par souci de lisibilité, les mesures du réseau Kcrumble sont moyennées sur 5 jours, celles de la Mortadelle sur 10 jours et celles de PAF sur 300 jours.

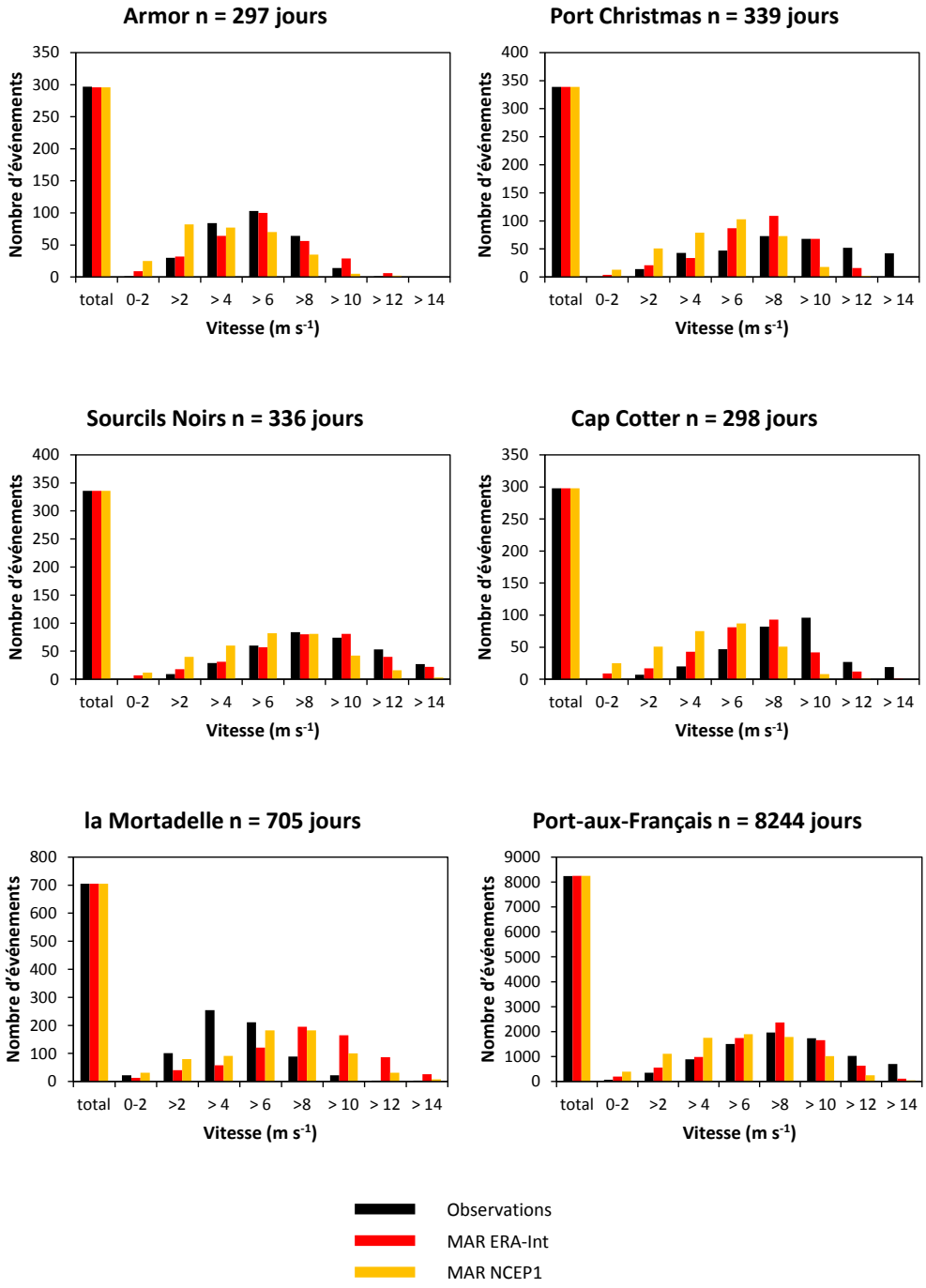

FIGURE H.3 – Comparaison entre le nombre d'événements de vent par classes de vitesse simulés par le MAR forcé par ERA-Interim et NCEP1 et mesurés aux 6 stations météorologiques.

TABLE H.2 – Evaluation de la vitesse du vent journalière simulée par le MAR par rapport aux observations aux 6 stations météorologiques : nombre d'observations (n), valeur moyenne mesurée à la station sur la période étudiée (Moy), RMSE (Root-Mean-Square Error), coefficient de corrélation (R, les valeurs en gras sont significatives à 95% selon un test de Student ($p < 0,05$)) et biais moyen annuel, en été (DJFMAM) et en hiver (JJASON).

Forçage	Station	n	Moy ($m\ s^{-1}$)	RMSE ($m\ s^{-1}$)	R	biais annuel ($m\ s^{-1}$)	biais été ($m\ s^{-1}$)	biais hiver ($m\ s^{-1}$)
ERA-Int	Armor	297	6,64	1,84	**0,70**	0,24	0,20	0,26
	Cotter	298	9,65	1,70	**0,78**	-1,93	-1,78	-2,06
	P. Christmas	339	9,77	2,30	**0,74**	-1,57	-1,44	-1,68
	S. Noirs	336	9,67	2,22	**0,74**	-0,58	-0,31	-0,81
	Mortadelle	705	5,94	3,29	**0,26**	3,11	3,26	2,96
	PAF	8244	9,64	2,29	**0,74**	-1,34	-1,17	-1,52
NCEP1	Armor	297		3,24	-0,01	-1,41	-1,32	-1,48
	Cotter	298		3,65	-0,01	-3,87	-3,51	-4,02
	P. Christmas	338		4,44	**-0,12**	-3,41	-2,88	-3,86
	S. Noirs	336		4,18	0,01	-2,38	-1,58	-3,05
	Mortadelle	705		3,79	-0,03	1,48	1,95	1,05
	PAF	18829		4,63	**-0,02**	-3.18	-2.60	-3.78

TABLE H.3 – Evaluation de l'humidité relative journalière simulée par le MAR par rapport aux observations aux 6 stations météorologiques : nombre d'observations (n), valeur moyenne mesurée à la station sur la période étudiée (Moy), RMSE (Root-Mean-Square Error), coefficient de corrélation (R, les valeurs en gras sont significatives à 95% selon un test de Student ($p < 0,05$)) et biais moyen annuel, en été (DJFMAM) et en hiver (JJASON).

Forçage	Station	n	Moy (%)	RMSE (%)	R	biais annuel (%)	biais été (%)	biais hiver (%)
ERA-Int	Armor	297	74,8	8,0	**0,52**	3,6	2,8	4,1
	Cotter	298	87,5	6,5	**0,70**	-5,4	-5,5	-5,2
	P. Christmas	168	86,2	6,6	**0,63**	2,5	0,9	5,2
	S. Noirs	336	81,8	6,7	**0,54**	-0,5	-0,7	-0,3
	Mortadelle	731	72,9	7,6	**0,39**	5,4	3,7	7,1
	PAF	4941	75,3	7,4	**0,64**	0,3	-1,6	2,3
NCEP1	Armor	297		24,7	0,04	7,6	6,9	8,1
	Cotter	298		12,7	0,03	-3,4	-4,1	-2,7
	P. Christmas	168		11,8	-0,04	2,8	0,8	6,2
	S. Noirs	336		11,2	-0,03	0,9	0,1	1,6
	Mortadelle	731		11,9	0,04	2,5	0,3	4,8
	PAF	4941		12,1	**0,22**	2,3	0,3	4,3

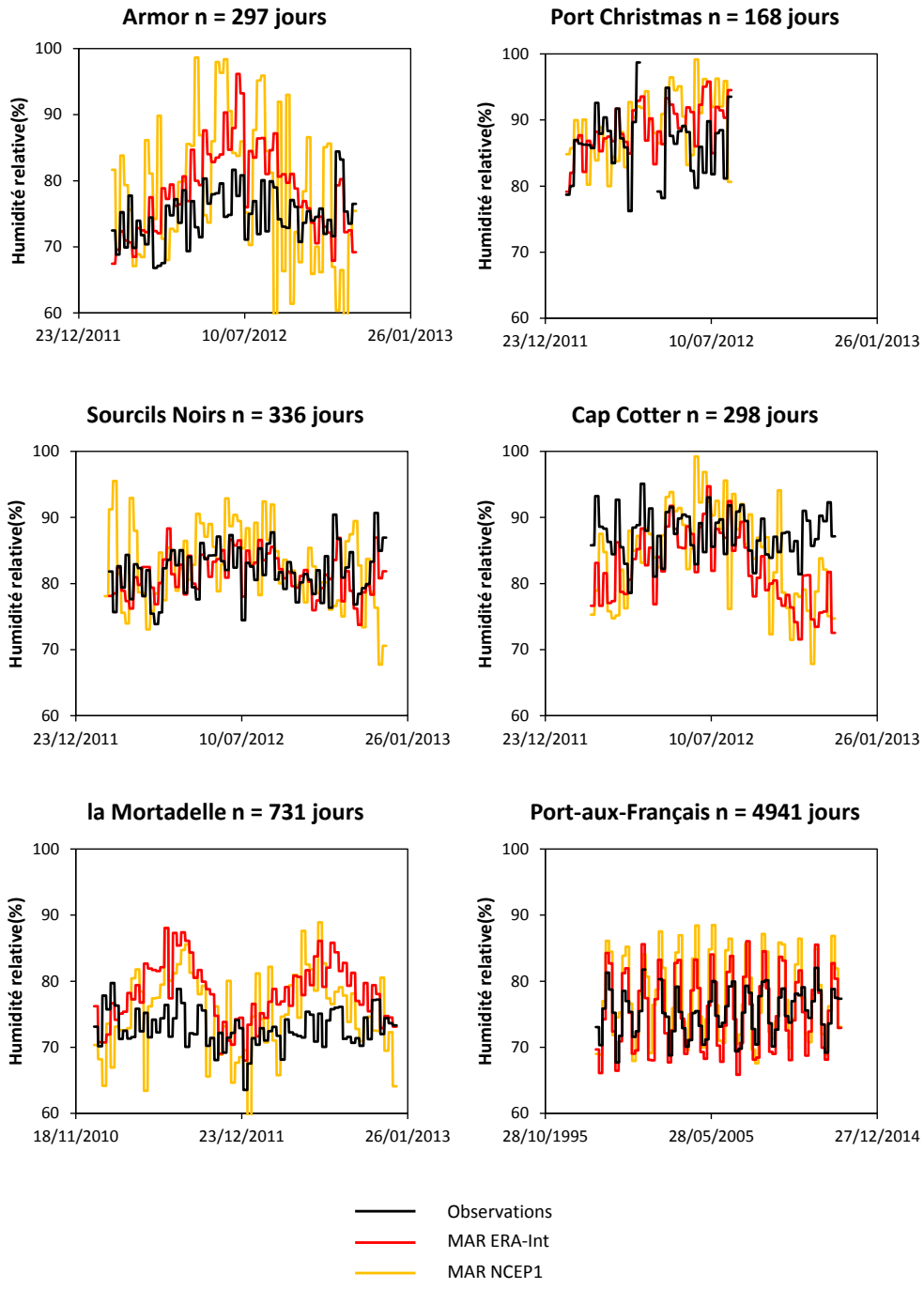

FIGURE H.4 – Séries temporelles de l'humidité relative en surface simulée par le MAR forcé par ERA-Interim et par NCEP1 en chaque point de grille contenant une station météorologique et de l'humidité relative en surface mesurée à cette station. Par souci de lisibilité, les mesures du réseau Kcrumble sont moyennées sur 5 jours, celles de la Mortadelle sur 10 jours et celles de PAF sur 70 jours.

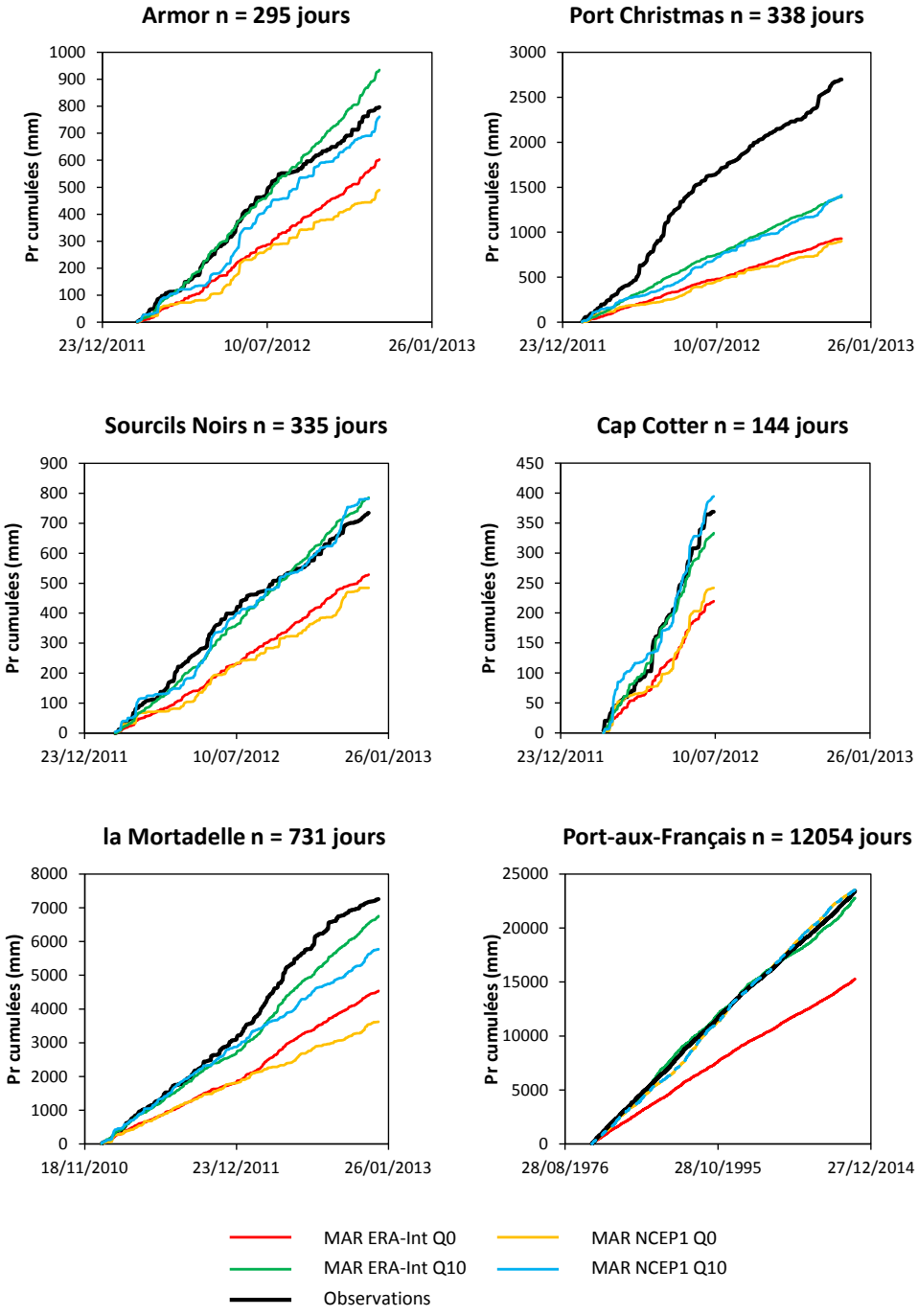

FIGURE H.5 – Séries temporelles des cumuls de précipitations (liquides et solides) journalières simulées par le MAR forcé par ERA-Interim et NCEP sans changement de l'humidité relative (Q0) et avec augmentation de 10% de l'humidité relative (Q10) en chaque point de grille contenant une station météorologique et des précipitations journalières mesurées à cette station. Notez qu'à Port-aux-Français, les courbes du MAr forcé par NCEP1 Q0 et NCEP1 Q10 sont confondues.

TABLE H.4 – Evaluation des précipitations journalières simulées par le MAR par rapport aux observations aux 6 stations météorologiques : nombre d'observations (n), valeur moyenne mesurée à la station sur la période étudiée (Moy), RMSE (Root-Mean-Square Error[1]), coefficient de corrélation (R, les valeurs en gras sont significatives à 95% selon un test de Student ($p < 0{,}05$)) et biais moyen annuel, en été (DJFMAM) et en hiver (JJASON).

Forçage	Station	n	Moy (mm j^{-1})	RMSE (mm j^{-1})	R	biais annuel (mm j^{-1})	biais été (mm j^{-1})	biais hiver (mm j^{-1})
ERA-Int Q0	Armor	295	2,7	3,8	**0,52**	-0,7	-1,1	-0,4
	Cotter	144	2,6	3,6	**0,57**	-1,0	-1,0	-1,3
	P. Christmas	8,0	338	10,5	**0,41**	-5,2	-7,1	-3,6
	S. Noirs	335	2,2	3,3	**0,51**	-0,6	-0,8	-0,4
	Mortadelle	731	10,0	14,9	**0,72**	-3,7	-4,5	-3,0
	PAF	12054	1,9	4,0	**0,52**	-0,6	-0,6	-0,6
NCEP1 Q0	Armor	295		5,7	-0,02	-1,0	-1,4	-0,8
	Cotter	144		5,5	0,01	-0,9	-0,9	-0,8
	P. Christmas	338		12,2	-0,01	-5,3	-7,4	-3,5
	S. Noirs	335		4,7	0,01	-0,7	-1,0	-0,6
	Mortadelle	731		20,9	0,02	-5,0	-6,2	-3,8
	PAF	22641		6,6	0,01	0,0	0,2	-0,1
ERA-Int Q10	Armor	295		3,9	**0,55**	0,5	0,1	0,7
	Cotter	144		3,7	**0,54**	-0,3	-0,2	-0,6
	P. Christmas	338		10,5	**0,41**	-3,9	-5,6	-2,4
	S. Noirs	335		3,3	**0,51**	0,2	-0,1	0,3
	Mortadelle	731		13,6	**0,74**	-0,7	-1,3	-0,1
	PAF	12054		4,0	**0,55**	0,1	0,0	0,1
NCEP1 Q10	Armor	295		6,4	-0,02	-0,1	-0,6	0,2
	Cotter	144		6,3	0,03	0,2	0,2	0,5
	P. Christmas	338		12,7	-0,02	-3,8	-6,0	-2,0
	S. Noirs	335		5,5	0,01	0,1	-0,1	0,4
	Mortadelle	731		21,9	0,04	-2,0	-3,2	-0,9
	PAF	22641		6,6	0,00	0,0	0,2	-0,2

TABLE H.5 – Pourcentage d'événements de précipitation 1) observés et simulés, 2) observés mais non simulés, 3) non observés mais simulés, et 4) ni observés ni simulés à chaque station météorologique et pour le MAR forcé par ERA-Interim et NCEP1 avec (Q10) et sans (Q0) augmentation de l'humidité. Les sommes 1+4 (accord entre simulations et observations) et 2+3 (désaccord entre simulations et observations) sont également renseignées.

Forçage	Station	1 (%)	2 (%)	3 (%)	4 (%)	1+4 (%)	2+3 (%)
ERA-Int Q0	Armor	63	6	19	12	75	25
	Cotter	57	7	17	19	76	24
	P. Christmas	81	10	6	3	84	16
	S. Noirs	68	4	21	7	75	25
	Mortadelle	63	5	22	10	73	27
	PAF	45	8	27	20	65	35
NCEP1 Q0	Armor	46	23	20	11	57	43
	Cotter	47	17	24	12	59	41
	P. Christmas	67	24	7	2	69	31
	S. Noirs	42	31	17	10	52	48
	Mortadelle	47	20	24	9	56	44
	PAF	39	18	29	14	53	47
ERA-Int Q10	Armor	64	5	21	10	74	26
	Cotter	60	4	24	12	72	28
	P. Christmas	85	6	7	2	87	13
	S. Noirs	70	3	21	6	76	24
	Mortadelle	65	2	25	8	73	27
	PAF	45	8	27	20	65	35
NCEP1 Q10	Armor	52	17	23	8	60	40
	Cotter	52	12	27	9	61	39
	P. Christmas	78	12	9	1	79	21
	S. Noirs	55	18	21	6	61	39
	Mortadelle	54	13	27	6	60	40
	PAF	39	18	29	14	53	47

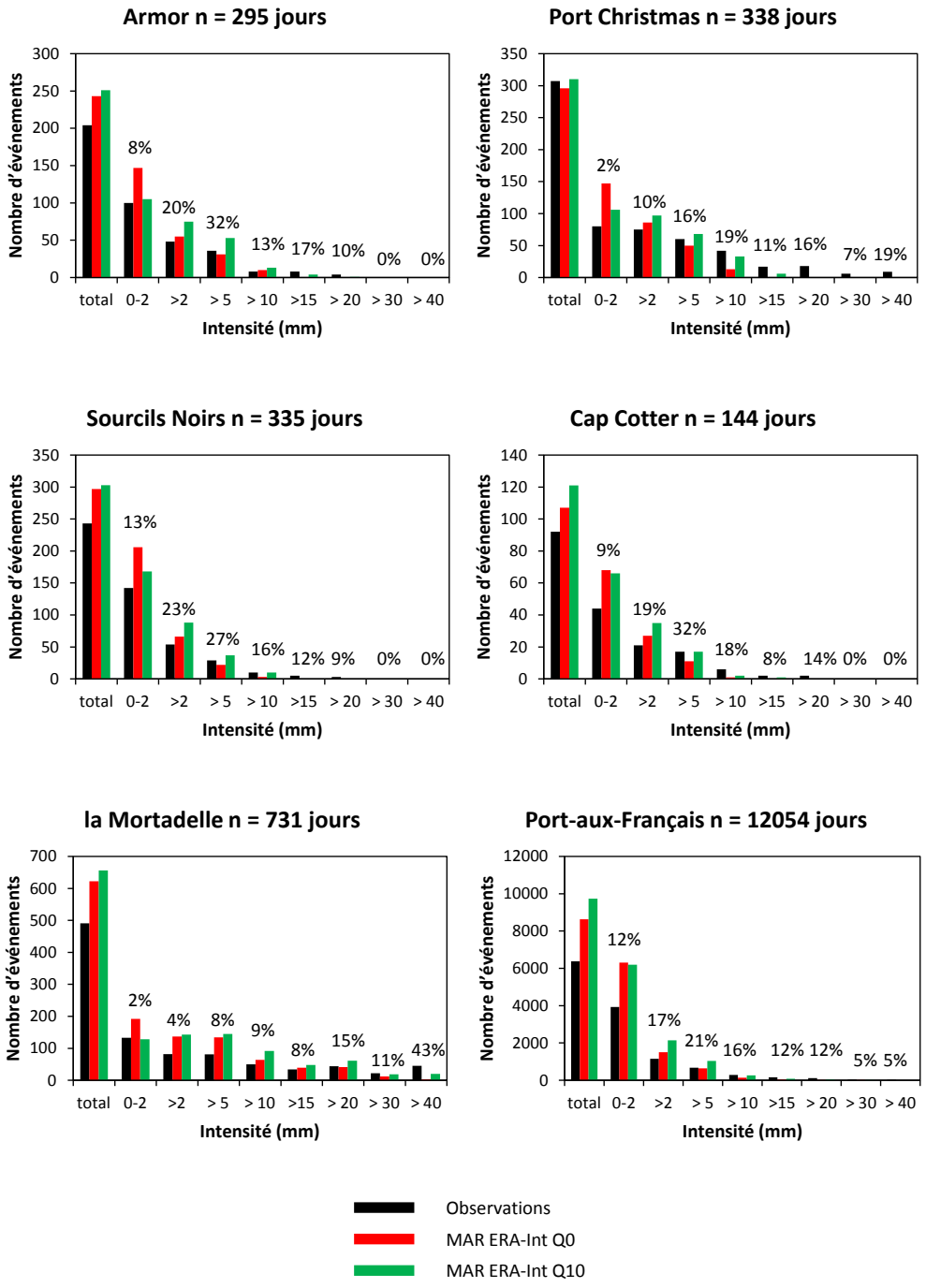

FIGURE H.6 – Comparaison entre le nombre d'événements de précipitations par classes d'intensité simulés par le MAR forcé par ERA-Interim avec (Q10) et sans (Q0) augmentation de l'humidité relative et mesurés aux 6 stations météorologiques. Les pourcentages indiqués au-dessus des histogrammes représentent la part de chaque classe d'intensité par rapport au cumul total de précipitations observées. Les résultats sont similaires pour la simulation forcée par NCEP1.

Références

Abram, N., Mulvaney, R., Vimeux, F., Phipps, S., Turner, J., and England, M. : Evolution of the Southern Annular Mode during the past millennium, Nature Climate Change, 4, 564–569, 2014.

Adler, R., Huffman, G., Chang, A., Ferraro, R., Xie, P.-P., Janowiak, J., Rudolf, B., Schneider, U., Curtis, S., Bolvin, D., Gruber, A., Susskind, J., Arkin, P., and Nelkin, E. : The version-2 global precipitation climatology project (GPCP) monthly precipitation analysis (1979-present), Journal of Hydrometeorology, 4, 1147–1167, 2003.

Agosta, C. : Évolution du bilan de masse de surface Antarctique par régionalisation physique et conséquences sur les variations du niveau des mers, Ph.D. thesis, Université Joseph Fourier, Grenoble, 2012.

Agosta, C., Favier, V., Krinner, G., Gallée, H., Fettweis, X., and Genthon, C. : High resolution modelling of the Antarctic surface mass balance, application for the twentieth, twenty first and twenty second centuries, Climate Dynamics, 41, 3247–3260, 2013.

Amante, C. and Eakins, B. : ETOPO1 1 arc-minute global relief model : procedures, data sources and analysis, NOAA Technical Memorandum NESDIS NGDC-24, 2009.

Anderson, B., Mackintosh, A., Stumm, D., George, L., Kerr, T., Winter-Billington, A., and Fitzsimons, S. : Climate sensitivity of a high-precipitation glacier in New Zealand, Journal of Glaciology, 56, 114–128, 2010.

Arnaud, F., Révillon, S., Poulenard, J., Boone, D., and Heirman, K. : First reconstruction of last millennium flooding activity on Kerguelen archipelago (50° S, sub-Antarctic Indian Ocean) from Lake Armor sediment : implications for southern hemisphere cyclonic circulation changes, Geophysical Research Abstracts, 11, 10 436, 2009.

Aubert De La Rue, E. : Remarques sur la disparition des glaciers de la Péninsule Courbet (Archipel de Kerguelen), TAAF Revue trimestrielle, pp. 3–19, 1967.

Bechtold, P., Bazile, E., Guichard, F., Mascart, P., and Richard, E. : A mass-flux convection scheme for regional and global models, Quarterly Journal of the Royal Meteorological Society, 127, 869–886, 2001.

Behera, S. and Yamagata, T. : Subtropical SST dipole events in the southern Indian Ocean, Geophysical Research Letters, 28, 327–330, 2001.

Bellair, P. : Un exemple de glaciation aberrante : les Îles Kerguelen, Com. Nati. Franc. Rech. Antarc., 11, 1–27, 1965.

Belleflamme, A., Fettweis, X., Lang, C., and Erpicum, M. : Current and future atmospheric circulation at 500 hPa over Greenland simulated by the CMIP3 and CMIP5 global models, Climate dynamics, 41, 2061–2080, 2013.

Bentley, M., Cofaigh, C., Anderson, J., Conway, H., Davies, B., Graham, A., Hillenbrand, C., Hodgson, D., Jamieson, S., Larter, R., Mackintosh, A., Smith, J., Verleyen, E., Ackert, R., Bart, P., Berg, S., Brunstein, D., Canals, M., Colhoun, E., Crosta, X., Dickens, W., Domack, E., Dowdeswell, J., Dunbar, R., Ehrmann, W., Evans, J., Favier, V., Fink, D., Fogwill, C., Glasser, N., Gohl, K., Golledge, N., Goodwin, I., Gore, D., Greenwood, S., Hall, B., Hall, K., Hedding, D., Hein, A., Hocking, E., Jakobsson, M., Johnson, J., Jomelli, V., Jones, R., Klages, J., Kristoffersen, Y., Kuhn, G., Leventer, A., Licht, K., Lilly, K., Lindow, J., Livingstone, S., Mass, G., McGlone, M., McKay, R., Melles, M., Miura, H., Mulvaney, R., Nel, W., Nitsche, F., O'Brien, P., Post, A., Roberts, S., Saunders, K., Selkirk, P., Simms, A., Spiegel, C., Stolldorf, T., Sugden, D., van der Putten, N., van Ommen, T., Verfaillie, D., Vyverman, W., Wagner, B., White, D., Witus, A., and Zwartz, D. : A community-based geological reconstruction of Antarctic Ice Sheet deglaciation since the Last Glacial Maximum, Quaternary Science Reviews, 100, 1–9, 2014.

Berthier, E., Arnaud, Y., Kumar, R., Ahmad, S., Wagnon, P., and Chevallier, P. : Remote sensing estimates of glacier mass balances in the Himachal Pradesh (Western Himalaya, India), Remote Sensing of Environment, 108, 327–338, 2007.

Berthier, E., Le Bris, R., Mabileau, L., Testut, L., and Remy, F. : Ice wastage on the Kerguelen Islands (49 degrees S, 69 degrees E) between 1963 and 2006, Journal of Geophysical Research, 114, doi :10.1029/2008JF001192, 2009.

Berthier, E., Schiefer, E., Clarke, G., Menounos, B., and Remy, F. : Contribution of Alaskan glaciers to sea-level rise derived from satellite imagery, Nature Geoscience, 3, 2010.

Björnsson, H., Pálsson, F., Gudmundsson, S., Magnússon, E., Adalgeirsdóttir, G., Jóhannesson, T., Berthier, E., Sigurdsson, O., and Thorsteinsson, T. : Contribution of Icelandic ice caps to sea level rise : trends and variability since the Little Ice Age, Geophysical Research Letters, 40, 1546–1550, 2013.

Blard, P.-H., Lavé, J., Pik, R., Wagnon, P., and Bourlès, D. : Persistence of full glacial conditions in the central Pacific until 15,000 years ago, Nature, 449, 591–594, 2007.

Brun, E., David, P., Sudul, M., and Brunot, G. : A numerical Model to Simulate Snowcover Stratigraphy for Operational Avalanche Forecasting, Journal of Glaciology, 38, 13–22, 1992.

Cai, W., Cowan, T., and Thatcher, M. : Rainfall reductions over Southern Hemisphere semi-arid regions : the role of subtropical dry zone expansion, Scientific reports, 2, doi :10.1038/srep00702, 2012.

Chen, J., Wilson, C., and Tapley, B. : Interannual variability of Greenland ice losses from satellite gravimetry, Journal of Geophysical Research, 116, doi :10.1029/2010JB007789, 2011.

Chinn, T., Fitzharris, B., Willsman, A., and Salinger, M. : Annual ice volume changes 1976–2008 for the New Zealand Southern Alps, Global and Planetary Change, 92, 105–118, 2012.

Cogley, J., Berthier, E., and Donoghue, S. : Glaciers of the Subantarctic islands, 2010.

Cogley, J., Hock, R., Rasmussen, L., Arendt, A., Bauder, A., Braithwaite, R., Jansson, P., Kaser, G., Möller, M., Nicholson, L., and Zemp, M. : Glossary of Glacier Mass Balance and Related Terms, IHP-VII Technical Documents in Hydrology, 86, IACS Contribution No. 2, UNESCO-IHP, Paris, 2011.

De Ridder, K. and Gallée, H. : Land surface-induced regional climate change in southern Israel, Journal of aAplied Meteorology, 37, 1470–1485, 1998.

Dee, D., Uppala, S., Simmons, A., Berrisford, P., Poli, P., Kobayashi, S., Andrae, U., Balmaseda, M., Balsamo, G., Bauer, P., Bechtold, P., Beljaars, A., van de Berg, L., Bidlot, J., Bormann, N., Delsol, C.and Dragani, R., Fuentes, M., Geer, A., Haimberger, L., Healy, S., Hersbach, H., Hólm, E., Isaksen, L., Kållberg, P., Köhler, M., Matricardi, M., McNally, A., Monge-Sanz, B., Morcrette, J.-J., Park, B.-K., Peubey, C., de Rosnay, P., Tavolato, C., Thépaut, J.-N., and Vitart, F. : The ERA-Interim reanalysis : Configuration and performance of the data assimilation system, Quarterly Journal of the Royal Meteorological Society, 137, 553–597, 2011.

Delworth, T. and Zeng, F. : Regional rainfall decline in Australia attributed to anthropogenic greenhouse gases and ozone levels, Nature Geoscience, 7, 583–587, 2014.

Deser, C., Phillips, A., Bourdette, V., and Teng, H. : Uncertainty in climate change projections : the role of internal variability, Climate Dynamics, 38, 527–546, 2012.

Dumont, M. : Détermination de l'albédo des surfaces enneigées par télédétection, Ph.D. thesis, Université Paris Est, 2010.

Dumont, M., Gardelle, J., Sirguey, P., Guillot, A., Six, D., Rabatel, A., and Arnaud, Y. : Linking glacier annual mass balance and glacier albedo retrieved from MODIS data, The Cryosphere, 6, 1527–1539, 2012.

Duynkerke, P. : Application of the E-ε turbulence closure model to the neutral and stable atmospheric boundary layer, Journal of the Atmospheric Sciences, 45, 865–880, 1988.

Duynkerke, P. and van den Broeke, M. : Surface energy balance and katabatic flow over glacier and tundra during GIMEX-91, Global and Planetary Change, 9, 17–28, 1994.

Ettema, J., van den Broeke, M., van Meijgaard, E., van de Berg, W., Bamber, J., Box, J., and Bales, R. : Higher surface mass balance of the Greenland ice sheet revealed by high-resolution climate modeling, Geophysical Research Letters, 36, doi :10.1029/2009GL038110, 2009.

Falvey, M. and Garreaud, R. : Regional cooling in a warming world : Recent temperature trends in the southeast Pacific and along the west coast of subtropical South America (1979–2006), Journal of Geophysical Research, 114, doi :10.1029/2008JD010519, 2009.

Farman, J., Gardiner, B., and Shanklin, J. : Large losses of total ozone in Antarctica reveal seasonal ClOx/NOx interaction, Nature, pp. 207–210, 1985.

Favier, L., Durand, G., Cornford, S., Gudmundsson, G., Gagliardini, O., Gillet-Chaulet, F., Zwinger, T., Payne, A., and Le Brocq, A. : Retreat of Pine Island Glacier controlled by marine ice-sheet instability, Nature Climate Change, 4, 117–121, 2014.

Favier, V. : Etude du bilan d'énergie de surface et de la production des écoulements de fonte d'un glacier des Andes d'Equateur : Relation glacier–climat en zone tropicale, Ph.D. thesis, Université Montpellier 2, Montpellier, 2004.

Favier, V., Agosta, C., Genthon, C., Arnaud, L., Trouvillez, A., and Gallée, H. : Modeling the mass and surface heat budgets in a coastal blue ice area of Adelie Land, Antarctica, Journal of Geophysical Research : Earth Surface (2003–2012), 116, 2011.

Favier, V., Verfaillie, D., Berthier, E., Menegoz, M., Jomelli, V., Kay, J., Ducret, L., Malbéteau, Y., Brunstein, D., Gallée, H., and Park, Y.-H. : The ozone hole as the main driver of dramatic glacier wastage in the sub-Antarctic region, Nature Geoscience, in review.

Fettweis, X., Franco, B., Tedesco, M., van Angelen, J., Lenaerts, J., van den Broeke, M., and Gallée, H. : Estimating Greenland ice sheet surface mass balance contribution to future sea level rise using the regional atmospheric climate model MAR, The Cryosphere, 7, 469–489, 2013.

Fitzharris, B., Chinn, T., and Lamont, G. : Glacier balance fluctuations an atmospheric circulation patterns over the Southern Alps, New Zealand, International Journal of Climate, 17, 745–763, 1997.

Fitzharris, B., Clare, G., and Renwick, J. : Teleconnections between Andean and New Zealand glaciers, Global and Planetary Change, 59, 159–174, 2007.

Fouquart, Y. and Bonnel, B. : Computations of solar heating of the earth's atmosphere- A new parameterization, Beiträge zur Physik der Atmosphäre, 53, 35–62, 1980.

Frenot, Y., Gloaguen, J.-C., Picot, G., Bougère, J., and Benjamin, D. : Azorella selago Hook. used to estimate glacier fluctuations and climatic history in the Kerguelen Islands over the last two centuries, Oecologia, 95, 140–144, 1993.

Frénot, Y., Gloaguen, J., and Trehen, P. : Climate change in Kerguelen Islands and colonization of recently deglaciated areas by Poa kerguelensis and P. annua, Antarctic communities : species, structure and survival, B. Battaglia, J. Valencia et DWH Walton eds., Cambridge University Press, Cambridge, pp. 358–366, 1997.

Frenot, Y., Gloaguen, J.-C., Van de Vijver, B., and Beyens, L. : Datation of some Holocene peat sediments and glacier fluctuations in the Kerguelen Islands, Comptes Rendus de l'Académie des Sciences, Série III-Sciences de la Vie - Life Sciences, 320, 567–573, 1997.

Fujiyoshi, Y., Kondo, H., Inoue, J., and Yamada, T. : Characteristics of precipitation and vertical structure of air temperature in the northern Patagonia, Bulletin of Glacier Research, 4, 15–23, 1987.

Funk, C. and Michaelsen, J. : A simplified diagnostic model of orographic rainfall for enhancing satellite-based rainfall estimates in data-poor regions, Journal of Applied Meteorology, 43, 1366–1378, 2004.

Gallée, H. and Duynkerke, P. : Air-snow interactions and the surface energy and mass balance over the melting zone of west Greenland during the Greenland Ice Margin Experiment., Journal of Geophysical Research, 102, 13 813–13 824, 1997.

Gallée, H. and Schayes, G. : Development of a three-dimensional meso-γ primitive equation model : Katabatic winds simulation in the area of Terra Nova Bay, Antarctica, Monthly Weather Review, 122, 671–685, 1994.

Gallée, H., Guyomarc'h, G., and Brun, E. : Impact of snow drift on the Antarctic ice sheet surface mass balance : possible sensitivity to snow-surface properties, Boundary-Layer Meteorology, 99, 1–19, 2001.

Gardelle, J., Berthier, E., and Arnaud, Y. : Slight mass gain of Karakoram glaciers in the early twenty-first century, Nature geoscience, 5, 322–325, 2012.

Gardelle, J., Berthier, E., Arnaud, Y., and Kääb, A. : Region-wide glacier mass balances over the Pamir-Karakoram-Himalaya during 1999-2011., The Cryosphere, 7, 1263–1286, 2013.

Gardner, A., Moholdt, G., Cogley, J., Wouters, B., Arendt, A., Wahr, J., Berthier, E., Hock, R., Pfeffer, W., Kaser, G., Ligtenberg, S., Bolch, T., Sharp, M., Ove Hagen, J., van den Broeke, M., and Paul, F. : A reconciled estimate of glacier contributions to sea level rise : 2003 to 2009, Science, 340, 852–857, 2013.

Garreaud, R., Vuille, M., Compagnucci, R., and Marengo, J. : Present-day South American climate, Palaeogeography, Palaeoclimatology, Palaeoecology, 281, 180–195, 2009.

Garreaud, R., Lopez, P., Minvielle, M., and Rojas, M. : Large-scale control on the Patagonian climate, Journal of Climate, 26, 215–230, 2013.

Gential, L. : Modélisation du bilan de masse en surface de la calotte glaciaire antarctique, Ph.D. thesis, Université Joseph Fourier, Grenoble, 2007.

Gillett, N., Kell, T., and Jones, P. : Regional climate impacts of the Southern Annular Mode, Geophysical Research Letters, 33, doi :10.1029/2006GL027721, 2006.

Giorgi, F. and Mearns, L. : Introduction to special section : Regional climate modeling revisited, Journal of Geophysical Research, 104, 6335–6352, 1999.

Gordon, J., Haynes, V., and Hubbard, A. : Recent glacier changes and climate trends on South Georgia, Global and Planetary Change, 60, 72–84, 2008.

Hall, D., Riggs, G., Salomonson, V., DiGirolamo, N., and Bayr, K. : MODIS snow-cover products, Remote Sensing of Environment, 83, 181–194, 2002.

Hall, K. : Evidence in favour of an extensive ice cover on sub-Antarctic Kerguelen Island during the last glacial, Palaeogeography, palaeoclimatology, palaeoecology, 47, 225–232, 1984.

Harper, J. and Humphrey, N. : High altitude Himalayan climate inferred from glacial ice flux, Geophysical research letters, 30, doi :10.1029/2003GL017329, 2003.

Harris, I., Jones, P., Osborn, T., and Lister, D. : Updated high-resolution grids of monthly climatic observations–the CRU TS3. 10 Dataset, International Journal of Climatology, 34, 623–642, 2014.

Hartmann, D., Klein Tank, A., Rusticucci, M., Alexander, L., Brönnimann, S., Charabi, Y., Dentener, F., Dlugokencky, E., Easterling, D., Kaplan, A., Soden, B., Thorne, P., Wild, M., and Zhai, P. : Observations : Atmosphere and Surface, in : Climate Change 2013 : The Physical Science Basis. Contribution of Working Group I to the Fifth Assessment Report of the Intergovernmental Panel on Climate Change, edited by Stocker, T., Qin, D., Plattner, G.-K., Tignor, M., Allen, S., Boschung, J., Nauels, A., Xia, Y., Bex, V., and Midgley, P., Cambridge University Press, 2013.

Heirman, K. : 'A wind of change' : changes in position and intensity of the southern hemisphere westerlies during oxygen isotope stages 3, 2 and 1, Ph.D. thesis, Ghent University, Ghent, Beligum, 2011.

Hock, R. : Temperature index melt modelling in mountain areas, Journal of Hydrology, 282, 104–115, 2003.

Hodgson, D., Graham, A., Roberts, S., Bentley, M., Ó Cofaigh, C., Verleyen, E., Vyverman, W., Jomelli, V., Favier, V., Brunstein, D., Verfaillie, D., Colhoun, E., Saunders, K., Selkirk, P., Mackintosh, A., Hedding, D., Nel, W., Hall, K., McGlone, M., Van der Putten, N., Dickens, W., and Smith, J. : Terrestrial and submarine evidence for the extent and timing of the Last Glacial Maximum and the onset of deglaciation on the maritime-Antarctic and sub-Antarctic islands, Quaternary Science Reviews, 100, 137–158, 2014.

Holmlund, P. and Fuenzalida, H. : Anomalous glacier responses to 20th century climatic changes in Darwin Cordillera, southern Chile, Journal of Glaciology, 41, 465–473, 1995.

Ivins, E., Watkins, M., Yuan, D.-N., Dietrich, R., Casassa, G., and Rülke, A. : On-land ice loss and glacial isostatic adjustment at the Drake Passage : 2003–2009, Journal of Geophysical Research, 116, doi :10.1029/2010JB007607, 2011.

Jacka, T., Budd, W., and Holder, A. : A further assessment of surface temperature changes at stations in the Antarctic and Southern Ocean, Annals of Glaciology, 29, 331–338, 2004.

Jacob, T., Wahr, J., Pfeffer, W., and Swenson, S. : Recent contributions of glaciers and ice caps to sea level rise, Nature, 482, 514–518, 2012.

Johannessen, O., Khvorostovsky, K., Miles, M., and Bobylev, L. : Recent Ice-Sheet Growth in the Interior of Greenland, Science, 310, 1013–1016, 2005.

Jomelli, V., Khodri, M., Favier, V., Brunstein, D., Ledru, M.-P., Wagnon, P., Blard, P.-H., Sicart, J.-E., Braucher, R., Grancher, D., Bourlès, D., Braconnot, P., and Vuille, M. : Irregular tropical glacier retreat over the Holocene epoch driven by progressive warming, Nature, 474, 196–199, 2011.

Jomelli, V., Favier, V., Vuille, M., Braucher, R., Martin, L., Blard, P.-H., Colose, C., Brunstein, D., He, F., Khodri, M., Bourlès, D., Leanni, L., Rinterknecht, V., Grancher, D., Francou, B., Ceballos, J., Fonceca, H., Liu, Z., and Otto-Bliesner, B. : A major advance of tropical Andean glaciers during the Antarctic cold reversal, Nature, 513, 224–228, 2014.

Kääb, A., Berthier, E., Nuth, C., Gardelle, J., and Arnaud, A. : Contrasting patterns of early twenty-first-century glacier mass change in the Himalayas, Nature, 488, 495–498, 2012.

Kalnay, E., Kanamitsu, M., Kistler, R., Collins, W., Deaven, D., Gandin, L., Iredell, M., Saha, S., White, G., Woollen, J., Zhu, Y., Leetmaa, A., Reynolds, R., Chelliah, M., Ebisuzaki, W., Higgins, W., Janowiak, J., Mo, K., Ropelewski, C., Wang, J., Roy, J., and Dennis, J. : The NCEP/NCAR 40-Year Reanalysis Project, Bulletin of the American Meteorological Society, 77, 437–471, 1996.

Kanamitsu, M., Ebisuzaki, W., Woollen, J., Yang, S.-K., Hnilo, J., Fiorino, M., and Potter, G. : The NCEP/NCAR 40-Year Reanalysis Project, Bulletin of the American Meteorological Society, 83, 1631–1643, 2002.

Kessler, E. : On the distribution and continuity of water substance in atmospheric circulation, Meteorological Monographs, 10, 1969.

Kistler, R., Collins, W., Saha, S., White, G., Woollen, J., Kalnay, E., Chelliah, M., Ebisuzaki, W., Kanamitsu, M., Kousky, V., van den Dool, H., Jenne, R., and Fiorino, M. : The NCEP-NCAR 50-year reanalysis : Monthly means CD-ROM and documentation, Bulletin of the American Meteorological society, 82, 247–267, 2001.

Kuipers Munneke, P., Ligtenberg, S., van den Broeke, M., and Vaughan, D. : Firn air depletion as a precursor of Antarctic ice-shelf collapse, Journal of Glaciology, 60, 205–214, 2014.

Larson, L. and Peck, E. : Accuracy of precipitation measurements for hydrologic modeling, Water Resources Research, 10, 857–863, 1974.

le Roux, P. and McGeoch, M. : Changes in climate extremes, variability and signature on sub-Antarctic Marion Island, Climatic Change, 86, 309–329, 2008.

Lefebre, F., Gallée, H., Van Ypersele, J.-P., and Greuell, W. : Modelling of snow and ice melt at ETH-Camp (West Greenland) : a study of surface albedo, Journal of Geophysical Research, 108, doi :10.1029/2001JD001160, 2002.

Lemke, P., Ren, J., Alley, R., Allison, I., Carrasco, J., Flato, G., Fujii, Y., Kaser, G., Mote, P., Thomas, R., , and Zhang, T. : Observations : Changes in Snow, Ice and Frozen Ground, in : Climate Change 2007 : The Physical Science Basis. Contribution of Working Group I to the Fourth Assessment Report of the Intergovernmental Panel on Climate Change, edited by Solomon, S., Qin, D., Manning, M., Chen, Z., Marquis, M., Averyt, K., Tignor, M., and Miller, H., Cambridge University Press, 2007.

Lenaerts, J., van den Broeke, M., Déry, S., König-Langlo, G., Ettema, J., and Munneke, P. : Modelling snowdrift sublimation on an Antarctic ice shelf, The Cryosphere, 4, 179–190, 2010.

Lenaerts, J., van den Broeke, M., van Wessem, J., van de Berg, W., van Meijgaard, E., van Ulft, L., and Schaefer, M. : Extreme Precipitation and Climate Gradients in Patagonia Revealed by High-Resolution Regional Atmospheric Climate Modeling, Journal of Climate, 27, 4607–4621, 2014.

Lin, Y.-L., Farley, R., and Orville, H. : Bulk parameterization of the snow field in a cloud model, Journal of Climate and Applied Meteorology, 22, 1065–1092, 1983.

Lopez, P., Sirguey, P., Arnaud, Y., Pouyaud, B., and Chevallier, P. : Snow cover monitoring in the Northern Patagonia Icefield using MODIS satellite images (2000-2006), Global and Planetary Change, 61, 103–116, 2008.

Lopez, P., Chevallier, P., Favier, V., Pouyaud, B., Ordenes, F., and Oerlemans, J. : A regional view of fluctuations in glacier length in southern South America, Global and Planetary Change, 71, 85–108, 2010.

Manatsa, D., Morioka, Y., Behera, S., Yamagata, T., and Matarira, C. : Link between Antarctic ozone depletion and summer warming over southern Africa, Nature Geoscience, 6, 934–939, 2013.

Melkonian, A., Willis, M., Pritchard, M., Rivera, A., Bown, F., and Bernstein, S. : Satellite-derived volume loss rates and glacier speeds for the Cordillera Darwin Icefield, Chile, The Cryosphere, 7, 823–839, 2013.

Michalakes, J., Dudhia, J., Gill, D., Klemp, J., and Skamarock, W. : Design of a next-generation regional weather research and forecast model, in : Towards Teracomputing, Proceedings of the eighth ECMWF workshop on the Use of Parallell Processors in Meteorology, pp. 117–124, 1998.

Moholdt, G., Hagen, J., Eiken, T., and Schuler, T. : Geometric changes and mass balance of the Austfonna ice cap, Svalbard, The Cryosphere, 4, 21–34, 2010a.

Moholdt, G., Nuth, C., Hagen, J., and Kohler, J. : Recent elevation changes of Svalbard glaciers derived from ICESat laser altimetry, Remote Sensing of Environment, 114, 2756–2767, 2010b.

Moholdt, G., Wouters, B., and Gardner, A. : Recent mass changes of glaciers in the Russian High Arctic, Geophysical Research Letters, 39, 2012.

Monin, A. and Obukhov, A. : Basic laws of turbulent mixing in the surface layer of the atmosphere, Contrib. Geophys. Inst. Acad. Sci. USSR, 24, 163–187, 1954.

Morcrette, J.-J. : Assessment of the ECMWF model cloudiness and surface radiation fields at the ARMSGP site, Monthly Weather Review, 130, 257–277, 2002.

Moss, R., Edmonds, J., Hibbard, K., Manning, M., Rose, S., Van Vuuren, D., Carter, T., Emori, S., Kainuma, M., Kram, T., Meehl, G., Mitchell, J., Nakicenovic, N., Riahi, K., Smith, S., Stouffer, R., Thomson, A., Weyant, J., and Wilbanks, T. : The next generation of scenarios for climate change research and assessment, Nature, 463, 747–756, 2010.

Nougier, J. : Aspects de morpho-tectonique glaciaire aux Iles Kerguelen, Revue de Géographie Physique et de Géologie Dynamique, 14, 499–505, 1972.

Nuth, C., Moholdt, G., Kohler, J., Hagen, J., and Kääb, A. : Svalbard glacier elevation changes and contribution to sea level rise, Journal of Geophysical Research, 115, 2010.

Nye, J. : The flow of glaciers and ice-sheets as a problem in plasticity, Proceedings of the Royal Society of London A, 207, 554–572, 1951.

Peterson, T., Karl, T., Jamason, P., Knight, R., and Easterling, D. : First difference method : Maximizing station density for the calculation of long-term global temperature change, Journal of Geophysical Research, 103, 25 967–25 974, 1998.

Pettit, E., Scambos, T., Heran, T., Mosley-Thompson, E., Bauer, R., Wellner, J., and Vernet, M. : Differing ice dynamics across the Antarctic Peninsula, in : Proceedings of the International Glaciological Society, URL http://www.igsoc.org/symposia/2014/chamonix/proceedings/procsfiles/procabstracts_65.htm#A0970, abstract 70A0970, 2014.

Poggi, A. : Etude comparative du bilan thermique en deux stations du glacier Ampère Iles Kerguelen, Zeitschrift für Gletscherkunde und Glazialgeologie, 13, 87–97, 1977a.

Poggi, A. : Heat Balance in ablation area of Ampere Glacier (Kerguelen Islands), Journal of Applied Meteorology, 16, 48–55, 1977b.

Pritchard, H., Ligtenberg, S., Fricker, H., Vaughan, D., Van den Broeke, M., and Padman, L. : Antarctic ice-sheet loss driven by basal melting of ice shelves, Nature, 484, 502–505, 2012.

Purich, A., Cowan, T., Min, S.-K., and Cai, W. : Autumn precipitation trends over Southern Hemisphere midlatitudes as simulated by CMIP5 models, Journal of Climate, 26, 8341–8356, 2013.

Quilty, P. : Origin and evolution of the sub-Antarctic islands : the foundation, in : Papers and Proceedings of the royal Society of tasmania, vol. 141, pp. 35–58, 2007.

Rabatel, A., Bermejo, A., Loarte, E., Soruco, A., Gomez, J., Leonardini, G., Vincent, C., and Sicart, J. : Can the snowline be used as an indicator of the equilibrium line and mass balance for glaciers in the outer tropics ?, Journal of Glaciology, 58, 1027–1036, 2012.

Rabatel, A., Francou, B., Soruco, A., Gomez, J., Cáceres, B., Ceballos, J., Basantes, R., Vuille, M., Sicart, J.-E., Huggel, C., Scheel, M., Lejeune, Y., Arnaud, Y., Collet, M., Condom, T., Consoli, G., Favier, V., Jomelli, V., Galarraga, R., Ginot, P., Maisincho, L., Mendoza, J., Menegoz, M., Ramirez, E., Ribstein, P., Suarez, W., Villacis, M., and Wagnon, P. : Current state of glaciers in the tropical Andes : a multi-century perspective on glacier evolution and climate change, The Cryosphere, 7, 81–102, 2013.

Radić, V. and Hock, R. : Regionally differentiated contribution of mountain glaciers and ice caps to future sea-level rise, Nature Geoscience, 4, 91–94, 2011.

Rayner, N., Brohan, P., Parker, D., Folland, C., Kennedy, J., Vanicek, M., Ansell, T., and Tett, S. : Improved analyses of changes and uncertainties in sea surface temperature measured in situ since the mid-nineteenth century : The HadSST2 dataset, Journal of Climate, 19, 446–469, 2006.

Reynolds, R., Smith, T., Liu, C., Chelton, D., Casey, K., and Schlax, M. : Daily high-resolution-blended analyses for sea surface temperature, Journal of Climate, 20, 5473–5496, 2007.

Rignot, E., Rivera, A., and Casassa, G. : Contribution of the Patagonia Icefields of South America to sea level rise, Science, 302, 434–437, 2003.

Rignot, E., Mouginot, J., Morlighem, M., Seroussi, H., and Scheuchl, B. : Widespread, rapid grounding line retreat of Pine Island, Thwaites, Smith, and Kohler glaciers, West Antarctica, from 1992 to 2011, Geophysical Research Letters, 41, 3502–3509, 2014.

Ritz, C., Rommelaere, V., and Dumas, C. : Modeling the evolution of Antarctic ice sheet over the last 420,000 years : Implications for altitude changes in the Vostok region, Journal of Geophysical Research, 106, 31 943–31 964, 2001.

Rivera, A., Corripio, J., Bravo, C., and Cisternas, S. : Glaciar Jorge Montt (Chilean Patagonia) dynamics derived from photos obtained by fixed cameras and satellite image feature tracking, Annals of Glaciology, 53, 147–155, 2012.

Sallée, J., Speer, K., and Morrow, R. : Response of the Antarctic Circumpolar Current to atmospheric variability, Journal of climate, 21, 3020–3039, 2008.

Scambos, T., Berthier, E., Haran, T., Shuman, C., Cook, A., Ligtenberg, S., and Bohlander, J. : Detailed ice loss pattern in the northern Antarctic Peninsula : widespread decline driven by ice front retreats, The Cryosphere Discussions, 8, 3237–3261, 2014.

Schaefer, M., Machguth, H., Falvey, M., and Casassa, G. : Modeling past and future surface mass balance of the Northern Patagonia Icefield, Journal of Geophysical Research : Earth Surface, 118, 571–588, 2013.

Schneider, C., Kilian, R., and Glaser, M. : Energy balance in the ablation zone during the summer season at the Gran Campo Nevado Ice Cap in the Southern Andes, Global and Planetary Change, 59, 175–188, 2007.

Shepherd, A., Ivins, E., Geruo, A., Barletta, V., Bentley, M., Bettadpur, S., Briggs, K., Bromwich, D., Forsberg, R., Galin, N., Horwath, M., Jacobs, S., Joughin, I., King, M., Lenaerts, J., Li, J., Ligtenberg, S., Luckman, A., Luthcke, S., McMillan, M., Meister, R., Milne, G., Mouginot, J., Muir, A., Nicolas, J., Paden, J., Payne, A., Pritchard, H., Rignot, E., Rott, H., Sϕrensen, L., Scambos, T., Scheuchl, B., Schrama, E., Smith, B., Sundal, A., van Angelen, J., van de Berg, W., van den Broeke, M., Vaughan, D., Velicogna, I., Wahr, J., Whitehouse, P., Wingham, D., Yi, D., Young, D., and Zwally, H. : A reconciled estimate of ice-sheet mass balance, Science, 338, 1183–1189, 2012.

Sinclair, M. : A diagnostic model for estimating orographic precipitation, Journal of Applied Meteorology, 33, 1163–1175, 1994.

Sirguey, P., Mathieu, R., and Arnaud, Y. : Subpixel monitoring of the seasonal snow cover with MODIS at 250 m spatial resolution in the Southern Alps of New Zealand : Methodology and accuracy assessment, Remote Sensing of Environment, 113, 160–181, 2009.

Smith, T. and Reynolds, R. : Improved extended reconstruction of SST (1854-1997), Journal of Climate, 17, 2466–2477, 2004.

Smith, T., Reynolds, R., Peterson, T., and Lawrimore, J. : Improvements to NOAA's historical merged land-ocean surface temperature analysis (1880-2006), Journal of Climate, 21, 2283–2296, 2008.

Stolarski, R., Krueger, A., Schoeberl, M., McPeters, R., Newman, P., and Alpert, J. : Nimbus 7 satellite measurements of the springtime Antarctic ozone decrease, Nature, 322, 808–811, 1986.

Takeuchi, Y., Naruse, R., Satow, K., and Ishikawa, N. : Comparison of heat balance characteristics at five glaciers in the southern hemisphere, Global and Planetary Change, 22, 201–208, 1999.

Taylor, K., Stouffer, R., and Meehl, G. : An Overview of CMIP5 and the Experiment Design, Bulletin of the American Meteorological Society, 93, 485–498, 2012.

Testut, L., Wöppelmann, G., Simon, B., and Téchiné, P. : The sea level at Port-aux-Français, Kerguelen Island, from 1949 to the present, Ocean Dynamics, 56, 464–472, 2006.

Thomas, R., Rignot, E., Casassa, G., Kanagaratnam, P., Acuña, C., Akins, T., Brecher, H., Frederick, E., Gogineni, P., Krabill, W., Manizade, S., Ramamoorthy, H., Rivera, A., Russell, R., Sonntag, J., Swift, R., Yungel, J., and Zwally, J. : Accelerated sea-level rise from West Antarctica, Science, 306, 255–258, 2004.

Thompson, D., Solomon, S., Kushner, P., England, M., Grise, K., and Karoly, D. : Signatures of the Antarctic ozone hole in Southern Hemisphere surface climate change, Nature Geoscience, 4, 741–749, 2011.

Trenberth, K.E.and Jones, P., Ambenje, P., Bojariu, R., Easterling, D., Klein Tank, A., Parker, D., Rahimzadeh, F., Renwick, J., Rusticucci, M., Soden, B., and Zhai, P. : Observations : Surface and Atmospheric Climate Change, in : Climate Change 2007 : The Physical Science Basis. Contribution of Working Group I to the Fourth Assessment Report of the Intergovernmental Panel on Climate Change, edited by Solomon, S., Qin, D., Manning, M., Chen, Z., Marquis, M., Averyt, K., Tignor, M., and Miller, H., Cambridge University Press, 2007.

Trüssel, B., Motyka, R., Truffer, M., and Larsen, C. : Rapid thinning of lake-calving Yakutat Glacier and the collapse of the Yakutat Icefield, southeast Alaska, USA, Journal of Glaciology, 59, 149–161, 2013.

Uppala, S., Kållberg, P., Simmons, A., Andrae, U., Bechtold, V., Fiorino, M., Gibson, J., Haseler, J., Hernandez, A., Kelly, G., Li, X., Onogi, K., Saarinen, S., Sokka, N., Allan, R., Andersson, E., Arpe, K., Balmaseda, M., Beljaars, A., Van De Berg, L., Bidlot, J., Bormann, N., Caires, S., Chevallier, F., Dethof, A., Dragosavac, M., Fisher, M., Fuentes, M., Hagemann, S., Hólm, E., Hoskins, B., Isaksen, L., Janssen, P., Jenne, R., Mcnally, A., Mahfouf, J.-F., Morcrette, J.-J., Rayner, N., Saunders, R., Simon, P., Sterl, A., Trenberth, K., Untch, A., Vasiljevic, D., Viterbo, P., and Woollen, J. : The ERA-40 re-analysis, Quarterly Journal of the Royal Meteorological Society, 131, 2961–3012, 2005.

Vallon, M. : Bilan de masse et fluctuations récentes du Glacier Ampère (Iles Kerguelen, TAAF), Zeitschrift für Gletscherkunde und Glazialgeologie, 13, 55–85, 1977a.

Vallon, M. : Topographie sous glaciaire du Glacier Ampère (Iles Kerguelen, TAAF), Zeitschrift für Gletscherkunde und Glazialgeologie, 13, 37–55, 1977b.

Vallon, M. : Glaciologie à Kerguelen, in : Actes du Colloque sur la Recherche Françaises dans les Terres Australes, Strasbourg, 1987.

Van der Putten, N., Verbruggen, C., Ochyra, R., Verleyen, E., and Frenot, Y. : Subantarctic flowering plants : pre-glacial survivors or post-glacial immigrants ?, Journal of Biogeography, 37, 582–592, 2010.

Vaughan, D., Comiso, J., Allison, I., Carrasco, J., Kaser, G., Kwok, R., Mote, P., Murray, T., Paul, F., Ren, J., Rignot, E., Solomina, O., Steffen, K., and Zhang, T. : Observations : Cryosphere, in : Climate Change 2013 : The Physical Science Basis. Contribution of Working Group I to the Fifth Assessment Report of the Intergovernmental Panel on Climate Change, edited by Stocker, T., Qin, D., Plattner, G.-K., Tignor, M., Allen, S., Boschung, J., Nauels, A., Xia, Y., Bex, V., and Midgley, P., Cambridge University Press, 2013.

Velicogna, I. and Wahr, J. : Greenland mass balance from GRACE, Geophysical Research Letters, 32, doi :10.1029/2005GL023955, 2005.

Verfaillie, D., Fily, M., Le Meur, E., Magand, O., Jourdain, B., Arnaud, L., and Favier, V. : Snow accumulation variability derived from radar and firn core data along a 600 km transect in Adelie Land, East Antarctic plateau, The Cryosphere, 6, 1345–1358, 2012.

Verfaillie, D., Favier, V., Menegoz, M., Kay, J., Jomelli, V., Berthier, E., and Gallée, H. : Reconciling southern hemisphere mid-latitude glacier wastage and climate change, Geophysical Research Letters, in prep.

Verfaillie, D., Favier, V., Dumont, M., Jomelli, V., Gilbert, A., Brunstein, D., Gallée, H., Rinterknecht, V., Menegoz, M., and Frenot, Y. : Recent glacier decline in the Kerguelen Islands (49° S, 69° E) derived from modeling, field observations and satellite data, Journal of Geophysical Research, submitted.

Villalba, R., Lara, A., Masiokas, M., Urrutia, R., Luckman, B., Marshall, G., Mundo, I., Christie, D., Cook, E., Neukom, R., Allen, K., Fenwick, P., Bonisegne, J., Srur, A., Morales, M., Araneo, D., Palmer, J., Cuq, E., Aravena, J., Holz, A., and LeQuesne, C. : Unusual Southern Hemisphere tree growth patterns induced by changes in the Southern Annular Mode, Nature Geoscience, 5, 793–798, 2012.

Wang, G. and Kay, W. : Climate-change impact on the 20th-century relationship between the Southern Annular Mode and global mean temperature, Scientific Reports, 3, doi :10.1038/srep02039, 2013.

Watelet, S. : 1979-2012 surface mass balance modelling of the Ellesmere Island using the regional climate model MAR, Master's thesis, Université de Liège, 2013.

Willis, M., Melkonian, A., Pritchard, M., and Ramage, J. : Ice loss rates at the Northern Patagonian Icefield derived using a decade of satellite remote sensing, Remote Sensing of Environment, 117, 184–198, 2012a.

Willis, M., Melkonian, A., Pritchard, M., and Rivera, A. : Ice loss from the Southern Patagonian Ice Field, South America, between 2000 and 2012, Geophysical Research Letters, 39, 2012b.

Wingham, D., Francis, C., Baker, S., Bouzinac, C., Brockley, D., Cullen, R., de Chateau-Thierry, P., Laxon, S., Mallow, U., Mavrocordatos, C., Phalippouc, L., Ratierb, G., Reyc, L., Rostand, F., Viaub, P., and Wallisa, D. : CryoSat : A mission to determine the fluctuations in Earth's land and marine ice fields, Advances in Space Research, 37, 841–871, 2006.

Wingham, D., Wallis, D., and Shepherd, A. : Spatial and temporal evolution of Pine Island Glacier thinning, 1995–2006, Geophysical Research Letters, 36, doi :10.1029/2009GL039126, 2009.

Yen, Y.-C. : Review of thermal properties of snow, ice and sea ice, Tech. rep., CRREL Hanover, 1981.

Yin, J. : A consistent poleward shift of the storm tracks in simulations of 21st century climate, Geophysical Research Letters, 32, doi :10.1029/2005GL023684, 2005.

Young, S. and Schofield, E. : Pollen evidence for late Quaternary climate changes on Kerguelen Islands, Nature, 245, 311–312, 1973a.

Young, S. and Schofield, E. : Palynological evidence for the late glacial occurrence of Pringlea and Lyallia on Kerguelen Islands, Rhodora, 75, 239–247, 1973b.

Zwally, H., Schutz, B., Abdalati, W., Abshire, J., Bentley, C., Brenner, A., Bufton, J., Dezio, J., Hancock, D., Harding, D., Herring, T., Minster, B., Quinn, K., Palm, S., Spinhirne, J., and Thomas, R. : ICESat's laser measurements of polar ice, atmosphere, ocean, and land, Journal of Geodynamics, 34, 405–445, 2002.

Zwally, H., Giovinetto, M., Li, J., Cornejo, H., Beckley, M., Brenner, A., Saba, J., and Yi, D. : Mass changes of the Greenland and Antarctic ice sheets and shelves and contributions to sea-level rise : 19922002, Journal of Glaciology, 51, 509–527, 2005.

Zwinger, T., Greve, R., Gagliardini, O., Shiraiwa, T., and Lyly, M. : A full Stokes-flow thermo-mechanical model for firn and ice applied to the Gorshkov crater glacier, Kamchatka, Annals of glaciology, 45, 29–37, 2007.

Liste des figures

Liste des tableaux